Akademia Górniczo-Hutnicza im. Stanisława Staszica w Krakowie

Wydział Fizyki i Informatyki Stosowanej

Rozprawa doktorska

Efekty neuromimetyczne w perowskitach i ich analogach
Neuromimetic effects in perovskites and their analogues

Autor: *mgr Piotr Zawal*

Dyscyplina główna: *Nauki fizyczne*

Dyscyplina dodatkowa: *Nauki biologiczne*

Pierwszy promotor: *prof. dr hab. Konrad Szaciłowski*

Drugi promotor: *prof. dr hab. Grzegorz Hess*

Kraków, 2022

Try again. Fail again. Fail better.
— Samuel Beckett

Oświadczenie autora rozprawy:

Oświadczam, świadom odpowiedzialności karnej za poświadczenie nieprawdy, że niniejszą rozprawę doktorską wykonałem osobiście i samodzielnie oraz że nie korzystałem z innych źródeł niż wymienione w pracy.

18 października 2022 r.

.....

mgr Piotr Zawal

Oświadczenia promotorów:

Niniejsza rozprawa jest gotowa do oceny przez recenzentów.

18 października 2022 r.

.....

prof. dr hab. Konrad Szaciłowski

.....

prof. dr hab. Grzegorz Hess

Granty badawcze:

Badania, których wyniki zostały przedstawione w niniejszej rozprawie, prowadzone były w ramach grantów Narodowego Centrum Nauki (UMO-2015/18/A/ST4/00058, UMO-2018/31/N/ST5/03215, UMO-2020/36/T/ST5/00421) oraz Akademii Górniczo-Hutniczej im. Stanisława Staszica w Krakowie ("Inicjatywa doskonałości - uczelnia badawcza").

Niniejsza rozprawa doktorska została wykonana w ramach Programu Operacyjnego Wiedza Edukacja Rozwój, nr projektu POWR.03.02.00-00-I004/16, współfinansowanego ze środków Unii Europejskiej.

Praca została wsparta infrastrukturą badawczą Akademickiego Centrum Materiałów i Nanotechnologii.

Podziękowania

Podczas studiów i badań, których efektem jest ta rozprawa doktorska, otrzymałem wsparcie od wielu osób — chciałbym tutaj okazać im wdzięczność za okazaną pomoc.

Przede wszystkim dziękuję pierwszemu promotorowi prof. dr. hab. Konradowi Szaciłowskiemu za nieustające wsparcie w eksploracji nowych pomysłów badawczych i ogrom przekazanej przez te wszystkie lata pracy wiedzy, ale ponad wszystko — za rozbudzenie pasji do nauki. Jestem wdzięczny za wprowadzenie mnie do tematyki memrystorów — możliwość pracy w tym projekcie była dla mnie niesamowitą okazją do rozwoju.

Podziękowania składam także prof. dr. hab. Grzegorzowi Hessowi — za wsparcie podczas studiów doktoranckich oraz pomoc w połączeniu dwóch różnych naukowych światów: memrystorów i neuronów.

Szczególne podziękowania należą się dr. Tomaszowi Mazurowi, który przez te wszystkie lata towarzyszył mi w pracach eksperymentalnych i wspierał naukowo oraz na każdej innej płaszczyźnie. Dziękuję za wszystkie rozmowy, rady i dyskusje! Nie dałbym rady ukończyć tej pracy bez Twojej pomocy.

Dziękuję także całej załodze Akademickiego Centrum Materiałów i Nanotechnologii, która zawsze wspierała mnie w moich pracach eksperymentalnych. ACMiN był miejscem pełnym otwartych, inteligentnych i wspierających osób — nie wyobrażam sobie lepszego miejsca do prowadzenia badań w ramach studiów doktoranckich. W szczególności dziękuję dr Sylwii Klejnie, Marii Lis, Dawidowi Przyczynie i Romie Wireckiej — dzięki Wam długie godziny w laboratoriach zawsze upływały w najlepszej atmosferze.

Jestem również wdzięczny mojej rodzinie i przyjaciołom, którzy wspierali mnie w tej przygodzie i udawali zrozumienie kiedy opowiadałem, czym się zajmuję.

Szczególnie dziękuję mojej żonie, Natalii — bez Twojego nieustannego wsparcia i pomocy ta praca nigdy by nie powstała.

Streszczenie

Rozwój elektroniki pozwolił na opracowanie wydajnych, powszechnie dostępnych i wszechstronnych urządzeń komputerowych. Mimo tego, algorytmy wykorzystywane w uczeniu maszynowym i sztucznej inteligencji wymagają przetwarzania tak dużych ilości danych, że stanowi to poważne wyzwanie dla konwencjonalnych komputerów. Ich architektura, w której procesor i pamięć stanowią odrębne układy, wymaga ciągłego przesyłania danych pomiędzy pamięcią i procesorem. Proces ten jest jednym z najistotniejszych ograniczeń mocy obliczeniowej współczesnych komputerów i stanowi wyzwanie dla szybkiego rozwoju sztucznej inteligencji.

Jednym z potencjalnych rozwiązań tego problemu są nowe paradygmaty obliczeniowe, na przykład przetwarzanie danych bezpośrednio w pamięci. Jego implementacja jest możliwa w memrystorach — elementach elektronicznych, które potrafią jednocześnie przetwarzać i przechowywać dane, dzięki czemu nie ma potrzeby przesyłania ich pomiędzy dwoma rozdzielonymi układami. W memrystorach informacja przechowywana jest w postaci konduktancji, która może być zmieniana za pomocą napięcia. W niektórych typach memrystorów przewodnictwo może być kontrolowane w szerokim zakresie, pozwalając na odejście od logiki dwuwartościowej stanowiącej podstawę funkcjonowania obecnych komputerów. Dzięki temu memrystory mogą naśladować sposób, w jaki sygnały przetwarzane są przez biologiczne neurony. W układzie nerwowym komunikacja odbywa się poprzez wzmacnianie i osłabianie połączeń synaptycznych pomiędzy neuronami wywołane krótkimi impulsami elektrycznymi. Miarą siły tego połączenia jest waga synaptyczna, a zmiany jej wartości — nazywane plastycznością synaptyczną — leżą u podstaw procesów uczenia się.

W memrystorach analogią do wagi synaptycznej jest zmienna konduktancja, która może być modulowana przez napięcie o zmiennej amplitudzie i częstotliwości. Dzięki niej memrystory są zdolne do odtworzenia niektórych rodzajów plastyczności synaptycznej obserwowanych w neuronach. Wśród takich efektów neuromorficznych (lub neuromimetycznych) znajdują się m. in. metaplastyczność, pamięć krótko- i długoterminowa oraz potencjalizacja i depresja. Dzięki ich obecności memrystory mogą zostać wykorzystane jako sztuczne synapsy przetwarzające sygnał w sposób analogiczny do biologicznych synaps.

Wśród materiałów wykorzystywanych do budowy memrystorów znajdują się hybrydowe organiczno-nieorganiczne perowskity halogenkowe. Do tej grupy perowskitów należą materiały będące jednymi z najbardziej wydajnych ogniw słonecznych, ale ich właściwości optoelektronicznie czynią je także interesującymi z punktu widzenia zastosowań w

optoelektronice i jako memrystory. Ich silne oddziaływanie ze światłem stwarza możliwość kontrolowania efektów memrystywnych i neuromorficznych nie tylko napięciem, ale także za pomocą światła.

Celem prowadzonych badań było zbadanie efektów neuromimetycznych w cienkich warstwach perowskitów oraz w materiałach do nich analogicznych. Zrozumienie mechanizmów fizycznych odpowiedzialnych za przełączanie rezystywne leżące u podstaw efektów neuromorficznych oraz ich pełnej charakterystyce woltamperometrycznej stanowi pierwszy krok do wykorzystania memrystorów perowskitowych w układach memrystywnych zdolnych do wydajnej implementacji algorytmów uczenia maszynowego, w których przetwarzanie sygnału inspirowane jest działaniem biologicznych neuronów.

W niniejszej rozprawie scharakteryzowano efekty neuromorficzne w perowskitach opartych o ołów i bizmut oraz związkach kompleksowych i kryształach jonowych bizmutu. Celem pracy było wyjaśnienie mechanizmów przełączania rezystywnego w memrystorach perowskitowych oraz ich powiązanie z efektami memrystywnymi i neuromimetycznymi. W tym celu materiały scharakteryzowano za pomocą metod spektroskopowych oraz woltamperometrycznych. Pokazano, że w memrystorach opartych o perowskity $CH_3NH_3PbI_3$ oraz $(CH_3NH_3)_3Bi_2I_9$ zmiana konduktancji memrystorów opiera się o modulację wysokości bariery energetycznej na złączu metalu i półprzewodnika (bariery Schottky'ego) wywołanej zapełnianiem i opróżnianiem stanów pułapkowych. Mechanizm ten pozwolił na odtworzenie efektów plastyczności synaptycznej, takich jak uczenie poprzez plastyczność synaptyczną zależną od częstotliwości (*spike-rate dependent plasticity* i *frequency facilitation*) oraz od korelacji czasowej i kolejności generowania potencjałów czynnościowych przez neuron pre- i postsynaptycznych (*spike-timing dependent plasticity*). W memrystorze opartym o kompleks bizmutu $[BiI_3(C_6H_5)_2SO_{1.5}]_4$ pokazano, że charakter uczenia jest zależy od orientacji bariery Schottky'ego i może być zmieniony poprzez wykorzystanie innego metalu w roli elektrody memrystora.

Pokazano, że w memrystorze opartym o perowskit $CH_3NH_3PbI_3$ efekty synaptyczne mogą być indukowane za pomocą światła. Wprowadzenie do memrystora materiału zdolnego do pułapkowania elektronów (nanocząstek azotku węgla) pozwala na modulowanie plastyczności indukowanej światłem — w memrystorze bez materiału pułapkującego światło powoduje wzmocnienie synaptyczne, a w urządzeniu z dodatkowym stanami pułapkowymi — osłabienie odpowiedzi synaptycznej.

Zmiana konduktancji memrystorów może odbywać się także poprzez tworzenie przewodzących filamentów powstających wskutek migracji defektów struktury krystalicznej w gradiencie zewnętrznego pola elektrycznego. Taki mechanizm przełączania zbadano w memrystorze opartym o związek bizmutu ($CH_4NH_9BiI_6$). Pokazano, że jest on zdolny do odtworzenia plastyczności synaptycznych opisywanych przez model biologicznego neuronu

leaky integrate and fire. Przeprowadzona symulacja sztucznej sieci neuronowej, w której jako parametry neuronów wykorzystano parametry memrystorów $CH_4NH_9BiI_6$, wykazała dokładność klasyfikacji pisma odręcznego na poziomie 94%.

Abstract

The rapid development of electronics has given rise to efficient, affordable and versatile computing devices. Despite that, algorithms that are utilized in machine learning and artificial intelligence require processing volumes of data so large, that they pose a significant challenge for conventional computers. Their architecture in which the processing unit and memory are physically separated requires to transfer the data between these two components constantly. This process significantly limits the processing power and poses an impediment to advancing the systems based on artificial intelligence.

This problem is addressed by new computational paradigms such as in-memory computing which can be implemented in memristors — electronic elements capable of processing and storing the data, thus eliminating the need to transfer it between two separate components. Memristors store information in the form of variable conductance which can be controlled by applying an external voltage to the device. In some types of memristors, the conductance can be incrementally tuned within a wide range, allowing to move from the canonical binary logic utilized by nowadays computers. Owing to tunable conductance, memristors can emulate the behaviour of neurons in a biologically faithful way. In the neural system, the communication between neurons relies on sending and receiving short electric spikes which lead to strengthening or weakening the synaptic connections between the participating cells. The measure of the connection strength is described by synaptic weight and its modulation — called synaptic plasticity — lies at the base of learning processes in the human brain.

In memristors, the analogy of synaptic weight is variable conductance which can be tuned by the amplitude or frequency of voltage spikes, allowing memristors to mimic some types of synaptic plasticity. Such effects are called neuromorphic or neuromimetic and include metaplasticity, short- and long-term memory, potentiation, depression and others. Owing to their presence, memristors can act as artificial synapses that process the signal in a biologically faithful manner.

Among the materials used in memristive devices, hybrid organic-inorganic halide perovskites are extensively investigated. This group of materials is utilized to build one of the most efficient solar cells but owing to their optoelectronic properties, perovskites are promising candidates for various optoelectronic and memristive devices as well. Due to their strong interaction with light, the response of perovskite memristors can be controlled not only by voltage but also by illumination.

The aim of the conducted research was to investigate the neuromorphic effects in thin layers of hybrid perovskites and their analogues. A deep understanding of physical

mechanisms resistive switching originates and full characterization of memristive and neuromorphic effects consist the first step towards the application of perovskite memristors in arrays to implement neuron-inspired machine learning algorithms.

In this thesis, I investigate neuromimetic responses in lead- and bismuth-based perovskites and in complexes and ionic compounds of bismuth. I mostly focus on explaining the physical mechanisms of resistive switching in memristors and their impact on memristive and neuromorphic effects. For this purpose, all materials have been characterized with spectroscopic and voltamperometric techniques. I show that in memristors based on $CH_3NH_3PbI_3$ and $(CH_3NH_3)_3Bi_2I_9$ the conductance is governed by the variable height of the energy barrier at the metal-semiconductor interface (the Schottky barrier) caused by population and depopulation of the trapping sites. The interface switching lead to almost analogue conductance tuning which in turn allowed for emulating such types of synaptic plasticity as frequency-based spike-rate dependent plasticity and spike-timing dependent plasticity which relies on the temporal order of the spikes in the pre- and postsynaptic neurons. In the memristor based on the bismuth complex compound $[BiI_3(C_6H_5)_2SO_{1.5}]_4$ we showed that the character of learning depends on the Schottky barrier orientation and can be altered simply by choosing different metal as one of the memristor electrical contacts.

I also present that in $CH_3NH_3PbI_3$ perovskite memristor synaptic effects can be induced with light. Incorporating an electron-trapping compound — the carbon nitride nanoparticles — as one of the memristor layers allows for modulating the light-induced plasticity. In the perovskite-only memristor, illumination leads to synaptic facilitation whereas synaptic depression was observed in the memristor with the additional trapping layer.

Apart from modulation of the barrier at the interface, the conductance changes may be caused by the creation of a conductive filament formed by crystal structure defects migrating in the gradient of an external electric field. Such mechanism was investigated in memristor based on bismuth ionic compound $(C_4H_9NH_3)_3BiI_6$. I show that it can be utilized to emulate neural behaviours described by the leaky integrate-and-fire neuron model. The artificial neural network simulation with parameters based on $CH_4NH_9BiI_6$ memristors switching characteristic shows high accuracy in classification tasks, reaching 94% in handwritten digit recognition.

Dorobek naukowy

Artykuły naukowe

1. Paczesny, J. Wybrańska, K; Niedziółka-Jönsson, J. Roźniecka, E.; Wadowska, M.; **Zawal, P**.; Malka, I.; Dzięcielewski, I.; Prochowicz, D.; Hołyst, R.; Fiałkowski, M. *Hollow Microtubes Made of Carbon, Boron and Gold: Novel Semiconducting Nanocomposite Material for Applications in Electrochemistry and Temperature Sensing*, RSC Adv. 2015, 5 (79), 64083–64090.

2. Wlaźlak, E.; Blachecki, A.; Bisztyga-Szklarz, M.; Klejna, S.; Mazur, T.; Mech, K.; Pilarczyk, K.; Przyczyna, D.; Suchecki, M.; **Zawal, P.**; Szaciłowski, K. *Heavy Pnictogen Chalcohalides: The Synthesis, Structure and Properties of These Rediscovered Semiconductors*, Chem. Commun. 2018, 54 (86), 12133–12162.

3. Wlaźlak, E., Marzec, M., **Zawal, P.**, Szaciłowski, K *Memristor in a Reservoir System—Experimental Evidence for High-Level Computing and Neuromorphic Behavior of PbI_2*, ACS Applied Materials & Interfaces, 2019, 11 (18), 17009-17018.

4. Mazur, T.[1], **Zawal, P.**[1], Szaciłowski, K. *Synaptic plasticity, metaplasticity and memory effects in hybrid organic-inorganic bismuth-based materials*, Nanoscale, 2019, 11 (3), 1080-1090.

5. Klejna, S., Mazur, T., Wlaźlak, E., **Zawal, P.**, Soo, H. S., Szaciłowski, K. *Halogen-containing semiconductors: From artificial photosynthesis to unconventional computing*, Coordination Chemistry Reviews, 2020, 415, 213316.

6. Przyczyna, D., **Zawal, P.**, Mazur, T., Strzelecki, M., Gentili, P. L., Szaciłowski, K. *In-materio neuromimetic devices: dynamics, information processing and pattern recognition*, Japanese Journal of Applied Physics, 2020, 59 (5), 050504.

[1]Wkład autorów w prowadzenie badań i przygotowanie artykułu był równy.

7. Wlaźlak, E., Kalinowska-Tłuścik, J., Przyczyna, D., **Zawal, P.**, Szaciłowski, K. *Bismuth triiodide complexes: Structure, spectroscopy, electronic properties, and memristive properties*, Journal of Materials Chemistry C, 2020, 8 (18), 6136-6148.

8. Wlaźlak, E., **Zawal, P.**, Szaciłowski, K. *Neuromorphic Applications of a Multivalued [$SnI_4(C_6H_5)_2SO_2$] Memristor Incorporated in the Echo State Machine*, ACS Applied Electronic Materials, 2020, 2 (2), 329-338

9. Lis, M., Onuma, S., Przyczyna, D., **Zawal, P.**, Mazur, T., Pilarczyk, K., Gentili, P. L., Kasai, S., Szaciłowski, K. *From Oscillatory Reactions to Robotics: A Serendipitous Journey Through Chemistry, Physics and Computation*, Handbook of Unconventional Computing, 2021, 1-79.

10. **Zawal, P.**[1], Mazur, T.[1], Lis, M., Chiolerio, A., Szaciłowski, K. *Light-Induced Synaptic Effects Controlled by Incorporation of Charge-Trapping Layer into Hybrid Perovskite Memristor*, Advanced Electronic Materials, 2022, 8 (4), 2100838.

Udział w konferencjach

Prezentacje plakatów naukowych:

– *Artificial synapses based on methylammonium bismuth iodides*, **P. Zawal**, T. Mazur, K. Szaciłowski, HYMA 2019: 6^{th} International Conference on Multifunctional, Hybrid and Nanomaterial, 11-–15 marca 2019, Sitges, Spain;

– *Synaptic effects in perovskites modified with nitrogen-enriched carbon quantum dots*, **P. Zawal**, T. Mazur, M. Lis, K. Szaciłowski, ISPPCC 2019: 23^{rd} International Symposium on the Photochemistry and Photophysics of Coordination Compounds, 14—19 lipca 2019, Hong Kong;

– *Light-induced synaptic effects in perovskites modified with heptazine quantum dots*, **P. Zawal**, T. Mazur, M. Lis, K. Szaciłowski, 2019 E-MRS Fall Meeting: symposium V, 16–19 września, 2019 Warszawa, Polska.

– *Light-induced synaptic-like effects in perovskite memristive device*, **P. Zawal**, T. Mazur, M. Lis, K. Szaciłowski, Materials Challenges for Memory, 11–13 kwietnia 2021, konferencja online.

Kierowanie projektami badawczymi

– Grant NCN PRELUDIUM 16, 2018/31/N/ST5/03215, *Optyczna modulacja efektu memrystywnego w halogenobizmutanach alkiloamoniowych*;

– Grant NCN ETIUDA 8, 2020/36/T/ST5/00421, *Efekty neuromimetyczne w perowskitach i ich analogach.*

Udział w projektach badawczych

– NCN MAESTRO 7, 2015/18/A/ST4/00058, *Nanostrukturalne układy neuromimetyczne*;

– Projekt badawczy *Post-perowskitowe materiały memrystywne do budowy hardware'owych sieci neuronowych* finansowany ze środków programu "Inicjatywa Doskonałości - Uczelnia Badawcza".

Zrealizowane staże naukowe

– Staż w Centre for Electronic Frontiers na Uniwersytecie w Southampton (Wielka Brytania) pod opieką dr. Dimitry Georgiadou w ramach grantu ETIUDA (07–10.2022).

Działania popularyzujące naukę

– Czynny udział w przygotowaniu pokazów podczas Festiwalu Nauki i Sztuki, Małopolskiej Nocy Naukowców oraz warsztatów dla Uniwersytetu Dzieci;

– Współautorstwo artykułu popularnonaukowego w Biuletynie AGH 147/2020.

Spis treści

Spis rysunków

ROZDZIAŁ 1

Wprowadzenie, motywacja i cel badań

1.1. Wstęp

Przetworzenie ogromnych ilości danych wytwarzanych codziennie przez przemysł i społeczeństwo stanowi duże wyzwanie dla współczesnych komputerów. Obecnie jednym z głównych obszarów rozwoju systemów przetwarzania danych stało się udoskonalanie zarówno komputerów, jak i procesów w taki sposób, aby były one w stanie efektywnie przetwarzać duże wolumeny danych. Tradycyjne podejścia, takie jak stosowanie złożonych algorytmów implementujących odpowiednią logikę, są coraz częściej zastępowane przez metody uczenia maszynowego, które znacznie wydajniej radzą sobie z niepełnymi i nieprecyzyjnymi danymi. Niestety, metody te wymagają dużej mocy obliczeniowej, co z kolei przekłada się na wysokie zużycie energii. W kontekście wpływu przetwarzania dużych ilości informacji na środowisko szacuje się, że w procesie trenowania dużego modelu sztucznej sieci neuronowej do przetwarzania języka naturalnego produkowana jest ilość CO_2, jaką średnio wytwarza człowiek w ciągu 7 lat [1].

Jednym z powodów dużej konsumpcji energii przez współczesne komputery jest ich budowa oparta na architekturze von Neumanna, w której jednostka obliczeniowa i pamięć stanowią odrębne, odseparowane od siebie układy [2]. Konieczność ciągłego przesyłania danych pomiędzy procesorem i pamięcią, wynikająca z wykonywania złożonych operacji matematycznych takich jak mnożenie wektorów i macierzy oraz latencja odczytu danych z pamięci są współcześnie jednymi z najistotniejszych ograniczeń rozwoju uczenia maszynowego i sztucznej inteligencji [3]. W odpowiedzi na te problemy rozwijane są dedykowane układy, takie jak Google TPU [4, 5, 6], w których obliczenia na macierzach i wektorach są wykonywanie znacznie wydajniej. Równocześnie proponowane są także rozwiązania wykorzystujące nowe paradygmaty obliczeniowe, które odchodzą od klasycznej architektury

von Neumanna i które naśladują sposób, w jaki informacje przetwarzane są przez mózg i neurony.

Mózg przetwarza informacje w znacznie bardziej wydajny i energooszczędny sposób niż robią to współczesne komputery. Szacuje się, że sztuczna inteligencja AlphaGo, znana przede wszystkim ze zwycięskiej rozgrywki z ówczesnym mistrzem świata w Go (gry, która poprzez bardzo dużą liczbę dostępnych kombinacji w każdym ruchu była uznawana za ekstremalnie trudną obliczeniowo dla komputerów), potrzebowała ok. 10 kW mocy [7]. Dla porównania, zapotrzebowanie ludzkiego mózgu wynosi ok. 20 W, a więc ponad 50 tys. razy mniej [8]. Biorąc pod uwagę te liczby, potencjalny zysk energetyczny wynikający z odejścia od klasycznej architektury komputerowej na rzecz rozwiązań inspirowanych sposobem przetwarzania informacji przez układy biologiczne może mieć ogromne znaczenie zarówno z punktu widzenia kosztów, jak i zmniejszenia energochłonności i w efekcie ograniczenia emisji gazów cieplarnianych do atmosfery.

Dostępne komercyjnie układy neuromorficzne, jak na przykład IBM TrueNorth czy Intel Loihi [9], oparte są o rozwiązania klasycznej technologii CMOS (ang. *Complementary Metal-Oxide Semiconductor)*. Układy te zaprojektowane zostały do wydajnego trenowania sieci neuronowych i charakteryzują się konsumpcją mocy na poziomie miliwatów. Rozwiązanie Intela pozwoliło na 300-krotne zmniejszenie zużycia energii w porównaniu do takich samych obliczeń wykonanych na układach graficznych GPU (ang. *graphics processing unit* i 150-krotne względem CPU [10]. Z kolei konwolucyjne sieci neuronowe zaimplementowane na układzie IBM są zdolne do przetworzenia do 2600 obrazów na sekundę przy zapotrzebowaniu mocy na poziomie 250 mW [11]. W ostatnich latach zaprezentowano także nowe rodzaje urządzeń, w których przetwarzanie sygnału odbywa się w sposób analogiczny do biologicznych synaps i które oparte są na na elementach fotonicznych [12], ferroelektrykach [13, 14], grafenie [15], a także na memrystorach.

Memrystory to urządzenia zdolne zarówno do przetwarzania jak i przechowywania informacji, które dzięki swoim właściwościom znalazły szerokie zastosowanie jako nieulotne pamięci [16], sztuczne synapsy [17, 18] oraz elementy układów neuromorficznych — urządzeń elektronicznych, które wykonują obliczenia w sposób inspirowany przetwarzaniem informacji przez układy neurobiologiczne, takie jak ludzki mózg [19, 20]. Wbudowana pamięć memrystorów pozwala na przetwarzanie i przechowywanie danych w tym samym miejscu, bez konieczności ich przesyłania pomiędzy procesorem a pamięcią. Podejście to nosi nazwę *in-memory computing*. Zatarcie granicy pomiędzy tymi dwoma procesami nie tylko pozwala na zwiększenie wydajności obliczeniowej poprzez obejście ograniczenia von Neumanna, ale także naśladuje sposób, w jaki informacje są przetwarzane w mózgu. Z tego powodu memrystory są szeroko badane pod względem ich zastosowania w nowych typach układów neuromimetycznych [21, 22].

1.2. Memrystory

Memrystory są elementami elektronicznymi, które przechowują informację w postaci zmiennej konduktancji. Z tego powodu o memrystorze można myśleć jako o rezystorze z pamięcią, z czego zresztą wynika jego nazwa (skrót od ang. *memory resistor*). Początkowo memrystory badane były głównie w kontekście ich zastosowania jako pamięci nieulotne (ang. *non-volatile memories*), np. w roli rezystywnych pamięci RAM [23]. Jednak ze względu na swoje właściwości, które pozwalają także na emulację zachowania biologicznych synaps i niektórych funkcji neuronów, a także możliwość łączenia memrystorów w skalowalne układy i integracji z układami wytworzonymi w technologii CMOS, są one obecnie uważane za bardzo obiecujące pod względem ich zastosowania w układach neuromorficznych.

Pierwszy działający memrystor został zaprezentowany przez Hewlett-Packard w 2008 roku [24], jednakże jego teoretyczny model opisano już niemal 40 lat wcześniej. W 1971 roku Leon Chua zapostulował istnienie czwartego — obok rezystora, kondensatora i cewki — elementu elektronicznego, który nazwał memrystorem [25]. Zasadę jego działania oparł na analogii z pozostałymi podstawowymi pasywnymi elementami elektronicznymi. Podczas gdy rezystancja R jest stałą proporcjonalności łączącą napięcie z prądem (Równ. 1.1), pojemność C ładunek z napięciem (Równ. 1.2) i induktancja L strumień magnetyczny z prądem (Równ. 1.3), memrystancja M określa relację pomiędzy strumieniem pola i ładunkiem (Równ. 1.4):

$$\mathrm{d}v = R\mathrm{d}i \tag{1.1}$$

$$\mathrm{d}q = C\mathrm{d}v \tag{1.2}$$

$$\mathrm{d}\phi = L\mathrm{d}i \tag{1.3}$$

$$\mathrm{d}\phi = M\mathrm{d}q \tag{1.4}$$

gdzie:

- v – napięcie
- i – prąd
- q – ładunek
- ϕ – strumień pola magnetycznego

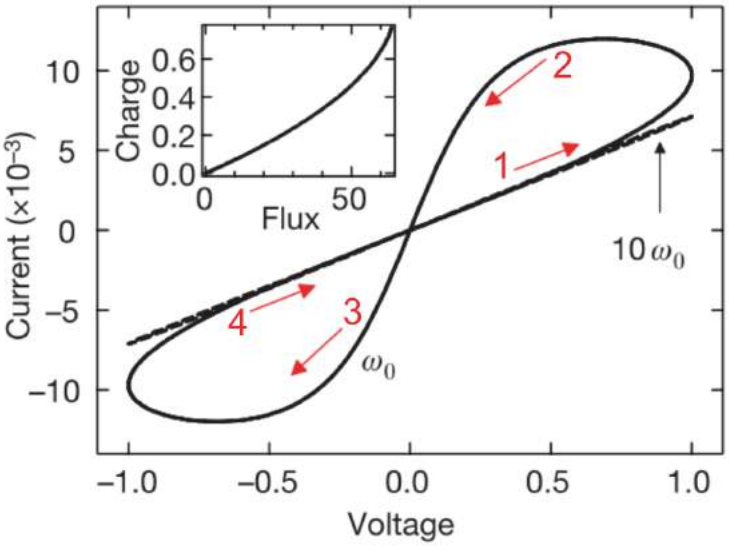

Rys. 1.1. Pętla histerezy idealnego memrystora poddanego bipolarnemu pomiarowi prądowo-napięciowemu o częstotliwości ω_0. Strzałki przedstawiają kierunek zmian napięcia. Pętla histerezy przecina się w zerze i dla wysokich częstotliwości ulega zwężeniu aż do całkowitego zaniku, przechodząc w zależność liniową [24].

W przeciwieństwie do rezystancji, będącej wartością stałą, memrystancja $M(q)$ jest funkcją ładunku, który przepłynął przez urządzenie. Prowadzi to do nieliniowej zależności pomiędzy prądem a napięciem, leżącej u podstaw najważniejszej cechy memrystorów: pętli histerezy w pomiarze prądowo-napięciowym $I-V$ (Rys. 1.1) [24]. W idealnym memrystorze, pętla jest symetryczna względem początku układu współrzędnych i przecina się przy wartości napięcia 0 V.[1] Jej szerokość zależy od częstotliwości zmian napięcia i ulega zwężeniu wraz jej wzrostem, przechodząc w zależność liniową dla odpowiednio wysokich częstotliwości.

Pętla histerezy w memrystorach jest manifestacją opóźnienia reakcji urządzenia na czynnik zewnętrzny. Za nieliniową zależność pomiędzy prądem a napięciem może odpowiadać wiele mechanizmów, takich jak przemieszczanie mobilnych jonów [28], defektów sieci krystalicznej materiału [29, 30], formowanie i niszczenie przewodzących filamentów [31, 32] lub przejścia fazowe [33]. Strzałki na Rys. 1.1 obrazują przebieg zmian napięcia w pomiarze $I-V$. Powyżej pewnego napięcia o dodatniej polaryzacji (strzałka 1) następuje zmiana konduktancji memrystora, prowadząca do wzrostu amplitudy prądu płynącego przez urządzenie. Wzrost konduktancji jest wynikiem zmian cech fizycznych materiału

[1] Jest to prawdą w przypadku idealnego memrystora, ale znane są memrystory, w których przecięcie jest obecne przy napięciach innych niż 0 V i które wynika z efektów pojemnościowych [26, 27].

memrystora, które, jeśli są stabilne, odpowiadają za efekt pamięci. Konduktancja memrystora pozostaje stała (strzałki 2 i 3), dopóki nie zostanie przekroczone napięcie progowe o przeciwnej polaryzacji, powyżej którego następuje powrót do pierwotnej wartości konduktancji (strzałka 4). Modulowanie konduktancji może odbywać się zarówno za pomocą prądu, jak i napięcia, a proces nazywany jest przełączaniem rezystywnym. Stany o niskiej i wysokiej konduktancji lub — równoważnie — o wysokiej i niskiej rezystancji najczęściej określa się jako *high-resistance state* (HRS) i *low-resistance state* (LRS).

1.2.1. Mechanizmy przełączania rezystywnego

W zależności od procesów fizycznych lub chemicznych wpływających na zmiany konduktancji materiału, wyróżnia się kilka mechanizmów przełączania rezystywnego. Kategoryzacja ta nie jest ustandaryzowana i w literaturze można znaleźć wiele umownych podziałów. W niniejszej pracy oparto się na klasyfikacji przedstawionej w artykule [34], gdyż uwzględnia ona większość opisanych mechanizmów fizykochemicznych. W ogólności mechanizmy przełączania rezystywnego można przypisać do trzech głównych grup: przełączanie związane z przejściami fazowymi materiału, przełączanie filamentowe (mechanizm elektromechaniczny i zmiany walencyjności) i przełączanie poprzez modyfikację parametrów złącza (mechanizm złączowy). Podział ten przedstawiono na Rys. 1.2.[2]

Przejście pomiędzy dwiema fazami leży u podstaw działania pamięci typu *phase change memory* (PCM). W urządzeniach tych przełączanie rezystywne i efekt pamięci wynikają z przejścia fazowego materiału aktywnego, które jest wywoływane przepływem prądu przez urządzenie. Ciepło wydzielone podczas tego procesu (ciepło Joule'a) prowadzi do krystalizacji lub amorfizacji materiału [35, 36, 37]. W pamięciach PCM, impulsy o niskim napięciu powodują lokalne wzrosty temperatury prowadzące do krystalizacji amorficznych obszarów materiału, co z kolei skutkuje wzrostem jego konduktancji. Przekroczenie pewnego napięcia progowego powoduje wydzielenie dużej ilości ciepła i w efekcie ponowną amorfizację materiału oraz jego przełączenie do HRS. Z tego powodu PCM są urządzeniami o przełączaniu *unipolarnym*, w którym przełączanie jest zależne od amplitudy napięcia, a nie od jego polaryzacji. Materiałami wykorzystywanymi w urządzeniach PCM są głównie chalkogenki, np. $Ge_2Sb_2Te_5$ [38, 39]. Obie formy tych związków — amorficzna i krystaliczna — są termodynamicznie stabilne przez długi czas, przechowując tym samym zapisany stan rezystywny. Choć mechanizm ten bywa klasyfikowany jako filamentowy,

[2]Istnieją również pamięci ferroelektryczne, w których za przełączanie rezystywne odpowiedzialna jest reorientacja domen ferroelektrycznych oraz wykorzystujące modulację tunelowego magnetooporu kontrolowanego przez spinowo spolaryzowany prąd [35]. Pamięci te nie posiadają jednak pętli histerezy przecinającej się w 0 V — jednej z najważniejszych cech memrystora — dlatego ich opis wykracza poza zakres niniejszej rozprawy.

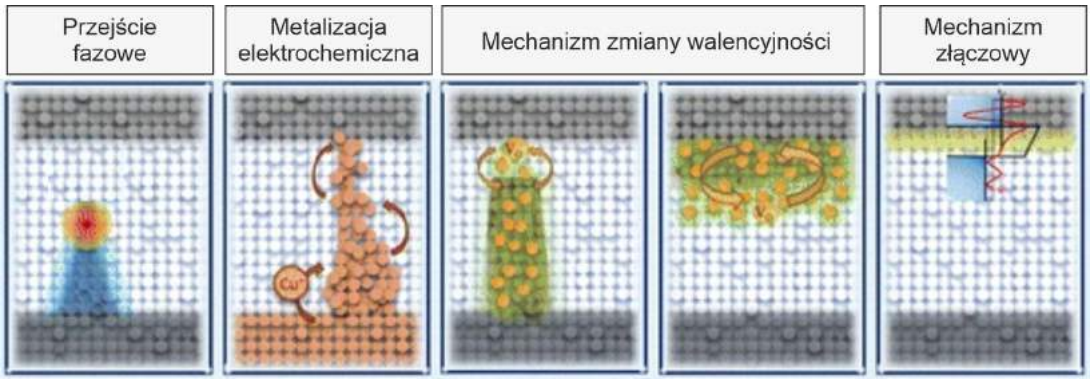

Rys. 1.2. Klasyfikacja mechanizmów przełączania rezystywnego. W mechanizmie związanymi z przejściami fazowymi przełączanie spowodowane jest przemianami materiału zachodzącymi wskutek lokalnych wzrostów temperatury wywołanych przepływem prądu. Mechanizm metalizacji elektrochemicznej oparty jest na tworzeniu przewodzącego filamentu z materiału elektrody. W mechanizmie zmiany walencyjności filament jest tworzony w wyniku migracji defektów struktury, ale przełączanie zachodzić może także przy równomiernej migracji defektów. Zmiany konduktancji w mechanizmie złączowym są wynikiem modulacji wysokości bariery energetycznej na złączu elektrody i materiału aktywnego memrystora. Na podstawie [34].

do zaobserwowania przełączania rezystywnego w tego typu pamięciach nie jest konieczne utworzenie filamentu łączącego obie elektrody, ale wystarczająca jest zmiana stosunku fazy krystalicznej do amorficznej.

Przełączanie filamentowe polega na utworzeniu przewodzącego filamentu w strukturze materiału. Łączy on ze sobą dwie elektrody, powodując przejście do LRS, a zniszczenie tego filamentu (np. przez napięcie o przeciwnej polaryzacji) sprowadza memrystor do początkowego HRS. Filament powstaje wskutek migracji defektów struktury krystalicznej lub kationów elektrody w gradiencie pola elektrycznego. Przekraczając pewne napięcie progowe, następuje wzrost filamentu pomiędzy elektrodami. Napięcie o przeciwnej polaryzacji powoduje migrację defektów lub kationów w przeciwnym kierunku, skutkując zniszczeniem filamentu. W zależności od rodzaju filamentu rozróżnia się podział na mechanizm elektrochemiczny (ang. *electrochemical mechanism*, ECM) oraz mechanizm zmiany walencyjności (ang. *valence-change mechanism*, VCM); czasami nazywa się je także odpowiednio kationowym i anionowym. W urządzeniach opartych o ECM przewodzący filament formowany jest przez atomy elektrochemicznie aktywnej elektrody metalicznej, np. Cu, Ag, Al, podczas gdy druga elektroda jest elektrochemicznie inertna, np. W, Pt, Ag. Dodatnie napięcie przyłożone do elektrody aktywnej A powoduje jej utlenienie do formy kationowej A^{n+}, a gradient pola elektrycznego wywołuje migrację kationów w stronę elektrody inertnej, na której ulegają redukcji, tworząc przewodzący metaliczny filament.

Mechanizm VCM obserwowany jest z kolei w niestechiometrycznych tlenkach metali przejściowych (np. TiO_x, HfO_x, WO_x) w strukturze których występują domieszki wynikające z nadmiaru lub niedostatku atomów tlenu w strukturze oraz w chalkogenkach (np. ZnTe, ZnSe), azotkach (AlN) i perowskitach ($SrTiO_3$, $SrZrO_3$, $BaTiO_3$) [40, 41, 42]. Migracja tych defektów, wywołana gradientem pola elektrycznego, skutkuje utworzeniem filamentu zbudowanego z defektów struktury krystalicznej. Cechą charakterystyczną przełączenia rezystywnego w tym mechanizmie są bardzo gwałtowne zmiany konduktancji oraz duża jej różnica pomiędzy stanami HRS i LRS. Przełączanie rezystywne w mechanizmie VCM nie zawsze musi być efektem utworzenia lub zniszczenia przewodzącego filamentu. Równomierna migracja defektów, np. wakancji tlenkowych $V_{\ddot{O}}$, w gradiencie pola elektrycznego może powodować równomierny wzrost obszaru zawierającego domieszki [24]. Ten typ przełączania charakteryzuje się mniej gwałtownymi zmianami konduktancji, niższym stosunkiem skrajnych stanów rezystywnych i szerszym zakresem napięć, w którym ono zachodzi. Istotną zaletą mechanizmu VCM jest obecność dodatkowych stanów rezystywnych pomiędzy skrajnymi stanami niskiego i wysokiego oporu, pozwalająca na zastosowanie tych memrystorów w układach analogowych i neuromorficznych [43].

Kolejnym rodzajem mechanizmu przełączania rezystywnego, w którym również istnieje możliwość przełączania memrystora do stanów pośrednich pomiędzy HRS i LRS

jest mechanizm złączowy. Za zmiany konduktancji odpowiedzialne są zmiany wysokości bariery energetycznej na złączu wywołane napięciem. Bariera energetyczna na granicy półprzewodnika i metalu powstaje w wyniku różnicy poziomów Fermiego tychże materiałów, a zmiana jej wysokości związana jest z procesami pułapkowania nośników ładunku w obszarze złącza.

Rozważając metal o pracy wyjścia Φ_M i półprzewodnik typu n o pracy wyjścia Φ_n, gdzie $\Phi_M > \Phi_n$, jeśli dochodzi do fizycznego kontaktu obu materiałów, musi także dojść do wyrównania poziomów Fermiego metalu E_{Fm} i półprzewodnika E_{Fn} poprzez przepływ nośników ładunku (Rys. 1.3(a)). Odbywa się on poprzez tunelowanie przez powstającą barierę potencjałów elektronów zajmujących wyższe stany energetyczne w paśmie przewodnictwa E_C półprzewodnika do nieobsadzonych stanów o niższej energii tuż nad poziomem Fermiego metalu. Tunelujące elektrony pozostawiają w półprzewodniku warstwę zubożoną, w której znajdują się dodatnio naładowane atomy donorów elektronów. W obszarze tej warstwy koncentracja elektronów jest zatem niższa, tym samym powodując wzrost wartości $E_C - E_{Fn}$ i zagięcie pasm energetycznych w obszarze złącza ((Rys. 1.3(b))), skutkujące pojawieniem się bariery energetycznej zwaną barierą Schottky'ego Φ_{SB} [44, 45], której wysokość określa równanie:

$$\Phi_{SB} = \Phi_M - \chi = eV_o + (E_c - E_{Fn}), \tag{1.5}$$

gdzie: χ — powinowactwo elektronowe, $V_o = \Phi_M - (\chi - \Phi_n)$ — potencjał kontaktowy metalu o pracy wyjścia Φ_M i półprzewodnika o pracy wyjścia Φ_n.

Polaryzacja urządzenia w kierunku przewodzenia powoduje przepływ elektronów z pasma przewodnictwa półprzewodnika do metalu, skutkując obniżeniem bariery Schottky'ego. Aby wystąpił efekt pamięci, elektrony muszą zostać spułapkowane w obszarze złącza, powodując trwałą zmianę wysokości bariery. Jeśli w obszarze złącza znajdują się nieobsadzone stany pułapkowe (Rys. 1.3(c)), następuje ich zapełnianie, powodujące obniżenie bariery Schottky'ego i przełączenie memrystora z HRS do LRS (Rys. 1.3(d)). Stan ten jest utrzymywany, dopóki memrystor nie zostanie spolaryzowany w kierunku zaporowym. Opróżnianie pułapek elektronowych skutkuje ponownym wzrostem bariery na złączu oraz powrotem do HRS. Mechanizm modulacji wysokości bariery jest odpowiedzialny za efekt pamięci w niektórych memrystorach opartych o organiczno-nieorganiczne hybrydowe perowskity [46], w których defekty struktury krystalicznej pełniące funkcję pułapek ładunku powstają w procesie syntezy perowskitu (np. poprzez niestechiometryczną proporcję substratów, proces krystalizacji prowadzony w niskiej temperaturze lub bez stosowania atmosfery gazu inertnego) [47].

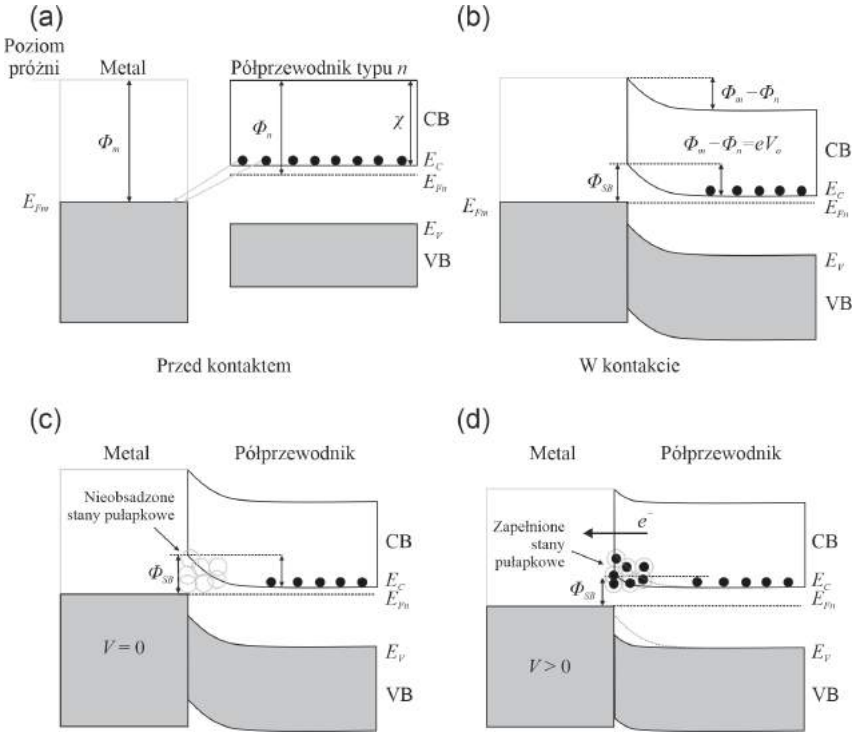

Rys. 1.3. (a) Powstawanie bariery Schottky'ego na przykładzie metalu i półprzewodnika typu n. Fizyczny kontakt (b) powoduje wyrównanie poziomów Fermiego obu tych materiałów poprzez przepływ elektronów z pasma przewodnictwa półprzewodnika E_C do stanów tuż nad pasmem Fermiego materiału E_{Fm}, skutkując wygięciem pasm na złączu i powstaniem bariery energetycznej. (c, d) Przełączanie rezystywne oparte na pułapkowaniu elektronów na złączu metal-półprzewodnik. (c) Przy braku zewnętrznego napięcia stanu pułapkowe pozostają nieobsadzone. (d) Spolaryzowanie złącza w kierunku przewodzenia powoduje przepływ elektronów z półprzewodnika do metalu i zapełnianie pułapek elektronowych w obszarze złącza, skutkując obniżeniem bariery Schottky'ego i przejściem z HRS do LRS. Polaryzacja w kierunku zaporowym powoduje opróżnianie pułapek elektronowych i zwiększenie wysokości bariery Schottky'ego skutkujące przejściem do HRS. Rysunki na podstawie [34, 44].

Przełączanie rezystywne oparte o mechanizm złączowy charakteryzuje się zwykle niższym stosunkiem konduktancji w LRS i HRS niż w memrystorach z przełączaniem filamentowym. Najistotniejszą cechą tego mechanizmu jest jednak prawie analogowy charakter zmiany konduktancji podczas przełączania. Pozwala on na przełączanie urządzenia do wielu przejściowych stanów rezystywnych pomiędzy HRS a LRS, co można wykorzystać do emulacji sposobu, w jaki informacje przetwarzają neurony, a co za tym idzie — do budowy urządzeń i układów neuromorficznych [48]. Szerzej mechanizm przełączania rezystywnego oparty o modulację bariery Schottky'ego i jego wykorzystanie do emulacji efektów neuromorficznych został opisany w sekcjach 2.4, 2.6 i 2.5 niniejszej rozprawy.

Brak widocznej zależności pomiędzy memrystancją a strumieniem pola magnetycznego (por. Równanie 1.4) był przedmiotem sporów, czy urządzenia wykazujące efekt przełączania rezystywnego należy uznać za memrystory [49, 50] lub wręcz podważających możliwość istnienia memrystora jako podstawowego elementu elektronicznego [51]. Z uwagi na zasadę działania tych urządzeń, bardziej precyzyjną nazwą są pamięci rezystywne. Jednak z uwagi na fakt, że fizyczne urządzenia posiadają najbardziej charakterystyczną cechę memrystora — przecinającą się w zerze pętlę histerezy — ze względu na ich funkcjonalne podobieństwo do cech idealnego memrystora, w literaturze przyjęło się nazywanie ich elementami memrystywnymi lub po prostu memrystorami [52, 53]. Mając na uwadze brak ścisłości tego nazewnictwa, dla przejrzystości niniejszej rozprawy powyższa terminologia została zachowana. Ponadto, w dalszej części pracy do opisu zachowania memrystorów zamiast memrystancji M używana jest konduktancja G, ponieważ dla napięć nieprzełączających (niższych od napięcia powodującego zmianę stanu memrystora) memrystor zachowuje się jak rezystor ohmowy, którego stan rezystywny jest określony wartością konduktancji.

1.2.2. Memrystory oparte o perowskity i ich analogi

Pierwszym odkrytym perowskitem był $CaTiO_3$, a nazwa tych minerałów pochodzi od nazwiska ich odkrywcy, L. A. Perovskiego. Obecnie perowskitami nazywana jest cała grupa związków o wzorze sumarycznym ABX_3 (gdzie A i B są kationami, a X anionem) krystalizujących w strukturze regularnej. Oprócz perowskitów nieorganicznych, wyróżnić można także hybrydowe organiczno-nieorganiczne perowskity. Ta grupa związków, ze względu na bardzo wydajną absorpcję promieniowania w szerokim zakresie spektralnym i wysoką wydajność generacji fotoindukowanych nośników ładunku, stała się bardzo atrakcyjna w kontekście ich zastosowania jako ogniwa słoneczne. Ich własności elektryczne pozwalają także na wykorzystanie perowskitów hybrydowych do budowy memrystorów.

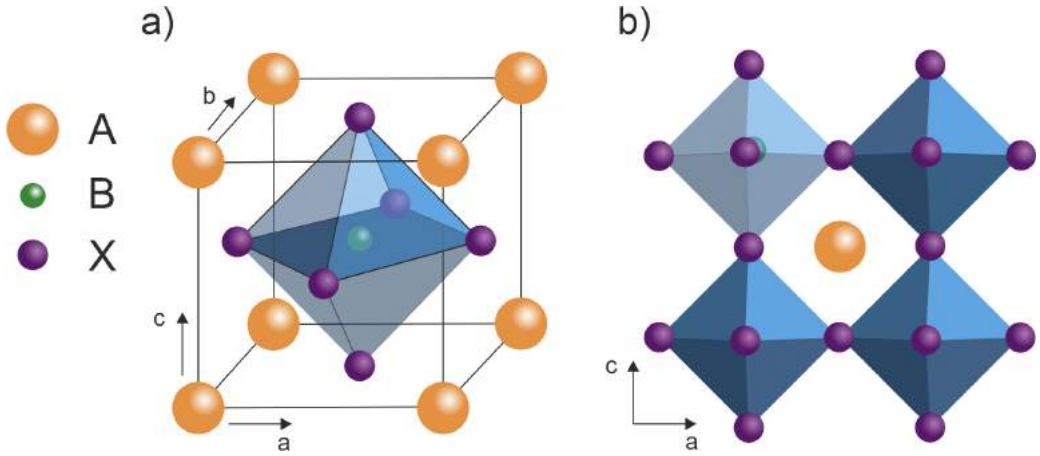

Rys. 1.4. (a) Komórka elementarna perowskitu. (b) Fragment sieci krystalicznej perowskitu krystalizującego w regularnym układzie krystalograficznym. Rysunek na podstawie [60].

W perowskitach hybrydowych A jest jednowartościowym kationem — np. metyloamoniowym $CH_3NH_3^+$ (MA^+) [54] lub formamidyniowym $CH_3(NH_2)_2^+$ (FA^+) [55]. W niektórych perowskitach wykorzystywanych w ogniwach słonecznych może być to także kation cezowy Cs^+, choć wtedy związek nie jest już perowskitem hybrydowym — chyba, że występuje w strukturze mieszanej z innymi kationem organicznym [56]. W miejscu B znajduje się dwuwartościowy kation nieorganiczny, np. Pb^{2+}, Sn^{2+} [57], Ge^{2+} [58], natomiast w pozycji X anion halogenkowy I^-, Cl^- lub Br^-.

Perowskity krystalizują w regularnym układzie krystalograficznym, utworzonym przez oktaedry $[BX_6]^{4-}$, w których kation B znajduje się w środku symetrii oktaedru, a aniony I^- umiejscowione są w jego narożach. W przestrzeniach pomiędzy oktaedrami znajduje się kation A^+. Aby utrzymać integralność sieci, musi być on dostatecznie mały, aby zmieścić się w przestrzenie pomiędzy nimi [59]. Rys. 1.4(a) przedstawia pojedynczą komórkę krystalograficzną perowskitu, a Rys. 1.4(b) fragment jego struktury.

Duża liczba badań poświęconych oddziaływaniu perowskitów ze światłem wynika z ich właściwości optoelektronicznych, które dodatkowo w stosunkowo łatwy sposób mogą być kontrolowane poprzez metody syntezy, zmianę składu i krystaliczności produktu. Wysoki współczynnik absorpcji pozwala na wydajną absorpcję fotonów, a w połączeniu z wysoką mobilnością nośników ładunku przekraczającą $10\,cm^2\,V^{-1}\,s^{-1}$, niską koncentracją stanów pułapkowych ($1\times10^{16}\,cm^{-3}$) oraz długą drogą swobodną nośników mniejszościowych (więcej niż 1 µm) pozwala na generowanie fotoprądów z wysoką wydajnością [61]. Wpływając z kolej na skład perowskitu lub na jego stopień krystaliczności (np. wymiarowość struktury krystalograficznej) możliwe jest kontrolowanie szerokości przerwy wzbronionej

oraz koncentracji defektów. Zmniejszenie szerokości przerwy pozwala na absorpcję szerszego zakresu światła, także z zakresu bliskiej podczerwieni; z drugiej strony, możliwość jej zwiększenia stwarza możliwości zastosowania perowskitów np. w diodach elektroluminescencyjnych [62, 63]. Z punktu widzenia zastosowań w urządzeniach memrystywnych, obecność defektów zdolnych do migracji w polu elektrycznym lub tworzących stany pułapkowe jest konieczna do wystąpienia efektów memrystywnych. Koncentracja defektów być kontrolowana poprzez np. niestechiometryczny stosunek prekursorów [18, 64] lub modyfikację warunków syntezy. Zależność tę opisano w publikacji streszczonej w rozdziale 2.4, a związek własności optoelektronicznych perowskitów z ich budową został szerzej opisany w rozdziale 2.1. Silne oddziaływanie perowskitów ze światłem pozwala na wpływanie z jego pomocą na własności memrystywne i efekty neuromimetyczne. Wyniki pomiarów badających wpływ światła na plastyczność synaptyczną oraz stan rezystywny memrystorów perowskitowych zostały opisane w rozdziale 2.6.

Ważnym czynnikiem opóźniającym lub wręcz powstrzymującym komercjalizację perowskitowych ogniw słonecznych jest fakt, że większość z urządzeń charakteryzujących się wysoką wydajnością konwersji światła na energię elektryczną oparta jest na ołowiu. Niestety, pierwiastek ten jest wysoce szkodliwy dla wszystkich organizmów żywych, powodując nieodwracalne uszkodzenia organów (np. mózgu) oraz niszcząc komórki poprzez zakłócenie ekspresji ich białek [65]. W ogniwach słonecznych wyeksponowanych na działanie warunków atmosferycznych, deszcz w łatwy sposób może zniszczyć strukturę perowskitu, powodując przeniknięcie ołowiu do środowiska. Ponadto, hybrydowe perowskity ołowiowe cechują się dużą wrażliwością na wilgoć, zmiany temperatury i promieniowanie ultrafioletowe, co w efekcie znacznie skraca czas życia urządzeń opartych o te materiały [66, 67]. Obecnie problemy te są adresowanie poprzez enkapsulację perowskitów zarówno w celu ochrony materiału przed czynnikami zewnętrznymi, jak i zapobieganiu przedostawaniu się ołowiu do środowiska lub stosowanie materiałów 2D (grafen, perowskity niskowymiarowe) odpornych na działanie wilgoci jako górne warstwy ogniwa [68]. Wyższą odporność na warunki środowiskowe uzyskuje się także np. przez podstawienie Pb^{2+} innym kationem, np. Ge^{2+} [69, 70], Sn^{2+} [71], Sb^{3+} [72], Bi^{3+} [73, 74]. Wśród nich bizmut, z niżej wymienionych powodów, wydaje się być dobrym kandydatem potencjalnie mającym szansę na zastąpienie ołowiu w perowskitowych ogniwach słonecznych:

– bizmut cechuje się niższą toksycznością niż ołów. Choć jest zaliczany do metali ciężkich, powszechnie występuje w środowisku i nie powoduje takich uszkodzeń w organizmach żywych jak ołów [75];

– jodobizmutany alkiloamoniowe cechują się wyższą odpornością na czynniki środowiskowe niż ich odpowiedniki zawierające ołów. Związki te wykazują stabilność struktury i parametrów fizykochemicznych bez żadnej enkapsulacji na przestrzeni tygodni [76, 64];

– wysoki współczynnik absorpcji — dla perowskitu bizmutowego wynosi 10^4–$10^5\,\mathrm{cm}^{-1}$ w szerokim zakresie promieniowania [77]. Jest to wartość porównywalna z perowskitami ołowiowymi [62];

– promień atomowy Bi^{3+} jest zbliżony do promienia atomowego Pb^{2+}. Struktura perowskitu formowana jest tylko wtedy, kiedy poszczególne atomu budujące sieć posiadają odpowiednie rozmiary mieszczące się w tzw. czynniku tolerancji Goldschmidta opisanym poniższym równaniem:

$$t = \frac{r_A + r_B}{\sqrt{2} r_X + r_B} \tag{1.6}$$

gdzie r_A, r_B i r_X to promienie jonowe odpowiednich kationów i anionów w perowskicie o stechiometrii ABX_3. Aby powstał materiał o strukturze perowskitu, wartość t musi mieścić się w przedziale 0.8–1. Ogranicza to wybór możliwych kationów tylko do tych o odpowiednio małym promieniu jonowym [78];

– kation Bi^{3+} jest izoelektronowy względem Pb^{2+} — oba posiadają elektrony $6s^2$ i charakteryzują się zbliżonymi właściwościami chemicznymi [79]. Pasmo przewodnictwa zbudowane jest z antywiążących orbitali powstałych po hybrydyzacji orbitali $6p$ ołowiu lub bizmutu oraz $5p$ jodu, a wysokie stany pasma walencyjnego powstają w wyniku hybrydyzacji tych samych orbitali jodu z orbitalami $6s$ metalu. Przejścia z orbitali $6s$ do $6p$ bizmutu są odpowiedzialne za wysoką absorpcję perowskitów bizmutowych pomimo szerszej niż dla perowskitów ołowiowych przerwy wzbronionej [77, 61].

Opisane powyżej właściwości leżą u podstaw zbliżonych właściwości optoelektronicznych perowskitów ołowiowych i ich analogów opartych o bizmut. Jednak ze względu na różną wartościowość tych dwóch pierwiastków, istotne różnice pojawiają się w strukturze krystalograficznej analogów bizmutowych. Aby sieć krystalograficzna pozostała obojętna elektrycznie, jodobizmutany alkiloamoniowe krystalizują w innej strukturze niż ich oparte na ołowiu odpowiedniki. Z uwagi na różnorodność tworzonych struktur, perowskity bizmutowe również można sklasyfikować pod względem ich wymiarowości na struktury na zero-, jedno-, dwu- i trójwymiarowe.

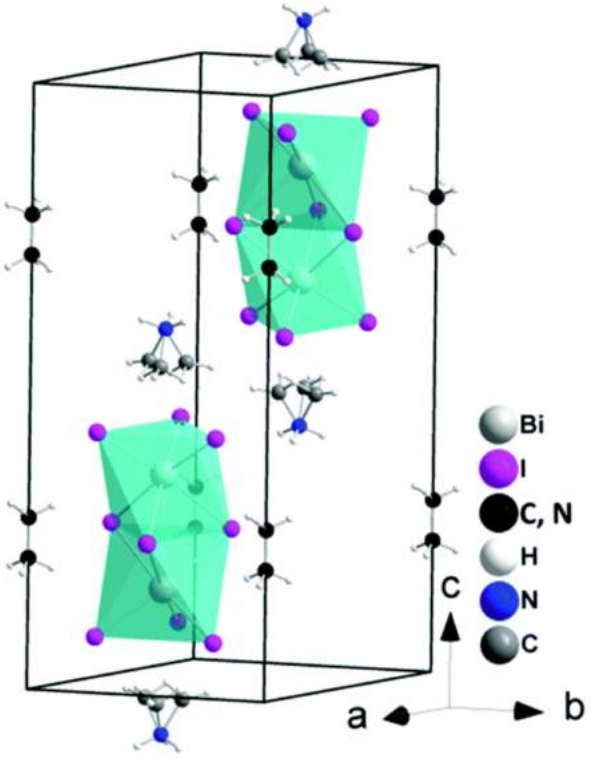

Rys. 1.5. Komórka elementarna $MABi_2I_9$ [81].

Bizmutowe struktury 0D powstają w wyniku reakcji jodku bizmutu(III) z jodkami tych samych kationów, z których krystalizowane są perowskity ołowiowe – najszerzej zbadanym związkiem w tej grupie jest jodobizmutan metyloamoniowy $MA_3Bi_2I_9$ (MA = CH_3NH_3), krystalizujący w układzie heksagonalnym (Rys. 1.5). Podobnie jak w $MAPbI_3$, pojedyncze oktaedry są tworzone przez kation Bi^{3+} i aniony jodkowe I^- znajdujące się w jego narożach, ale zamiast narożami połączone są płaszczyznami oktaedru wyznaczonymi przez trzy atomy jodu tworząc dimer [80]. Kolejne bioktaedry w strukturze krystalicznej oddzielone są kationami A^+ (w tym przypadku kationem metyloamoniowym $CH_3NH_3^+$, ale może być to m. in. kation cezowy Cs^+ lub formamidyniowy $CH_3(NH_2)_2^+$).

Podobnie jak w przypadku perowskitów ołowiowych, zmiana wymiarowości powodowana jest poprzez podstawienie poszczególnych elementów struktury innymi pierwiastkami lub związkami. Na przykład struktury 2D otrzymywane są poprzez domieszkowanie jednowartościowym kationem nieorganicznym o mniejszym promieniu jonowym niż Bi^{3+} (K^+, NH_4^+) bądź podstawienie Br^- lub Cl^- w miejsce I^- i charakteryzują się strukturą regularną [75].

Choć oddziaływanie perowskitów bizmutowych ze światłem jest słabsze niż perowskitów ołowiowych, to właściwości memrystywne tych materiałów są do siebie zbliżone. Obecność defektów strukturalnych i barier na złączach perowskit/elektroda powoduje

obecność pętli histerezy w pomiarach prądowo-napięciowych $I - V$ oraz efektów synaptycznych w pomiarach impulsowych [76, 64]. Z wyżej opisanych powodów jodobizmutany alkiloamoniowe, jako związki analogiczne do perowskitów ołowiowych, zostały wybrane do badań efektów neuromimetycznych, których wyniki przedstawiono w sekcjach 2.4 oraz 2.7 niniejszej rozprawy rozprawy doktorskiej.

1.3. Memrystory jako sztuczne synapsy

1.3.1. Plastyczność synaptyczna

Komórki nerwowe są podstawową jednostką tworzącą układ nerwowy. Typowy neuron zbudowany jest z ciała komórki (inaczej somy lub perikarionu), aksonu i dendrytów, za pomocą których neuron odbiera sygnały od innych neuronów lub receptorów (dendryt) i przesyła je do kolejnych (akson). Połączenie między dwiema komórkami nerwowymi, utworzone przez zakończenie aksonu jednego neuronu i dendryt drugiego nazywane jest synapsą. Nie jest to jednak połączenie fizyczne, ponieważ neurony odseparowane są od siebie szczeliną synaptyczną — przestrzenią o szerokości od ok. 20–500 nm, w zależności od typu neuronu [82]. Szacuje się, że w korze mózgowej ludzkiego mózgu znajduje się nawet ok. 5×10^{11} mld neuronów, a każdy z nich komunikuje się poprzez synapsy z 10^4 innymi neuronami. Ze względu na rodzaj przekazywanego bodźca, synapsy dzieli się na elektryczne i chemiczne. Oba te typy są liczne w układzie nerwowym, ale synapsy chemiczne występują w nim w dużo większej liczbie. Podstawowymi sygnałami elektrofizjologicznymi w układzie nerwowym są potencjały czynnościowe — krótkotrwałe, trwające ok. 2 ms przejściowe zmiany polaryzacji błony neuronu [83, 84]. Rozprzestrzeniając się wzdłuż aksonu, potencjały czynnościowe są odpowiedzialne za przekazywanie informacji do innych neuronów. Związana z aktywnością neuronalną plastyczność połączeń synaptycznych jest zjawiskiem leżącym u podstaw procesów uczenia w ludzkim mózgu.

Szczegółowy model wiążący procesy uczenia z plastycznością synaptyczną wywołaną przez jednoczesną lub niemal jednoczesną aktywację połączonych neuronów został zaproponowany w połowie XX wieku. W 1949 roku Donald Hebb sformułował zasadę, wedle której skorelowana czasowo aktywacja neuronu presynaptycznego i neuronu postsynaptycznego powoduje wzmocnienie połączenia synaptycznego [86]. Jeśli neuron presynaptyczny powoduje aktywację neuronu postsynaptycznego i w tym samym czasie sam jest aktywny, to stopniowo będzie stawał się coraz bardziej wydajny w aktywacji neuronu postsynaptycznego. Później odkryto, że jeśli to aktywność neuronu postsynaptycznego poprzedza aktywność neuronu presynaptycznego, to korelacja ta prowadzi do osłabienia

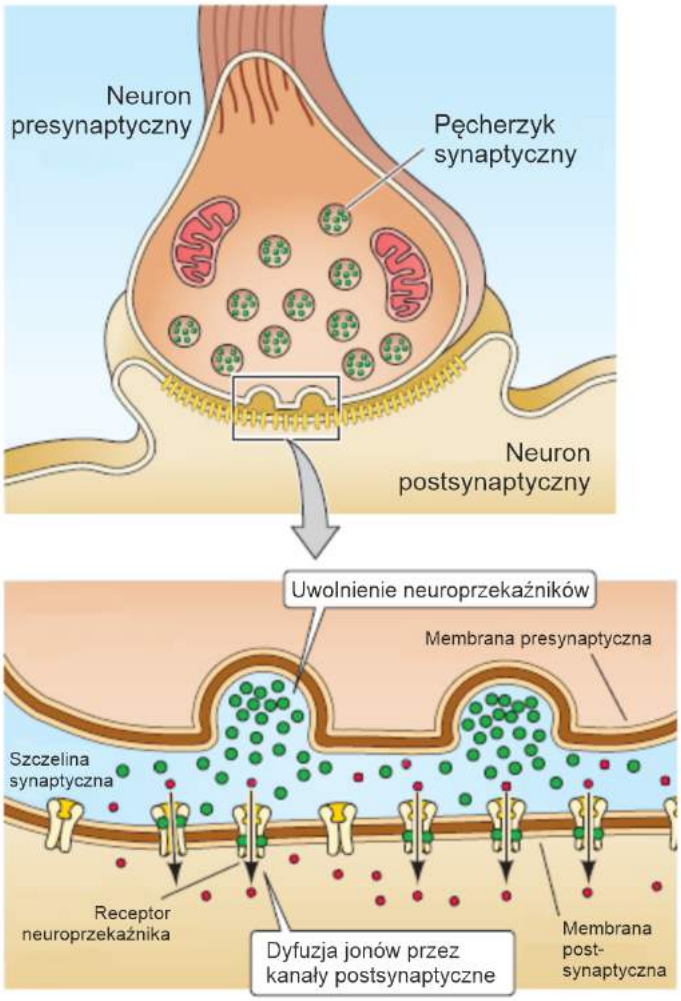

Rys. 1.6. Schematyczne przedstawienie budowy i działania synapsy chemicznej. Neuron presynaptyczny uwalnia cząsteczki neuroprzekaźnika, które wiążą się z odpowiednimi receptorami neuronu postsynaptycznego. Po związaniu cząsteczek neuroprzekaźnika kanały jonowe otwierają się, co pozwala na dyfuzję jonów do wnętrza komórki postsynaptycznej i generowanie prądów postsynaptycznych. Rysunek na podstawie [85].

połączenia synaptycznego.[3] Te zmiany wydajności połączenia synaptycznego manifestują się jako długotrwałe wzmocnienie synaptyczne (ang. *long-term potentiation*, LTP) i długotrwałe osłabienie synaptyczne (ang. *long-term depression*).

Na poziomie fizjologicznym przekaźnictwo synaptyczne zachodzi poprzez dyfuzję cząsteczek neuroprzekaźnika (neurotransmiterów) od neuronu presynaptycznego do postsynaptycznego przez szczelinę synaptyczną (Rys. 1.6). Ich uwolnienie do szczeliny jest odpowiedzią na pobudzenie zakończenia neuronu przez potencjał czynnościowy [82]. Wiążąc się z odpowiednimi receptorami w błonie neuronu postsynaptycznego, powodują dyfuzję jonów do jego wnętrza. W przypadku synaps pobudzających, w których neuroprzekaźnikiem jest glutaminian, w zależności od sposobu aktywacji synapsy może dojść do jej długotrwałego wzmocnienia lub osłabienia (depresji), co przejawia się, odpowiednio, jako powiększenie lub zmniejszenie pobudzających prądów postsynaptycznych, powstających w wyniku aktywacji receptorów dla glutaminianu. Plastyczność synaptyczna występuje również w synapsach hamujących, w których neuroprzekaźnikiem jest kwas gamma-aminomasłowy [82].

Wpływ na siłę połączenia synaptycznego ma także korelacja czasowa impulsów pre- i postsynaptycznych oraz ich kolejność. Zależność ta nosi nazwę *spike-timing-dependent plasticity* (STDP) [88]. W tym rodzaju plastyczności synaptycznej do LTP dochodzi, kiedy aktywność neuronu presynaptycznego poprzedza aktywność neuronu postsynaptycznego; LTD jest natomiast wynikiem aktywności neuronu postsynaptycznego poprzedzającej aktywność neuronu presynaptycznego (Rys. 1.7). W zależności od kolejności aktywności neuronów, możliwe jest zatem osłabienie lub wzmocnienie połączenia synaptycznego. Siła tego połączenia (waga synaptyczna) zależy od korelacji czasowej — im mniejszy interwał czasowy pomiędzy potencjałami czynnościowymi neuronów tym większa amplituda zmian siły. Gdy czas pomiędzy aktywnościami neuronów wzrasta, amplituda maleje. Z powodu tych właściwości STDP jest formą uczenia opisaną przez prawa sformułowane przez Hebba opisywane jest jako uczenie Hebba (ang. *Hebbian learning*), a krzywa przedstawiona na Rys. 1.7(a) krzywą uczenia Hebba.

Inną formą plastyczności synaptycznej jest *spike-rate-dependent plasticity*. W tym rodzaju plastyczności siła połączenia synaptycznego zależy od częstotliwości generowania impulsów przez neuron presynaptyczny. Im większa częstotliwość, tym większa amplituda zmian wagi synaptycznej [89, 90]. Oprócz długotrwałych form plastyczności synaptycznej, istnieją także krótkotrwałe procesy jej zmian, które również pełnią rolę w procesach nauki: krótkotrwałe wzmocnienie synaptyczne (ang. *short-term facilitation*, STP) i krótkotrwałe

[3]Oryginalna praca Hebba nie zawierała opisu osłabienia synaptycznego; model tego zjawiska został zaproponowany w późniejszym czasie [87].

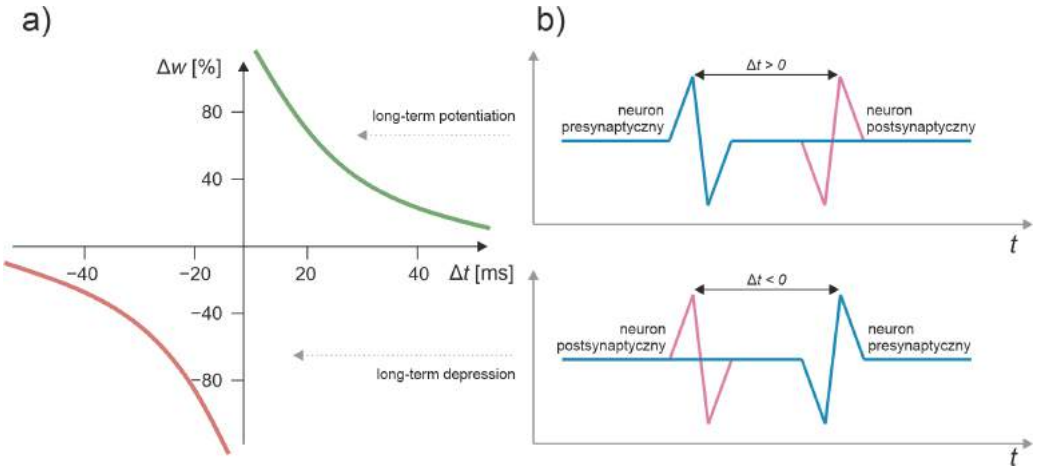

Rys. 1.7. (a) Funkcja opisująca STDP. W zależności od kolejności sygnałów generowanych prze neurony, waga synaptyczna δw ulega wzmocnieniu (*long-term potentiation*) lub osłabieniu (*long-term depression*. Amplituda tych zmian jest zależna od czasu pomiędzy impulsami δt. Rysunek na podstawie [92]. (b) Kolejność impulsów powodująca LTP i LTD. Neuron presynaptyczny generujący impuls przed neuronem postsynaptycznym prowadzi do wzmocnienia synaptycznego; jeśli kolejność impulsów zostaje odwrócona, połączenie synaptyczne ulega osłabieniu.

osłabienie synaptyczne (ang. *short-term depression*, STD). Odmianą STP jest np. *paired-pulse facilitation* (PPF), gdzie stosuje się jedynie dwa identyczne bodźce a amplituda prądu postsynaptycznego, powstającego w odpowiedzi na drugi bodziec, jest tym większa niż odpowiedź na pierwszy bodziec, im krótszy jest czas pomiędzy bodźcami [91].

Opisane powyżej formy nie są wszystkimi formami plastyczności synaptycznej, ale są najszerzej opisane w kontekście efektów neuromorficznych. Z tego powodu w niniejszej rozprawie poświęcono im najwięcej uwagi.

1.3.2. Efekty neuromimetyczne

Dzięki obecności pośrednich stanów rezystywnych pomiędzy skrajnymi HRS i LRS memrystory są zdolne do przetwarzania sygnałów w sposób zbliżony do biologicznych neuronów. Uzyskanie odpowiedzi prądowej o charakterystyce zbliżonej do opisanych wyżej krzywych uczenia się w neuronach możliwe jest dzięki przełączeniu memrystora do stanów pośrednich. Takie zjawiska nazywa się efektami neuromimetycznymi lub neuromorficznymi. Do tej pory w memrystorach opisano wiele typów naśladujących plastyczność synaptyczną, m. in. STDP [93, 94], SRDP [18], *spike-voltage-dependent plasticity*

[95], *paired-pulse faciliation*, plastyczność krótkotrwałą czy metaplastyczność [96]. Podobieństwo tych efektów pozwoliło na przetworzenie sygnałów pochodzących od neuronów przez układ memrystorów [97, 98].

Memrystory wykazujące efekty neuromorficzne bywają nazywane sztucznymi synapsami. Analogia ta dotyczy nie tylko funkcjonalności, ale także budowy urządzeń memrystywnych. Przełączanie rezystywne (w zależności od mechanizmu) opiera się na migracji wewnątrz struktury memrystora nośników ładunku lub defektów struktury krystalograficznej. Przyłożenie napięcia pomiędzy dolną i górną elektrodą (neuron presynaptyczny i postsynaptyczny) wywołuje ruch nośników wewnątrz materiału (odpowiednik synapsy), powodując przełączenie memrystora w stan o wyższej konduktancji. Skutkuje to przepływem prądu o wyższej amplitudzie (wzmocnienie synaptyczne, potencjacja), a odwrotny proces — przełączenie do stanu o niższej konduktancji — zmniejsza jego amplitudę (osłabienie synaptyczne, depresja). W tym kontekście, waga synaptyczna Δw jest względną różnicą prądu zmierzonego przed przyłożeniem napięcia I_{before} i po przyłożeniu napięcia przełączającego I_{after}.

$$\Delta w = \frac{I_{after} - I_{before}}{I_{before}} \tag{1.7}$$

Na Rys. 1.8(a) przedstawiono krzywą uczenia Hebba uzyskaną w pomiarze STDP zarejestrowaną w komórkach hipokampu szczura z widocznymi gałęziami potencjacji i depresji [88]. Rys. 1.8(b) przedstawia z kolei krzywą STDP zarejestrowaną w memrystorze opartym o jodobizmutan metyloamoniowy. Zgodnie z postulatem Hebba, efekt ten uzyskano przykładając impulsy napięcia odpowiednio do górnej i dolnej elektrody i zmniejszając interwał czasowy pomiędzy nimi oraz odwracając ich kolejność aby uzyskać efekt przeciwny. Wynik ten dowodzi, że memrystory zdolne są do przetwarzania sygnału w sposób podobny do neuronów.

1.3.3. Zastosowanie memrystorów w układach neuromorficznych

Układy obliczeniowe oparte na memrystorach mogą być odpowiedzią na wąskie gardło architektury von Neumanna. Możliwość przechowywania i przetwarzania danych w jednym układzie elektronicznym eliminuje konieczność ciągłego przesyłania tych danych pomiędzy procesorem i pamięcią — procesu, którego znanego jako *memory wall* i stanowiącego obecnie największe ograniczenie szybkości przetwarzania danych przez współczesne komputery [35].

Ograniczenie to nie istnieje w układach memrystorowych. Dzięki temu, że nie ma potrzeby przesyłania danych, operacje matematyczne takie jak mnożenie macierzy i wektorów czy regresja liniowa wykonywane są przez memrystory z dużo wyższą szybkością niż

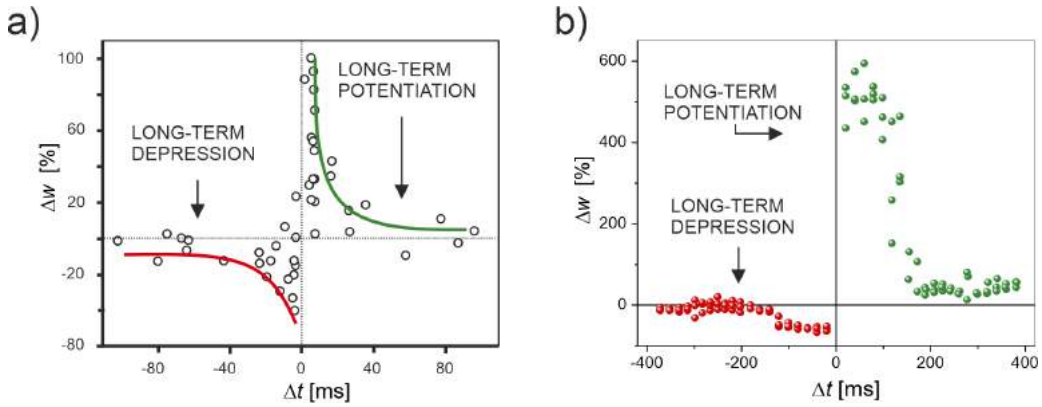

Rys. 1.8. Porównanie STDP w biologicznych neuronach i w memrystorze. (a) Krzywa uczenia Hebba zmierzone w neuronach hipokampu szczura. Reprodukcja z [88]. (b) Krzywa uczenia Hebba uzyskane w memrystorze wykorzystującym jodobizmutan metyloamoniowy jako materiał aktywny [64].

przez klasyczne układy elektroniczne [99, 100]. Możliwość przechowywania wielu stanów logicznych informacji w formie konduktancji urządzenia pozwala także na zbudowanie hardware'owych sztucznych sieci neuronowych, w których memrystory — dzięki wysokiej wydajności wykonywania operacji mnożenia macierzowego — pozwalają na szybszy proces trenowania sieci oraz równocześnie przechowują wyniki tych operacji w postaci wag synaptycznych [101, 102]. Szerszy opis zastosowania układów memrystorowych do wykonywania operacji matematycznych oraz sieci neuronowych opartych na memrystorach znajduje się w rozdziale 2.3, a wykorzystanie ich w roli układów kryptograficznych w rozdziale 2.2.

Memrystory perowskitowe także mogą być łączone w układy i przechowywać zapisaną w nich informację, charakteryzując się przy tym czasami retencji sięgającymi nawet 7×10^9 s i krótkimi czasami przełączania rzędu 200 ps, dzięki czemu energia potrzebna do przełączenia stanu rezystywnego jest na poziomie tej w biologicznych synapsach [103, 104]. Ze względu na możliwość emulowania plastyczności synaptycznej, częściej niż jako układy pamięciowe memrystory perowskitowe badane są w kontekście implementacji modeli sztucznych sieci neuronowych, w których są one wykorzystywane są jako węzły (neurony) sieci. Na przykład sieć neuronowa oparta na perowskicie $PEA_2MA_{n-1}Pb_nI_{3n+1}$ (PEA — kation fenyloetyloamoniowy) zbudowana z 784 neuronów w warstwie wejściowej sieci oraz trzech warstw o wymiarach $5 \times 4 \times 5$ jest w stanie z wysoką wydajnością klasyfikować obrazy. Na podstawie zbioru zawierającego zdjęcia odzieży i obuwia uzyskano dokładność rozpoznawania typu przedmiotu na poziomie 86% [103]. Sieć neuronowa oparta na

$MAPbBr_3$, w której parametry pojedynczych neuronów oparto na charakterystyce uczenia Hebba w pomiarze STDP, jest w stanie rozpoznawać odręczne pismo z dokładnością 80.8% [105]. Zbliżony wynik uzyskano także dla sztucznej sieci neuronowej opartej $MAPbI_3$, w której dokładność na tym samym zbiorze danych wyniosła 81.8% [106]. Przykład memrystywnej sztucznej sieci neuronowej opartej o jodobizmutan butyloamoniowy $(C_4H_9NH_3)_3BiI_6$, której dokładność klasyfikacji pisma odręcznego wynosi 94%, przedstawiono w artykule streszczonym w rozdziale 2.7.

1.3.3.1. Układy memrystywne w optoelektronice

Równie ciekawym przykładem zastosowania memrystorów perowskitowych są układy optoelektroniczne. Przykładem jest macierz perowskitowych nanodrutów $FAPbI_3$ osadzonych na elastycznym podłożu, która może pełnić funkcje biomimetyczne, naśladując funkcje fotoreceptorów w siatkówce ludzkiego oka [107]. Urządzenie charakteryzuje się wysoką czułością w szerokim zakresie intensywności światła (od $0.3\,\mu W\,cm^{-2}$ do $50\,mW\,cm^{-2}$) i zdolne jest do rozpoznawania wzorów optycznych w całym zakresie światła widzialnego (400–810 nm). Układ fototranzystorów o hybrydowej strukturze $CsPb(Br_{1-x}I_x)_3/MoS_2$ jest w stanie emulować adaptację sensoryczną — obniżenie odpowiedzi na bodziec (w tym przypadku światło) podczas ciągłej ekspozycji na niego, będącą istotną funkcją układu nerwowego [108].

Efekt pamięci w memrystorze może być także wywołany światłem. W macierzy memrystorów $MAPbBr_3$, w których stan rezystywny jest kontrolowany poprzez selektywne oświetlanie wybranych pikseli, zapisana informacja może zostać odczytana poprzez pomiar stanów rezystywnych poszczególnych memrystorów [109].

Interakcja światła z procesami przełączania rezystywnego otwiera drzwi nowym zastosowaniom układów memrystorów w optoelektronicznych układach neuromorficznych. Dzięki silnemu oddziaływaniu ze światłem, hybrydowe perowskity wydają się być jednymi z najbardziej obiecujących materiałów. Opisane wyżej badania stanowią pierwsze kroki w kierunku budowy urządzeń, które dzięki swoim właściwościom mogą pełnić niektóre funkcje sztucznego oka. Mogą także znaleźć zastosowanie w neuromorficznych układach optoelektronicznych wykorzystywanych przez szeroko pojęte rozwiązania oparte na uczeniu maszynowym i sztucznej inteligencji. Przykład indukowania efektów synaptycznych światłem w memrystorze perowskitowym przedstawiono w rozdziale 2.6.

1.4. Motywacja i cel badań

Memrystory mogą przetwarzać informacje w sposób zbliżony do neuronów — zjawiska te nie są jednak wciąż w pełni poznane, a związek efektów neuromimetycznych ze procesami fizycznymi w materiale nie jest w całości zbadany.

Celem prowadzonych przeze mnie badań było powiązanie własności fizykochemicznych cienkich warstw perowskitów i materiałów do nich analogicznych z efektami neuromimetycznymi oraz zbadanie możliwości odtworzenia efektów neuromimetycznych w tych materiałach. Zrozumienie fizycznych podstaw tych efektów pozwoli na projektowanie materiałów o określonych parametrach optoelektronicznych i memrystywnych.

Motywacją do badania perowskitów oraz materiałów o zbliżonej budowie i składzie były ich właściwości optoelektroniczne, potencjalnie pozwalające na kontrolowanie efektów memrystywnych za pomocą światła. Możliwość wykorzystania chemicznych metod ich syntezy pozwala na stosunkowo łatwe zmiany stechiometrii materiału i pozwala na wpływanie na jego właściwości fizykochemiczne, a w efekcie także memrystywne i neuromorficzne.

Niniejsza rozprawa składa się z cyklu prac przedstawiających metodologię i opis efektów neuromimetycznych w różnego typu materiałach na bazie hybrydowych organiczno-nieorganicznych perowskitów halogenkowych oraz materiałów o powiązanym składzie. Łączy w sobie syntezę, charakterystykę materiałową i badanie właściwości memrystywnych urządzeń opartych o perowskity lub materiały analogiczne w kontekście efektów neuromimetycznych.

Przedstawione w niniejszej rozprawie powiązanie mechanizmów fizycznych z efektami neuromimetycznymi w perowskitach i ich analogach stanowi krok na drodze ich wykorzystania w neuromorficznych układach elektronicznych.

ROZDZIAŁ 2

Streszczenia artykułów wchodzących w skład rozprawy

W skład niniejszej rozprawy wchodzą streszczenia poniższych artykułów naukowych:

1. Klejna, S., Mazur, T., Wlaźlak, E., **Zawal, P.**, Soo, H. S., Szaciłowski, K. *Halogen-containing semiconductors: From artificial photosynthesis to unconventional computing*, Coordination Chemistry Reviews, 2020, 415, 213316.

2. Lis, M., Onuma, S., Przyczyna, D., **Zawal, P.**, Mazur, T., Pilarczyk, K., Gentili, P. L., Kasai, S., Szaciłowski, K. *From Oscillatory Reactions to Robotics: A Serendipitous Journey Through Chemistry, Physics and Computation*, Handbook of Unconventional Computing, 2021, 1-79.

3. Przyczyna, D., **Zawal, P.**, Mazur, T., Strzelecki, M., Gentili, P. L., Szaciłowski, K. *In-materio neuromimetic devices: dynamics, information processing and pattern recognition*, Japanese Journal of Applied Physics, 2020, 59 (5), 050504.

4. Mazur, T.*, **Zawal, P.***, Szaciłowski, K. *Synaptic plasticity, metaplasticity and memory effects in hybrid organic-inorganic bismuth-based materials*, Nanoscale, 2019, 11 (3), 1080-1090.

5. Wlaźlak, E., Kalinowska-Tłuścik, J., Przyczyna, D., **Zawal, P.**, Szaciłowski, K. *Bismuth triiodide complexes: Structure, spectroscopy, electronic properties, and memristive properties*, Journal of Materials Chemistry C, 2020, 8 (18), 6136-6148.

6. **Zawal, P.***, Mazur, T.*, Lis, M., Chiolerio, A., Szaciłowski, K. *Light-Induced Synaptic Effects Controlled by Incorporation of Charge-Trapping Layer into Hybrid Perovskite Memristor*, Advanced Electronic Materials, 2022, 8 (4), 2100838.

*Wkład autorów w prowadzenie badań i przygotowanie artykułu był równy.

7. **Zawal, P.**, Das, D., Gryl, M., Sławek, A., Abdi, G., Gerouville, E., Marciszko-Wiąckowska, M., Marzec, M., Hess, G., Georgiadou, D., Szaciłowski, K. *Leaky integrate-and-fire model and short-term synaptic plasticity emulated in a novel bismuth-based diffusive memristor*, (...)

Artykuły 1-3 są artykułami przeglądowymi i stanowią wprowadzenie teoretyczne oraz naznaczają kontekst niniejszej pracy. Artykuł 1 opisuje własności optoelektroniczne perowskitów, podczas gdy artykuły 2 i 3 skupiają się na zastosowaniach memrystorów w układach elektronicznych.

Artykuły 4-7 są artykułami badawczymi, w których opisano efekty neuromorficzne w perowskitach i ich analogach oraz innych materiałach. Artykuły 5 i 7 nie dotyczą perowskitów ani materiałów analogowych, jednak ze względu na interesujące opisane w nich efekty neuromorficzne zdecydowano na włączenie ich do niniejszej rozprawy.

Na czas składania niniejszej rozprawy doktorskiej artykuł 7 znajduje się w procesie recenzji. Badania w nim zawarte stanowią jednak bardzo istotną część niniejszej rozprawy i opisują nowe rodzaje efektów neuromimetycznych oparte o filamentowy mechanizm przełączania rezystywnego, dlatego uznano, że artykuł ten powinien także stanowić jej część.

Poniższe streszczenia dotyczą jedynie tych fragmentów artykułów, w których przygotowaniu brałem bezpośredni udział bądź wykonywałem pomiary i przeprowadzałem analizę wyników. Wyjątek stanowi streszczenie artykułu 5, w którym aby wyjaśnić zaobserwowane efekty neuromimetyczne konieczne było także streszczenie fragmentu pracy dotyczącego fizycznego mechanizmu powstawania bariery energetycznej na złączu półprzewodnika i metalu. Ponadto symulacja sztucznej sieci neuronowej w streszczeniu artykułu 7 przeprowadzona została przez innego współautora artykułu na podstawie wyznaczonych przeze mnie parametrów memrystora.

2.1. Halogen-containing semiconductors: From artificial photosynthesis to unconventional computing

2.1.1. Wstęp

Hybrydowe perowskity jodkowo-ołowiowe o wzorze sumarycznym $CH_3NH_3PbI_3$, początkowo badane jako sensybilizatory w ogniwach słonecznych opartych o TiO_2, w krótkim czasie zyskały duże zainteresowanie ze względu na bardzo wysoką wydajność generowania nośników ładunku w wyniku absorpcji fotonów. W przeciągu zaledwie 10 lat badań, wydajność perowskitowych ogniw słonecznych osiągnęła niemal 26% [110] i zbliża się już do teoretycznego limitu wydajności wynoszącego dla perowskitów hybrydowych ok. 30% [111]. W połączeniu z niskimi kosztami produkcji oraz chemicznymi metodami wytwarzania umożliwiającymi łatwą modyfikację własności optoelektronicznych perowskitów, stały się one jednymi z najszerzej badanych materiałów w obszarze konwersji energii słonecznej na prąd.

W artykule opisano właściwości optoelektroniczne hybrydowych perowskitów halogenkowych w kontekście ich interakcji ze światłem. Dla zachowania klarowności tekstu określenie *perowskit* w niniejszym streszczeniu używane jest w kontekście grupy hybrydowych materiałów o strukturze perowskitu, bez ograniczenia jedynie do perowskitu jodkowo-ołowiowego.

2.1.2. Streszczenie

Po absorpcji fotonu o energii wyższej niż szerokość przerwy wzbronionej materiału generowane są ekscytony, które (przy braku rekombinacji) ulegają dysocjacji do pary elektron-dziura. Powstałe w tym procesie swobodne nośniki ładunku przenoszone są przez kolejne warstwy transportowe ogniwa do elektrod. Zaabsorbowane światło konwertowane jest więc na energię elektryczną, a wysoką wydajność konwersji perowskity zawdzięczają swoim własnościom optoelektronicznym.

Jedną z tych własności jest wysoki współczynnik absorpcji, który określa drogę swobodną fotonu przed jego absorpcją w materiale i w perowskicie jodkowo-ołowiowym wynosi on 1×10^4–$1 \times 10^5\,\mathrm{cm}^{-1}$. W połączeniu ze stromą krawędzią absorpcji i niskimi wartościami energii Urbacha świadczącymi o niskiej koncentracji pułapek nośników ładunku w obrębie przerwy wzbronionej, perowskity mogą zaabsorbować nawet 90 % promieniowania z zakresu 300–500 nm.

Kolejną cechą poprawiającą wydajność ogniwa jest niska energia dysocjacji ekscytonów, wynosząca ok. 5–16 meV, a zatem niższa niż wartość kT w temperaturze pokojowej

(ok. 26 meV). Cecha ta sprzyja generowaniu swobodnych nośników ładunku zamiast ekscytonów.

Droga dyfuzji elektron-dziura w jodkowo-ołowiowych perowskitach przekracza 100 nm, ale jej wartość w materiałach o pokrewnym składzie może być znacznie wyższa. W perowskitach z mieszanymi anionami Pb-Cl wynosi ona 1 µm, a w monokrystalicznych perowskitach z kationem formamidyniowym 6.6 µm (dla $FAPbI_3$) lub nawet 19 µm (dla $FAPbBr_3$). Dzięki tak dużym wartościom drogi dyfuzji oraz wysokiemu współczynnikowi absorpcji, nośniki ładunku mogą być przetransportowane do elektrod zanim zajdzie ich rekombinacja.

Własności optoelektroniczne perowskitów mogą być modulowane poprzez podstawienie każdego ze składników struktury perowskitu. Zależność szerokości przerwy wzbronionej od składu perowskitu te przedstawiono na Rys. 2.1. Wymiana kationu i anionu w perowskicie powoduje zmiany wielkości jego komórki elementarnej, co w efekcie wpływa na własności optoelektroniczne. Poprzez całkowite lub częściowe podstawienie anionów i kationów w strukturze perowskitu, możliwe jest manipulowanie szerokością jego przerwy wzbronionej w szerokim zakresie energii. Przerwa wzbroniona $CH_3NH_3PbI_3$ wynosi ok. 1.5–1.6 eV (wartości te odpowiadają zakresowi długości fali 775–826 nm). Podstawienie anionu jodkowego I^- anionem Br^- lub Cl^- prowadzi do przesunięcia hipsochromowego i zwiększenia szerokości przerwy wzbronionej do ok. 2.28 eV dla $CH_3NH_3PbBr_3$ i ok. 2.95 eV dla $CH_3NH_3PbCl_3$.

Z punktu widzenia zastosowania w ogniwach słonecznych, bardziej pożądane jest jednak zmniejszenie szerokości przerwy wzbronionej celem absorpcji szerszego zakresu promieniowania, co można osiągnąć poprzez zmianę kationu organicznego. Podstawienie kationu metyloamoniowego kationem formamidyniowym skutkuje przesunięciem batochromowym krawędzi absorpcji o ok. 20 nm do wartości ok. 806 nm.

Podstawienie kationu nieorganicznego zwykle skutkuje bardziej skomplikowanymi zmianami szerokości przerwy wzbronionej. Wymieniając część atomów ołowiu w $CH_3NH_3PbI_3$ na atomy cyny, zależność przerwy wzbronionej od ułamka molowego atomów cyny w strukturze ma nieliniowy charakter odstępujący od liniowej zależności (empirycznego prawa Vegarda) obserwowanej dla podstawień kationu organicznego i anionu.

Przez silne oddziaływanie ze światłem, w perowskitach zaobserwowano wiele zjawisk zachodzących pod jego wpływem. Przy ciągłym oświetleniu obserwowana jest fotoindukowana migracja jonów. W wyniku pułapkowania fotogenerowanych nośników ładunku w przypowierzchniowych stanach pułapkowych, powstałe pole elektryczne powoduje migrację anionów jodkowych zgodnie z gradientem tego pola. W przypadku mieszanych struktur zawierających różne rodzaje anionów, fotoindukowana migracja prowadzi do segregacji fazowej. W perowskicie $CH_3NH_3Pb(Br_xI_{1-x})$ aniony jodkowe i bromkowe migrują

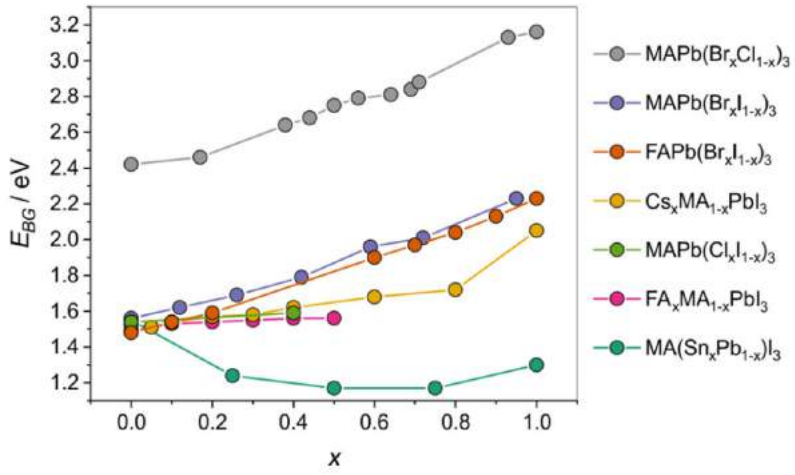

Rys. 2.1. Zależność szerokości przerwy wzbronionej od składu wybranych związków o strukturze perowskitu. W przypadku podstawienia ołowiu atomami cyny, widoczne jest odstępstwo od liniowego prawa Vegarda.

tworząc domeny z dużą koncentracją anionów jodkowych o małej przerwie wzbronionej i domeny z dużą koncentracją anionów bromkowych o większej przerwie wzbronionej, powodując powstanie dodatkowych pułapek elektronowych. Z punktu widzenia wydajności ogniw słonecznych, procesy migracji i segregacji są niekorzystnymi zjawiskami, ponieważ obniżają wydajność ogniwa i mogą prowadzić do szybszej degradacji struktury perowskitu.

Innym przykładem interakcji perowskitów ze światłem jest rozszerzanie sieci krystalicznej pod wpływem ciągłego oświetlania, prowadzące do relaksacji lokalnych naprężeń sieci, w efekcie zwiększając wydajność ogniwa. Oświetlając perowskity podczas ich syntezy, otrzymuje się materiały o wyższej krystaliczności i lepszych parametrach w kontekście ich zastosowania w ogniwach słonecznych.

W ostatnich latach badane są także perowskity o zredukowanej wymiarowości struktury krystalograficznej, które oprócz wyższej stabilności względem konwencjonalnej struktury 3D posiadają własności optoelektroniczne pozwalające na ich wykorzystanie nie tylko w roli ogniw słonecznych (szczególnie w układach mieszanych perowskitów 2D i 3D), ale także jako materiały elektroluminescencyjne.

W porównaniu do perowskitów 3D, niskowymiarowe perowskity składają się z pojedynczej (2D) lub wielu (quasi-2D) warstw nieorganicznych odseparowanych od siebie przez molekuły organiczne, a ich skład opisuje równanie $R_2A_{n-1}B_nX_{3n+1}$, gdzie R jest alkiloamoniowym kationem separującym n warstw nieorganicznych. Powszechnie klasyfikuje się perowskity 2D ($n = 1$), quasi-2D ($n = 2 - 5$) i quasi-3D ($n > 5$), które przy

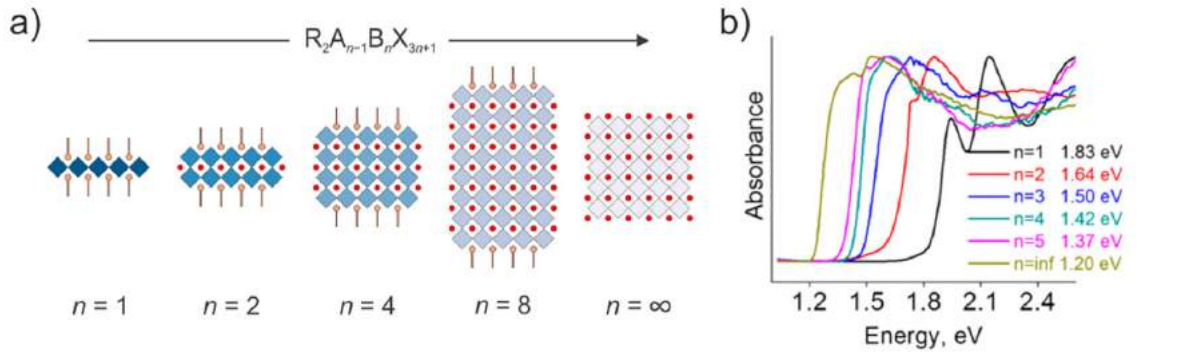

Rys. 2.2. Modulacja przerwy wzbronionej niskowymiarowych perowskitów. (a) Schemat zmiany wymiarowości perowskitu wraz ze zmianą liczby warstw nieorganicznych n od struktury 2D ($n = 1$), poprzez struktury quasi-2D i quasi-3D aż do 3D ($n = \infty$). (b) Przesunięcie krawędzi absorpcji dla $(BA)_2MA_{n-1}Sn_nI_{3n+1}$ w stronę wyższych energii wraz z malejącą liczbą warstw nieorganicznych n.

wyższej liczbie warstw ($n \to \infty$) uznawane są za struktury 3D. Rysunki struktur 3D, 2D i pośrednich przedstawiono na Rys. 2.2(a).

Szerokość przerwy wzbronionej perowskitów niskowymiarowych może być kontrolowana w taki sposób, aby pokryć cały zakres światła widzialnego. Efekt ten można osiągnąć zmieniając liczbę warstw nieorganicznych n. W związku o wzorze $(BA)_2MA_{n-1}Pb_nI_{3n+1}$ (gdzie BA — kation butyloamoniowy $C_4H_9NH_3^+$) krawędź absorpcji przesuwa się w stronę wyższych energii wraz z malejącą liczbą n; dla struktury 3D ($n \to \infty$) wynosi 1.50 eV, rosnąc kolejno do 1.91 eV ($n = 4$), 2.03 eV ($n = 3$) i 2.17 eV ($n = 2$) i finalnie osiągając wartość 2.43 eV dla struktury 2D ($n = 1$). Podobne zmiany zaobserwowano także w $(BA)_2MA_{n-1}Sn_nI_{3n+1}$, gdzie przerwa wzbroniona dla perowskitu 3D wzrasta z 1.20 eV do 1.83 eV dla perowskitu 2D (Rys. 2.2(b)). Innym sposobem manipulowania szerokością przerwy wzbronionej jest także zmiana kationu separującego warstwy nieorganiczne na kation o innym rozmiarze.

Z powodu różnicy stałych dielektrycznych pomiędzy warstwami nieorganicznymi i kationem separującym te warstwy oraz powstawaniem studni potencjału dla niskowymiarowych struktur o $n \leq 2$, materiały te na widmach absorpcji cechują się wyraźnym pasmem ekscytonowym (widocznym na Rys. 2.2(b) dla $n = 1$), które świadczy o generacji ekscytonów o wysokiej energii wiązań. Możliwość kontroli parametrów ekscytonów ma istotne znaczenie w zastosowaniach perowskitów w urządzeniach elektroluminescencyjnych, gdyż wydajność kwantowa fotoluminescencji jest skorelowana z energią wiązania ekscytonów. Obecna wydajność diod elektroluminescencyjnych opartych o perowskity 2D

wynosi 18.2 % w szerokim zakresie spektralnym. Dzięki możliwościom kontroli przerwy wzbronionej perowskitów, otrzymano także diody emitujące światło białe.

Innym potencjalnym zastosowaniem niskowymiarowych perowskitów są fotodetektory. Przypuszcza się, że duże kationy organiczne w roli warstw separujących obniżają koncentrację defektów w materiale, co w fotodetektorach przekłada się na niski poziom szumu elektronowego i wysokie czułości rzędu 10^{13} Jonesów. Ponadto, dichroizm wynikający z anizotropii optycznej perowskitów 2D pozwala na detekcję promieniowania o zadanej polaryzacji i przy wielu długościach fali.

Ostatnim z opisanych zastosowań jest wykorzystanie perowskitów 2D w elektronice spinowej (spintronice) poprzez modulowanie efektu gigantycznego rozszczepienia spinowego (tzw. duży efekt Rashby, ang. *giant Rashba splitting*). W niskowymiarowych perowskitach na poziomie struktury wynika on ze zniesienia symetrii inwersji, które jest efektem sprzężenia spin-orbita spowodowanego przemieszczeniem wiązań pomiędzy ciężkimi pierwiastkami w strukturze (Pb, I). Zniesienie degeneracji powoduje separację stanów energetycznych związanych ze spinem elektronu. Wielkość tego efektu może być dodatkowo kontrolowana poprzez zmianę wymiarowości. Czyni to perowskity niskowymiarowe interesującymi materiałami do zastosowań w spintronice.

2.1.3. Podsumowanie

W dwóch sekcjach artykułu omówiono powiązanie własności optoelektronicznych ze strukturą perowskitów. Kontrola szerokości przerwy wzbronionej w perowskitach 3D odbywa się przede wszystkim poprzez domieszkowanie poszczególnych składników struktury innymi pierwiastkami, pozwalając na jej zmianę w szerokich zakresach oraz zwiększenie stabilności struktury perowskitowej. W perowskitach niskowymiarowych efekt ten osiągany jest przede wszystkim poprzez zmianę wymiarowości perowskitu. Wymiarowość pozwala także na kontrolę innych właściwości optoelektronicznych materiału, np. energii wiązań ekscytonów czy rozszczepienia spinowego. Opisane szerokie możliwości kontroli tych parametrów poprzez zmianę parametrów struktury krystalicznej materiału czynią perowskity bardzo interesującymi materiałami pod względem ich wykorzystania w ogniwach słonecznych, fotodetektorach czy elektronice spinowej.

2.2. In-materio neuromimetic devices: dynamics, information processing and pattern recognition

2.2.1. Wstęp

W artykule przedstawiono zastosowanie memrystorów w fizycznie nieklonowalnych funkcjach (ang. *physically unclonable function*, PUF). Są to fizyczne urządzenia, których zadaniem jest zapewnienie unikalnej sygnatury użytkownika — tzw. odcisku palca (ang. *fingerprint*) — w celu zapewnienia bezpieczeństwa weryfikacji. Poprzez zestaw trudnych do podrobienia cech fizycznych, urządzenia takie są niemal niemożliwe do zduplikowania, zapewniając zwiększone bezpieczeństwo względem innych systemów uwierzytelniania przy niższych kosztach. W artykule zawarto opis cech memrystorów, które pozwalają na ich wykorzystanie w urządzeniach PUF oraz opis implementacji urządzenia opartego na macierzy memrystorów.

2.2.2. Streszczenie

Smartfony stały się uniwersalnym narzędziem w codziennym życiu, służąc między innymi do przechowywania wrażliwych danych, takich jak dokumenty tożsamości, oraz do uwierzytelniania i autoryzacji użytkownika w operacjach finansowych. W wymienionych zastosowaniach wymagających bezpieczeństwa szczególnie istotny jest rozwój metod, pozwalających na bezpieczne i pewne uwierzytelnienie. Obecne systemy uwierzytelniania opierają się na statycznej pamięci RAM i nieulotnych pamięciach jednokrotnego zapisu, ale zastosowania te wymagają dodatkowych układów szyfrujących lub podpisów cyfrowych, co komplikuje ich zastosowanie. Dodatkowo wymagają one ciągłego zasilania.

Tańszą alternatywą są układy PUF, które dla każdego sygnału wejściowego c (tzw. *challenge*) generują unikalną odpowiedź r (*response*) według równania $r = f(c)$, a pary *challenge-response* przechowywane są w zabezpieczonej bazie danych. Jeśli odpowiedź na dany sygnał znajduje się w bazie danych, użytkownik lub urządzenie jest uwierzytelniane. Korzyścią tego rozwiązania jest fakt, iż odpowiedź generowana jest na podstawie fizycznych parametrów urządzenia i nie musi być przechowywana w pamięci w postaci klucza, wykluczając tym samym konieczność ciągłego zasilania. Układy PUF wymagają kilku cech aby pełnić rolę systemów uwierzytelniania:

1. Odpowiedź musi być niemożliwa do przewidzenia i unikalna dla każdego sygnału wejściowego. Wymaganie to oznacza, że funkcja generująca parę *challenge-response* nie może być trywialna.

2. Odpowiedź na dany sygnał wejściowy musi być powtarzalna. W odróżnieniu od generatorów liczb losowych, wielokrotne podawanie takiego samego sygnału wejściowego musi skutkować zawsze taką samą odpowiedzią.

3. Nawet posiadając kompletną wiedzę o budowie danego układu PUF, niemożliwe jest zbudowanie innego urządzenia o identycznych parametrach (nieklonowalność urządzenia).

Wymagania te mogą zostać spełnione poprzez zmienność cech urządzenia wynikającą z procesu produkcyjnego bądź z wewnętrznej zmienności parametrów fizycznych urządzenia lub materiału, przez co prawdopodobieństwo wytworzenia dwóch urządzeń o takich samych parametrach jest niskie, nawet jeśli zostaną one otrzymane w jednym procesie produkcyjnym. Dzięki temu niemożliwe jest wytworzenie kopii układu PUF o takich samych parametrach. Unikalny zestaw parametrów fizycznych urządzenia zapewnia także unikalną odpowiedź na zadany sygnał wejściowy i dopóki parametry te nie ulegną zmianie, odpowiedź urządzenia jest powtarzalna.

Jednymi z elementów elektronicznych, które można wykorzystać w układach PUF są nieulotne pamięci i memrystory, w których przełączanie rezystywne opiera się na tworzeniu i niszczeniu filamentu przewodzącego poprzez przyłożenie napięcia o odpowiedniej amplitudzie i polaryzacji, zmieniając stan urządzenia na wysoko i nisko przewodzący. Zjawisko to jest w pewnym stopniu stochastyczne, przez co tworzenie i niszczenie filamentu zachodzi nie przy danej wartości napięcia, ale w pewnym zakresie napięć. Dzięki tej zmienności, jeśli początkowy stan urządzenia jest nieznany, niemożliwe jest przewidzenie jaki prąd popłynie przez urządzenie, nie można bowiem określić czy przewodzący filament ulegnie utworzeniu lub zniszczeniu. Aby zwiększyć bezpieczeństwo, memrystory łączone są w układy typu *crossbar*, w których poszczególne elementy połączone są siatką elektrod w macierze (Rys. 2.3(a)).

W macierzach memrystorów wybór elementu odbywa się poprzez przyłożenie napięcia pomiędzy odpowiednimi elektrodami. Na Rys. 2.3(b) przez element wybrany poprzez przyłożenie napięcia V_c pomiędzy dwiema zaznaczonymi elektrodami, przez memrystor o konduktancji G_{ij} płynie prąd (niebieska strzałka) o amplitudzie zależnej od wartości konduktancji. Czerwoną strzałką oznaczono prąd *sneak-path* płynący przez memrystory sąsiadujące z wybranym memrystorem. Odpowiedź układu jest zatem funkcją napięcia, prądu płynącego przez element o konduktancji G_{ij} oraz prądów *sneak-path* płynących przez sąsiadujące elementy o nieznanej konduktancji. O ile zjawisko to jest niekorzystne w kontekście wykorzystania macierzy memrystorów jako układów pamięci lub układów obliczeniowych, to w układach PUF zwiększa ono bezpieczeństwo poprzez zwiększenie złożoności odpowiedzi układu na zadany sygnał wejściowy.

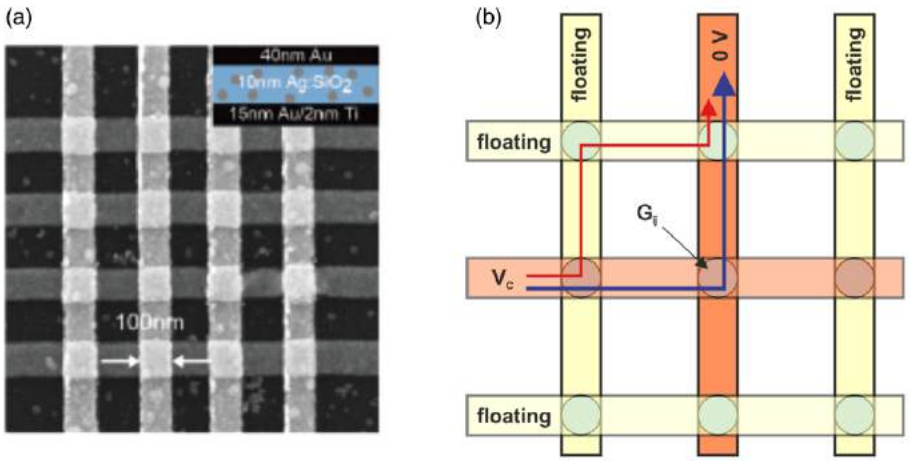

Rys. 2.3. Implementacja układu PUF z wykorzystaniem memrystorów połączonych w macierz *crossbar*. (a) Zdjęcie SEM macierzy memrystorów 4×4 [112]. (b) Schemat budowy układu PUF opartego na macierzy memrystorów 3×3. Przyłożenie napięcia V_c i 0 V pomiędzy pomarańczowymi elektrodami i pozostawieniu innych elektrod bez połączenia (*challenge*) powoduje przepływ prądu przez memrystor o konduktancji G_{ij} (niebieska strzałka) oraz prądu *sneak-path* (czerwona strzałka) poprzez sąsiednie elementy. Mierzony prąd (*response*) jest zdefiniowany przez stan całego układu i parametry fizyczne każdego z jego elementów.

2.2.3. Podsumowanie

We fragmencie artykułu opisano cechy układów typu PUF i przedstawiono wykorzystanie memrystorów połączonych w macierz typu *crossbar* jako fizyczną implementację układu. Zmienność parametrów fizycznych memrystorów oraz stochastyczna natura przełączania rezystywnego opartego na tworzeniu i niszczeniu przewodzącego filamentu sprawia, że nawet urządzenia wyprodukowane w jednakowym procesie różnią się charakterystyką prądowo-napięciową. Możliwość kontrolowania konduktancji memrystorów oraz organizacji w macierze typu *crossbar* pozwala na stworzenie silnych i niemożliwych do sklonowania układów PUF.

2.3. From Oscillatory Reactions to Robotics: A Serendipitous Journey Through Chemistry, Physics and Computation

2.3.1. Wstęp

Współczesnym komputerom coraz trudniej sprostać zapotrzebowaniom narzucanym przez szybki rozwój sztucznej inteligencji (ang. *artificial intelligence*, AI). Trenowanie zaawansowanych modeli AI wymaga znacznej mocy obliczeniowej, tym samym zużywając duże ilości energii — szacuje się, że sztuczna inteligencja AlphaGo podczas rozgrywki w grę w Go zużyła 50 tys. razy więcej energii niż mózg człowieka. Przekłada się to na emisje bardzo dużych ilości CO_2 do atmosfery — nawet kilkukrotnie przewyższających te, które emituje samochód w czasie całego cyklu jego użytkowania.

Rozwój nowego typu układów elektronicznych, lepiej dostosowanych do potrzeb sztucznej inteligencji, umożliwia bardziej efektywne trenowanie modeli AI, obniżając tym samym konsumpcję energii i ograniczając emisję CO_2. W takich układach, nazywanych układami neuromorficznymi, informacje przetwarzane są w sposób naśladujący przetwarzanie sygnałów przez neurony. Inaczej niż we współczesnych komputerach, dane nie muszą być przetwarzane przez procesor i przesyłane do pamięci, gdzie są przechowywane. W układach memrystywnych elementy pamięciowe są wykorzystywane jednocześnie do przetwarzania i przechowywania informacji. Podejście takie nazywa się przetwarzaniem *in materio* (w materiale).

Termin „przetwarzanie neuromorficzne" sięga lat 50 ubiegłego wieku, ale pierwsze układy zostały opracowane dopiero 30 lat później. Opierały się one całkowicie na elektronice analogowej, ale dzisiaj mianem neuromorficznych określa się wiele różnych rodzajów układów cyfrowych, analogowych oraz modeli sztucznych sieci neuronowych zaimplementowanych sprzętowo lub jako programy komputerowe. Rozwój memrystorów i pamięci z przełączaniem rezystywnym oraz sprzęt na nich oparty wydają się być w tym kontekście szczególnie obiecujące, ponieważ potrafią one jednocześnie przetwarzać i przechowywać informacje, pozwalając na połączenie koncepcji *in materio* i przetwarzania neuromorficznego.

Poniższe streszczenie dotyczy sekcji *1.3.1* rozdziału. Część wyprowadzeń matematycznych w niniejszym streszczeniu rozwinięto w porównaniu do oryginalnej publikacji tak, aby przedstawić je w bardziej klarowny sposób.

2.3.2. Streszczenie

Pierwsze układy memrystorów były zintegrowane z klasycznymi układami CMOS (ang. *complementary metal–oxide–semiconductor*), w których — dzięki zmiennemu oporowi — pełniły funkcję przerzutników i przełączników regulujących przepływ prądu.

Wykorzystując charakterystykę tych zjawisk zaproponowano układy implementujące logikę opartą wyłącznie na memrystorach: *memristor-aided logic* (MAGIC). Memrystory pozwalają na zwiększanie lub zmniejszanie swojej konduktancji w zależności od kierunku płynącego przez nie prądu. Dzięki temu bramki logiczne AND i OR mogą być zbudowane z dwóch memrystorów o antyrównoległej orientacji; bramki NOT, NOR i NAND zbudować zaś można z trzech memrystorów. Ponadto, w przeciwieństwie do tranzystorów, memrystory są elementami dwuelektrodowymi i mogą być organizowane w warstwach ułożonych jedna na drugiej. Pozwala to na ich skalowanie w dodatkowym – w porównaniu do układów tranzystorów — wymiarze i w efekcie na efektywniejsze wykorzystanie dostępnego miejsca na chipie.

Trenowanie modeli sztucznych sieci neuronowych oraz wykonywanie operacji matematycznych takich jak transformacje liniowe (np. dyskretna transformacja Fouriera, dyskretna transformacja cosinusowa) wymaga manipulacji strukturami danych o dużych rozmiarach. Na przykład trenowanie głębokiej sieci neuronowej (sztucznej sieci neuronowej składającej się z wielu warstw neuronów, tzw. warstw ukrytych) może w pojedynczej iteracji wymagać aktualizacji wartości milionów wag synaptycznych. Wyniki tych obliczeń wykonanych przez procesor są ciągle wysyłane do i przywoływane z pamięci komputera. Niestety, proces ten ze względu na czaso- i energochłonność postrzegany jest jako jedna z najbardziej istotnych przeszkód w rozwoju technik uczenia maszynowego. Rozwiązaniem tego problemu mogą być układy memrystorów, które potrafią jednocześnie przetwarzać i przechowywać dane. Dzięki temu przesyłanie danych nie jest już konieczne, gdyż pamięć i układ obliczeniowy znajdują się na tym samym chipie. W efekcie ogranicza to zużycie energii i skraca czas potrzebny na wykonanie obliczeń.

Fundamentalną operacją matematyczną wykorzystywaną w trenowaniu i wnioskowaniu modeli AI jest mnożenie macierzy. Może ono być zaimplementowane na macierzy memrystorów podobnej do tej przedstawionej na Rys. 2.3 z wykorzystaniem praw Ohma i Kirchoffa. Zgodnie z prawem Ohma, prąd I przepływający przez przewodzący element o konduktancji G jest proporcjonalny do U pomiędzy końcami tego elementu:

$$I = G \cdot U \tag{2.1}$$

Dla danego napięcia U amplituda prądu I płynącego przez memrystor jest zależna od jego stanu rezystywnego określonego przez konduktancję G.

Prawo Kirchoffa mówi z kolei, że suma prądów wpływająca do węzła musi być równa sumie prądów wypływających z tego węzła. W macierzy memrystory ułożone są tak, że w danej kolumnie lub rzędzie kontakt elektryczny każdego memrystora połączony jest ze wspólną elektrodą. Dzięki temu pojedynczy memrystor M_{ij} o konduktancji G_{ij} może być zaadresowany poprzez przyłożenie napięcia U_{ij} pomiędzy rzędem i i kolumną j. Elektroda, na której mierzony jest prąd zwykle jest uziemiona. Zgodnie z prawem Kirchoffa, prąd I_j mierzony na tej elektrodzie jest sumą wszystkich prądów płynących przez memrystory G_{ij} w danej kolumnie:

$$I_j = \sum_{i}^{m} G_{ij} U_i \tag{2.2}$$

Napięcia przyłożone do poszczególnych rzędów macierzy o wymiarach $m \times n$ mogą zostać zapisane w formie wektorowej jako:

$$\mathbf{U} = \begin{bmatrix} U_1 & U_2 & \dots & U_i & \dots & U_m \end{bmatrix} \tag{2.3}$$

Analogicznie zapisać można prądy zmierzone na każdej z elektrod macierzy:

$$\mathbf{I} = \begin{bmatrix} I_1 & I_2 & \dots & I_j & \dots & I_n \end{bmatrix} \tag{2.4}$$

Każdy memrystor w układzie charakteryzowany jest przez konduktancję G_{ij}. Dla układu memrystorów o wymiarach $m \times n$ wielkości te przedstawić można w postaci macierzowej:

$$\mathbf{G} = \begin{bmatrix} G_{11} & G_{12} & \dots & G_{1j} & \dots & G_{1n} \\ G_{21} & G_{22} & \dots & G_{2j} & \dots & G_{2n} \\ \vdots & \vdots & \vdots & \vdots & \ddots & \vdots \\ G_{m1} & G_{m2} & \dots & G_{mj} & \dots & G_{mn} \end{bmatrix} \tag{2.5}$$

Prąd płynący przez macierz memrystorów jest zatem dany równaniem:

$$\mathbf{I} = \mathbf{G} \times \mathbf{U} \tag{2.6}$$

Równanie to pokazuje, że mnożenie wektorów i macierzy w układach jest realizacją koncepcji obliczeń *in materio* — obliczenia wykonywane są w jednym układzie, bez konieczności transferu danych. Na przykład wykorzystywane w zagadnieniach klasyfikacji metody regresji liniowej i regresji logistycznej w układach memrystorów mogą być rozwiązane w zaledwie jednym kroku. Dodatkowo, przeprowadzenie bardziej skomplikowanych obliczeń, jak np. dzielenia macierzowy, jest możliwe z wykorzystaniem dodatkowych elementów elektronicznych. Te cechy układów memrystywnych sprawiają, że są one

obiecującymi rozwiązaniami w rozwoju technik uczenia maszynowego i sztucznych sieci neuronowych.

Zasada działania sztucznych sieci neuronowych jest w luźny sposób oparta na matematycznym modelu neuronu — jest on węzłem sieci, który przetwarza otrzymaną informację i przesyła do kolejnego węzła sieci. Kolejne węzły sieci połączone są ze sobą „synapsami", a siła tych połączeń opisana jest „wagą synaptyczną". W typowej sztucznej sieci neuronowej neurony ułożone są w połączone ze sobą warstwy, a proces trenowania (uczenia) sieci oparty jest o modulację wag synaptycznych pomiędzy neuronami. Sygnał wyjściowy pojedynczego neuronu y_j jest zatem sumą sygnałów od wszystkich neuronów x_i w poprzedniej warstwie mnożoną przez wagi synaptyczne w_{ij}:

$$y_j = \sum_i w_{ij} x_i \tag{2.7}$$

Proste sieci neuronowe zawierają tylko jedną warstwę, ale do implementacji bardziej skomplikowanych modeli wykorzystuje się sieci o większej ich liczbie (tzw. głębokie sieci neuronowe). W dalszej kolejności sygnał wyjściowy neuronu przetwarzany jest przez tzw. funkcję aktywacji, która określa, czy sygnał ma aktywować neurony w kolejnej warstwie. Najczęściej wykorzystywane funkcje to m. in. ReLU (ang. *Rectified Linear Unit*), tangens hiperboliczny czy funkcja sigmoidalna.

Dobór odpowiedniego algorytmu trenowania sieci neuronowych może mieć duży wpływ na jej finalną wydajność. W jednym z najpowszechniej wykorzystywanych algorytmów — propagacji wstecznej — sygnał z ostatniej warstwy neuronów (warstwy wyjściowej) jest porównywany z poprawnymi wartościami. Różnica między nimi przekazywana jest to pierwszej (wejściowej) warstwy sieci, dopóki błąd ten nie zostanie zminimalizowany. Wytrenowana w ten sposób sieć neuronowa może zostać wykorzystana do wielu różnych zadań, jak klasyfikacja lub rozpoznawanie obrazów.

Memrystory posiadają wszystkie cechy wymagane do fizycznej implementacji sieci neuronowych: wiele stanów rezystywnych, niską energię potrzebną do zmiany tych stanów i pamięć pozwalającą na trwały zapis stanu. Pamięci rezystywne (ang. *resistive random switching memory*, ReRAM lub RRAM) mogą przechowywać 6.5 bitów informacji, a pamięci typu PCM nawet 8 bitów. Energia potrzebna do zmiany ich stanów jest rzędu femtojouli, co jest wartością zbliżoną do energii zużywanej przez biologiczne neurony. Trwałość stanów rezystywnych mierzona jest natomiast w latach.

Porównując Równania 2.2 i 2.7 można zauważyć podobieństwo wyjaśniające, dlaczego macierze memrystorów mogą służyć jako fizyczne implementacje sieci neuronowych. Do tej pory pokazano ich efektywność m. in. w rozpoznawaniu twarzy czy rozpoznawaniu pisma odręcznego, w którym osiągają one dokładność 89.9%. Sieci o innej architekturze (konwolucyjne sieci neuronowe) potrafią osiągnąć uzyskać rzędu 96.9% oraz osiągają podobnie

dużą efektywność w rozpoznawaniu obiektów (zwierząt i maszyn) na zdjęciach. Układy te pozwalają także na dużo szybsze mnożenie macierzy i wektorów - szacuje się, że układy memrystywne mogą wykonywać te operacje na poziomie $115\,\mathrm{TOPS\,W^{-1}}$ (TOPS — *tera operations per second*, jednostka określająca liczbę operacji na sekundę). Dla porównania, klasyczna architektura CMOS wykonuje je na poziomie $7\,\mathrm{TOPS\,W^{-1}}$. Dodatkowo szacuje się, że wykonując obliczenia w sposób neuromorficzny, układy memrystorów mogą ograniczyć zużycie energii nawet tysiąckrotnie.

Należy mieć jednak na uwadze także wyzwania stojące na drodze rozwoju neuromorficznych układów memrystywnych. Różnica parametrów memrystorów produkowanych w tym samym procesie,[2] nieliniowa zależność konduktancji od impulsów napięcia i różnica charakterystyk przełączania z HRS do LRS oraz w przeciwnym kierunku są odpowiedzialne za niższą dokładność predykcji sieci neuronowych. Problemy te są adresowane poprzez dobór wąskich zakresów napięć przełączających, w których powyższe procesy posiadają odpowiednie (pożądane) charakterystyki oraz poprzez pomiar parametrów wszystkich elementów macierzy memrystorów tak, aby dynamika przełączania rezystywnego każdego z nich mogła zostać uwzględniona w algorytmach trenowania sieci neuronowych. Podejścia te są jednak czasochłonne i mogą stanowić duże wyzwanie dla komercjalizacji memrystywnych układów neuromorficznych.

Z drugiej strony, możliwość odtworzenia przez memrystory efektów neuromimetycznych takich jak STDP i uczenie hebbowskie stwarzają potencjał do implementacji sieci neuronowych typu SNN (ang. *spiking neural networks*). Ten typ sieci wiernie naśladuje procesy uczenia zachodzące w mózgu, przez co jest w stanie wydajnie przetwarzać obrazy lub ludzką mowę. Podobnie jak w biologicznych neuronach, sygnał przekazywany jest w formie ciągu krótkich impulsów i tylko odpowiednie sekwencje tych impulsów aktywują kolejne neurony. Zmiany wag synaptycznych oparte są o reguły uczenia takie jak STDP, w której amplituda zmian wagi synaptycznej zależy od odstępu czasowego pomiędzy impulsem pre- i postsynaptycznym. Nawet sieci typu SNN o niewielkiej liczbie synaps są w stanie wydajnie przetwarzać dynamiczne wzory wizualne, pochłaniając przy tym niewielkie ilości energii. Pierwsze sprzętowe sieci SNN są już dostępne komercyjnie, choć rozwiązania te bazują na elektronice CMOS. Są to m. in. superkomputer SpiNNaker, Loihi (Intel) oraz TrueNorth (IBM).

[2]Warto zauważyć, że z punktu widzenia zastosowania memrystorów w układach PUF opisanych w Rozdz. 2.2 jest to pożądana cecha.

2.3.3. Podsumowanie

W części rozdziału opisano wykorzystanie układów memrystorów do mnożenia wektorów i macierzy — operacji matematycznej leżącej u podstaw uczenia maszynowego i trenowania sztucznych sieci neuronowych. Dzięki cechom memrystorów procesy te mogą być wykonywane znacznie efektywniej. Brak konieczności przesyłania danych pomiędzy układami elektronicznymi pozwala na zwiększenie szybkości obliczeń przy jednoczesnym ograniczeniu konsumpcji energii.

Pierwsze fizyczne implementacje sztucznych sieci neuronowych na układach memrystorów pokazują, że mogą one z wysoką dokładnością klasyfikować wzorce wizualne. Fakt, że w układach memrystywnych może zostać zaimplementowanych wiele różnych rodzajów sztucznych sieci neuronowych sprawia, że sprzęt na nich oparty może znaleźć zastosowanie w wielu różnych dziedzinach sztucznej inteligencji.

2.4. Synaptic plasticity, metaplasticity and memory effects in hybrid organic-inorganic bismuth-based materials

2.4.1. Wstęp

Przełączanie rezystywne w memrystorach może być konsekwencją wielu różnych mechanizmów. Jednym z nich jest mechanizm złączowy oparty o modulację wysokości bariery Schottky'ego. Przełączanie tego typu charakteryzuje się stosunkowo niewielką różnicą pomiędzy stanami HRS i LRS, ale jego dynamika ma charakter zbliżony do analogowego. Umożliwia to kontrolowanie konduktancji urządzenia w sposób, który pozwala na stopniowe przełączanie między stanami z wykorzystaniem wielu stanów pośrednich. Cecha ta umożliwia bardzo dokładne odtworzenie zjawisk synaptycznych w memrystorze.

W artykule opisano własności memrystywne i neuromimetyczne jodobizmutanu metyloamoniowego — analogu perowskitu opartego o bizmut o wzorze $(CH_3NH_3)_3Bi_2I_9$ (MABiI) wraz z jego charakterystyką spektroskopową.

2.4.2. Streszczenie

W artykule przedstawiono urządzenie memrystywne, w którym warstwę aktywną stanowi jodobizmutan metyloamoniowy umieszczony pomiędzy dolną elektrodą z ITO i górną elektrodą miedzianą jak na Rys. 2.4(a). Artykuł podzielony jest na dwie części: pierwszą z nich stanowi charakterystyka materiałowa MABiI wykonana z wykorzystaniem skaningowej mikroskopii elektronowej, dyfrakcji promieniowania rentgenowskiego oraz spektroskopii absorpcyjnej roztworów i spektroskopii transmisyjnej UV-Vis cienkich warstw. Pomiary wykonano dla warstw o różnym stopniu zdefektowania (Rys. 2.4(b)). Druga część artykułu obejmuje pomiary prądowo-napięciowe składające się na charakterystykę własności memrystywnych oraz pomiary efektów neuromorficznych: uczenia i zapominania, STDP, SRDP i metaplastyczności.

Na Rys. 2.5(a) przedstawiono pętle histerezy zmierzone dla MABiI zsyntetyzowanego z różnych stosunków prekursorów. Obecność w pomiarach prądowo napięciowych (I-V) pętli histerezy przecinającej się przy pewnej wartości napięcia jest jedną z cech charakterystycznych memrystora. Podczas zwiększania napięcia od 0 V do 3 V, przy wartości ok. 0.5 V nachylenie odpowiedzi prądowo-napięciowej ulega wyraźniej zmianie, co wynika ze stopniowego przełączania memrystora ze stanu HRS do LRS (ten kierunek przełączenia bywa nazywany procesem *SET*). Podczas przemiatania od 3 V do −3 V układ początkowo pozostaje w LRS, o czym świadczy liniowy charakter zależności prądowo-napięciowej, ale

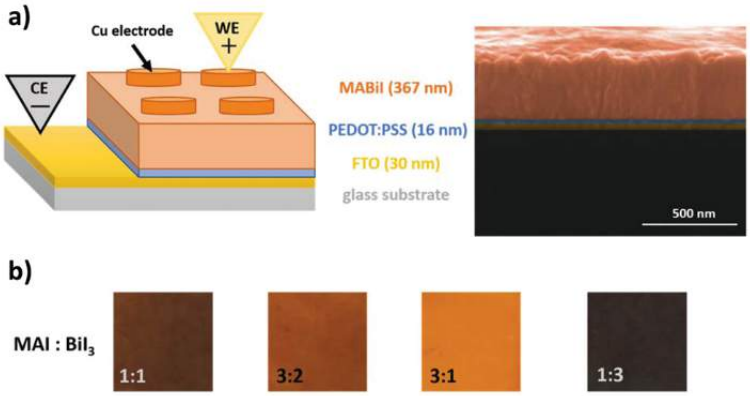

Rys. 2.4. (a) Schemat urządzenia memrystywnego zbudowanego z materiału aktywnego MABiI umieszczonego pomiędzy dwiema elektrodami przewodzącymi Cu i FTO. Po prawej: zdjęcie SEM przekroju poprzecznego memrystora wraz z grubościami poszczególnych warstw. (b) Optyczne fotografie MABiI zsyntetyzowanego z roztworów o różnym stosunku prekursorów. Zróżnicowania barwa wynika ze zdefektowania materiałów.

przy wartości ok. $-2\,\mathrm{V}$ amplituda prądu zaczyna stopniowo maleć, co wynika z przełączenia z LRS do HRS (proces *RESET*). Układ pozostaje w tym stanie podczas ostatniej części przebiegu od $-3\,\mathrm{V}$ do $0\,\mathrm{V}$.

Pętlę histerezy o najwęższej charakterystyce zaobserwowano dla stosunku 3 : 2 — jest to materiał stechiometryczny, a zatem charakteryzujący się najniższą liczbą defektów, co przekłada się na najwęższą pętlę histerezy. Zmieniając zdefektowanie materiału poprzez odejście od stosunku stechiometrycznego, uzyskano poszerzenie pętli. Każdy z bardziej zdefektowanych materiałów charakteryzował się większym stosunkiem HRS do LRS w ujemnym zakresie napięć, co świadczy o lepszych właściwościach memrystywnych materiałów niestechiometrycznych.

Jedną z cech charakterystycznych dla memrystorów jest zwężenie pętli histerezy wraz ze wzrostem szybkości przemiatania napięciem. W perowskitach może być ono konsekwencją ograniczonej ruchliwości nośników ładunku wewnątrz materiału, m. in. kationów metyloamoniowych i wakancji lub anionów jodkowych [113, 114]. W memrystorze opartym na MABiI pętla posiadała zbliżony kształt nawet dla częstotliwości przemiatania wynoszących $20\,\mathrm{V\,s^{-1}}$ (Rys. 2.5(b)), co sugeruje, że za efekt przełączania rezystywnego odpowiadają nośniki o wysokiej ruchliwości, np. elektrony. Elektronowy mechanizm przewodnictwa jest charakterystyczny dla przełączania rezystywnego opartego o barierę Schottky'ego. Za efekt memrystywny mogą także odpowiadać *metal-induced gap states* (MIGS)

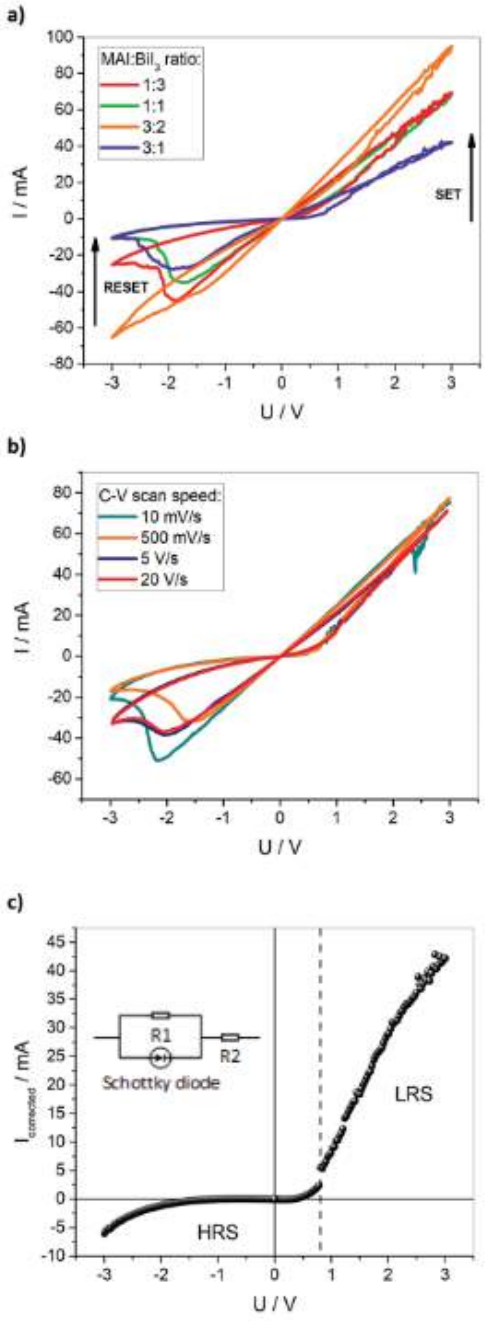

Rys. 2.5. (a) Pętle histerezy w pomiarze $I - V$. Szerokość pętli jest zależna od stechiometrii roztworu prekursorów — pętla jest najwęższa dla próbki stechiometrycznej (3:2). (b) Brak widocznej zależności szerokości pętli histerezy od szybkości przemiatania napięciem świadczy o tym, że proces odpowiadający za przełączanie rezystywne jest stosunkowo szybki. Sugeruje to, że jest związany z transportem elektronów, a nie np. defektów struktury. (c) Część pętli histerezy zmierzona w memrystorze MABiI 3:1 o charakterystyce diodowej. Przełączenie następuje przy napięciu 0.8 V

— stany powstałe na złączu metal-półprzewodnik, które pojawiają się w obszarze przerwy wzbronionej półprzewodnika na skutek oddziaływania jego stanów powierzchniowych z elektronami w metalu. Kontakt metalu z półprzewodnikiem wymusza wyrównanie poziomów Fermiego, pozostawiając puste stany elektronowe w obszarze złącza [115, 116]. Modulacja bariery Schottky'ego następuje poprzez zapełnianie i opróżnianie tych stanów, co przekłada się na obserwowaną pętlę histerezy, a efekt pamięci jest z kolei wynikiem stabilności termodynamicznej tychże stanów. Dodatnia polaryzacja elektrody metalicznej powoduje przepływ elektronów z pasma walencyjnego półprzewodnika do metalu, zapełniając pułapki elektronowe na złączu i obniżając wysokość bariery Schottky'ego, tym samym powodując przejście z HRS do LRS (por. Rys. 1.3(c) i (d)). W ujemnym zakresie potencjałów akceptorowe stany elektronowe są stopniowo opróżniane wraz ze wzrostem napięcia, przywracając barierę Schottky'ego do pierwotnej wysokości i powodując przejście z LRS do HRS.

Obecność bariery na złączu MABiI/Cu wyjaśnia także asymetryczny kształt pętli histerezy oraz jej diodową charakterystykę w stanie HRS, co przedstawia Rys. 2.5(c). Powyżej napięcia 0.8 V następuje zmiana charakteru przewodnictwa z diodowej na ohmowe oraz przełączenie z HRS do LRS. Wykorzystując teorię emisji termoelektronowej i równanie diody Richardsona, na podstawie przebiegu $I - V$ oszacowano wysokość bariery Schottky'ego na 0.55 eV.

W memrystorach retencja stanów jest zależna od wartości napięcia przełączającego — wysokie wartości napięcia przełączają memrystory do bardziej stabilnych stanów, skutkując dłuższymi czasami retencji [117]. W memrystorze MABiI zmierzono stabilność stanów przełączając układ znajdujący się w HRS za pomocą napięcia o różnej amplitudzie i odczytując stan układu 10 s po przełączeniu oraz następnie po 30 min (Rys. 2.6). Ujemne napięcia nie powodowały istotnych zmian stanu rezystywnego. Stabilne stany otrzymano dla napięć 1.5 V i wyższych, podczas gdy w układzie przełączonym napięciem 1 V zaobserwowano postępującą relaksację z LRS do HRS. Różne wartości prądów po przełączeniu napięciami 1.5 V, 2 V i 3 V pokazują, że układ posiada przynajmniej trzy odróżnialne i stabilne stany rezystywne, pozwalając na przechowywanie w memrystorze więcej niż jednego bitu informacji. Cecha ta jest niezwykle istotna z punktu widzenia zastosowania memrystora w obliczeniowych układach neuromorficznych oraz do indukcji efektów neuromimetycznych [118].

Efekty neuromimetyczne w memrystorach indukowane są poprzez stymulację układu impulsami napięcia. Kontrolując przełączanie rezystywne oraz wykorzystując trwałość tych stanów, za pomocą sekwencji napięcia o różnej amplitudzie, polaryzacji, częstotliwości i kształcie impulsów możliwe jest przetwarzanie sygnału w sposób analogiczny do plastyczności synaptycznej. Odtworzenie synaptycznego uczenia się i zapominania poprzez

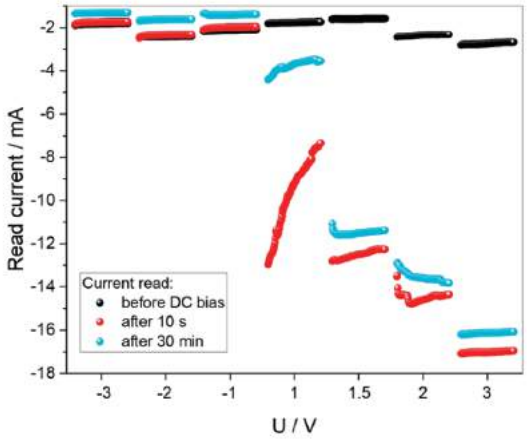

Rys. 2.6. Zależność stabilności stanów rezystywnych memrystora MABiI od amplitudy napięcia przełączającego. Stan układu odczytano mierząc prąd płynący przez memrystor po przyłożeniu napięcia $-0.5\,\mathrm{V}$ przez 10 s. Czarny kolor przedstawia stan układu przed przyłożeniem napięcia przełączającego. Po przełączeniu memrystora do LRS za pomocą dodatniego napięcia i HRS za pomocą ujemnego, stan układu odczytano po 10 s (kolor czerwony) i następnie po 30 min (kolor niebieski).

stopniowy wzrost lub obniżenie amplitudy prądu uzyskano przy użyciu krótkich impulsów o polaryzacji dodatniej (uczenie) i ujemnej (zapominanie). Procesy te charakteryzują się zróżnicowaną dynamiką — stała czasowa uczenia (czyli przełączanie memrystora z HRS do LRS) była niemal cztery razy dłuższa niż stała czasowa zapominania (przełączanie z LRS do HRS). Jest to efektem charakterystyki diodowej urządzenia — transfer nośników ładunku jest łatwiejszy w kierunku przewodnictwa diody niż w kierunku zaporowym.

Najważniejszą część artykułu stanowi charakterystyka efektu metaplastycznego w memrystorze MABiI. W badaniach neurofizjologicznych metaplastyczność definiuje się jako „plastyczność plastyczności synaptycznej". Oznacza to, że występowanie, kierunek i amplituda zmian wydajności synaptycznej może być modyfikowana również pod wpływem innych czynników, niż tylko chwilowa aktywność połączenia synaptycznego. Istotny wpływ metaplastyczny na plastyczność ma wcześniejsza aktywność synapsy. W eksperymentach na memrystorach miarą siły połączenia pomiędzy neuronami jest waga synaptyczna zdefiniowana jako względny wzrost prądu przed i po eksperymencie, określony dla zadanego napięcia czytającego zgodnie z Równaniem 1.7. W mózgu zmiany wagi synaptycznej następują w wyniku aktywności sieci neuronalnych podczas procesów uczenia. Zgodnie z teorią Hebba, wzrost wagi jest wynikiem sytuacji, w której neuron presynaptyczny przez dany okres w sposób powtarzalny stymuluje neuron postsynaptyczny, a jej spadek wywoływany jest przez odwrotną kolejność stymulacji neuronów [86]. *Spike-timing-dependent plasticity*

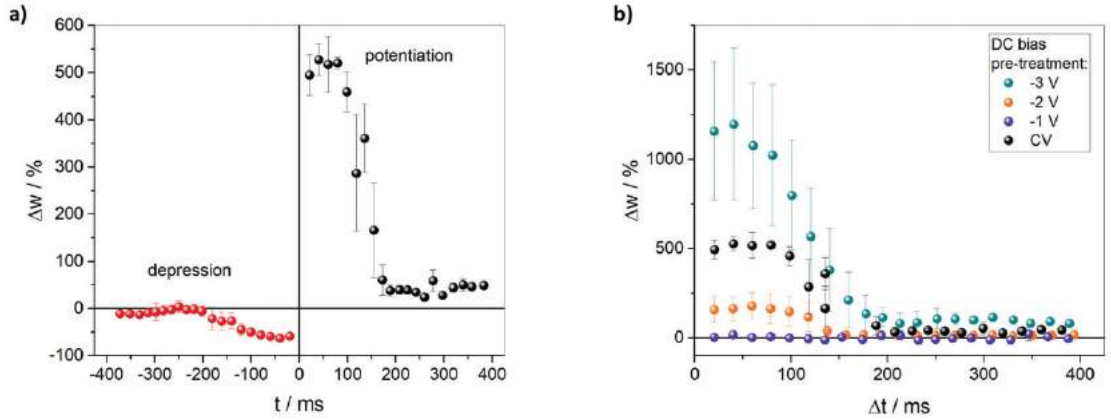

Rys. 2.7. Uczenie typu STDP i modulacja metaplastyczna krzywych uczenia. (a) Antysymetryczna krzywa uczenia hebbowskiego z wyraźnym rozróżnieniem potencjacji i depresji. (b) Gałąź potencjacji krzywej uczenia na próbce o stechiometrii 3 : 1 z modulacją metaplastyczną uzyskaną poprzez przyłożenie do układu napięcia o różnej amplitudzie przed wykonaniem pomiaru STDP. CV oznacza wykonanie pełnego pomiaru prądowo-napięciowego jako procedurę modulującą. Zmiany wartości wagi synaptycznej Δw pokazują, że za pomocą napięcia można modulować amplitudę jej zmian w gałęzi potencjacji. Przebieg napięciowy do otrzymania krzywej uczenia hebbowskiego składał się z bipolarnych trójkątnych impulsów trwających 400 ms o amplitudzie ± 1.6 V. W celu modulacji wagi synaptycznej Δw interwał czasowy pomiędzy impulsami był zmniejszany od 400 ms do 20 ms.

(STDP) jest jedną z form uczenia hebbowskiego. W tym eksperymencie zarówno neuron postsynaptyczny jak i presynaptyczny generują potencjał czynnościowy, a modulacja wagi synaptycznej Δw jest zależna w głównej mierze od dwóch czynników:

(a) kolejności generowania impulsów - jeśli neuron presynaptyczny generuje sygnał przed neuronem postsynaptycznym, dochodzi do wzmocnienia synaptycznego. W sytuacji odwrotnej, kiedy sygnał generowany przez neuron postsynaptyczny pojawia się wcześniej niż ten od neuronu presynaptycznego, połączenie synaptyczne ulega osłabieniu.

(b) interwału czasowego - im krótszy jest czas pomiędzy generacją impulsów w obu neuronach, tym większa jest amplituda zmian wagi synaptycznej.[3]

Ten rodzaj uczenia w memrystorze MABiI odtworzono kontrolując kolejność i interwał czasowy pomiędzy impulsami napięcia dostarczanymi do elektrody Cu i ITO. Rys. 2.7(a)

[3]Zależność ta często wyrażana jest frazą: *Neurons that fire together, wire together.* - Donald Hebb

przedstawia antysymetryczną krzywą uczenia hebbowskiego otrzymaną w pomiarze STDP z widocznymi osłabieniem (depresja) i wzmocnieniem synaptycznym (potencjacja). Amplituda zmian wagi synaptycznej Δw może zostać dodatkowo wzmocniona lub osłabiona w zależności od procedury modulującej wykonywanej przed pomiarem, co przedstawiono na Rys. 2.7(b). Dla napięcia $-1\,\mathrm{V}$ nie zaobserwowano istotnych zmian wagi synaptycznej wraz ze zmniejszaniem interwału czasowego pomiędzy impulsami pre- i postsynaptycznymi, ale dla $-2\,\mathrm{V}$ maksymalne wartości Δw uległy zmniejszeniu do ok. 200 % względem domyślnej procedury modulującej, dla której wynosiły ok. 500 %. Zwiększając amplitudę napięcia do $-3\,\mathrm{V}$ uzyskano wzrost maksymalnej wartości Δw do ok. 1200 %. Wyniki te świadczą o tym, że metaplastyczna modulacja może — w zależności od procedury modulującej zastosowanej przed pomiarem STDP — zarówno zwiększać, jak i zmniejszać amplitudę odpowiedzi synaptycznej, pozwalając na modulację sygnału w obu kierunkach.

Zbadana zależność amplitudy zmian wagi synaptycznej Δw w zależności od stechiometrii roztworu prekursorów pokazuje, że największe wzmocnienie i osłabienie synaptyczne zaobserwowano dla próbki o stechiometrii 3:1, a więc z nadmiarem MAI w roztworze względem stechiometrycznego składu MABiI. Jako że próbki wykrystalizowane z roztworów niestechiometrycznych charakteryzują się większą koncentracją defektów struktury krystalicznej, sugeruje to, że za efekty plastyczności synaptycznej odpowiedzialne są stany pułapkowe generowane przez te defekty.

Inne rodzaje plastyczności synaptycznej również mogą być modulowane metaplastycznie. Do indukcji *spike-rate-dependent plasticity* (SRDP) wykorzystano ciąg krótkich impulsów napięciowych o jednakowej amplitudzie. W klasycznym pomiarze SRDP amplituda zmian wagi synaptycznej mierzona jest jako funkcja częstotliwości impulsów. Aby pokazać modulację metaplastyczną, zachowano stały interwał czasowy $\Delta t = 30\,\mathrm{ms}$ pomiędzy impulsami o amplitudzie 1.2 V. Jako procedurę modulującą wykorzystano impulsy napięcia o różnej amplitudzie i o jednakowym czasie trwania 2 s, a Δw obliczono z wykorzystaniem Równania 1.7 na podstawie odczytu stanu układu przed i po pomiarze SRDP wykonanym przy napięciu $-0.5\,\mathrm{V}$. Wyniki pomiaru przedstawiono na Rys. 2.8. Dla zakresu napięć od $-3\,\mathrm{V}$ do $-0.5\,\mathrm{V}$ układ pozostawał w zakresie potencjacji, ale amplituda zmian Δw malała wraz ze obniżaniem wartości napięcia modulującego. Dla napięcia $-0.5\,\mathrm{V}$ układ znalazł się w zakresie depresji, o czym świadczy ujemna wartość Δw.

Otrzymane wyniki pokazują, że modulujące efekty metaplastyczne mogą zapewnić dużą elastyczność zmian odpowiedzi synaptycznej w pomiarach STDP i SRDP.

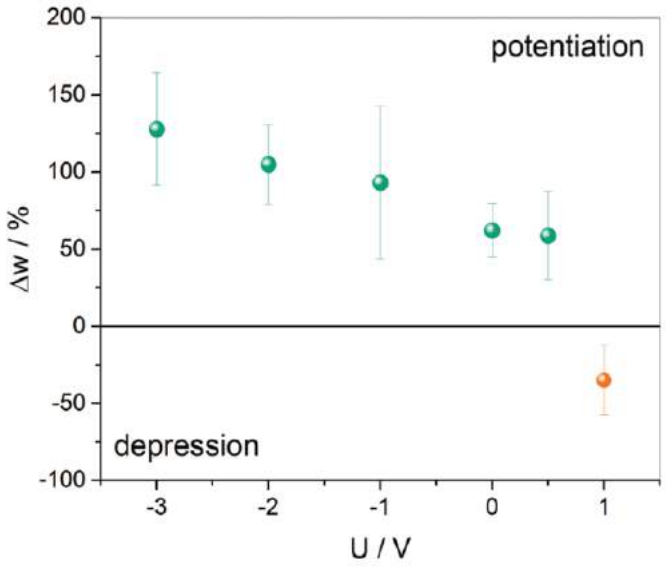

Rys. 2.8. Modulacja metaplastyczna wagi synaptycznej Δw w pomiarze SRDP otrzymana poprzez stymulację układu przed pomiarem za pomocą napięcia o różnej amplitudzie. Dla zakresu napięć modulujących od $-3\,\mathrm{V}$ do $-0.5\,\mathrm{V}$ połączenie synaptyczne ulega potencjacji. Wraz z obniżaniem napięcia modulującego obserwowany jest spadek amplitudy zmian wagi synaptycznej, a dla $-1\,\mathrm{V}$ zaobserwowano depresję połączenia synaptycznego.

2.4.3. Podsumowanie

W pracy pokazano memrystor oparty o analog perowskitu — jodobizmutan metyloamoniowy, w którym scharakteryzowano efekty memrystywne: pętlę histerezy i retencję stanów rezystywnych oraz plastyczności synaptycznej: uczenie Hebba w pomiarze STDP oraz SRDP. Jako mechanizm fizyczny odpowiedzialny za przełączanie rezystywne wskazano modulację wysokości bariery Schottky'ego na złączu MABiI/Cu poprzez zapełnianie i opróżnianie stanów pułapkowych w pobliżu złącza. Jako mechanizm wyjaśniający efekty synaptyczne opisane w artykule zaproponowano istnienie stanów pułapkowych o różnym czasie pułapkowania ładunków.

Najważniejszym odkryciem opisanym w artykule jest modulacja metaplastyczna odpowiedzi synaptycznej, za pomocą której, poprzez wykorzystanie odpowiedniej procedury modulacyjnej, możliwe jest wzmocnienie lub osłabienie wagi synaptycznej. Efekt ten może potencjalnie być korzystny dla zastosowania memrystorów opartych o MABiI w zastosowaniach neuromorficznych, pozwalając na uzyskanie dodatkowych i rozróżnialnych stanów rezystywnych, które mogą zostać wykorzystane do implementacji w tych urządzeniach logiki wielowartościowej.

2.5. Bismuth triiodide complexes: Structure, spectroscopy, electronic properties, and memristive properties

2.5.1. Wstęp

W artykule przedstawiono charakterystykę materiałową i memrystywną grupy związków kompleksowych bizmutu z dużymi ligandami organicznymi. Efekty neuromimetyczne zbadano w kompleksie $[BiI_3(C_6H_5)_2SO_{1.5}]_4$, będącym półprzewodnikiem o szerokości przerwy wzbronionej wynoszącej 2.37 eV. Kształt i charakter pętli histerezy w pomiarze woltamperometrycznym $I - V$ świadczy o tym, że mechanizm przełączania oparty jest o modulację wysokości bariery energetycznej (bariery Schottky'ego) na złączu kompleksu i metalu, z którego wytworzona jest górna elektroda.

W kontekście efektów neuromimetycznych, fragment artykułu skupia się na powiązaniu właściwości bariery Schottky'ego z charakterystyką STDP. W zależności od metalu wykorzystanego w roli górnej elektrody, charakter bariery ulega zmianie, wpływając na charakterystykę memrystywną i neuromimetyczną urządzeń. W artykule pokazano, że memrystory oparte o kompleks $[BiI_3(C_6H_5)_2SO_{1.5}]_4$ z elektrodami Cu i Au wykazują przeciwne charaktery uczenia hebbowskiego w pomiarze STDP, co jest konsekwencją różnej orientacji bariery energetycznej na złączu kompleks/metal.

2.5.2. Streszczenie

W ogólnym przypadku kierunek bariery Schottky'ego na złączu metalu i półprzewodnika warunkowany jest wartością prac wyjścia tych materiałów. Jeśli praca wyjścia metalu ϕ_M jest wyższa od pracy wyjścia półprzewodnika ϕ_S ($\phi_M > \phi_S$), elektrony przepływają z metalu do półprzewodnika dopóki poziomy Fermiego ulegną wyrównaniu. Po osiągnięciu równowagi, pasma półprzewodnika ulegają wygięciu w górę, tworząc barierę na złączu (Rys. 2.9(a)). W sytuacji odwrotnej, kiedy $\phi_S > \phi_M$, pasma ulegają wygięciu w przeciwną stronę, ponieważ elektrony płyną wówczas od metalu do półprzewodnika. W efekcie powstaje bariera o przeciwnej orientacji (Rys. 2.9(c)).

Przeprowadzone pomiary woltamperometryczne różnią się jednak znacząco charakterem odpowiedzi, co sugeruje, że bariery w urządzeniach z elektrodą Cu i Au mają przeciwne orientacje. Prace wyjścia Au (5.2 eV), Cu (4.6 eV) i $[BiI_3(C_6H_5)_2SO_{1.5}]_4$ (5.24 eV) wykazują jednak dosyć zbliżone wartości, co sugeruje, że na orientację bariery Schottky'ego wpływ muszą mieć także inne efekty.

Pierwszym z nich mogą być defekty struktury krystalicznej, w szczególności stany powierzchniowe. Stanami powierzchniowymi określa się lokalne poziomy energetyczne znajdujące się na powierzchni materiału, ale energetycznie leżące w obszarze przerwy wzbronionej. W półprzewodnikach typu n stany powierzchniowe naładowane są ujemnie, powodując wygięcie pasm do góry; w półprzewodnikach typu p pasma wygięte są w dół z powodu dodatniego ładunku na powierzchni.

Kolejnym ważnym w przypadku związku $[BiI_3(C_6H_5)_2SO_{1.5}]_4$ czynnikiem wpływającym na barierę jest tworzenie wiązań chemicznych pomiędzy kompleksem a elektrodą Cu. Powstanie wiązań I—Cu wprowadza dodatkowy ujemny ładunek na złączu. Sumaryczny ładunek w obrębie złącza definiuje wysokość bariery Schottky'ego i w zależności od znaku, może on także wpłynąć na jej orientację.

Ostatnim z czynników są *metal-induced gap states* opisane szerzej w rozdziale 2.4. Jeśli $\phi_M > \phi_S$, to podczas tworzenia złącza elektrony płynące z półprzewodnika do metalu zostają spułapkowane w stanach MIGS, polaryzując złącze ujemnie. W przypadku przeciwnym, kiedy $\phi_S > \phi_M$, sumaryczny ładunek złącza jest dodatni.

Poszczególne wkłady w charakter bariery energetycznej na złączu są bardzo trudne do oszacowania, ale sumaryczny charakter bariery jest możliwy do określenia podstawie pomiarów $I - V$. W dodatnim zakresie napięć memrystor $[BiI_3(C_6H_5)_2SO_{1.5}]_4$ (będący półprzewodnikiem typu p) z elektrodą Au przełącza się ze stanu LRS do HRS. Jeśli przy braku zewnętrznego napięcia sumaryczny ładunek na złączu jest dodatni, to dodatnia polaryzacja elektrody powoduje przepływ elektronów z półprzewodnika do metalu i tym samym zwiększenie sumarycznego dodatniego ładunku na złączu. Wówczas bariera Schottky'ego rośnie, powodując przejście z LRS do HRS. Ujemna polaryzacja powoduje przepływ elektronów do półprzewodnika, które zapełniają stany pułapkowe i obniżają wysokość bariery.

W tym samym materiale z elektrodą Cu w pomiarach $I - V$ kierunek przełączania rezystywnego jest przeciwny: w dodatnim zakresie napięć następuję przejście z HRS do LRS. Sugeruje to, że sumaryczny ładunek na złączu jest ujemny — jeśli przy przy dodatniej polaryzacji Cu bariera Schottky'ego ulega obniżeniu, to świadczy to o opróżnianiu obsadzonych pułapek elektronowych. W efekcie memrystor przełącza się z HRS do LRS. Na podstawie tych pomiarów można stwierdzić, że przełączanie memrystora $[BiI_3(C_6H_5)_2SO_{1.5}]_4$/Cu warunkowane jest zmianami wysokości bariery przedstawionymi na Rys. 2.9(a) i (b), a układu $[BiI_3(C_6H_5)_2SO_{1.5}]_4$/Au na Rys. 2.9(c) i (d).

W efekcie, w zależności od metalu elektrody, przełączanie w memrystorze $[BiI_3(C_6H_5)_2SO_{1.5}]_4$ następowało w kierunku zgodnym (dla Cu) lub przeciwnym (dla Au) z ruchem wskazówek zegara, zgodnie z procesami opisanymi na panelach Rys. 2.9. Oprócz

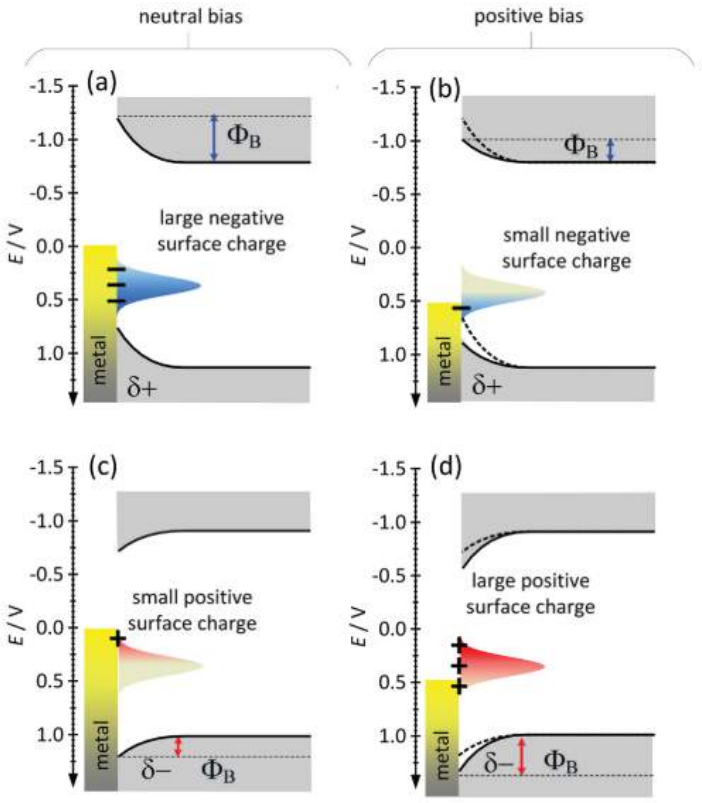

Rys. 2.9. Zależność orientacji i wysokości bariery na złączu metal/półprzewodnik w zależności od ładunku powierzchniowego i zewnętrznego napięcia. (a) Bariera na złączu metalu i półprzewodnika o ujemnym ładunku powierzchniowym ulega obniżeniu przy dodatniej polaryzacji metalu wskutek opróżniania stanów pułapkowych (b). (c) W przypadku bariery powstałej na złączu metalu i półprzewodnika o dodatnim ładunku powierzchniowym, dodatnia polaryzacja metalu powoduje zapełnianie dostępnych stanów pułapkowych i zwiększenie wysokości bariery (d).

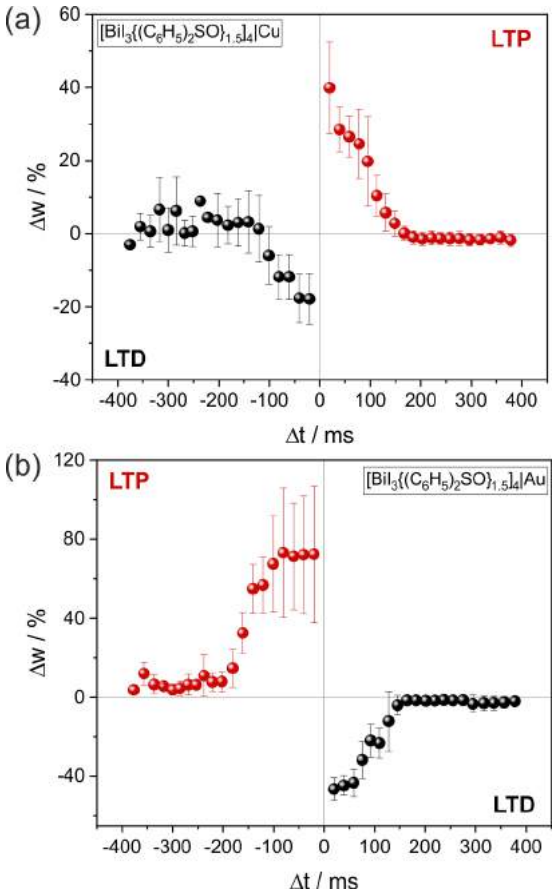

Rys. 2.10. Różne rodzaje STDP zmierzone w memrystorze $[BiI_3(C_6H_5)_2SO_{1.5}]_4$ z elektrodą górną Cu (a) i Au (b). Charakter uczenia Hebba zmienia się w zależności od metalu elektrody — dla Cu zaobserwowano uczenie hebbowskie, a dla Au uczenie antyhebbowskie.

własności memrystywnych, mają one także wpływ na efekty neuromimetyczne w materiale — wyniki pomiarów STDP przedstawiono na Rys. 2.10.

W memrystorze z elektrodą Cu zmierzono krzywą uczenia hebbowskiego (Rys. 2.10(a)). Wzrost wagi synaptycznej Δw następował wtedy, kiedy impuls elektryczny docierał najpierw do elektrody presynaptycznej (którą w tym przypadku stanowił tlenek cyny domieszkowany fluorem, FTO), a następnie do elektrody postsynaptycznej. Jeśli kolejność ta ulega odwróceniu i impuls dociera najpierw do elektrody postsynaptycznej, a później do presynaptycznej, następowała potencjacja. W obu rodzajach plastyczności, wraz ze zmniejszaniem interwału czasowego pomiędzy impulsami rośnie amplituda zmian Δw.

Charakter uczenia uległ zmianie dla elektrody Au (Rys. 2.10(b)). W tym memrystorze następowało wzmocnienie, jeśli impuls aplikowany jest najpierw do elektrody postsynaptycznej, a następnie presynaptycznej. Analogiczna zmiana zachodzi dla depresji, która w tym urządzeniu ma miejsce przy stymulacji elektrody presynaptycznej przed elektrodą postsynaptyczną. Zmiana elektrody z Cu na Au spowodowała więc odwrócenie charakteru uczenia, który znany jest jako uczenie antyhebbowskie.

Zmiana uczenia z hebbowskiego na antyhebbowskie jest wynikiem tych samych procesów, które wpływają na kierunek przełączania rezystywnego. Jako, że waga synaptyczna Δw jest względną różnicą amplitud prądów przed i po przyłożeniu sekwencji impulsów przełączających (zgodnie z Równ. 1.7), to kierunek przełączania pomiędzy stanami rezystywnymi warunkuje jej znak. Przełączenie HRS $\rightarrow$ LRS odpowiada wzmocnieniu, a LRS $\rightarrow$ HRS osłabieniu. Odwrócenie charakteru uczenia jest zatem wynikiem zmiany kierunku przełączania rezystywnego wywołanego różnym charakterem barier Schottky'ego na złączu kompleksu z Au i Cu.

2.5.3. Podsumowanie

We fragmencie artykułu pokazano wpływ orientacji bariery Schottky'ego na efekty neuromorficzne w memrystorze opartym o związek kompleksowy o wzorze $[BiI_3(C_6H_5)_2SO_{1.5}]_4$. Pokazano, że zmieniając jedynie metal elektrody, charakter krzywej uczenia w pomiarze STDP ulega zmianie z hebbowskiego na antyhebbowski, co jest konsekwencją przeciwnej orientacji bariery Schottky'ego na złączu półprzewodnika z Cu i Au.

Możliwość uzyskania dwóch przeciwnych rodzajów krzywych uczenia wydaje się być obiecująca w kontekście ich wykorzystania w sieciach neuronowych SNN. Neurony o dwóch przeciwnych regułach uczenia — hebbowskiej i antyhebbowskiej — mogą zostać wykorzystane w niektórych algorytmach trenowania sieci SNN, pozwalając na uzyskanie dokładności rozpoznawania odręcznie pisanych cyfr ze zbioru MNIST (Modified National Institute of Standards and Technology) na poziomie zbliżonym do ludzkich możliwości [119].

2.6. Light-Induced Synaptic Effects Controlled by Incorporation of Charge-Trapping Layer into Hybrid Perovskite Memristor

2.6.1. Wstęp

Unikalne własności optoelektroniczne hybrydowych perowskitów ołowiowych, które czynią je wydajnymi ogniwami fotowoltaicznymi, mogą zostać także wykorzystane do indukowania efektów neuromorficznych w memrystorze za pomocą światła. Wysoki współczynnik absorpcji perowskitów i niska energia dysocjacji ekscytonów oraz długa droga swobodna nośników ładunku pozwalają na wydajną generację prądu w wyniku absorpcji fotonu. Efekty memrystywne są natomiast wynikiem modulacji bariery Schottky'ego na złączu perowskitu i metalu. Połączenie tych cech czyni perowskity potencjalnie interesującymi kandydatami do zastosowań w optoelektronice przetwarzającej sygnały w sposób neuromorficzny.

W artykule opisano sztuczną synapsę zbudowaną z metyloamoniowego jodku ołowiu, w której wykorzystano dodatkową warstwę nanocząstek niestechiometrycznej formy polimerycznej azotku węgla C_3N_4 (CN-NPs), której obecność w strukturze urządzenia pozwoliła na zmianę odpowiedzi synaptycznej indukowanej światłem. Jest to wynikiem zdolności azotków węgla do pułapkowania ładunku na długi czas sięgający nawet kilku godzin [120]. Motywacją do wykorzystania azotków węgla była weryfikacja hipotezy czy pułapkowanie ładunku przez te związki wpłynie na odpowiedź memrystywną i synaptyczną memrystora perowskitowego poprzez modyfikację bariery na złączu perowskit/CN-NPs lub CN-NPs/ITO.

2.6.2. Streszczenie

W artykule przedstawiono porównanie dwóch memrystorów, których strukturę można przedstawić następująco:

1. ITO/OIP/Au
2. ITO/CN-NPs/OIP/Au,

gdzie ITO — tlenek indu domieszkowany cyną (elektroda dolna), OIP (skrót z ang. *organic-inorganic perovskite*) — metyloamoniowy perowskit jodkowo-ołowiowy o wzorze $CH_3NH_3PbI_3$ pełniący rolę warstwy aktywnej, CN-NPs — nanocząstki azotku węgla C_3N_4 stanowiące warstwę pułapkującą ładunek, Au — napylona warstwa złota (elektroda górna). Schematy urządzeń przedstawiono na Rys. 2.11(d).

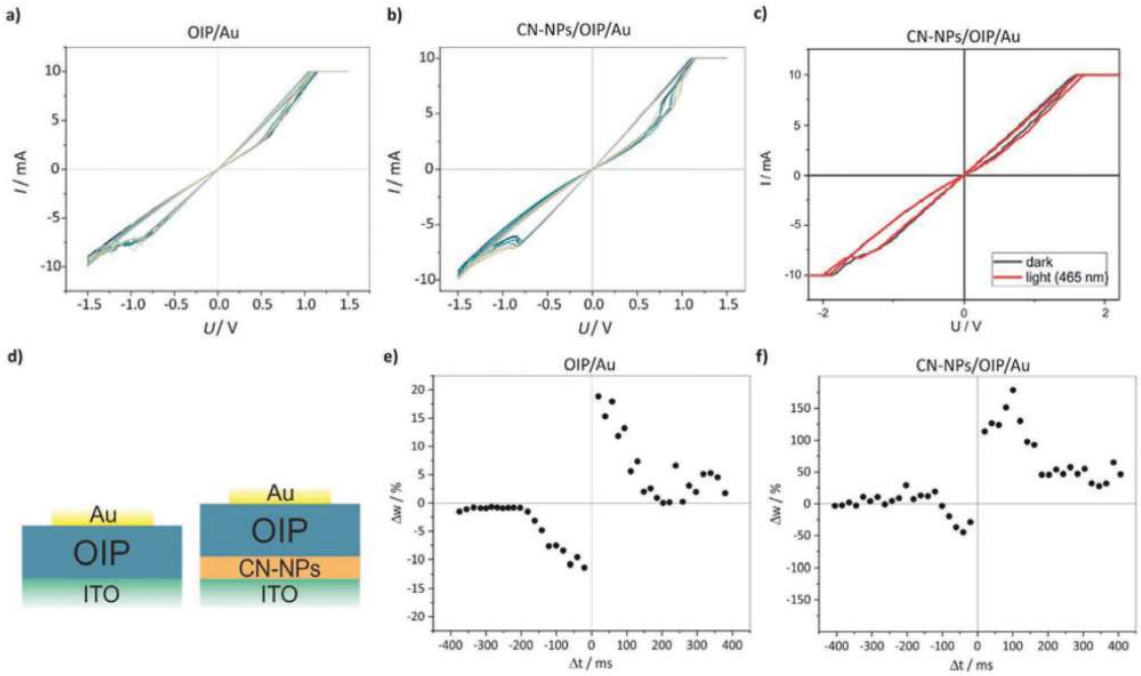

Rys. 2.11. Pętle histerezy memrystora (a) OIP/Au i (b) CN-NPs/OIP/Au wskazujące na memrystywny charakter urządzeń. (c) Brak zmian pętli histerezy podczas pomiaru w świetle i w ciemności. (d) Schematyczne przedstawienie budowy memrystorów. (e, f) Uczenie hebbowskie w pomiarze STDP zmierzone w memrystorze (e) bez oraz (f) z warstwą CN-NPs. Oba urządzenia wykazują antysymetryczny przebieg krzywej uczenia, ale amplituda zmian wagi synaptycznej Δw jest wielokrotnie wyższa w urządzeniu z warstwą CN-NPs.

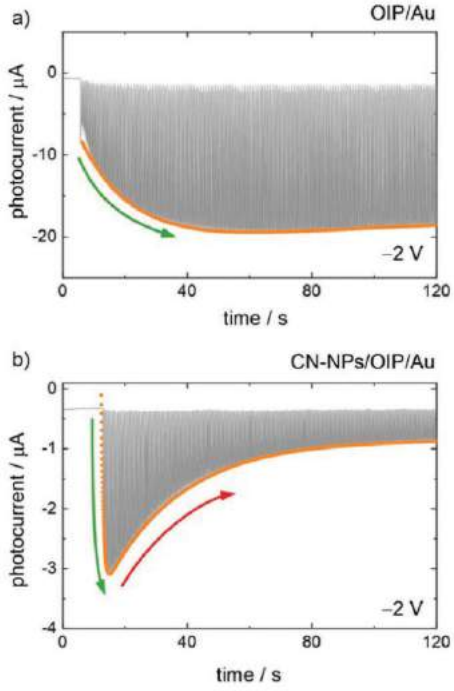

Rys. 2.12. Zmiana dynamiki generowania fotoprądów w memrystorze bez oraz z warstwą pułapkującą CN-NPs. (a) Amplituda fotoprądów w memrystorze ITO/OIP/Au rośnie nieliniowo aż to osiągnięcia *plateau*, naśladując krótkotrwałe wzmocnienie synaptyczne (ang. *short-term facilitation*, STF). (b) Fotoprądy w memrystorze ITO/CN-NPs/OIP/Au po gwałtownym wzroście zaczynają maleć analogicznie do długotrwałego osłabienia synaptycznego (ang. *long-term depression*, LTD).

Oba badane urządzenia posiadały zbliżoną charakterystykę prądowo-napięciową $I-V$ w zakresie w zakresie $\pm 1.5\,\mathrm{V}$ o stosunkowo wąskiej pętli histerezy oraz bipolarnym przełączaniu rezystywnym (Rys. 2.11(a) i (b)). W urządzeniu z warstwą CN-NPs nie zaobserwowano zmian w charakterystyce $I-V$ w ciemności ani podczas ciągłego naświetlania memrystora światłem o długości fali 465 nm.

Oba urządzenia wykazywały także antysymetryczną krzywą uczenia hebbowskiego w pomiarze STDP, przy czym amplituda zmian wagi synaptycznej była ponad sześciokrotnie wyższa w urządzeniu z warstwą CN-NPs (por. Rys. 2.11(e) i (f)). Warstwa pułapkująca ładunek nie wywołała zatem jakościowej zmiany charakteru odpowiedzi synaptycznej. Uzyskano ją natomiast, kiedy do indukcji efektów neuromorficznych zamiast napięcia wykorzystano impulsy światła i zmierzono dynamikę zmian generowanego fotoprądu.

Memrystory naświetlano od strony przezroczystej elektrody dolnej impulsami światła o częstotliwości 5 Hz, długości fali 465 nm i mocy $60\,\mathrm{mW\,cm^{-2}}$. Oba urządzenia wykazywały znacząco różną dynamikę generacji fotoprądów, którą przedstawiono na Rys. 2.12. W

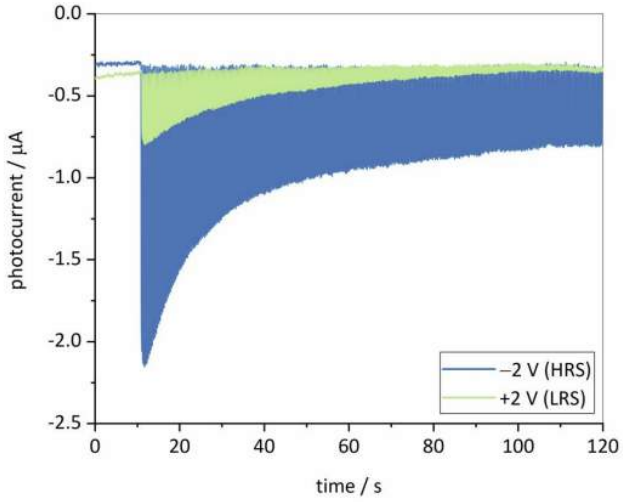

Rys. 2.13. Zależność amplitudy fotoprądów od stanu rezystywnego w memrystorze CN-NPs/OIP/Au. Fotoprądy w stanie HRS mają wyższą amplitudę od stanu LRS przy zachowaniu takiej samej dynamiki generacji fotoprądów.

memrystorze OIP/Au zaobserwowano stopniowy wzrost amplitudy fotoprądów, który po ok. 45 s osiągnął wartość maksymalną. Efekt ten jest odpowiada krótkotrwałemu wzmocnieniu synaptycznemu w neuronach (ang. *short-term facilitation*, STF), będącego formą plastyczności synaptycznej.

W memrystorze CN-NPs/OIP/Au (Rys. 2.12b)), po szybkim wzroście fotoprądów trwającym ok. 2 s, nastąpiło stopniowe zmniejszenie ich amplitudy, co stanowi efekt analogiczny do długotrwałej depresji synaptycznej (*long-term depression*, LTD), zachodzącej w biologicznych układach w warunkach obniżenia poziomu neurotransmiterów, które przenoszą sygnały pomiędzy neuronami. Efekty te sklasyfikowano odpowiednio jako krótko- i długotrwałe formy plastyczności synaptycznej na podstawie wyznaczonych stałych czasowych.

Amplituda fotoprądów jest także zależna od stanu rezystywnego memrystora. Rys. 2.13 przedstawia fotoprądy zmierzone w memrystorze CN-NPs/OIP/Au w dwóch różnych stanach rezystywnych. Fotoprądy zmierzone w stanie HRS charakteryzowały się kilkukrotnie wyższą amplitudą niż fotoprądy w LRS, ale dynamika odpowiedzi układu pozostała taka sama dla obu stanów. Efekt ten można zatem wykorzystać do odczytu stanu memrystora za pomocą światła. Korzyścią płynącą z optycznego czytania stanu jest fakt, iż wielokrotny odczyt za pomocą napięcia może doprowadzić do zmiany stanu układu. Z kolei odczyt światłem, generujący prądy o ok. 1000-krotnie niższej amplitudzie, minimalizuje to ryzyko, pozwalając na większą liczbę cykli odczytów stanu układu.

2.6.3. Podsumowanie

W artykule przedstawiono wpływ dodania warstwy warstwy pułapkującej ładunek do memrystora opartego o perowskit ołowiowo-jodkowy na jego odpowiedź prądową i fotoprądową. Obecność warstwy nie zmieniła charakteru odpowiedzi prądowej, ale znacząco wpłynęła na dynamikę generacji fotoprądów, prowadząc do zmiany typu odpowiedzi synaptycznej. Oba urządzenia wykazywały zbliżoną jakościowo odpowiedź w pomiarach STDP, ale w pomiarach z wykorzystaniem impulsów światła dla memrystora bez warstwy pułapkującej uzyskano wzmocnienie synaptyczne, które uległo przejściu w osłabienie synaptyczne w memrystorze z warstwą CN-NPs. Pokazano ponadto, że stan rezystywny może zostać odczytany za pomocą światła, co potencjalnie pozwoli na zwiększenie liczby cykli odczytu bez wpływania na stan memrystora.

W artykule zaproponowano prawdopodobny mechanizm wyjaśniający zaobserwowane efekty. Jednoczesna obecność dwóch różnych rodzajów plastyczności synaptycznej — indukowanej napięciem i indukowanej światłem — jest wynikiem pułapkowania ładunków na złączu Au/OIP oraz oraz w warstwie CN-NPs. Zapełnianie stanów pułapkowych na złączu OIP/Au powoduje stopniowe obniżenie bariery Schottky'ego, prowadząc do wzrostu amplitudy fotoprądów. Z kolei pułapkowanie ładunku w CN-NPs skutkuje modulacją wysokości bariery na złączach OIP/CN-NPs, obniżając amplitudę fotoprądów.

2.7. Leaky integrate-and-fire model and short-term synaptic plasticity emulated in a novel bismuth-based diffusive memristor

2.7.1. Wstęp

Memrystory, ze względu na czas retencji informacji w nich zapisanych, można podzielić na dwie grupy: nieulotne i ulotne. Pierwsze z nich po wyłączeniu napięcia potrafią utrzymać stan rezystywny przez długi czas, sięgający od minut do miesięcy, pozwalając na ich wykorzystanie jako pamięci. W memrystorach z pamięcią ulotną, wyłączenie napięcie powoduje spontaniczny powrót do HRS w krótkim czasie (od nanosekund do sekund). Choć nie przechowują informacji w sposób trwały, ulotność ich pamięci może być wykorzystana do emulacji zachowania neuronów.

Komunikacja pomiędzy neuronami odbywa się poprzez wysyłanie i odbieranie krótkich impulsów elektrycznych. Impuls ten powoduje uwolnienie cząsteczek neurotransmitera do szczeliny synaptycznej, które — docierając do neuronu postsynaptycznego — wywołują ciąg reakcji prowadzących do dyfuzji kationów Na^+ z płynu zewnątrzkomórkowego do wnętrza neuronu. Jeśli napływ tych jonów jest odpowiednio duży, błona komórkowa ulega depolaryzacji i, po przekroczeniu progu pobudliwości, neuron generuje potencjał czynnościowy. Następnie potencjał błony powraca do swojej wartości spoczynkowej.

Jednym z modeli opisujących dynamikę zmian potencjału błony komórkowej neuronu jest model *leaky integrate-and-fire* (LIF). Opisuje on powrót potencjału membrany do wartości spoczynkowej niezależnie od tego, czy impuls został wygenerowany czy nie (np. przez zbyt małą dyfuzję Na^+ i nieosiągnięcie przez błonę neuronu wartości progowej). Uwzględnia także fakt, że wytworzenie potencjału czynnościowego jest tym bardziej prawdopodobne, im częściej neuron otrzymuje impulsy od innego neuronu. Prawdopodobieństwo to spada natomiast, jeśli czas pomiędzy impulsami staje się dłuższy.

W memrystorach ulotnych analogią relaksacji potencjału błony komórkowej jest spontaniczny powrót z LRS do HRS. Niniejszy artykuł przedstawia charakterystykę materiałową oraz memrystywną i neuromorficzną memrystora opartego o nowy typ związku: jodobizmutan butyloamoniowy (BABI). Mechanizm przełączania rezystywnego w tym memrystorze opiera się o utworzenie filamentu przewodzącego powodującego przejście z HRS do LRS. Po wyłączeniu napięcia filament spontanicznie zanika, powodując powrót do HRS. W artykule pokazano, że zachowanie to pozwala na odtworzenie niektórych funkcji synaptycznych opisywanych przez model LIF.

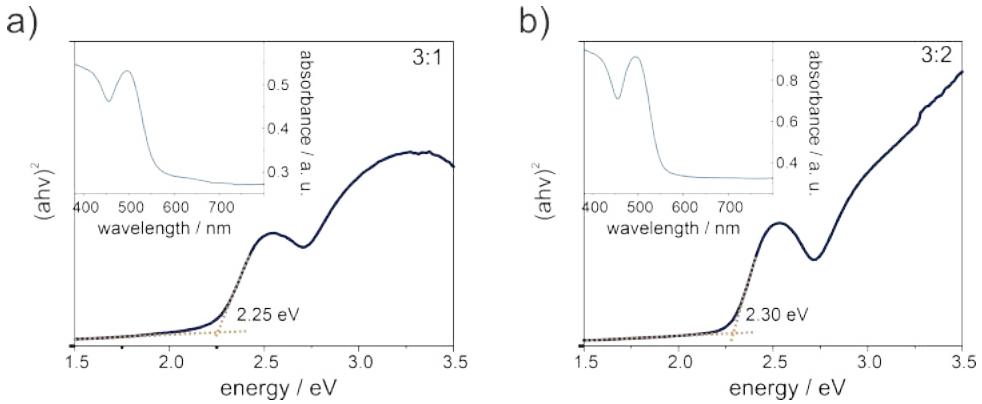

Rys. 2.14. Wykresy Tauca cienkich warstw BABI zsyntetyzowanych z roztworu o stosunku BAI:BiI_3 3:1 (a) i 3:2 (b). Mniejsze wykresy przedstawiają odpowiednie widma absorpcyjne. Nadmiar BiI_3 powoduje wzrost optycznej przerwy wzbronionej z 2.25 eV do 2.30 eV.

2.7.2. Streszczenie

Jodobizmutan butyloamoniowy (BABI) jest związkiem o składzie zbliżonym do jodomizbutanu metyloamoniowego (MABiI), który krystalizuje w strukturze zbliżonej do perowskitu. Poprzez analogię z MABiI zakładano, że stechiometria związku będzie opisana wzorem $A_3Bi_2I_9$, gdzie A jest kationem alkiloamoniowym. Pomiary dyfrakcji rentgenowskiej wykazały jednak, że BABI jest kryształem jonowym o stechiometrii A_3BiI_6 i wzorze sumarycznym $(CH_3NH_3)_3BiI_6$, krystalizującym w rombowym układzie krystalograficznym. Związek ten, pomimo podobieństwa substratów, nie jest zatem perowskitem.

Przeprowadzono pomiary spektroskopii refleksyjnej na dwóch cienkich warstwach BABI: pierwszej zsyntetyzowanej z roztworu stechiometrycznego i drugiej wykrystalizowanej z roztworu niestechiometrycznego o stosunku jodku butyloamoniowego do jodku bizmutu(III) wynoszącym 3:2. Nadmiar BiI_3 wykorzystano, aby wprowadzić do materiału dodatkowe defekty struktury krystalicznej. Widma absorpcyjne przedstawiono na wstawkach na Rys. 2.14. Do oszacowania szerokości przerw wzbronionych wykorzystano wykresy Tauca przy założeniu prostej przerwy energetycznej. W niestechiometrycznej próbce przerwa wzbroniona wzrosła z 2.25 eV do 2.30 eV, co może być wyjaśnione efektem Bursteina-Mossa. Efektem zaburzenia stechiometrii związku jest wzrost koncentracji domieszek, które zapełniają dostępne stany w pobliżu dolnej krawędzi pasma przewodnictwa. Stany te w efekcie przestają być dostępne dla elektronów wzbudzanych poprzez absorpcję fotonu, które wymagają wyższych energii do wzbudzenia do pasma przewodnictwa. W konsekwencji powoduje to wzrost optycznej przerwy wzbronionej. Obserwacja ta jest także pośrednim dowodem na wzrost koncentracji defektów struktury krystalograficznej materiału wykrystalizowanego z niestechiometrycznego roztworu. Widma uzyskane

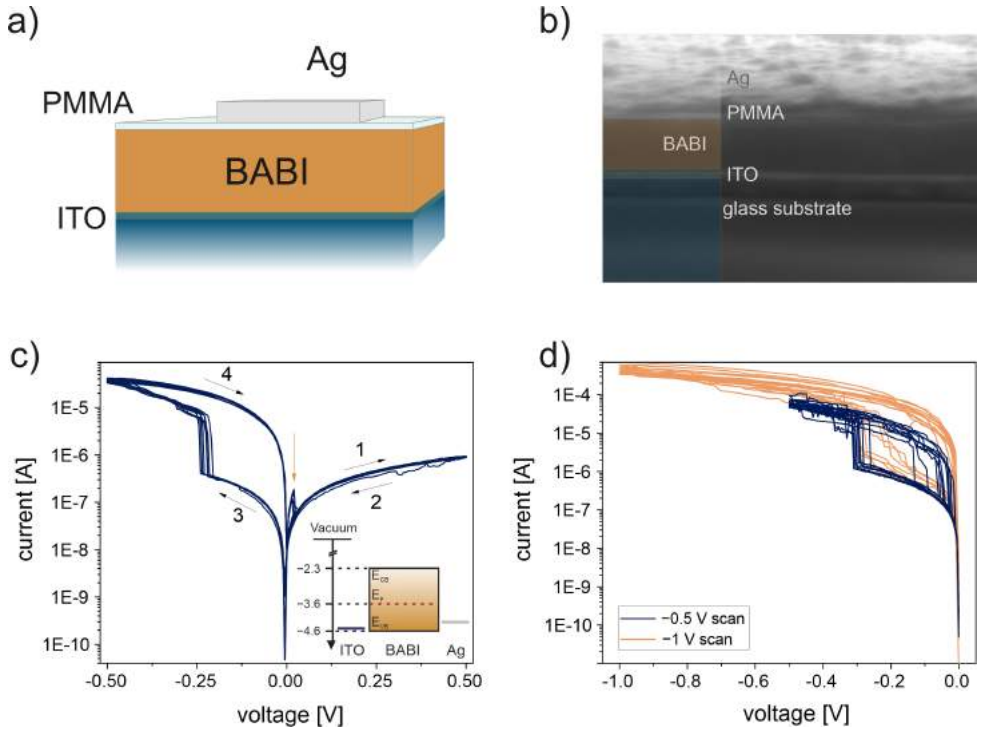

Rys. 2.15. (a) Budowa memrystora BABI. (b) Zdjęcie przekroju poprzecznego memrystora wykonane techniką skaningowej mikroskopii elektronowej z zaznaczonymi warstwami. (c) 10 kolejnych pomiarów $I-V$ ze strzałkami pokazującymi kierunek zmian napięcia. Wstawka przedstawia strukturę elektronową memrystora. (d) Pomiary $I-V$ jedynie w zakresie ujemnych napięć pokazujące, że stan LRS nie jest utrzymywany pomiędzy kolejnymi pomiarami.

w pomiarach spektroskopii fotoelektronów w zakresie ultrafioletu wskazują, że defektami tymi są wakancje jodkowe. Liczne badania perowskitów halogenkowych wskazują, że wakancje jodkowe migrować w gradiencie pola elektrycznego, tworząc przewodzące filamenty i powodować zmiany stanu rezystywnego memrystorów.

Memrystor zbudowano z warstwy aktywnej BABI osadzonej na przewodzącym podłożu tlenku cynowo-indowego (ITO). Jako elektrodę górną wykorzystano Ag. Aby zapobiec reakcji Ag z BABI, wykorzystano cienką warstwę polimetakrylanu metylu (PMMA). Schemat budowy przedstawiono na Rys. 2.15(a), a zdjęcie przekroju poprzecznego urządzenia wykonane techniką skaningowej mikroskopii elektronowej na Rys. 2.15(b).

Memrystor BABI charakteryzuje się pętlą histerezy w pomiarze prądowo-napięciowym $I-V$ widoczną jedynie w ujemnym zakresie napięć (Rys. 2.15(c)). Przejście z HRS do LRS zachodzi przy niskim napięciu ok. $-0.23\,\mathrm{V}$ i ma skokowy charakter, co jest charakterystyczne dla mechanizmu przełączania rezystywnego opartego o tworzenie filamentów

przewodzących. Zmiana polaryzacji napięcia w pomiarze $I-V$ pokazuje jednak, że filament ten jest nietrwały — w dodatnim zakresie napięć memrystor powraca do HRS, o czym świadczą niskie prądy i brak pętli histerezy. W niektórych przebiegach zaobserwowano moment zaniku filamentu przy niskich dodatnich napięciach, co zaznaczono pomarańczową strzałką na Rys. 2.15(c). Pomiary $I-V$ przeprowadzone wyłącznie w ujemnym zakresie napięć (Rys. 2.15(d)) pokazują, że stan LRS nie jest utrzymywany pomiędzy kolejnymi pomiarami, co świadczy o zaniku filamentu. Niskie napięcia, przy których zachodzi przełączanie sugerują także niską energię aktywacji defektów za nie odpowiedzialnych. Wykonując pomiary woltamperometryczne w szerokim zakresie temperatur oszacowano, że wynosi ona ok. 0.1 eV — wartość ta odpowiada wartościom energii aktywacji dla migracji wakancji jodkowych w perowskitach.

Niestabilność filamentu i spontaniczny powrót z LRS do HRS pozwala na odtworzenie efektów opisanych przez model LIF. Na Rys. 2.16(a) przedstawiono prąd wywołany krótkimi impulsami napięcia trwającymi 100 ms. Napięcie −300 mV nie wywołało żadnego impulsu prądowego, ale wraz ze wzrostem jego amplitudy do −500 mV, −800 mV i −1000 mV widoczny jest wzrost liczby impulsów prądowych. Napięcie −1500 mV powoduje przepływ prądu przez memrystor niemal przy każdym impulsie napięcia. Rys. 2.16(b) pokazuje prawdopodobieństwo zmierzenia impulsu prądowego w funkcji napięcia. Im wyższe napięcie, tym wyższe prawdopodobieństwo zaobserwowania impulsu prądowego. W neuronach opisanych przez model LIF, aby neuron wygenerował potencjał czynnościowy, zmiana potencjału błony neuronu musi być odpowiednio duża. Dopiero po jej przekroczeniu powstaje impuls przekazywany do kolejnego neuronu. Również w memrystorze BABI dopiero napięcie o amplitudzie wyższej niż −1000 mV powoduje powstanie impulsów prądowych.

Model LIF opisuje także, że wraz ze wzrostem częstotliwości stymulacji neuronu rośnie prawdopodobieństwo wygenerowania potencjału czynnościowego. Ten rodzaj plastyczności synaptycznej — wzmocnienie częstotliwościowe (ang. *frequency facilitation*) — odtworzono w memrystorze BABI poprzez przyłożenie do urządzenia impulsów napięcia o rosnącej częstotliwości (Rys. 2.17). Przy częstotliwości 200 Hz generowane są impulsy o amplitudzie nieprzekraczającej 100 µA; przy 2000 Hz amplituda większości impulsów jest prawie czterokrotnie wyższa.

W artykule przedstawiono także symulację sieci neuronowej, której parametry węzłów wyznaczono na podstawie charakterystyk prądowo-napięciowych memrystora BABI (Rys. 2.18). Sztuczna sieć składała się z warstwy wejściowej zawierającej 400 neuronów, warstwy ukrytej (100 neuronów) i warstwy wyjściowej (10 neuronów) (Rys. 2.18). Do trenowania sieci wykorzystano zbiór MNIST zawierający 10 000 zdjęć odręcznie pisanych cyfr, a do oszacowania dokładności klasyfikacji wykorzystano zbiór zawierający 60000

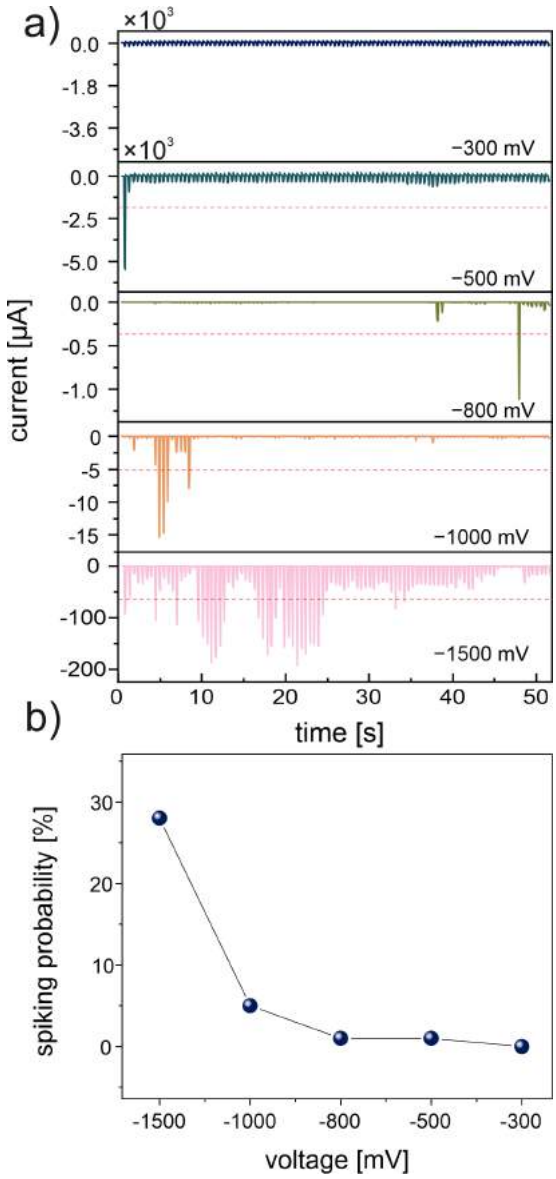

Rys. 2.16. (a) Impulsy prądowe wywołane poprzez przyłożenie impulsów napięciowych. Wraz ze wzrostem ich amplitudy rośnie liczba obserwowanych impulsów prądowych. Czerwoną przerywaną linią oznaczono amplitudę prądu, powyżej której sygnał klasyfikowano jako „impuls generowany przez neuron". (b) Prawdopodobieństwo generowania impulsu (o amplitudzie wyższej niż zaznaczona linią na panelu (a)).

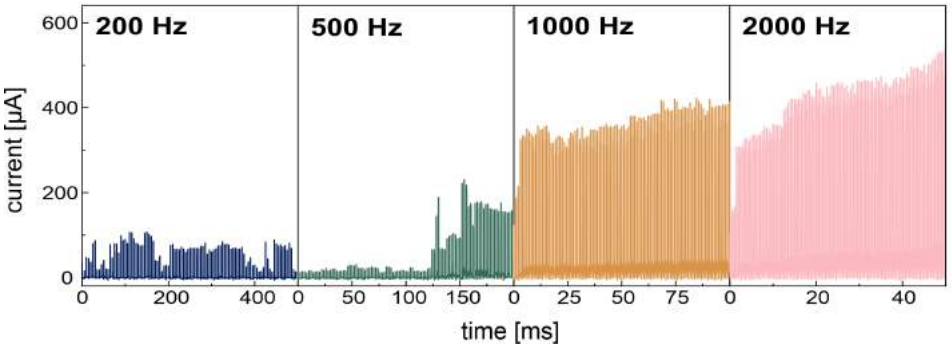

Rys. 2.17. Wzmocnienie synaptyczne przedstawione jako wzrost amplitudy prądu płynącego przez memrystor wraz ze wzrostem częstotliwości impulsów napięciowych.

obrazów. Sztuczna sieć neuronowa o zaprezentowanej architekturze była zdolna do rozpoznania cyfr z dokładnością ok. 94% osiągniętą w jedynie 20 cyklach trenowania. Wynik ten pokazuje, że sieci neuronowe oparte o memrystory mają duży potencjał w szeroko pojętych zastosowaniach związanych ze sztuczną inteligencją.

2.7.3. Podsumowanie

W artykule przedstawiono memrystor o ulotnej pamięci oparty o nowy typ związku: jodobizmutan butyloamoniowy. Przełączanie w tym materiale oparte jest o migrację wakancji jodkowych w polu elektrycznym, które tworzą przewodzący filament powodujący przejście z HRS do LRS. Nietrwałość tego filamentu powoduje spontaniczny powrót do HRS i odpowiada za ulotną pamięć urządzenia.

Efekt ulotności pamięci wykorzystano do odtworzenia w memrystorze BABI funkcji neuronu opisywanego przez model LIF. Pokazano, że impulsy prądowe generowane są tylko przez napięcie o odpowiedniej wartości, a amplituda impulsów zależy od częstotliwości stymulacji memrystora. Analogiczne efekty w neuronach opisywane są w modelu LIF.

Przeprowadzona symulacja sieci neuronowej, w której wykorzystano charakterystykę przełączania rezystywnego BABI, osiągnęła dokładność klasyfikacji odręcznie pisanych cyfr na poziomie 94%. Tak wysoki wynik sugeruje, że w macierze memrystorów BABI mogą z powodzeniem służyć do implementacji modeli sztucznych sieci neuronowych.

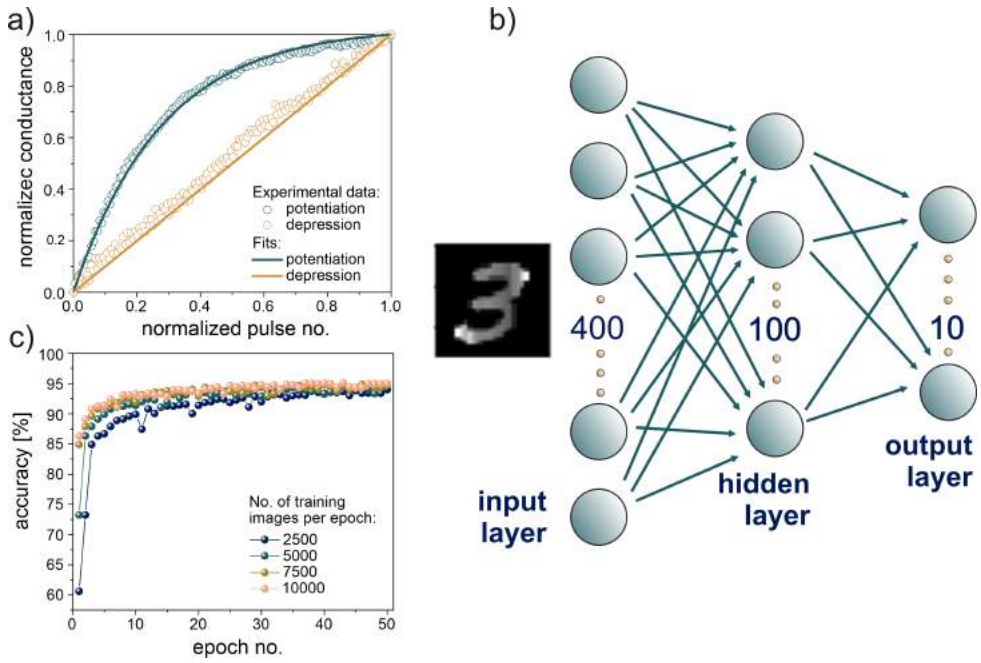

Rys. 2.18. (a) Zmiana konduktancji w funkcji liczby impulsów. Obie wielkości zostały znormalizowane. (b) Schemat budowy sztucznej sieci neuronowej wykorzystanej w symulacji. (c) Dokładność klasyfikacji odręcznie pisanych liczb osiąga poziom 94% w ok. dwudziestu cyklach trenowania.

ROZDZIAŁ 3

Podsumowanie

Badania opisane w niniejszej rozprawie doktorskiej skupiają się na efektach neuromimetycznych w memrystorach opartych o materiały o strukturze perowskitu oraz materiałach analogicznych. Rozdziały 2.1, 2.2 i 2.3 stanowią wprowadzenie teoretyczne do tematyki doktoratu. Pierwszy z nich poświęcony jest właściwościom optoelektronicznym perowskitów oraz ich związkowi ze budową tych materiałów. Dwa kolejne rozdziały skupiają się na potencjalnym zastosowaniu memrystorów w układach służących do przetwarzania informacji. W rozdziałach od 2.4 do 2.7 streszczono prace eksperymentalne, w których przedstawiono właściwości memrystywne i neuromimetyczne materiałów perowskitowych, analogicznych i pokrewnych oraz opisano mechanizmy fizyczne leżące u podstaw tych efektów.

Fragment artykułu przeglądowego streszczony w rozdziale 2.1 opisuje własności optoelektroniczne materiałów o strukturze perowskitu, szczególnie w kontekście oddziaływania tych materiałów ze światłem. Przedstawiono w nim także zależność szerokości przerwy wzbronionej od składu perowskitów oraz możliwość jej modulowania za pomocą domieszkowania bądź całkowitego podstawienia poszczególnych składników struktury. Na przykładzie perowskitów 2D, quasi-2D i 3D opisano związek zredukowanej wymiarowości materiału z jego właściwościami optoelektronicznymi, przedstawiając także przykłady zastosowań tych materiałów.

W rozdziale 2.2 przybliżono zastosowanie elementów memrystywnych w układach elektronicznych służących do uwierzytelnienia tożsamości użytkownika — fizycznie nieklonowalnych funkcjach. Nawet jeśli memrystory zostały wyprodukowane w tym samym procesie, posiadają pewną wariancję parametrów fizycznych, prowadzących do niejednakowej odpowiedzi elektrycznej. Przedstawiono wykorzystanie tej cechy do budowy układów o unikalnej i niemożliwej do sklonowania odpowiedzi.

Rozdział 2.3 kontynuuje opis zastosowania memrystorów w układach macierzowych, ale w zastosowaniu do wykonywania obliczeń na wektorach i macierzach. Duża efektywność memrystorów w wykonywaniu tych operacji sprawia, że mogą one przetwarzać duże struktury danych wydajniej niż procesory. Opisano, w jaki sposób mnożenie wektorów i macierzy jest realizowane w macierzach memrystorów oraz w jaki sposób operacje te wykorzystywane są do implementacji sieci neuronowych w fizycznych układach memrystywnych.

W artykule naukowym opisanym w rozdziale 2.4 opisano efekty memrystywne oraz efekty plastyczności synaptycznej w memrystorze opartym o perowskit bizmutowy. Pokazano, że przełączanie rezystywne wywołane jest modulacją wysokości bariery energetycznej na złączu elektrody metalicznej oraz perowskitu. Najistotniejszą część pracy stanowi charakterystyka efektów neuromimetycznych, których nie zbadano wcześniej w perowskicie bizmutowym. Oprócz plastyczności synaptycznych STDP i SRDP pokazano, że amplituda zmian odpowiedzi memrystora w tych pomiarach może być kontrolowana za pomocą napięcia, co pozwoliło na odtworzenie efektu metaplastycznego.

Artykuł streszczony w rozdziale 2.5 zawiera bardziej szczegółowy opis wpływu charakterystyki bariery Schottky'ego na złączu półprzewodnika i metalu na właściwości memrystywne i neuromimetyczne. Modyfikację parametrów złącza prowadząca do różnej charakterystyki bariery Schottky'ego uzyskano poprzez zmianę metalu elektrody. W zależności od orientacji bariery, w pomiarze STDP otrzymano — w zależności od użytego materiału — uczenie Hebba lub anty-Hebba, w których potencjalizacja i depresja występują przy odwrotnej kolejności impulsów pre- i postsynaptycznych.

W streszczeniu w rozdziale 2.6 pokazano, że efekty plastyczności synaptycznej oprócz napięcia mogą być indukowane także za pomocą światła. Dzięki silnemu oddziaływaniu ze światłem perowskit jodkowo-ołowiowy może wydajnie generować fotoprądy, których dynamika pozwala na odtworzenie efektów neuromorficznych. Wprowadzając do struktury memrystora materiał zdolny do pułapkowania ładunku doprowadzono do zmiany charakteru odpowiedzi synaptycznej. W memrystorze bez warstwy pułapkującej impulsy światła powodowały wzmocnienie synaptyczne, które ulegało przejściu w osłabienie w memrystorze z wprowadzoną warstwą. Pokazano ponadto, że za pomocą światła można odczytywać stan rezystywny memrystora zapisany za pomocą napięcia.

Rozdział 2.7 zawiera charakterystykę neuromimetyczną memrystora o pamięci ulotnej opartym o jodobizmutan butyloamoniowy (BABI). W memrystorze tym za przełączanie rezystywne odpowiedzialne jest tworzenie filamentu przewodzącego zbudowanego z wakancji jodkowych, a przyczyną nietrwałości stanów rezystywnych jest jego spontaniczny zanik. Dynamika tego typu przełączania pozwoliła na odtworzenie w memrystorze efektów opisanych modelem neuronu *leaky integrate-and-fire*. Potencjał zastosowania memrystora

BABI w układach neuromorficznych zbadano przeprowadzając symulację sztucznej sieci neuronowej, parametry której oparto na charakterystyce przełączania rezystywnego memrystora. Sieć osiągnęła wysoką dokładność w rozpoznawaniu odręcznie pisanych cyfr na poziomie 94%.

Badania zaprezentowane w niniejszej rozprawie są skoncentrowane na charakterystyce efektów neuromorficznych. Niektóre z nich, takie jak efekt metaplastyczny, indukowana światłem plastyczność synaptyczna i przetwarzanie sygnału w analogii do neuronów opisanych modelem *leaky integrate-and-fire* zostały scharakteryzowane w tych materiałach po raz pierwszy. Przedstawione w rozprawie badania są badaniami podstawowymi — zrozumienie fizycznych podstaw efektów neuromorficznych stanowi konieczny krok do rozwoju układów memrystywnych składających się z większej liczby elementów.

Bibliografia

[1] Emma Strubell, Ananya Ganesh i Andrew McCallum. „*Energy and policy considerations for modern deep learning research*". W: *AAAI 2020 - 34th AAAI Conference on Artificial Intelligence* (2020), s. 1393–13696. ISSN: 2159-5399. DOI: *10.1609/aaai.v34i09.7123*.

[2] J. von Neumann. „*First draft of a report on the EDVAC*". W: *IEEE Annals of the History of Computing* 15.4 (1993), s. 27–75. ISSN: 1058-6180. DOI: *10.1109/85.238389*.

[3] Onur Mutlu i in. „*Processing data where it makes sense: Enabling in-memory computation*". W: *Microprocessors and Microsystems* 67 (czer. 2019), s. 28–41. ISSN: 0141-9331. DOI: *10.1016/J.MICPRO.2019.01.009*.

[4] Thomas N. Theis i H. S. Philip Wong. „*The End of Moore's Law: A New Beginning for Information Technology*". W: *Computing in Science and Engineering* 19.2 (2017), s. 41–50. ISSN: 15219615. DOI: *10.1109/MCSE.2017.29*.

[5] Mark Horowitz. „*Computing's energy problem (and what we can do about it)*". W: *2014 IEEE International Solid-State Circuits Conference Digest of Technical Papers (ISSCC)*. T. 57. IEEE, lut. 2014, s. 10–14. ISBN: 978-1-4799-0920-9. DOI: *10.1109/ISSCC.2014.6757323*.

[6] Norman P. Jouppi i in. „*In-Datacenter Performance Analysis of a Tensor Processing Unit*". W: *Proceedings of the 44th Annual International Symposium on Computer Architecture*. T. Part F1286. New York, NY, USA: ACM, czer. 2017, s. 1–12. ISBN: 9781450348928. DOI: *10.1145/3079856.3080246*.

[7] Fei Yue Wang i in. „*Where does AlphaGo go: From church-turing thesis to AlphaGo thesis and beyond*". W: *IEEE/CAA Journal of Automatica Sinica* 3.2 (kw. 2016), s. 113–120. ISSN: 23299274. DOI: *10.1109/JAS.2016.7471613*.

[8] David Silver i in. „*Mastering the game of Go with deep neural networks and tree search*". W: *Nature* 529 (2016). DOI: *10.1038/nature16961*.

[9] Mike Davies i in. „*Loihi: A Neuromorphic Manycore Processor with On-Chip Learning*". W: *IEEE Micro* 38.1 (sty. 2018), s. 82–99. ISSN: 0272-1732. DOI: *10.1109/MM.2018.112130359*.

[10] Peter Blouw i in. „*Benchmarking Keyword Spotting Efficiency on Neuromorphic Hardware*". W: *Proceedings of the 7th Annual Neuro-inspired Computational Elements Workshop on - NICE '19*. New York, New York, USA: ACM Press, 2019, s. 1–8. ISBN: 9781450361231. DOI: *10.1145/3320288.3320304*.

[11] Steven K. Esser i in. „*Convolutional networks for fast, energy-efficient neuromorphic computing*". W: *Proceedings of the National Academy of Sciences* 113.41 (paź. 2016), s. 11441–11446. ISSN: 0027-8424. DOI: *10.1073/pnas.1604850113*.

[12] Bhavin J. Shastri i in. „*Photonics for artificial intelligence and neuromorphic computing*". W: *Nature Photonics 2021 15:2* 15.2 (sty. 2021), s. 102–114. ISSN: 1749-4893. DOI: *10.1038/s41566-020-00754-y*.

[13] Sören Boyn i in. „*Learning through ferroelectric domain dynamics in solid-state synapses*". W: *Nature Communications* 8.1 (kw. 2017), s. 14736. ISSN: 2041-1723. DOI: *10.1038/ncomms14736*.

[14] S. Oh, H. Hwang i I. K. Yoo. „*Ferroelectric materials for neuromorphic computing*". W: *APL Materials* 7.9 (wrz. 2019), s. 091109. ISSN: 2166532X. DOI: *10.1063/1.5108562*.

[15] Mohammad Taghi Sharbati i in. „*Low-Power, Electrochemically Tunable Graphene Synapses for Neuromorphic Computing*". W: *Advanced Materials* 30.36 (wrz. 2018), s. 1802353. ISSN: 1521-4095. DOI: *10.1002/ADMA.201802353*.

[16] Qiang Cao i in. „*Nonvolatile Multistates Memories for High-Density Data Storage*". W: *ACS Applied Materials & Interfaces* (2020). ISSN: 1944-8244. DOI: *10.1021/acsami.0c10184*.

[17] Leon Chua, Valery Sbitnev i Hyongsuk Kim. „*Hodgkin-Huxley Axon is Made of Memristors*". W: *International Journal of Bifurcation and Chaos* 22.03 (2012), s. 1230011. ISSN: 0218-1274. DOI: *10.1142/S021812741230011X*.

[18] Zhengguo Xiao i Jinsong Huang. „*Energy-Efficient Hybrid Perovskite Memristors and Synaptic Devices*". W: *Advanced Electronic Materials* 2.7 (lip. 2016), s. 1600100. ISSN: 2199160X. DOI: *10.1002/aelm.201600100*.

[19] Meiran Zhao i in. „*Reliability of analog resistive switching memory for neuromorphic computing*". W: *Applied Physics Reviews* 7.1 (mar. 2020), s. 011301. ISSN: 1931-9401. DOI: *10.1063/1.5124915*.

[20] Xinjiang Zhang i in. „*Neuromorphic Computing with Memristor Crossbar*". W: *Physica Status Solidi (A) Applications and Materials Science* 215.13 (2018), s. 1–16. ISSN: 18626319. DOI: *10.1002/pssa.201700875*.

[21] Wei Wang i in. „*Learning of spatiotemporal patterns in a spiking neural network with resistive switching synapses*". W: *Science Advances* 4.9 (2018), s. 1–9. ISSN: 23752548. DOI: *10.1126/sciadv.aat4752*.

[22] Daniele Ielmini i Stefano Ambrogio. „*Neuromorphic computing with resistive switching memory devices*". W: *Advances in Non-Volatile Memory and Storage Technology*. Second Edi. Elsevier Ltd., 2019, s. 603–631. ISBN: 9780081025840. DOI: *10.1016/b978-0-08-102584-0.00017-6*.

[23] Hyojung Kim i in. „*Halide perovskites for resistive random-access memories*". W: *Journal of Materials Chemistry C* 7.18 (maj 2019), s. 5226–5234. ISSN: 2050-7526. DOI: *10.1039/C8TC06031B*.

[24] Dmitri B. Strukov i in. „*The missing memristor found*". W: *Nature* 453.7191 (maj 2008), s. 80–3. ISSN: 1476-4687. DOI: *10.1038/nature06932*.

[25] Leon O. Chua. „*Memristor—The Missing Circuit Element*". W: *IEEE Transactions on Circuit Theory* 18.5 (1971), s. 507–519. ISSN: 00189324. DOI: *10.1109/TCT.1971.1083337*.

[26] V Biolkova, D. Biolek i Z Biolek. „*Pinched hysteretic loops of ideal memristors, memcapacitors and meminductors must be 'self-crossing'*". W: *Electronics Letters* 47.25 (2011), s. 1385–1387. ISSN: 0013-5194. DOI: *10.1049/el.2011.2913*.

[27] Massimiliano Di Ventra i Yuriy V. Pershin. „*On the physical properties of memristive, memcapacitive and meminductive systems*". W: *Nanotechnology* 24.25 (2013), s. 255201. ISSN: 09574484. DOI: *10.1088/0957-4484/24/25/255201*.

[28] Yan Wang i in. „*Synergies of Electrochemical Metallization and Valance Change in All-Inorganic Perovskite Quantum Dots for Resistive Switching*". W: *Advanced Materials* 30.28 (lip. 2018), s. 1800327. ISSN: 09359648. DOI: *10.1002/adma.201800327*.

[29] Rafael Schmitt i in. „*Design of Oxygen Vacancy Configuration for Memristive Systems*". W: *ACS Nano* 11.9 (2017), s. 8881–8891. ISSN: 1936086X. DOI: *10.1021/acsnano.7b03116*.

[30] Sung Kyu Kim i in. „*Direct Observation of Conducting Nanofilaments in Graphene-Oxide-Resistive Switching Memory*". W: *Advanced Functional Materials* 25.43 (2015), s. 6710–6715. ISSN: 16163028. DOI: *10.1002/adfm.201502734*.

[31] Selina La Barbera, Dominique Vuillaume i Fabien Alibart. „*Filamentary switching: Synaptic plasticity through device volatility*". W: *ACS Nano* 9.1 (2015), s. 941–949. ISSN: 1936086X. DOI: *10.1021/nn506735m*.

[32] Qi Liu i in. „*Real-Time Observation on Dynamic Growth/Dissolution of Conductive Filaments in Oxide-Electrolyte-Based ReRAM*". W: *Adv. Mater* 24 (2012), s. 1844–1849. DOI: *10.1002/adma.201104104*.

[33] Roberto Carboni i Daniele Ielmini. „*Stochastic Memory Devices for Security and Computing*". W: *Advanced Electronic Materials* 5.9 (2019), s. 1–27. ISSN: 2199160X. DOI: *10.1002/aelm.201900198*.

[34] S Bagdzevicius i in. „*Interface-type resistive switching in perovskite materials*". W: *Journal of Electroceramics* 39.1-4 (grud. 2017), s. 157–184. ISSN: 1385-3449. DOI: *10.1007/s10832-017-0087-9*.

[35] Daniele Ielmini i H.-S. Philip Wong. „*In-memory computing with resistive switching devices*". W: *Nature Electronics* 1.6 (czer. 2018), s. 333–343. ISSN: 2520-1131. DOI: *10.1038/s41928-018-0092-2*.

[36] Matthias Wuttig i Noboru Yamada. „*Phase-change materials for rewriteable data storage*". W: *Nature Materials 2007 6:11* 6.11 (2007), s. 824–832. ISSN: 1476-4660. DOI: *10.1038/nmat2009*.

[37] Aravinthan Athmanathan i in. „*Multilevel-Cell Phase-Change Memory: A Viable Technology*". W: *IEEE Journal on Emerging and Selected Topics in Circuits and Systems* 6.1 (mar. 2016), s. 87–100. ISSN: 21563357. DOI: *10.1109/JETCAS.2016.2528598*.

[38] Noboru Yamada i in. „*Rapid-phase transitions of GeTe-Sb2Te3 pseudobinary amorphous thin films for an optical disk memory*". W: *Journal of Applied Physics* 69.5 (czer. 1998), s. 2849. ISSN: 0021-8979. DOI: *10.1063/1.348620*.

[39] Xilin Zhou i in. „*Carbon-doped Ge2Sb2Te5 phase change material: A candidate for high-density phase change memory application*". W: *Applied Physics Letters* 101.14 (paź. 2012), s. 142104. ISSN: 0003-6951. DOI: *10.1063/1.4757137*.

[40] Anja Wedig i in. „*Nanoscale cation motion in TaOx, HfOx and TiOx memristive systems*". W: *Nature Nanotechnology 2015 11:1* 11.1 (wrz. 2015), s. 67–74. ISSN: 1748-3395. DOI: *10.1038/nnano.2015.221*.

[41] Hee Ju Yun i Byung Joon Choi. „*Effects of moisture and electrode material on AlN-based resistive random access memory*". W: *Ceramics International* 45.13 (wrz. 2019), s. 16311–16316. ISSN: 0272-8842. DOI: *10.1016/J.CERAMINT.2019.05.157*.

[42] Deok Hwang Kwon i in. „*Atomic structure of conducting nanofilaments in TiO2 resistive switching memory*". W: *Nature Nanotechnology 2010 5:2* 5.2 (sty. 2010), s. 148–153. ISSN: 1748-3395. DOI: *10.1038/nnano.2009.456*.

[43] Sieu D. Ha i Shriram Ramanathan. „*Adaptive oxide electronics: A review*". W: *Journal of Applied Physics* 110.7 (paź. 2011), s. 071101. ISSN: 0021-8979. DOI: *10.1063/1.3640806*.

[44] S. O. Kasap. „*Principles of Electronic Materials and Devices*". 4 wyd. McGraw-Hill Education, 2018, s. 978. ISBN: 978-0-07-802818-2.

[45] S.M. Sze i Kwok K. Ng. „*Physics of Semiconductor Devices Physics of Semiconductor Devices*". T. 10. 1995, s. 739–751. ISBN: 978-3-319-03001-2.

[46] Xinwei Guan i in. „*Light-Responsive Ion-Redistribution-Induced Resistive Switching in Hybrid Perovskite Schottky Junctions*". W: *Advanced Functional Materials* 28.3 (sty. 2018), s. 1–11. ISSN: 16163028. DOI: *10.1002/adfm.201704665*.

[47] Tae-Hee Hee Han i in. „*Interface and Defect Engineering for Metal Halide Perovskite Optoelectronic Devices*". W: *Advanced Materials* 1803515 (2019), s. 1–35. ISSN: 15214095. DOI: *10.1002/adma.201803515*.

[48] Yuetong Fang i in. „*Advances in Halide Perovskite Memristor from Lead-Based to Lead-Free Materials*". W: *ACS Applied Materials and Interfaces* 13.15 (2021), s. 17141–17157. ISSN: 19448252. DOI: *10.1021/acsami.1c03433*.

[49] Sascha Vongehr i Xiangkang Meng. „*The missing memristor has not been found*". W: *Scientific Reports* 5.1 (grud. 2015), s. 11657. ISSN: 20452322. DOI: *10.1038/srep11657*.

[50] Jinsun Kim i in. „*An Experimental Proof that Resistance-Switching Memory Cells are not Memristors*". W: *Advanced Electronic Materials* 6.7 (lip. 2020), s. 2000010. ISSN: 2199-160X. DOI: *10.1002/aelm.202000010*.

[51] Isaac Abraham. „*The case for rejecting the memristor as a fundamental circuit element*". W: *Scientific Reports* 8.1 (2018), s. 1–9. ISSN: 20452322. DOI: *10.1038/s41598-018-29394-7*.

[52] Leon Chua. „*If it's pinched it's a memristor*". W: *Semiconductor Science and Technolgy* 29.10 (paź. 2014), s. 104001. ISSN: 0268-1242. DOI: *10.1088/0268-1242/29/10/104001*.

[53] Abu Sebastian i in. „*Memory devices and applications for in-memory computing*". W: *Nature Nanotechnology* 15.7 (lip. 2020), s. 529–544. ISSN: 1748-3387. DOI: *10.1038/s41565-020-0655-z*.

[54] Olga Malinkiewicz i in. „*Perovskite solar cells employing organic charge-transport layers*". W: *Nature Photonics* 8.2 (2014), s. 128–132. ISSN: 17494885. DOI: *10.1038/nphoton.2013.341*.

[55] Ayan A. Zhumekenov i in. „*Formamidinium Lead Halide Perovskite Crystals with Unprecedented Long Carrier Dynamics and Diffusion Length*". W: *ACS Energy Letters* 1.1 (2016), s. 32–37. ISSN: 23808195. DOI: *10.1021/acsenergylett.6b00002*.

[56] Michael Saliba i in. „*Cesium-containing triple cation perovskite solar cells: improved stability, reproducibility and high efficiency*". W: *Energy & Environmental Science* 9.6 (2016), s. 1989–1997. DOI: *10.1039/c5ee03874j*.

[57] Fan Zuo i in. „*Binary-Metal Perovskites Toward High-Performance Planar-Heterojunction Hybrid Solar Cells*". W: *Advanced Materials* 26.37 (paź. 2014), s. 6454–6460. ISSN: 1521-4095. DOI: *10.1002/ADMA.201401641*.

[58] Ming-Gang Ju i in. „*Lead-Free Mixed Tin and Germanium Perovskites for Photovoltaic Application*". W: *Journal of the American Chemical Society* 139.23 (czer. 2017), s. 8038–8043. ISSN: 0002-7863. DOI: *10.1021/jacs.7b04219*.

[59] Giulia Grancini i Mohammad Khaja Nazeeruddin. „*Dimensional tailoring of hybrid perovskites for photovoltaics*". W: *Nature Reviews Materials* 4.1 (2019), s. 4–22. ISSN: 20588437. DOI: *10.1038/s41578-018-0065-0*.

[60] Loredana Protesescu i in. „*Dismantling the "Red Wall" of Colloidal Perovskites: Highly Luminescent Formamidinium and Formamidinium–Cesium Lead Iodide Nanocrystals*". W: *ACS Nano* 11.3 (mar. 2017), s. 3119–3134. ISSN: 1936-0851. DOI: *10.1021/acsnano.7b00116*.

[61] Javad Shamsi i in. „*Metal Halide Perovskite Nanocrystals: Synthesis, Post-Synthesis Modifications, and Their Optical Properties*". W: *Chemical Reviews* 119.5 (mar. 2019), s. 3296–3348. ISSN: 15206890. DOI: *10.1021/acs.chemrev.8b00644*.

[62] Stefaan De Wolf i in. „*Organometallic halide perovskites: Sharp optical absorption edge and its relation to photovoltaic performance*". W: *Journal of Physical Chemistry Letters* 5.6 (mar. 2014), s. 1035–1039. ISSN: 19487185. DOI: *10.1021/jz500279b*.

[63] Zhi-Kuang Tan i in. „*Bright light-emitting diodes based on organometal halide perovskite*". W: *Nature Nanotechnology* 9.August (2014), s. 1–6. ISSN: 1748-3387. DOI: *10.1038/nnano.2014.149*.

[64] Tomasz Mazur, Piotr Zawal i Konrad Szaciłowski. „*Synaptic plasticity, metaplasticity and memory effects in hybrid organic-inorganic bismuth-based materials*". W: *Nanoscale* 11.3 (2019), s. 1080–1090. ISSN: 20403372. DOI: *10.1039/c8nr09413f*.

[65] Bruce S. Gillis, Zarema Arbieva i Igor M. Gavin. „*Analysis of lead toxicity in human cells*". W: *BMC genomics* 13.1 (lip. 2012). ISSN: 1471-2164. DOI: *10.1186/1471-2164-13-344*.

[66] Lei Shi i in. „*Accelerated Lifetime Testing of Organic-Inorganic Perovskite Solar Cells Encapsulated by Polyisobutylene*". W: *ACS Applied Materials and Interfaces* 9.30 (2017), s. 25073–25081. ISSN: 19448252. DOI: *10.1021/acsami.7b07625*.

[67] Joel Troughton, Katherine Hooper i Trystan M. Watson. „*Humidity resistant fabrication of CH3NH3PbI3 perovskite solar cells and modules*". W: *Nano Energy* 39.June (wrz. 2017), s. 60–68. ISSN: 22112855. DOI: *10.1016/j.nanoen.2017.06.039*.

[68] G Grancini i in. „*One-Year stable perovskite solar cells by 2D/3D interface engineering.*" W: *Nature communications* 8 (2017), s. 15684. ISSN: 2041-1723. DOI: *10.1038/ncomms15684*.

[69] Nacereddine Lakhdar i Abdelkader Hima. „*Electron transport material effect on performance of perovskite solar cells based on CH3NH3GeI3*". W: *Optical Materials* 99 (sty. 2020), s. 109517. ISSN: 0925-3467. DOI: *10.1016/J.OPTMAT.2019.109517*.

[70] Ping Ping Sun i in. „*Theoretical insights into a potential lead-free hybrid perovskite: substituting Pb 2+ with Ge 2+*". W: *Nanoscale* 8.3 (sty. 2016), s. 1503–1512. ISSN: 20403372. DOI: *10.1039/C5NR05337D*.

[71] Feng Hao i in. „*Solvent-Mediated Crystallization of CH3NH3SnI3 Films for Heterojunction Depleted Perovskite Solar Cells*". W: *Journal of the American Chemical Society* 137.35 (wrz. 2015), s. 11445–11452. ISSN: 0002-7863. DOI: *10.1021/jacs.5b06658*.

[72] Karunakara Moorthy Boopathi i in. „*Solution-processable antimony-based light-absorbing materials beyond lead halide perovskites*". W: *Journal of Materials Chemistry A* 5.39 (2017), s. 20843–20850. ISSN: 20507496. DOI: *10.1039/c7ta06679a*.

[73] Chunfeng Lan i in. „*Effect of lead-free (CH3NH3)3Bi2I9perovskite addition on spectrum absorption and enhanced photovoltaic performance of bismuth triiodide solar cells*". W: *Journal of Alloys and Compounds* 701 (2017), s. 834–840. ISSN: 09258388. DOI: *10.1016/j.jallcom.2017.01.169*.

[74] Robert L.Z. Z Hoye i in. „*Methylammonium Bismuth Iodide as a Lead-Free, Stable Hybrid Organic-Inorganic Solar Absorber*". W: *Chemistry - A European Journal* 22.8 (2016), s. 2605–2610. ISSN: 15213765. DOI: *10.1002/chem.201505055*.

[75] Sanam Attique i in. „*A Potential Checkmate to Lead: Bismuth in Organometal Halide Perovskites, Structure, Properties, and Applications*". W: *Advanced Science* 7.13 (lip. 2020), s. 1903143. ISSN: 2198-3844. DOI: *10.1002/advs.201903143*.

[76] Bohee Hwang i Jang-Sik Lee. „*Lead-free, air-stable hybrid organic–inorganic perovskite resistive switching memory with ultrafast switching and multilevel data storage*". W: *Nanoscale* 10.18 (maj 2018), s. 8578–8584. ISSN: 2040-3364. DOI: *10.1039/C8NR00863A*.

[77] Ajinkya Bhorde i in. „*Highly stable and Pb-free bismuth-based perovskites for photodetector applications*". W: *New Journal of Chemistry* 44 (2020), s. 11282. ISSN: 1144-0546. DOI: *10.1039/d0nj01806f*.

[78] Yongping Fu i in. „*Metal halide perovskite nanostructures for optoelectronic applications and the study of physical properties*". W: *Nature Reviews Materials* 4.3 (2019), s. 169–188. ISSN: 20588437. DOI: *10.1038/s41578-019-0080-9*.

[79] C. Soykan i H. Gocmez. „*The physical properties of bismuth replacement in lead halogen perovskite solar cells: CH3NH3Pb1-xBixI3 compounds by ab-initio calculations*". W: *Results in Physics* 13 (czer. 2019), s. 102278. ISSN: 22113797. DOI: *10.1016/j.rinp.2019.102278*.

[80] Johnpaul K Pious i in. „*Bismuth-Based Zero-Dimensional Perovskite-like Materials: Effect of Benzylammonium on Dielectric Confinement and Photoconductivity*". W: *Chemistry of Materials* 32.6 (2020), s. 2647–2652. ISSN: 15205002. DOI: *10.1021/acs.chemmater.0c00390*.

[81] Kai Eckhardt i in. „*Crystallographic insights into (CH3NH3)3(Bi2I9): A new lead-free hybrid organic-inorganic material as a potential absorber for photovoltaics*". W: *Chemical Communications* 52.14 (lut. 2016), s. 3058–3060. ISSN: 1364548X. DOI: *10.1039/c5cc10455f*.

[82] Alan Longstaff. „*Krótkie wykłady. Neurobiologia.*" I. Warszawa: Wydawnictwo Naukowe PWN, 2012, s. 561. ISBN: 68897512.

[83] Jianshi Tang i in. „*Bridging Biological and Artificial Neural Networks with Emerging Neuromorphic Devices: Fundamentals, Progress, and Challenges*". W: *Advanced Materials* 31.49 (grud. 2019). ISSN: 15214095. DOI: *10.1002/adma.201902761*.

[84] Adam H. Marblestone i in. „*Physical principles for scalable neural recording*". W: *Frontiers in Computational Neuroscience* 0.OCT (paź. 2013), s. 137. ISSN: 16625188. DOI: *10.3389/FNCOM.2013.00137/BIBTEX*.

[85] Dale Purves i in. „*Neurosciences.*" Red. Dale Purves i in. 6 wyd. T. 52. 10. Sunderland, Massachusetts: Oxford University Press, paź. 2018, 22N–9N. ISBN: 9781605353807.

[86] Donald O Hebb. „*The organization of behavior: A neurophysiological approach*". New York: Wiley i Sons, 1949.

[87] G. S. Stent. „*A physiological mechanism for Hebb's postulate of learning.*" W: *Proceedings of the National Academy of Sciences of the United States of America* 70.4 (1973), s. 997–1001. ISSN: 00278424. DOI: *10.1073/pnas.70.4.997*.

[88] Guo-qiang Bi i Mu-ming Poo. „*Synaptic Modifications in Cultured Hippocampal Neurons: Dependence on Spike Timing, Synaptic Strength, and Postsynaptic Cell Type*". W: *The Journal of Neuroscience* 18.24 (grud. 1998), s. 10464–10472. ISSN: 0270-6474. DOI: *10.1523/JNEUROSCI.18-24-10464.1998*.

[89] Wei He i in. „*Enabling an integrated rate-temporal learning scheme on memristor*". W: *Scientific Reports* 4 (2014). ISSN: 20452322. DOI: *10.1038/srep04755*.

[90] Chiara Bartolozzi. „*Synaptic Plasticity in Neuromorphic Systems*". Red. Christian Mayr i in. T. 24. Frontiers Research Topics 4. Frontiers Media SA, 2016, s. 20–22. ISBN: 9782889198771. DOI: *10.3389/978-2-88919-877-1*.

[91] Youngjun Park i Jang Sik Lee. „*Artificial Synapses with Short- and Long-Term Memory for Spiking Neural Networks Based on Renewable Materials*". W: *ACS Nano* 11.9 (2017), s. 8962–8969. ISSN: 1936086X. DOI: *10.1021/acsnano.7b03347*.

[92] Sen Song, Kenneth D Miller i L F Abbott. „*Competitive Hebbian learning through spike-timing-dependent synaptic plasticity*". W: *Nature Neuroscience* 3.9 (2000), s. 919–926. ISSN: 10976256. DOI: *10.1038/78829*.

[93] D.A. A. Lapkin i in. „*Spike-timing-dependent plasticity of polyaniline-based memristive element*". W: *Microelectronic Engineering* 185-186 (2018), s. 43–47. ISSN: 01679317. DOI: *10.1016/j.mee.2017.10.017*.

[94] Ayoub H Jaafar i in. „*Reversible optical switching memristors with tunable STDP synaptic plasticity: A route to hierarchical control in artificial intelligent systems*". W: *Nanoscale* 9.43 (2017), s. 17091–17098. ISSN: 20403372. DOI: *10.1039/c7nr06138b*.

[95] Sung Il Kim i in. „*Dimensionality Dependent Plasticity in Halide Perovskite Artificial Synapses for Neuromorphic Computing*". W: *Advanced Electronic Materials* 5.9 (mar. 2019), s. 1900008. ISSN: 2199160X. DOI: *10.1002/aelm.201900008*.

[96] Zheng Hua Tan i in. „*Synaptic Metaplasticity Realized in Oxide Memristive Devices*". W: *Advanced Materials* 28.2 (2016), s. 377–384. ISSN: 15214095. DOI: *10.1002/adma.201503575*.

[97] Alexantrou Serb i in. „*Memristive synapses connect brain and silicon spiking neurons*". W: *Scientific Reports* 10.1 (2020), s. 2590. ISSN: 2045-2322. DOI: *10.1038/s41598-020-58831-9*.

[98] Isha Gupta i in. „*Real-time encoding and compression of neuronal spikes by metal-oxide memristors*". W: *Nature Communications* 7.1 (wrz. 2016), s. 1–9. ISSN: 20411723. DOI: *10.1038/ncomms12805*.

[99] Zhong Sun i in. „*One-step regression and classification with cross-point resistive memory arrays*". W: *Science Advances* 6.5 (sty. 2020), eaay2378. ISSN: 2375-2548. DOI: *10.1126/sciadv.aay2378*.

[100] Zhong Sun i in. „*Solving matrix equations in one step with cross-point resistive arrays*". W: *Proceedings of the National Academy of Sciences of the United States of America* 116.10 (2019), s. 4123–4128. ISSN: 10916490. DOI: *10.1073/pnas.1815682116*.

[101] Zhongrui Wang i in. „*Reinforcement learning with analogue memristor arrays*". W: *Nature Electronics* 2.3 (mar. 2019), s. 115–124. ISSN: 25201131. DOI: *10.1038/s41928-019-0221-6*.

[102] Hongsik Jeong i Luping Shi. „*Memristor devices for neural networks*". W: *Journal of Physics D: Applied Physics* 52.2 (2019). ISSN: 13616463. DOI: *10.1088/1361-6463/aae223*.

[103] Seung Ju Kim i in. „*Vertically aligned two-dimensional halide perovskites for reliably operable artificial synapses*". W: *Materials Today* 52 (sty. 2022), s. 19–30. ISSN: 1369-7021. DOI: *10.1016/J.MATTOD.2021.10.035*.

[104] Yuting Zhang i in. „*Three-dimensional perovskite nanowire array-based ultrafast resistive RAM with ultralong data retention*". W: *Science Advances* 7.36 (wrz. 2021). ISSN: 23752548. DOI: *10.1126/SCIADV.ABG3788*.

[105] Rohit Abraham John i in. „*Ionotronic Halide Perovskite Drift-Diffusive Synapses for Low-Power Neuromorphic Computation*". W: *Advanced Materials* 30.51 (grud. 2018), s. 1805454. ISSN: 09359648. DOI: *10.1002/adma.201805454*.

[106] Seonggil Ham i in. „*Photonic Organolead Halide Perovskite Artificial Synapse Capable of Accelerated Learning at Low Power Inspired by Dopamine-Facilitated Synaptic Activity*". W: *Advanced Functional Materials* 29.5 (lut. 2019), s. 1806646. ISSN: 16163028. DOI: *10.1002/adfm.201806646*.

[107] Leilei Gu i in. „*A biomimetic eye with a hemispherical perovskite nanowire array retina*". W: *Nature* 581 (2020). DOI: *10.1038/s41586-020-2285-x*.

[108] Seongin Hong i in. „*Sensory Adaptation and Neuromorphic Phototransistors Based on CsPb(Br1– xIx)3 Perovskite and MoS2 Hybrid Structure*". W: *ACS Nano* 14.8 (sierp. 2020), s. 9796–9806. ISSN: 1936-0851. DOI: *10.1021/acsnano.0c01689*.

[109] Xinwei Guan i in. „*A monolithic artificial iconic memory based on highly stable perovskite-metal multilayers*". W: *Applied Physics Reviews* 7.3 (2020). ISSN: 19319401. DOI: *10.1063/5.0009713*.

[110] NREL. „*Best Research-Cell Efficiency Chart | Photovoltaic Research | NREL*". 2019.

[111] Bin Yang i in. „*Perovskite Solar Cells with Near 100% Internal Quantum Efficiency Based on Large Single Crystalline Grains and Vertical Bulk Heterojunctions*". W: *Journal of the American Chemical Society* 137.29 (2015), s. 9210–9213. ISSN: 15205126. DOI: *10.1021/jacs.5b03144*.

[112] R. Zhang i in. „*Nanoscale diffusive memristor crossbars as physical unclonable functions*". W: *Nanoscale* 10.6 (2018), s. 2721–2726. ISSN: 2040-3364. DOI: *10.1039/C7NR06561B*.

[113] Xiaojian Zhu i Wei D. Lu. „*Optogenetics-Inspired Tunable Synaptic Functions in Memristors*". W: *ACS Nano* 12.2 (lut. 2018), s. 1242–1249. ISSN: 1936086X. DOI: *10.1021/acsnano.7b07317*.

[114] Yongbo Yuan i in. „*Photovoltaic Switching Mechanism in Lateral Structure Hybrid Perovskite Solar Cells*". W: *Advanced Energy Materials* 5.15 (sierp. 2015), s. 1–7. ISSN: 16146840. DOI: *10.1002/aenm.201500615*.

[115] H Vázquez i in. „*Energy level alignment at organic heterojunctions: Role of the charge neutrality level*". W: *Physical Review B* 71.4 (sty. 2005), s. 041306. ISSN: 1098-0121. DOI: *10.1103/PhysRevB.71.041306*.

[116] Tomonori Nishimura, Koji Kita i Akira Toriumi. „*Evidence for strong Fermi-level pinning due to metal-induced gap states at metal/germanium interface*". W: *Applied Physics Letters* 91.12 (2007), s. 23702. ISSN: 00036951. DOI: *10.1063/1.2789701*.

[117] Sylvain Saïghi i in. „*Plasticity in memristive devices for spiking neural networks*". W: *Frontiers in Neuroscience* 9.MAR (mar. 2015), s. 1–16. ISSN: 1662-453X. DOI: *10.3389/fnins.2015.00051*.

[118] Spyros Stathopoulos i in. „*Multibit memory operation of metal-oxide bi-layer memristors*". W: *Scientific Reports* 7.1 (grud. 2017), s. 17532. ISSN: 2045-2322. DOI: *10.1038/s41598-017-17785-1*.

[119] Che-Chia Chia Chang i in. „*Interchangeable Hebbian and Anti-Hebbian STDP Applied to Supervised Learning in Spiking Neural Network*". W: s. 1–15. DOI: *10.1109/IEDM.2018.8614648*.

[120] Vincent Wing-hei Lau i in. „*Dark Photocatalysis: Storage of Solar Energy in Carbon Nitride for Time-Delayed Hydrogen Generation*". W: *Angewandte Chemie International Edition* 56.2 (sty. 2017), s. 510–514. ISSN: 14337851. DOI: *10.1002/anie.201608553*.

ROZDZIAŁ 4

Załączniki do rozprawy

4.1. Artykuły naukowe wchodzące w skład rozprawy

Coordination Chemistry Reviews 415 (2020) 213316

Contents lists available at ScienceDirect

Coordination Chemistry Reviews

journal homepage: www.elsevier.com/locate/ccr

Review

Halogen-containing semiconductors: From artificial photosynthesis to unconventional computing

Sylwia Klejna [a,1], Tomasz Mazur [a,1], Ewelina Wlaźlak [a,1], Piotr Zawal [a,b,1], Han Sen Soo [c,*], Konrad Szaciłowski [a,*]

[a] Academic Center for Materials and Nanotechnology, AGH University of Science and Technology, al. Mickiewicza 30, 30-059 Kraków, Poland
[b] Faculty of Physics and Applied Computer Science, AGH University of Science and Technology, al. Mickiewicza 30, 30-059 Kraków, Poland
[c] Division of Chemistry and Biological Chemistry, School of Physical and Mathematical Sciences, Nanyang Technological University, 21 Nanyang Link, Singapore 637371, Singapore

ARTICLE INFO

Article history:
Received 24 January 2020
Received in revised form 19 March 2020
Accepted 23 March 2020
Available online 7 April 2020

Keywords:
Semiconductors
Metal halide perovskites
Photocatalysis
Artificial photosynthesis
Photovoltaics
Memristors
Neuromimetic technologies

ABSTRACT

Unconventional computing and artificial photosynthesis seem to be completely unrelated fields of research. However, both technologies try to sustain the development of our civilization despite the flood of information and limited energy resources. In this review, we will show that the same materials – namely organic–inorganic metal halide perovskites and other iodine-based semiconductors – are materials of choice for both fields of scientific and technological activity. This contribution reviews the most up-to-date achievements in the fields of artificial photosynthesis and neuromimetic unconventional computing that utilize metal halide perovskites or other heavy metal-halogen compounds as active materials. Recent advances about photocatalysis and perovskite photovoltaics are also added to demonstrate the versatility of the applications that result from the peculiar geometric and electronic structures of iodine-based semiconductors.

Contents

* Corresponding authors.
E-mail addresses: hansen@ntu.edu.sg (H.S. Soo), szacilow@agh.edu.pl (K. Szaciłowski).
[1] These authors have equally contributed to the manuscript and are listed in an alphabetic order.

https://doi.org/10.1016/j.ccr.2020.213316
0010-8545/

1. Introduction

Energy and information are the two main 'fuels' powering modern society [1]. In an information-driven world, its effective acquisition, processing, and storage is a matter of utmost importance. Fast information processing and storage, however, is extremely energy-demanding. In 2016, data centers were estimated to have consumed over 416 TWh of electric energy, more than the United Kingdom during the same period (300 TWh) [2]. It is also estimated that energy consumption related to information storage and processing accounts for 3.2% of the total anthropogenic carbon dioxide emissions [2]. The amount of energy used by data centers continues to double every four years, meaning that they have the fastest-growing carbon footprint of any area within the information technology (IT) sector [2].

A human brain (cerebrum) contains approximately 10–20 billion neurons, with around 55–70 billion in the cerebellum [3,4]. Each neuron forms approximately 10^4 connections, which altogether yields about 100 trillion (1×10^{14}) synaptic connections within an average human brain [5]. This impressive network is dense as each cubic millimeter of neural tissue contains up to 10^9 synaptic junctions. While the brain typically constitutes only 2% of the body mass, it consumes 20% of the energy demand at rest. Despite the tremendous energetic efficiencies of neural systems, which remain in striking contrast with computer systems, the brain is still the most energy-demanding organ in a human body [6].

Existing computer technologies are largely based on semiconductor materials, and their development is an example of an extraordinarily successful history [7]. However, despite their unprecedented achievements, current classical computational paradigms encompass only a small subset of all computational possibilities [8]. There is a very broad class of computational substrates and paradigms, which utilize dynamic physical systems and can be successfully exploited as computing media [9].

Through billions of years of evolution, Nature has created various miraculous structures of unprecedented performance. All living organisms are enormously complex structures capable of energy harvesting and information processing. These processes have various manifestations in different domains and kingdoms of life. From all the energetic transformations, photosynthesis may not be the most ubiquitous (due to the abundance of fungi and bacteria), but it is likely to be one of the most efficient and important processes of energy harvesting [10]. All living creatures (and also viruses, which are excluded from the tree of life [11]) use nucleic acids as the principal information carrier. Among all living entities, animals have developed the most advanced information-related structure – the neural system that finally yielded consciousness, creativity, and technological developments. Therefore, Nature can be considered as an unlimited source of inspiration for all branches of science and technology.

Bioinspiration can originate from various levels of organization and functionalities of biological structures: macrostructures, microstructures, and molecules/nanostructures. The structural features that modulate the colors of insects, gecko's feet, and lotus leaves are some of the best known natural smart materials that have been the source of inspiration for various functional materials, some of which are already commercialized. For these examples, the natural structure serves as an inspiration for a novel material with the performance related to the original. Artificial enzymes are another category of bioinspired molecules. In this case, the functionality and principle of operation are copied from a natural system, but the structure of the artificial enzyme may not be related to the natural counterpart at all, although some crude structural analogies can still be found [12]. This research was stimulated by the superior catalytic performance of enzymes over other catalytic systems, the high cost and low stability of natural enzymes, as well as the difficulty in their recycling. Initially, the artificial enzymes were based on various receptor structures (e.g. cyclodextrins, cyclophanes) equipped with active site mimics [12,13]. Years of intense research in that field resulted in myriads of new supramolecular assemblies with catalytic activities. Further development of artificial enzymes resulted in the incorporation of catalytically active metal centers into supramolecular scaffolds of artificial enzymes [14,15]. These structures combine the advantages of transition metal catalysis with the structural flexibility and specific binding of both natural enzymes and various supramolecular receptors. The newest trend in the development of artificial enzymes encompasses the application of naturally developed peptide scaffolds (thus benefitting from millennia of evolution and genetic memory) with artificial metal centers. This approach resembles bionics, in which hybrid systems and devices are being developed [16,17].

The next step in this biomimetic track is the development of nanozymes – artificial nanostructures with enzyme-like catalytic activities [18]. They are usually based on various nanoparticles, sometimes encapsulated in appropriate shells. The next step involves the integration of several nanocomponents into a single 'shell', which can sometimes be natural proteins devoid of any catalytic properties or just an artificial polymer scaffold [19]. Despite the intense research in this field, there is a lot of work needed to overcome some challenges such as the possibility of a wide range of catalyzed reactions, mimicking of the protein scaffold, optimization according to the Sabatier principle [20], multifunctionality, and a wide range of practical applications [21–23]. The final concept in biomimetic catalytic systems encompasses the combination of the nanoenzyme concept with single-atom catalysis [24].

Some of the 'killer applications' of biomimetic catalytic processes are artificial photosynthesis and other bioinspired energy harvesting technologies [25]. It is a response to the increasing demand for cheap and clean energy and fuels. It should be the cleanest source of fuels, and if appropriate catalysts are developed. Furthermore, it may be the cheapest one. Natural photosynthesis involves several subsequent steps, each of which involves highly-specialized molecular assemblies: light antennae harvesting the sunlight, charge separation systems, and redox centers capable of water oxidation, and protomotoric-force-powered ATP synthase [25–27]. Photosynthesis is powered by visible photons and the light-harvesting antennae are tuned to the available light. Electronic excitation in the antenna migrates from chromophore to chromophore and ultimately to the reaction center, where is converted into the chemical energy in a multi-step redox reaction. Thus, reconstruction of the photosynthesis in an artificial system requires the reproduction of the same functionalities. Numerous approaches, involving various chromophores like porphyrins and phthalocyanines, ruthenium-bipyridine dendrimers, and other species (molecular and supramolecular) were commonly applied as light-harvesting antennae. Quinones, (like those in a natural photosynthetic system), fullerenes, ferrocene derivatives, and other electrochemically active inorganic species are also used in

artificial charge separation systems. Catalytic centers in artificial photosynthetic systems usually contain metal complexes that can catalyze water oxidation and carbon dioxide reduction. The substrates in artificial photosynthesis, in a broad sense of this term, do not need to be limited to water and carbon dioxide, since other forms of easily accessible substrates can be used. The same principle applies to the final product – in artificial systems, hydrogen gas, carbon monoxide, formic acid, and methanol are usually considered as the final products, but hydrocarbons have also been obtained [28,29]. For instance, the fabrication of biomass (including carbohydrates) in an artificial photosynthetic system was recently achieved with the support of hydrogen consuming bacteria in a device called the *Bionic Leaf* [30].

Bioinspiration in information processing is embodied in artificial neural networks, and machine learning approaches towards artificial intelligence, genetic algorithms, and unconventional computational platforms [31]. Neural networks are usually software implementations of learning and pattern recognition or classification algorithms based on the architecture principles of the operation of neural systems, hardware implementations are also possible, although they have been relatively rare up to now. Whereas neural networks require laborious training, the machine learning approach provides systems with the ability to automatically learn and improve from experience without being explicitly programmed. In the simplest approach, developed already in the 1980s century, the neural network is composed of nodes connected via weighted synaptic links. The structure containing at least two layers of software-implemented neurons is referred to as a perceptron [32]. Neural networks mimic the topology of neural tissue. Software neurons are connected with software synapses, and the coupling strength (or so-called synaptic weight) is optimized during the training phase to achieve the desired result. Whereas software implementations of neural networks are common and pretty advanced, there are only a few hardware implementations that have been developed by the largest players in the field: Hewlett-Packard, IBM, Intel Corporation, and the Samsung Group [33–35]. All these implementations are based on classical silicon-based electronics, but hybrid solutions with memristors and analog or digital components are also available [36–38]. The next step should involve a closer look at the structures and functions of nervous systems at the cellular and molecular levels, and finding synthetic structures that can imitate some information-related functionalities of neurons and synapses, followed by their incorporation into complex circuitry – also with a certain dose of randomness. Randomness and stochasticity in the brain may be the source of creativity. In artificial systems, they seem to be the key ingredients in fault-resistant information processing systems [39–41].

Memristive elements, with an ideal memristor, which is postulated to be the fourth passive primitive electronic element [42,43], are usually considered as a *Holy Grail* of electronics and modern information technologies [44–48]. Memristors are nonlinear electronic elements exhibiting the notably high dynamic variance of its properties in response to external stimuli, such as voltage or charge. Therefore, the state of a memristor can be drastically changed with a small input stimulus, which also may lead to chaotic behavior. Memristors usually show a negative differential resistance (NDR), which accelerates the response speed up to the chaotic level [49]. This makes them even more similar to neurons and synapses.: L. Chua, the pioneer of memristor science, has recently stated that biological neurons are "poised at the edge of chaos", [50,51] and they should respond to minute perturbations of the input. Such behavior was recently observed in memristive devices (*vide infra*). Memristors are usually considered as novel memory components [52], but numerous memristive elements, which does not exhibit electrical properties suitable for memory applications (such as fast and energy-efficient switching between states with high ON/OFF ratios) can be applied in various signal and information processing systems with great success. These prototypical constructs are domains of the vigorously developing field of *in-materio computing*: science at the edge of information sciences, chemistry, and physics [9,53,54].

Serendipitously, the main working horse of photovoltaics – lead halide perovskites [55,56] – proved to be useful for two important biomimetic technologies: artificial photosynthesis and neuromimetic information processing. These materials also present extremely interesting spectral and structural properties and can significantly contribute to the development of various fields of chemistry and physics.

This review focuses on two biomimetic processes: artificial photosynthesis and artificial neural networks. Interestingly, both processes can be realized with very similar coordination chemistry systems – lead iodide perovskites and related materials. This review briefly introduces the structures and properties of iodide-based semiconductors, their photocatalytic and photovoltaic properties, and their applications in artificial photosynthesis and the construction of memristors, which are inanimate equivalents of synapses [57,58]. All these applications are consequences of the unique crystal and electronic structure of heavy p-block element coordination polymers with iodide ligands.

2. Introducing the heroes – why iodine-based semiconductors

Silver and copper halides were the first binary halide semiconductors that were studied in detail. The metal ions are either tetracoordinate, forming a diamond-like structure (e.g. CuF, CuCl, CuBr, CuI, and AgI) or hexacoordinate, forming a rock salt lattice (e.g. AgF, AgCl, and AgBr) [59]. Recently, the semiconducting properties of tin, lead, and bismuth halides have also been explored. Among all halide-based semiconductors, the iodine compounds are characterized by the smallest bandgap energies, but also the lowest stabilities, especially due to hydrolysis. The hexacoordinate units present in the structures of PbI_2 and BiI_3 can be also be found in perovskites and other iodoplumbate and iodobismuthate compounds, the diversity of which is remarkable [60–63].

Furthermore, iodine, and to a lower extent, bromine, are halogens with the most intriguing reactivity, which leads to the formation of amazing structures, like large polyatomic anions such as polybromides [64] and polyiodides [65], which also can serve as ligands [66]. Among the polyiodide species, materials with semiconducting properties can be also be found [67–70]. The main application of triiodide salts, however, is the redox mediator in dye-sensitized solar cells [71–73]. The formation of halogen-bonded structures [74–78] and hypervalent compounds [79,80] further increases the diversity of iodine-based compounds and supramolecular structures.

Heavy crystallogen (group IV) and pnictogen (group V) halides tend to prefer lower oxidation state [81] and adopt a variety of crystal structures ranging from ionic crystals, *e.g.* SnF_2 [82], PbF_2 [83], $PbCl_2$ [84], and BiF_3 [85], to two-dimensional (2D) layered structures, *e.g.* $SnCl_2$ [86], $SnBr_2$ [87], SnI_2 [88], $PbCl_2$ [89], $PbBr_2$ [90], PbI_2 [91], SbF_3 [92], $BiCl_3$ [93], $BiBr_3$ [94], and BiI_3 [95], to molecular or quasimolecular solid crystals, *e.g.* $SbCl_3$ [96], $SbBr_3$ [97], and SbI_3 [98].

The source of crystallographic diversity and common polymorphism comes from the high variability of the coordination numbers of heavy metals [81,99,100]. These structures are often characterized by stereochemical distortions caused by the nonbonding valence electrons of the metal atom, ns^2. The stability of the higher oxidation states (Sn^{+4}, Pb^{+4}, Sb^{+5}, Bi^{+5}) decreases down the groups and, for a given metal, strongly decreases from the fluoride (ionic

character) to the iodide (covalent character). The general rule is a trend towards lower *M-X* bond strengths with increasing atomic numbers, destabilized by electronegative substituents, which is further enhanced by the relativistic effects [101]. The band gap for these semiconductors ranges from ~5 eV to 1.2 eV and decreases from the fluoride to the iodide for a given metal [102]. The electronic structure is typical for materials containing post-transition metals with a ns^2 electronic configuration and is characterized by the hybridized anti-bonding metal *s*-orbitals with halogen *p*-orbitals at the top of the valence band, and extended *p*-states at the bottom of the conduction band [102–113].

An interest in iodide-based semiconductors has greatly increased upon the rediscovery of lead halide perovskites [114,115] and pnictogen chalcohalides [116,117] as materials for photovoltaics, photocatalysis, and optoelectronics. Later on, the search for more friendly substitutes of lead halide perovskites has focused researchers' attention on elpasolites, also known as double perovskites, a family of materials with much larger tailorability and flexibility [118–120].

The term perovskite is a general name for a series of cubic face-centered crystalline phases with ABX_3 stoichiometry, where A and B are cations (usually inorganic, but numerous organic derivatives are also known) and X is an anion (usually oxide or halide, but other possibilities are also known). To attain a neutral charge, the charges of the ions that constitute the structure must obey a rule (1):

$$q_A + q_B = -3q_X \tag{1}$$

Phases of other lattice types (hexagonal, monoclinic, orthorhombic, tetragonal and trigonal) are also known. Frequently found combinations, include, but are not limited to:

$q_X = -1$, $(q_A, q_B) = (1, 2)$, for example, $CsPbI_3$;
$q_X = -2$, $(q_A, q_B) = (1, 5)$, for example, $NaNbO_3$;
$q_X = -2$, $(q_A, q_B) = (2, 4)$, for example, $BaTiO_3$;
$q_X = -3$, $(q_A, q_B) = (4, 5)$, for example, $ThTaN_3$.

The importance of perovskites was recognized for the first time upon the discovery of the dielectric and ferroelectric properties of barium titanate ($BaTiO_3$) [121], and later on by the discovery of high-T_c cuprate superconductors [122]. The idealized structure of perovskite is based on corner-sharing octahedra, with one of the cations (B) located within the octahedron, while the other (A) occupies the void and has cuboctahedral coordination (Fig. 1).

Several variations on the main perovskite structure are possible, but the local coordination environment around the cation B remains unchanged. However, the placement of the cations A and the way the octahedra are arranged and connected may vary to a great extent, leading to structures of numerous dimensionalities, even with the same cationic charges. Adjustments of the size of cation A is a common tool for control of the dimensionality. They are formed according to two different reactions, depending on the cation size. For small cations, A_{small}, the most common process follows the reaction (2):

$$A_{small}X + BX_2 = A_{small}BX_3 \tag{2}$$

Voluminous cations (A_{large}), like decylammonium, or p-methylbenzylammonium yield phases of different compositions for the 2D structures (3):

$$2\,A_{large}X + BX_2 = (A_{large})_2BX_4 \tag{3}$$

In the case of a mixture of cations, layered structures can be formed according to (4):

$$(n-1)A_{small}BX_3 + (A_{large})_2BX_4 = (A_{small})_{n-1}(A_{large})_2B_nX_{3n+1} \tag{4}$$

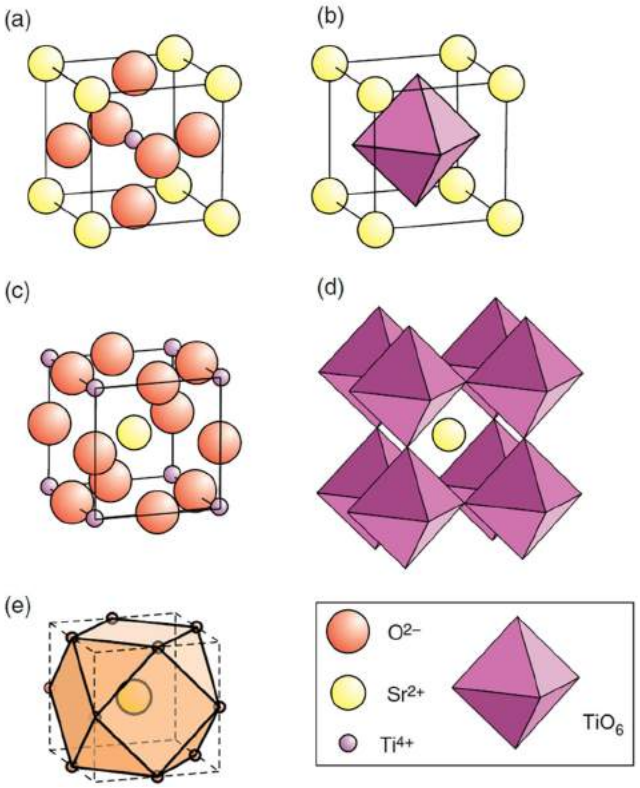

Fig. 1. The idealized perovskite structure of $SrTiO_3$: (a) the atom positions with Sr^{2+} at the cell origin; (b) a TiO_6 octahedral coordination polyhedron; (c) the atom positions with Ti^{4+} at the cell origin; (d) a TiO_6 octahedral polyhedron framework with Sr^{2+} at the cell center, and (e) a cuboctahedral cage site. Reproduced from Ref. [121] with permission. Copyright Wiley & Sons, Ltd. 2016.

All these variations, and also the substitutions at the B and X positions, are possible as long as the perovskite lattice remains stable. The perovskite lattice is rigid because the unit cell does not have any adjustable atomic position parameters. Therefore, any change in the composition must be reflected in a change of a lattice parameter. This parameter is a sum of the cation–anion bond length and the cubic cell edge *a* is equal to the double bond length $d_{B\text{-}X}$ (5):

$$a = 2d_{B-X} \tag{5}$$

The width of a cubooctahedral cage, $a \times 2$, is equal to the doubled bond length A-X (6):

$$a\sqrt{2} = 2d_{A-X} \tag{6}$$

The ratio of these two terms (7):

$$t = \frac{d_{A\text{-}X}}{\sqrt{2}d_{B\text{-}X}} \tag{7}$$

expressed also using ionic radii (8):

$$t = \frac{r_A + r_X}{\sqrt{2}(r_B + r_X)} \tag{8}$$

is called the *Goldschmidt tolerance factor* (7) or the *empirical Goldschmidt tolerance factor* (8). This factor is equal to unity in the case of an ideal perovskite structure. Nonetheless, the Goldschmidt tolerance factor itself does not yield unambiguous predictions of the crystal structure of a compound in question. Therefore, another factor called the octahedral factor (μ) was introduced (9):

$$\mu = \frac{r_B}{r_X} \tag{9}$$

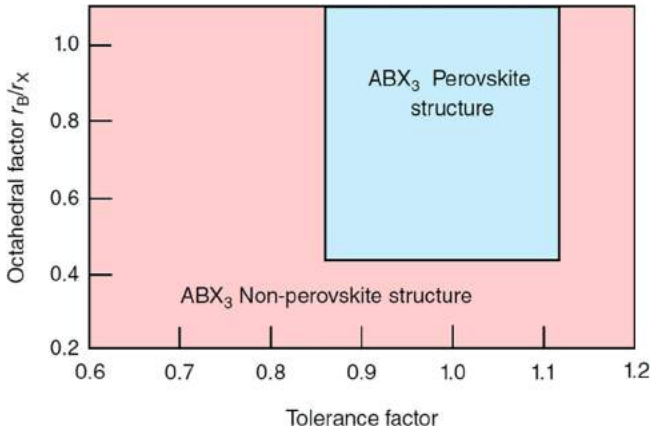

Fig. 2. Structure-field map of the octahedral factor μ versus the tolerance factor t for ABX_3 halide phases. Reproduced from Ref. [121] with permission. Copyright Wiley & Sons, Ltd. 2016.

These two parameters together allow the generation of structure stability maps that can be used to design new materials of perovskite structure (Fig. 2) [121].

One of the most important classes of perovskite materials, from this paper's perspective, are organic–inorganic lead halide perovskites and structural variations of them. It should be noted that despite the common misconception, they are not organometallic compounds since there are no direct bonds between carbon and metal atoms. The lattice can be described as a three-dimensional (3D) heteropolar network (with mixed ionic and covalent interactions) combined with a zero-dimensional (molecular) organic component. There are purely electrostatic interactions between these two components. Strong hybridization, i.e. orbital overlap within the octahedral framework, is responsible for the low effective masses of the charge carriers, namely 0.15 m_e for the electron and 0.12 m_e for the hole [123]. This allows a high mobility band transport, which (along with the low and easily tunable bandgap energy) makes them materials of choice for photovoltaic applications. The high atomic numbers of both components of the network (i.e. lead and iodine) suggest significant contributions from relativistic effects [124].

Organic cations (e.g. methylammonium) within the perovskite lattice are ca. 6 Å apart. Their large permanent dipole moment of 2.29 D and their proximity yield dipole–dipole interaction energies of 25 meV, which is comparable to thermal energy at room temperature. Therefore, this class of perovskite materials has shown complex ferroelectric behavior. This results in the formation of a local structure containing domains of low and high electrostatic potential. The inner topology of these materials (even monocrystals) resembles those of bulk heterojunctions [125].

Moreover, iodine redox chemistry contributes to the extraordinary properties of the lead halide perovskites. Usually, vacancies, interstitials, and other defects have a detrimental influence on the solar cell performance due to charge carrier trapping, which limits the cell voltage or charge carrier recombination, and also the cell current. Interestingly, metal halide perovskites are very defect-tolerant. It was recently reported that depending on the condition, detrimental traps could be easily induced during the synthesis of perovskites (via hydrolysis and acid-catalyzed oxidation of iodide) or these traps can be deactivated by post-synthetic treatment with mild oxidizing agents. The post-synthesis exposure to mild oxidizing agents can transform the harmful hole traps into kinetically inactive electron traps. Furthermore, it explains why layers prepared with a slight deficiency of iodide have better optoelectronic performance [126].

All the features mentioned above, together with the low cost and abundance of the precursors and the relative simplicity of fabrication [127], make iodine-based semiconductors: perovskites and elpasolites especially, materials of choice for various emerging technologies.

3. Crystal and electronic structure of perovskite semiconductors

Perovskites of the type ABX_3 possess crystal structures consisting of an inorganic octahedral network of the unit BX_3 with A-site cations contained within the voids of this framework, see (Fig. 3).

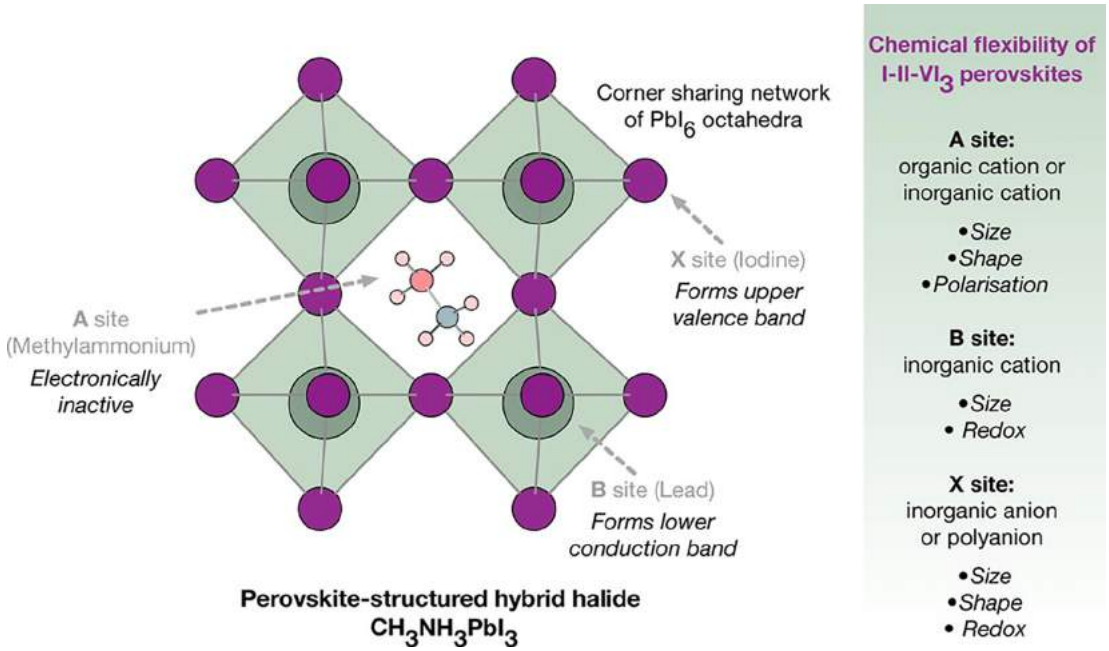

Fig. 3. Schematic of the perovskite structure ABX_3 indicating the A, B, and X lattice sites. Note that for larger molecular A cations, layered perovskites are formed. Beyond the halide perovskites, a wider range of stoichiometries and superstructures are known, e.g., the Ruddlesden–Popper, Aurivillius, and Dion–Jacobson phases. Reproduced from Ref. [125] with the permission of the American Chemical Society.

For this crystal system class, materials databases with structures and properties of new compounds are available [128]. The corners of the octahedra are occupied by halide anions (X = Cl^-, Br^-, I^-) and the center position by divalent metal cations (Sn^{2+}, Pb^{2+}). The pairwise substitution, *i.e.* replacing two divalent metal cations with one trivalent and one monovalent cations, leads to double perovskites with the general formula A_2BCX_6 (B = Bi^{3+}, Sb^{3+}; C = Cs^+, Ag^+) [129–132]. According to the tolerance factor for the three-dimensional (3D) halide perovskites [133], the A-site cation is limited to a small number of ions including $CH_3NH_3^+$, $HC(NH_2)_2^+$, Cs^+, and Rb^+. Incorporating larger cations results in lower dimensionality structures due to the disruption of the 3D octahedral framework.

3.1. 3D perovskites

The common characteristic of perovskites is the structural and compositional flexibility with accessible cubic, tetragonal, orthorhombic, trigonal, and monoclinic polymorphs depending on the tilt and rotation of the BX_6 polyhedra in the lattice (Fig. 4) [134]. The phase transitions are reversible and can be stimulated by temperature, pressure, or an electric field. For example, the crystal phase of the hybrid lead halide perovskite $MAPbI_3$ (MA = methylammonium) [135] changes from a lower symmetry at low temperature to higher symmetry with increasing temperatures, see (Fig. 5). $MAPbI_3$ features an orthorhombic (*Pnma*) to tetragonal (*I*4/*mcm*) phase change at 162 K, and subsequently a to cubic ($Pm\bar{3}m$) phase change at 328 K [136–139]. The origin of these phase changes is the orientational disorder of the molecular sublattice, $CH_3NH_3^+$, in the case of $MAPbI_3$ (C_{3v} symmetry), which increases with higher temperatures. Thus, the molecular cation appears ordered in the orthorhombic phase, becomes 2D disordered in the tetragonal phase, and then becomes isotropically 3D disordered - with free rotation with the inorganic tilts in the cubic phase [140]. Fig. 6 shows the geometrical structures of the orthorhombic and tetragonal phases of $MAPbI_3$, illustrating the variety of methylammonium orientations. To add to the structural complexity of perovskites, some of them, *e.g.* $HC(NH_2)_2PbI_3$ (FAPI)

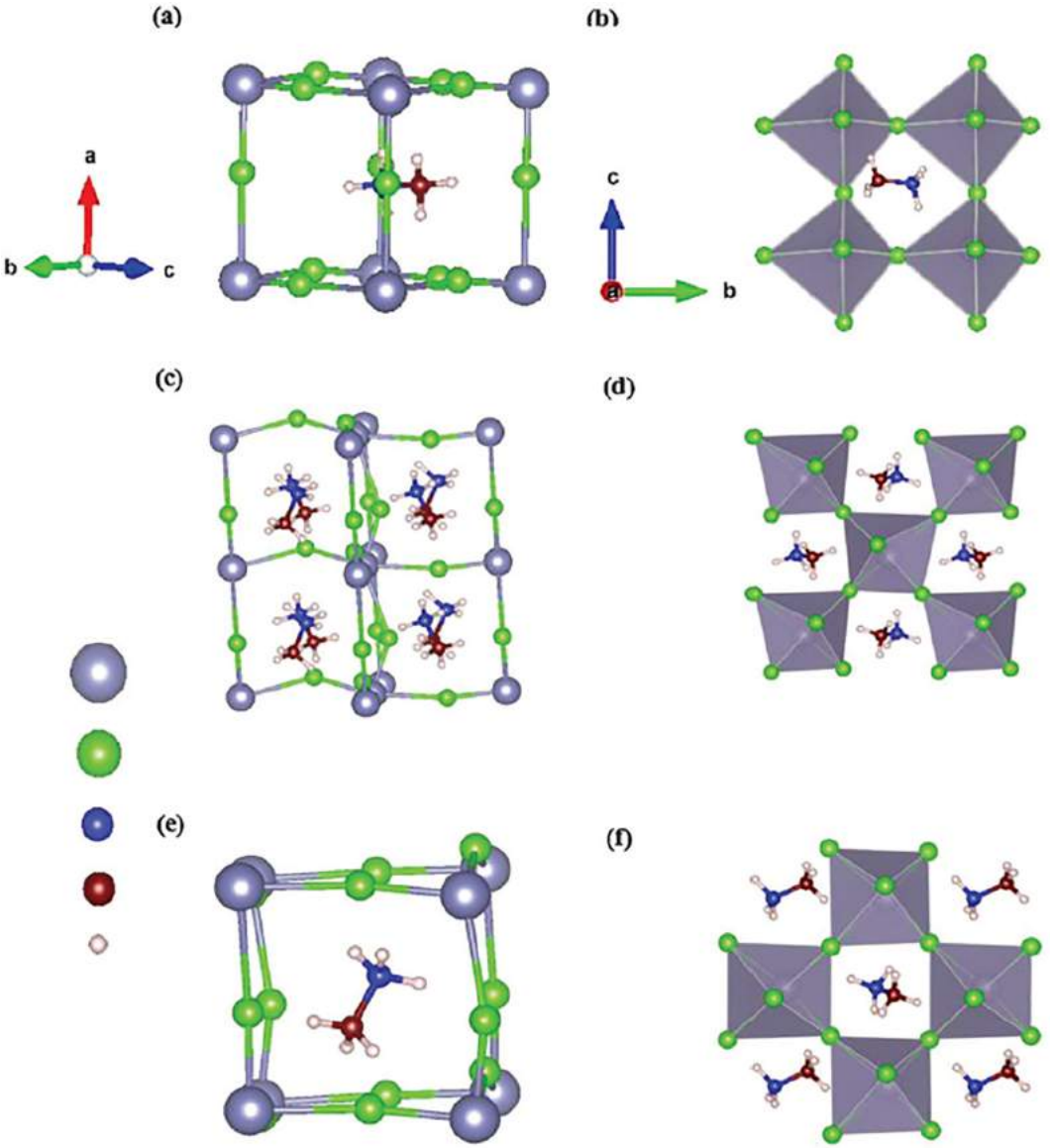

Fig. 4. Geometrical structures of $CH_3NH_3SnCl_3$ in the (a)-(b) cubic phase, (c)-(d) monoclinic phase, and (e)-(f) triclinic phase. The left panel shows the side views, and the right panel shows the structure in polyhedron diagrams (grey: tin; green: chlorine; blue: carbon; brown: nitrogen; pink: hydrogen). Reproduced from Ref. [142] with the permission of the Royal Chemical Society.

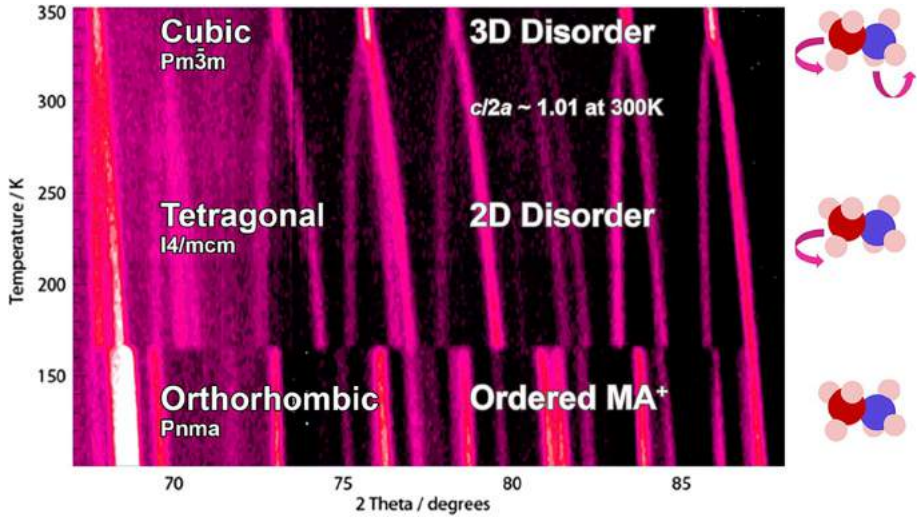

Fig. 5. Temperature-dependent (100–352 K) powder neutron diffraction patterns of $CH_3NH_3PbI_3$, illustrating the low to high-temperature phase transitions. Reproduced from Ref. Ref. [140]with the permission of the Copyright American Chemical Society.

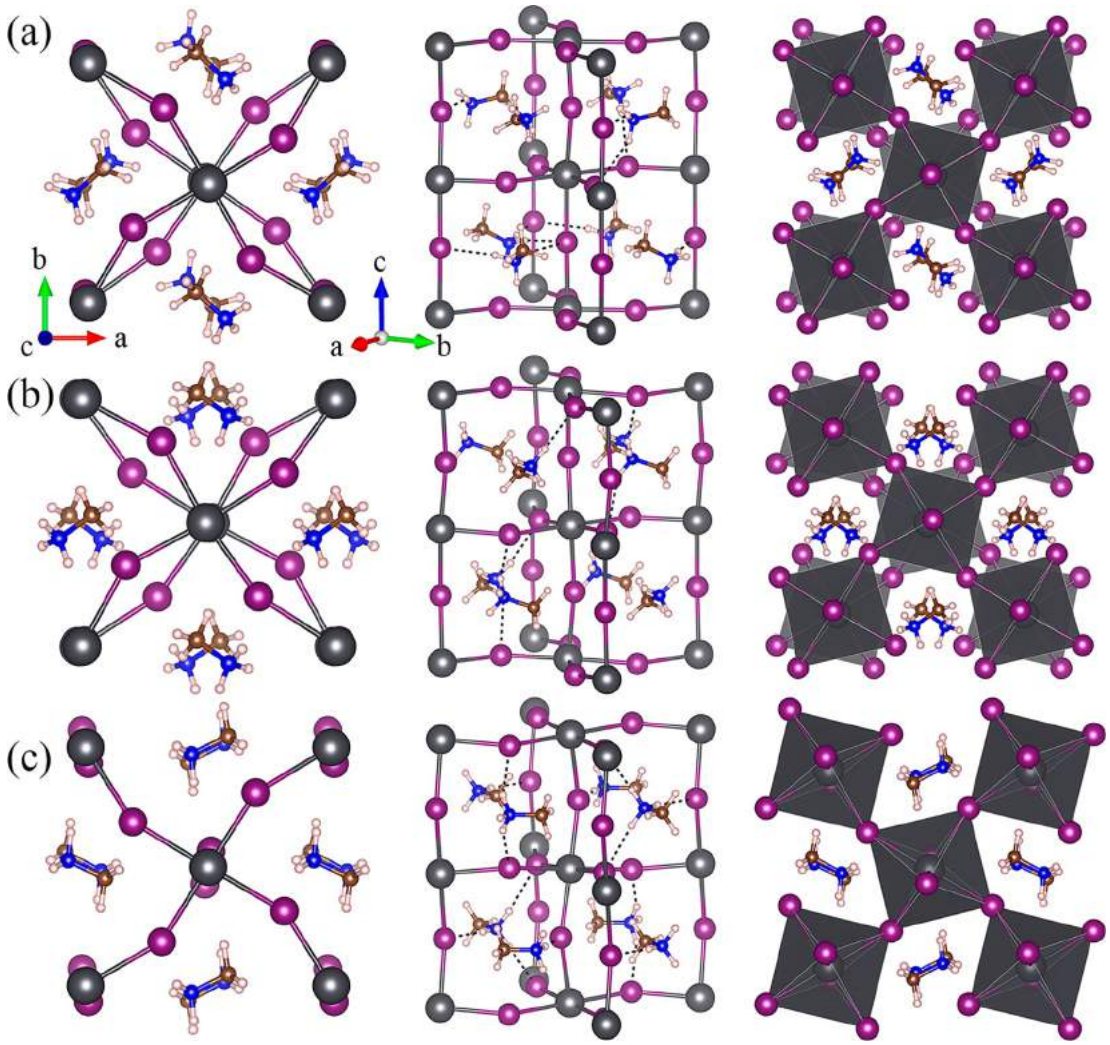

Fig. 6. Geometrical structures of $MAPbI_3$ in the (a) tetragonal phase with a parallel distribution of the methylammonium cations, (b) tetragonal phase with a vertical distribution of the methylammonium cations, and (c) orthorhombic phase. The left panel is a top view, the middle panel is a side view, and the right panel shows the structure in polyhedron graphs (dark gray: lead; purple: iodine; brown: carbon; blue: nitrogen; pink: hydrogen). Reproduced from Ref. [156] with the permission of the American Chemical Society.

and $CsSnI_3$, exhibit the phase competition between corner-sharing octahedra and the edge-sharing octahedral molecular crystals [141]. This means that the perovskites exist in a general disordered state with coherent structural domains of the nanoscale length [139].

This dynamic physical softness [143] means that the bond lengths, angles, and the atomic orbital overlaps change with temperature, which further means that the electronic structures are also temperature-sensitive [144–149]. Therefore, it should be noted that studying the electronic structure of hybrid perovskites presents a challenge in materials modeling, which has been discussed in recent reviews [150,151]. However, the organic cation was shown to play an indirect role in the electronic properties as the frontier orbitals have contributions only from the inorganic framework [152,153]. Thus, the basic electronic structure is marginally affected by random [146,154] or collective [155,156] methylammonium orientation [157]. In a more detailed study, it was demonstrated that at room temperature, a variety of apolar (antiferroelectric) as well as polar (ferroelectric) methylammonium dipole configurations are accessible, where the latter gives rise to a strong band bending [158]. The molecular and lattice polarization of hybrid perovskites, the ferroelectric effect, can be tuned by the choice of the asymmetric organic cation [159].

Although the local and semi-local exchange–correlation functionals fortuitously deliver the bandgap energy of bulk $MAPbI_3$ [155,160,161], to properly describe the complex nature of a halide perovskite, with its subtle electronic structure, it is necessary to consider relativistic effects of spin–orbit coupling (SOC), many-body effects, and van der Waals interactions [123,142,162–169]. In the case of $MAPbI_3$, the valance band is mainly contributed by Pb-*s* and I-*p* orbitals, while the conduction band is derived from the Pb-*p* states. For perovskites structures that lack centers of inversion symmetry, the relativistic spin splittings of bands are observed – the Rashba-Dresselhaus effect (Fig. 7) [123,170]. The band gaps of hybrid perovskites increase with increasing cell volume and decreasing pressure [171]. For smaller molecular cations, lower bandgap energies should be observed [125]. However, Amat et al. showed that replacing methylammonium with formamidiniuminduced a bandgap reduction, which was rationalized by the modulation of the Pb–I bond character due to the size effects and the enhanced hydrogen bonding between the molecular and the inorganic network [172]. In contrast, the bandgap changes due to the X-site substitution are influenced by the electronic states of the anion, similarly as in the binary halides. Thus, the bandgap energy decreases from Cl to Br to I. The band gaps for $MAPbCl_3$ and $MAPbI_3$ differs by as much as 0.6 eV [173]; the bandgap energy of $FAPbBr_3$ decreases from 2.23 eV to 1.48 eV for $FAPbI_3$ [174]; the band gaps of $MASnI_3$, $FASnI_3$, and $CsSnI_3$ are nearly the same [171]. The B-site substitution of Pb by Sn is promising, resulting in a decreased bandgap (1.1 eV) and a reduced effective mass of holes [175], but is diminished by the poor stability against oxidation [176]. The effective masses of the carriers decrease from chlorine to iodine, as demonstrated for $MASnX_3$ [142,177] and $CsPbX_3$ [178] and are anisotropic, which is an effect of the different octahedral rotations [179].

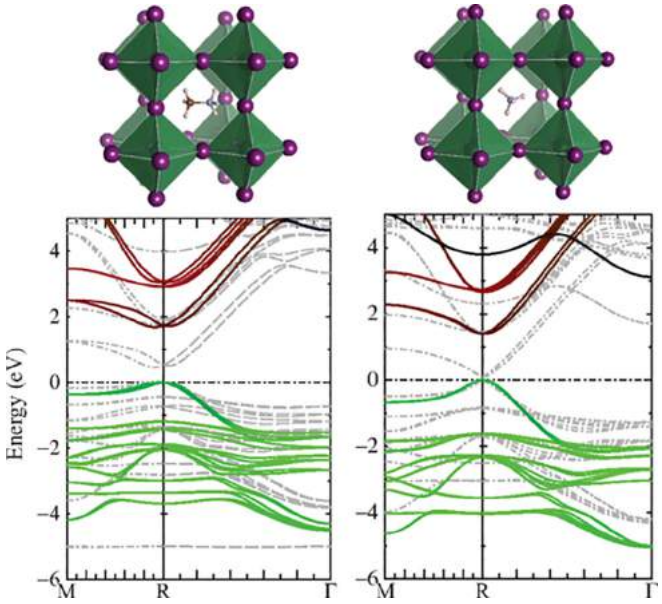

Fig. 7. The electronic band structure for $CH_3NH_3PbI_3$ (left) and NH_4PbI_3 (right) obtained from the quasiparticle self-consistent *GW* theory. The relativistic Rashba-Dresselhaus splitting of the lower conduction band is visible due to the presence of $CH_3NH_3^+$ in the hybrid perovskite resulting in a non-centrosymmetric crystal. The zero on the energy scale denotes the valence band maximum. The bands are colored according to their orbital character: green depicts I 5*p*, red depicts Pb 6*p*, and blue depicts Pb 6*s*. The light-gray dashed lines show the corresponding bands obtained from local density approximation (LDA) DFT. Reproduced from Ref. [123] with the permission of the American Physical Society.

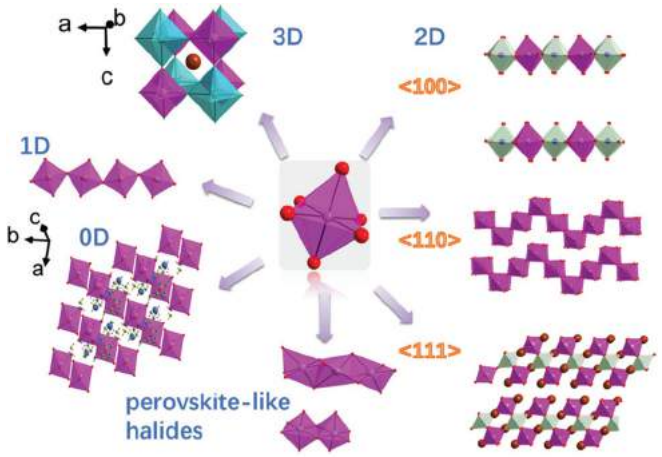

Fig. 8. Standard-perovskites (3D), 2D perovskites with different types of layers (2D, ⟨1 0 0⟩, ⟨1 1 0⟩, ⟨1 1 1⟩), chains of octahedra in 1D perovskites, discrete octahedra separated by organic cations (0D) and perovskite-like halides with moieties of edge- and face-sharing octahedra. Reproduced from Ref. [204] with permission of the Royal Chemical Society.

3.2. Low-dimensional perovskites

In the low dimensional perovskites the 3D inorganic framework is broken into sheets (2D), wires (1D) or isolated BX_6 octahedra (0D), as illustrated in Fig. 8 [180–182]. The two-dimensional perovskites consist of single or multiple inorganic layers separated by organic molecules and have the general formula $R_2A_{n-1}B_nX_{3n+1}$, where R is the alkylammonium cation acting as a spacer and *n* denotes the number of inorganic layers [183]. The common arbitrary classification includes 2D (*n* = 1), quasi-2D (*n* = 2–5) and quasi-3D (*n* > 5) perovskites, which further converge to 3D structures for large (i.e. approaching infinity) values of *n* [184]. According to the different octahedral connectivity and the stacking orientation of inorganic layers with respect to the cubic primary structure, the 2D architectures can be divided into three structural types: (1) the ⟨1 0 0⟩-oriented – the Ruddlesden–Popper phase [185,186], the Dion-Jacobson phase [187], alternating cation in the interlayer space (ACI) phases [188] and the special case of double perovskites forming mono- and bilayer nanosheets, *e.g.* $(BA)_4AgBiBr_8$ (BA = butylammonium) and $(BA)_2CsAgBiBr_7$ [189]; (2) the ⟨1 1 0⟩-oriented – corrugated perovskites [190–193];

(3) the ⟨1 1 1⟩-oriented defective perovskites [194]. These structural variations are presented in Fig. 8. The ⟨1 0 0⟩-oriented phases represent the largest 2D perovskite family. The one-dimensional perovskites form nanowires (linear or zig-zag) from corner-sharing, edge-sharing, or face-sharing octahedral units, which are surrounded by organic cations. The zero-dimensional perovskites are essentially molecular solids with isolated octahedral anions or clusters surrounded by the organic cations. Similar to the 3-D perovskites, the physical properties of these compounds can be tuned through suiting of the organic cation, halide and metal components [195]. The reduction in dimensionality allows for a plethora of organic cations that can be intercalated to obtain desired properties and yields a remarkable degree of structural versatility and complexity [196], as discussed in many recent review papers [197–201,202,203].

The organic cations act as insulating barriers that confine the charge carriers in the directions depending on the dimensionality reduction. Thus, with direct consequences on the electronic properties, 2D structures feature behavior of quantum well, 1D perovskites are characterized by quantum wire and 0D perovskites by quantum dots, as highlighted in Fig. 9 [205]. Quantum confinement leads to the band narrowing and band edge shifts, resulting in decreased width of bands and effective masses and the increased bandgap energy. For layered structures, the systematic increase of the bandgap energy with decreasing thickness (*n*-value) of the perovskite layer along with the decreased number of sub-bands in the band structure is observed [185,186,206–208]. At the origin of such trends, dictated by the dimensionality reduction, is the structure deprivation of the hydrogen or halogen bonding at the organic–inorganic interface, resulting in less disperse valence band maximum and thus increased bandgap [209,210]. The organic cation energetic levels can be tuned by changing the electron-withdrawing/donating character which leads to the formation of localized states, either in the organic or the inorganic part [211,212]. The electronic properties can be further altered by the connectivity modes formed in the inorganic networks [213]. As a general trend, the bandgap energy follows the increasing trend "corner-sharing < edge-sharing < face-sharing", due to the increasing lone pair stabilization in these structures. These lone pairs, that localize deep within the valence band, while the energy of the bottom of the conduction band increases [214–216]. The band dispersion also depends on the distance between the octahedral layers, thus on the thickness of the organic spacer, highlighting the importance of the long-range Coulombic interactions. For instance, in case of $(BdA)_2PbI_4$, $(HdA)_2PbI_4$ and $(OdA)_2PbI_4$ (BdA = butyldiammonium, HdA = hexyldiammonium, OdA = octyldiammonium) series of perovskites which differ in the length of alkyl chains, the reported limit of interaction between the inorganic planes was less than 6 Å [217]. This limit was inferred from the observation of the dispersion that became flatter in the order of the increased length of the spacer BdA > HdA > OdA. In 0-D structures, the isolation of the metal halide octahedra by the wide-band-gap organic ligands reaches the maximum and completely deters the metal-halogen interactions, resulting in the distinct electronic band structures that involve localized orbitals centered at the metal halide octahedral units, as exemplified for $(C_4N_2H_{14}X)_4SnX_6$ [181,215] or Cs_4PbBr_6 [218].

Further consequences of quantum confinement involve crystal properties becoming highly anisotropic, very sensitive to the structural features, and significantly different from those of 3D structures. The band dispersion is sizable in the direction of reciprocal space corresponding to the stacking axis of octahedral motifs, thus reducing the effect of quantum confinement [187,188]. The directional dependence of the effective masses was also observed. The charge carrier effective masses are smaller for the in-plane directions within the inorganic planes and are much larger perpendicular to the inorganic plane, that is, a direction between two inorganic planes separated by the organic molecules [183,217,219]. The Rashba-Dresselhaus spin-splitting is expected to occur along one of the in-plane axes [220,221].

4. Interactions with light

4.1. 3D perovskite structures

Among iodide-based materials, the lead halide perovskites gained tremendous attention from researchers because of their strong interactions with light. Since the landmarking papers that described the first application of halide perovskites (HaPs) as sensitizers in TiO_2-based solar cells, and the later research using these materials as active layers in solar cells, the field of photovoltaics (PVs) has witnessed a tremendous growth of interest for inexpensive and solution-processable solar cells [222,223]. Nowadays,

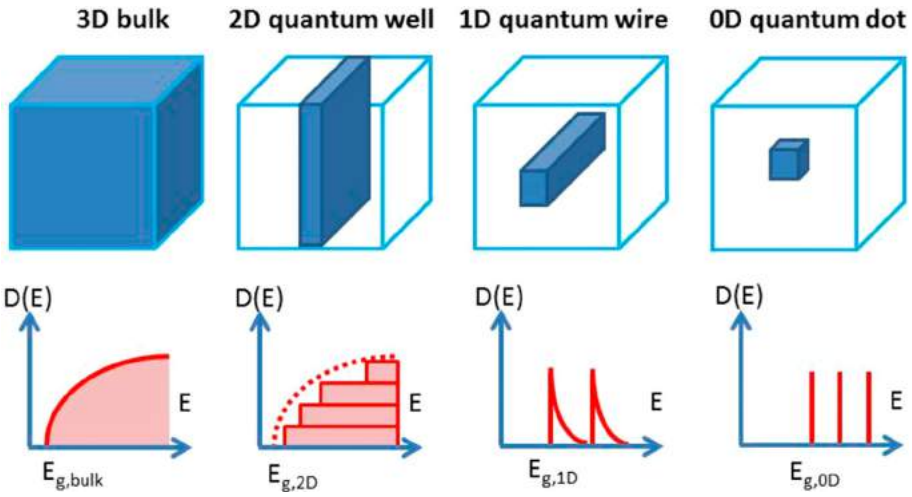

Fig. 9. Schematic representation of a three-dimensional (3D) bulk semiconductor and the related two-dimensional (2D), one-dimensional (1D), and zero-dimensional (0D) quantum nanostructures. The joint density of states D(E) between the conduction band (CB) and the valence band (VB) is represented as a function of the energy, assuming infinite confinement potentials and an effective mass model for both the CB and the VB. The quantum confinement also results in increased bandgap energy when compared to the bulk material. The 3D density of states (DOS) can be reconstructed by merging 2D DOS related to electronic sub-bands in both the CB and VB. Reproduced from Ref. [205] with permission of the American Chemical Society.

hybrid organic–inorganic perovskites (HOIPs) remain one of the most intensively studied materials for light-harvesting applications, owing to the rapid and tremendous advance in the photon-to-electron conversion of HOIP-based solar cells. In less than 10 years of research, the power conversion efficiencies (PCEs) of perovskite solar cells (PSCs) increased from 9.7% [224] in 2012 to 22.7% in 2018 [225]. Currently, the highest PCE values were obtained for solar cells based on single-crystal perovskites [226] and mixed perovskites with complex stoichiometry, such as $(FAPbI_3)_{0.95}(MAPbBr_3)_{0.05}$ (22.7%) [227,228], $Cs_5(MA_{0.17}FA_{0.83})_{0.95}$-$Pb(I_{0.83}Br_{0.17})_3$ (21.1%) [229], the efficiency of which can be even further enhanced to excess 23% with charge transport layers engineering [230]. Even higher values of PCE equal to 25.2% were obtained for perovskite/silicon tandem systems [231]. With such rapid progress, it is presumed that PSCs are on the good pathway towards reaching their theoretical efficiency limit of 31%, which is nearly equal to that achievable by gallium arsenide (GaAs) solar cells [232] and closely approaches the Shockley-Queisser limit for single-junction solar cells [233]. These exceptionally high-efficiency values originate primarily from the high absorption coefficients, long charge carrier lifetimes, long diffusion lengths, and low exciton binding energies.

Within a solar cell, the HaP layer is usually sandwiched in a vertical configuration between carrier-selective transport layers. The popular choices for electron-transporting layers (ETLs) are: TiO_2, and SnO_2 , and the commonly used materials for hole-transporting layers (HTLs) are: $N^2,N^2,N^{2\prime},N^{2\prime},N^7,N^7,N^{7\prime},N^{7\prime}$-octakis(4-methoxyphenyl)-9,9′-spirobi[9H-fluorene]-2,2′,7,7′-tetramine (spiro-OMeTAD) and poly(triarylamine) (PTAA). Careful selection of these layers helps to improve the electronic structure of a solar cell via effective extraction of the photogenerated charge carriers at the interfaces and facilitates the transport of electrons and holes through the ETL and HTL, respectively [230]. Upon absorption of a photon of sufficient energy (i.e. higher than the bandgap width), the generated excitons or free charge carriers are further split or collected with the corresponding transporting layer. The absorption coefficient determines how far the incident photon can penetrate the material before it is absorbed. With the absorption coefficients on the order of 10^4-10^5 cm^{-1} [234] and very steep absorption edges [235] (Fig. 10a), the perovskite layers can absorb up to 90% of the incident light within 300–500 nm [236]. The steep absorption onsets with low Urbach energies indicates the lack of trapping sites within the bandgap of the perovskites. Along with the photoluminescence (PL) peak, these features often serve as benchmarks for determining the crystallinity and quality of the material [237,238].

The other feature responsible for the extraordinarily high PCEs is the direct generation of free carriers instead of excitons upon photon absorption. The exciton binding energy in 3D HaPs was initially determined to fall within the range of 2–55 meV, but recently it has been directly measured to be as low as 16 meV [239]. Moreover, it has been shown that binding energy decreases with increasing temperatures and can be as low as 5–6 meV [240,241]. With binding energies significantly lower than kT ~ 26 meV at room temperature (298 K), upon the photon absorption, free carriers are generated rather than excitons, strongly facilitating the separation of electron and hole [242]. The photogenerated free carriers need to be transported to the electrodes before the recombination processes occur. The electron-hole diffusion length in $MAPbI_3$ HaP exceeds 100 nm

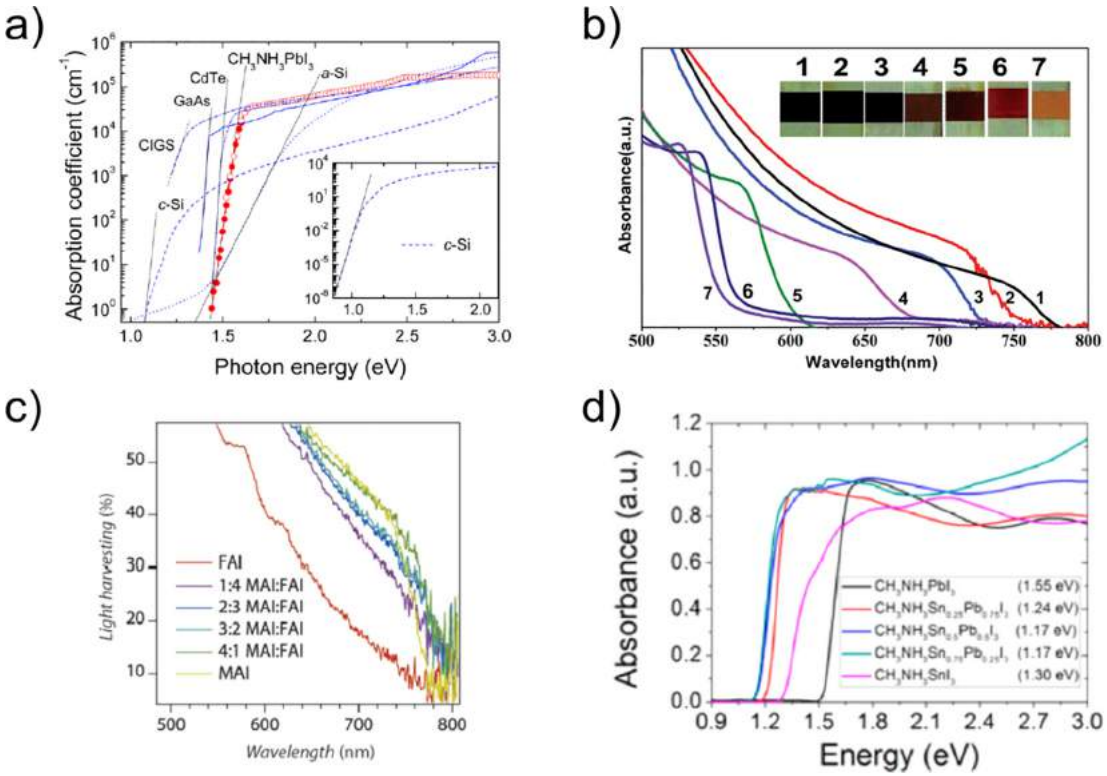

Fig. 10. Bandgap engineering of lead iodide perovskite with component mixing. (a) The bandgap of $MAPbI_3$ falls within a range of 1.5–1.6 eV, and the sharp absorption onset is at ~786–794 nm. (b) Incorporation of Br^- into the structure blue-shifts the absorption onset to ~ 550 nm, corresponding to a bandgap of ~2.2 eV. (c) Substitution of methylammonium with formamidiniumin the A-site of the perovskite ABX_3 structure results in a red-shift of the absorption edge of ~20 nm and (d) replacing the Pb^{2+} with Sn^{2+} in the B-site decreases the bandgap to 1.3 eV. Panel (a) has been reproduced from Ref. [237] with permission of the American Chemical Society, panel (b) has been reproduced from Ref. [247], CC BY-NC 3.0, panel (c) has been reproduced from Ref. [250] with the permission of Wiley and panel (d) has been reproduced from Ref. [252] with permission of the American Chemical Society.

[243], while the one for the mixed Pb-Cl HaP exceeds 1 μm [244]. In single-crystalline $FAPbI_3$ and $FAPbBr_3$, the diffusion length can reach values even as high as 6.6 μm and 19 μm, respectively. In polycrystalline $FAPbI_3$, the determined diffusion length is 3.1 μm [244,24521]. These values are significantly higher than (or, in the case of $MAPbI_3$, at least comparable with) the absorption depth. This means that photogenerated electrons and holes can be efficiently collected before they recombine with the ETL and HTL, respectively.

In recent years, a significant number of studies were devoted to investigating the optoelectronic properties of perovskite solid solutions. The incorporation of ions of different sizes affects the size of the unit cell, which further affects the optoelectronic structure. In this manner, mixing and substitution of components in the perovskite structure enable tuning of the bandgap over a wide range spanning from the near-infrared to the near-ultraviolet wavelengths.

The exchange of halide anions in the X-site shifts the absorption onset towards higher energies (Fig. 10b). The bandgap of pure $MAPbI_3$ is reported to be between 1.5 and 1.6 eV [151,237,246]. The addition of smaller Br atoms to the structure in $MAPb(I_{1-x}Br_x)_3$ results in the widening of the bandgap due to electronic effects [116] and the contraction of the perovskite unit cell. The absorption onset shifts hypsochromically from ~786–794 nm (1.56–1.58 eV) for pure iodide-based perovskites to ~544–556 nm (2.23–2.28 eV) for bromide-rich mixed structures and the onsets become more steep with increasing Br content (Fig. 10b) [247,248]. The substitution of chlorine for bromine shifts the absorption further towards shorter wavelengths, resulting in onset at ~420 nm for pure $MAPbCl_3$ [249].

However, in terms of applications in PV, it is more desirable to extend the absorption onset into the red region to enhance solar light harvesting. The absorption edge redshift can be obtained via substitution of the methylammonium cation with a more voluminous FA, which will cause an expansion of the perovskite structure. Incorporation of formamidinium into $MAPbI_3$ results in a bathochromic absorption onset shift of ca. 20 nm [250] (Fig. 10c) and improves the stability of the $FAPbI_3$ phase. Similar effects have been shown in the more complex mixed $(FAPbI_3)_{1-x}(MAPbBr_3)_x$ structures as well [251].

Finally, the bandgap tuning can be achieved with B-site inorganic cation substitution as well. Replacing Pb with Sn results in a narrowing of the bandgap from 1.55 eV for $MAPbI_3$ to 1.30 eV in $MASnI_3$ [252] (Fig. 10d). Interestingly, the dependence of the bandgap on the Sn molar fraction is not subjected to the linear Vegard's law, but changes in an anomalous, non-linear fashion. After an initial decrease from ~1.57 for pure $MAPbI_3$ to 1.17–1.24 eV for mixed $MA(Sn_xPb_{1-x})I_3$, the bandgap then increases again to 1.30 for $MASnI_3$. This nonlinear behavior can be better approximated by a parabola according to the van Vechten-Bergstresser rule, which states that the bandgap of solid solutions of two semiconductors can be described with a quadratic function of the molar fractions of the components [253]. A similar quadratic dependence was observed for the mixed halide perovskite $MAPb(Br_xI_{1-x})I_3$ [248]. The nonlinear relationship between the bandgap and the structural composition is relatively common for mixed perovskites and was observed in many other compositions (Fig. 11) [247,252,254]. The possibility of precisely tuning the bandgap has proven to be of particular importance for solar cell research. The currently best-performing perovskite-based solar cells include both cation (MA, FA) and halide (I, Br) mixtures [227,229].

Even though the solar cell efficiency record is held by the hybrid perovskites, the inorganic perovskites have been extensively investigated for solar cell applications as well. Despite that the fact that the A-site organic cation can be replaced with a smaller Cs^+ while still maintaining the perovskite structure (t = 0.8), the introduced lattice distortion significantly affects the structural stability. Up to when this review was written, the best performing solar cell based on $CsPbI_3$ has achieved a PCE of more than 15% PCE [258]. The bandgaps of these materials can be tuned by replacement of the halide anion or inorganic cation. In the first case, swapping I^- with Br^- widens the bandgap from 1.73 eV for $CsPbI_3$ to ~2.26 eV for $CsPbBr_3$ [259]. Substitution of Pb^{2+} with Sn^{2+} brings the bandgap to 1.30 eV [260], while incorporation of Cs^+ to $MAPbI_3$ results in an increase of E_{BG} to 2.05 eV (Fig. 11). In contrast to the hybrid HaPs, the bandgap tuning via halide mixing usually follows the linear Vegard's law [259,261], however, with some exceptions [257].

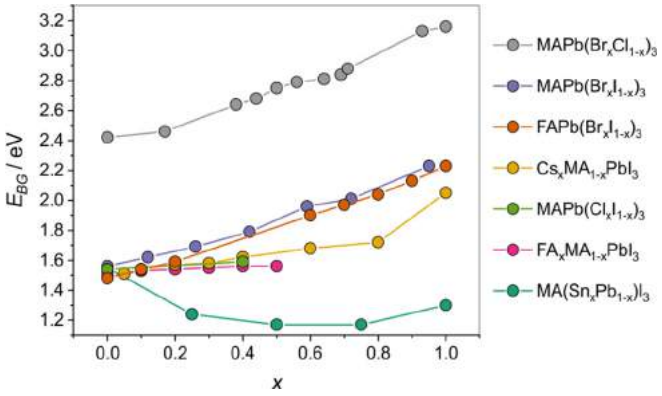

Fig. 11. The dependence of the bandgap value on the composition of the perovskite for selected compounds. Bandgap values were taken from Refs. [73,247,252,255–257].

Furthermore, due to the strong and complex interactions with light, many other interesting photo-induced phenomena occur in lead halide perovskites. A particularly interesting one is the light-induced ion migration. Upon illumination, many of the photogenerated electrons are become trapped at near-surface vacancies. This perturbation gives rise to a photoinduced intrinsic electric field, which induces iodide species migration and results in a net reduction in the vacancy densities in pure $MAPbI_3$ [262,263]. Notably, the phenomenon of light-dependent iodide vacancy migration phenomena may be responsible for the hysteretic behavior of lead halide perovskites [264], and it may be utilized to mimic the behavior of biological synapses [257].

The migration of ions under the illumination becomes a more complex phenomenon in the case of mixed-anion perovskites. However, despite being the most efficient method for bandgap tuning, halide mixing introduces instabilities in the material for some compositions, which further leads to light-induced phase segregation [265]. For example, in mixed $MAPb(Br_xI_{1-x})_3$ perovskites, under illumination, bromide and iodide anions under illumination diffuse through the lattice into high-bandgap Br-rich and low-bandgap I-rich domains, resulting in the creation of charge traps near the band edges [265,266]. They observed that the sub-bandgap absorption increased and the photoluminescence shifted towards the red region. The trap creation was found to be fully reversible and after relaxation in the dark, the photogenerated carriers relax back into lower energy states. In general, ion migration is an undesirable phenomenon, since it can introduce temporal changes in solar cell efficiency. Moreover, it was reported that ion migration induced by constant illumination, and may lead to faster degradation of the perovskite structure [267,268]. Interestingly, the light-induced halide segregation can be counteracted with A-site cation mixing [269].

Another example of perovskite-light interaction is lattice expansion under constant illumination. It has been found that light soaking causes the perovskite lattice to expand in a uniform

fashion, which leads to relaxation of the local lattice strains, therefore improving the PCE [270]. It has also been shown that light illumination accelerates the formation of the perovskite structure, affecting the endmost crystal density and influencing the PCE [271].

Apart from solar cells, HaPs have been extensively investigated for light-emitting applications as well. To this day, red- [272], green- [273], and blue-emitting [274] perovskite-based LEDs (PeLEDs) with external quantum efficiencies (EQEs) reaching ~20% have been reported, approaching the efficiencies of the best-performing organic LEDs [275].

4.2. Low-dimensional perovskites

Control of the crystal structure dimensionality has been proven to be a powerful technique to tune and modify the optoelectronic properties of perovskites. Recently, low-dimensional perovskites gained huge amounts of researchers' attention due to the improved stability over canonical 3D structures. For this reason, they were first used as an encapsulating top layer for conventional 3D PSCs. However, their structural flexibility and considerably different optoelectronic properties from their 3D analogs made them attractive materials for light-emitting applications and PSCs, especially in mixed 2D/3D systems for PSCs [276]. Low-dimensional perovskites consist of single (2D) or multiple (quasi-2D) inorganic layers separated by organic molecules and have the general formula $R_2A_{n-1}B_nX_{3n+1}$, where R is an alkylammonium cation acting as a spacer and n denotes the number of inorganic layers (Fig. 12a). The common arbitrary classification includes 2D (n = 1), quasi-2D (n = 2–5) and quasi-3D (n > 5) perovskites, which further converge to 3D structures for large (i.e. approaching infinity) values of n.

The bandgap of low-dimensional perovskites can be tuned to cover the entire visible range. The bandgap engineering can be performed in a twofold manner: by increasing the number of layers n and by the replacement of structural components. In $(C_4H_9NH_3)_2MA_{n-1}Pb_nI_{3n+1}$, the absorption edge moves towards higher energies with decreasing n, shifting progressively from 1.50 eV for 3D (n = ∞), through 1.91 eV (n = 4), 2.03 eV (n = 3), 2.17 eV (n = 2), to 2.43 eV for n = 1 [185]. When the inorganic Pb^{2+} cation is replaced with Sn^{2+}, the bandgap can be tuned in range from 1.20 eV (n = ∞) to 1.83 eV (n = 1) [277] (Fig. 12b). The substitution of the organic spacer with phenylethylammonium cation (PEA) in $PEA_2MA_{n-1}Pb_nI_{3n+1}$ produces bandgaps of 1.94 eV and 2.36 eV for n = 1 and n = 3, respectively [278]. The structural flexibility of the low-dimensional perovskites and the plethora of possible compositional modifications allow for very broad, but yet precise tuning of the optoelectronic properties.

Due to the discrepancy between the dielectric constants of the inorganic and spacer layer or quantum confinement in the case of for $n \leq 2$, low-dimensional perovskites exhibit strong excitonic behavior. Unlike in 3D perovskites, stable excitons with binding energies approaching a few hundreds of meV can be formed. The increasing number of layers and therefore increasing the thickness of the 2D perovskites scale this energy value down. However, even for big n values, it is predicted that the exciton binding energy will be dozens of times higher than that of 3D perovskites [219]. The distinct excitonic peaks were observed in lead-based perovskites up to 4 layers. Interestingly, for Sn-based compounds, the excitonic peak is visible only for n = 1, which is presumably due to the lower dielectric constant of Sn [185,277]. The control over excitonic behavior is highly demanded in the LED application, as the photoluminescence quantum yield is correlated with the binding energy of the exciton. So far, 2D perovskite LEDs with external quantum efficiencies (EQEs) reaching 18.2% and broad spectral emission have been presented [275]. Recently, several PeLEDs with white-light emission were reported, owing to their broad luminescence spectra to defect-assisted radiative recombination [279].

Beyond LEDs, 2D perovskites have been utilized to achieve low-threshold lasing and amplified spontaneous emission at room temperature [280]. The population inversion is facilitated by ultrafast energy transfer processes between quantum wells with different n values. An energy cascade is formed spontaneously during the synthesis, making these materials very desirable in the field of on-chip integrated nanophotonics.

Another feasible application of low-dimensional perovskites is their use in photodetectors. It is presumed that large organic cations suppress defect formation, which translates to low electronic noise and an extraordinary detectivity reaching 10^{13} Jones [281]. Notably, recent research showed that the linear dichroism that emerged from the optical anisotropy of 2D perovskites enabled polarization-sensitive detection at multiple wavelengths, opening up a promising avenue for applications in polarized optoelectronics [282].

The unique properties in low-dimensional perovskites include the tunable giant Rashba splitting, which strongly enhances the spin-to-charge conversion efficiency, and makes these materials extensively investigated for applications in spintronics [220]. The Rashba splitting occurs due to the lack of the inversion symmetry, which originates from spin-orbital coupling caused by the displacement of the bonds between the heavy elements (Pb, I) [260]. The splitting results in the removal of spin-degeneration of the bands, giving rise to two branches with the opposite spin-aligned electronic states [220]. The possibility of modulating this effect by manipulation of the 2D structure provides control over the Rashba splitting, making low-dimensional HaPs promising candidates for spintronic devices [283,284].

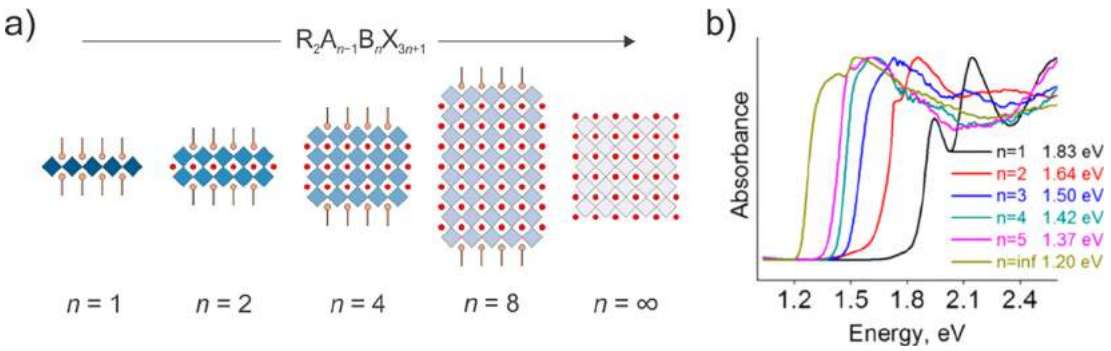

Fig. 12. Bandgap tuning of low-dimensional perovskites. (a) Schematic representation of the perovskite unit cell dimensionality, evolving from 2D (n = 1) to 3D structures (n = ∞). (b) The bandgap of Sn-based 2D perovskites increases from 1.20 eV ($MASnI_3$, n = ∞) to 1.83 eV ($(BA)_2SnI_4$, n = 1) as the dimensionality is reduced (a) [276]. A distinct excitonic peak is visible for the material with n = 1, suggesting significantly lower exciton binding energies than their Pb-based analogs. Panel (b) has been reproduced from Ref. [277] with the permission of the American Chemical Society.

5. Photocatalysis

Photocatalysis can be described as the light-to-energy combined with substrate-to-product conversions. There are several prerequisites for these phenomena to happen in chemical systems and the concomitant chemical reaction to occur. First and foremost, the photocatalytic material electronic band structures, and thus their energies, must be aligned in proper ways to overcome the first energy barriers of the processes. A photon of sufficient energy generates an electron-hole pair. After that, the material electronic structure should additionally sustain and support this process in two dimensions: time and space. Both entities can then remain separated and further transported throughout the structure, usually allowing for desired oxidations or reductions, among other reactions.

Historically, photocatalysis was considered very unselective because of the involvement of (very reactive) radical species. In the previous decade, this landscape changed, and thus, most of the scientific efforts nowadays are set towards highly selective photocatalysis [285]. Other crucial parameters to be enhanced in the course of research are conversion rates and yield. Halide-based materials are being investigated in these contexts. Among the most popular photocatalytic materials, iodides are not top choices. TiO_2 is still considered to be one of the most common candidates for most photocatalytic processes. Nevertheless, several interesting systems with iodides can be found in the literature – with both theoretical and experimental studies. Photocatalytic theories, concepts, and realization strategies, along with their thorough understanding, are cornerstones to another of the main topics of this review: artificial photosynthesis applications.

5.1. Bandgap and band alignment modifications in BiOX (X = F, Cl, Br or I) and their hybrids – a photoacatalytic approach

Historically, pure TiO_2 or modified TiO_2 were widely employed as photocatalysts, yet during the last decade, bismuth oxyhalides (BiOX, X = Cl, Br, I) have been tested numerous photocatalytic applications, including CO_2 conversion, water splitting, or organic pollutant abatement via redox processes. Among them, one of the most commonly researched is BiOI - considered as non-toxic and also a low-cost alternative to lead-based organic–inorganic perovskites (OIP) [286] with an electronic structure being also defect-tolerant (see the electronic structure section or another review of our group [116]). To date, most of the reports concerning BiOX photocatalysts are focused on the decomposition of organic pollutants. Good and thorough reviews on this subject have been published recently [116,117,287,288]. Thus, we will just underline the most interesting, new, or omitted articles contributing to the topic of BiOX photocatalysis here.

Each of the halides (Cl, Br, I) play a significant role in the electron structure composition in the compound and influences the bandgap: BiOCl (~3.2 eV), BiOBr (~2.7 eV), and BiOI (~1.7 eV). These numbers slightly differ, depending on the modifications made to materials. For example, hierarchical nanoplate microspheres of BiOX (X = Cl, Br, I) have bandgaps of 3.2 eV, 2.64, and 1.77 eV, respectively [289]. This is an example of the structure–property correlation. In general, the bulk material properties, especially photocatalytic ones, can be changed. And for the electronic band constitution, they can be fine-tuned by several modification strategies.

From the group of bismuth oxyhalides BiOX, BiOI has an optimal width of the bandgap for visible light absorption and a sufficient absorption coefficient for these wavelengths. The band positions and gaps for BiOX are presented in Fig. 13 relative to the potentials of water splitting (pH = 0) [290,291]. Within the scope of this review, most of the described photocatalytic tests will be based on the degradation of organic compounds, since these show potential for both industrial and ecological applications.

The first and most common method of tuning the photocatalytic activity of bismuth oxyhalides is the modulation of the microstructure. This approach has been used for some time, firstly with the synthesis of micron-sized structures, such as the BiOBr microspheres reported in 2009 for the photooxidation of NO in the gas phase [292]. They were effective photocatalysts mostly due to changes in the bandgap of 2.5 eV and also due to the hierarchical structure.

Structural changes can go down to nanometric sizes. These nanomaterials possess unique quantum chemical properties. For photocatalysis, one of the most significant property is the increase in their active surface. Nanomaterials can be of several dimensions, including 0D (nanoparticles), 1D (fibers, rods, and wires), 2D (plates and sheets), and 3D (hierarchical ordering). Just recently, a series of BiOCl catalyst nanoparticles have been synthesized [293]. The reported method allows for precise control of the surface termination, bandgap, and photocatalytic activity for Rhodamine B decomposition.

A second modification method of BiOX is heterologous hybridization. This method is widely used for any type of photocatalysts since single component catalysts usually do not reach the application stage, often due to photocorrosion or because their bandgap energy is too large. This is why multi-component materials are used by the addition of metals, semiconductors, and co-catalysts. Most synthetic methods for BiOX produce p-type semiconductors [294], with some exceptions for thin films [295] or bulk [296] BiOI. For the p-type semiconductors, the metal nanoparticles can act as electron reservoirs, accelerating the charge transport of electrons from the BiOX VB to metal nanoparticles, while the photogenerated holes stay in the CB of BiOX [297]. Due to more efficient separation of electron-hole pairs, superoxide radical and singlet oxygen were produced, which can be used for bisphenol A removal. The same type of improved interfacial charge transfer was also reported for Bi nanoparticles deposited on $BiOBr_xI_{1-x}$ [298].

There have been cases of metallic Au and Ag doping on BiOX connected with surface plasmon resonance (SPR)-related effects. The oscillating free electrons in the metal can be transferred to the CB of BiOX, leaving holes in the metal nanoparticles. This is a competitive process to the BiOX-to-metal electron transfer, and both can happen simultaneously.

Some of these photocatalytic systems can be used for water purification systems, such as the Ag/BiOI and Ag/AgI/BiOI presented by Lin et al. [299]. One of the benefits of these materials is their usually straightforward method of synthesis by (photo)reduction or solvothermal processing.

Various semiconductors have been used to make hybrid materials with BiOX. Depending on the relative alignment of the VB/CB, there are three types of planar heterojunctions as presented in Fig. 14a. A similar analysis can be done for core–shell semiconductor nanoparticles (Fig. 14b). Among the planar heterojunctions and the straddling gaps (type I), staggered gaps (type II), and broken gaps (type III), type II heterojunctions are considered to be the most effective hybrid. The VB/CB bands are aligned with each other, thus allowing efficient charge carrier transfer: electrons from the higher to lower CB, and holes from the lower to higher VB. Furthermore, in the case of core/shell nanoparticles, various types of heterojunctions are responsible for the diversity of charge carrier confinement schemes [300].

A specific type II heterojunction has been named a Z scheme. For a thorough description, we suggest reading a review from 2016 by H. Li [303] and in 2017 by J. Low [304]. Briefly, Z-scheme systems mimic the charge separation mechanism from

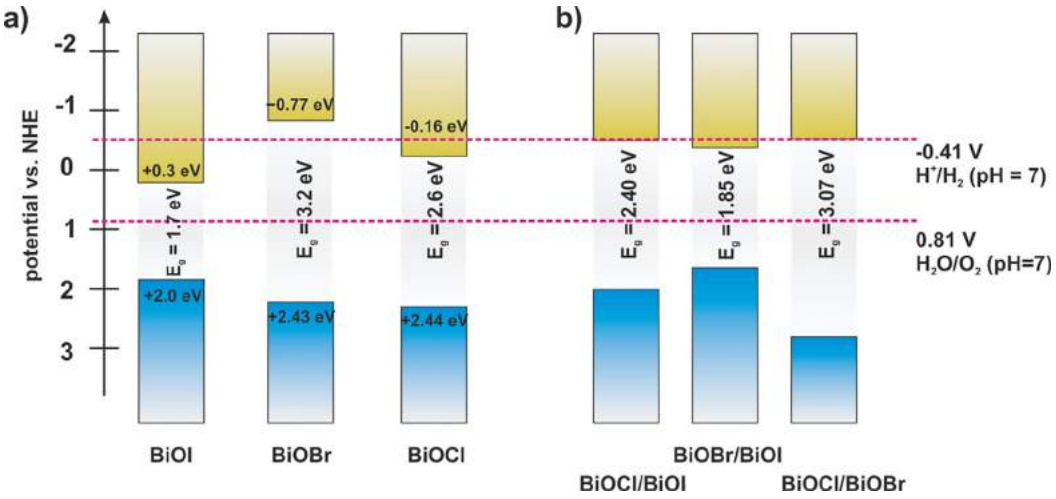

Fig. 13. (a) Band alignment and bandgaps of BiOX films compared to the potentials of water splitting at pH 0 and 7 [290]. (b) Calculated (HSE06) bandgaps of selected BiOX heterojunctions [291].

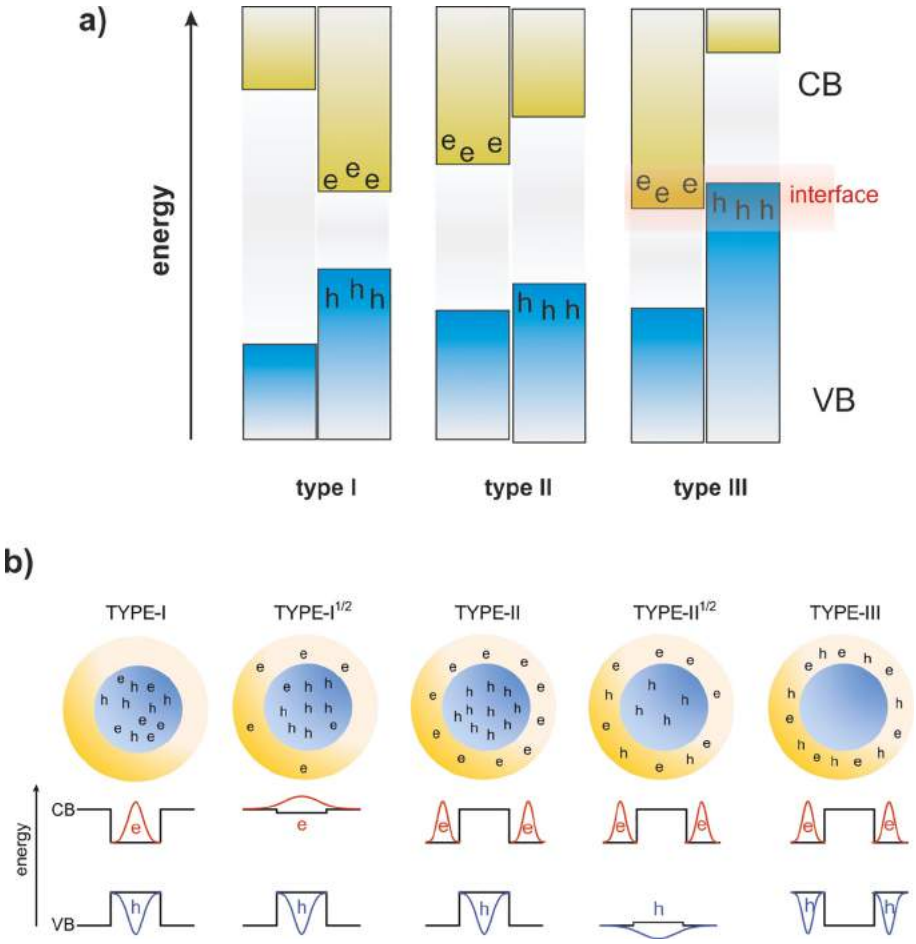

Fig. 14. Different types of semiconductor heterojunctions for a) planar heterostructures and b) materials in core–shell nanoparticles. The figure depicts charge carrier confinement and the radial probability functions for the lowest energy electrons (red line) and holes (blue line). Adapted from Refs. [298,300].

natural photosynthesis, and semiconductors can act as analogous photosystems I and II, conjugated by a cascade of redox mediators (Fig. 15a). Some of the oxyhalides are used in Z-scheme applications. Hybrids made of g-C_3N_4/BiOCl [305] were described to be photocatalytically active for rhodamine B degradation, without any charge mediators, just like the direct Z-scheme system presented in Fig. 15c. For the same photocatalytic reaction, the AgBr/BiOBr connected through Ag nanoparticles [306] have been utilized in a solid-state electron mediator scheme (Fig. 15b).

With proper band alignment, the heterojunctions can be used for the effective narrowing of the bandgaps for photocatalysts. The wide-bandgap semiconductor (e.g. BiOCl) can act as an actual

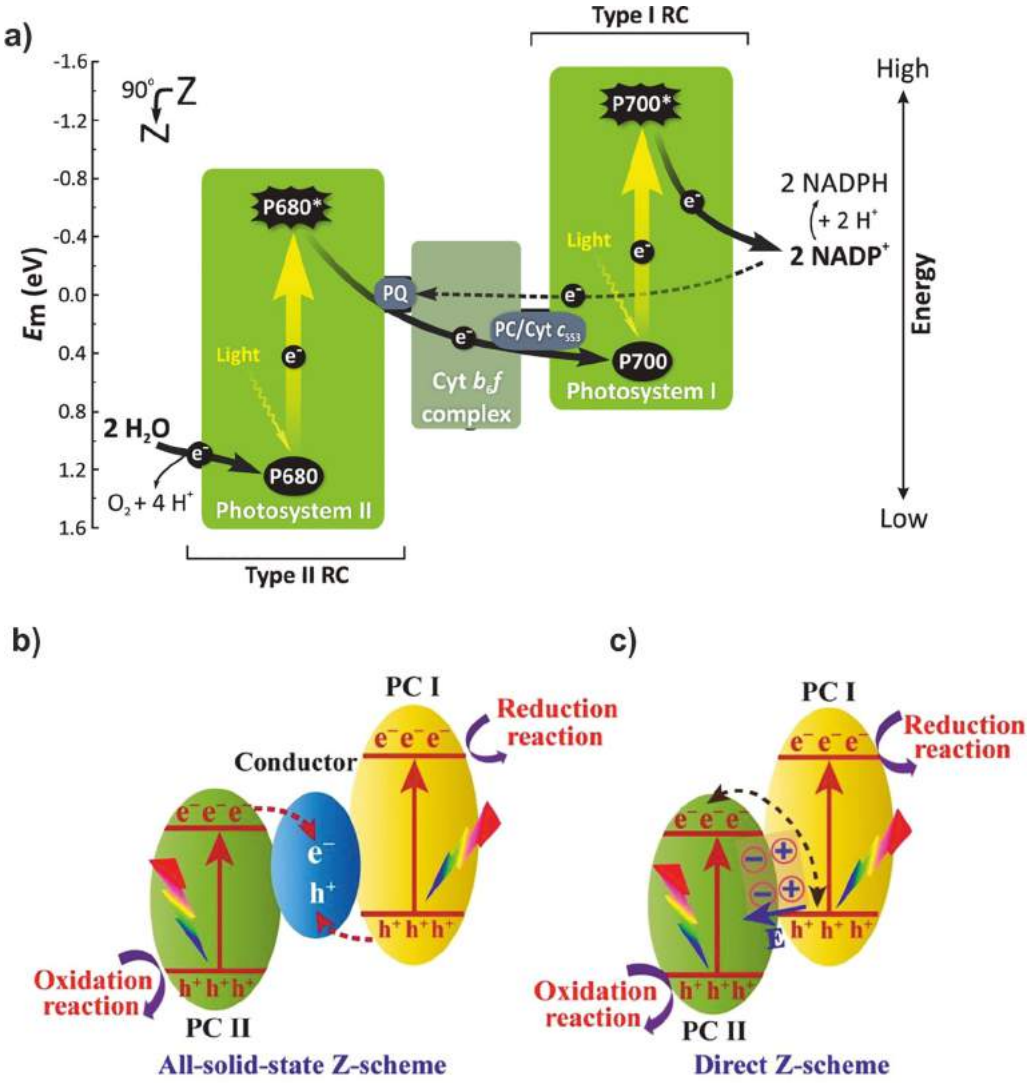

Fig. 15. (a) Photosystems I and II and conjugated by a photochemical cascade. Reprinted with permissions from Ref. [301]. Copyright 2018 by Elsevier. Heterojunction mimetic systems (b) with a solid-state, metal nanoparticle electron mediator, and (c) without an electron mediator. Reprinted with permissions from Ref. [302].

catalyst for such systems, possessing the strong oxidation/reduction ability, while the necessary electron-hole pairs are created due to the presence of the narrow-band gap semiconductor. By the introduction of n-type wide bandgap semiconductors such as (TiO_2 [307], ZnO, and Bi_2O_3 [308,309]) one can design hybrids with BiOI (bandgap energy < 1.8 eV) acting as an efficient photosensitizer. These are examples of creating p-n junction photocatalysts with enhanced charge separation and transfer properties.

Several authors report that it is not only the relative band positions which influence the photocatalytic activity. For Bi/BiOBr [310] and BiOI/BiOCl heterojunctions [311] crystal facets at the interface can regulate photogenerated electron diffusion distances. All these factors, in turn, can tune the performance for direct water splitting [291]. Based on theoretical calculation other $BiOX^1/BiOX^2$ should facilitate enough charge carrier generation, separation, and flow to sustain both water splitting redox processes, i.e. H^+ reduction to H_2 and H_2O oxidation to O_2 (cf. Fig. 13b).

In nanostructured AgI/BiOI composites [312] band alignment supports photogenerated electrons and holes localized on BiOI and AgI, respectively. This improves material photostability and increases the amounts of reactive oxygen species generated, which results in better reactivity compared to organic dye degradation processes [313].

Photosensitization of BiOX can be achieved with the use of carbon materials such as graphene [314,315] or carbon nanotubes [316]. Thin films of BiOI on graphene (GR) can be prepared with nanoflake morphologies [317]. The graphene in this system has anti-reflectance and light-trapping properties. Also, the graphene addition has been found to increase the number of separated charge carriers, which in turn increased the rate of methylene blue photodegradation.

Lately, more sophisticated hybrids have been made, and example of which is graphitic carbon nitride ($g\text{-}C_3N_4$), a new metal-free semiconductor, immobilized with BiOI on flexible supports [318]. The resulting material has enhanced photocurrent densities and was tested for the degradation of rhodamine B and also the reduction of Cr(VI), with good reusability in each example. The $g\text{-}C_3N_4$/BiOI heterojunction has another positive effect on photocatalytic properties because of the high recombination rate and low charge mobility rate of the photogenerated electron-hole pairs on $g\text{-}C_3N_4$ are circumvented. The presence of $g\text{-}C_3N_4$ also extended the visible light absorption form 500 nm to 650 nm and enhanced the charge separation properties. The electrons are transported into the more positive conduction band of BiOI due to the internal electric field gradient [319,320].

One more approach for material modification is based on the doping of metal or non-metal ions directly into the BiOX crystal structure. Owing to the similarities in ionic radii, Bi^{3+} can be exchanged with Mn^{3+}, Zn^{2+}, Cu^{2+}, or Fe^{3+}. These dopants improve the photocatalytic activity by the introduction of additional electronic states in the bandgap region. Sometimes, the metal ions can also inhibit the recombination rate of the electron-hole pairs. Another variation of the structural design is by vacancy generation. For example, BiOI with oxygen defects exhibits better photodegradation activity for formaldehyde [321]. The vacancies acted in favor of the separation and transport of generated charge carriers.

The BiOX mixed halides can also be doped to introduce isolated energy states below the CB or above the VB of the starting BiOX material, which allows for continuous bandgap tuning. This was reported for a $BiOBr_xI_{1-x}$ solid-solution comprising two-dimensional nanoplates. When the percentage of iodide increased, a significant decrease in the bandgap energy occurred (2.87 eV–1. 89 eV), yielding in greater efficiency towards rhodamine B degradation and higher stability during the photocatalysis [322].

By using a heavy doping strategy, Shang et al. modified BiOBr to become $Bi_{24}O_{31}Br_{10}$. The changes of the stoichiometric ratios of Bi to O to Br influenced the orbital hybridization and raised the conduction band level [323]. This resulted in enhanced photocatalytic water splitting with dramatically increased H_2 production.

Since 2014, there have been many other examples of graphene/BiOX nanocomposites that utilize at least two of the modification strategies described before. One of the reported ideas involves a heterojunction of non-stoichiometric BiOF, and non-stochiometric BiOI supported on graphene oxide (GO) [324]. The photocatalytic tests on the degradation of organic pollutants suggested that the composites performed superior to each of the individual constituting compounds. Ag nanoparticle/BiOI junctions with graphene derivative supports were also presented with increased photon absorption and inhibited recombination of charge carriers [325]. The photocatalytic degradation of rhodamine B could reach 99% in 2 h for this system. A parallel system used reduced graphene oxide (rGO) as the support to become Ag/BiOI/rGO. Similar to the GO supported analog, the charge separation and photocurrent density increased, making Ag/BiOI/rGO even better for diclofenac degradation [326,327]. Further improvements to these photocatalytic systems include the use of carbon nanofibers for supporting the AgBr/BiOBr heterojunctions, which resulted in an open-porous structure with heterojunction/support effects that accelerated rhodamine B degradation [327].

Another way to functionalize BiOX catalysts, apart from the above-mentioned modifications, is the surface engineering, by the introduction of more hydroxyl termination groups as one of the examples. The materials were synthesized as nanosheets, and the surface termination was enhanced, which induced greater photoreactivity towards organic pollutant decomposition [328].

5.2. Other halide-based photocatalytic systems

Apart from BiOX and halide perovskites, there are still several underexplored systems. Among the alternatives, antimony sulfoiodide (SbSI) has been proposed as a promising material for the photocatalytic degradation of organic dyes [329]. Despite its low surface area, the photodegradation activity of SbSI for methyl orange decomposition is high, due to the reactive surfaces of the 1D nanorods organized inside 3D urchin shapes. SbSI can also be modified with carbon nanotubes (CNTs) to enhance the stability and rate of photocatalytic dye degradation [330]. Another sulfoiodide material that has been described is a BiSI/MoS2 hydrothermally synthesized nanocomposite [331] which exhibited higher stability and activity than both constituents alone.

6. Artificial photosynthesis in perovskite systems

Metal halide perovskites, especially the ones containing small organic ammonium cations, have undergone a renaissance and received intensive attention over the past decade for photovoltaic and other optoelectronic applications [55,115,332–334]. As mentioned before, there have already been multiple reviews on the use of the traditional 3D perovskites [115,332–334] and the lower dimensional Ruddlesden-Popper phases in solar cells [55,335]. Notably, despite the reported successes of halide perovskites for these device purposes, there has been a relative scarcity of their introduction in artificial photosynthesis, despite the desirable optical properties common to all these functions.

To understand how and why metal halide perovskites can be beneficial in the context of artificial photosynthesis (AP), one needs to understand what AP entails and the desirable aspects of perovskites in fulfilling the requirements. Fundamentally, photosynthesis is the use of light (gr. $\varphi\acute{\alpha}o\varsigma$ = light) to assemble products (gr. $\sigma\upsilon\nu\tau\acute{\iota}\theta\eta\mu\iota$ = to put together). Natural photosynthesis by green plants can be distilled into the following equation:

$$CO_2 + 6H_2O \rightarrow C_6H_{12}O_6(\text{glucose}) + 6O_2 \quad (10)$$

Essentially, green plants harvest sunlight as the energy source to split water in the light-dependent reactions and subsequently channel the reducing equivalents (nicotinamide adenine dinucleotide phosphate, NADPH) for carbon–carbon bond formation reactions using CO_2. AP is thus an attempt to achieve the same objectives of collecting solar energy to prepare chemicals with manmade technology. With the inspiration and lessons learned from studying natural photosynthesis, AP has become synonymous with specific reactions such as water splitting or CO_2 reduction. However, we will adopt the more general and basic definition of photosynthesis described above, which is the use of light to produce chemicals, with the following caveats to distinguish photosynthesis from photocatalysis [336]. Photocatalysis is a kinetic concept where light is needed mainly to overcome an activation barrier for an otherwise thermodynamically favorable reaction, whereas photosynthesis utilizes light to facilitate reactions that are thermodynamically uphill and not spontaneous [336]. AP is thus a way to harness solar energy for chemical processes that will store the energy across two half-reactions in fungible chemicals that can be fuels or feedstocks for other reactions.

To operate effectively for AP, the ideal material should possess the following properties:

(i) Panchromatic or substantial visible light absorption to collect as much of the solar spectrum as feasible;
(ii) high quantum yields for charge separation so that the absorbed photons are utilized for chemical reactions;
(iii) suitable band levels to mediate the desired catalytic processes;
(iv) high thermal, photochemical, oxidative, and aqueous stability to function for extended periods under illumination in the air;
(v) affordable and composed of earth-abundant elements to be economically viable;
(vi) non- or minimally-toxic to be used in large scales without creating end-of-life pollution problems.

In light of these requirements, numerous materials have been explored for AP, including metal chalcogenides [337,338], pnictides [339], halides and their mixed ion forms [340]. No single material has emerged as the leading candidate that can fulfill all the desired properties, but there are now fairly established insights about the different classes of materials. For instance, metal oxides

tend to be oxidatively and hydrolytically stable within certain pH conditions [337], but exhibit limited visible absorption capabilities since the valence bands predominantly consist of contributions by the low-lying O 2p orbitals. Conversely, metal oxynitrides [341,342] and oxyhalides [340] usually harvest larger portions of the solar spectrum, but are susceptible to hydrolysis, especially at high pH. Consequently, the search for suitable photocatalytic materials for AP is still ongoing.

In this context, metal halide perovskites have demonstrated characteristics that are commonly appealing to optoelectronic devices and AP. Over the past decade, perovskites such as methylammonium lead iodide ($MAPbI_3$), formamidinium lead iodide ($FAPbI_3$), and other mixed ion variants have been (re)discovered and found to be panchromatic, and display longlived photoexcited states, high photoconductivity, and efficient charge extraction behavior. Moreover, the constituents are relatively affordable main group elements. Owing to the hydrolytic and oxidative instability of the perovskites containing the small organic ammonium or alkali metal cations in the 3D perovskites, lower-dimensional 2D and 1D Ruddlesden-Popper phases with more hydrophobic interlayers have been increasingly popular in photovoltaic applications [335]. Besides, although lead is patently toxic and unsuitable for large-scale implementation, lead-free and less toxic alternatives containing Bi, Sb and Sn have been explored for various devices.

Thus, it is apparent that the initial hurdles in extrapolating metal halide perovskites into the realm of AP, including the solvent stability and lead toxicity, will likely be overcome eventually by the parallel progresses made to solve the same problems in optoelectronic devices. The following sections discuss the evolution of three approaches in the past decade by which perovskites were used for AP. Initially, 3D perovskites, especially $MAPbI_3$, operated solely as efficient, light-harvesting photovoltaics, and the generated photocurrents were directed toward simple water splitting or CO_2 reduction devices. As the encapsulation and nanostructuring technologies improved, $MAPbI_3$ could be protectively isolated from solvents, so the perovskite could be incorporated into tandem light-absorbing photoelectrochemical cells, even for water splitting reactions. Lately, more oxidatively and hydrolytically stable 3D and lower dimensional perovskites, as well as lead-free variants [343], have been directly introduced for AP, paving the way for another frontier in perovskite applications.

6.1. Indirect methods I: perovskite photovoltaics for artificial photosynthesis

After the rapid rise in solar-to-electric power conversion efficiencies (PCEs) from 3.8 to 17.9% in less than five years [222,335], it was evident that perovskite photovoltaics could challenge the dominance of semiconductors such as Si and CdTe and could potentially be employed as light-harvesting materials for AP [55,115,332–335]. The most popular perovskite that kickstarted this renaissance was $MAPbI_3$, which exists in a black, tetragonal perovskite phase at room temperature [335]. Its crystal structure consists of corner-shared PbI_6 octahedra in a 3D cubic lattice, with almost uniform Pb-I bond lengths of 3.17 Å for the axial iodides and 3.11 Å for the equatorial iodides [344]. The respectable PCEs partly arose from the high current densities above 20 mA cm^{-2} that were achievable for mixed ion variants of $MAPbI_3$ upon illumination under AM 1.5G conditions [345]. In turn, the high photocurrents that could be generated were then exploited as early as 2014 for solar-driven water splitting [345].

As illustrated in Fig. 16a, two state-of-the-art $MAPbI_3$ perovskite solar cells were connected in tandem to separately power the anode and cathode for water oxidation to O_2 and proton

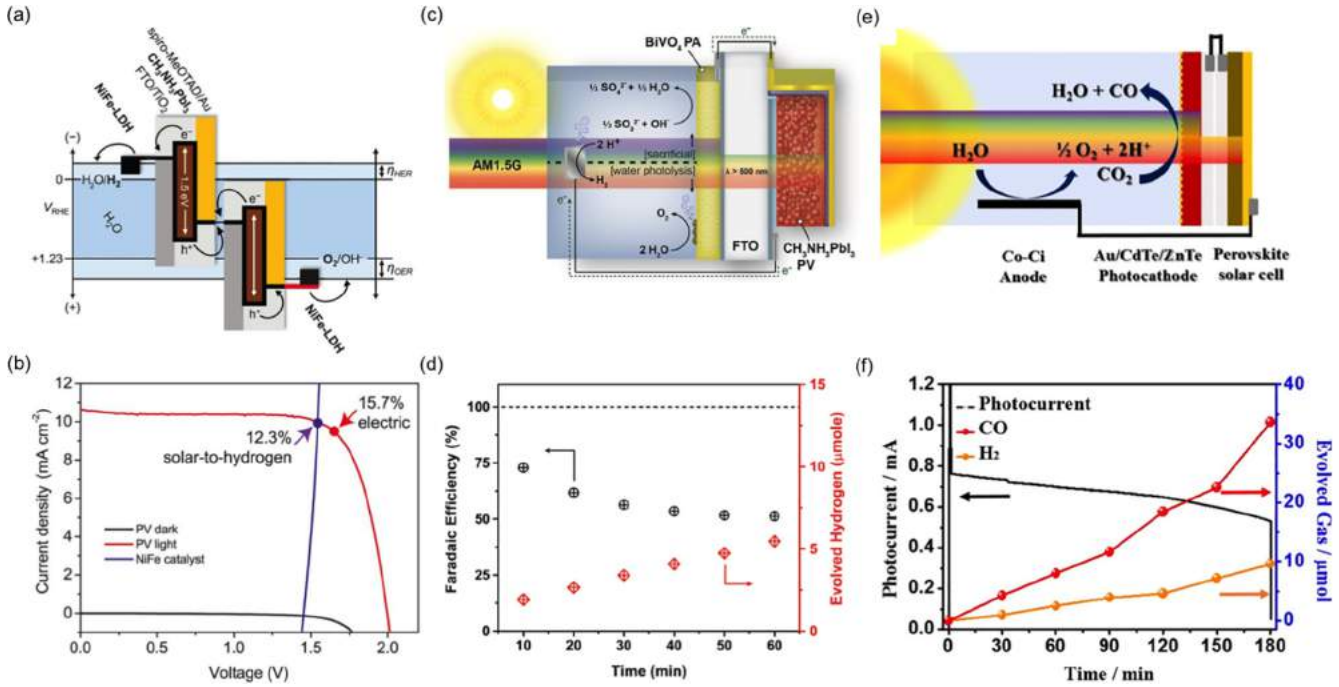

Fig. 16. (a) Energy level diagram of a $CH_3NH_3PbI_3$ PV tandem cell combined with NiFe layered double hydroxide as the electrocatalysts for overall water splitting. (b) *J-V* curves are illustrating the high solar-to-hydrogen conversion efficiency by the cell in (a) under simulated AM 1.5G solar irradiation. Both (a) and (b) have been reproduced with permission from Ref. [345]. Copyright 2014 by the American Association for the Advancement of Science. (c) Schematic of the complementary light harvesting by a tandem $CH_3NH_3PbI_3$-$BiVO_4$ photoanode for water oxidation with cobalt phosphate as the catalyst. (d) Faradaic efficiency and amount of evolved H_2 when the photoanode in (c) is coupled to Pt for H_2 evolution. Both (c) and (d) have been reproduced with permission from Ref. [347]. Copyright 2015 by the American Chemical Society. (e) Diagram of a similar approach for complementary light harvesting by a tandem $CH_3NH_3PbI_3$ PV-Au/CdTe/ZnTe photocathode for CO_2 reduction coupled to a cobalt bicarbonate anode for water oxidation. (f) Chronoamperometry and the corresponding CO and H_2 produced in 3 h by the PEC in (e). Both (e) and (f) have been reproduced with permission from Ref. [348]. Copyright 2016 by the American Chemical Society.

reduction to H_2, respectively [345]. Each perovskite photovoltaic cell was capable of harvesting light up to 800 nm and providing a photocurrent density of 21.3 mA cm^{-2} and an open-circuit voltage of 1.06 V, which resulted in PCEs of 17.3% [345]. Since the thermodynamic potential for water splitting is 1.23 V, at least two of the perovskite solar cells were necessary to provide the potentials for the individual half-reactions. To overcome the unfavorable kinetics of the water-splitting catalytic processes, chemically resistant nickel (Ni) foam deposited with nickel and iron layered double hydroxides (NiFe-LDH) were introduced as the actual catalysts in 1 M NaOH solutions [345]. Remarkably, this tandem perovskite photovoltaic water splitting device could achieve the standard photocurrent of 10 mA cm^{-2}, which would translate to a solar-to-H_2 conversion efficiency of 12.3% (Fig. 16b), among the highest efficiencies even now and at levels that could potentially become economically viable [345]. The water-splitting device would be operating at close to its maximum power point of 9.61 mA cm^{-2} at 1.63 V, with a PCE of 15.7% (Fig. 16b) [345]. This simple, pioneering demonstration of highly efficient water splitting by perovskite photovoltaics already underscored the value of perovskites in steering AP research.

Following this early work, the same team led by Grätzel and other coworkers at Nanyang Technological University, Singapore, created a different variant of a tandem perovskite-Fe_2O_3 water splitting device [346]. Instead of using two high-efficiency perovskite photovoltaic cells to supply the necessary energy, a Mn-doped hematite (Fe_2O_3) photoanode was coated with cobalt phosphate (Co-Pi) and employed as the water oxidation catalyst [346]. By assembling these tandem light absorbers in series and introducing Pt as the H_2 evolution catalyst, they were able to attain overall unassisted water splitting with photopotential of up to 1.87 V and solar-to-H_2 conversion efficiency of 2.4% [346]. Several advances in this system include the higher affordability and robustness of the Fe_2O_3 photoanode over a second perovskite photovoltaic cell, although 1 M NaOH still had to be used and the H_2 production efficiency was lower. In a similar conceptual design, Kamat and coworkers developed a tandem $MAPbI_3$-$BiVO_4$ water splitting device, where a $BiVO_4$ photoanode coated with CoPi as well, was the O_2 evolution catalyst (Fig. 16c) [347]. This system could operate in neutral pH conditions and accomplished a solar-to-H_2 conversion efficiency of 2.5% under AM 1.5G illumination [347], similar in performance to the one with Fe_2O_3 as the photoanode. A major drawback of this tandem water-splitting cell was that the Faradaic efficiency of H_2 evolution declined over time (Fig. 16d), which was attributed to side-reactions when sacrificial reagents were introduced [347]. Both these examples illustrate the feasibility of combining perovskite photovoltaics for tandem light absorption with more affordable, traditional semiconductor photoanodes in water splitting AP systems.

In a related approach, Ko, Lee, and their coworkers combined a $MAPbI_3$ photovoltaic cell in tandem with a ZnO@ZnTe@CdTe core–shell nanorod array as the *photocathode* (Fig. 16e), underlining the versatility of the perovskite solar cells [348]. Analogous to the photoanode cells described previously, the ZnO@ZnTe@CdTe semiconductor photocathode harvests the higher energy wavelengths below 580 nm, while $MAPbI_3$ collects the remaining photons up to around 800 nm [348]. After depositing Au nanoparticles on the photocathode as co-catalysts, a $MAPbI_3$ solar cell with an open-circuit voltage of 1.04 V and a short-circuit current density of 20.86 mA cm^{-2} (PCE of 16.31%) was stacked in tandem [348]. The cell was then operated under unbiased conditions with a cobalt bicarbonate (Co-Ci) anode on Ni foam for O_2 evolution in CO_2-saturated $KHCO_3$ aqueous solutions under the standard AM 1.5 G conditions [348]. As shown in Fig. 16f, respectable Faradaic efficiencies of up to 81.9% and CO selectivity over H_2 of at least 74.9% were obtained [348].

As mentioned previously, it was believed that 3D metal halide perovskites such as $MAPbI_3$, while exhibiting remarkable light absorption and charge separation behavior as well as high PCEs as photovoltaics, were inherently too hydrolytically, oxidatively, and photochemically unstable to be directly exposed to solvents for AP purposes [335]. The activation barrier for the decomposition of $MAPbI_3$ is merely 80 kJ mol^{-1}, while its enthalpy of formation is only −404 kJ mol^{-1}, suggesting that it can readily degrade to its constituents under mild heating [349]. Moreover, the typical open-circuit voltage of around 1.1 V and below for perovskites meant that the valence and conduction band levels were probably unsuitable for directly mediating some of the thermodynamically challenging reactions such as water oxidation to O_2. These early examples highlight how perovskite photovoltaics could still be utilized for driving AP reactions by isolating them from the catalytic processes and exclusively exploiting them only as efficient light harvesters. Furthermore, by combining in tandem with another perovskite solar cell or other semiconductor photoelectrodes, the necessary potentials for reactions such as water splitting and CO_2 reduction reactions could be acquired, thus paving the way for subsequent improvements in perovskite optoelectronic technologies to be incorporated into the design of AP systems.

6.2. Indirect methods II: encapsulated perovskites for artificial photosynthesis

Since it became evident that metal halide perovskites were effective chromophores for AP, there had been growing interest in their incorporation into photoelectrodes in wired or wireless systems to serve as catalysts for water splitting. In an advance over Kamat's earlier design, Lee and coworkers incorporated $MAPbI_3$ directly into a photoanode with tandem light absorption by 3% Mo-doped $BiVO_4$ [350]. To ensure the photochemical stability of the $MAPbI_3$ after exposure to aqueous environments, the perovskite was first sandwiched between TiO_2 (as the electron transport layer) and a poly(triarylamine) (PTAA as the hole transport layer), before a 70 nm Au electrode was deposited on the PTAA by thermal evaporation (Fig. 17a) [350]. This Au layer was then sealed with a cover glass and epoxy to become water-proof [350]. The tandem light absorber was then attached using Ag paste to connect with the Co-Ci coated Mo-doped $BiVO_4$ film that had been deposited on FTO plates to create the photoanode for water oxidation to O_2 [350].

The key differences over the previous system by Kamat and coworkers are that the $BiVO_4$ had undergone additional treatment by hydrogenation and doping with Mo, and there is a direct interface between the $BiVO_4$ and $MAPbI_3$. The former is crucial in improving the charge extraction behavior over $BiVO_4$ alone, as observed by the high photocurrent densities of 3.5 mA cm^{-2} (Fig. 17b), and a corresponding higher average solar-to-H_2 conversion efficiency of 4.3% (c.f. to 2.5% above) in a wired system [350]. The latter is attractive in that a completely wireless, monolithic "artificial leaf" could be created by integrating the tandem $MAPbI_3$-$BiVO_4$ photoanode with Pt, which resulted in a device that operated with a respectable average solar-to-H_2 conversion efficiency of 3.0% [350]. Although the performance of the standalone artificial leaf architecture was poorer, likely due to higher Ohmic resistance at the interfaces of the device [350], these wireless systems are appealing for certain applications such as portable, distributed solar fuel devices, which can be used in remote places with poor electrical infrastructure.

Besides tandem light-absorbing unbiased devices, $MAPbI_3$ has also been incorporated into a single junction photoanode and passivated with a thin Ni layer for photoelectrochemical water oxidation [351]. As illustrated in Fig. 17c, the bandgap energy of $MAPbI_3$

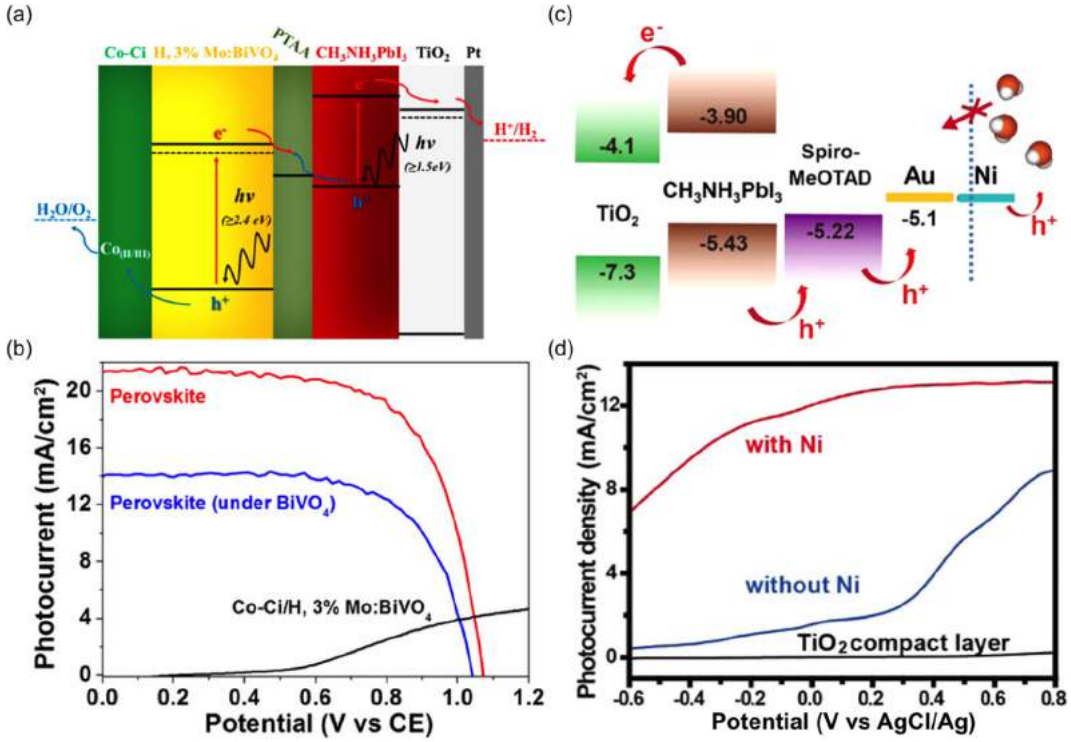

Fig. 17. (a) Energy level diagram of a $CH_3NH_3PbI_3$ light harvester integrated into a wireless photoelectrochemical system with Mo-doped $BiVO_4$ as a photoanode. The perovskite is encapsulated with cobalt carbonate (Co-Ci) as the water oxidation catalyst and Pt as the proton reduction catalyst for overall water splitting. (b) *J-V* curves of the photoelectrochemical cell in (a), where the intersection of the perovskite and the $BiVO_4$ curves (~4 mA/cm^2) is the anticipated operating point for water splitting. Both (a) and (b) have been reproduced with permission from Ref. [350]. Copyright 2015 by the American Chemical Society. (c) Illustration of the band alignments of a $CH_3NH_3PbI_3$-only light harvester sealed in a photoanode with a Ni coating for photoelectrochemical water oxidation. (d) Comparison of the photocurrent densities showing the dramatic improvement in activity with the additional Ni coating in (c). Both (c) and (d) have been reproduced with permission from Ref. [351]. Copyright 2015 by the American Chemical Society.

is around 1.53 V [351], which exceeds the thermodynamic requirement of 1.23 V needed for water splitting. In principle, $MAPbI_3$ alone should be capable of functioning as the light harvester in AP without the need for another tandem chromophore. Zheng and coworkers created a photoanode by sandwiching $MAPbI_3$ between a compact, electron-transporting TiO_2 layer and spiro-MeOTAD as a hole-transporting layer, the latter of which was coated with Au as the electrode [351]. To ensure that the perovskite was physically protected from the aqueous environment and also facilitate water oxidation, an 8 nm thin Ni layer was deposited by magnetron sputtering [351]. Remarkably, in the presence of 0.1 M Na_2S as a sacrificial electron donor in a pH 12.8 alkaline solution, the Ni coated photoanode showed a dramatic increase in photocurrent density over the photoanode without Ni, achieving above the 10 mA cm^{-2} standard at 0 V vs AgCl/Ag (Fig. 17d) [351]. This encapsulated $MAPbI_3$ photoanode was then connected with a Pt cathode, and the photoelectrochemical cell was irradiated under one sun with no external bias to achieve overall water splitting [351].

Although this example verified that $MAPbI_3$, when suitably encapsulated, could function without a tandem light absorber for AP reactions like water splitting, the long-term performance was still not ideal. The high initial photocurrent density decreased dramatically and plateaued around 2 mA cm^{-2} after only 15 min owing to deterioration of the device by electrolyte penetration through the Ni and Au layers [351]. Patently, although $MAPbI_3$ is an effective light harvester for photovoltaics and AP, there are limitations to how much engineering can overcome in terms of the stability of the 3D perovskites when exposed to solvents. Alternative metal halide perovskites that are inherently more photochemically and hydrolytically stable would be vital for further applications in AP, some recent examples of which will be discussed in the next section.

6.3. Direct artificial photosynthesis with robust perovskites: beyond photofuel production

Although it was known that $MAPbI_3$ was hydrolytically unstable when exposed to moisture, Nam and coworkers demonstrated that judicious management of the coordination chemistry of Pb^{2+}, I^-, and H^+ ions in water could counterintuitively stabilize the black tetragonal perovskite phase at room temperature. PbI_2 has low solubility in water (K_{sp} = 4.4 × 10^{-9} at 20 °C) [352] but is known to dissolve as the I^- concentration increases to form PbI_3^- and PbI_4^{2-} ions [353]. Nam and coworkers astutely hypothesized that maintaining high concentrations of H^+ would increase the hydrogen bonding interactions among water molecules and reduce the likelihood of water intercalation into the crystal structure of $MAPbI_3$ in water [354]. Moreover, high concentrations of I^- would promote the formation of PbI_3^- ions [353]. Thus, a combined high concentration of HI should then be favorable for the stabilization and precipitation of the black tetragonal $MAPbI_3$ perovskite phase, instead of the formation of the almost colorless monohydrate ($MAPbI_3{\cdot}H_2O$) or the yellow dihydrate ($MA_4PbI_6{\cdot}2H_2O$) [354].

Remarkably, when the excess precipitates in the presence of increasing [HI] from 0.1 M to 6.06 M were examined by powder X-ray diffraction, there was a gradual but clear transition from PbI_2 to $MAPbI_3{\cdot}H_2O$ and finally to $MAPbI_3$ once the HI concentration was above 3.16 M (Fig. 18a) [354]. A detailed phase mapping was conducted by using different concentrations of $HClO_4$ and KI, which confirmed that elevated concentrations of both H^+ and I^- were necessary for the precipitate to be predominantly perovskite

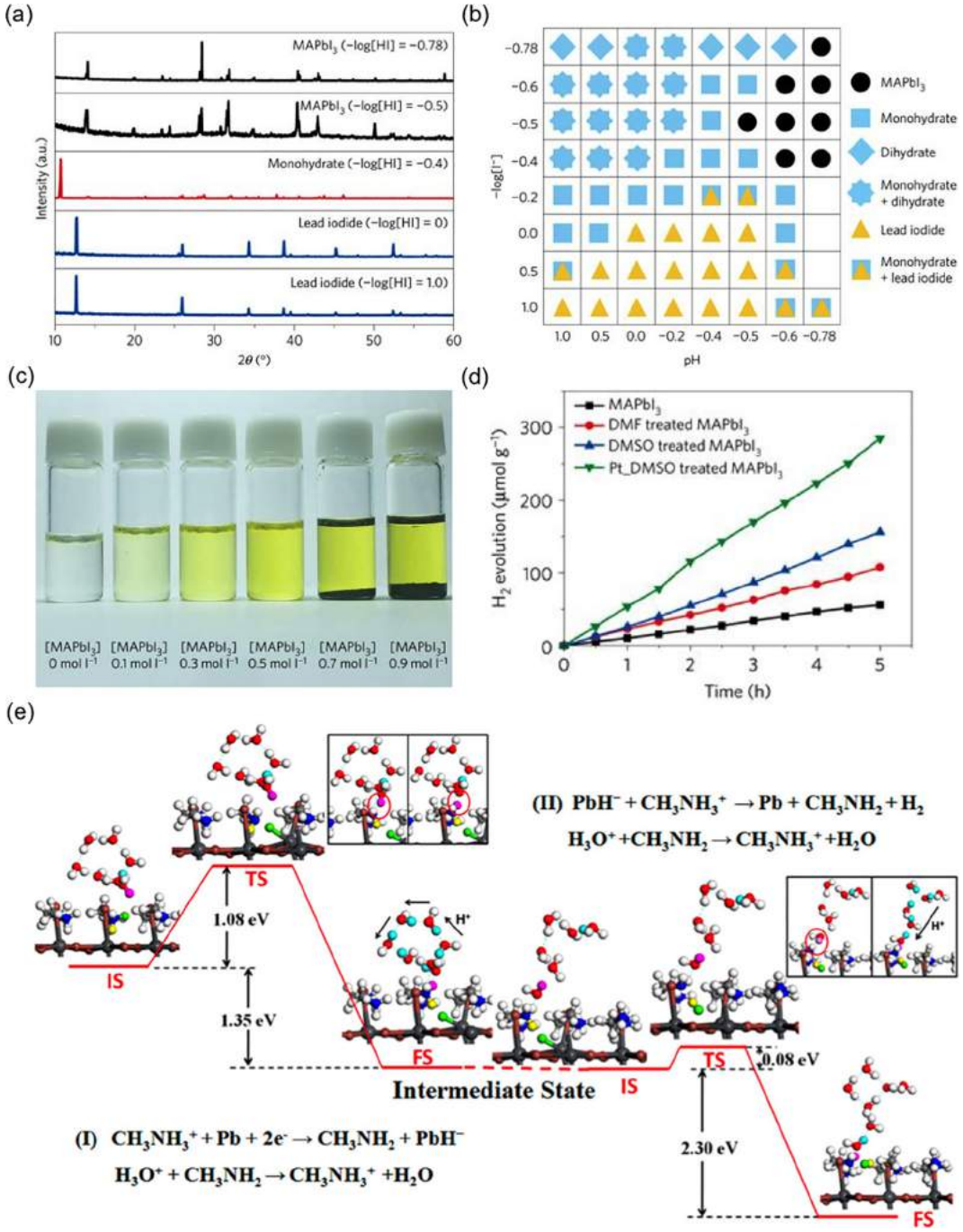

Fig. 18. (a) XRD patterns of the precipitates in HI solutions of different concentrations saturated with CH_3PbI_3. (b) Phase diagram of CH_3PbI_3 at different concentrations of H^+ and I^-. (c) Photographs of different amounts of CH_3PbI_3 added to 6.06 M HI solutions, showing that the perovskite phase is stable at high concentrations. (d) Comparison of the H_2 evolution activity of CH_3PbI_3 annealed under different solvents, with and without a Pt co-catalyst. Parts (a) - (d) have been reproduced with permission from Ref. [354]. Copyright 2016 by Nature Springer. (e) Reaction pathway for the Pb-activated, amine-assisted H_2 evolution from the surface of CH_3PbI_3 in acidic solutions derived from quantum mechanical calculations. This image has been reproduced with permission from Ref. [355]. Copyright 2018 by the American Chemical Society.

$MAPbI_3$ (Fig. 18b) [354]. Interestingly, even in 6.06 M HI, $MAPbI_3$ was still somewhat soluble, dissolving to give MA^+ and PbI_3^- ions, until the solution became saturated and $MAPbI_3$ was stable and could be precipitated above 0.7 M (Fig. 18c) [354]. The identity of the perovskite was verified with other techniques such as optical absorption and UV photoelectron spectroscopy [354].

Having shown that $MAPbI_3$ was stable in concentrated HI solutions, Park et al. demonstrated that independently synthesized perovskite could be employed in AP to split HI into H_2 and I_3^- upon visible light (>475 nm) irradiation [354]. Under their reaction conditions, $MAPbI_3$ impressively functioned as heterogeneous H_2 evolution photocatalysts from HI for a least 160 h [354]. They also found that special thermal annealing of $MAPbI_3$ films under polar solvents such as DMSO, and the introduction of Pt as a co-catalyst dramatically improved the H_2 evolution activity (Fig. 18d) to reach a solar-to-H_2 efficiency of 0.81% [354]. Goddard and coworkers subsequently used aqueous quantum mechanics calculations to propose a Pb-activated, amine-assisted reaction mechanism for this H_2 evolution reaction [355]. The most feasible predicted pathway involves protonation by MA^+ of surface Pb with

empty coordination sites to form Pb-H intermediates after visible light irradiation to overcome a 1.08 eV activation barrier (Fig. 18e) [355]. In the subsequent step, another MA^+ cation reacts with the hydridic Pb-H to form H_2, with a low barrier of only 0.08 eV (Fig. 18e) [355]. Owing to the high HI concentration, a Grotthus chain mechanism from H_3O^+ in solution rapidly replenishes the MA^+ cations in both steps [355]. In summary, the teams of Nam and Goddard have shown that a perceptive understanding of the coordination chemistry of $MAPbI_3$, by manipulating the ionic strengths of its constituents, enabled the groundbreaking demonstration of the popular 3D perovskite in H_2 evolution for AP from aqueous conditions.

Besides $MAPbI_3$, another 3D perovskite that has recently found applications in AP is the orthorhombic $CsPbBr_3$. $CsPbBr_3$ possesses several advantages over $MAPbI_3$, namely (i) Cs^+ is not thermally volatile and labile like MA^+; (ii) the Pb-Br bond dissociation energy is higher than that of the Pb-I bond, so $CsPbBr_3$ is thermodynamically more stable and less soluble; (iii) the Br^- ion has a higher redox potential than the I^- ion, so $CsPbBr_3$ will be oxidatively more stable and should have a more positive valence band level (+1.2 V vs. SCE) [356]. Conversely, the more positive valence band level of $CsPbBr_3$ is associated with larger bandgap energy (2.4 eV) than $MAPbI_3$ (1.5 eV) and hence diminished light-harvesting capabilities [356]. With these properties in view, the enhanced solvent stability of $CsPbBr_3$ nanocrystals for oxidative photocatalysis was exploited for some of the first demonstrations of perovskites for pollutant degradation and organic synthesis [356–358].

Wu and coworkers reported that $CsPbBr_3$ nanocubes with around 10 nm edges were found to catalyze the oxidative dimerization of thiophenol to diphenyl disulfide in dichloromethane under ambient atmospheric conditions and white LED illumination (Fig. 19a) [356]. They observed an external quantum yield of 3.6% at room temperature and expanded the substrate scope to produce 12 disulfide compounds by homo- and hetero-coupling of aromatic and aliphatic thiols [356]. The same $CsPbBr_3$ nanocubes were then used for C–H activation of tertiary amines followed by oxidative coupling with phosphite esters in toluene, also under ambient air and white light (Fig. 19b) [356]. Likewise, a reasonable substrate scope of 13 products was shown, emphasizing the general applicability of the nanocrystals [356]. During detailed studies on the mechanism of the thiol coupling, Wu et al. observed a hypsochromic shift in the absorbance edge, which was attributed to anion exchange of the Br^- in $CsPbBr_3$ with Cl from the dichloromethane solvent [356]. Lead halide perovskites are reputed to undergo facile and even topotactic anion exchange owing to the relatively weak lead-halide bonds and the unusually high ion mobilities [335]. Most interestingly, the authors mentioned that when both photocatalytic reactions were conducted in the absence of air, H_2 evolution was observed, although conversions and yields were lower [356]. Nonetheless, this simultaneous production of value-added organic products like disulfides and phosphites by oxidative photocatalysis, while a fuel like H_2 is generated, is an instance of the more general form of AP one of our team has been promoting [336].

Shortly after Wu's work was reported, Yan and coworkers reported the introduction of $MAPbBr_3$ and $CsPbBr_3$ nanocrystals of sizes between 2 and 100 nm for photocatalysis [359]. Likewise, they found that $CsPbBr_3$ was chemically more stable under their reaction conditions [359], likely because Cs^+ would not be affected by the base added and the 3D perovskite nanocrystals would remain intact, whereas MA^+ would be deprotonated and become volatilized as methylamine. They used the $CsPbBr_3$ nanocrystals to effect reductive C–C bond formation between α-bromoketones and aldehydes (Fig. 19c) in the presence of secondary amines as both the co-catalyst and base [359]. The photoexcited $CsPbBr_3$ was proposed to reduce the α -bromoketone to generate a nucleophilic radical, while the secondary amine and aldehyde would convert to an enamine in a dark reaction [359]. Subsequently, the enamine would get oxidized by holes from the photoexcited $CsPbBr_3$ and combine with the nucleophilic radical to eventually produce α -alkylated aldehydes [359]. A modest substrate scope was demonstrated with 12 products, including a derivative of cholesterol, and turnover numbers of up to 52,000 were recorded [359], suggesting that $CsPbBr_3$ could indeed be employed in a range of promising AP reactions. Nonetheless, although the $CsPbBr_3$ was reused for at least four cycles, Zhu et al. reported that

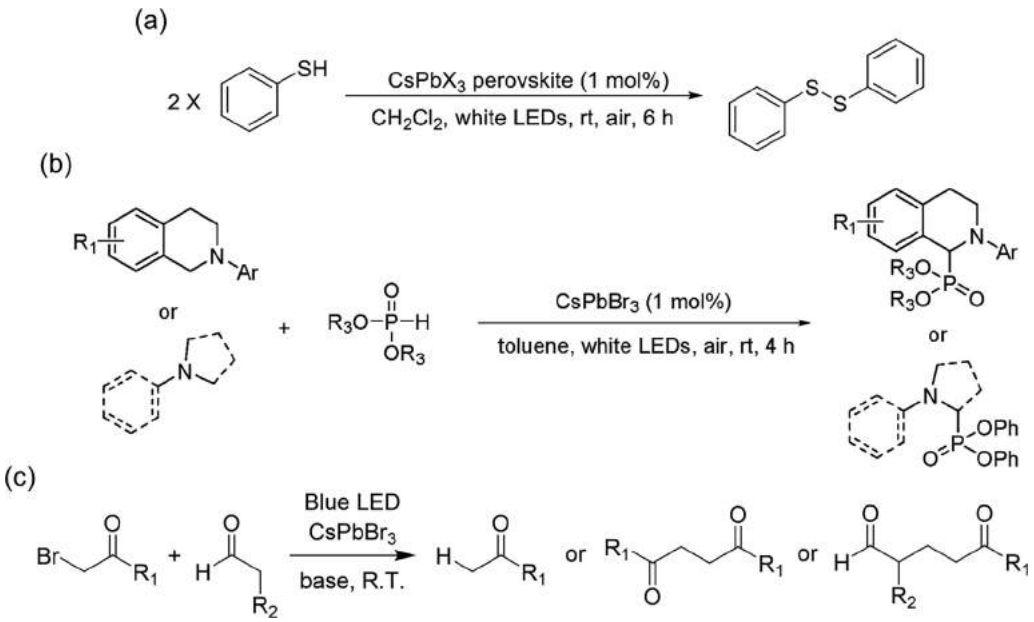

Fig. 19. Examples of photoredox catalytic reactions by moderately stable $CsPbBr_3$ nanocrystals in (a) oxidative coupling of thiols, (b) C–H activation, and cross-dehydrogenative between tertiary amines and phosphites, and (c) reductive dehalogenation, dimerization, and α -alkylation of aldehydes. Both (a) and (b) have been reproduced with permission from Ref. [356]. Copyright 2018 by the Royal Society of Chemistry. Part (c) has been adapted from Ref. [359] with permission from the American Chemical Society.

aliquots of water completely deactivated and dissolved the perovskites [359], which will be ruinous for the broader utility of these 3D perovskites for AP in aqueous media.

Although it appeared that $CsPbBr_3$ nanocrystals could be directly used for AP, there had also been attempts to improve their catalytic activity by integrating 6 nm $CsPbBr_3$ quantum dots (QDs) with graphene oxide (GO) to form a composite (Fig. 20a) [360]. Both the $CsPbBr_3$ QDs and the $CsPbBr_3$ QD/GO composite were then employed for photocatalytic CO_2 reduction in ethyl acetate as a solvent and sacrificial electron donor [360]. As illustrated in Fig. 20b, there was a >99% selectivity for CO_2 reduction in the absence of water, with CO and CH_4 being the most and second most abundant products respectively [360]. It also appeared that the GO was beneficial in giving higher yields of the CO_2 reduction products and higher external quantum efficiencies than just the QDs alone [360]. Through electrochemical impedance and time-resolved photoluminescence spectroscopic measurements, the authors proposed that GO served not only to improve the stability of $CsPbBr_3$ but also facilitated more effective charge extraction from the perovskite [360]. However, the sacrificial oxidation of ethyl acetate and the hydrolytic instability remain undesirable in the use of $CsPbBr_3$ in AP, thus motivating the development of more sustainable perovskite alternatives.

Since the re-emergence of lead halide perovskites for photovoltaics, there have been parallel developments in the search for more oxidatively and hydrolytically robust, as well as less toxic alternatives. In this context, Karunadasa and coworkers have reported several groundbreaking results in the development of lead-free double perovskites containing Bi^{3+}, Ag^{+}, and Cs^{+} instead [129–132]. These double perovskites retain the same 3D metal-halide lattice but have general formulae of $A^{+}_2B^{+}C^{3+}X_6$ (A = alkali metal or MA, B = Ag or Tl, C = Bi or Sb) instead of the ABX_3 for 3D lead halide perovskites [129–132]. The double perovskites, an example of which is $Cs_2AgBiBr_6$, possess several coordination chemistry advantages over the lead halide perovskite, namely (i) they are lead-free and comprise much less toxic elements; (ii) the higher charge of the C cation (e.g. Bi^{3+}) results in stronger metal-halide bond strengths, higher thermodynamic stability, and lower solubility; and (iii) the larger number of components offers greater substitutional variability in the choice of ions that can fulfill the Goldschmidt tolerance factor to form stable perovskites. Nonetheless, the light-harvesting and charge extraction efficiencies of the double perovskites have so far underperformed those of the lead halide perovskites, thus limiting their wider adoption in optoelectronic devices.

Despite these shortcomings, double perovskites have been successfully applied for AP recently. Kuang and coworkers prepared 9.5 nm $Cs_2AgBiBr_6$ nanocubes with bandgaps of around 2.52 eV, corresponding to a hypsochromic shift due to quantum confinement effects compared to the 1.95 eV of the bulk form [361]. The structure of this double perovskite consists of corner-bridged alternating octahedra of $BiBr_6$ and $AgBr_6$ in a 3D cubic lattice, with Cs^{+} ions in the interstitial spacing [361]. The nanocrystals were found to be stable for over three weeks in non-coordinating solvents such as chloroform and octane, and at least five days in ethyl acetate. $Cs_2AgBiBr_6$ has an indirect bandgap and the nanocrystals have average photoluminescence lifetimes of 7.5 ns, which is longer than diffusion control [361]. Based on the band levels obtained

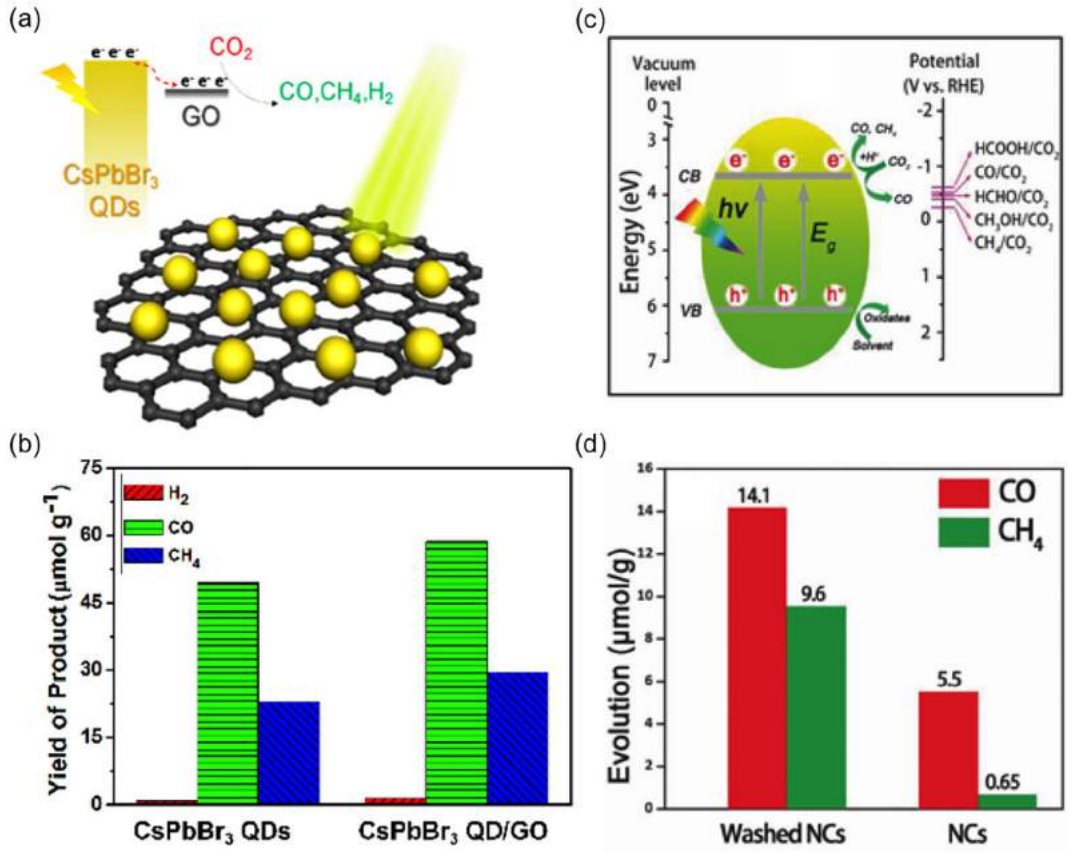

Fig. 20. (a) Illustration of the relative conduction band levels for CO_2 photoreduction by a composite of $CsPbBr_3$ QDs dispersed over GO. (b) Improved yields of CO and CH_4 after 12 h of irradiation for the composite in (a) over $CsPbBr_3$ QDs alone. Both (a) and (b) have been reproduced with permission from Ref. [360]. Copyright 2017 by the American Chemical Society. (c) Energy and potential levels of the $Cs_2AgBiBr_6$ double perovskite nanocrystals for CO_2 photoreduction. (d) Comparison of the improved CO_2 photoreduction activity after removal of the organic surfactants from the $Cs_2AgBiBr_6$ nanocrystals in (c). Parts (c) and (d) have been adapted from reference [361] with permission from Wiley-VCH Verlag GmbH & Co. KGaA.

by photoelectron spectroscopy in the air (PESA) and optical measurements (Fig. 20c), the conduction band electrons should have sufficient potential for multielectron CO_2 reduction to several products [129,361]. Accordingly, the authors used the $Cs_2AgBiBr_6$ nanocrystals for photocatalytic CO_2 reduction in ethyl acetate as a solvent and sacrificial electron donor under AM 1.5G solar simulation and observed CO and CH_4 as the predominant products (Fig. 20d) [361]. They also discovered that after rinsing away the excess surfactants which could interfere with charge extraction, there was a 6.5 times increase in the electrons consumed (Fig. 20d), corresponding to an external quantum efficiency of 0.028% at 398 nm [361]. Most impressively, the $Cs_2AgBiBr_6$ nanocrystals could retain their structure and phase uniformity at 55% relative humidity for 90 days, light soaking under 70 mW cm^{-2} for 500 h, or heating at 100 °C for 300 h [361]. However, the nanocrystals were still susceptible to ligand detachment and eventual degradation in protic solvents such as isobutanol [361].

Given the poor hydrolytic stability of double perovskites, different strategies to achieve hydrophobic and more robust perovskites will be beneficial. Karunadasa and coworkers demonstrated that lowering the dimensionality of the 3D $Cs_2AgBiBr_6$ to the 2D Ruddlesden-Popper phases for $(BA)_4AgBiBr_8$ and $(BA)_2CsAgBiBr_7$ (BA = butylammonium) resulted in mono- and bilayer metal halide nanosheets with tetragonal distortions in the Ag-Br octahedral [189]. The axial Ag-Br bonds contracted to 2.6–2.7 Å, whereas the equatorial Ag-Br bonds expanded to 3.0–3.1 Å, which was attributed to a pseudo-Jahn-Teller effect from mixing of the filled 4d orbitals and the empty 5 s orbitals [189]. These lower-dimensional perovskites have even more substitutional versatility and electronic diversity and have been found to be favorable for photovoltaics [335], alluding to similar advantages for applications in AP.

In light of these benefits, one of our team had recently reported hydrophobic lead and tin 2D perovskites intercalated by C_{16} long hexadecylammonium (HDA) cation as water-resistant materials for photoredox catalysis and AP [362]. The structures of the $(HDA)_2PbI_4$ and $(HDA)_2SnI_4$ perovskites were studied by powder (Fig. 21a) and single crystal (Fig. 21b) X-ray diffraction, with the

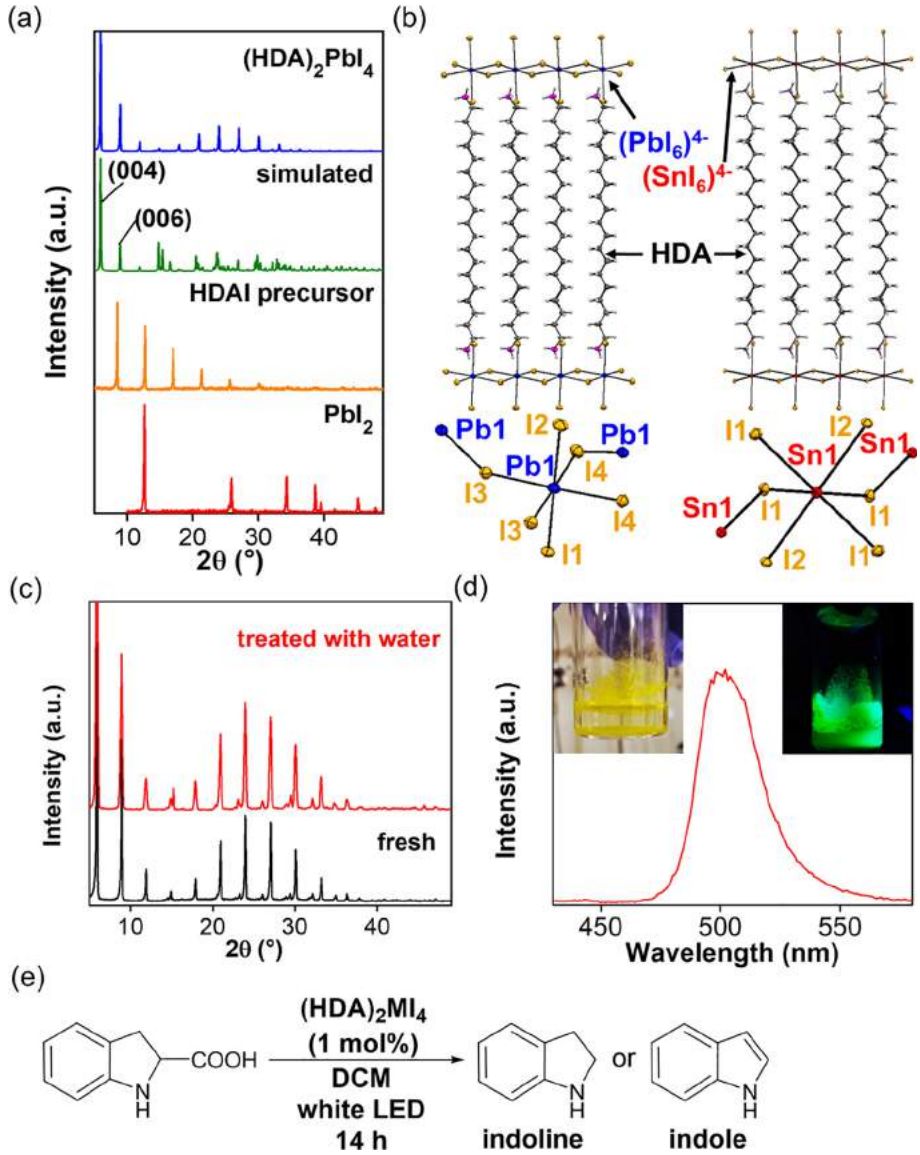

Fig. 21. (a) Comparison of the powder XRD patterns $(HDA)_2PbI_4$ and its precursors. (b) Solid-state structures of $(HDA)_2PbI_4$ and $(HDA)_2SnI_4$ obtained by single-crystal XRD. (c) Powder XRD patterns of $(HDA)_2PbI_4$ highlighting its stability after stirring in water for at least 30 min. (d) PL data of $(HDA)_2PbI_4$ after photoexcitation at 350 nm in water, demonstrating that the optical properties are retained. (e) Examples of the photocatalytic decarboxylation and dehydrogenation reactions mediated by the Pb and Sn 2D perovskites. Reproduced from [362] with the permission of Wiley-VCH Verlag GmbH & Co. KGaA.

latter confirming the remarkably stacked C_{16} hydrophobic chains intercalated between corner-shared MI_6 (M = Pb or Sn) octahedra in 2D nanosheets [362]. Unlike the $(BA)_4AgBiBr_8$ and $(BA)_2CsAgBiBr_7$ double perovskites, which had tetragonal distortion for the Ag-Br octahedral, the metal-halide bond lengths for both the Pb and Sn perovskites were fairly uniform at 3.1–3.2 Å, with bond angles close to 90° at each metal center (Fig. 21b) [362]. Presumably, the main group Pb and Sn nuclei do not experience the same pseudo-Jahn-Teller effect as Ag since the former have s^2 electronic configurations, whereas the latter has empty s orbitals. As anticipated, owing to the extremely hydrophobic HDA cation, $(HDA)_2PbI_4$ was structurally unchanged even after suspension in water for 30 min (Fig. 21c) and was even photoluminescent (Fig. 21d) at room temperature. Contact angle measurements gave an average of 98.4°, verifying the hydrophobicity of this 2D perovskite [362].

Although $(HDA)_2PbI_4$ and $(HDA)_2SnI_4$ were isolated and fully characterized, the Sn perovskite was still vulnerable to air oxidation from Sn^{II} to Sn^{IV}, thus limiting its broader applications [362]. $(HDA)_2PbI_4$ was further characterized by variable temperature, steady-state, and ultrafast time-resolved optical spectroscopy, as well as PESA [362]. The valence band maximum has been estimated to be +1.2 V versus the normal hydrogen electrode, and the bandgap energy is 2.3 eV, while the photoluminescence lifetime is up to 3.0 ns, suggesting that $(HDA)_2PbI_4$ may be suitable as heterogeneous photocatalysts for oxidative reactions [362]. Accordingly, both $(HDA)_2PbI_4$ and $(HDA)_2SnI_4$ were found to be suitable for the photooxidation of indoline-2-carboxylic acid in dichloromethane under 48 W LED illumination at room temperature. In the absence of air, decarboxylation occurred to give indoline in an overall redox neutral process, whereas a further dehydrogenation to indole took place when the reaction was performed in the air (Fig. 21e) [362]. The reaction showed tolerance to electron-donating and electron-withdrawing functional groups, including halide substituents that could be further derivatized. Although $(HDA)_2SnI_4$ was not oxidatively stable, it was still shown to be viable for the photocatalysis, albeit with lower yields. This was a crucial demonstration that Pb-free variants were also feasible for AP reactions. $(HDA)_2PbI_4$ could be recovered by centrifugation and reused in the photocatalysis, while the compositional integrity was verified by both powder X-ray diffraction and X-ray photoelectron spectroscopy [362].

As illustrated in the examples covered above, metal halide perovskites have been shown to be functional heterogeneous photocatalysts for many AP reactions. The initial concerns about the solvent stability had been overcome on several pathways, including managing the ionic strengths in solution [354], utilizing structures that possessed stronger metal halide bonds [356,359,360], employing double perovskites with higher bond strengths [361], and lowering the dimensionality with hydrophobic organic cations [362]. Unfortunately, the most widely used perovskites still contain highly toxic elements such as Pb and Tl, but the recent results with double perovskites have expanded the compositional diversity to include eco-friendlier materials. We anticipate that the combination of double perovskites and lower dimensionality [189,335,362] will pave the way forward in the development of metal halide perovskites that can fulfill most, if not all the desired criteria for materials which will be applied in AP in the near future.

7. Let's count on iodide-based semiconductors – implementations of unconventional computational techniques

A neuromorphic approach is one of the most influential trends in information processing nowadays [362] and memristors (and other memristive and memfractive elements) and considered as the main building blocks of such systems. There is a plethora of original papers and reviews on the synaptic properties of memristors, as well as simple neural networks built thereon. Many of the most important findings have been compiled in a series of specialized books [52,363–368]. Here, we will focus on more complex aspects of information processing by utilizing the dynamics of memristive elements. The dynamic aspects of the neuromorphic approach toward computation can be summarized in Latin as *repetitio est mater studiorum*, which means "repetition is the mother of learning". This phrase has been adopted by scholars since the middle ages, and is a simple recipe for learning: any information repeated several times has a greater chance to be remembered than a single event. It must be noted; however, that continuous repetition of false information may lead to self-generated misinformation [369] or purposeful deception [370], well-documented sociological phenomena [371], which according to some opinions, may have happened in the case of research on memristors [372]. In the brain, repetitive training rule is realized twofold: a signal might appears several times, and as a result, a specific synaptic connections form, or the signal appears once, and it circulates between the brain structures due to the presence of feedback loop [373,374]. In order to mimic such a neural system, one needs a synaptic-like device to store the information/signal, preferably as a value somewhere between 0 and 1. Memristors have such functions, which is, and it is one of several reasons why they attract special attention in the field of neuromorphic computing [375–377]. Furthermore, such an artificial system, in order to process information efficiently, needs to show a complex internal dynamics.

The memristor is a two-terminal passive device that has memory. Namely, it has at least two different resistive states at the same potential, and the state depends on the history of the device. The device was postulated in the 1970s by Leon Chua on the basis of theoretical symmetry relations between differential equations describing a resistor (current vs voltage), a capacitor (voltage vs charge), and an inductor (current vs magnetic flux) [42]. Originally, the memristor was supposed to associate the voltage with magnetic flux. Due to the relation of units, a new element should also be described by resistance, which, in contrast to resistors, should be a function of electric charge. This theoretical circuit element was named *memristor* - a combination of memory and resistor. Interestingly, application of other symmetry rules yields the same analytical description of the memristor [378]. The physical realization of a memristor was announced in 2008 by researchers from HP Labs [379]. This report, being a source of exasperation for some researchers, has initiated a long discussion on the existence of memristors as physical devices, especially in the context of fundamental circuit element [380–382]. It also initiated the 'memristor rush', which led to thousands of theoretical and experimental papers published in following years [383]. Recently the existence of ideal memristors was invalidated on experimental grounds [384,385]. Interestingly, at the same time, a first report on a memristive element operating on magnetic flux was published [386]. The most important fingerprint of a memristor is a characteristic pinched loop in the current–voltage plane [48,387]. Various circuit elements bearing this feature have been reported much earlier than the idea of a memristor itself [43,388].

The founding father of the idea has no problem with the use of the term *memristor*, but several more cautious authors prefer to use the term *memristive device*, which is more general (and also refers to three and more-terminal devices having synaptic-like behaviour) but creates additional confusion. Introduction of a more generalized concept of memfractance makes the whole story even more complex [389–391]. The fundamental issues on the existence of memristors are, of course, not purely semantical disputes. Readers interested in this vivid discussion are encouraged to follow the

vigorous exchanges within the original papers [378,380–382,384–386,392]. Controversies aside, passive nonlinear memory elements do exist [393], some of which have pinched hysteresis loops, while others are without it. These devices, called memristors or memristive elements for the sake of simplicity, have bright futures not only as storage information units but also for information processing. The observation of a pinched hysteresis loop in the current–voltage characteristics of the device is the simplest way to determine the presence of memory-like features in the passive, two-terminal memristive devices that exhibit nonvolatile (and sometimes also volatile) memory. The mechanisms behind the memristive hysteresis loops are diverse. The change from a high to a low resistive state can be a result of the formation of conductive filaments [394–396], modulation of the Schottky barrier height [397,398], ion or dopant migration [399], or a combination of these processes (Fig. 22) [400].

In the case of memristors, different synaptic features were demonstrated: long-term potentiation and depression (LTP, LTD), short-time potentiation and depression (STP, STD), spike-timing-dependent potentiation (STDP), spike-rate dependent potentiation (SRDP), pulse pair facilitation (PPF), measurement of excitatory postsynaptic current (EPSC), and different forms of metaplasticity [376,401]. Most publications describe the performance of a single device, but recently more and more often, chips built as arrays of memristors are designed for use for a particular application or a generalized approach towards IA implementation [376]. In contrast to inorganic oxide or chalcogenide-based memristors, the incorporation of the halogen-containing memristive device in a larger system to perform a certain task is uncommon [33,397].

One of the crucial parameters here is the variable resistance that can be used for information storage. Metal oxide-based memristors are the most intensively studied devices due to their usually large ON/OFF ratios [402]. It is a result of the filamentary mechanism. The abrupt changes of resistance typical for most memristors are not ideal in analog applications [403]. These applications require devices with continuous resistivity change, even with very limited ON/OFF switching ratios. The brain is an analog device, and the synaptic weights in our brain are not represented with 0's and 1's, but rather as various values somewhere in between. Such criteria fit the definitions of memristors, where mechanisms are based on the Schottky barrier height modulation.

Memristors can be utilized as synaptic devices in various hardware implementations of artificial neural networks (e.g. perceptrons) and in digital electronics using a so-called MAGIC (memristor-aided logic) approach [404]. Memristors based on interfacial switching (cf. Fig. 22a-c) are not very well suited for these kinds of applications, but they paradoxically offer much more. Due to the 'soft' switching characteristics, they are perfectly suited for the processing of analog signals in dynamic systems. Such an approach is usually referred to as *reservoir computing*. In general terms, the reservoir is a dynamical system with fading memory that echoes the state property. The state of the system is a function of its history, and the input signal influences the evolution of a dynamic system in real-time. Memristive elements can be easily transformed into reservoir computing systems, especially into single node echo state machines, which are systems where delayed feedback loops provide the internal dynamics of the system and fading memory features. Details on the theory, construction, and properties of reservoir systems can be found elsewhere in numerous specialized papers and are out of the scope of this review [405–409]. In the presented examples, the role of the reservoir node is played by a single memristor.

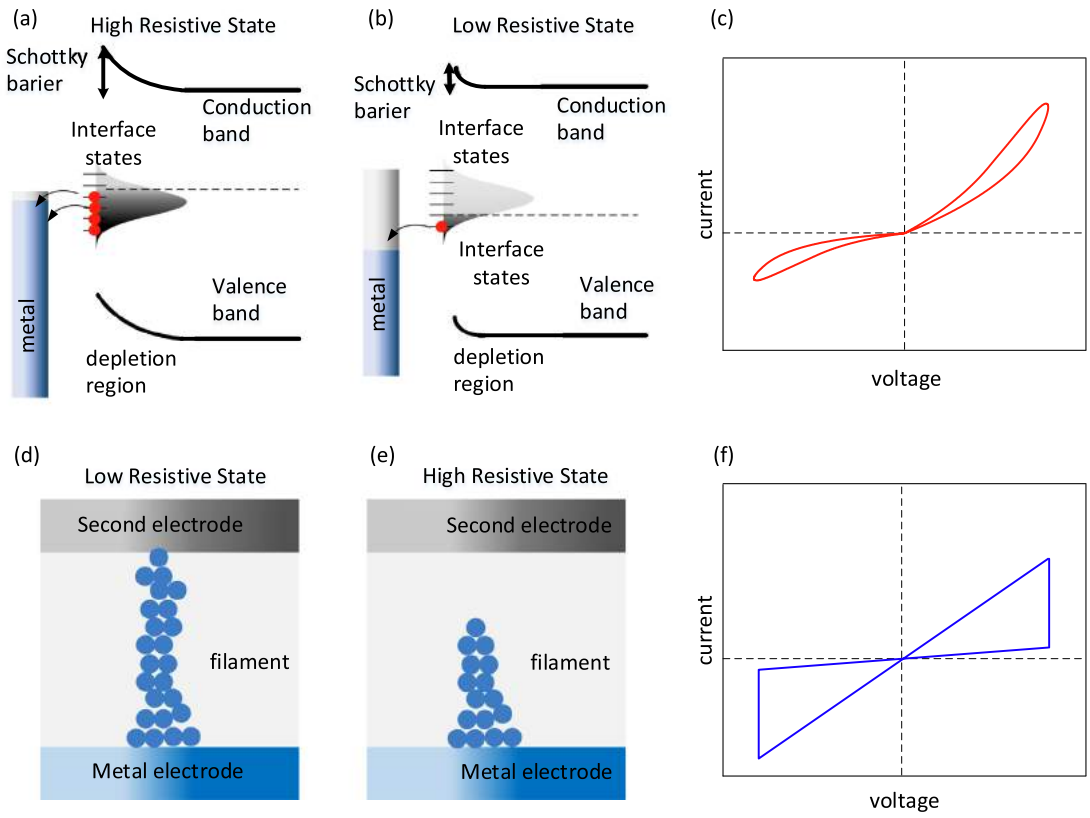

Fig. 22. Two of the most common mechanisms of resistive switching: the modulation of the Schottky barrier value (a,b) and the conductive filament formation (e,d), with the corresponding idealized hysteresis curves (c, f); the dashed lines correspond to zero current and voltage values.

Thorough review articles about memristors and memristive (or even photomemristive) devices have already been presented [376,402,410–413]. Here, we explore the lead halides, tin iodide complexes, and lead and tin halide perovskites as the materials used in the memristive devices, described in this chapter because some of our team have taken a steps towards the application of the memristive device in a specific task, which involves a different type of recurrent signals in the synaptic experiments.

Lead halides and a molecular complex of tin tetraiodide were recently described in terms of their synaptic properties, as central layers of ITO/PbX_2/metal and FTO/$[SnI_4\{(C_6H_5)_3SO\}_2]$/Cu devices [397,398]. These memristors have layered structures and were prepared by spin-coating solutions of the compounds on the fluorine-doped tin oxide (FTO) or indium tin oxide (ITO) surfaces. In the case of lead halides, the second electrodes were composed of various metals (e.g. Cu, Ag, Au, Al), while the device based on the organic–inorganic complex has a piece of copper as the second contact. The layer structure of the device is presented in Fig. 22c. Fig. 22d shows that the surface of FTO/$[SnI_4\{(C_6H_5)_3SO\}_2]$ is polycrystalline. The devices have, to some extent, similar current–voltage (*IV*) hysteresis loops with the anticlockwise directions of propagation and gradual changes from high resistive to a low resistive state. The latter is an important property of the device in terms of analog computing [403].

The long-term memory of both ITO/PbI_2/Cu [397] and FTO/$[SnI_4\{(C_6H_5)_3SO\}_2]$/Cu [398] devices were used to perform classification tasks. For this purpose, an individual memristor was incorporated into the system, according to Fig. 23a. The signal is then introduced to the system as the voltage difference between the electrodes of the memristor. The sourcemeter, amplifier, and the delay line create a feedback loop in which signals can circulate. Such a system is called a Single Node Echo State Machine and is a type of recurrent neural network or reservoir system.Fig. 24.

To understand how the signal processing in such a system works, one should focus on the *IV* characteristics of the memristors. First of all, the presented devices have unsymmetrical, rectifying characteristics (Fig. 23a, b). As a result, the initially introduced symmetrical signal is reduced to its upper (positive) half after several cycles. The more cycles there are, the higher the deformation of the input signal. A second important feature of the *IV* pattern is the threshold potential above which the current starts to grow significantly. In the ITO/PbI_2/Cu memristor, it is about 0.5 V–0.7 V. In the classification experiment, a set of sinusoidal signals of amplitude in the 1.0 Vpp to 2.2 Vpp range were introduced to the system one by one. The signals with the amplitudes lower than 1.85 Vpp vanished after several cycles, while signals of higher (or equal to 1.85 Vpp) amplitudes persisted in the system infinitely. This is a simple example of signal classification according to its amplitude. What is important to notice is the threshold value of 1.8 Vpp, which corresponds well with the threshold value from the *IV* characteristic (1.8 Vpp/2 = 0.9 V). In the classification process, the threshold value can be modulated in a reasonable range with the amplifier incorporated in the feedback loop.

As an additional result of the classification experiment, the device changed its state from a high resistance state (HRS) to a

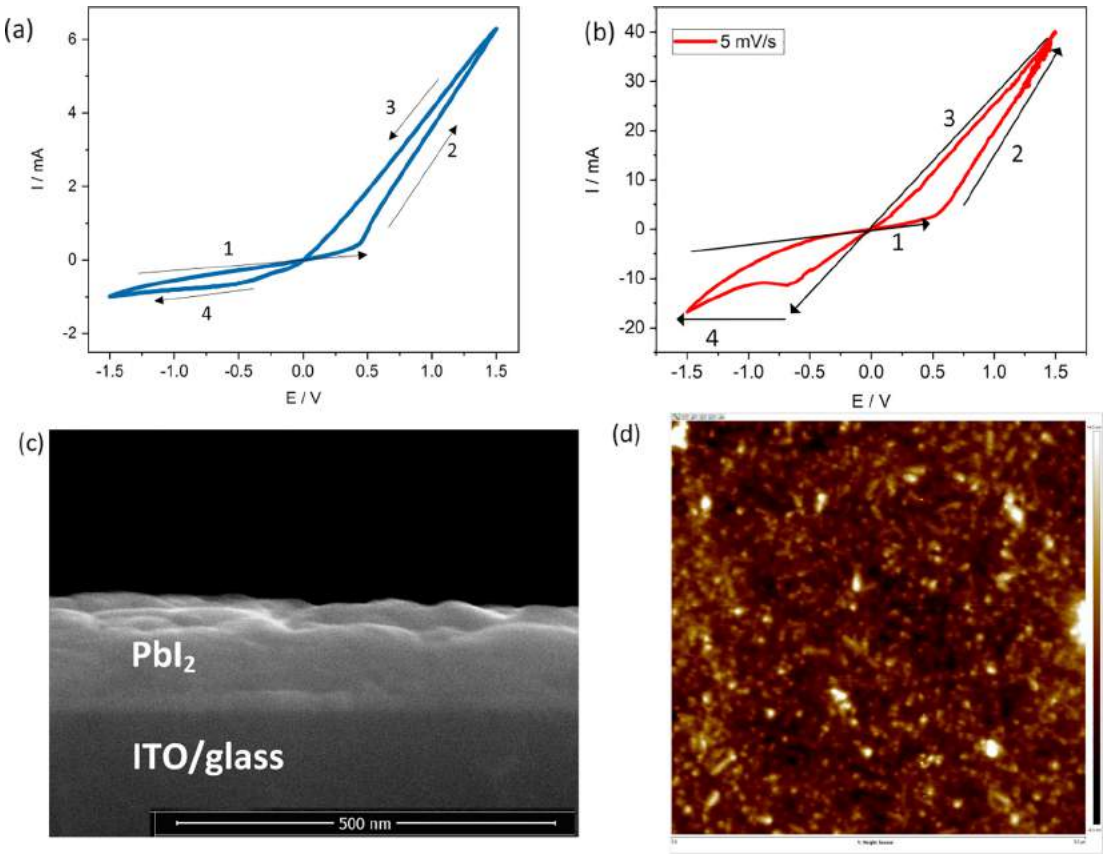

Fig. 23. The current–voltage characteristics of (a) ITO/PbI_2/Cu recorded with a 100 mV/s scan rate, and (b) FTO/$[SnI_4\{(C_6H_5)_3SO\}_2]$/Cu recorded with 100 mV/s scan rate. (c) A cross-section of the PbI_2/ITO/glass structure. (d) An AFM image of the spin-coated layer of $[SnI_4\{(C_6H_5)_3SO\}_2]$. Adapted from Refs. [397] and [398] with the permission from the American Chemical Society.

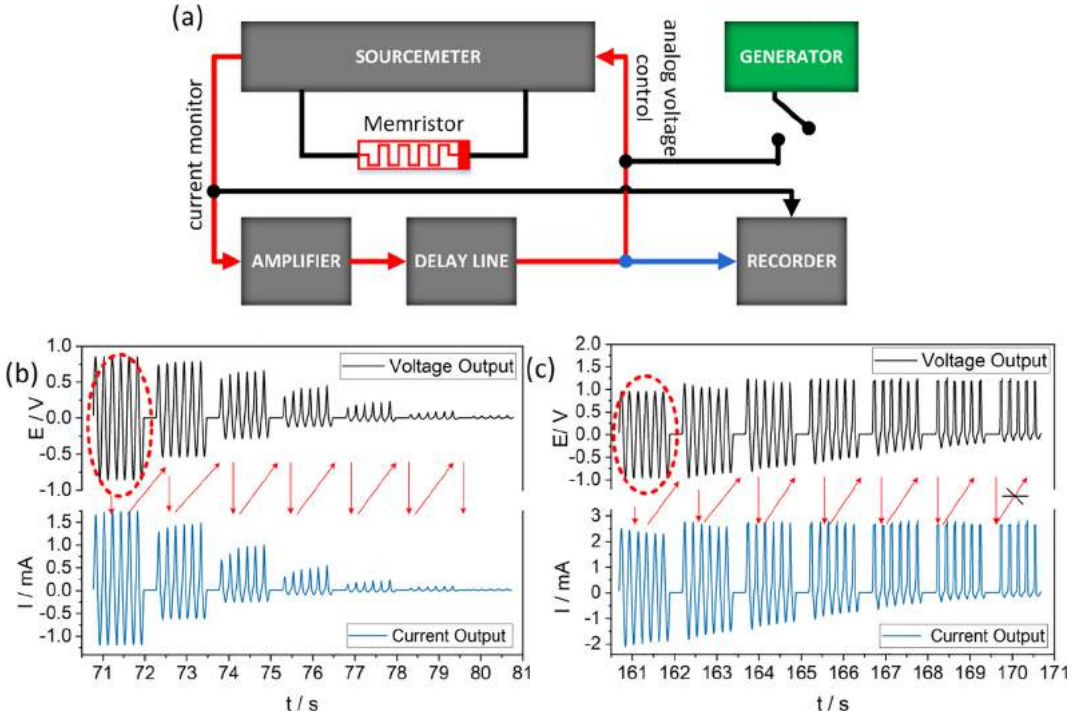

Fig. 24. A representation of the reservoir system. The red arrows indicate the feedback loop created by a connecting sourcemeter, an amplifier, and the delay line (a). Two scenarios may be observed in the system: once introduced, the signal decreases slightly in each cycle to finally vanish (b), or the signal increases in each loop and can sustain itself (c). Adapted from [397] with the permission of the American Chemical Society (ACS).

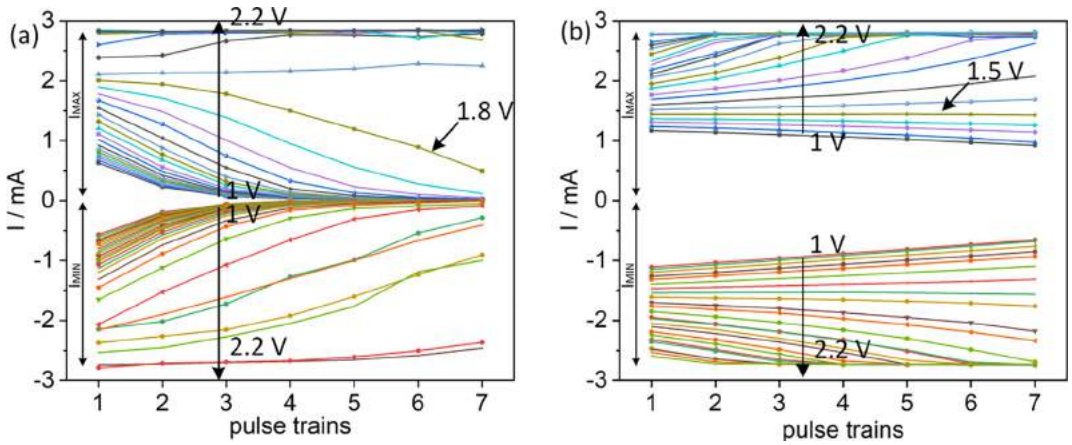

Fig. 25. A summary of the classification experiment: The maximum and minimum amplitudes of the current signals recorded in seven cycles for signals of amplitudes in the 1.0 to 2.2 Vpp potential range. The initial state of the memristor is the HRS (a) and LRS (b). Adapted from Ref. [397] with the permission of the American Chemical Society.

low resistance state (LRS) (Fig. 25a, b). It is a consequence of the above-mentioned rectifying properties of the presented memristor. The initial signal was symmetrical and sinusoidal, but every time it went through the nonlinear memristor node, it became more and more asymmetrical and only the upper, positive part of the initial input survived in the system. As a result, the positive part of the signal changes the state of the device, and we can say that the system learns the information.

A similar approach was taken in a recent publication that reported the properties of an FTO/[$SnI_4\{(C_6H_5)_3SO\}_2$]/Cu composite; however, the signals have a pulse shape and duration of 10 ms or 100 ms (Fig. 26). Shorter pulses were insufficient to perform clear classification of the signals but allowed the observation of the stochastic behavior of the system, which is a type of behavior typical for biological systems (Fig. 27). Sometimes the signal to sustain itself in the loop lasted 20 s, whereas sometimes, the signal vanished after less than 5 s.

In another approach, the fading memory of perovskite synapses ($MAPbBr_3$, $FAPbBr_3$, $CsPbBr_3$) synapses was used to perform simple learning of certain patterns [414]. John et al. divided their investigations into short and long-term memory experiments, but the retention of the conductance state was less than 20 min. In some applications, especially in the field of reservoir computing, this property is not a disadvantage but a very desired feature: fading

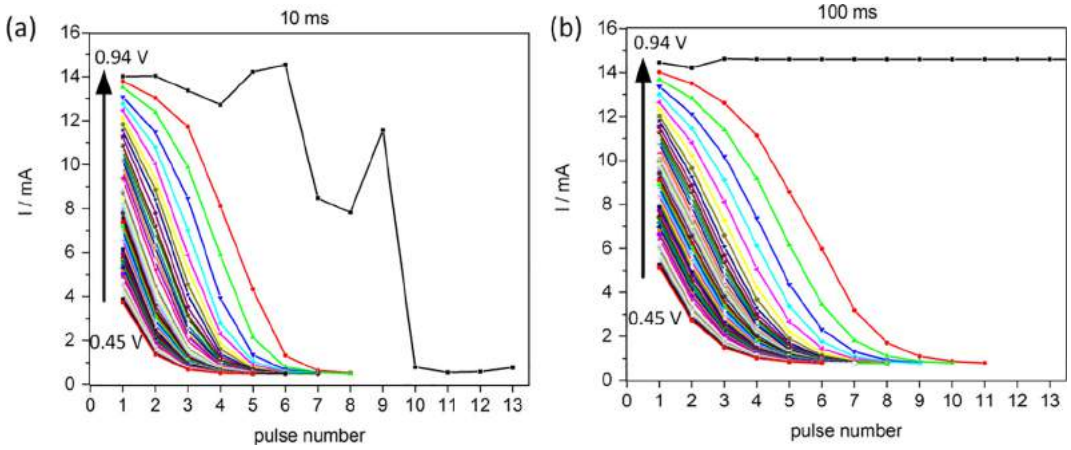

Fig. 26. A summary of a classification experiment performed in the reservoir system with an FTO/[$SnI_4\{(C_6H_5)_3SO\}_2$]/Cu memristor incorporated as a nonlinear node. (a) The 10 ms pulses are too short to be classified, while (b) the introduction of 100 ms pulses results in a classification process. The amplitude ranges in both experimental series were 0.45 to 0.94 V. Adapted from [398] with the permission of the American Chemical Society (ACS).

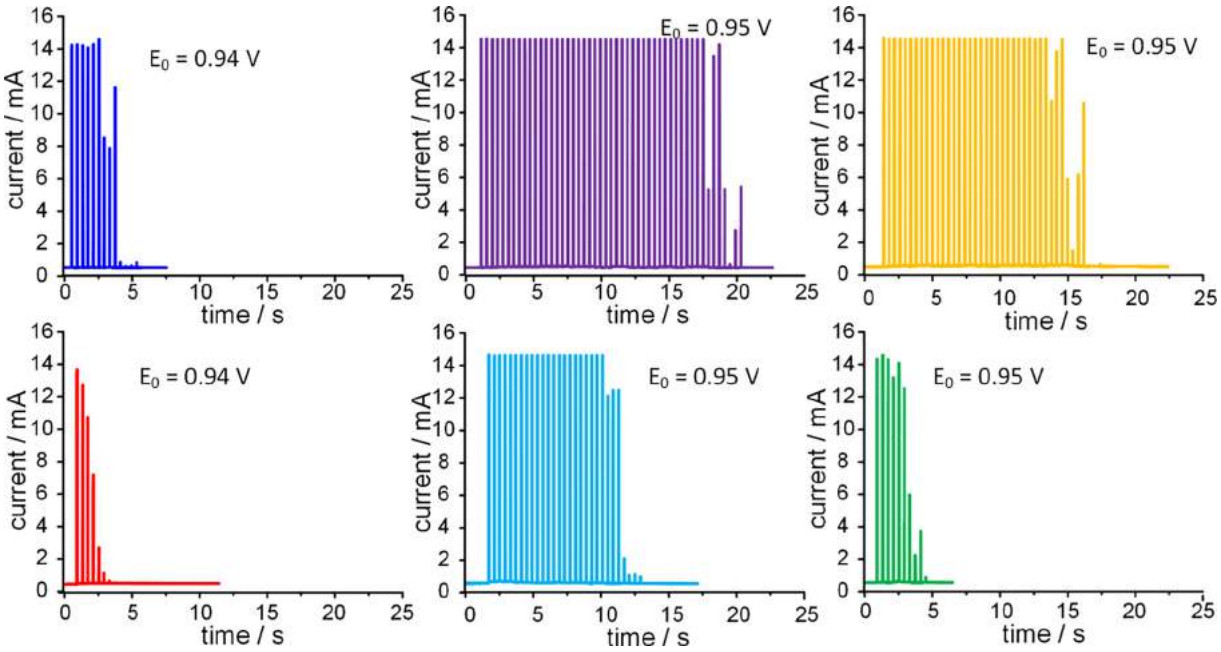

Fig. 27. A stochastic behavior is observed in a reservoir system with an FTO/[$SnI_4\{(C_6H_5)_3SO\}_2$]/Cu memristor incorporated as a nonlinear node. The duration of the initial signals was 10 ms, with the initial amplitude presented near each of the current responses. Adapted from Ref. [398] with the permission of the American Chemical Society (ACS).

memory is a key feature of reservoir computing systems [407]. A large group of memristive devices is memristors based on organic–inorganic halide perovskites [411].

The device under the test was prepared by spin-coating a 100 nm layer of the halide perovskite on the PEDOT:PSS covered ITO-coated glass [414]. The second contact was obtained by evaporation of 4,7-diphenyl-1,10-phenanthroline (Bphen), calcium, and aluminum. The plasticity of presented synapses is attributed to the ionic movements in those materials. The 4x4 array of perovskite synapses was trained to remember the letter N with 5 V (10 s) pulses (Fig. 28). Due to the diffusive character of the perovskite, 5 min after the initial training, 80% of the conductance state was retained, which decreased to 50% after 10 min, and further down to 30% after 15 min. When the array was left for 20 min, the pattern was completely forgotten. Voltage impulses shorter than the training one were sufficient to restore the initial weights of the pixels after the loss of 50% of the conductance, by applying an impulse of 5 V for a duration of only 2 s.

The presented device has some tolerance for noise. An input that contains pulses (5 V, 10 s) coding the letter 'N', but also spurious and random 10 s impulses of 1.5 V, was also delivered to the device in order to test the robustness against a non-ideal input (Fig. 29). The pixels that received the 5 V signals responded with increased conductance, while the random signals with a smaller amplitude of 1.5 V did not change the state of the device; therefore, the noise was ignored. John et al. utilized the knowledge about the

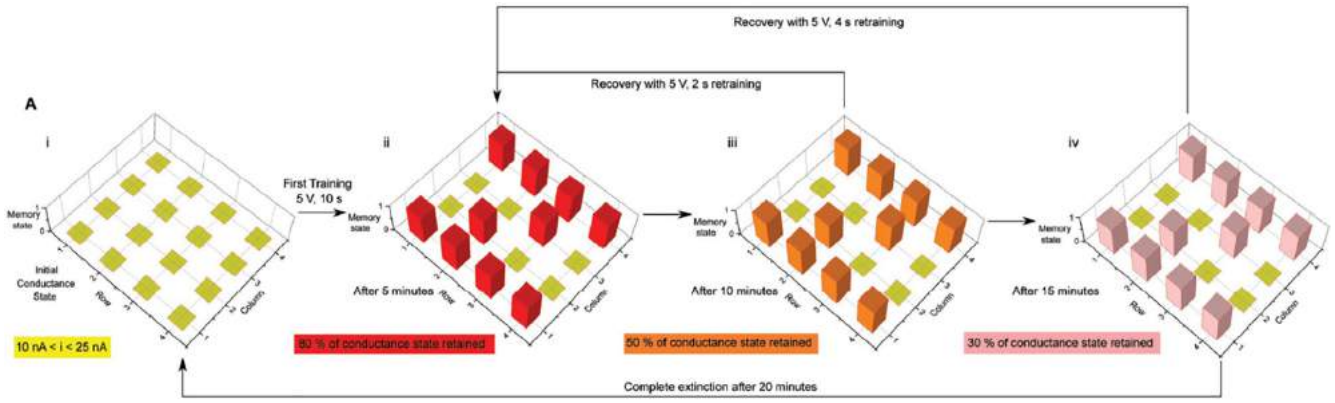

Fig. 28. A halide perovskite memory array of memristive synapses. The device has the following architecture: ITO/PEDOT:PSS/$MAPbBr_3$/Bphen/Ca/Al. Adapted from Ref. [414] with the permission of Wiley.

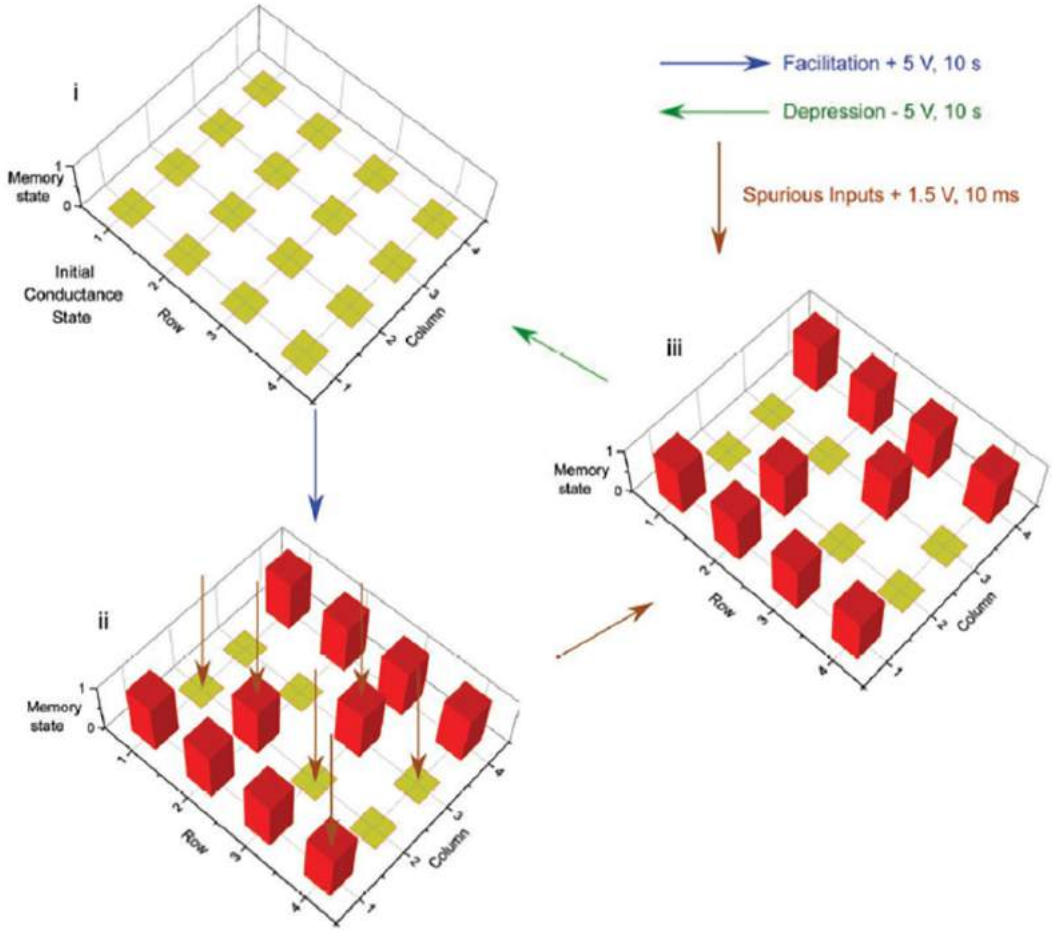

Fig. 29. Fault tolerance of the halide perovskite memory array based on an ITO/PEDOT:PSS/$MAPbBr_3$/Bphen/Ca/Al device. The random impulses of 1.5 V (brown arrows) do not influence the conductivity of the pixels. Adapted from Ref. [414] with the permission of Wiley.

current–voltage characteristic of the presented synapses. The voltage threshold above which the device starts to increase its conductivity is between 2.0 and 2.5 V, so the positive signals below these values should not modify the synaptic weights [414].

Besides the proof of concept experiments regarding simple pattern learning, John et al. highlighted the role of repetition in the transition from short-term memory to long-term memory. Fig. 30a shows how increasing excitatory postsynaptic currents during the application of pulse trains with frequencies higher than 16 Hz. In the above-described experiments, the repetition of the impulses shorter than the training sustains the memory of the array. Fig. 30b highlights the influence of the number of pulses on the final conductance state: the more pulses, the higher the final conductivity of the device [414].

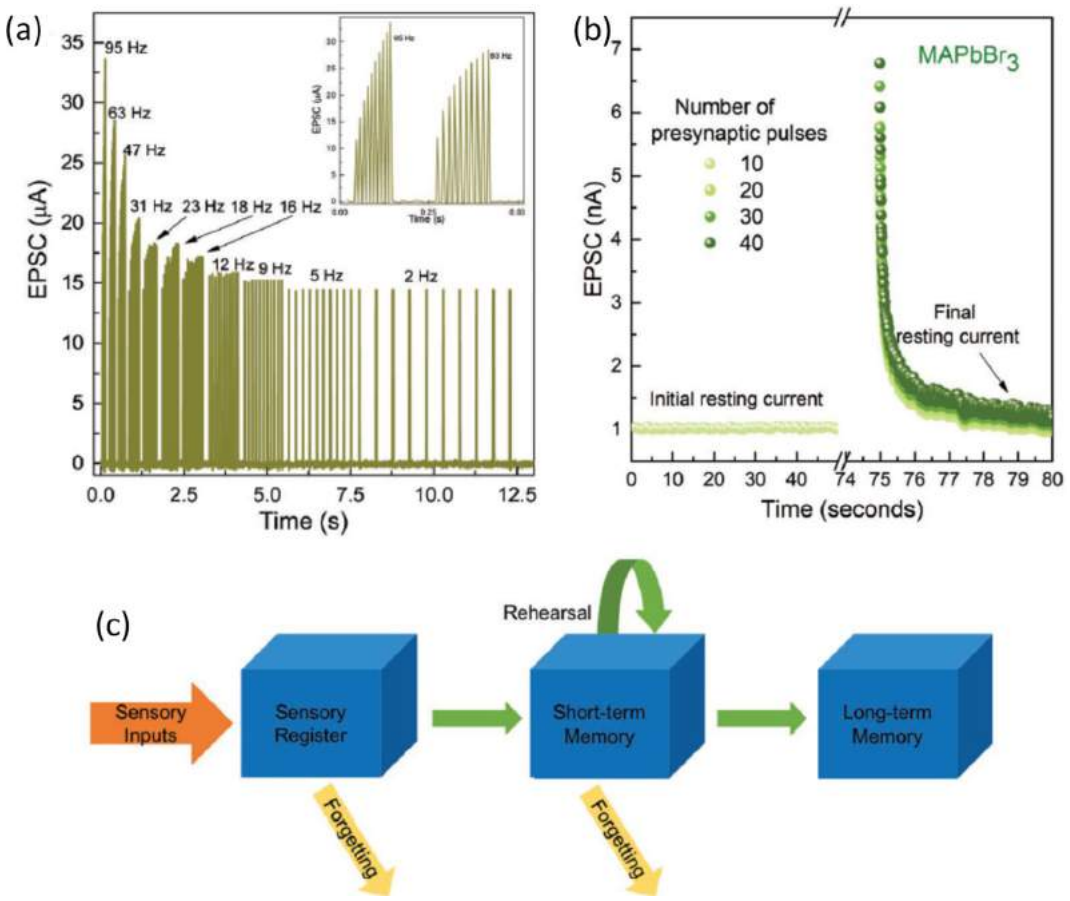

Fig. 30. (a) The response of ITO/PEDOT:PSS/$MAPbBr_3$/Bphen/Ca/Al synapses to pulse trains of different frequencies. (b) Long-term potentiation in response to various repetitions of presynaptic pulses. (c) A schematic of the route of a single sensory input from the sensory register to long-term memory. The rehearsal process allows the facilitation of the information from short-term memory to long-term memory. Adapted from Ref. [414] with the permission of Wiley.

8. Concluding remarks

The exceptional properties of metal halide semiconductors, especially those containing heavy halogen atoms, have found applications in various, sometimes unrelated fields. All these applications, however, creatively use the electric and optical peculiarities of these materials, including high absorptivity, exceptionally high charge carrier mobility, ferroelectric behavior, and hysteretic properties. The applications mentioned in this review span from photovoltaics and photocatalysis, artificial photosynthesis (which may be regarded as a combination of the two previous fields), to unconventional computing, especially neuromimetic computing, reservoir computing, and other highly advanced information processing paradigms. Thus, we propose that the serendipitously discovered, iodine-based semiconductors will remain in the limelight of various modern technologies in the near future.

Declaration of Competing Interest

The authors declare that they have no known competing financial interests or personal relationships that could have appeared to influence the work reported in this paper.

Acknowledgments

Authors acknowledge the financial support from the Polish National Science Center within the MAESTRO (grant agreement No. UMO-2015/18/A/ST4/00058) and PRELUDIUM (grant agreement No. UMO-2015/19/N/ST5/00533) projects. P.Z. has been partly supported by the EU Project POWR.03.02.00-00-I004/16. H. S.S. is supported by Singapore Ministry of Education Academic Research Fund Tier 1 grants RG 111/18 and RT 05/19, and also Agency for Science, Technology and Research (A*STAR) AME IRG grants A1783c0002, A1783c0003, and A1783c0007.

References

[1] G.E. Mobus, M.C. Kalton, Principles of Systems Science, Springer, New York, 2016.
[2] C. Truemann, Why Data Centres Are the New Frontier in the Fight against Climate Change, 2019,https://www.computerworld.com/article/3431148/why-data-centres-are-the-new-frontier-in-the-fight-against-climate-change.html, accessed: January 10th, 2020.
[3] C.S. von Bartheld, J. Bahney, S. Herculano-Houzel, J. Comp. Neurol. 524 (2016) 3865–3895.
[4] F.A.C. Azevedo, L.R.B. Carvalho, L.T. Grinberg, J.M. Farfel, R.E.L. Ferretti, R.E.P. Leite, W.J. Filho, R. Lent, S. Herculano-Houzel, J. Comp. Neurol. 513 (2009) 532–541.
[5] S.J. Finnema, N.B. Nabulsi, T. Eid, K. Detyniecki, S.-F. Lin, M.-K. Chen, R. Dhaher, D. Matuskey, E. Baum, D. Holden, D.D. Spencer, J. Mercier, J. Hannestad, Y. Huang, R.E. Carson, Sci. Transl. Med. 8 (2016) 348ra396.
[6] K. Szaciłowski, Infochemistry. Information Processing at the Nanoscale, John Wiley & Sons, Chichester, 2012.
[7] B. Lojek, History of Semiconductor Engineering, Springe-Verlag, Berlin, 2007.
[8] S. Stepney, Physica D 237 (2008) 1157–1164.
[9] C. Horsman, S. Stepney, R.C. Wagner, V. Kendon, Proc. Royal. Soc. A 470 (2014) 20140182.
[10] L.R. Milgrom, The Colours of Life, Oxford, 1997.
[11] D. Moreira, P. López-García, Nat. Rev. Microbiol. 7 (2009) 306–311.
[12] R. Breslow, Artificial Enzymes, Wiley-VCH Verlag, Weinheim, 2005.
[13] Y. Murakami, J.-I. Kikuchi, Y. Hisaeda, O. Hayashida, Chem. Rev. 96 (1996) 721–758.

[14] F. Schwizer, Y. Okamoto, T. Heinisch, Y. Gu, M.M. Pellizzoni, V. Lebrun, R. Reuter, V. Köhler, J.C. Lewis, T.R. Ward, Chem. Rev. 118 (2018) 142–231.
[15] M. Dieguéz, J.E. Bäckvall, O. Pàmies, Artificial Metalloenzymes and Metalldnazymes in Catalysis, Wiley-VCH Verlag, Wienheim, 2018.
[16] R. Jung, Biohybrid Systems: Nerves, Interfaces and Machines, Wiley-VCH Verlag, Weinheim, 2011.
[17] G.G. Wallace, S. Moulton, R.M.I. Kapsa, M. Higgins, Organic Bionics, Wiley-VCH Verlag, Weinheim, 2012.
[18] Y. Zhou, B. Liu, R. Yang, J. Liu, Bioconjugate Chem. 28 (2017) 2903–2909.
[19] J. Wu, S. Li, H. Wei, Chem. Commun. 54 (2018) 6520–6530.
[20] G. Rothenberg, Catalysis. Concepts and Green Applications, Wiley-VCH Verlag, Weinheim, 2008.
[21] H. Wei, E. Wang, Chem. Soc. Rev. 42 (2013) 6060–6093.
[22] J. Wu, X. Wang, Q. Wang, Z. Lou, S. Li, Y. Zhu, L. Qin, H. Wei, Chem. Soc. Rev. 48 (2019) 1004–1076.
[23] X. Wang, Y. Hu, H. Wei, Inorg. Chem. Frontiers 3 (2016) 41–60.
[24] S. Lin, H. Wei, Sci. China Life Sci. 62 (2019) 710–712.
[25] V.I. Vullev, J. Phys. Chem. Lett. 2 (2011) 503–508.
[26] K. Möbius, Chem. Soc. Rev. 29 (2000) 129–139.
[27] M.A.L. Abrahamsson, Electron Transfer in Ruthenium-Manganese Complexes for Artificial Photosynthesis, Acta Universitatis Upsaliensis, Uppsala, 2001.
[28] H. Zhou, J. Guo, P. Li, T. Fan, D. Zhang, J. Ye, Sci. Rep. 3 (2013) 1667.
[29] T. Wu, C. Zhu, D. Han, Z. Kang, L. Niu, Nanoscale 11 (2019) 22980–22988.
[30] D.K. Dogutan, D.G. Nocera, Acc. Chem. Res. 52 (2019) 3143–3148.
[31] S. Stepney, A. Adamatzky, Inspired by Nature, Springer International Publishing, Cham, 2018.
[32] M. Minsky, S. Papert, Perceptrons. An Introduction to Computational Geometry, MIT Press, Cambridge, 1988.
[33] Z. Wang, S. Joshi, S. Savel'ev, W. Song, R. Midya, Y. Li, M. Rao, P. Yan, S. Asapu, Y. Zhuo, H. Jiang, P. Lin, C. Li, J.H. Yoon, N.K. Upadhyay, J. Zhang, M. Hu, J.P. Strachan, M. Barnell, Q. Wu, H. Wu, R.S. Williams, Q. Xia, J.J. Yang, Nat. Electron. 1 (2018) 137–145.
[34] Z. Wang, S. Joshi, S.E. Savel'ev, H. Jiang, R. Midya, P. Lin, M. Hu, N. Ge, J.P. Strachan, Z. Li, Q. Wu, M. Barnell, G.-L. Li, H.L. Xin, R.S. Williams, Q. Xia, J.J. Yang, Nat. Mater. 16 (2016) 101.
[35] C. Ríos, N. Youngblood, Z. Cheng, M. Le Gallo, W.H.P. Pernice, C.D. Wright, A. Sebastian, H. Bhaskaran, Sci. Adv. 5 (2019) eaau5759.
[36] A. Serb, A. Khiat, T. Prodromakis, Nat. Commun. 9 (2018) 2170.
[37] Q. Hong, L. Zhao, X. Wang, Neurocomputing 330 (2019) 11–16.
[38] H. Kim, M.P. Sah, C. Yang, T. Roska, L.O. Chua, Proc. IEEE 100 (2012) 2061–2070.
[39] B. Kosko, Noise, Viking, New York, 2006.
[40] M. Privman, Isr. J. Chem. 51 (2011) 118–131.
[41] M.C. Soriano, S. Ortín, L. Keuninckx, L. Appelant, IEEE Trans. Neural Networks 26 (2015) 388–393.
[42] L.O. Chua, IEEE Trans. Circ. Theor. 18 (1971) 507–519.
[43] T. Prodromakis, C. Toumazou, L. Chua, Nat. Mater. 11 (2012) 478–481.
[44] L. Chua, If it's pinched it's a memristor, in: R. Tetzlaff (Ed.), Memristors and Memristive Systems, Springer, New York, 2014, pp. 17–90.
[45] L. Chua, Radioengineering 24 (2015) 319–368.
[46] O. Krestinskaya, A.P. James, L.O. Chua, IEEE Trans. Neural Networks Learning Syst. 31 (2019) 1-20.
[47] Z.I. Mannan, S.P. Adhikari, C. Yang, R.K. Budhathoki, H. Kim, L.O. Chua, IEEE Trans. Neural Networks Learning Syst. 30 (2019) 3458–3470.
[48] L. Chua, Semicond. Sci. Technol. 29 (2014) 104001.
[49] D.S. Jeong, K.M. Kim, S. Kim, B.J. Choi, C.S. Hwang, Adv. Electron. Mater. 2 (2016) 1600090.
[50] L.O. Chua, Nanotechnology 24 (2013) 383001.
[51] L. Chua, V. Sbitnev, H. Kim, Int. J. Bifurc. Chaos 22 (2012) 1250098.
[52] D. Ielmini, R. Waser, Resistive Switching. From Fundamentals of Nanoionic Redox Processes to Memristive Device Applications, Viley-VCH, Weinheim, 2016.
[53] S. Stepney, S. Rasmussen, M. Amos, Computational Matter, Springer, Cham, 2018.
[54] X. Zhang, Y. Zhuo, Q. Luo, Z. Wu, R. Midya, Z. Wang, W. Song, R. Wang, N.K. Upadhyay, Y. Fang, F. Kiani, M. Rao, Y. Yang, Q. Xia, Q. Liu, M. Liu, J.J. Yang, Nat. Commun. 11 (2020) 51.
[55] B. Saparov, D.B. Mitzi, Chem. Rev. 116 (2016) 4558–4596.
[56] N.G. Park, M. Graetzel, T. Miyasaka, Organic-Inorganic Halide Perovskite Photovoltaics. From Fundamentals to Device Architectures, Springer International Publishing, Switzerland, 2016.
[57] Z. Lv, Y. Zhou, S.-T. Han, V.A.L. Roy, Mater. Today 21 (2018) 537–552.
[58] S.G. Kim, J.S. Han, H. Kim, S.Y. Kim, H.W. Jang, Adv. Mater. Technol. 3 (2018) 1800457.
[59] L.I. Berger, Semiconductor Materials, CRC Press, Bocs Raton, 1997.
[60] L.-M. Wu, X.-T. Wu, L. Chen, Coord. Chem. Rev. 253 (2009) 2787–2804.
[61] A.N. Usoltsev, M. Elshobaki, S.A. Adonin, L.A. Frolova, T. Derzhavskaya, P.A. Abramov, D.V. Anokhin, I.V. Korolkov, S.Y. Luchkin, N.N. Dremova, K.J. Stevenson, M.N. Sokolov, V.P. Fedin, P.A. Troshin, J. Mater. Chem. A 7 (2019) 5957–5966.
[62] A.J. Dennington, M.T. Weller, Dalton Trans. 47 (2018) 3469–3484.
[63] V.Y. Kotov, A.B. Ilyukhin, A.A. Korlyukov, A.F. Smolyakov, S.A. Kozyukhin, New J. Chem. 42 (2018) 6354–6363.
[64] M.E. Easton, A.J. Ward, B. Chan, L. Radom, A.F. Masters, T. Maschmeyer, Phys. Chem. Chem. Phys. 18 (2016) 7251–7260.
[65] P.H. Svensson, L. Kloo, Chem. Rev. 103 (2003) 1649–1684.
[66] S.A. Adonin, M.N. Sokolov, V.P. Fedin, Coord. Chem. Rev. 367 (2018) 1–17.
[67] H. Yu, L. Yan, Y. He, H. Meng, W. Huang, Chem. Commun. 53 (2017) 432–435.
[68] E. Wlaźlak, J. Kalinowska-Tłuścik, W. Nitek, S. Klejna, K. Mech, W. Macyk, K. Szaciłowski, ChemElectroChem 5 (2018) 3486–3497.
[69] T. Poręba, M. Ernst, D. Zimmer, P. Macchi, N. Casati, Angew. Chem. Int. Ed. 58 (2019) 6625–6629.
[70] S. Madhu, H.A. Evans, V.V.T. Doan-Nguyen, J.G. Labram, G. Wu, M.L. Chabinyc, R. Seshadri, F. Wudl, Angew. Chem. Int. Ed. 55 (2016) 8032–8035.
[71] H. Tributsch, Coord. Chem. Rev. 248 (2004) 1511–1530.
[72] C.A. Bignozzi, R. Argazzi, R. Boaretto, E. Busatto, S. Carli, F. Ronconi, S. Caramori, Coord. Chem. Rev. 257 (2013) 1472–1492.
[73] J. Wu, Z. Lan, J. Lin, M. Huang, Y. Huang, L. Fan, G. Luo, Chem. Rev. 115 (2015) 2136–2173.
[74] P. Politzer, J.S. Murray, T. Clark, Phys. Chem. Chem. Phys. 12 (2010) 7748–7757.
[75] P. Politzer, J.S. Murray, T. Clark, Phys. Chem. Chem. Phys. 15 (2013) 11178–11189.
[76] L.C. Gilday, S.W. Robinson, T.A. Barendt, M.J. Langton, B.R. Mullaney, P.D. Beer, Chem. Rev. 115 (2015) 7118–7195.
[77] G. Cavallo, P. Metrangolo, R. Milani, T. Pilati, A. Priimagi, G. Resnati, G. Terraneo, Chem. Rev. 116 (2016) 2478–2601.
[78] H. Wang, W. Wang, W.J. Jin, Chem. Rev. 116 (2016) 5072–5104.
[79] V.V. Zhdankin, P.J. Stang, Chem. Rev. 108 (2008) 5299–5358.
[80] A. Yoshimura, V.V. Zhdankin, Chem. Rev. 116 (2016) 3328–3435.
[81] A.F. Wells, Structural Inorganic Chemistry, 5th ed., Oxford Science Publications, London, 1984.
[82] G. Denes, J. Pannetier, J. Lucas, J. Solid State Chem. 33 (1980) 1–11.
[83] N.H. Kolderup, Miner. Abstr. 3 (1924), 340-340.
[84] H. Braekken, Z. Kristallogr. 83 (1932) 222.
[85] A.K. Cheetham, N. Norman, Acta Chem. Scand. A 28 (1974) 55–60.
[86] J.M. van den Berg, Acta Crystallogr. 14 (1961) 1002–1003.
[87] I. Abrahams, D.Z. Demetriou, J. Solid State Chem. 149 (2000) 28–32.
[88] R.A. Howie, W. Moser, I.C. Trevena, Acta Crystallog. B 28 (1972) 2965–2971.
[89] Y.Z. Nozik, L.E. Fykin, L.A. Muradyan, Kristallografiya 21 (1976) 38–40.
[90] W. Nieuwenkamp, J.M. Bijvoet, Z. Kristallogr. 84 (1933) 49.
[91] R.S. Mitchell, Z. Kristallogr. 111 (1959) 372.
[92] A.J. Edwards, J. Chem. Soc. A (1970) 2751-2753, https://doi.org/10.1039/J19700002751.
[93] S.C. Nyburg, G.A. Ozin, S.T. Szymanski, Acta Crystallog. B 28 (1972) 2885.
[94] H. von Benda, Z. Kristallogr. 151 (1980) 271.
[95] H. Braekken, Z. Kristallogr. 74 (1930) 67.
[96] I. Lindqvist, A. Niggli, J. Inorg. Nucl. Chem. 2 (1956) 345–347.
[97] D.W. Cushen, R. Hulme, J. Chem. Soc. (1962) 2218-2222, https://doi.org/10.1039/JR9620002218.
[98] J. Trotter, T. Zobel, Z. Kristallogr. 123 (1966) 67.
[99] B. Palosz, J. Phys.: Condens. Matter 2 (1990) 5285–5295.
[100] B. Winkler, M.T. Dove, E.K.H. Salje, M. Leslie, B. Palosz, J. Phys.: Condens. Matter 3 (1991) 539–550.
[101] M. Hargittai, Chem. Rev. 100 (2000) 2233–2302.
[102] A. Jain, S.P. Ong, G. Hautier, W. Chen, W.D. Richards, S. Dacek, S. Cholia, D. Gunter, D. Skinner, G. Ceder, K.A. Persson, APL Mater. 1 (2013) 011002.
[103] J. Terra, D. Guenzburger, Phys. Rev. B 39 (1989) 50–56.
[104] P. Ravindran, A. Delin, R. Ahuja, B. Johansson, S. Auluck, J.M. Wills, O. Eriksson, Phys. Rev. B 56 (1997) 6851–6861.
[105] I.V. Murin, A.V. Petrov, I.I. Tupitsyn, R.A. Évarestov, Phys. Solid State 40 (1998) 211–212.
[106] S. Escalante, R. Vargas, A. Vela, J. Phys. Chem. A 103 (1999) 5590–5601.
[107] J. Bordas, J. Robertson, A. Jakobsson, J. Phys. C: Solid State 11 (1978) 2607–2621.
[108] A.J. Lehner, H. Wang, D.H. Fabini, C.D. Liman, C.-A. Hébert, E.E. Perry, M. Wang, G.C. Bazan, M.L. Chabinyc, R. Seshadri, Appl. Phys. Lett. 107 (2015) 131109.
[109] I.C. Schlüter, M. Schlüter, Phys. Rev. B 9 (1974) 1652–1663.
[110] J. Robertson, J. Phys. C: Solid State 12 (1979) 4753–4766.
[111] B.M. Nitsovich, V.M. Kramar, N.K. Kramar, International Conference on Correlation Optics, SPIE, 1999.
[112] R. Ahuja, H. Arwin, A. Ferreira da Silva, C. Persson, J.M. Osorio-Guillén, J. Souza de Almeida, C. Moyses Araujo, E. Veje, N. Veissid, C.Y. An, I. Pepe, B. Johansson, J. Appl. Phys. 92 (2002) 7219–7224.
[113] M. Yagmurcukardes, F.M. Peeters, H. Sahin, Phys. Rev. B 98 (2018) 085431.
[114] M.B. Faheem, B. Khan, C. Feng, M.U. Farooq, F. Raziq, Y. Xiao, Y. Li, ACS Energy Lett. 5 (2020) 290–320.
[115] A.K. Jena, A. Kulkarni, T. Miyasaka, Chem. Rev. 119 (2019) 3036–3103.
[116] E. Wlaźlak, A. Blachecki, M. Bisztyga-Szklarz, S. Klejna, T. Mazur, K. Mech, K. Pilarczyk, D. Przyczyna, M. Suchecki, P. Zawal, K. Szaciłowski, Chem. Commun. 54 (2018) 12133–12162.
[117] J.-R. Xiao, S.-H. Yang, F. Feng, H.-G. Xue, S.-P. Guo, Coord. Chem. Rev. 347 (2017) 23–47.
[118] S.E. Creutz, E.N. Crites, M.C. De Siena, D.R. Gamelin, Nano Lett. 18 (2018) 1118–1123.
[119] F. Giustino, H.J. Snaith, ACS Energy Lett. 1 (2016) 1233–1240.
[120] L. Mao, S.M.L. Teicher, C.C. Stoumpos, R.M. Kennard, R.A. DeCrescent, G. Wu, J. A. Schuller, M.L. Chabinyc, A.K. Cheetham, R. Seshadri, J. Am. Chem. Soc. 141 (2019) 19099–19109.
[121] R.J.D. Tilley, Perovskites. Structure-Property Relationships, John Wiley & Sons Ltd., Chichester, 2016.

[122] J.G. Bednorz, K.A. Müller, Z. Phys, B Cond. Mat. 64 (1986) 189–193.
[123] F. Brivio, K.T. Butler, A. Walsh, M. van Schilfgaarde, Phys. Rev. B 89 (2014) 155204.
[124] Z. Wei, D. Guo, J. Thieme, C. Katan, V.M. Caselli, J. Even, T.J. Savenije, Nat. Commun. 10 (2019) 5342.
[125] A. Walsh, J. Phys. Chem. C 119 (2015) 5755–5760.
[126] D. Meggiolaro, S.G. Motti, E. Mosconi, A.J. Barker, J. Ball, C. Andrea Riccardo Perini, F. Deschler, A. Petrozza, F. De Angelis, Energy Environ. Sci. 11 (2018) 702–713.
[127] C.C. Stoumpos, M.G. Kanatzidis, Adv. Mater. 28 (2016) 5778–5793.
[128] C. Kim, T.D. Huan, S. Krishnan, R. Ramprasad, Sci. Data 4 (2017) 170057.
[129] A.H. Slavney, T. Hu, A.M. Lindenberg, H.I. Karunadasa, J. Am. Chem. Soc. 138 (2016) 2138–2141.
[130] A.H. Slavney, L. Leppert, D. Bartesaghi, A. Gold-Parker, M.F. Toney, T.J. Savenije, J.B. Neaton, H.I. Karunadasa, J. Am. Chem. Soc. 139 (2017) 5015–5018.
[131] A.H. Slavney, L. Leppert, A. Saldivar Valdes, D. Bartesaghi, T.J. Savenije, J.B. Neaton, H.I. Karunadasa, Angew. Chem. Int. Ed. Engl. 57 (2018) 12765–12770.
[132] M.D. Smith, B.A. Connor, H.I. Karunadasa, Chem. Rev. 119 (2019) 3104–3139.
[133] F.S. Galasso, Structure, Properties and Preparation of Perovskite-Type Compounds, Pergamon, 1969.
[134] A.M. Glazer, Acta Crystallog. B 28 (1972) 3384–3392.
[135] T. Baikie, Y. Fang, J.M. Kadro, M. Schreyer, F. Wei, S.G. Mhaisalkar, M. Graetzel, T.J. White, J. Mater. Chem. A 1 (2013) 5628–5641.
[136] M.T. Weller, O.J. Weber, P.F. Henry, A.M. Di Pumpo, T.C. Hansen, Chem. Commun. 51 (2015) 4180–4183.
[137] N. Onoda-Yamamuro, T. Matsuo, H. Suga, J. Phys. Chem. Solids 51 (1990) 1383–1395.
[138] Y. Kawamura, H. Mashiyama, K. Hasebe, J. Phys. Soc. Jpn. 71 (2002) 1694–1697.
[139] C.C. Stoumpos, C.D. Malliakas, M.G. Kanatzidis, Inorg. Chem. 52 (2013) 9019–9038.
[140] J.M. Frost, A. Walsh, Acc. Chem. Res. 49 (2016) 528–535.
[141] M.T. Weller, O.J. Weber, J.M. Frost, A. Walsh, J. Phys. Chem. Lett. 6 (2015) 3209–3212.
[142] L.-Z. Wang, Y.-Q. Zhao, B. Liu, L.-J. Wu, M.-Q. Cai, Phys. Chem. Chem. Phys. 18 (2016) 22188–22195.
[143] A. Poglitsch, D. Weber, J. Chem. Phys. 87 (1987) 6373–6378.
[144] A.N. Beecher, O.E. Semonin, J.M. Skelton, J.M. Frost, M.W. Terban, H. Zhai, A. Alatas, J.S. Owen, A. Walsh, S.J.L. Billinge, ACS Energy Lett. 1 (2016) 880–887.
[145] L.D. Whalley, J.M. Skelton, J.M. Frost, A. Walsh, Phys. Rev. B 94 (2016) 220301.
[146] E. Mosconi, C. Quarti, T. Ivanovska, G. Ruani, F. De Angelis, Phys. Chem. Chem. Phys. 16 (2014) 16137–16144.
[147] W.A. Saidi, S. Poncé, B. Monserrat, J. Phys. Chem. Lett. 7 (2016) 5247–5252.
[148] C. Quarti, E. Mosconi, J.M. Ball, V. D'Innocenzo, C. Tao, S. Pathak, H.J. Snaith, A. Petrozza, F. De Angelis, Energy Environ. Sci. 9 (2016) 155–163.
[149] M.H. Du, J. Mater. Chem. A 2 (2014) 9091–9098.
[150] L.D. Whalley, J.M. Frost, Y.-K. Jung, A. Walsh, J. Chem. Phys. 146 (2017) 220901.
[151] W.-J. Yin, J.-H. Yang, J. Kang, Y. Yan, S.-H. Wei, J. Mater. Chem. A 3 (2015) 8926–8942.
[152] C. Quarti, E. Mosconi, F. De Angelis, Phys. Chem. Chem. Phys. 17 (2015) 9394–9409.
[153] G. Giorgi, J.-I. Fujisawa, H. Segawa, K. Yamashita, J. Phys. Chem. C 118 (2014) 12176–12183.
[154] J. Ma, L.-W. Wang, Nano Lett. 15 (2015) 248–253.
[155] A.M.A. Leguy, P. Azarhoosh, M.I. Alonso, M. Campoy-Quiles, O.J. Weber, J. Yao, D. Bryant, M.T. Weller, J. Nelson, A. Walsh, M. van Schilfgaarde, P.R.F. Barnes, Nanoscale 8 (2016) 6317–6327.
[156] W. Geng, L. Zhang, Y.-N. Zhang, W.-M. Lau, L.-M. Liu, J. Phys. Chem. C 118 (2014) 19565–19571.
[157] M.A. Pérez-Osorio, R.L. Milot, M.R. Filip, J.B. Patel, L.M. Herz, M.B. Johnston, F. Giustino, J. Phys. Chem. C 119 (2015) 25703–25718.
[158] C. Quarti, E. Mosconi, F. De Angelis, Chem. Mater. 26 (2014) 6557–6569.
[159] J.M. Frost, K.T. Butler, F. Brivio, C.H. Hendon, M. van Schilfgaarde, A. Walsh, Nano Lett. 14 (2014) 2584–2590.
[160] Y. Wang, T. Gould, J.F. Dobson, H. Zhang, H. Yang, X. Yao, H. Zhao, Phys. Chem. Chem. Phys. 16 (2014) 1424–1429.
[161] F. Brivio, A.B. Walker, A. Walsh, APL Mater. 1 (2013) 042111.
[162] P. Azarhoosh, S. McKechnie, J.M. Frost, A. Walsh, M. van Schilfgaarde, APL Mater. 4 (2016) 091501.
[163] E. Menéndez-Proupin, P. Palacios, P. Wahnón, J.C. Conesa, Phys. Rev. B 90 (2014) 045207.
[164] J. Even, L. Pedesseau, C. Katan, Phys. Chem. Chem. Phys. 16 (2014) 8697–8698.
[165] L. Protesescu, S. Yakunin, M.I. Bodnarchuk, F. Krieg, R. Caputo, C.H. Hendon, R. X. Yang, A. Walsh, M.V. Kovalenko, Nano Lett. 15 (2015) 3692–3696.
[166] X. Lao, X. Li, H. Ågren, G. Chen, Nanomaterials 9 (2019).
[167] J. Even, L. Pedesseau, J.-M. Jancu, C. Katan, J. Phys. Chem. Lett. 4 (2013) 2999–3005.
[168] L. Lang, J.-H. Yang, H.-R. Liu, H.J. Xiang, X.G. Gong, Phys. Lett. A 378 (2014) 290–293.
[169] M.R. Filip, F. Giustino, Phys. Rev. B 90 (2014) 245145.
[170] M. Kepenekian, R. Robles, C. Katan, D. Sapori, L. Pedesseau, J. Even, ACS Nano 9 (2015) 11557–11567.
[171] I. Borriello, G. Cantele, D. Ninno, Phys. Rev. B 77 (2008) 235214.
[172] A. Amat, E. Mosconi, E. Ronca, C. Quarti, P. Umari, M.K. Nazeeruddin, M. Grätzel, F. De Angelis, Nano Lett. 14 (2014) 3608–3616.
[173] E. Mosconi, A. Amat, M.K. Nazeeruddin, M. Grätzel, F. De Angelis, J. Phys. Chem. C 117 (2013) 13902–13913.
[174] G.E. Eperon, S.D. Stranks, C. Menelaou, M.B. Johnston, L.M. Herz, H.J. Snaith, Energy Environ. Sci. 7 (2014) 982–988.
[175] P. Umari, E. Mosconi, F. De Angelis, Sci. Rep. 4 (2014) 4467.
[176] A. Walsh, G.W. Watson, J. Phys. Chem. B 109 (2005) 18868–18875.
[177] J. Feng, B. Xiao, J. Phys. Chem. C 118 (2014) 19655–19660.
[178] S. Baroni, S. de Gironcoli, A. Dal Corso, P. Giannozzi, Rev. Mod. Phys. 73 (2001) 515–562.
[179] A. Filippetti, A. Mattoni, Phys. Rev. B 89 (2014) 125203.
[180] J. Calabrese, N.L. Jones, R.L. Harlow, N. Herron, D.L. Thorn, Y. Wang, J. Am. Chem. Soc. 113 (1991) 2328–2330.
[181] H. Lin, C. Zhou, Y. Tian, T. Siegrist, B. Ma, ACS Energy Lett. 3 (2018) 54–62.
[182] K. Liang, D.B. Mitzi, M.T. Prikas, Chem. Mater. 10 (1998) 403–411.
[183] Z. Shi, Z. Cao, X. Sun, Y. Jia, D. Li, L. Cavallo, U. Schwingenschlögl, Small 15 (2019) 1900462.
[184] C.M.M. Soe, G.P. Nagabhushana, R. Shivaramaiah, H. Tsai, W. Nie, J.-C. Blancon, F. Melkonyan, D.H. Cao, B. Traoré, L. Pedesseau, M. Kepenekian, C. Katan, J. Even, T.J. Marks, A. Navrotsky, A.D. Mohite, C.C. Stoumpos, M.G. Kanatzidis, Proc. Natl. Acad. Sci. 116 (2019) 58.
[185] C.C. Stoumpos, D.H. Cao, D.J. Clark, J. Young, J.M. Rondinelli, J.I. Jang, J.T. Hupp, M.G. Kanatzidis, Chem. Mater. 28 (2016) 2852–2867.
[186] C.C. Stoumpos, C.M.M. Soe, H. Tsai, W. Nie, J.-C. Blancon, D.H. Cao, F. Liu, B. Traoré, C. Katan, J. Even, A.D. Mohite, M.G. Kanatzidis, Chem 2 (2017) 427–440.
[187] L. Mao, W. Ke, L. Pedesseau, Y. Wu, C. Katan, J. Even, M.R. Wasielewski, C.C. Stoumpos, M.G. Kanatzidis, J. Am. Chem. Soc. 140 (2018) 3775–3783.
[188] C.M.M. Soe, C.C. Stoumpos, M. Kepenekian, B. Traoré, H. Tsai, W. Nie, B. Wang, C. Katan, R. Seshadri, A.D. Mohite, J. Even, T.J. Marks, M.G. Kanatzidis, J. Am. Chem. Soc. 139 (2017) 16297–16309.
[189] B.A. Connor, L. Leppert, M.D. Smith, J.B. Neaton, H.I. Karunadasa, J. Am. Chem. Soc. 140 (2018) 5235–5240.
[190] D.B. Mitzi, S. Wang, C.A. Feild, C.A. Chess, A.M. Guloy, Science 267 (1995) 1473.
[191] M. Daub, C. Haber, H. Hillebrecht, Eur. J. Inorg. Chem. 2017 (2017) 1120–1126.
[192] E.R. Dohner, A. Jaffe, L.R. Bradshaw, H.I. Karunadasa, J. Am. Chem. Soc. 136 (2014) 13154–13157.
[193] L. Mao, Y. Wu, C.C. Stoumpos, M.R. Wasielewski, M.G. Kanatzidis, J. Am. Chem. Soc. 139 (2017) 5210–5215.
[194] K.M. McCall, C.C. Stoumpos, S.S. Kostina, M.G. Kanatzidis, B.W. Wessels, Chem. Mater. 29 (2017) 4129–4145.
[195] D.B. Mitzi, J. Chem. Soc., Dalton Trans. (2001) 1-12, https://doi.org/10.1039/B007070J.
[196] K.S. Aleksandrov, Kristallografiya 40 (1995) 279–301.
[197] L. Mao, C.C. Stoumpos, M.G. Kanatzidis, J. Am. Chem. Soc. 141 (2019) 1171–1190.
[198] L.N. Quan, B.P. Rand, R.H. Friend, S.G. Mhaisalkar, T.W. Lee, E.H. Sargent, Chem. Rev. 119 (2019) 7444–7477.
[199] Y. Fu, H. Zhu, J. Chen, M.P. Hautzinger, X.Y. Zhu, S. Jin, Nat. Rev. Mater. 4 (2019) 169–188.
[200] W.A. Dunlap-Shohl, Y. Zhou, N.P. Padture, D.B. Mitzi, Chem. Rev. 119 (2019) 3193–3295.
[201] X.-G. Zhao, D. Yang, J.-C. Ren, Y. Sun, Z. Xiao, L. Zhang, Joule 2 (2018) 1662–1673.
[202] G. Grancini, M.K. Nazeeruddin, Nat. Rev. Mater. 4 (2018) 4–22.
[203] Y. Zhang, J. Liu, Z. Wang, Y. Xue, Q. Ou, L. Polavarapu, J. Zheng, X. Qi, Q. Bao, Chem. Commun. 52 (2016) 13637–13655.
[204] Z. Song, J. Zhao, Q. Liu, Inorg. Chem. Frontiers 6 (2019) 2969–3011.
[205] C. Katan, N. Mercier, J. Even, Chem. Rev. 119 (2019) 3140–3192.
[206] K. Tanaka, T. Kondo, Sci. Technol. Adv. Mat. 4 (2003) 599–604.
[207] A. Bala, A.K. Deb, V. Kumar, J. Phys. Chem. C 122 (2018) 7464–7473.
[208] D. Sapori, M. Kepenekian, L. Pedesseau, C. Katan, J. Even, Nanoscale 8 (2016) 6369–6378.
[209] S. Sourisseau, N. Louvain, W. Bi, N. Mercier, D. Rondeau, F. Boucher, J.-Y. Buzaré, C. Legein, Chem. Mater. 19 (2007) 600–607.
[210] N. Mercier, S. Poiroux, A. Riou, P. Batail, Inorg. Chem. 43 (2004) 8361–8366.
[211] S. Maheshwari, T.J. Savenije, N. Renaud, F.C. Grozema, J. Phys. Chem. C 122 (2018) 17118–17122.
[212] L. Mao, H. Tsai, W. Nie, L. Ma, J. Im, C.C. Stoumpos, C.D. Malliakas, F. Hao, M.R. Wasielewski, A.D. Mohite, M.G. Kanatzidis, Chem. Mater. 28 (2016) 7781–7792.
[213] Z. Deng, G. Kieslich, P.D. Bristowe, A.K. Cheetham, S. Sun, APL Mater. 6 (2018) 114202.
[214] L. Mao, P. Guo, M. Kepenekian, I. Hadar, C. Katan, J. Even, R.D. Schaller, C.C. Stoumpos, M.G. Kanatzidis, J. Am. Chem. Soc. 140 (2018) 13078–13088.
[215] M.E. Kamminga, G.A. de Wijs, R.W.A. Havenith, G.R. Blake, T.T.M. Palstra, Inorg. Chem. 56 (2017) 8408–8414.
[216] M.E. Kamminga, H.-H. Fang, M.R. Filip, F. Giustino, J. Baas, G.R. Blake, M.A. Loi, T.T.M. Palstra, Chem. Mater. 28 (2016) 4554–4562.
[217] D. Phuyal, M. Safdari, M. Pazoki, P. Liu, B. Philippe, K.O. Kvashnina, O. Karis, S. M. Butorin, H. Rensmo, T. Edvinsson, L. Kloo, J.M. Gardner, Chem. Mater. 30 (2018) 4959–4967.

[218] J. Yin, P. Maity, M. De Bastiani, I. Dursun, O.M. Bakr, J.-L. Brédas, O.F. Mohammed, Sci. Adv. 3 (2017) e1701793.
[219] J.C. Blancon, A.V. Stier, H. Tsai, W. Nie, C.C. Stoumpos, B. Traoré, L. Pedesseau, M. Kepenekian, F. Katsutani, G.T. Noe, J. Kono, S. Tretiak, S.A. Crooker, C. Katan, M.G. Kanatzidis, J.J. Crochet, J. Even, A.D. Mohite, Nat. Commun. 9 (2018) 2254.
[220] Y. Zhai, S. Baniya, C. Zhang, J. Li, P. Haney, C.-X. Sheng, E. Ehrenfreund, Z.V. Vardeny, Sci. Adv. 3 (2017) e1700704.
[221] X. Chen, H. Lu, Z. Li, Y. Zhai, P.F. Ndione, J.J. Berry, K. Zhu, Y. Yang, M.C. Beard, ACS Energy Lett. 3 (2018) 2273–2279.
[222] A. Kojima, K. Teshima, Y. Shirai, T. Miyasaka, J. Am. Chem. Soc. 131 (2009) 6050–6051.
[223] M.M. Lee, J. Teuscher, T. Miyasaka, T.N. Murakami, H.J. Snaith, Science 338 (2012) 643.
[224] S. Shao, J. Liu, G. Portale, H.H. Fang, G.R. Blake, G.H. ten Brink, L.J.A. Koster, M. A. Loi, Adv. Energy Mater. 8 (2018).
[225] J. Feng, X. Zhu, Z. Yang, X. Zhang, J. Niu, Z. Wang, S. Zuo, S. Priya, S. Liu, D. Yang, Adv. Mater. 30 (2018) 1801418.
[226] Z. Chen, B. Turedi, A.Y. Alsalloum, C. Yang, X. Zheng, I. Gereige, A. AlSaggaf, O. F. Mohammed, O.M. Bakr, ACS Energy Lett. 4 (2019) 1258–1259.
[227] W.S. Yang, B.-W. Park, E.H. Jung, N.J. Jeon, Y.C. Kim, D.U. Lee, S.S. Shin, J. Seo, E. K. Kim, J.H. Noh, S.I. Seok, Science 356 (2017) 1376–1379.
[228] E.H. Jung, N.J. Jeon, E.Y. Park, C.S. Moon, T.J. Shin, T.-Y. Yang, J.H. Noh, J. Seo, Nature 567 (2019) 511–515.
[229] M. Saliba, T. Matsui, J.-Y. Seo, K. Domanski, J.-P. Correa-Baena, M.K. Nazeeruddin, S.M. Zakeeruddin, W. Tress, A. Abate, A. Hagfeldt, M. Grätzel, Energy Environ. Sci. 9 (2016) 1989–1997.
[230] N.J. Jeon, H. Na, E.H. Jung, T.-Y. Yang, Y.G. Lee, G. Kim, H.-W. Shin, S. Il Seok, J. Lee, J. Seo, Nat. Energy 3 (2018) 682–689.
[231] F. Sahli, J. Werner, B.A. Kamino, M. Bräuninger, R. Monnard, B. Paviet-Salomon, L. Barraud, L. Ding, J.J. Diaz Leon, D. Sacchetto, G. Cattaneo, M. Despeisse, M. Boccard, S. Nicolay, Q. Jeangros, B. Niesen, C. Ballif, Nat. Mater. 17 (2018) 820–826.
[232] W.E.I. Sha, X. Ren, L. Chen, W.C.H. Choy, Appl. Phys. Lett. 106 (2015) 221104.
[233] S. Rühle, Solar Energy 130 (2016) 139–147.
[234] M.A. Green, A. Ho-Baillie, H.J. Snaith, Nat. Photonics 8 (2014) 506–514.
[235] C. Barugkin, J. Cong, T. Duong, S. Rahman, H.T. Nguyen, D. Macdonald, T.P. White, K.R. Catchpole, J. Phys. Chem. Lett. 6 (2015) 767–772.
[236] P. Docampo, J.M. Ball, M. Darwich, G.E. Eperon, H.J. Snaith, Nat. Commun. 4 (2013) 1–6.
[237] S. De Wolf, J. Holovsky, S.J. Moon, P. Loper, B. Niesen, M. Ledinsky, F.J. Haug, J. H. Yum, C. Ballif, J. Phys. Chem. Lett. 5 (2014) 1035–1039.
[238] F. Yang, M. Wilkinson, E.J. Austin, K.P. O'Donnell, Phys. Rev. Lett. 70 (1993) 323-326.
[239] A. Miyata, A. Mitioglu, P. Plochocka, O. Portugall, J.T.-W. Wang, S.D. Stranks, H.J. Snaith, R.J. Nicholas, Nat. Phys. 11 (2015) 582–587.
[240] J. Even, L. Pedesseau, C. Katan, J. Phys. Chem. C 118 (2014) 11566–11572.
[241] Y. Yamada, T. Nakamura, M. Endo, A. Wakamiya, Y. Kanemitsu, IEEE J. Photovoltaics 5 (2015) 401–405.
[242] V. D'Innocenzo, G. Grancini, M.J. Alcocer, A.R. Kandada, S.D. Stranks, M.M. Lee, G. Lanzani, H.J. Snaith, A. Petrozza, Nat. Commun. 5 (2014) 3586.
[243] G. Xing, N. Mathews, S. Sun, S.S. Lim, Y.M. Lam, M. Grätzel, S. Mhaisalkar, T.C. Sum, Science 342 (2013) 344–347.
[244] S.D. Stranks, G.E. Eperon, G. Grancini, C. Menelaou, M.J.P. Alcocer, T. Leijtens, L.M. Herz, A. Petrozza, H.J. Snaith, Science 342 (2013) 341–344.
[245] A.A. Zhumekenov, M.I. Saidaminov, M.A. Haque, E. Alarousu, S.P. Sarmah, B. Murali, I. Dursun, X.-H. Miao, A.L. Abdelhady, T. Wu, O.F. Mohammed, O.M. Bakr, ACS Energy Lett. 1 (2016) 32–37.
[246] Q. Chen, N. De Marco, Y. Yang, T.-B. Song, C.-C. Chen, H. Zhao, Z. Hong, H. Zhou, Y. Yang, Nano Today 10 (2015) 355–396.
[247] S.A. Kulkarni, T. Baikie, P.P. Boix, N. Yantara, N. Mathews, S. Mhaisalkar, J. Mater. Chem. A 2 (2014) 9221–9225.
[248] J.H. Noh, S.H. Im, J.H. Heo, T.N. Mandal, S.I. Seok, Nano Lett. 13 (2013) 1764–1769.
[249] R. Comin, G. Walters, E.S. Thibau, O. Voznyy, Z.-H. Lu, E.H. Sargent, J. Mater. Chem. C 3 (2015) 8839–8843.
[250] N. Pellet, P. Gao, G. Gregori, T.-Y. Yang, M.K. Nazeeruddin, J. Maier, M. Grätzel, Angew. Chem. Int. Ed. 53 (2014) 3151–3157.
[251] N.J. Jeon, J.H. Noh, W.S. Yang, Y.C. Kim, S. Ryu, J. Seo, S.I. Seok, Nature 517 (2015) 476–480.
[252] F. Hao, C.C. Stoumpos, R.P. Chang, M.G. Kanatzidis, J. Am. Chem. Soc. 136 (2014) 8094–8099.
[253] J.A. Van Vechten, T.K. Bergstresser, Phys. Rev. B 1 (1970) 3351–3358.
[254] Q. Tai, K.-C. Tang, F. Yan, Energy Environ. Sci. 12 (2019) 2375–2405.
[255] J. Chen, J. Xu, L. Xiao, B. Zhang, S. Dai, J. Yao, ACS Appl. Mater. Interfaces 9 (2017) 2449–2458.
[256] N.K. Kumawat, A. Dey, A. Kumar, S.P. Gopinathan, K.L. Narasimhan, D. Kabra, ACS Appl. Mater. Interfaces 7 (2015) 13119–13124.
[257] H. Choi, J. Jeong, H.-B. Kim, S. Kim, B. Walker, G.-H. Kim, J.Y. Kim, Nano Energy 7 (2014) 80–85.
[258] P. Wang, X. Zhang, Y. Zhou, Q. Jiang, Q. Ye, Z. Chu, X. Li, X. Yang, Z. Yin, J. You, Nat. Commun. 9 (2018).
[259] C.C. Stoumpos, C.D. Malliakas, J.A. Peters, Z. Liu, M. Sebastian, J. Im, T.C. Chasapis, A.C. Wibowo, D.Y. Chung, A.J. Freeman, B.W. Wessels, M.G. Kanatzidis, Cryst. Growth Des. 13 (2013) 2722–2727.
[260] I. Chung, J.-H. Song, J. Im, J. Androulakis, C.D. Malliakas, H. Li, A.J. Freeman, J.T. Kenney, M.G. Kanatzidis, J. Am. Chem. Soc. 134 (2012) 8579–8587.
[261] D. Sabba, H.K. Mulmudi, R.R. Prabhakar, T. Krishnamoorthy, T. Baikie, P.P. Boix, S. Mhaisalkar, N. Mathews, J. Phys. Chem. C 119 (2015) 1763–1767.
[262] D.W. deQuilettes, W. Zhang, V.M. Burlakov, D.J. Graham, T. Leijtens, A. Osherov, V. Bulović, H.J. Snaith, D.S. Ginger, S.D. Stranks, Nat. Commun. 7 (2016) 11683.
[263] Y. Deng, Z. Xiao, J. Huang, Adv. Energy Mater. 5 (2015) 1500721.
[264] A.K. Jena, T. Miyasaka, Hysteresis characteristics and devide stability, in: N.G. Park, M. Graetzel, T. Miyasaka (Eds.), Organic-Inorganic Halide Perovskite Photovoltaics. From Fundamentals to Device Architectures, Springer International Publishing, Switzerland, 2016.
[265] W. Mao, C.R. Hall, A.S.R. Chesman, C. Forsyth, Y.-B. Cheng, N.W. Duffy, T.A. Smith, U. Bach, Angew. Chem. Int. Ed. 58 (2019) 2893–2898.
[266] E.T. Hoke, D.J. Slotcavage, E.R. Dohner, A.R. Bowring, H.I. Karunadasa, M.D. McGehee, Chem. Sci. 6 (2015) 613–617.
[267] H. Yuan, E. Debroye, K. Janssen, H. Naiki, C. Steuwe, G. Lu, M. Moris, E. Orgiu, I. H. Uji, F. De Schryver, P. Samori, J. Hofkens, M. Roeffaers, J. Phys. Chem. Lett. 7 (2016) 561–566.
[268] N.N. Shlenskaya, N.A. Belich, M. Grätzel, E.A. Goodilin, A.B. Tarasov, J. Mater. Chem. A 6 (2018) 1780–1786.
[269] D.P. McMeekin, G. Sadoughi, W. Rehman, G.E. Eperon, M. Saliba, M.T. Horantner, A. Haghighirad, N. Sakai, L. Korte, B. Rech, M.B. Johnston, L.M. Herz, H.J. Snaith, Science 351 (2016) 151–155.
[270] H. Tsai, R. Asadpour, J.-C. Blancon, C.C. Stoumpos, O. Durand, J.W. Strzalka, B. Chen, R. Verduzco, P.M. Ajayan, S. Tretiak, J. Even, M.A. Alam, M.G. Kanatzidis, W. Nie, A.D. Mohite, Science 360 (2018) 67.
[271] A. Ummadisingu, L. Steier, J.-Y. Seo, T. Matsui, A. Abate, W. Tress, M. Grätzel, Nature 545 (2017) 208–212.
[272] B. Zhao, S. Bai, V. Kim, R. Lamboll, R. Shivanna, F. Auras, J.M. Richter, L. Yang, L. Dai, M. Alsari, X.-J. She, L. Liang, J. Zhang, S. Lilliu, P. Gao, H.J. Snaith, J. Wang, N.C. Greenham, R.H. Friend, D. Di, Nat. Photonics 12 (2018) 783–789.
[273] K. Lin, J. Xing, L.N. Quan, F.P.G. De Arquer, X. Gong, J. Lu, L. Xie, W. Zhao, D. Zhang, C. Yan, W. Li, X. Liu, Y. Lu, J. Kirman, E.H. Sargent, Q. Xiong, Z. Wei, Nature 562 (2018) 245–248.
[274] Q. Wang, X. Wang, Z. Yang, N. Zhou, Y. Deng, J. Zhao, X. Xiao, P. Rudd, A. Moran, Y. Yan, J. Huang, Nat. Commun. 10 (2019) 5633.
[275] Y. Cao, N. Wang, H. Tian, J. Guo, Y. Wei, H. Chen, Y. Miao, W. Zou, K. Pan, Y. He, H. Cao, Y. Ke, M. Xu, Y. Wang, M. Yang, K. Du, Z. Fu, D. Kong, D. Dai, Y. Jin, G. Li, H. Li, Q. Peng, J. Wang, W. Huang, Nature 562 (2018) 249–253.
[276] M. Yuan, L.N. Quan, R. Comin, G. Walters, R. Sabatini, O. Voznyy, S. Hoogland, Y. Zhao, E.M. Beauregard, P. Kanjanaboos, Z. Lu, D.H. Kim, E.H. Sargent, Nat. Nanotechnol. 11 (2016) 872–877.
[277] D.H. Cao, C.C. Stoumpos, T. Yokoyama, J.L. Logsdon, T.-B. Song, O.K. Farha, M. R. Wasielewski, J.T. Hupp, M.G. Kanatzidis, ACS Energy Lett. 2 (2017) 982–990.
[278] X. Gan, O. Wang, K. Liu, X. Du, L. Guo, H. Liu, Sol. Energy Mater. Sol. Cells 162 (2017) 93–102.
[279] D.Y. Park, S.-J. An, C. Lee, D.A. Nguyen, K.-N. Lee, M.S. Jeong, J. Phys. Chem. Lett. 10 (2019) 7942-7948.
[280] H. Zhang, Q. Liao, Y. Wu, Z. Zhang, Q. Gao, P. Liu, M. Li, J. Yao, H. Fu, Adv. Mater. 30 (2018) e1706186.
[281] W. Peng, J. Yin, K.-T. Ho, O. Ouellette, M. De Bastiani, B. Murali, O. El Tall, C. Shen, X. Miao, J. Pan, E. Alarousu, J.-H. He, B.S. Ooi, O.F. Mohammed, E. Sargent, O.M. Bakr, Nano Lett. 17 (2017) 4759–4767.
[282] Y. Liu, Z. Wu, X. Liu, S. Han, Y. Li, T. Yang, Y. Ma, M. Hong, J. Luo, Z. Sun, Adv. Opt. Mater. 7 (2019) 1901049.
[283] J. Yin, P. Maity, L. Xu, A.M. El-Zohry, H. Li, O.M. Bakr, J.-L. Brédas, O.F. Mohammed, Chem. Mater. 30 (2018) 8538–8545.
[284] G. Long, C. Jiang, R. Sabatini, Z. Yang, M. Wei, L.N. Quan, Q. Liang, A. Rasmita, M. Askerka, G. Walters, X. Gong, J. Xing, X. Wen, R. Quintero-Bermudez, H. Yuan, G. Xing, X.R. Wang, D. Song, O. Voznyy, M. Zhang, S. Hoogland, W. Gao, Q. Xiong, E.H. Sargent, Nat. Photonics 12 (2018) 528–533.
[285] J. Kou, C. Lu, J. Wang, Y. Chen, Z. Xu, R.S. Varma, Chem. Rev. 117 (2017) 1445–1514.
[286] R.E. Brandt, V. Stevanović, D.S. Ginley, T. Buonassisi, MRS Commun. 5 (2015) 265–275.
[287] H. Cheng, B. Huang, Y. Dai, Nanoscale 6 (2014) 2009–2026.
[288] K. Sharma, V. Dutta, S. Sharma, P. Raizada, A. Hosseini-Bandegharaei, P. Thakur, P. Singh, J. Ind. Eng. Chem. 78 (2019) 1–20.
[289] X. Zhang, Z. Ai, F. Jia, L. Zhang, J. Phys. Chem. C 112 (2008) 747–753.
[290] D.S. Bhachu, S.J.A. Moniz, S. Sathasivam, D.O. Scanlon, A. Walsh, S.M. Bawaked, M. Mokhtar, A.Y. Obaid, I.P. Parkin, J. Tang, C.J. Carmalt, Chem. Sci. 7 (2016) 4832–4841.
[291] Z.-K. Tang, W.-J. Yin, Z. Le, B. Wen, D.-Y. Zhang, L.-M. Liu, W.-M. Lau, Sci. Rep. 6 (2016) 32764.
[292] Z. Ai, W. Ho, S. Lee, L. Zhang, Environ. Sci. Technol. 43 (2009) 4143–4150.
[293] X. Sun, M. Wang, N.X. Qian, X.Y. Sun, C. Liu, X. Zhang, R. Rao, Y.Q. Ma, Appl. Surf. Sci. 489 (2019) 1030–1041.
[294] S.K. Poznyak, A.I. Kulak, Electrochim. Acta 35 (1990) 1941–1947.
[295] N.T. Hahn, S. Hoang, J.L. Self, C.B. Mullins, ACS Nano 6 (2012) 7712–7722.
[296] P. Kwolek, K. Szaciłowski, Electrochimica Acta 104 (2013) 448–453.
[297] C. Chang, L. Zhu, Y. Fu, X. Chu, Chem. Eng. J. 233 (2013) 305–314.
[298] C. Zheng, C. Cao, Z. Ali, Phys. Chem. Chem. Phys. 17 (2015) 13347–13354.
[299] H. Lin, Y. Zhao, Y. Wang, J. Cao, S. Chen, Mater. Lett. 132 (2014) 141–144.

[300] J. Oszajca, A. Podborska, K. Szaciłowski, Molecules on: semiconductors: toward molecular logic, in: W.A. Goddard, D.W. Brenner, S.E. Lyshevski, G.J. Iafrate (Eds.), Handbook of Nanoscience, Engineering, and Technology, CRC Press, Boca Raton, 2012.
[301] Govindjee, D. Shevela, Front. Plant Sci. 2 (2011).
[302] Q. Xu, L. Zhang, J. Yu, S. Wageh, A.A. Al-Ghamdi, M. Jaroniec, Mater. Today 21 (2018) 1042–1063.
[303] H. Li, W. Tu, Y. Zhou, Z. Zou, Adv. Sci. 3 (2016) 1500389.
[304] J. Low, C. Jiang, B. Cheng, S. Wageh, A.A. Al-Ghamdi, J. Yu, Small Methods 1 (2017) 1700080.
[305] Y. Bai, P.-Q. Wang, J.-Y. Liu, X.-J. Liu, RSC Adv. 4 (2014) 19456–19461.
[306] L. Ye, J. Liu, C. Gong, L. Tian, T. Peng, L. Zan, ACS Catal. 2 (2012) 1677–1683.
[307] X. Zhang, H. Yang, B. Zhang, Y. Shen, M. Wang, Adv. Mater. Interfaces 3 (2016) 1500273.
[308] S. Han, J. Li, K. Yang, J. Lin, Chin. J. Catal. 36 (2015) 2119–2126.
[309] Y. Cong, Y. Ji, Y. Ge, H. Jin, Y. Zhang, Q. Wang, Chem. Eng. J. 307 (2017) 572–582.
[310] Y. Guo, Y. Zhang, N. Tian, H. Huang, ACS Sust. Chem. Eng. 4 (2016) 4003–4012.
[311] L. Sun, L. Xiang, X. Zhao, C.-J. Jia, J. Yang, Z. Jin, X. Cheng, W. Fan, ACS Catal. 5 (2015) 3540–3551.
[312] H. Cheng, B. Huang, Y. Dai, X. Qin, X. Zhang, Langmuir 26 (2010) 6618–6624.
[313] C. He, Q. Zhang, J. Yang, Z. Xu, D. Shu, C. Shan, L. Zhu, W. Liao, Y. Xiong, Visible-Light-Induced Activity of AgI-BiOI Composites for Removal of Organic Contaminants from Water and Wastewater in N. Shamim, V.K. Sharma (Eds.) Sustainable Nanotechnology and the Environment: Advances and Achievements, American Chemical Society, Washington, 2013.
[314] H. Huang, K. Liu, Y. Zhang, K. Chen, Y. Zhang, N. Tian, RSC Adv. 4 (2014) 49386–49394.
[315] H. Liu, W.-R. Cao, Y. Su, Z. Chen, Y. Wang, J. Colloid Interface Sci. 398 (2013) 161–167.
[316] J. Niu, P. Dai, K. Wang, Z. Zhang, Q. Zhang, B. Yao, X. Yu, Mater. Technol. 34 (2019) 506–514.
[317] L.A. Mabuti, I.K.S. Manding, C.C. Mercado, RSC Adv. 8 (2018) 42254–42261.
[318] X. Zhou, C. Shao, S. Yang, X. Li, X. Guo, X. Wang, X. Li, Y. Liu, ACS Sust. Chem. Eng. 6 (2018) 2316–2323.
[319] K.M. Alam, P. Kumar, P. Kar, U.K. Thakur, S. Zeng, K. Cui, K. Shankar, Nanoscale Adv. 1 (2019) 1460–1471.
[320] J. Di, J. Xia, S. Yin, H. Xu, L. Xu, Y. Xu, M. He, H. Li, J. Mater. Chem. A 2 (2014) 5340–5351.
[321] W. Fan, H. Li, F. Zhao, X. Xiao, Y. Huang, H. Ji, Y. Tong, Chem. Commun. 52 (2016) 5316–5319.
[322] X. Zhang, C.Y. Wang, L.W. Wang, G.X. Huang, W.K. Wang, H.Q. Yu, Sci. Rep. 6 (2016).
[323] J. Shang, W. Hao, X. Lv, T. Wang, X. Wang, Y. Du, S. Dou, T. Xie, D. Wang, J. Wang, ACS Catal. 4 (2014) 954–961.
[324] J.Y. Fu, L.W. Chen, Y.M. Dai, F.Y. Liu, S.T. Huang, C.C. Chen, Mol. Catal. 455 (2018) 214–223.
[325] S. Zhong, B. Wang, H. Zhou, C. Li, X. Peng, S. Zhang, J. Alloys Compd. 806 (2019) 401–409.
[326] W. Li, R. Yu, M. Li, N. Guo, H. Yu, Y. Yu, Chemosphere 218 (2019) 966–973.
[327] G. Jiang, Z. Wei, H. Chen, X. Du, L. Li, Y. Liu, Q. Huang, W. Chen, RSC Adv. 5 (2015) 30433–30437.
[328] X. Wang, Y. Zhang, C. Zhou, D. Huo, R. Zhang, L. Wang, Appl. Catal. B: Environ. 268 (2019) 118390.
[329] M. Tamilselvan, A.J. Bhattacharyya, RSC Adv. 6 (2016) 105980–105987.
[330] M. Tasviri, Z. Sajadi-Hezave, Mol. Catal. 436 (2017) 174–181.
[331] S. Bargozideh, M. Tasviri, New J. Chem. 42 (2018) 18236–18241.
[332] M. Grätzel, Acc. Chem. Res. 50 (2017) 487–491.
[333] J. Seo, J.H. Noh, S.I. Seok, Acc. Chem. Res. 49 (2016) 562–572.
[334] C.C. Stoumpos, M.G. Kanatzidis, Acc. Chem. Res. 48 (2015) 2791–2802.
[335] T.M. Koh, K. Thirumal, H.S. Soo, N. Mathews, ChemSusChem 9 (2016) 2541–2558.
[336] M. Dokic, H.S. Soo, Chem. Commun. 54 (2018) 6554–6572.
[337] L.K.-S. Ng, E.J.-C. Tan, T.W. Goh, X. Zhao, Z. Chen, T.C. Sum, H.S. Soo, Appl. Mater. Today 15 (2019) 192–202.
[338] S. Anantharaj, S.R. Ede, K. Sakthikumar, K. Karthick, S. Mishra, S. Kundu, ACS Catal. 6 (2016) 8069–8097.
[339] M.G. Kibria, Z. Mi, J. Mater. Chem. A 4 (2016) 2801–2820.
[340] J. Li, H. Li, G. Zhan, L. Zhang, Acc. Chem. Res. 50 (2017) 112–121.
[341] M. Higashi, K. Domen, R. Abe, Energy Environ. Sci. 4 (2011) 4138–4147.
[342] Q. Wang, K. Domen, Chem. Rev. 120 (2020) 919–985.
[343] Z. Hong, D. Tan, R.A. John, Y.K.E. Tay, Y.K.T. Ho, X. Zhao, T.C. Sum, N. Mathews, F. Garcia, H.S. Soo, iScience 16 (2019) 312–325.
[344] Z. Fan, H. Xiao, Y. Wang, Z. Zhao, Z. Lin, H.-C. Cheng, S.-J. Lee, G. Wang, Z. Feng, W.A. Goddard, Y. Huang, X. Duan, Joule 1 (2017) 548–562.
[345] J. Luo, J.H. Im, M.T. Mayer, M. Schreier, M.K. Nazeeruddin, N.G. Park, S.D. Tilley, H.J. Fan, M. Grätzel, Science 345 (2014) 1593–1596.
[346] Gurudayal, D. Sabba, M.H. Kumar, L.H. Wong, J. Barber, M. Grätzel, N. Mathews, Nano Lett. 15 (2015) 3833–3839.
[347] Y.S. Chen, J.S. Manser, P.V. Kamat, J. Am. Chem. Soc. 137 (2015) 974–981.
[348] Y.J. Jang, I. Jeong, J. Lee, J. Lee, M.J. Ko, J.S. Lee, ACS Nano 10 (2016) 6980–6987.
[349] B. Brunetti, C. Cavallo, A. Ciccioli, G. Gigli, A. Latini, Sci. Rep. 6 (2016) 31896.
[350] J.H. Kim, Y. Jo, J.H. Kim, J.W. Jang, H.J. Kang, Y.H. Lee, D.S. Kim, Y. Jun, J.S. Lee, ACS Nano 9 (2015) (1829) 11820–11821.
[351] P. Da, M. Cha, L. Sun, Y. Wu, Z.S. Wang, G. Zheng, Nano Lett. 15 (2015) 3452–3457.
[352] H.L. Clever, F.J. Johnston, J. Phys. Chem. Ref. Data 9 (1980) 751–784.
[353] O.E. Lanford, S.J. Kiehl, J. Am. Chem. Soc. 63 (1941) 667–669.
[354] S. Park, W.J. Chang, C.W. Lee, S. Park, H.-Y. Ahn, K.T. Nam, Nat. Energy 2 (2016) 16185.
[355] L. Wang, H. Xiao, T. Cheng, Y. Li, W.A. Goddard 3rd, J. Am. Chem. Soc. 140 (2018) 1994–1997.
[356] W.-B. Wu, Y.-C. Wong, Z.-K. Tan, J. Wu, Catal. Sci. Technol. 8 (2018) 4257–4263.
[357] S. Schünemann, H. Tüysüz, Eur. J. Inorg. Chem. 2018 (2018) 2350–2355.
[358] M.-Z. Yang, Y.-F. Xu, J.-F. Liao, X.-D. Wang, H.-Y. Chen, D.-B. Kuang, J. Mater. Chem. A 7 (2019) 5409–5415.
[359] X. Zhu, Y. Lin, Y. Sun, M.C. Beard, Y. Yan, J. Am. Chem. Soc. 141 (2019) 733–738.
[360] Y.F. Xu, M.Z. Yang, B.X. Chen, X.D. Wang, H.Y. Chen, D.B. Kuang, C.Y. Su, J. Am. Chem. Soc. 139 (2017) 5660–5663.
[361] L. Zhou, Y.F. Xu, B.X. Chen, D.B. Kuang, C.Y. Su, Small 14 (2018) e1703762.
[362] Z. Hong, W.K. Chong, A.Y.R. Ng, M. Li, R. Ganguly, T.C. Sum, H.S. Soo, Angew. Chem. Int. Ed. Engl. 58 (2019) 3456–3460.
[363] Q. Yu, H. Tang, J. Hu, K.C. Tan, Neuromorphic Cognitive Systems. A Learning and Memory Centered Approach, Springer International Publishing AG, Cham, Switzerland, 2017.
[364] I. Vourkas, G.C. Sirakoulis, Memristor-Based Nanoelectronic Computing Circuits and Architectures, Springer International Publishing, Heidelberg, 2016.
[365] A. Adamatzky, L. Chua, Memristor Networks, Springer, New York, 2014.
[366] L. Chua, G.C. Sirakoulis, A. Adamatzky, Handbook of Memritsor Networks, Springer Nature, Switzerland, 2019.
[367] R. Tetzlaff, Memristors and Memristive Systems, Springer Science, Heidelberg, 2014.
[368] A. Adamatzky, G. Chen, Chaos, CNN, Memristors and Beyond, World Scientific, Singapore, 2012 https://doi.org/10.1142/8590.
[369] K. Pickel, Memory 12 (2004) 14–26.
[370] X. Hu, H. Chen, G. Fu, Front. Psychol. 3 (2012).
[371] D. Miller, Sociology, propaganda and psychological operations, in: M. Dawson, B. Fowler, D. Miller, A. Smith (Eds.), Stretching the Sociological Imagination, Palgrave Macmillan, London, 2015.
[372] S. Vongehr, arXiv, 1205.6129 (2012).
[373] Z. Gao, M. Proietti-Onori, Z. Lin, M.M. Ten Brinke, H.-J. Boele, J.-W. Potters, T.J. H. Ruigrok, F.E. Hoebeek, C.I. De Zeeuw, Neuron 89 (2016) 645–657.
[374] A.L. Person, K. Khodakhah, Neuron 89 (2016) 427–430.
[375] S. Jiang, S. Nie, Y. He, R. Liu, C. Chen, Q. Wan, Mater. Today Nano 8 (2019) 100059.
[376] C. Sung, H. Hwang, I.K. Yoo, J. Appl. Phys. 124 (2018) 151903.
[377] Y.V. Pershin, M. Di Ventra, Proc. IEEE 100 (2011) 2071–2080.
[378] F.Z. Wang, IEEE Trans. Circ. Syst. 60 (2013) 616–623.
[379] D.B. Strukov, G.S. Snider, D.R. Stewart, R.S. Williams, Nature 453 (2008) 80–83.
[380] S. Vongehr, X. Meng, Sci. Rep. 5 (2015) 11657.
[381] I. Abraham, Sci. Rep. 8 (2018) 10972.
[382] K.M. Sundqvist, D.K. Ferry, L.B. Kish, Fluct. Noise Lett. 16 (2017) 1771001.
[383] L.O. Chua, IEEE Micro 38 (2018) 7–12.
[384] J. Kim, Y.V. Pershin, M. Yin, T. Datta, M. Di Ventra, arXiv, 1909.07238 (2019).
[385] Y.V. Pershin, M. Di Ventra, J. Phys. D: Appl. Phys. 52 (2018) 01LT01.
[386] F.Z. Wang, L. Li, L. Shi, H. Wu, L.O. Chua, J. Appl. Phys. 125 (2019) 054504.
[387] S.P. Adhikari, M.P. Sah, H. Kim, L.O. Chua, IEEE Trans. Circuits Syst. 60 (2013) 3008–3021.
[388] T. Prodromakis, Two centuries of memristors, in: A. Adamatzky, G. Chen (Eds.), Chaos, Cnn, Memristors and Beyond, WORLD SCIENTIFIC, 2012, p. 564.
[389] M.-S. Abdelouahab, R. Lozi, L. Chua, Int. J. Bifurc. Chaos 24 (2014) 1430023.
[390] J.T. Machado, Commun. Nonlinear Sci. Numer. Simulat. 18 (2013) 264–275.
[391] K. Biswas, G. Bohannan, R. Caponetto, A.M. Lopes, J.A.T. Machado, Fractional Order Devices, Springer Nature, Cham, 2017.
[392] L. Chua, Appl. Phys. A 102 (2011) 765–783.
[393] S. Westerlund, Phys. Scr. 43 (1991) 174–179.
[394] H.N. Tran, T.J. Raeber, Z.C. Zhao, D.R. McKenzie, A.S. Holland, D.G. McCulloch, B.J. Murdoch, J.G. Partridge, MRS Commun. 8 (2018) 1104–1110.
[395] W. Sun, B. Gao, M. Chi, Q. Xia, J.J. Yang, H. Qian, H. Wu, Nat. Commun. 10 (2019) 3453.
[396] T.-H. Lee, H.-G. Hwang, J.-U. Woo, D.-H. Kim, T.-W. Kim, S. Nahm, ACS Appl. Mater. Interfaces 10 (2018) 25673–25682.
[397] E. Wlaźlak, M. Marzec, P. Zawal, K. Szaciłowski, ACS Appl. Mater. Interfaces 11 (2019) 17009–17018.
[398] E. Wlaźlak, P. Zawal, K. Szaciłowski, ACS Appl. Electron. Mater. 2 (2020) 329–338.
[399] B. Hwang, J.-S. Lee, Sci. Rep. 7 (2017) 673.
[400] M. Hansen, M. Ziegler, L. Kolberg, R. Soni, S. Dirkmann, T. Mussenbrock, H. Kohlstedt, Sci. Rep. 5 (2015) 13753.
[401] Q. Wu, H. Wang, Q. Luo, W. Banerjee, J. Cao, X. Zhang, F. Wu, Q. Liu, L. Li, M. Liu, Nanoscale 10 (2018) 5875–5881.
[402] B. Mohammad, A. Jaoude Maguy, V. Kumar, M. Al Homouz Dirar, A. Nahla Heba, M. Al-Qutayri, N. Christoforou, Nanotechnol. Revs., 5 (2016) 311 https://doi.org/10.1515/ntrev-2015-0029.
[403] Y. Chen, G. Liu, C. Wang, W. Zhang, R.-W. Li, L. Wang, Mater. Horiz. 1 (2014) 489–506.

[404] S. Kvatinsky, D. Belousov, S. Liman, G. Satat, N. Wald, E.G. Friedman, A. Kolodny, U.C. Weiser, IEEE Trans. Circuits Syst. II: Exp. Briefs 61 (2014) 895–899.
[405] V. Athanasiou, Z. Konkoli, On mathematics of universal computation with generic dynamical systems, in: A. Adamatzky, S.G. Akl, G.C. Sirakoulis (Eds.), From Parallel to Emergent Computing, CRC Press, London, 2019.
[406] Z. Konkoli, S. Nichele, M. Dale, S. Stepney, Reservoir computing with computational matter, in: S. Stepney, S. Rasmussen, M. Amos (Eds.), Computational Matter, Springer, Cham, Switzerland, 2018.
[407] Z. Konkoli, Int. J. Parallel Emergent Distrib. Syst. 33 (2018) 121–143.
[408] Z. Konkoli, Reservoir computing, in: A. Adamatzky (Ed.), Unconventional Computing. A Volume of the Encyclopedia of Complexity and Systems Science, Springer Nature, New York, 2018.
[409] V. Athanasiou, Z. Konkoli, Int. J. Parallel Emergent Distrib. Syst. 33 (2018) 367–386.
[410] Y. Li, Z. Wang, R. Midya, Q. Xia, J.J. Yang, J. Phys. D: Appl. Phys. 51 (2018) 503002.
[411] X. Zhao, H. Xu, Z. Wang, Y. Lin, Y. Liu, InfoMat 1 (2019) 183–210.
[412] E. Wlaźlak, D. Przyczyna, R. Gutierrez, G. Cuniberti, K. Szaciłowski, Jap. J. Appl. Phys., 59 (2020) SI0801.
[413] K. Pilarczyk, E. Wlaźlak, D. Przyczyna, A. Blachecki, A. Podborska, V. Anathasiou, Z. Konkoli, K. Szaciłowsk, Coord. Chem. Rev. 365 (2018) 23–40.
[414] R.A. John, N. Yantara, Y.F. Ng, G. Narasimman, E. Mosconi, D. Meggiolaro, M.R. Kulkarni, P.K. Gopalakrishnan, C.A. Nguyen, F. De Angelis, S.G. Mhaisalkar, A. Basu, N. Mathews, Adv. Mater. 30 (2018) 1805454.

Japanese Journal of Applied Physics

The Japan Society of Applied Physics

STAP REVIEW

In-materio neuromimetic devices: dynamics, information processing and pattern recognition

Japanese Journal of Applied Physics **59**, 050504 (2020)
https://doi.org/**10.35848/1347-4065/ab82b0**

In-materio neuromimetic devices: dynamics, information processing and pattern recognition

Dawid Przyczyna[1,2†], Piotr Zawal[1,2†], Tomasz Mazur[1†], Marcin Strzelecki[3], Pier Luigi Gentili[4*], and Konrad Szaciłowski[1*]

[1]*Academic Centre for Materials and Nanotechnology, AGH University of Science and Technology, al. Mickiewicza 30, 30-059 Kraków, Poland*
[2]*Faculty of Physics and Applied Computer Science, AGH University of Science and Technology, al. Mickiewicza 30, 30-059 Kraków, Poland*
[3]*Faculty of Creativity, Interpretation and Music Education, Academy of Music in Kraków, ul. Św. Tomasza 43, 31-027 Kraków, Poland*
[4]*Department of Chemistry, Biology, and Biotechnology; University of Perugia, 06123 Perugia, Italy*

[*]E-mail: pierluigi.gentili@unipg.it; szacilow@agh.edu.pl
[†]These authors have equally contributed to the manuscript.

Received February 14, 2020; revised March 11, 2020; accepted March 24, 2020; published online May 1, 2020

The story of information processing is a story of great success. Todays' microprocessors are devices of unprecedented complexity and MOSFET transistors are considered as the most widely produced artifact in the history of mankind. The current miniaturization of electronic circuits is pushed almost to the physical limit and begins to suffer from various parasitic effects. These facts stimulate intense research on neuromimetic devices. This feature article is devoted to various *in materio* implementation of neuromimetic processes, including neuronal dynamics, synaptic plasticity, and higher-level signal and information processing, along with more sophisticated implementations, including signal processing, speech recognition and data security. Due to the vast number of papers in the field, only a subjective selection of topics is presented in this review.

Supplementary material for this article is available online

1. Introduction

The story of information processing is a story of great success. Todays' microprocessors are integrated circuits of unprecedented complexity and MOSFET transistors are considered as the most widely produced component in the history of mankind, with a total number of fabricated devices easily exceeding several sextillions (10^{21})[1)] The contemporary microprocessor contains approximately 3.95×10^9 transistors.[2)] In a human, there are an estimated 10–20 billion neurons in the cerebral cortex and 55–70 billion neurons in the cerebellum.[3)] A human brain is, therefore, the most complex information processing structure, as each of the ca. 8×10^{10} neurons may form up to 10^4 synaptic connections with other neurons. Brain's ability to learn and adapt is a consequence if its dynamically changing topology of synaptic connections, plasticity of individual connections, high redundancy and multilevel dynamics at various geometrical and temporal scales.

These facts stimulate intense research on neuromimetic devices. Their performance, at the present stage of development, cannot be compared with natural systems, but provides stimulation for other fields of investigation, including chemistry, physics, electronics, and computer sciences.

This feature article is devoted to various *in materio* implementations of neuromimetic processes, including neuronal dynamics, synaptic plasticity, and higher-level signal and information processing. From the plethora of various *in-materio* implementation of information processing, involving inorganic and organic materials, polymers, various molecular species, as well as biopolymers and even living organisms[4)] we have chosen a handful of wet photochromic systems and semiconducting materials. This selection is by no means exhaustive, but sufficient to illustrate the main research directions as well as current trends in *in-materio* neuromimetic computing.

2. Mimicking neural dynamics

Human intelligence emerges from the complex structural and dynamical properties of our nervous system. The primary cellular elements of our nervous systems are neurons. The ultimate computational power of our nervous system relies on the dynamical properties of neurons and their networks. Every neuron is a nonlinear dynamic system,[5,6)] and according to some theoretical analysis can be regarded as a biological memristive element.[7–9)] Some neurons operate in the oscillatory regime. They are called pacemaker neurons and fire action potentials periodically. Pacemaker neurons generate rhythmic activities in neural networks involved in the neocortex, basal ganglia, thalamus, locus coeruleus, hypothalamus, ventral tegmentum area, hippocampus, and amygdala.[10)] These structures are associated with sleep, wakefulness, arousal, motivation, addiction, memory consolidation, cognition, and fear.

Excitable neurons are another type of neurons present in the nervous system. Excitability can be twofold—"tonic" or "phasic". When neurons react to a constant excitatory signal by firing a sequence of spikes, they are classified as "tonic". On the other hand, excitability is "phasic", when neurons react in an analog manner and shoot only once, when receiving a sharp excitatory signal. Excitatory "tonic" neurons are present e.g. in the cortex whereas "phasic" excitable neurons act e.g. in the auditory brainstem (involved in precise timing computations) and in the spinal cord.[11,12)]

Finally, there are chaotic neurons. Chaotic neurons are quite common in the nervous system because the intrinsic dynamic instability facilitates the extraordinary ability of neural networks to adapt.[6,13)]

It is possible to mimic the dynamics of neurons by selecting specific chemical systems and maintaining them out-of-equilibrium.[14)] One of the most widespread examples is the Belousov–Zhabotinsky (BZ) reaction. Other popular models are memristive elements and circuits,[7–9)] as well as some (photo)electrochemical systems, especially those with self-excitable oscillations.[15)]

The dynamics of neural networks can be mimicked in reservoir computing systems: unconventional computational systems exhibiting a dynamic behavior, internal dynamics,

fading memory and echo state property. They are usually based on a nonlinear node (e.g. memristor) which at the same time provides memory features, an input layer which provides information/signal to be processed, a delayed feedback loop, which provides internal dynamics of the system and a readout layer, the part of the reservoir system which reflects the internal state of the reservoir, thus providing the echo state property. The readout layer is the only part of the system that may undergo training. Details on theory, construction, and properties of reservoir systems can be found elsewhere in numerous specialized papers and are out of the scope of this review.[16–21)]

2.1. The case of the BZ reaction

The BZ reaction is a catalyzed oxidative bromination of malonic acid in aqueous acidic solution (1):

$$2BrO_3^-{}_{(aq)} + 3CH_2(COOH)_{2(aq)} + 2\,H^+_{(aq)} \rightarrow 2BrCH(COOH)_{2(aq)} + 3CO_{2(g)} + 4H_2O_{(l)}. \quad (1)$$

Various metal ions or metal-complexes, such as either cerium ions or ferroin [i.e. tris-(1,10-phenanthroline)-iron(II)] or tris(2,2′-bipyridyl)dichloro-ruthenium(II) ($Ru(bpy)_3^{2+}$) can serve as catalyst. The mechanism of the BZ is quite complicated because it consists of many elementary steps. Briefly, when the concentration of the intermediate bromide (Br^-) is higher than its critical value, the reaction proceeds by a set of elementary steps wherein the catalyst maintains the reduced state, and the solution is red-colored in the presence of ferroin. During these elementary steps, bromide is consumed. As soon as the concentration of Br^- is lower than its critical value (that corresponds to 5×10^{-6} $[BrO_3^-]$), the reaction proceeds through another set of elementary steps, where mono-electronic transformations are involved, and the catalyst goes from the reduced to the oxidized state. In the presence of the indicator ferroin, the solution becomes blue. When the concentration of the oxidized state of the catalyst becomes high, another set of reactions becomes important where bromide is produced. As soon as the bromide concentration becomes again higher than its critical value, the solution switches from blue to red, and the cycle repeats. A BZ reaction in its reduced state is like a resting neuron in its hyperpolarized state. When the BZ reaction feels a small perturbation, it maintains its reduced state. On the other hand, when the perturbation is sufficiently strong, slightly above a critical threshold value, it responds by moving temporarily to its oxidized state and then recovering its original reduced state. By a careful choice of the boundary conditions (i.e. concentrations of the reagents, temperature, and flow rate, in case the reaction is performed in an open system), it is possible to have the BZ reaction in either the oscillatory or the tonic excitable or the chaotic regime.[22)] The BZ reaction in the oscillatory regime is a good model of real pacemaker cells. Pacemaker cells have their internal rhythm, but external stimuli can alter their timing. In pacemaker cells, information about a stimulus is encoded by changes in the timing of individual action potentials, and it is used to rule proprioception and motor coordination for running, swimming and flying.[23)] In a similar way to neurons, the BZ reaction in the oscillatory regime can be perturbed in its timing by both inhibitors and activators. Bromide is an example of an inhibitor, whereas Ag^+ is an example of an activator, or more precisely of an anti-inhibitor because its addition removes bromide, forming an AgBr precipitate. The effect of injection of either Br^- or Ag^+ is immediate, and the BZ reaction restores the initial period quickly, after one or a few more cycles, if it is carried out in an open system such as a continuous-flow stirred tank reactor (CSTR). The CSTR guarantees a replenishment of fresh reagents and the elimination of the products. The response of the system is phase-dependent, where for the phase of addition we mean the ratio

$$\varphi = \frac{\tau}{T_0}. \quad (2)$$

In (2), τ is the "time delay", i.e. the time since the most recent spike occurred, and T_0 is the period of the previous oscillations. The addition of Br^- leads always to a delay in the appearance of a spike. In other words, $\Delta T = T_{pert} - T_0$ (T_{pert} is the period of the perturbed oscillation) is always positive. The higher the phase of the addition of Br^-, the larger the ΔT.[24)] The addition of silver ion decreases the period unless it is injected in small quantities and at a low phase, inducing a slight lengthening of the period of oscillations.

Since the information within our brain is encoded as a pattern of activity of neural networks, it is compelling to study the coupling between artificial neurons and the corresponding dynamics. The coupling among real neurons takes place through discrete chemical pulses of neurotransmitters released by the synapses of a neuron and collected by the dendrites of other neurons. Therefore, it is useful to focus on pulse-coupled oscillators. The study of two pulse-coupled BZ oscillators, implemented in two physically separated CSTRs, may be viewed as the chemical analog of the two pulse-coupled pacemaker cells. The dynamics of two pseudo-neurons has been investigated under both symmetrical inhibitory and/or excitatory coupling.[25,26)] The latency caused by the propagation of action potentials has been emulated employing a delay between the appearance of a spike and the release of a pseudo-neurotransmitter. Both symmetrical and asymmetrical coupling can give rise to many temporal patterns. For example, mutual and symmetrical inhibitory coupling generates either anti-phase, in-phase or irregular oscillations depending on the time delay and concentration of the inhibitor; when τ is zero and $[Br^-]$ is large, suppression of oscillations in one artificial neuron model—that is maintained in its reduced state—has been observed. Even the mutual and symmetrical excitatory coupling generates different dynamical regimes: the so-called master and slave condition, bursting behavior, fast anti-phase oscillations, and suppression of oscillations with the suppressed oscillator maintained in its oxidized state. Further patterns have been achieved with mixed excitatory-inhibitory coupling and with the symmetrical coupling of two unequal BZ oscillators.[27)] All these dynamical patterns emulate the reasoning code of pairs of real neurons. However, the main drawback of these artificial systems is their hybrid nature. The chemical coupling is ruled by a silicon-based computer (see Fig. 1). To contrive chemical oscillators that can couple autonomously, it is useful to focus on optical signals and photo-sensitive oscillators.

2.2. Optical communication among artificial neuron models

The oscillatory BZ reaction with cerium ions as catalysts gives rise to appreciable transmittance oscillations in the UV part of the electromagnetic spectrum [see Fig. 2(a)]. If a UV

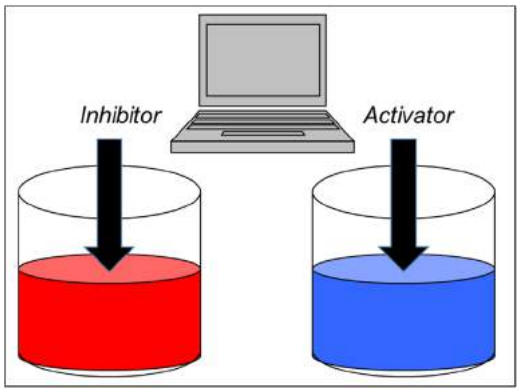

Fig. 1. (Color online) Scheme of a computer-controlled coupling between two BZ reactions performed in two distinct CSTRs.

radiation with constant intensity crosses the BZ reaction, its transmitted intensity is modulated. In other words, the BZ reaction transmits a UV output, whose intensity oscillates, and the frequency of oscillations coincides with the intrinsic frequency of the BZ. When ferroin is introduced as either the catalyst or the redox indicator, large transmittance oscillations are recordable in all the visible region of the spectrum [see Fig. 2(b)]. Therefore, the BZ reaction becomes suitable to transmit a visible oscillatory signal. Transmittance oscillations in the visible spectrum and oscillatory red luminescence are recordable in case $Ru(bpy)_3^{2+}$ is chosen as the catalyst [see Fig. 2(c)].

The periodic UV or visible radiation, transmitted or emitted by the BZ reaction, can be sent to luminescent and photochromic compounds.[28)] Luminescent and thermally reversible photochromic compounds are good models of phasic excitable neurons. They respond to a steady excitatory signal with analog output of emitted light or color saturation. Moreover, they "relax", i.e. they recover the initial state upon cessation of the excitatory signal. When the BZ reaction transmits a periodic excitatory optical signal to the photo-excitable receiver, constituted by either a luminescent or a photochromic compound, a master-and-slave relationship is always established. The light emitted by the luminescent compound or the saturation of the color generated by the photochromic compound oscillate with the same frequency of the BZ. The oscillations of the optical signals of the transmitter and the receiver are in-phase or out-of-phase depending on the response rate of the "slave": if it is fast, the synchronization is in phase, whereas if it is slow, the sync is out-of-phase.

Photochromic materials find further applications in neuromimetic systems based on optical signals. Photo-reversible photochromic compounds allow to implement memory effects: if they are direct photo-reversible photochromes, UV and visible signals promote and inhibit their colorations, respectively. Furthermore, when a photochromic compound receives excitatory optical signals at the bottom of a liquid column, wherein there are either laminar or turbulent convective motions of the solvent generated by a vertical thermal gradient, it gives rise to a hydrodynamic photochemical oscillator that originates chaotic spectrofluorimetric signals.[29–31)] A hydrodynamic photochemical oscillator can mimic a chaotic neuron. If it sends its chaotic excitatory signal to a luminescent compound, the latter synchronizes in-phase and emits an aperiodic fluorescence signal having the same chaotic features of the transmitter.[32)]

Finally, the intrinsic spectral evolution of every photochromic compound that transforms from one form to the other under irradiation, generates either positive or negative feedback actions. The optical feedback actions produced by every photochromic compound act on both itself and other photo-sensitive neuro-mimetic systems that are optically connected to the photochrome. Therefore, recurrent networks can be implemented by using photochromic compounds.[28)] The feedback actions of every photochrome are wavelength-dependent because its photo-excitability, which depends on the product $\varepsilon\Phi$, where ε is its absorption coefficient and Φ is its photochemical quantum yield, is also wavelength-dependent. Therefore, photochromic compounds allow implementing neuromodulation,[33)] which is the alteration of neuronal and synaptic properties in the context of neuronal circuits, allowing anatomically defined circuits to produce multiple outputs reconfiguring networks into different functional circuits.[34)]

When photochromic and luminescent compounds are combined with luminescent oscillatory reactions, such as the chemiluminescent Orbán transformation, they allow implementing even feed-forward networks wherein optical signals travel unidirectionally.[28)] The recurrent and feed-forward networks implemented so far with oscillatory and photo-excitable chemical systems consist of two or, at most, three nodes that communicate through an optical code. The UV and visible signals can play both excitatory and inhibitory effects. Within the networks, phenomena of in-phase, out-of-phase, anti-phase, and phase-locking synchronizations have been observed as it occurs in networks of real neurons that communicate through the chemical code of

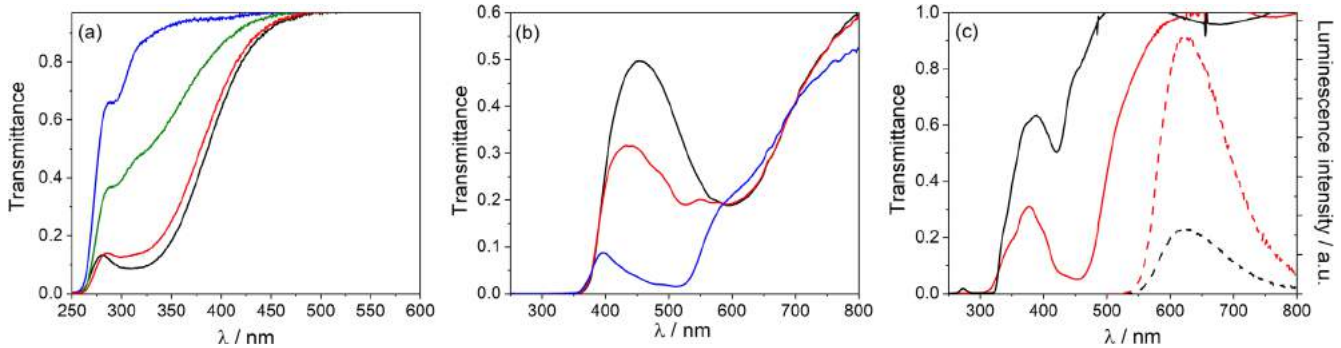

Fig. 2. (Color online) Transmittance oscillations for the BZ with cerium ions (a), with ferroin (b), and with $Ru(bpy)_3^{2+}$ (c). The dashed spectra in (c) represent the oscillations in the red luminescence of $[Ru(bpy)_3]^{2+}$.

neurotransmitters. Three communication architectures have been devised, labeled as α, β, and γ, respectively. In the α architecture, the transmitter and the receiver are in the same cuvette and the same phase, possibly with one component chemically protected by micelles. In the β architecture, the transmitter and the receiver are in the same cuvette but two immiscible phases. In the γ architecture, the transmitter and the receiver are in two distinct cuvettes. The networks have been attained by hybridizing or upgrading the α, β, and γ architectures.[28] All these optical communications do not require an external source of information, such as computer software, to be guided, but they are spontaneous and maintained out-of-equilibrium by chemical and electromagnetic energies.

2.3. An artificial neuron in photoelectrochemical system

Various photoelectrochemical processes have been considered as a computational platform for quite a long-time.[35] The basis of these processes was a photoelectrochemical photocurrent switching effect (PEPS)[36,37] observed in numerous surface-modified semiconductors[38] as well as in highly defected bulk semiconductors like cadmium sulfide,[39] bismuth sulfoiodide[40] and bismuth oxyiodide.[41] The effect was utilized for the implementation of various binary logic gates, reconfigurable logic gates,[42,43] combinatorial logic circuits[44–47] and arithmetic systems.[48] Later the PEPS-based devices were used to implement ternary logic functions,[49] ternary combinatorial circuits[50] and fuzzy logic systems (FLSs).[38,50] The analysis of the PEPS effect and its applications were based solely on the thermodynamics of modified semiconducting materials, whereas the kinetic aspects of photocurrent generation were neglected. The involvement of kinetic factors leads to new switching phenomena with potentials applications in information processing.[51]

Detailed photoelectrochemical studies of cadmium sulfide—multiwalled carbon nanotubes composite have shown a peculiar dynamic behavior of this material subjected to short pulses of light.[52] The photoelectrodes prepared from this composite material, when subjected to a series of light pulses, generate photocurrent pulses, the intensity of which depends on the history of the photoelectrode. In more detail, it depends on past illumination history: the second pulse yields a photocurrent of higher intensity when the interval between pulses is short enough. The response of the electrode towards trains of pulses of various frequencies are shown in Fig. 3. Quite surprisingly, the dependence of the photocurrent spike intensity on time interval between pulses is described by a bi-exponential equation, like in the case of living plastic neurons.[53]

Hebbian learning[54] is based on the plastic properties of synapses. Synaptic plasticity is the process that strengthens or weakens the connection between neurons as a consequence of the time sequence of firing events. It was figuratively described as "neurons wire together if they fire together".[55] This process is usually described by bi-exponential Eq. (3):[56,57]

$$W(\Delta t) = \begin{cases} A_+ \exp(-\Delta t/\tau_a) + |A_-| \exp(-\Delta t/\tau_c) & \text{for } \Delta t \geqslant 0 \\ A_+ \exp(\Delta t/\tau_b) + |A_-| \exp(\Delta t/\tau_d) & \text{for } \Delta t < 0 \end{cases}, \quad (3)$$

where Δt is the time interval between post- and presynaptic signals, $\tau_\pm$ are the time constants and $A_\pm$ are the parameters determined by the synaptic weights. The upper part of the formula (the $\Delta t \geqslant 0$ case) describes the potentiation mode (i.e. an increase of synaptic weight as a consequence of the decreased time interval between events), whereas the lower one (the $\Delta t < 0$ case) the depression mode. In the described case only the potentiation mode has been observed, therefore the response function can be simplified to (4):[52]

$$f(\Delta t) = \alpha_1 \exp(-\Delta t/T_1) + \alpha_2 \exp(-\Delta t/T_2) + \beta, \quad (4)$$

where $\alpha_{1,2}$ and $T_{1,2}$ are relevant fitting parameters while β is only a scale factor, which is irrelevant for the data interpretation. The result of the fitting procedure is presented in Fig. 3(c). A good match was found (χ^2 around 1.1×10^{-3}) with the following set of fitting parameters: $\alpha_1 = 3.014 \pm 0.034$, $\alpha_2 = 4.80 \pm 0.21$, $T_1 = 116.4 \pm 3.7$ ms, $T_2 = 6.88 \pm 0.31$ ms, and $\beta = 1.722 \pm 0.024$. It is noteworthy that the time constants are of comparable value to the ones obtained for biological structures.[56,58]

The mechanism of the plastic processes observed in the CdS-MWCNT composite is relatively simple. Photoexcitation of the material within the fundamental absorption of cadmium results in the promotion of electrons from the valence to the conduction band (process **1** in Fig. 4). Some electrons may undergo thermal relaxation to the valence band (**1′**). The observed photocurrent is a consequence of interfacial electron transfer to the conducting substrate (**2**) accompanied by the redox reaction with the redox mediator (iodide anions in the studied case) present in the electrolyte (**2′**). In the presence of carbon nanotubes, acting as additional electron traps the process (**3**) competes with photocurrent generation (**2**). The recombination process (**3′**) must be significantly slow, therefore the lifetime of trapped electrons is in order of tenths of a second. Partial filling of the nanotube-related trap states results in increased photocurrent intensities.

The SPICE model [Fig. 5(a)] proves the correctness of the proposed mechanism. Photoelectrode based on the CdS-MWCNT material was modeled by three *RC* loops, which simulate the behavior of a nanoparticulate electrode as suggested in previous reports.[37,60] The nanotube trapping site was modeled by an additional R_TC_T loop. The capacitance of this part was set to be 50 times larger (500 nF) than the ones used in the other *RC* loops. This choice is justified by a very high electric capacitance of carbon nanotubes.[61] The equivalent circuit contains also other elements: R_a describes the ohmic resistance of the electrolyte, whereas R_b is the electron transfer resistance of the CdS-MWCNT junction. Two diodes in the circuit represent Schottky junctions between conducting support and the material (D_a) and between carbon nanotubes and semiconductor nanoparticles (D_T). These diodes provide unidirectional electron transfer from the conduction band to the conducting substrate (D_a) and from the conduction band to the nanotube traps (D_T).

The application of change pulses results in trains of output potential of characteristics very close to the experimental ones [cf. Fig. 5(b)]. Removal of the charge trapping subcircuit (red in Fig. 5) results in a disappearance of the learning effect [Fig. 5(c)]. Very recently it was found that similar effects can be observed in other highly defected nanocrystalline CdS modifications. Very similar photoelectrochemical neuromimetic devices were based on a 1:1 mixture of hexagonal and tetragonal polymorphs of cadmium sulfide [Fig. 4(b)]. In this

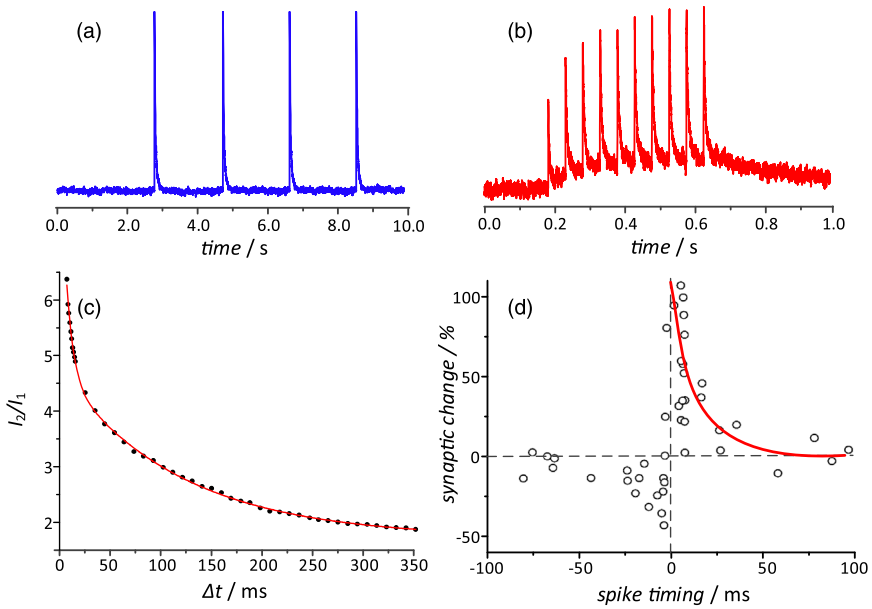

Fig. 3. (Color online) The response of the artificial synapse upon illumination (450 nm) with 2 s (a) and with 50 ms (b) time intervals between light pulses. The plasticity of the studied synaptic system with the fit line described by Eq. (2) (b) is compared to the plasticity of hippocampal glutamatergic neurons in culture (d) (data are taken from Ref. 53). Reproduced from Ref. 52 with permission from Wiley.

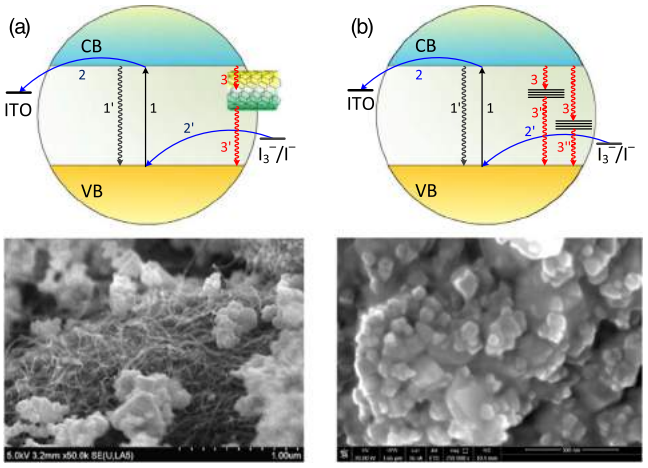

Fig. 4. (Color online) The mechanism responsible for the synaptic behavior of the CdS/MWCNT-based device (a) and hexagonal/tetragonal CdS mixtures (b) along with SEM images of studied materials. Adapted from Refs. 52, 59.

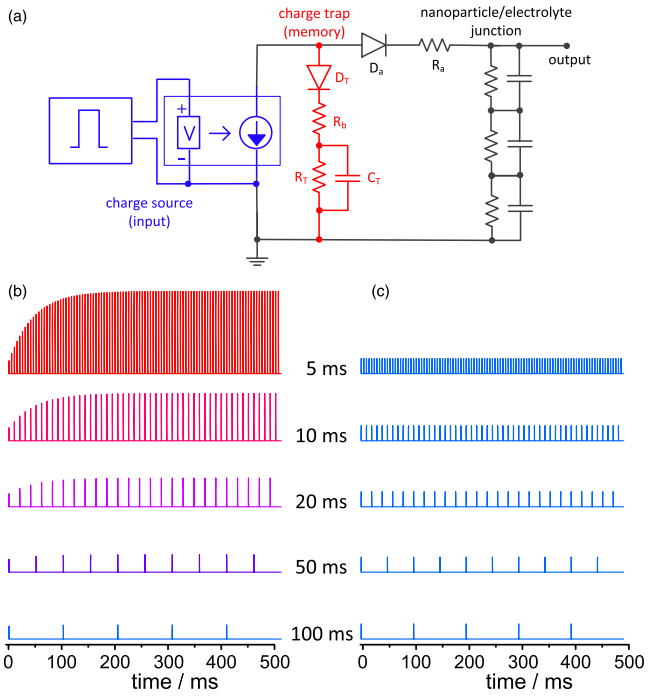

Fig. 5. (Color online) The equivalent electronic circuit employed to describe the ITO/MWCNTs/CdS photoelectrodes (a) and the simulated time-dependent response of the equivalent circuit to the pulsed stimulation characterized by various repetition intervals. Two cases were taken into consideration: in the first one the branch responsible for charge trapping/de-trapping events (related to the presence of MWCNTs) was introduced (b) and in the second one it was removed (c). Reproduced from Ref. 52 with permission from Wiley.

particular case, the bi-exponential learning curve was also observed ($\chi^2 = 6.23 \times 10^{-5}$), but the fitting parameters were significantly different ($\alpha_1 = 0.218 \pm 0.013$, $\alpha_2 = 0.339 \pm 0.014$, $T_1 = 167 \pm 23$ ms, $T_2 = 20 \pm 4$ ms, and $\beta = 1.00 \pm 0.01$).[59)]

3. Processing fuzzy logic with molecules

Human intelligence has the remarkable power of handling both accurate and vague information. Vague information is coded through the words of our natural languages. We have the remarkable capability to reason, speak, discuss, and make rational decisions without any quantitative measurement and any numerical computation, in an environment of uncertainty, partiality, and relativity of truth. A major challenge is the design of neuromimetic devices that have the capabilities of human intelligence to compute with words.[62)] The imitation of the human ability to compute with words is still challenging. One of the approaches that can offer a satisfying approximation is fuzzy logic-based models.

3.1. Some key concepts of fuzzy logic

Fuzzy logic has been defined as a rigorous logic of vague and approximate reasoning.[63)] Fuzzy logic is based on the theory of fuzzy sets proposed by the engineer Lotfi Zadeh in 1965.[64)] A fuzzy set is different from a classical Boolean set because it breaks the law of Excluded Middle. An item may belong to a fuzzy set and its complement at the same

time, with the same or different degrees of membership. The degree of membership (μ) of an element to a fuzzy set can be any number included between 0 and 1. It derives that fuzzy logic is an infinite-valued logic. Fuzzy logic can be used to describe any nonlinear cause and effect relation by building a FLS. The construction of an FLS requires three fundamental steps. First, the granulation of all the variables in fuzzy sets. The number, position, and shape of the fuzzy sets are context-dependent. Second, the graduation of all the variables: each fuzzy set is labeled by a linguistic variable, often an adjective. Third, the relations between input and output variables are described through syllogistic statements of the type "If…, Then….", which are named as fuzzy rules.

The "If…" part is called the antecedent and involves the labels chosen for the input fuzzy sets. The "Then…" part is called the consequent and involves the labels chosen for the output fuzzy sets. When we have multiple inputs, these are connected through the AND, OR, NOT operators.[65] In formulating the fuzzy rules, we must consider all the possible scenarios, i.e. all the possible combinations of input fuzzy sets. At the end of the three-steps procedure, an FLS is built; it is a predictive tool or a decision support system for the particular phenomenon it describes.

Every FLS is constituted by three components: A fuzzifier, a fuzzy inference engine, and a defuzzifier. A fuzzifier is based on the partition of all the input variables in fuzzy sets. It transforms the crisp values of the input variables in degrees of membership to the input fuzzy sets. The fuzzy inference engine is based on fuzzy rules. It turns on all the rules that involve the fuzzy sets activated by the crisp input values. Finally, the Defuzzifier is based on the fuzzy sets of the output variables, and it transforms the collection of the output fuzzy sets, activated by the rules, in crisp output values. Fuzzy logic is a good model of the human ability to compute with words because there are some structural and functional analogies between any FLS and the human nervous system (HNS).[66]

3.2. The fuzziness of the HNS

The HNS comprises three elements: (I) the sensory system; (II) the central nervous system; (III) the effectors' system. The sensory system catches physical and chemical signals and transduces them in electro-chemical information that is sent to the brain. In the brain, information is integrated, stored, and processed. The outputs of the cerebral computations are electro-chemical commands sent to the components of the effectors' system, i.e. glands and muscles.[67] The sensory system includes visual, auditory, somatosensory, olfactory, and gustatory subsystems. Each type of sensory subsystem encodes four features of a stimulus: modality, intensity, time evolution, and spatial distribution.

The power of distinguishing these features derives from the hierarchical structure of every sensory system. In fact, for each sensory system, we have, at the smallest level, a collection of distinct molecular switches. At an upper level, we have a set of distinct sensory cells: each cell contains many replicas of a specific molecular switch. Finally, at the highest level, we have many replicas of the different receptor cells that are organized in a tissue whose structure depends on the architecture of the sensory organ. For instance, in the case of the visual system, we have four types of photoreceptor proteins (each one absorbing a specific portion of the visible spectrum); four types of cells (one rod and three types of cones), each one having many replicas of one of the four types of photoreceptor proteins. Finally, we have many replicas of the different cells disposed on a photo-sensitive tissue, the retina, with the rods spread on the periphery, and the cones concentrated in the fovea.

Consequently, the information of a stimulus is encoded hierarchically. The collection of four types of photoreceptor proteins plays like an ensemble of four distinct molecular fuzzy sets. The information regarding the modality of the stimulus is encoded as degrees of membership of the stimulus to the four molecular fuzzy sets; that is, it is encoded as fuzzy information at the molecular level ($\bar{\mu}_{\mathrm{ML}}$). The four types of cells play like cellular fuzzy sets. The information regarding the intensity is encoded as degrees of membership of the stimulus to the cellular fuzzy sets, that is, as fuzzy information at the cellular level ($\bar{\mu}_{\mathrm{CL}}$). Finally, the array of the many replicas of the receptive cells plays like an array of cellular fuzzy sets, and the information regarding the spatial distribution of the stimulus is encoded as degrees of membership to the array of cells, that is, as fuzzy information at the organ level ($\bar{\mu}_{\mathrm{OL}}$). The total information of the stimulus will be the composition of the fuzzy information encoded at the three levels. For instance, in the case of the photoreceptor system, the total information will be a matrix of data reproducing the array of cells on the retina. Each element of the matrix will be the product of two terms: the fuzzy information encoded at the molecular level times that encoded at the cellular level.

The sensory cells produce graded potentials that are analog signals. The information of such signals is usually converted into the firing rate of the action potential trains. Often, the action potentials are produced by an architecture of afferent neurons that integrate the information regarding the spatial distribution of the stimuli. Every afferent neuron has a receptive field that works as a fuzzy set encompassing specific receptor cells.[68] The action potentials generated by the afferent neurons are the ideal code for sending the information up to the brain. In the cerebral cortex, various areas are having different intrinsic rhythms.[69] They form a neural dynamic space partitioned in overlapped cortical fuzzy compartments. Such cortical fuzzy sets are activated at different degrees by separate attributes of the perceptions and produce a meaningful experience of the external and internal worlds.

3.3. The best strategies to implement FLSs

In electronics, the best implementations of FLSs have been achieved through analog circuits, although fuzzy logic is routinely processed in digital electronic circuits. More recently, fuzzy logic has also been processed by using molecules, macromolecules, and chemical transformations. All the methods proposed for processing fuzzy logic can be sorted out in three main strategies.[68] The first strategy is an imitation of the "fuzzy parallelism" of the sensory subsystems described in the previous paragraph. The second is the "conformational fuzziness" of molecules and macromolecules that exist as an ensemble of conformers, whose distribution is context-dependent. The third is the "quantum fuzziness" that hinges on the decoherence of overlapped quantum states originating continuous, smooth, analog input-output relationships between macroscopic variables when it involves large amounts of molecules. In the next paragraphs, examples of the three strategies are described.

3.3.1. The "fuzzy parallelism" of the biologically inspired photochromic FLSs. As we have seen in paragraph 3.2, the human visual system grounds on four photoreceptor proteins: three for daily vision in color and one for night vision in black and white. All of them have 11-*cis* retinal as the chromophore. However, the four photoreceptors have different absorption spectra in the visible region, because they differ in the amino-acidic composition. The absorption spectra of the four photoreceptor proteins behave as "molecular fuzzy sets". The spectral composition of a light stimulus is encoded as degrees of membership of the light to these "molecular fuzzy sets". Moreover, the millions of replicas of the three photoreceptor proteins within each photoreceptor cell allow determining the intensity of the signals at every wavelength. The imitation of the way we distinguish colors has allowed devising chemical systems that extend human vision to the UV.[70] Such chemical systems are based on direct thermally reversible photochromic compounds. Direct photochromic species usually absorb just in the UV. The criteria to mix the direct photochromic compounds and generate Biologically inspired photochromic fuzzy logic (BIPFUL) systems that extend the human ability to distinguish electromagnetic frequencies to the UV region have been the following ones. First, the absorption bands of the closed uncolored (Un) forms were assumed to be input fuzzy sets. Second, the absorption bands of the open colored (Col) forms were assumed to be output fuzzy sets. Third, the algorithm expressing the degree of membership of the UV radiation, having the intensity $I_0(\lambda_{irr})$ at the wavelength λ_{irr}, to the absorption band of the ith compound is given by (5):

$$\mu_{UV,i} = \Phi_{PC,i}(\lambda_{irr}) I_0(\lambda_{irr})(1 - 10^{-\varepsilon_{Un,i} C_{0,i} l}). \quad (5)$$

In Eq. (5), $\Phi_{PC,i}(\lambda_{irr})$ is the photochemical quantum yield of photo-coloration, $\varepsilon_{Un,i}$ the absorption coefficient at λ_{irr} for the ith photochromic species, and $C_{0,i}$ is its analytical concentration. Finally, the equation expressing the activation of the ith output fuzzy sets is (6):

$$A_{Co,i} = \frac{\varepsilon_{Co,i}(\lambda_{an})}{k_{\Delta,i}} \mu_{UV,i}. \quad (6)$$

In Eq. (6), $A_{Co,i}$ is the absorbance at the wavelength λ_{an} into the visible and due to the colored form of the ith photochromic species; $\varepsilon_{Co,i}(\lambda_{an})$ is its absorption coefficient, and $k_{\Delta,i}$ is its kinetic constant of the bleaching reaction. Each absorption spectrum recorded at the photo-stationary state will be the sum of as many terms represented by Eq. (6) as there are photochromic components present within the BIPFUL system. Some BIPFUL systems consisting of from three to five photochromic compounds have been proposed.[71] They allow the three regions of the UV spectrum, UV-A, UV-B, and UV-C, to be discriminated because the wavelengths belonging to the three UV regions originate from distinct colors.

An example of a quaternary BIPFUL system is shown in Fig. 6. It is constituted by four direct thermally reversible photochromic compounds (labeled as **1**, **2**, **3**, and **5**).[70] It becomes green, gray, and orange when it is irradiated by frequencies belonging to the UV-A, UV-B, and UV-C regions, respectively. It works both in the liquid phase (the concentrations of the species involved are reported in Fig. 6) and on a cellulosic white paper.

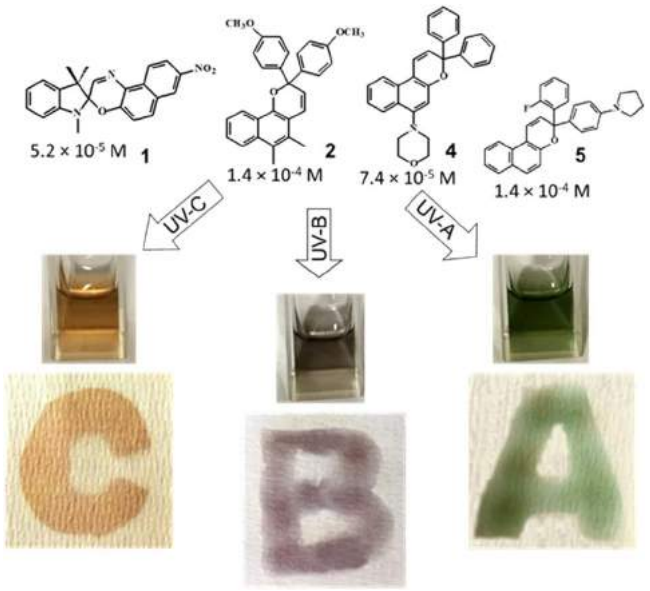

Fig. 6. (Color online) A quaternary BIPFL system constituted by the direct thermally reversible photochromic compounds **1**, **2**, **4**, and **5**; this BIPFUL system becomes green, grey, and orange when it is irradiated by frequencies belonging to the UV-A, UV-B, and UV-C regions, respectively. Its sensory activity works both in the liquid phase and on a white paper made of cellulose.

The imitation of other sensory subsystems, described as hierarchical fuzzy systems, wherein distinct molecular and cellular fuzzy sets work in parallel, will allow to design new artificial sensory systems. These new artificial sensory systems will have the power to extract the essential features of stimuli and will contribute to the recognition of variable patterns.

3.3.2. The fuzziness of conformers. Every molecular or macromolecular compound that exists as an ensemble of conformers works as a fuzzy set.[68,72] The types and amounts of different conformers depend on the physical and chemical contexts. Every compound is like a word of the natural language, whose meaning is context-dependent. Conformational dynamism and heterogeneity enable context-specific functions to emerge in response to changing environmental conditions and allow the same compound to be used in multiple settings. It is possible to quantify the fuzziness of every compound by determining the fuzzy entropy (7):

$$H = -\frac{1}{\log(n)} \sum_{i=1}^{n} \mu_i \log(\mu_i), \quad (7)$$

wherein n is the number of conformers and μ_i is the relative weight of the ith conformer.

The fuzziness of a macromolecule is usually more pronounced than that of a simpler molecule. Among proteins, those completely or partially disordered are the fuzziest.[73] Their remarkable fuzziness makes them multifunctional and suitable to moonlight, i.e. play distinct roles, depending on their context.[74]

3.3.3. From quantum to fuzzy logic. The elementary unit of quantum information is the qubit. The qubit, $|\Psi\rangle$, is a quantum system that has two accessible states, labeled as $|0\rangle$

and $|1\rangle$, and it exists as a superposition of them (8):

$$|\Psi\rangle = a|0\rangle + b|1\rangle. \quad (8)$$

In Eq. (8), a and b are complex numbers that satisfy the normalization condition $|a|^2 + |b|^2 = 1$. The two states, $|0\rangle$ and $|1\rangle$, work as two fuzzy sets. The $|\Psi\rangle$ state belongs to both $|0\rangle$ and $|1\rangle$ with degrees that are $|a|^2$ and $|b|^2$, respectively. Any logic operation on a qubit manipulates both states, simultaneously. If a molecular system is a superposition of n qubits, any operation on it manipulates 2^n states, simultaneously. Therefore, it is evident the alluring parallelism of quantum logic. However, deleterious interactions between the quantum system and the surrounding environment can cause the decoherence of the quantum states.[75] The decoherence induces the collapse of any qubit in one of its two accessible states, either $|0\rangle$ or $|1\rangle$, with probabilities $|a|^2$ and $|b|^2$, respectively.

Whenever the decoherence is unavoidable, the single microscopic units can be used to process discrete logics, i.e. binary or multi-valued crisp logics depending on the original number of qubits.[76,77] Advanced microscopic techniques, reaching the atomic resolution, are required to carry out the computations with single particles. Alternatively, large assemblies of particles, e.g. molecules, can be used to make computations. However, vast collections of molecules (amounting to the order of the Avogadro's number) are bulky materials. The inputs and outputs for making computations become macroscopic variables that can change continuously. The functions linking input and output variables can be either steep or smooth. Steep sigmoid functions are suitable to implement discrete logic. In contrast, both linear and nonlinear smooth functions are suitable to build FLSs.[78]

Many FLSs have been built by using the emission of light as preferable output because it bridges the gap between the microscopic and the macroscopic world. For instance, the fluorescence of 6(5 H)-phenanthridinone depends smoothly on the hydrogen bonding donation ability of the solvent (HBD) and the temperature.[79] The fluorescence of tryptophan, both as an isolated molecule and bonded to the serum albumin, depends smoothly on the temperature and the amount of the quencher flindersine.[80] Further examples are a ruthenium complex, whose fluorescence depends on Fe^{2+} and F^-,[81] and europium bound to a metal-organic framework, which depends on metal cations, such as Hg^{2+} and Ag^+.[82]

With a multi-responsive chromogenic compound, belonging to the class of spirooxazine, all the fundamental fuzzy logic gates, AND, OR, and NOT, have been implemented.[83] The protons, Cu^{2+}, and Al^{3+} ions have been used as inputs and the color coordinates (R, G, B) or the colorability of the chromogenic compound as outputs. Then, other platforms have been proposed. For example, a multi-state tantalum oxide memristive device[84] and an anthraquinone-modified titanium dioxide electrode.[50] All these case studies demonstrate that fuzzy logic can be processed by unconventional chemical systems showing analog physical-chemical input-output relationships in either the liquid or the solid phase. They are alternative to the conventional way of processing fuzzy logic, which is based on electronic circuits and signals.

4. Classification and transformation of simple signals

All material-based real devices operating at realistic conditions are best described by fractional differential equations, as it was demonstrated in the case of a capacitor by Svante Westerlund in 1991 in a seminal paper with a mind-twisting title "Dead matter has memory!".[85] This concept was further extended towards other fundamental devices.[86,87] It implies, that *in-materio* components exhibit some forms of memory, which is a consequence of internal dynamics. Therefore these systems and devices are naturally suited for signal processing and also can be incorporated, as active nodes, into signal classification devices. The following sections will present some selected applications in this field, which also relate to neuromorphic information processing.

4.1. Generation of higher harmonics in memristive devices

The second harmonic generation (SHG) involves generating signals (e.g. optical or electrical) the frequencies of which are twice as high as the fundamental frequency, hence often this effect is called frequency doubling. The generation of higher harmonics is observed in nonlinear resistors, but in this case, the largest spectral weight falls on the fundamental frequency.[88] One of the simplest electronic circuits capable of implementing electrical frequency doubling is a diode bridge. It can be shown on the basis of the Fourier analysis that the diode bridge achieves 4.5% efficiency for SHG and 18.9% for higher harmonics in relation to input power.[89] Oskoee et al.[90] initially suggested the potential for SHG for strongly memristive systems. In an attempt at improving SHG efficiencies, Cohen et al.[88] performed a quantitative analysis based on the memristor model for a single element as well as for the memristor bridge. The results show a significant improvement in performance in SHG generation, at 16.9% for a single element and 40.3% for a memristor bridge. Based on the above simulation results, the potential of memristive structures in applications related to SHG has been shown.

Literature describing research on SHG present in hardware memristive structures is sparse. Majzoub et al. performed an analysis of the influence of higher harmonic components of the recorded current on the pinched hysteresis loop.[91] Authors used a commercially available device (KNOWM Inc.) to show, that higher harmonic components are crucial to form the pinched hysteresis loop. By filtering the components above second harmonic, authors obtained distortionless response of the device, without losing functionality in digital applications of AND/OR logic gates simulation. To benefit from the higher complexity of the system and get as close as possible to high interconnectivity of biological nervous structure Avizienis et al.[92] have studied the neuromorphic atomic switch network (ASN). Presented ASN was fabricated through electroless self-assembly of silver nanowires from the $AgNO_3$ solution which was added to SU-8 (epoxy-based negative resist) with patterned Cu posts. The oxidation reaction of Cu seeds with the $AgNO_3$ solution leads to the formation of an extremely interconnected structure (10^9 junctions per cm^2) of silver nanowires with variable morphology. Gas-phase sulfurization of the obtained network enables the formation of memristive metal-insulator-metal ($Ag|Ag_2S|Ag$) junctions. Analysis of the network properties showed the memristive nature of the junctions after activation through unidirectional electrical sweeps which were associated with the formation of conducting filaments (CFs). Moreover, studied ASN exhibited a pronounced increase in the magnitude of higher harmonic generation (Fig. 7) after

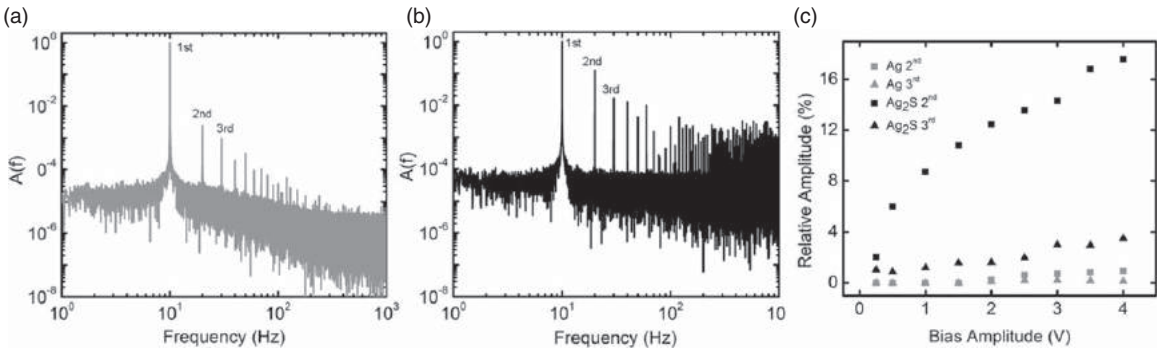

Fig. 7. Fourier transform spectra for control device (a) and functionalized network (b), both subjected to 10 Hz, 2 V stimulation. Second and third harmonic relative amplitudes in the function of bias voltage show a significant increase in SHG for the functionalized network (black) in comparison with the control device [grey, (c)]. Reproduced from Ref. 92 with permission from the Public Library of Science.

system functionalization due to an increase in the number of hard switching junctions.[90)]

4.2. Amplitude discrimination

The amplitude-discrimination of voltage is the inherent property of memristors. Only pulses with sufficient amplitude can affect the resistive state of the memristive device. In general, the resistive state is dependent on the history applied current and voltage, enabling storage and adjustable changes of the device's conductance. Specific voltage pulse can transfer the memristor from one state [e.g. high resistance state (HRS)] to another [e.g. low resistance state (LRS)].

Memristors employed in a reservoir system can act as a simple amplitude classifier. In general, the resistive state of the memristive device is dependent on the history of the applied current and voltage. Furthermore, exploiting the nonlinear *I*–*V* dependence, one can gradually switch the resistance to the other state with the pulses of sufficient amplitude and proper polarity. These inherent properties of memristors can be utilized for the amplitude classification with employing the memristor in the feedback loop. It has been reported that lead iodide (PbI_2) incorporated in a single node echo-state network with a delayed feedback loop can efficiently discriminate input voltage pulses on the basis of their amplitude.[93)] The PbI_2|Cu device shows a distinct rectifying characteristic, which leads to the amplification of forward bias pulses and the reduction of reverse bias pulses. In this simplified reservoir system, the output signal—after a delay time—is routed back to the input. As the number of feedback cycles increases, some signals gain the intensity and the others are attenuated, leading to an amplitude classification. If the signal voltage exceeded the threshold value of 1.85 V_{pp}, the signal was amplified. On the contrary, lower voltage amplitudes were decreased over the course of subsequent. As another example, $[SnI_4((C_6H_5)_2SO)_2]$/Cu in echo state machine can perform similar classification based on both amplitude and duration of the input voltage.[94)] Higher the amplitude and longer the duration, the signal propagated longer in the feedback loop before the full attenuation.

4.3. Frequency discrimination

Most basic frequency discrimination for neuromorphic memristor-based devices is the spike-rate-dependent plasticity (SRDP) learning strategy. If the frequency of spike train exceeds the threshold value, the short term effects, such as signal intensity decay can be overcome and each next spike has increased intensity, until reaching plateau level. This way of frequency processing has its instant limits—a range of frequencies between threshold and plateau values. The resolution of frequency detection is also associated with the length of individual pulses. The realization of these ideas is possible with the incorporation of several memristive materials, for example, organolead trihalide perovskites (or organic–inorganic perovskites).[95)] Even transistors, such as nanoparticles/organic memory transistors which are equivalent to leaky memory devices and have kind of STP-like characteristics can be used as very simple frequency discriminators.[96,97)] Presented strategy is unfortunately insufficient for a wide variety of frequencies and lacks scientific elegance—one still needs dedicated software and von-Neumann architecture-based hardware elements to detect measure and correctly categorize output signals.

Advancement of the above methodology would be to use STP or LTP (short- and long-time plasticity) effects associated with threshold frequency. Experimentally this behavior was shown by He in 2014[98)] for the sandwich-like structure of Pt/FeO_x/Pt. To observe this effect one must put the spike train similar to the biological firing curve. The spikes are inspired by the firing behavior of biological neurons—and consist of two pulses. The first one is a very short but high-amplitude pulse, followed by a wide and low-amplitude pulse in the opposite direction. It is a necessary condition to realize bidirectional weight change. At the same time, this is the limitation of the method as the input impulses must be properly shaped in order to distinguish between their frequency. Low-frequency spikes (below 10 kHz) tent to induce long-term depression by decreasing the conductivity of the memristor. On the contrary, 20 kHz spikes accumulate positive constituting pulses, causing an increase of the conductance—c.f. Figs. 8(a) and 8(b).

Similarly, better frequency resolution than mere SRDP can also be obtained by directly using the learning rules of Bienenstock–Cooper–Munro according to whom the synapse's weight can exhibit either be strengthened (potentiation) or weakened (depression) even when subjected to the same spike trains. Memristive devices with WO_x between metal (Pt) electrodes additionally to STP/LTP regimes utilize the so-called "sliding threshold frequency" as the frequency classification rule.[99)] Historical synaptic activity influences device performance—periods of increased activity are followed by higher frequency threshold for synaptic weight

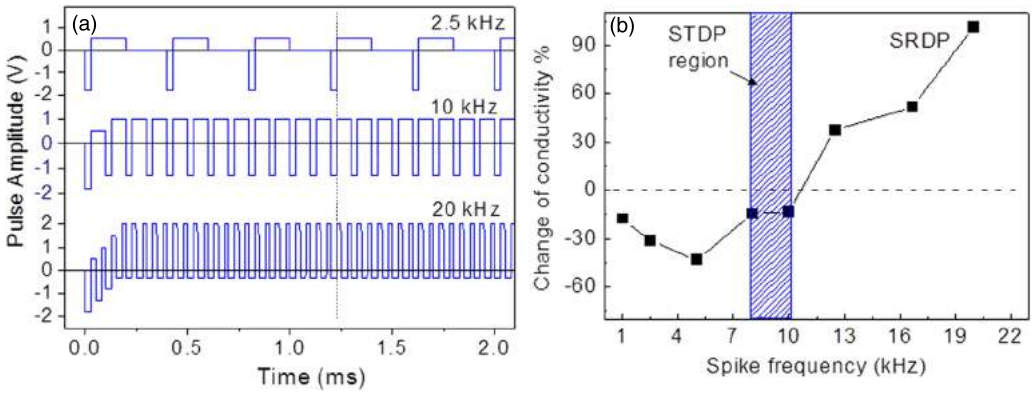

Fig. 8. (Color online) Spike waveforms, similar to biological neural spikes at different presynaptic firing frequency. Signal intensification is detected after crossing the frequency threshold (a). Emulated spike-rate-dependent plasticity (SRDP) learning rule for memristor build of iron oxide (b). Such behavior is also reported for real-life synapses. Reproduced from Ref. 98 according to the Creative Commons CC-BY-NC-ND licence.

potentiation and periods of lighter intensity—as presented in Fig. 9(a) for biological neurons.

This behavior was repeated artificially [Fig. 9(b)]—after 200 Hz stimulation, synaptic weight increased and the concomitant 10 Hz stimulation caused current drop [step 2 in Fig. 9(b)]. After that 1 Hz stimulation and 10 Hz stimulation caused increase in output current [step 4 in Fig. 9(b)]. Figure 9(c) shows results for stimulation with different frequency (20, 50 and 100 kHz) and then five probing pulses. After stimulation these probing pulses, depending in turn on their own frequency, result in either weakening or strengthening of the synaptic weight. The higher the pre-stimulation before probing pulses, the higher frequency probing pulse is needed to strengthen the synapse—this effect is similar to the one observed in biological systems. In addition to frequency discrimination, pretreatment of the sample influences also amplitude threshold [Fig. 9(d)].

The learning/forgetting effect with the frequency threshold was also reported for ZnO memristive devices.[101] Described devices possessed a biorealistic rate-dependent synaptic plasticity, mimicking biological systems, has been demonstrated in the rectifying diode-like Pt/n-ZnO/SiO_{2-x}/Pt synaptic heterostructures. Among others, the SRDP rule, the STP and LTP retention, and frequency sliding threshold simultaneously exist in the device. The paired pulse facilitation phenomenon along with the SRDP learning rule was discovered to similarly follow the plasticity behavior of that in the actual synapse. The frequency sliding threshold was explored to show the dynamic stability of the synaptic weight depending on spike train time spacing and frequency. In whole, frequency discrimination signal processing help emulated human-like "Learning-Forgetting-Relearning" synaptic behavior. These findings will serve as cornerstones for dynamic hardware-based neuromorphic systems.

Discrimination of periodic signals of various waveforms according to their frequency should be also possible. It is an obvious fact that due to the switching dynamics memristors are frequency-sensitive elements. At sufficiently high frequencies they may behave like linear memristors, whereas their nonlinear features emerge as low-frequency range. Therefore, it should be possible to build a reservoir system similar to the previously described, which selectively amplifies signals of frequencies lower than the threshold value and attenuates signal of higher frequencies (or vice versa). Such behavior is not a unique feature in classical analog electronics: any bandpass filter (active or passive) can perform similarly. The expected advantage of reservoir memristive devices in comparison to analog filters is a very high slope of their frequency characteristics, especially if they are embedded into a single node echo state machine[93,94] as shown in Fig. 10.

In such systems, low-frequency signals should be amplified, whereas the signals of frequencies higher than the characteristic cut-off frequency should be slowly attenuated. The signal matching the cut-off frequency should remain unchanged. The same type of devices can be also used for more advanced signal processing due to gradual change in the signals' symmetry due to partial rectification at the Schottky junction of the memristor.

Some of the above-described effects were implemented for memristive devices and perform frequency discrimination functions, amplitude-discrimination functions alongside with other time-oriented functions in patented solutions.[102] The sum of output currents, thus overall resistivity of the aggregated memristors network, is dependable on the input signal frequency level—making it possible to switch the device between states if the input signal is greater than a threshold frequency.

5. Classification of complex acoustic patterns

Dynamics of resistance changes in memristors as well as their highly nonlinear characteristics seem to be key features in their application is signal processing and classification. Furthermore, they can be incorporated into feedback loops yielding single node echo state machines (or other types of reservoir computers) with a superb performance in signal classification. In the case of reservoir computing training of the reservoir is not required, the classification of the input signal relies on the internal dynamics of the reservoir. The only point that requires training is a readout layer—simple artificial neural network (software-based), single layer perceptron or a simple signal processing circuit. Despite obvious utility of memristive elements in such computational tasks the reports on experimental verification of memristor applicability in signal classification/processing are scarce, however, the number of theoretical works, including numerical simulations, is increasing. The reason is purely technological—analog memristors (vide infra) are an emerging class of devices and require a lot of fundamental and technological studies.

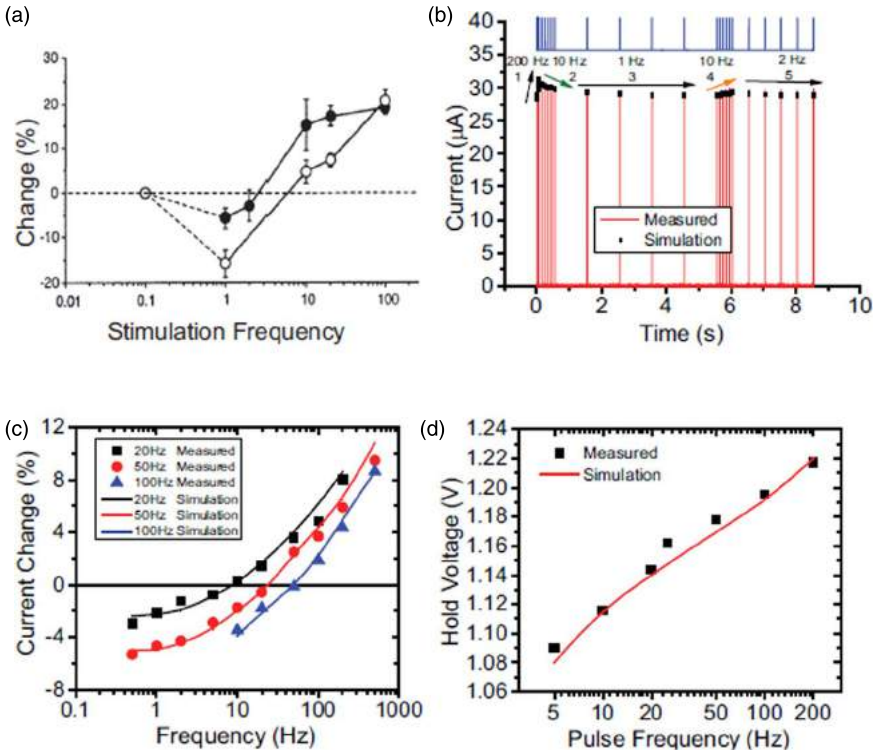

Fig. 9. (Color online) Activity-dependent plasticity (STP/LTP rules) and sliding threshold effects in memristors. Relative change in synaptic weight as a function of stimulation frequency for two different cases. Low stimulation frequency results in depression and high stimulation frequency results in facilitation. The threshold moves to a lower frequency for filled symbols (low activity period) compared to the normal condition (open symbols). Data obtained in rat visual cortex.[100] (a) Memristor response to consecutive programming pulse trains at different frequencies. The 10 Hz pulse train caused a decrease of current in step 2 following strong stimulation in step 1, but the current increase in step 4 following weak stimulation in step 3. Black squares: Simulation results from the memristor model using experimental parameters. (b) Memristor current change as a function of the stimulation frequency after the memristor has been exposed to different levels of activities. Pulse trains consisting of five pulses (1.2 V, 1 ms) with different repetition frequencies were used to program the memristor. Black squares, red circles, and blue triangles represent experimental data. The solid lines are simulation results from the memristor model using experimental parameters. (c) Measured threshold hold voltage as a function of previous activity (represented by different pulse frequency). The device was stimulated by pulse trains with the same repetition frequency of 50 Hz but different amplitudes. Black squares: Experimental data. Solid line: Simulation results from the memristor model using experimental parameters. (d) Reprinted from Ref. 99 with the permission of Wiley.

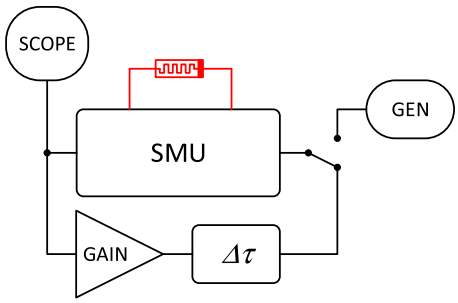

Fig. 10. (Color online) A scheme of a memristor-based single node echo machine: SMU stands for a source-measure unit, GAIN for an amplifier, SCOPE for oscilloscope/signal recorder $\Delta\tau$ for a delay line and GEN for arbitrary function generator.

There are two principal categories of memristors, which can be tentatively called analog and digital ones.[103,104] Analog memristors gradually change their internal state due to interfacial switching processes (e.g. Schottky barrier height modulation) or dopant migration. As a result, these devices can store not only binary data but also analog data. Materials that show the interface-switching behavior are still under development. Moreover, the accuracy in controlling the memristance value in analog memristors is still considered to be a big concern, however, recent studies on pulse and signal classification define the safe limits of their applicability.[93,94,105] On the contrary, most memristors reported so far operate according to the filamentary switching mechanism. In filamentary switching, memristors can have either a HRS or a LRS and therefore the systems based on these devices are considered error-tolerant. On the other hand, the application of binary memristors significantly limits the computational performance of memristive systems. The computational power of memristive devices can be further improved by utilization of their dynamic properties, e.g. in reservoir computer systems.[106]

The concept of signal classification based on the dynamic behavior of memristor was reported by Tanaka et al.[107] In this report authors demonstrate the applicability of linear-drift-based memristors in discrimination between sine and triangular waves of the same amplitude within a refined range of frequencies. The system used two different topologies of reservoir networks: ring and small-world topology (a network, in which most nodes are not neighbors of one another, but the neighbors of any given node are likely to be neighbors of each other and most nodes can be reached from every other node by a small number of hops or steps), as shown in Fig. 11.

Such a system computes an output potential at each node and these values are fed into two nodes of a perceptron. The input of a perceptron node h_i ($i = 1, 2$) is a weighted sum of

inputs from reservoir node (9):

$$h_i(t) = \sum_j w_{i,j} x_j(t). \tag{9}$$

Sigmoidal activation function was used to compute the output state of the perceptron nodes (10):

$$y_i(t) = \frac{1}{1 + e^{-h_i(t)}}. \tag{10}$$

Training of the reservoir involves optimization of weights to achieve the (0,1) output state for sine-wave input and the (1,0) for the triangular one. The systems provided good separability of the waveforms at a sufficiently high number of reservoir nodes coupled with the perceptron: 2 in the case of ring topology and 5 in the case of small-world topology. On the other hand, the ring topology works efficiently only in the case of identical elements, even a small variation in memristor characteristics significantly reduces the performance of the system. The introduction of additional connectivities in the circuit (small-world topology) results in a variability-tolerant system, however, a larger number of readout connections (blue arrows in Fig. 11) is required for optimal performance.

Similar capabilities, even without the trained readout layer should be also observed in a single node echo state machine with a nonlinear node of appropriate characteristics. Composite waveforms, with Fourier spectra covering a significantly large range of frequencies, should yield a complex dynamic behavior: some spectral components should be amplified, whereas some others attenuated. This may lead to a binary classification of waveform shapes. It can be further extended by an appropriate readout layer.

5.1. Classification of musical objects

Music is the most ubiquitous human activity independently on any social and cultural attributes or intellectual abilities. Music belongs to human universals,[108] however, according to some opinions, it does not convey any biologically-relevant information.[109] According to Guerino Mazzola music provides a platform of communication between symbolic and emotional layers.[110] Music, like information, is a notion very difficult to define in precise terms. Different cultures developed different concepts of music, where different elements determine the identity of particular music. However, at the fundamental level, one may indicate some components common to all music, like the use of discrete pitches or the presence of rhythmic patterns.[111] Dislike speech, music is not meant for explicit communication purposes, but it triggers various emotional responses in recipients due to aesthetical feelings. On the other hand, music is a very well-organized structure, as not every combination of sounds should be considered as music, however, the modern musicological approach provides a piece of evidence that any purposeful combination of sounds can be considered as music.[112,113] Going to the extreme, even silence (a lack of purposeful sound) can be considered music, with famous *4′33′* by John Cage as the most prominent example.[114] In the simplest approach, however, music can be defined as an appropriate time sequence of quantized acoustic frequencies (Fig. 12). These frequencies are called steps in a musical scale, and along with rhythm and timbre are principal constituents to any musical piece. In the music of European origin, an octave (an interval between frequencies f and 2 f) is divided into 12 steps, called semitones, but other musical systems (the Middle East and India) use smaller intervals (microtones). Also, there exist many different tuning systems, and octave divisions (like Balinese and Javanese gamelan systems). A characteristic feature of European music is the specific concept of musical harmony, which may be considered as a key component of theory and practice. Musical harmony is a complex notion reflected in: (i) the pure content of the ensemble of frequencies heard at given time (also including a timbre of an individual note), (ii) the musical content—the verticality of the chord (a set of notes played simultaneously) and (iii) the position and relation of a chord in relation to the melody at given moment.[115,116] Despite well-established musical theories[115] the automated classification of intervals, chords and clusters and recognition of consonance and dissonance has been not achieved. The reason for this may be that there are three types of factors responsible for the phenomenon of musical harmony: physical (acoustical), physiological (mechanism of auditory perception), and culturally determined cognitive processes. There are many different styles of musical harmony (culturally and historically determined), but the fundamental to all of these is a basic notion of dissonance and consonance, which is of psycho-acoustical nature. Although, different dissonant or consonant sonorities may be differently aesthetically evaluated within a particular musical style or genre. Furthermore, the understanding of physical nature of dissonance and consonance is still not fully established,[109] however various approaches beyond classical

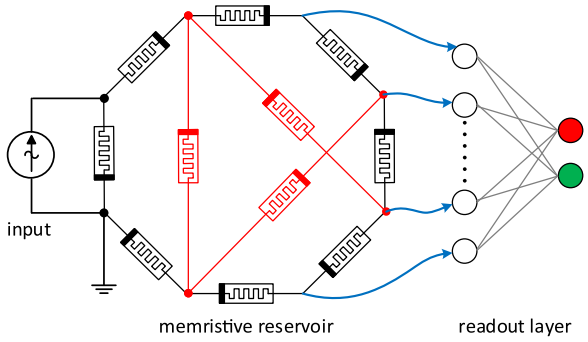

Fig. 11. (Color online) Schematic representation of a memristive reservoir computing system in two different topologies: ring (only black memristors) and small-world (black and red memristors). In the studied case the readout layer was a one later perceptron with a sigmoidal activation function. Adapted from Ref. 107.

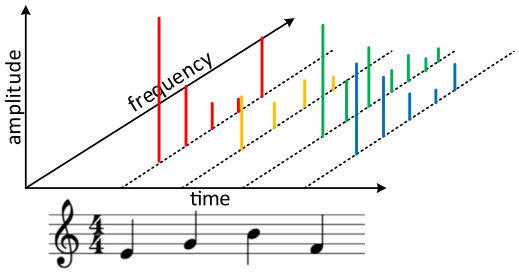

Fig. 12. (Color online) 3D representation of music as a time sequence of tones of different frequency (pitch) and spectral characteristics (timbre). Adapted from Ref. 115.

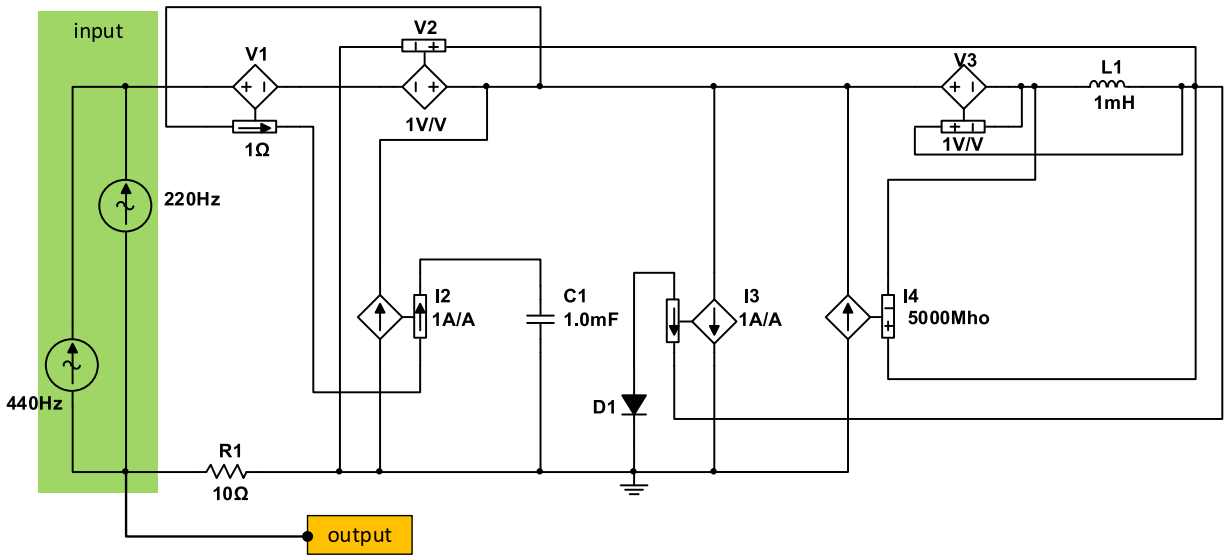

Fig. 13. (Color online) Circuit by Song et al. transforming a diode into a memristor.[120] Two sine-wave current sources are used as an input, whereas the voltage drop on resistor *R*1 is used as an output.

Helmholtz curve of sensory dissonance has been developed.[117–119]

Photoelectrochemical reservoir systems, based on wide bandgap semiconductors (neat or modified with simple coordination compounds) cannot compete with photonic devices in terms of speed or efficiency. They operate, however, in a frequency domain corresponding to the audible range. Therefore, we have turned our attention to the classification of acoustic signals. There are a plethora of different data sets that require advanced processing techniques, including ECG and EEG signals, automated speech analysis or the classification of music. We have found the latter as the most suitable one to be addressed in the photoelectrochemical system due to its internal, well-defined structure based on the Pythagorean geometry.[109,115,121]

Before the experimental verification of this idea series of numerical simulations for a simple memristive device (a memristor in series with a resistor) have been performed. As the numerical model, an example given by Song et al. was implemented in Multisim (Fig. 13), in which a nonlinear circuit element (a diode) is converted into memristor by mutator circuit based on a capacitor and an inductor connected by a series of voltage- and current-controlled voltage- and current sources.[120] It can be observed, that pure tones (single sine waves of frequencies which belong to the natural scale) yield simple memristor-like pinched hysteresis loops (Fig. 14). When a sum of two signals, which form a consonant combination (e.g. perfect octave, perfect fifth or perfect fourth) is applied to the circuit, a stable loop is observed as well, but with an increased number of lobes (Fig. 15). In the case of an interval which is considered dissonant (e.g. triton), the observed characteristics becomes quasi-random (the simulation was too short to justify if the signal is truly chaotic or not), but the trajectory is confined inside the hysteresis loop defined by the lower frequency tone [Fig. 15(c)]. Therefore, the memristor hysteresis loop can be considered as an attractor for the unstable behavior of the memristor-based circuit.

This result is fully consistent with the chaotic behavior of memristive circuits, especially the so-called Chua circuit (a double loop circuit of a memristor, resistor, and two capacitors).[122] This numerical experiment proves the utility of reservoir computing in the processing of acoustic signals, which has been recently postulated on the basis of theoretical models.[123] Surprisingly, the results are consistent with the results of neurophysiological studies on the perception of music by humans and monkeys.[124,125] In conclusion, this experiment opens a new path into a field of interdisciplinary investigations: the application of molecular systems to the analysis, in the short term, but maybe also to the creation of music in the future. This idea has been recently successfully developed by Professor Eduardo R. Miranda in a series of biocomputing experiments with *Physarum* slime mold[126–129] and follows the cross-boundary research at the interface of the information theory, music, and physical sciences.[130] The analogy between the human perception of music and the reservoir perception of simple intervals may be misleading. It does not mean that a simple reservoir is as sensitive as a human ear, but rather it may suggest that memristive systems may provide a universal problem-solving power and with appropriate operation can solve numerous problems, which cannot be easily addressed using other approaches. The combination of reservoirs with logic devices (Boolean or fuzzy) may lead to a substantial increase of complexity and computing efficiency. The first reports on practical combinations of the Boolean logic and the reservoir computing are already available.[131,132]

As a result of experiments with memristive reservoir a set of musical compositions was designed. In one of those compositions, titled *Reservoir study no. 1*, a feedback loop of a length of 555 ms was used to transform music being played by an ensemble of musicians. The process resulted in harmonic and timbral fluctuations of particular aesthetic quality. The repetitive character of those fluctuations reflects continuous processes taking place within the reservoir. It starts with short improvisations on the keyboard, followed by a slowly evolving tune with many almost identical bars—this evolution illustrates the evolution of a signal within a single node echo state machine. In the middle of the piece, the changes accumulate and trigger the reservoir to the chaotic state, which is illustrated by improvisations and a series of

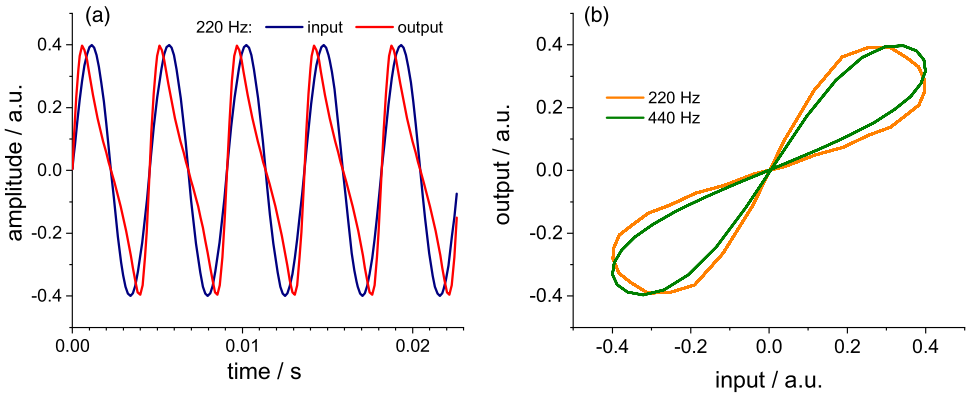

Fig. 14. (Color online) Simulated responses of a resistor-memristor circuit subjected to the voltage signal modulated with 220 Hz sine (a) and corresponding *I*–*V* (input/output) hysteresis loop for 200 and 440 Hz sine waves (b).

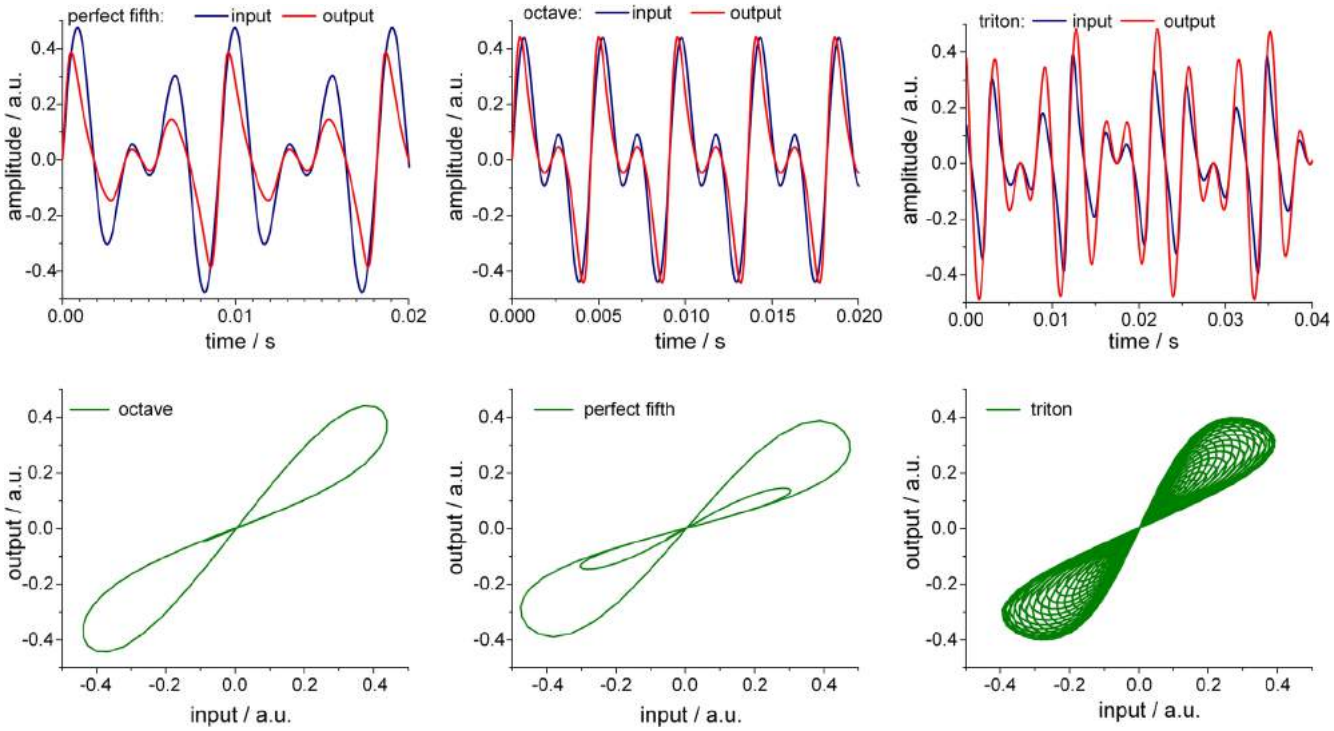

Fig. 15. (Color online) Simulated responses of a resistor-memristor circuit subjected to the voltage signal modulated with two sine waves: 220 Hz + 440 Hz [octave, (a)], 220 Hz + 330 Hz [perfect fifth, (b)] and 220 Hz + 309.375 Hz [triton, (c)].

glissandi giving an impression of musical chaos. This acoustic chaos calms down, which is a musical illustration of amplitude death in dynamic systems—a set of coupled oscillators reaches a quiet stationary state.[133] Finally, the constant pace is established again. It indicates the spontaneous rebirth of oscillations[134] which leads to final chords—a musical embodiment of the results of reservoir computation. The piece was designed, completed and performed by The Nano Consort (Konrad Szaciłowski—cello, Dawid Przyczyna, Kacper Pilarczyk—guitars, Marcin Strzelecki—keyboard, Dominika Peszko, Piotr Zieliński—piano) during concert in Krakow Opera House, September 16th, 2019 (Fig. 16, please see the supplementary video file, available online at stacks.iop.org/JJAP/59/050504/mmedia, of the world premiere recording of this composition).

5.2. Speech processing and classification

Speech recognition is a fundamental yet complex problem for AI systems of the modern era. Speech is the most common means of communication among the human race, therefore the automated speech recognition system finds numerous applications. Verbal communication is a trivial task in everyday life, but this becomes a complex phenomenon when ported to the machines. The complexity of this task originates from an extremely rich vocabulary of a single language (hundreds of thousands of words), variations of the pronunciations and dialects of the same words, and variations in a timbre, rhythm of speech and personal characteristics. The speech of children and non-native speakers adds additional complications to this already very complicated task.[135] Therefore, automated speech recognition is a complex problem in the field of artificial intelligence.[136] Software solutions include Fourier and wavelet analysis followed by artificial neural network-based classification of spectral features.[137] The most promising approach, however, is based on neuro-inspired speech recognition, involving reservoir computing.[138–140] Although there are many advances reported on this front with software simulations, the solutions are not scalable to port it to the hardware of an intelligent machine. Therefore, hardware-based

Fig. 16. (Color online) Photos taken on September 16th, 2019 during the rehearsal (left) and the world premiere (right) of Reservoir Study No. 1.

solutions based on memristors and other nonlinear elements are considered as potential candidates to embed acoustic frequency signal analysis and classification (vide supra). An addition of oscillatory characteristics (or other dynamic features) should increase the performance of the computing system based on small networks.[141,142)]

Up to now, there is only one reported experimental evidence of successful human speech recognition in a hardware system. The device reported by Romera et al.[143)] is based on four spin-torque oscillators based on the PtMn/$Co_{71}Fe_{29}$/Ru/$Co_{60}Fe_{20}B_{20}$/$Co_{70}Fe_{30}$/MgO/$Fe_{80}B_{20}$/MgO/Ta/Ru magnetic tunnel junctions fabricated by ultrahigh vacuum magnetron sputtering. The FeB layer presents a structure with a single magnetic vortex as the ground state. In a small region called the vortex core (of about 12 nm diameter at remanence for our materials), the magnetization spirals out of plane. Under direct current injection and the action of the spin transfer torques, the core of the vortex steadily gyrates around the center of the dot with a frequency in the range of 150–450 MHz for the oscillators reported in the cited paper.[143)] A set of English vowels was used as an input. Because usually the formant frequencies of a human voice are within the range of 500–3500 Hz, and the magnetic nano-oscillators have the characteristic frequencies in the MHz range, the formant frequencies were used to synthesize the pair of input signals (f_A, f_B) as linear combinations of three principal formant frequencies. These high-frequency signal I_{RFA} and I_{RFA}, calculated on the basis of 37 female voices, served as input into neuromimetic classification device [Figs. 17(a), 17(b)]. The device itself contains four oscillating magnetic tunneling junctions connected into a circuit driven with DC currents to maintain radio frequency oscillations. Microwave signals recorded as an output and used for vowel recognition [Figs. 17(d), 17(e)]. The correlation maps involving two input signal were generated [Fig. 17(f)] for various vowels represented on f_A, f_B plane [Fig. 17(g)].

The performance of this system was compared with a multilayer perceptron trained to use 12 formant frequencies. The software-based speech recognition tool, with ca. 100 trained weights yields a recognition rate of 97%. In comparison, the oscillatory network with four oscillators yields a recognition rate of 84% with 30 training parameters.

This is an impressive result taking into account a small number of control parameters, energy efficiency and a small footprint of the device: each of the spin oscillators has a diameter of ca. 375 nm. These results demonstrate, how oscillatory dynamics can improve pattern recognition, especially in the case of dynamic patterns. These types of behavior have been previously observed in other coupled oscillatory systems operating at the edge of chaos.[144,145)]

6. Transformation of signals—towards memristive cryptography

Signal and information processing involves significant security issues. From Ancient times information was considered as a high value, therefore a lot of efforts were paid to protect sensitive information. The big branch of information science is devoted to information security issues. Cryptography (from Greek *κρυπτός* "hidden, secret" and *γράφειν* "to write") is the science and technology of secure communication in the presence of adversaries trying to prevent the users from achieving privacy, integrity, and availability of data. More generally, cryptography is about constructing and analyzing protocols that prevent third parties or the public from reading private messages. Various aspects in information security such as data confidentiality, data integrity, and authentication, are central to modern cryptography.[146)]

This is especially important in the era of the Internet of Things, a ubiquitous network of transmitting, computing, storage, and information retrieval devices. Therefore, in order to provide privacy and security to the users, various cryptographic techniques are used. In currently used devices most of the solutions are software-based, but the tremendous progress in unconventional and neuromimetic *in-materio* computing creates unique cryptographic solutions. It should be noted, however, that there are no complete *in-materio* cryptographic systems up to date, but some cryptographic primitives have been already implemented or at least demonstrated in numerical models. They include random number generation, identity verification via physical unclonable functions, hashing functions and ciphering/deciphering of messages.[147)]

6.1. Chaos and random number generation

The generation of random numbers is essential for many areas of economic importance. This type of numbers is a

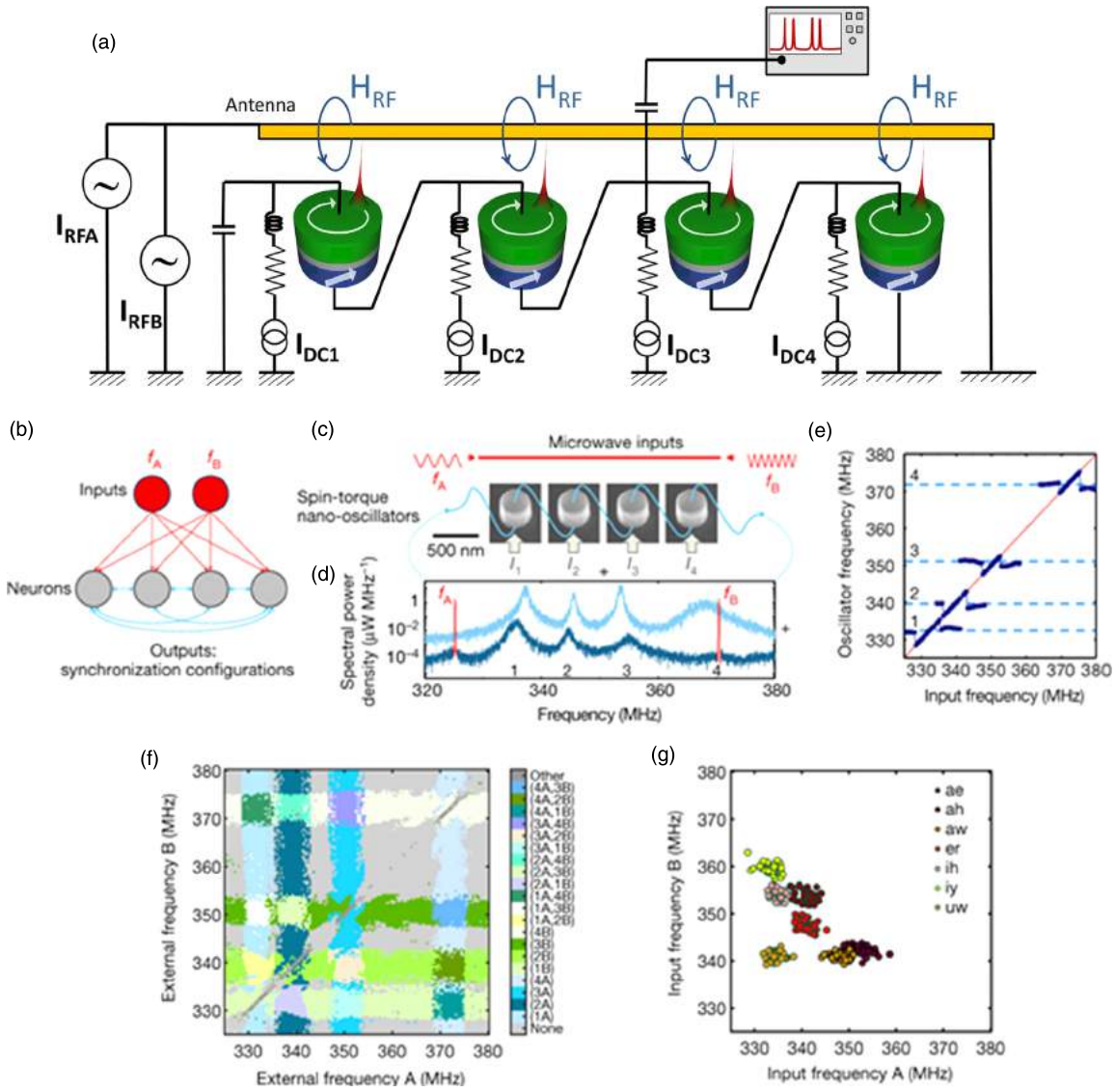

Fig. 17. (Color online) The four coupled vortex nano-oscillators. I_{RFA} and I_{RFB} are the microwave currents injected in the strip line by the two microwave sources. H_{RF} is the resulting microwave field. I_{DC1-4} are the applied direct currents (a). Scheme of the emulated neural network (b). Scheme of the experimental set-up with four spin-torque nano-oscillators electrically connected in series and coupled through their own emitted microwave currents. Two microwave signals encoding information in their frequencies f_A and f_B are applied as inputs to the system through a strip line, which translates into two microwave fields. The total microwave output of the oscillator network is recorded with a spectrum analyzer (c). Microwave output emitted by the network of four oscillators without (light blue) and with (dark blue) the two microwave signals applied to the system. The two curves have been shifted vertically for clarity. The four peaks in the light blue curve correspond to the emissions of the four oscillators. The two narrow red peaks in the dark blue curve correspond to the external microwave signals with frequencies f_A and f_B (d). Evolution of the four oscillator frequencies when the frequency of external source A is swept. One after the other, the oscillators phase-lock to the external input when the frequency of the source approaches their natural frequency. In the locking range, the oscillator frequency is equal to the input frequency (e). Experimental synchronization map as a function of the frequencies of the external signals f_A and f_B. Each color corresponds to a different synchronization state (f). Inputs applied to the system, represented in the (f_A, f_B) plane. Each color corresponds to a different spoken vowel, and each data point corresponds to a different speaker (g). Reproduced from Ref. 143 with permission of Springer Nature.

fundamental building block of many areas of science and technology—cryptography, stochastic modeling and probabilistic computation (Monte Carlo) as well as e-commerce, gambling, and finance-related areas.[148,149] These areas rely heavily on random numbers and could not function without them. For this reason, it is important to develop new technologies that allow the generation of such numbers.

Generally, random numbers used in various applications are pseudo-random. They are generated through software programs based on some mathematical formula that, if run again with the same "seed", would give the same determined output. It's clear that this is an issue, especially from the point of view of cryptography, therefore, it is important to have a reliable random number generator that will produce unique sequences in each run. Compared to software solutions, a hardware approach poses a more secure option that can act as a cryptographic key. Hardware systems for generation of random numbers are referred to as true random number generators (TRNG).[150] They are based on various physical processes, such as thermal noise,[151] photoelectric effect[152] or quantum phenomena[153] to name a few. Due to their fluctuating nature, these processes enable obtaining random numbers by digitizing generated signals. For example, thermal noise based TRNG operate through amplification of noise coming from resistors, avalanche diode or Zener diode. Another classic example is based on the nuclear decay

of radioactive atoms, which is measured by a Geiger counter attached to a PC.[154] More advanced solutions employ chaotic laser systems mounted on the optical table.[155]

Novel TRNG technologies include systems based on memristive junctions or electronic circuits coupled with memristive elements. Employment of memristive structures is beneficial from the point of view of possible integration with existing CMOS architecture as well as their fast and energy-efficient operation. Essentially, TRNG based on memristive devices employs observed intrinsic stochasticity of resistive switching related phenomena which act as an entropy source. In that regard, three main approaches are studied, namely—stochastic noise, stochastic switching time and stochastic switching voltage.[156] One of the first TRNG hardware implementations based on resistive switching was presented by Huang. et al.[157] Random telegraph noise (RTN) observed in low conductivity state of W/TiN/TiON/SiO_2/Si memristive device was used as the source of randomness. RTN is based on the random physical process of trapping/detrapping of charge carriers between e.g. defect sites in the crystal lattice. However, the received 0/1 bit distribution strongly depended on the applied potential so additional circuit elements and post-processing steps (e.g. Von Neumann correction) were necessary. On the other hand, undesirable property—from the point of view of data storage—of device-to-device and cycle-to-cycle variability of operation observed in memristive devices was used by Balatti et al. as a source of randomness.[158,159] Due to non-volatile character of Cu/AlO_x and Ti/HfO_x based memristive devices, a pair of SET/RESET voltage pulses needed to be used for generation of every bit. In both approaches cited above, additional post-processing stages were necessary to realize the true randomness of the obtained bits. Despite this fact, presented solutions failed some of the National Institute of Standards and Technology (NIST) randomness tests.[160] A slightly different approach was used by Jiang et al. to simplify the required operations hence obtainment of random bits was more straightforward.[161] In the presented research authors used the intrinsic stochasticity of the delay time in pulse-induced switching between low and high conductive states as the basis for randomness. Moreover, used memristive structure (Ag/Ag:SiO_2—operation of which is based on ionic diffusion) demonstrates volatile action in the form of self-OFF switching which reduces power consumption. The presented memristive device passed all NIST randomness tests without any post-processing. Further refinement of the concept was presented by Woo et al.[162] where stochasticity of volatile relaxation time was also used as another source of randomness (Fig. 18). What's more, operation of Pt/HfO_2/TiN memristive structure is based on electron trapping/detrapping which is generally faster and has lower power consumption in comparison to ionic diffusion mentioned *vide supra*.[163,164]

Photochromic dyes can be a platform for wetware random pattern generation. An exemplary device of this kind is based on a quartz cell (uncapped) filled with an acetone solution of a photochromic dye, e.g. 3-dihydro-1,3,3-trimethyl-8′-nitro-spiro[2H-indole-2,3′-[3 H]naphth[2,1-b][1,4]oxazine][29] or 6-morpholino-3-(4-morpholinophenyl)-3-phenyl-3H-naphtho [2,1-b]pyran.[165] The cell is illuminated at the bottom with a focused UV radiation (375 nm). Illumination induces two processes: (i) photoisomerization of colorless oxazine into colored merocyanine dye and (ii) heating of the acetone solution. The photochemical process itself is a simple photoisomerization process and does not involve any auto-catalytic step, but two simple unimolecular reactions, which, in a stirred solution easily reach the photostationary state, give rise to chaotic spectrophotometric signals. The large amplitude oscillations shown in Fig. 19 are observed only when enough (3 ml) photochromic solution is maintained in an uncapped cuvette and UV irradiation is carried out at the bottom of the solution. The oscillations are induced solely by the hydrodynamic instability of the solution, which is heated at the bottom and cooled form the surface via evaporation. The detailed analysis demonstrates positive values of the largest Lyapunov exponent ($\lambda = 0.045$), clearly indicating that the time series of the photochromic hydrodynamic oscillator are chaotic, and corresponding strange attractors with the fractal dimension $D = 10.71$.[165]

6.2. Physical unclonable functions

In the era of Internet of Things, one of the main challenges is to provide safe and reliable verification methods. During the

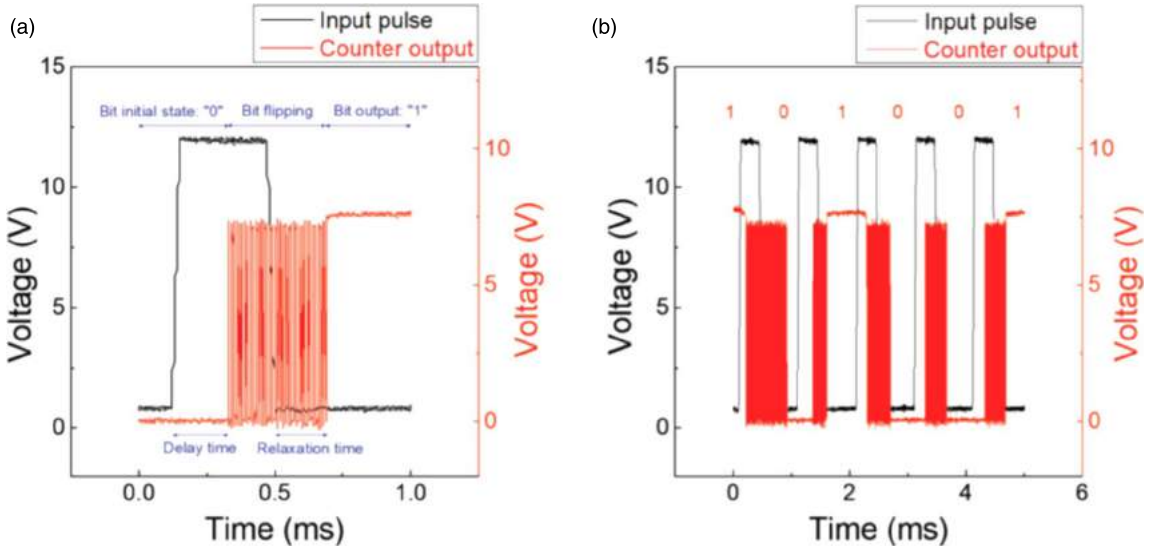

Fig. 18. (Color online) Signal registered during random number generation by Pt/HfO2/TiN memristive device for a single bit (a) and a stream of bits (b). Stochasticity of delay time, relaxation time and switching of the device ("bit flipping") are shown. Reproduced from Ref. 150 with the permission of Wiley.

recent decade, smartphones have become a universal and ubiquitous tool for a plethora of tasks, from mail and social media communication, through storage of secure information to financial operations. Since these devices often function as an authentication token for the user, the development of reliable authentication methods remains a challenging task that needs to be addressed.[166] Current authentication systems involve static random-access memory and non-volatile electrically erasable programmable read-only memories for the storage of the secret key. Unfortunately, these devices usually need to be combined with hardware encryption and/or digital signatures, which results in complex and expensive design.[167] This leads to increased manufacturing costs and high power consumption, as they demand a constant power supply.

A promising, less expensive alternative for authentication and key generation are physical unclonable functions (PUFs). In principle, PUFs can be regarded as a black-box challenge-response system which returns a response $r = f(c)$ upon inquiry of an input challenge c. For a given challenge, PUF generates a unique response. Such challenge-response pairs

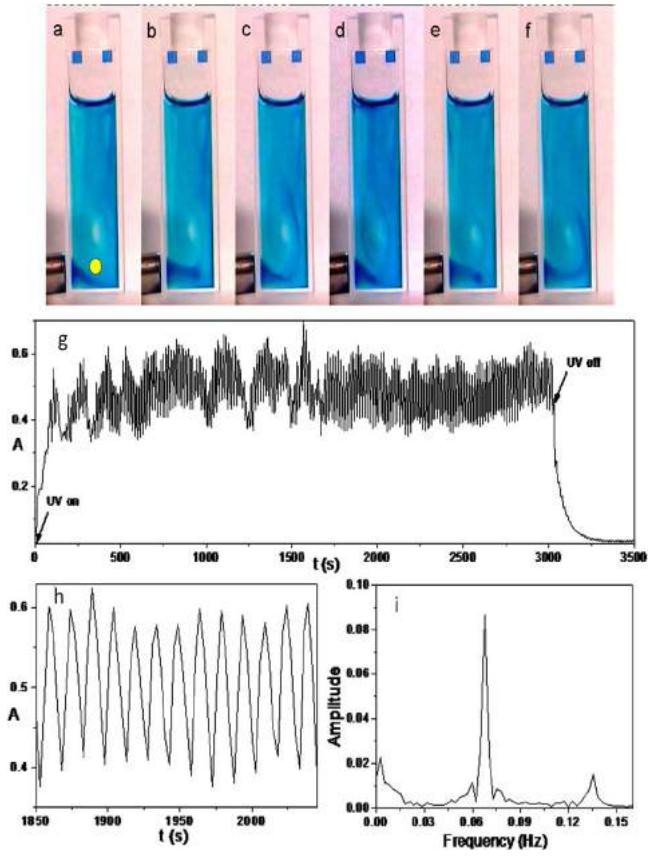

Fig. 19. (Color online) Photochromic compound (concentration $9.4 \times 10-5$ M) in methanol during the photocoloration stage. The snapshots in the first row are of the uncapped cuvette at 162 (a), 169 (b), 180 (c), 189 (d), 199 (e), and 209 s (f) after the beginning of UV irradiation. Oscillations recorded at 612 nm for the photochrome ($8.8 \times 10-5$ M) in acetone in an uncapped cuvette. Graph (g) shows the entire dynamical evolution: the first part refers to the stage of UV irradiation (UV on), whereas the second part starts when the UV is off; (h) zoom of the kinetics showing large, regular oscillations, whose Fourier spectrum (calculated between 1850 and 2045 s) is depicted in (i). Ambient conditions: $T_{initial} = 298.5$ K, $T_{final} = 298.6$ K; $P_{initial} = 967.0$ hPa, $P_{final} = 966.2$ hPa. The height of the solution was 3.10 cm at the beginning ($h_{initial}$) and 3.00 cm at the end (h_{final}) of the experiment. The yellow spot in (a) indicates the place where the absorptivity of the solution was followed spectrophotometrically. Reproduced from Ref. 29 with permission from the American Chemical Society.

(CRPs) are stored in a secure database.[168] When the response matches the input challenge, the device is authenticated. In this way, the authentication key is derived from the internal physical characteristics of the device instead of being stored in the digital memory and the constant power supply is no longer necessary.

In general, to be considered practical for hardware security applications, PUFs have to meet a few requirements.[169] First of all, the response of the device upon challenge query must be reproducible. Unlike TRNGs, the responses generated by the PUF should be very similar among many identical challenge inquiries.

Secondly, the response must be impossible to predict (or even completely random) and unique. The first demand can be satisfied with the manufacturing variability or with the innate variability of physical parameters of the devices: due to uncontrollable parameter variance during the production, the probability of producing two devices with identical authentication fingerprint is very low. Thereby, two different, but identically manufactured PUFs, while being inquired by the identical challenge will produce distinguishable responses, thus satisfying the requirement for the uniqueness.

Moreover, even with the complete knowledge of the PUF architecture, it should be impossible to reproduce the device. The "unclonability" of the function relies on the concept that it is impractical—both in the terms of costs and time—to reproduce the response of the device. Since the response function originates from the physical characteristics of the device, the out-of-control manufacturing variabilities guarantee that it is impossible to recreate the characteristics of the device even if the adversary could gain access to the device and get to know the space of CRPs.

Finally, the $f(c)$ and r should not be bound with any trivial mathematical relationship. This prevents the adversary from predicting the functionality of the PUFs based on the known response.

PUF devices have already been implemented with the use of non-volatile memories (NVMs) and memristors. In the latter devices, the information is written by changing the resistance of the memory from one state with given conductance to another. One of the mechanisms responsible for the resistive switching phenomena relies on the creation and rupture of CFs. The large concentration of defects, for example, oxygen vacancies or metallic ions injected from the active electrode, can migrate in the electric field.[170] When a positive voltage is applied to the top electrode, where the density of the defects is higher, the defects electromigrate towards the bottom electrode and change the conductivity of the device from the HRS to the LRS. When a negative voltage is applied to the electrode of the device in LRS state, the field-driven migration towards the top electrode results in resistive switching to the original HRS state.

The generation and rupture of CFs that governs the transition between states are, to some extent, stochastic. Therefore, the voltage at which the switching occurs can differ between the devices and the switching cycles. It is noteworthy that this variability does not originate solely from the manufacturing process, but is inherent in the resistive switching mechanism.[171] The switching voltage and resistance variations are the main reasons restraining memristors from their application in resistive RAMs. However, the

inability to precisely predict the current flowing through the memristors with an unknown resistive state makes them potential candidates for PUFs. One of the key requirements for PUF commercialization is a large space of the CRPs, which cannot be obtained for simple architectures relying on single elements. The amount of CPRs can be significantly increased with the PUF implementation exploiting the crossbar arrays of memristors.

The idea of crossbar array PUFs exploits the sneak-path currents, which are a result of an indirect biasing of the array elements.[168] These currents are generally highly undesirable in crossbar memristor systems for memory applications, but due to their nature can serve as a response for an input challenge. If the resistive states in the crossbar array are randomly distributed, then the output current measured upon challenge inquiry is also random. Even if the production process introduces some spatial correlation between the elements of the array, the resistive states can be randomized by one-time programming.[168]

In the crossbar implementation, the set of memristors is connected into an array with perpendicular crossbars acting as top and bottom electrodes [Fig. 20(a)]. The simplest challenge query is realized by biasing row i and column j with voltage V_C and 0, respectively, while other electrodes are left floating.[170] The output current, besides the current flowing through element G_{ij}, will also include a number of sneak-path currents, being a result of an indirect biasing the array elements at the floating electrodes [see Fig. 20(b)]. Thereby, the measured current (the response) becomes a complicated function of the voltage, current flowing through G_{ij} and the unknown conductances of neighboring array elements. This concept of the challenge inquiry can be extended to an arbitrary number of electrodes to make the response function more complex.[168] In general, such PUF can be composed of any NVM elements. However, one can benefit from memristors' nonlinear I–V characteristics to improve the PUF safety.[173,174] The unpredictable variance of physical properties in combination with the adjustable resistive states and possibility to fabricate high-dimensional stack architectures make memristors extremely promising candidates for strong PUFs.[173]

6.3. Hash functions

A hash function is a cryptographic primitive, an algorithm that maps any message of arbitrary size into a fixed size (in the terms of a number of bits) number. The hash function should be a one-way function, i.e. a function which is practically infeasible to invert. The ideal cryptographic hash function has the following main properties: (i) it is deterministic, meaning that the same message always results in the same hash; (ii) it is quick to compute the hash value for any given message; (iii) it is infeasible to generate a message that yields a given hash value; (iv) it is infeasible to find two different messages with the same hash value and finally (v) a small change to a message should change the hash value so extensively that the new hash value appears uncorrelated with the old hash value.[175]

A memristor array-based hash function has been suggested by Azriel and Kvatinsky.[176] It is based on a write disturb phenomenon, a phenomenon based on parasitic currents in memristive crossbar arrays. Such arrays suffer from sneak paths—parasitic currents through unused memory cells, which distort information during the read operation and modify unselected cells during the write operation. A secure hash function is created on the basis of the state of the whole array of memristors—all memristors contribute to the hash state. Information used to generate hash is written to some cells of the array—the addresses of these cells are computed based on the message itself and a previous state of an array. Because write disturb mitigation is implemented, during the write operation, in addition to the target cell, other cells are modified. This procedure produces a unique signature of each message, being the function of a message itself and all previous messages processes in the device.

A similar hashing protocol, yet much simpler, can be implemented in dynamic photoelectrochemical devices showing short time memory features and (preferably) nonlinear light-intensity photocurrent response. In the absence of a short memory feature, the photocurrent intensity generates at a semiconducting photoelectrode can be expressed as a function of a light flux (11):[51]

$$i_{ph}(\varphi) = i_0^A(1 - e^{-k_A\varphi(t)}) - i_0^C(1 - e^{-k_C\varphi(t)}), \tag{11}$$

where i_0^A, i_0^C are saturation currents for anodic and cathodic components (which in turn strongly and nonlinearly depend on electrode potential, and k_A, k_C are materials-dependent constants. In the simplest case saturation photocurrent intensity at applied potential U can be formulated for both cathodic and anodic component as (12):

$$i_0(\varphi) = \alpha\varphi\sqrt{\frac{2e\varepsilon\varepsilon_0}{N_D}(U - V_{\mathrm{FB}})}, \tag{12}$$

where N_D is the doping density, α is the absorption coefficient and V_{FB} is the flat band potential of the material. Application of additional charge trapping centers (e.g. carbon nanotubes, nanoparticles of different semiconducting material or conductive polymer coating) contributes to the fading memory feature with characteristic quenching constant (k_q) and corresponding memory persistence time (t_0). This leads to the final expression of the form (13):

$$i_{ph}(\varphi(t), t) = i_0^A(1 - e^{-k_A\varphi(t)})\left(1 - \int_{t-t_0}^{t} e^{-k_q\varphi(t)}dt\right) - i_0^C(1 - e^{-k_C\varphi(t)}), \tag{13}$$

where i_0 is given by the expression above. This makes the hashing unidirectional, due to the properties of the definite integral.

6.4. Memristive cryptographic systems

In common language scrambling and encryption are sometimes used as synonyms, yet one should distinguish that the latter is usually connected with digital signal processing. Analog signals data scrambler possesses intrinsic high entropy and thus generates fully random, or at least pseudo-random, outputs. As for the actual realization of the scrambling process—the original signal is modified—usually, some of its components are transposed or inverted. For the above reasons scramblers are frequently called "randomizers". The idea behind the hardware-based implementation is to replace numerically expensive hashing functions (vide cryptocurrencies and the whole electrical/numerical consumptions) with a generator based on the

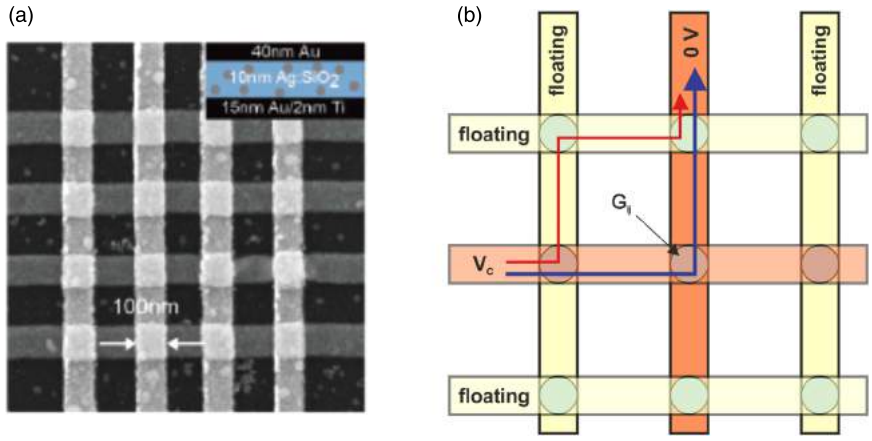

Fig. 20. (Color online) PUF implementations with a crossbar array of memristors. (a) SEM image of a 4 × 4 memristor array. (b) Schematic drawing of PUF composed of a 3 × 3 array of memristors. Upon biasing crossbars to V_C and 0 with other electrodes left floating (the challenge), the measured output current (the response) is composed of the current flowing through directly biased element G_{ij} (blue arrow) and sneak-path current (red arrow). Panel (a) was reproduced from Ref. 172 with permission from the Royal Society of Chemistry.

intrinsic discrepancies between each individual memristive pixels/cells. Such applications have been intensively studied, yet so far theoretically.[176)]

Data scrambling, despite being designed for analog signal, is also used in digitized information –consisting of many following 0 s and 1 s. Data scrambler effectively truncates the number of similar bits, making the information more light-weight. In current IT systems data scrambling functions/algorithms/concepts are also used for removing or truncating most sensitive data. Such processes are principle irreversible.

Chaotic systems can be exploited to generate apparently random sequences that serve as a basis for various cryptographic techniques.[149)] One of the applications of chaotic time series is to hide an encrypted message by mixing it with a chaotic signal.[177)] Chaotic dynamics are, by definition, aperiodic, extremely sensitive to the initial conditions, and unpredictable in the long-term.[178)] Any chaotic signal can, therefore, mask a secret message. The sender takes the message $m(t)$ and adds it to a chaotic signal $c(t)$, creating an incomprehensible secret message $s(t)$:

$$s(t) = m(t) + c(t). \tag{14}$$

Other operations convoluting messages with chaotic keys can be also used.

Any unauthorized adversary can detect only a chaotic signal, which sounds/looks like meaningless noise. With an appropriate, synchronized source of a chaotic signal, it is possible, however, to recover the initial message. Chaotic Chua oscillator and related memristive circuits generate truly chaotic time series,[9,179–182)] therefore they are proposed as novel cryptographic engines that can operate with analog (e.g. acoustic) and digital messages in real-time. The software implementation of this approach works spectacularly, especially on graphical data.[183)]

The software model of this system was checked on a famous photo of Lena Forsén, shot by photographer Dwight Hooker, cropped from the centerfold of the November 1972 issue of *Playboy* magazine (Fig. 21).[184)] A set of two synchronized chaotic oscillators provide enough security in the transmission of graphical content. Application of a simple image scrambling protocol (inverting odd lines and columns followed by column permutation) and subsequent pixel-by-pixel XOR operation with the output of Chua's memristor-based oscillator yields a chaotic "pepper-and-salt" type image. A more developed security algorithm, also based on Chua's oscillators was reported by Arpacı et al.[185)] Application of hyperchaotic oscillators and additionally, a complex scrambling algorithm provides even better data protection and additionally giver better error resistance. The efficiency of this encryption process can be illustrated by a comparison of two very different images encrypted using the same protocol and the same settings of the generator (Fig. 22).

7. Conclusions

By drawing a simple comparison between the ability to process information in silico and that by biological neuronal structures, faster does not necessarily mean better. The emergence of extraordinary performance in the pattern recognition resulting from the high complexity of the nervous system and its operation at the edge of chaos[186)] maximized our chances of survival and enabled the rise of civilization as we know today. It seems to be a natural step to draw inspiration from the neural structures and transfer their functionalities into artificial systems. The imitation of human intelligence can be achieved by pursuing the idea of implementing fuzzy logic and a complex dynamic behavior with molecules and nanoscale systems and by boosting the research line of neuromorphic engineering.

The examples presented in this paper demonstrate that both wetware and memristive hardware enable efficient computation within dynamic systems with memory. This approach seems to circumvent the problem of a von Neumann bottleneck. In classical computational systems information is stored in the memory and all calculations are done within a microprocessor, therefore constant data flow slows down computation and consumes a lot of energy. Dynamic systems (both solid-state and wetware) provide a unique opportunity of computation within memory—a novel computational paradigm, which however requires new algorithms and new system architectures.

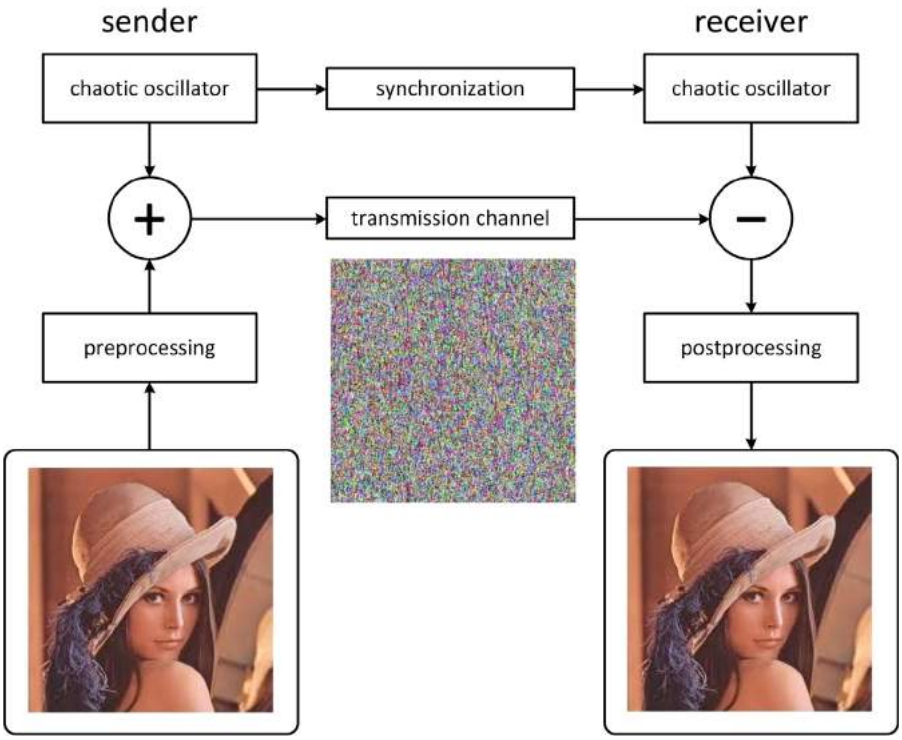

Fig. 21. (Color online) A scheme of chaotic cryptography system based on two coupled Chua chaotic oscillators. Original graphical data are taken from Ref. 183 according to the CC 4.0 license.

Fig. 22. (Color online) Demonstration of efficiency and robustness of memristor-based chaotic cryptography: two different input data (a), (c) yield very similar noise-like outputs (b), (d). The addition of extra noise to the communication channel (e) still allows a successful decoding of the message (f). Reproduced from Ref. 185 with the permission of Elsevier.

In the field of neuromorphic engineering, the exploitation of exhaustible, slow and bulky oscillatory reactions has strong limitations compared to much faster and easily scalable traditional electronic components and memristors. By implementing neuromimetic devices through unconventional chemical systems and materials, we intend to promote the development of the Chemical Artificial Intelligence (CAI).[14] The purpose of CAI is to mimic some of the

performances of the human intelligence by using not software or the conventional hardware of the electronic computers based on the von Neumann architecture, but rather unconventional chemical systems in wetware or new hardware-based on unconventional materials and phenomena.

As a far-fetched vision, we may predict that other oscillatory chemical reactions besides the BZ and the Orbán oscillators,[187] and after miniaturizing them by micro-beads, microcapsules, and compartmentalization through micelles, liposomes, and micro-emulsions,[188–190] the use of a wetware (i.e. solutions) rather than a hardware (solid state devices), and of electromagnetic radiation instead of chemicals or electrons, will bring two great benefits. First, in biological multicellular systems, which are complex out-of-equilibrium "soups" of chemicals, the phenomena of long-range coupling, mediated by diffusive chemicals, exist. Such long-range coupling phenomena, not possible in the solid state, enlarge the computing power of the whole system because they originate collective oscillations and waves. Finally, the encoding of information by UV-visible radiation will guarantee very fast propagation of messages, easy tunability of their content, and a wealthy code for futuristic brain-like computing machines. Finally, CAI will boost the development of soft robotics. Soft robots, also called "chemical robots", will be easily miniaturized and implanted in living beings.[191–193] They will interplay with cells and organelles for biomedical applications. They will become auxiliary elements of the human immune system to defeat diseases that are still incurable.

Acknowledgments

The authors thank Ewelina Wlaźlak, Andrew Adamatzky and Zoran Konkoli for numerous stimulating discussions on reservoir computing, memristive systems, unconventional computing, and signal processing. The authors acknowledge the financial support from the Polish National Science Center within the MAESTRO project (grant agreement No. UMO-2015/18/A/ST4/00058). DP and PZ have been partly supported by the EU Project POWR.03.02.00-00-I004/16.

1) R. Reis, "Challenges in the design of integrated systems for IoT," *Internet of Things. A Confluence of Many Disciplines. IFIPIoT 2019. IFIP Advances in Information and Communication Technology* (Springer, Cham), Vol. 574.
2) Y. Sun et al., arXiv:1911.11313 (2019).
3) C. S. von Bartheld, J. Bahney, and S. Herculano-Houzel, J. Comp. Neurol. **524**, 3865 (2016).
4) A. Adamatzky (ed.) *Advances in Physarum Machines. Sensing and Computing with Slime Mold* (Springer International Publishing, Cham, 2016).
5) E. M. Izhikevich, *Dynamical Systems in Neuroscience* (MIT Press, Cambridge, MA, 2007).
6) M. I. Rabinovich, P. Verona, A. I. Selverston, and H. D. I. Abarbanel, Rev. Mod. Phys. **78**, 1213 (2006).
7) L. Chua, Radioengineering **24**, 319 (2015).
8) L. O. Chua, V. Sbitnev, and H. Kim, Int. J. Bifurc. Chaos **22**, 1230011 (2012).
9) L. O. Chua, Nanotechnology **24**, 383001 (2013).
10) J.-M. Ramirez, A. K. Tryba, and F. Peña, Curr. Opin. Neurobiol. **14**, 665 (2004).
11) X. Meng, G. Huguet, and J. Rinzel, Discrete Contin. Dyn. Syst. A **32**, 2729 (2012).
12) S. A. Prescott, *Excitability: Types I, II and III* (Springer, New York, 2013) Encyclopedia of Computational Neuroscience.
13) H. Korn and P. Faure, C. R. Biol. **326**, 787 (2003).
14) P. L. Gentili, RSC Adv. **3**, 25523 (2013).
15) E. Wlaźlak, D. Przyczyna, R. Gutierrez, G. Cuniberti, and K. Szaciłowski, Jpn. J. Appl. Phys. **59**, SI0801 (2020).
16) V. Athanasiou and Z. Konkoli, *On Mathematics of Universal Computation with Generic Dynamical SystemsFrom Parallel to Emergent Computing* (CRC Press, London, 2019).
17) K. Pilarczyk, E. Wlaźlak, D. Przyczyna, A. Blachecki, A. Podborska, V. Anathasiou, Z. Konkoli, and K. Szaciłowski, Coord. Chem. Rev. **365**, 23 (2018).
18) Z. Konkoli, S. Nichele, M. Dale, and S. Stepney, *Reservoir Computing With Computational Matter in Computational Matter* (Springer, Cham, 2018).
19) Z. Konkoli, Int. J. Parallel Emergent Distrib. Syst. **33**, 121 (2018).
20) Z. Konkoli, *Reservoir Computing in Unconventional Computing. A Volume of the Encyclopedia of Complexity and Systems Science* (Springer Nature, New York, 2018).
21) V. Athanasiou and Z. Konkoli, Int. J. Parallel Emergent Distrib. Syst. **33**, 367 (2018).
22) I. R. Epstein and J. A. Pojman, *An Introduction to Nonlinear Chemical Dynamics* (Oxford University Press, New York, 1998).
23) A. T. Winfree, Science **197**, 761 (1977).
24) P. L. Gentili, V. Horvath, V. K. Vanag, and I. R. Epstein, Int. J. Uncov. Comput. **8**, 177 (2012).
25) V. Horvath, D. J. Kutner, J. T. Chavis Iii, and I. R. Epstein, Phys. Chem. Chem. Phys. **17**, 4664 (2015).
26) V. Horvath, P. L. Gentili, V. K. Vanag, and I. R. Epstein, Angew. Chem. Int. Ed. **51**, 6878 (2012).
27) A. I. Lavrova and V. K. Vanag, Phys. Chem. Chem. Phys. **16**, 6764 (2014).
28) P. L. Gentili, M. S. Giubila, R. Germani, A. Romani, A. Nicoziani, A. Spalletti, and B. M. Heron, Angew. Chem. Int. Ed. **56**, 7535 (2017).
29) P. L. Gentili, M. Dolnik, and I. R. Epstein, J. Phys. Chem. C **118**, 598 (2014).
30) K. Hayashi, H. Gotoda, and P. L. Gentili, Chaos **26**, 053102 (2016).
31) P. L. Gentili, H. Gotoda, M. Dolnik, and I. R. Epstein, Chaos **25**, 013104 (2015).
32) P. L. Gentili, M. S. Giubila, R. Germani, and B. M. Heron, Dyes Pigments **156**, 149 (2018).
33) B. Bartolomei, B. M. Heron, and P. L. Gentili, Rend. Fis. Acc. Lincei **31**, 39 (2020).
34) P. S. Katz and R. J. Calin-Jageman, *Neuromodulation* (Amsterdam, Netherlands, 2009) Encyclopedia of Neuroscience.
35) S. Gawęda, A. Podborska, W. Macyk, and K. Szaciłowski, Nanoscale **1**, 299 (2009).
36) K. Szaciłowski and W. Macyk, Comp. Rend. Chim. **9**, 315 (2006).
37) M. Hebda, G. Stochel, K. Szaciłowski, and W. Macyk, J. Phys. Chem. B **110**, 15275 (2006).
38) K. Pilarczyk, B. Daly, A. Podborska, P. Kwolek, V. A. D. Silverson, A. P. de Silva, and K. Szaciłowski, Coord. Chem. Rev. **325**, 135 (2016).
39) A. Podborska, B. Gaweł, Ł. Pietrzak, I. B. Szymańska, J. K. Jeszka, W. Łasocha, and K. Szaciłowski, J. Phys. Chem. C **113**, 6774 (2009).
40) P. Kwolek, K. Pilarczyk, T. Tokarski, J. Mech, J. Irzmański, and K. Szaciłowski, Nanotechnology **26**, 105710 (2015).
41) P. Kwolek and K. Szaciłowski, Electrochim. Acta **104**, 448 (2013).
42) K. Szaciłowski, W. Macyk, and G. Stochel, J. Am. Chem. Soc. **128**, 4550 (2006).
43) K. Szaciłowski and W. Macyk, Solid-State Electron. **50**, 1649 (2006).
44) K. Lewandowska, A. Podborska, P. Kwolek, T.-D. Kim, K.-S. Lee, and K. Szaciłowski, Appl. Surf. Sci. **319**, 285 (2014).
45) K. Lewandowska and K. Szaciłowski, Aust. J. Chem. **64**, 1409 (2011).
46) S. Gawęda, G. Stochel, and K. Szaciłowski, Chem. Asian J. **2**, 580 (2007).
47) W. Macyk, G. Stochel, and K. Szaciłowski, Chem. Eur. J. **13**, 5676 (2007).
48) J. Mech, R. Kowalik, A. Podborska, P. Kwolek, and K. Szaciłowski, Aust. J. Chem. **63**, 1330 (2010).
49) M. Warzecha, M. Oszajca, K. Pilarczyk, and K. Szaciłowski, Chem. Commun. **51**, 3559 (2015).
50) A. Blachecki, J. Mech-Piskorz, M. Gajewska, K. Mech, K. Pilarczyk, and K. Szaciłowski, Chem. Phys. Chem. **18**, 1798 (2017).
51) A. Podborska, M. Suchecki, K. Mech, M. Marzec, K. Pilarczyk, and K. Szaciłowski, Nat. Commun. **11**, 854 (2020).
52) K. Pilarczyk, A. Podborska, M. Lis, M. Kawa, D. Migdał, and K. Szaciłowski, Adv. Electron. Mater. **2**, 1500471 (2016).
53) G. Q. Bi and M. M. Poo, J. Neurosci. **18**, 10464 (1998).
54) D. O. Hebb, *The Organization of Behavior: A Neuropsychological Theory* (Wiley, New York, 1949).

55) S. Lowel and W. Singer, Science **255**, 209 (1992).
56) W. Gerstner and W. M. Kistler, Biol. Cybern. **87**, 404 (2002).
57) R. Legenstein, D. Pecevski, and W. Maass, PLoS Comput. Biol. **4**, e10000180 (2008).
58) I. R. Fiete, W. Senn, C. Z. H. Wang, and R. H. R. Hahnloser, Neuron **65**, 563 (2010).
59) D. Przyczyna, M. Lis, K. Pilarczyk, and K. Szaciłowski, Molecules **24**, 2738 (2019).
60) K. Szaciłowski, W. Macyk, and G. Stochel, J. Mater. Chem. **16**, 4603 (2006).
61) C. Rutherglen and P. Burke, Nano Lett. **7**, 3296 (2007).
62) L. A. Zadeh, *A New Direction in AI - Toward a Computational Theory of PerceptionsComputational Intelligence. Theory and Applications* (Springer, Berlin, 2001).
63) L. A. Zadeh, IEEE Comput. Intell. Mag. **3**, 11 (2008).
64) L. A. Zadeh, Inform. Control **8**, 338 (1965).
65) J. M. Mendel, Proc. IEEE **83**, 345 (1995).
66) P. L. Gentili, Int. J. Intell. Fuzzy Syst. **27**, 2137 (2014).
67) G. Paxinos and J. K. Mai, *The Human Nervous System* (Elsevier, San Diego, CA, 2004).
68) P. L. Gentili, Molecules **23**, 2074 (2018).
69) K. R. Gegenfurtner, Nat. Rev. Naurosci. **4**, 563 (2003).
70) P. L. Gentili, A. L. Rightler, B. M. Heron, and C. D. Gabbutt, Chem. Commun. **52**, 1474 (2016).
71) P. L. Gentili, A. L. Rightler, B. M. Heron, and C. D. Gabbutt, Dyes Pigments **135**, 169 (2016).
72) P. L. Gentili, Dyes Pigments **110**, 235 (2014).
73) M. Fuxreiter, Molecules **23**, 3008.
74) C. J. Jeffery, Biochem. Soc. Trans. **42**, 1679 (2014).
75) W. H. Zurek, Phys. Today **44**, 36 (1991).
76) K. Szaciłowski, Chem. Rev. **108**, 3481 (2008).
77) A. P. de Silva, *Molecular Logic-based Computation* (The Royal Society of Chemistry, Cambridge, 2012).
78) P. L. Gentili, Chem. Phys. Chem. **12**, 739 (2011).
79) P. L. Gentili, Chem. Phys. **336**, 64 (2007).
80) P. L. Gentili, J. Phys. Chem. A **112**, 11992 (2008).
81) S. Karmakar, M. Nandi, S. Mukherjee, and S. Baitalik, Inorg. Chim. Acta **454**, 76 (2017).
82) X.-Y. Xu and B. Yan, Adv. Funct. Mater. **27**, 1700247 (2017).
83) P. L. Gentili, Phys. Chem. Chem. Phys. **13**, 20335 (2011).
84) D. Bhattacharjee, W. Kim, A. Chattopadhyay, R. Waser, and V. Rana, Sci. Rep. **8**, 8 (2018).
85) S. Westerlund, Phys. Scr. **43**, 174 (1991).
86) K. Biswas, G. Bohannan, R. Caponetto, A. M. Lopes, and J. A. T. Machado, *Fractional Order Devices* (Springer Nature, Cham, 2017).
87) J. A. Tenreiro Machado and A. M. Lopes, Comm. Nonlinear Sci. Num. Simul. **70**, 343 (2019).
88) G. Z. Cohen, Y. V. Pershin, and M. Di Ventra, Appl. Phys. Lett. **100**, 133109 (2012).
89) C. K. Alexander, *Fundamentals of Electric Circuits* (McGraw-Hill, New York, 2009).
90) E. N. Oskoee and M. Sahimi, Phys. Rev. E **83**, 031105 (2011).
91) S. Majzoub, A. Elwakil, C. Psychalinos, and B. Maundy, AEU Int. J. Electron. Commun. **111**, 152923 (2019).
92) A. V. Avizienis, H. O. Sillin, C. Martin-Olmos, H. H. Shieh, M. Aono, A. Z. Stieg, and J. K. Gimzewski, PLoS One **7**, e42772 (2012).
93) E. Wlaźlak, M. Marzec, P. Zawal, and K. Szaciłowski, ACS Appl. Mater. Interfaces **11**, 17009 (2019).
94) E. Wlaźlak, P. Zawal, and K. Szaciłowski, ACS Appl. Electron. Mater. **2**, 329 (2020).
95) Z. Xiao and J. Huang, Adv. Electron. Mater. **2**, 1600100 (2016).
96) S. Saïghi et al., Front. Neurosci. **9** (2015).
97) F. Alibart, S. Pleutin, O. Bichler, C. Gamrat, T. Serrano-Gotarredona, B. Linares-Barranco, and D. Vuillaume, Adv. Funct. Mater. **22**, 609 (2012).
98) W. He, K. Huang, N. Ning, K. Ramanathan, G. Li, Y. Jiang, J. Sze, L. Shi, R. Zhao, and J. Pei, Sci. Rep. **4**, 4755 (2014).
99) C. Du, W. Ma, T. Chang, P. Sheridan, and W. D. Lu, Adv. Func. Mater. **25**, 4290 (2015).
100) A. Kirkwood, M. G. Rioult, and M. F. Bear, Nature **381**, 526 (1996).
101) A. S. Sokolov, Y.-R. Jeon, S. Kim, B. Ku, and C. Choi, NPG Asia Mater. **11**, 5 (2019).
102) M. A. Keane, J. R. Koza, and M. J. Streeter, Nature **453**, 80 (2016).
103) Y. Chen, G. Liu, C. Wang, W. Zhang, R.-W. Li, and L. Wang, Mater. Horiz. **1**, 489 (2014).
104) S. N. Truong, S.-J. Ham, and K.-S. Min, Nanoscale Res. Lett. **9**, 629 (2014).
105) T. Mazur, P. Zawal, and K. Szaciłowski, Nanoscale **11**, 1080 (2019).
106) G. Tanaka, T. Yamane, J. B. Heroux, R. Nakane, N. Kanazawa, S. Takeda, H. Numata, D. Nakano, and A. Hirose, Neural Netw. **115**, 100 (2019).
107) G. Tanaka, R. Nakane, T. Yamane, S. Takeda, D. Nakano, S. Nakagawa, and A. Hirose, *Waveform Classification by Memristive Reservoir ComputingNeural Information Processing* (Springer, Cham, 2017) Vol. 4.
108) D. E. Brown, *Human Universals* (McGraw-Hill, New York, 1991).
109) J. G. Roederer, *The Physics and Psychophysics of Music* (Springer, New York, 2008).
110) G. Mazzola, M. Mannone, Y. Pang, M. O'Brien, and N. Torunski, *All About Music. The Completye Ontology: Realities, Semiotics, Communication and Embodiment* (Springer Nature, Cham, 2016).
111) S. Brown and J. Jordania, Psychol. Music **41**, 229 (2011).
112) J. Demers, *Listening through the Noise. The Aesthetics of RExperimental Electronic Music* (Oxford University Press, New York, 2010).
113) E. Priest, *Boring Formless Nonsense. Exprimetal Music and the Aesthetics of Future* (Bloomsbury, New York, 2013).
114) D. Daniels and I. Arms (ed.) *Sounds Like Silence: John Cage 4′33″* (Spector Books, Leipzig, 2018).
115) D. Paret and S. Sibony, *Musical Techniques* (Wiley, Hoboken NJ, 2017).
116) W. A. Sethares, *Tuning, Timbre, Spectrum, Scales* (Springer, London, 2005).
117) K. J. Hsu and A. J. Hsu, Proc. Natl. Acad. Sci. **87**, 938 (1990).
118) M. J. Tramo, P. A. Cariani, B. Delgutte, and L. D. Braida, Ann. N.Y. Acad. Sci. **930**, 92 (2001).
119) R. Parncutt and G. Hair, J. Interdisc. Music. Studies **5**, 119 (2011).
120) D. Song, X. Ren, M. Lv, M. Li, H. Zhou, and Y. Zu, J. Comput. Commun. **1**, 5 (2013).
121) G. T. Toussaint, *The Geometry of Music. What Makes a "Good" Rhythm Good?* (CRC Press, Boca Raton, FL, 2013).
122) A. I. Ahamed, K. Srinivasan, K. Murali, and M. Lakshaman:, Int. J. Bifurc. Chaos **21**, 737 (2011).
123) L. Keuninckx, J. Danckraert, and G. Van der Sande, Cogn. Comput. **9**, 315 (2017).
124) Y. I. Fishman, I. O. Volkov, M. D. Noh, C. Garell, H. Bakken, J. C. Arezzo, M. A. Howard, and M. Steinschneider, J. Neurophysiol. **86**, 2761 (2001).
125) G. M. Bidelman and A. Krishnan, J. Neurosci. **29**, 13165 (2009).
126) E. R. Miranda and E. Braund, *Experiments in Musical Biocomputing: Towards new kinds of Processor for Audio and MusicAdvances in Unconventional Computing. Prototypes, Models and Algorithms* (Springer, Cham, 2017) Vol. 2.
127) E. R. Miranda and E. Braund, Symmetry Cult. Sci. **28**, 7 (2017).
128) E. Braund and E. R. Miranda, J. Bionic Eng. **14**, 151 (2017).
129) E. R. Miranda, A. Adamatzky, and J. Jones, J. Bionic Eng. **8**, 107 (2011).
130) E. R. Miranda, *Guide to Unconventional Computing for Music* (Springer, Berlin, 2017).
131) N. D. Haynes, M. C. Soriano, D. P. Rosin, I. Fischer, and D. J. Gauthier, Phys. Rev. E **91**, 020801(R) (2015).
132) M. C. Soriano, S. Ortín, L. Keuninckx, and L. Appelant, IEEE Trans. Neural Networks **26**, 388 (2015).
133) G. Saxena, A. Prasad, and R. Ramaswamy, Phys. Rep. **521**, 205 (2012).
134) H. Onuma, A. Okubo, M. Yokokawa, M. Endo, A. Kurihashi, and H. Sawahata, J. Phys. Chem. A **115**, 14137 (2011).
135) H. K. Kim, M. Kim, and Y. R. Oh, *Non-Native Pronunciation Variation Modeling for Automatic Speech RecognitionAdvances in Speech Recognition* (IntechOpen, London, 2010).
136) M. A. Rafique, B. G. Lee, and M. Jeon, Electron. Lett **52**, 1428 (2016).
137) M. H. Farouk, *Application of Wavelets in Speech Processing* (Springer Nature, Cham, 2018).
138) D. Verstraeten, B. Schrauwen, and D. Stroobandt, "Reservoir-based techniques for speech recognition," Proc. 2006 IEEE Int. Joint Conf. on Neural Networks Vancouver, 2006.
139) F. A. Araujo et al., Sci. Rep. **10**, 328 (2020).
140) A. Ghani, T. M. McGinnity, L. Maguire, L. McDaid, and A. Belatreche, *Neuro-Inspired Speech Recognition Based on Reservoir Computing Advances in Speech Recognition* (IntechOpen, London, 2010).
141) H. Jaeger and H. Haas, Science **304**, 78 (2004).
142) M. Lukoševičius and H. Jaeger, Comput. Sci. Rev. **3**, 127 (2009).
143) M. Romera et al., Nature **563**, 230 (2018).
144) V. K. Vanag, Chaos **29**, 033106 (2019).
145) K. Srinivasen, I. Tiwari, and P. Parmananda, Europhys. Lett. **123**, 60003 (2018).

146) J. van Leeuwen, *Handbook of Theoretical Computer Science* (MIT Press, Cambridge, MA, 1994).
147) A. P. James, Eur. Phys. J.: Spec. Top. **228**, 2301 (2019).
148) M. Stipčević and Ç. K. Koç, *True Random Number Generators in Open ProblemsMathematics and Computational Science* (Springer, Cham, 2014).
149) L. Kocarev and S. Lian, *Chaos-Based Cryptography* (Springer, Berlin, 2011).
150) V. Fischer and M. Drutarovský, "True random number generator embedded in reconfigurable hardware," Proc. Int. Workshop on Cryptographic Hardware and Embedded Systems, 2002 (Berlin).
151) M. Bucci, L. Germani, R. Luzzi, A. Trifiletti, and M. Varanonuovo, IEEE Trans. Comput. **52**, 403 (2003).
152) M. Stipčević and B. M. Rogina, Rev. Sci. Instrum. **78**, 045104 (2007).
153) A. Stefanov, N. Gisin, O. Guinnard, L. Guinnard, and H. Zbinden, J. Mod. Opt. **47**, 595 (2000).
154) Y. Yoshizawa et al., J. Jpn. Soc. Comp. Statist. **12**, 67 (1999).
155) A. Argyris, S. Deligiannidis, E. Pikasis, A. Bogris, and D. Syvridis, Opt. Express **18**, 18763 (2010).
156) R. Carboni and D. Ielmini, *Applications of Resistive Switching Memory as Hardware Security Primitive Applications of Emerging Memory Technology* (Springer, Berlin, 2020).
157) C.-Y. Huang, W. C. Shen, Y.-H. Tseng, Y.-C. King, and C.-J. Lin, IEEE Electron Device Lett. **33**, 1108 (2012).
158) S. Balatti, S. Ambrogio, Z. Wang, and D. Ielmini, IEEE J. Emerg. Sel. Top. Curcuits Syst. **5**, 214 (2015).
159) S. Balatti, S. Ambrogio, R. Carboni, V. Milo, Z. Wang, A. Calderoni, N. Ramaswamy, and D. Ielmini, IEEE Trans. Electron Devices **63**, 2029 (2016).
160) A. Rukhin, J. Soto, J. Nechvatal, M. Smid, and E. Barker, NIST Special Publication 800-22.Rev.1a, 2001.
161) H. Jiang, D. Belkin, S. E. Savel'ev, S. Lin, Z. Wang, Y. Li, S. Joshi, R. Midya, C. Li, and M. Rao, Nat. Commun. **8**, 1 (2017).
162) K. S. Woo, Y. Wang, J. Kim, Y. Kim, Y. J. Kwon, J. H. Yoon, W. Kim, and C. S. Hwang, Adv. Electron. Mater. **5**, 1800543 (2019).
163) J. H. Yoon, K. M. Kim, S. J. Song, J. Y. Seok, K. J. Yoon, D. E. Kwon, T. H. Park, Y. J. Kwon, X. Shao, and C. S. Hwang, Adv. Mater. **27**, 3811 (2015).
164) J. J. Yang, D. B. Strukov, and D. R. Stewart, Nat. Nanotechnol. **8**, 13 (2013).
165) P. L. Gentili, M. S. Giubila, and B. M. Heron, ChemPhysChem **18**, 1831 (2017).
166) M. Uddin, A. S. Shanta, M. B. Majumder, M. S. Hasan, and G. S. Rose, Memristor Crossbar PUF based Lightweight Hardware Security for IoT in Proc. IEEE Int. Conf. on Consumer Electronics (ICCE), 2019 (Las Vegas).
167) C. Herder, M. D. Yu, F. Koushanfar, and S. Devadas, Proc. IEEE **102**, 1126 (2014).
168) L. Gao, P. Y. Chen, R. Liu, and S. Yu, IEEE Trans. Electron Devices **63**, 3109 (2016).
169) R. Carboni and D. Ielmini, *Applications of Resistive Switching Memory as Hardware Security PrimitiveApplications of Emerging Memory Technology* (Springer, Singapore, 2020).
170) D. Ielmini and H.-S. P. Wong, Nat. Electron. **1**, 333 (2018).
171) A. Chen, IEEE Electron Device Lett. **36**, 138 (2015).
172) R. Zhang, H. Jiang, Z. R. Wang, P. Lin, Y. Zhuo, D. Holcomb, D. H. Zhang, J. J. Yang, and Q. Xia, Nanoscale **10**, 2721 (2018).
173) H. Nili, G. C. Adam, B. Hoskins, M. Prezioso, J. Kim, M. R. Mahmoodi, F. M. Bayat, O. Kavehei, and D. B. Strukov, Nat. Electron. **1**, 197 (2018).
174) Y. Gao, D. C. Ranasinghe, S. F. Al-Sarawi, O. Kavehei, and D. Abbott, Sci. Rep. **5**, 12785 (2015).
175) S. Al-Kuwari, J. H. Davenport, and R. J. Bradford, Crypt. Eprint. Arch. 565 (2011).
176) L. Azriel and S. Kvatinsky, "Towards a memristive hardware secure hash function (MemHash)," Proc. IEEE Int. Symp. on Hardware Oriented Security and Trust (HOST), 2017 (Mclean).
177) K. M. Cuomo and A. V. Oppenheim, Phys. Rev. Lett. **71**, 65 (1993).
178) P. L. Gentili, *Untangling Complex Systems. A Grand Challenge for Science* (CRC Press, Boca Raton, FL, 2018).
179) Y. Tao, W. Chai Wah, and L. O. Chua, IEEE Trans. Circ. Syst. **44**, 469 (1997).
180) T. Matsumoto, L. Chua, and M. Komuro, IEEE Trans. Circuits Syst. **32**, 797 (1985).
181) L. Pivka, C. W. Wu, and A. Huang, J. Franklin Inst. **331**, 705 (1994).
182) P. Deregel, J. Circuits Syst. Comput. **3**, 309 (1993).
183) A. S. Andreatos and A. P. Leros, J. Eng. Sci. Technol. Rev. **6**, 90 (2013).
184) D. Hooker, *Playboy Magazine* **19/11**, centerfold (1972).
185) B. Arpacı, E. Kurt, and K. Çelik, Eng. Sci. Technol. Int. J. (2019).
186) M. G. Kitzbichler, M. L. Smith, S. R. Christensen, and E. Bullmore, PLoS Comput. Biol. **5**, e1000314 (2009).
187) P. L. Gentili and J.-C. Micheau, J. Photochem. Photobiol. C100321 (2019).
188) M. M. Hanczyc, S. M. Fujikawa, and J. W. Szostak, Science **302**, 618 (2003).
189) M. M. Hanczyc, T. Toyota, T. Ikegami, N. Packard, and T. Sugawara, J. Am. Chem. Soc. **129**, 9386 (2007).
190) J. Čejková, T. Banno, M. M. Hanczyc, and F. Štěpánek, Artif. Life **23**, 528 (2017).
191) M. Hagiya, A. Konagaya, S. Kobayashi, H. Saito, and S. Murata, Acc. Chem. Res. **47**, 1681 (2014).
192) H. Hess and J. L. Ross, Chem. Soc. Rev. **46**, 5570 (2017).
193) S. Kassem, A. T. L. Lee, D. A. Leigh, A. Markevicius, and J. Solà, Nat. Chem. **8**, 138 (2016).

Dawid Przyczyna is a Ph.D. candidate conducting his research at the Academic Center of Materials and Nanotechnology, AGH. In previous years he has conducted research on solid electrolytes for lithium-ion batteries, on the basis of which he received a master's degree. Currently he has changed his scientific interests and mainly deals with unconventional computation, neuromorphic engineering, and memristive devices.

Piotr Zawal is a Ph.D. candidate in physics at AGH University of Science and Technology in Krakow. He received his M.Sc. degrees in Chemistry and Nanotechnology from Jagiellonian University in 2016, working on photocatalysis and optical magnetometry. His current research interests focus is on the investigation of artificial synapses and optoelectronic devices based on hybrid perovskites.

Tomasz Mazur obtained his Ph.D. in 2015 (Jagiellonian University, Krakow, Poland), then moved, as a postdoctoral researcher, to UNIST (Ulsan, Republic of South Korea). Currently he works at AGH, Krakow, Poland where he develops memristive material information processing systems. His research is focused on perovskite-based neuromimetic devices, alongside with flexible electronics.

Marcin Strzelecki is a music theorist and composer, instrumentalist, digital media artist, and music critic. Associated with the Academy of Music in Krakow, where he lectures on contemporary music analysis and advanced techniques of musical composition, in particular computer-assisted composition. He collaborates with the Krakow Academy of Fine Arts, leading projects related to "sound art" and sound installations. As a music theorist, he conducts empirically oriented research on the foundations of musical creativity, such as cognitive and acoustic limitations, using advanced information processing techniques. Recently, his research concerns the perception of musical harmony and timbre, music stylometry and artificial intelligence techniques used in composing music.

Pier Luigi Gentili received his Ph.D. in Chemistry from the University of Perugia in 2004. His research and teaching activities are focused on Complex Systems. He is author of the book titled "Untangling Complex Systems: A Grand Challenge for Science" published by CRC Press in 2018. He trusts in the research line of Natural Computing for understanding Complex Systems. He is using Systems Chemistry to mimic some performances of human intelligence and develop Chemical Artificial Intelligence (CAI). He has several collaborations and work experience in many laboratories, such as the "Photochemistry and Photophysics Group" of the University of Perugia (Italy); the "Nonlinear Dynamics Group" of the Brandeis University (USA); the "European Laboratory of Nonlinear Optics" in Florence (Italy); the "Center for Photochemical Sciences" of the Bowling Green State University (USA); the "Laboratory of Computational Chemistry and Photochemistry" of University of Siena (Italy).

Konrad Szaciłowski graduated from the Faculty of Chemistry, Jagiellonian University (Kraków, Poland) in 1995 (M.Sc.) and 2000 (Ph.D.). After habilitation (2008) he has moved from Jagiellonian University to AGH University of Science and Technology. Now he is a group leader at the Academic Center of Materials and Nanotechnology. His initial interest in photochemistry and spectroscopy of coordination compounds has gradually evolved towards molecular and nanoscale logic devices and finally towards unconventional computing. At the moment his main research interests encompass the design of inorganic materials for memristive applications, mimicking of neutral and synaptic processes in inanimate systems, reservoir computing and relations of musical harmony with other fields of science. He is an author of the book "Infochemistry: Information processing at nanoscale" (Wiley 2012) and numerous papers in fields of coordination chemistry, material science, spectroscopy, catalysis, and electrochemistry. In his free time he enjoys classical music, philately and single malts from Islay and Speyside.

https://doi.org/10.1142/9789811235740_0001

Chapter 1

From Oscillatory Reactions to Robotics: A Serendipitous Journey Through Chemistry, Physics and Computation

Maria Lis*, Shu Onuma†, Dawid Przyczyna*,‡, Piotr Zawal*,‡, Tomasz Mazur*, Kacper Pilarczyk*, Pier Luigi Gentili¶, Seiya Kasai† and Konrad Szaciłowski*

*Academic Centre for Materials and Nanotechnology, AGH University of Science and Technology, Kraków, Poland

†Research Center for Integrated Quantum Electronics and Graduate School of Information Science and Technology, Hokkaido University, Sapporo, Japan

‡Faculty of Physics and Applied Computer Science, AGH University of Science and Technology, Kraków, Poland

¶Department of Chemistry, Biology, and Biotechnology, University of Perugia, Perugia, Italy

The continuous search for more efficient and energy-effective computing technologies drives researchers into various fields, seemingly not related to computing at all. It turns out, however, that system dynamics is the powerful computational medium, irrespectively of the physical nature of the system itself. This review presents a *potpourri* of systems and devices which share the common feature — they evolve in time, respond to the external signals and are thus suitable for information processing. It makes them useful for computational purposes and even for such demanding applications as autonomous robotics.

Det er vanskeligt at spå, især når det gælder Fremtiden
Karl Kristian Vilhelm Steincke (1880–1963)

1.1. Introduction

Modern society is mostly driven by information. Entering the era of Big Data and the Internet of Things created the need for fast and energy-efficient devices for information acquisition, transmission, processing, and storage. Information storage and processing is, however, an extremely energy-demanding task. In 2016, data centers all over the world were estimated to have consumed over 416 TWh of electric energy, more than the United Kingdom during the same period (300 TWh).[1] It can be estimated that ca 3.2% of total anthropogenic emission of carbon dioxide is a result of high performance computation. It should also be noted that the amount of energy consumed by supercomputing centres doubles every four years. This fact makes the search for novel, bioinspired and energy-efficient computing a socially and environmentally important field.

On the other hand, Nature has created an extremely complex and energy-efficient computing system based on wetware: a human brain. It comprises ca. 10–20 billion neurons in the cerebral cortex and additionally 55–70 billion neurons in the cerebellum.[2] The structural complexity is a result of a large number of connections between neurons: up to 10^4 synaptic connections with other neurons for each neuron. Therefore, the network with 9×10^{10} nodes with 4×10^{14} dynamically weighted links is an uncopiable system, and despite great efforts with still unknown structure and capabilities.[3] This amazing structure gives us creativity and intelligence. It also stimulates research of computing systems that mimic some odbrain's functionalities, like speech or face recognition. This is a domain of *artificial intelligence* (AI).

Most software and hardware AI implementations try to mimic the complexity of nervous systems using digital (binary) and rigorously deterministic algorithms, which is just a next step in the development of classical Turing machine.[4] Artificial systems (hopefully) lack creativity, their goals are formulated by humans and embedded in hardware and/or software. Despite the fact that the development of a truly creative AI is usually likened to Pandora's box, as can be seen in catastrophic science-fiction movies, there is an ongoing

intense research in this field. The concepts of AI have also cross-fertilized other fields of science, including chemistry and material science. As a result, *molecular logic*,[5–10] *molecular computing*,[11,12] *unconventional computing*[13,14] and *in-materio computing*[15] have emerged as independent — but partially overlapping — fields of research.

In materio computing can in principle use any kind of material, provided it shows some responsiveness to external stimuli, nonlinear properties, memory features, and internal dynamics.[15] The computational efficiency of the material and complexity of problems that it can solve depend on the properties of the material under study. The most interesting are materials called by E.W. Plummer *schizophrenic* — materials that develop a multitude of different "personalities" upon physical stimulation. More technically, computational materials should have numerous ground states of different properties (optical, electrical) and the material should be easily switched from one state to the other.[16] Very similar requirements are posed for materials applied in soft robotics,[17] and more interestingly, some soft robotic materials and structures can be directly used as a computational medium.[18–21] In this context materials and systems with internal dynamics (*e.g.*, chemical oscillators) seem to be of special interest.[22,23]

The key concept in neuromorphic and unconventional information processing is dynamics. Neural systems of human and animals are usually understood as an extremely complex system of partially coupled oscillators.[24,25] To make the whole system more convoluted, these oscillators, depending on their own history and the environment, may enter numerous distinct oscillatory modes.[26] Therefore, dynamic systems are considered as the most promising unconventional computing platform.[27–30] One of the unconventional computing paradigms — *reservoir computing* — very naturally exploits extensively dynamic features of various physical systems.[31–33] Quite unexpectedly, reservoir computing, despite its complexity and inherent difficulties in construction of efficient reservoirs became a field of vigorous studies. Nobody expected reservoir computing![34] Dynamics

of complex systems is also naturally associated with delayed feedback, which originated from a finite velocity of signal propagation or processing. This delay can be understood as a form of memory of a dynamic system (1.1)[35]:

$$\frac{dx}{dt} = f\left(x\left(t\right), x\left(t-\tau\right)\right) \tag{1.1}$$

where f denotes a nonlinear function and τ is the delay time. Because the current state of the system, that is, $x\left(t_0\right)$, depends on its own history, this dynamics in many cases can be controlled and harnessed for computing.[33]

The chapter focuses on computational properties of switchable materials (applied, e.g., in memristors) as well as oscillatory systems (chemical and electrochemical oscillators), especially in the context of reservoir computing (single node echo state machines) for sensing, signal processing, control, and autonomous robotics applications.

1.2. Systems Dynamics as a Computational Platform

Human intelligence emerges from the complex structural and dynamical features of our nervous system. The cellular building blocks of our nervous system are neurons. The ultimate computational power of our nervous system relies on the neural dynamics and the behavior of neural networks.[36] Every neuron is a nonlinear dynamic system.[24,37] Neurons can work in the either oscillatory, chaotic, or excitable regime. Every neuron responds to inputs by changing the value of its transmembrane potential. When a neuron is at rest, it usually has a negative transmembrane potential. The neuron is said to be hyperpolarized. If it receives inhibitory signals, the transmembrane potential becomes more negative, that is, the degree of hyperpolarization increases. On the other hand, if the neuron receives excitatory signals, its transmembrane potential becomes less negative, and the neuron depolarizes. When the excitatory signal is so strong that the transmembrane potential reaches a threshold value, then, the neuron fires an action potential. An action potential is a swift modification of the transmembrane potential of the neuron, which, at first, jumps from a negative to a positive value

(the neuron depolarizes), and then, becomes negative again (the neuron restores the hyperpolarization state) in a few milliseconds. The action potential propagates through the axon of the neuron as an electrochemical wave,[38] until it reaches the synapses of the neuron where it is transduced in chemical signals. The chemical signals are the neurotransmitters that are released to the dendrites of other connected neurons. A neuron in oscillatory or chaotic regime fires action potentials periodically or chaotically, respectively. A neuron in the excitable regime can show three types of response: type I, II, and III. Under a constant excitatory input, type I and type II excitable neurons are capable of spiking repetitively across a broad range of frequencies depending on the intensity of the input. Type I (5–150 spikes/s) and type II (75–150 spikes/s) neurons are said to have "tonic" excitability. Type III excitability is said to be "phasic" because it responds with an analog signal without firing action potentials, unless it receives an extreme and short excitation. Phasic excitable neurons are particularly useful to encode the occurrence and time of rapid change in the stimulus. They can perform coincidence detection, as for inputs from two ears, with extraordinary, submillisecond, temporal precision. The computational power of neural networks hinges on the synchronization phenomena the neurons can originate.

Development of alternative computing approaches requires exploration of various dynamic systems, harnessing their nonlinearity and exploration of memory features. Next step involves development of computing planform using various materials and substrates and exploring various physical phenomena. Up to now the material criteria for the best alternative computing system are not known, however the exploitation of nonlinearity and dynamics point towards reservoir computing as a paradigm of choice. Unfortunately, the generalized design principles for reservoirs are still lacking.[39] Therefore, software reservoirs are usually optimized by brute force search,[40] whereas *in materio* implementations require trial-and-error selection of materials and device configurations followed by laborious manual tuning. Fortunately, some tools to evaluate the performance of reservoirs have been developed. They include measures of their

nonlinearity, Lyapunov stability, computational capacity, and fading memory.[39,41–45]

There exist chemical systems in liquid solutions, which can mimic all the possible dynamics of neurons. Examples of these systems are the well-known Belousov–Zhabotinsky reaction,[46,47] the Orbán reaction, the photochromic and luminescent compounds, in the presence or not of convective motions of the solvent.[48,49] The information is encoded through the intensities and the spectral compositions of the lights they transmit and/or emit.[50]

Other examples of systems which possess a great neuromimetic potential can be found among the electrochemical oscillators. Probably the best known electrochemical oscillator is the mercury beating heart — a spectacular experimental demonstration of periodic oscillations of liquid mercury contacted with oxidizing electrolyte. The first works in this field have been reported over two centuries ago independently by Alessandro Volta and William Henry,[51] whereas the first more detailed study on this phenomenon was reported by Friedlib Ferdinand Runge.[52] Other well-known electrochemical oscillatory systems have been reported by Koper[53] and Lev.[54] The indium/thiocyanate electrochemical oscillator is based on reduction of indium(III) by thiocyanate, which is affected by the potential applied to the electrode.[53] Furthermore, this oscillator has an interesting feature — mix-mode oscillation and "chaotic" regions which can be found in biological systems as was mentioned earlier in this work.

Since their discovery in the eighteenth century, enormous progress has been made not only in understanding their chemical nature processes and their nonlinear dynamics.[55,56] These systems are also postulated as computing[27] and decoding systems.[57] Although the appearance of oscillations in electrochemical systems may have different origins, the presence of coupling between reactive sites[58] allows us to consider electrochemical oscillators as a future platform for artificial neuromimetic systems and devices. Furthermore, related phenomena are considered as a soft robotic platform[59] with embedded intelligence[60] and has already been used for control of robots.[61]

1.2.1. *Wet oscillating systems*

The Belousov–Zhabotinsky (BZ) reaction is an oxidative bromination of malonic acid in aqueous acidic solution (1.2).

$$2\mathrm{BrO}^{-}_{3(\mathrm{aq})} + 3\mathrm{CH}_2(\mathrm{COOH})_{2(\mathrm{aq})} + 2H^{+}_{(\mathrm{aq})} \rightarrow 2\mathrm{BrCH}(\mathrm{COOH})_{2(\mathrm{aq})} + 3\mathrm{CO}_{2(\mathrm{g})} + 4\mathrm{H}_2\mathrm{O}_{(l)} \quad (1.2)$$

It is catalyzed by various metal ions or metal-complexes. Examples are cerium ions, tris-(1,10-phenanthroline)-iron(II) (ferroin) and tris(2,2′-bipyridyl)ruthenium(II), $[\mathrm{Ru(bpy)_3}]^{2+}$. When the cerium ions are selected, the BZ originates periodic large transmittance oscillations in the UV. In the presence of ferroin, the color of the solution changes periodically from blue to red and back to blue. Finally, with $[\mathrm{Ru(bpy)_3}]^{2+}$, the BZ seesaws from orange to green and back to orange, and it emits periodic luminescent flashes of red light. Furthermore, in the presence of $[\mathrm{Ru(bpy)_3}]^{2+}$, the BZ reaction is photosensitive to both the UV and the blue-green lights.[62] Recently, the ferroin-based BZ system has been reported to respond to white[63] and green[61] light.

The Orbán reaction is an oxidative degradation of thiocyanate by hydrogen peroxide in aqueous alkaline solution (1.3).

$$4\mathrm{H_2O_2} + \mathrm{SCN}^{-} \rightarrow \mathrm{HSO}^{-}_{4} + \mathrm{NH}^{+}_{4} + \mathrm{HCO}^{-}_{3} + \mathrm{H_2O} \quad (1.3)$$

It is catalyzed by copper ions, and when luminol is added, it gives rise to periodic chemiluminescent flashes of blue light. It is also sensitive to the blue light.[64]

The BZ and the Orbán reactions can mimic the dynamics of the pacemaker, tonic excitable, and chaotic neurons. Since they originate spikes of transmitted or emitted UV–visible radiation, they encode information through their optical signals.[50] They can establish optical communication with luminescent and photochromic compounds. Luminescent compounds respond to an excitatory optical signal by emitting light. On the other hand, photochromic compounds react by changing their color and hence the spectral composition of the light they transmit.[49] Both luminescent and photochromic compounds

are good models of the neurons in the phasic excitable regime because they respond in an analog manner to external optical stimuli. When the photochromic or the luminescent compounds are in the presence of hydrodynamic convective motion of the solvent, triggered by suitable thermal gradient, they can originate either periodic or chaotic optical signals.[65–67]

The optical communication between the oscillatory, chaotic, and excitable artificial neuron models allow to obtain "in-phase", "out-of-phase", "anti-phase", and "phase-locking" synchronization phenomena analogous to those popping up in real neural networks.[50] The photochromism finds further applications in neuromorphic engineering. Photo-reversible photochromic compounds allow to implement memory effects: if they are direct photo-reversible photochromes, UV and visible signals promote and inhibit their colorations, respectively. Furthermore, the intrinsic spectral evolution of every photochromic compound that transforms from one form to the other under irradiation generates either positive or negative feedback actions. The optical feedback actions produced by every photochromic compound act on both itself and other photo-sensitive artificial neuron models that are optically connected to the photochrome. Therefore, it is easy to devise recurrent networks by selecting photochromes with proper spectral properties. The feedback actions of every photochrome are wavelength-dependent because its photo-excitability, which depends on the product $\mathcal{E}\Phi$, where $\mathcal{E}$ is its absorption coefficient, and Φ is its photochemical quantum yield, is also wavelength-dependent. Therefore, photochromic compounds allow to implement neuromodulation. Neuromodulation is the alteration of neuronal and synaptic properties in the context of neuronal circuits, allowing anatomically defined circuits to produce multiple outputs reconfiguring networks into different functional circuits.[68]

1.2.2. *Electrochemical oscillators*

Nature with all its processes, the more elaborate or completely simple ones, is an extremely vast source of human inspiration in laboratory and in everyday life. Looking for solutions that enable precise reflection of the reality, especially in such a complex aspect

as brain activity and learning, can lead humanity to a brighter future, better medical treatments, or self-learning computers. In this section the electrochemical oscillators will be presented as a contender for further considerations on their future use in neuromimetics and information technologies.

The history of electrochemical oscillators dates back to 1828 when Fechner[69] observed a new type of dissolution of silver on iron in an acidified solution of silver nitrate — nonlinear and periodic. Since the 19th century, electrochemical oscillators focused scientific attention not only as a curious abnormality but as a new type of system which can be the future of computing *in materio*[22] or mimicking biological systems.[70] Figure 1.1 shows the oscillations recorded in various neural tissues,[71] whereas Figure 1.2(a) various electrocorrosive oscillations.[72] The similarities between these two oscillatory systems are clearly visible.

After many years of investigations, the phenomena behind the electrochemical oscillations of two common features emerged from different types of mechanisms: (i) negative charge-transfer resistance (occurs in the potential window when oxidation rate decreases with more oxidation potential or reduction rate decreases with higher reduction potential) and (ii) external resistive component weakens the controlling potential (as a result of, e.g., forming passive film on the electrode). Moreover, if one looks closely on the curves depicting such oscillations then one will find characteristic regions of (1) rapid increase of current to maximum value, (2) current decrease with the slowing rate, (3) acceleration of current decreasing rate to the minimum value on which it remains until the whole process resumes. This basic model of electrochemical oscillators helps to divide interesting processes from each other and focus on steps underlying its origin.[73]

Concerning electrochemical oscillators as a group of processes presenting periodic and even chaotic phenomena, they can be divided into two main categories: anodic and cathodic. A vast majority of cases found in the literature are based on anodic polarization of metals associated with instabilities during passivation or due to porosity of oxide film/electrode surface.[74] A general conclusion can be made: if in the system a region with non-steady processes can

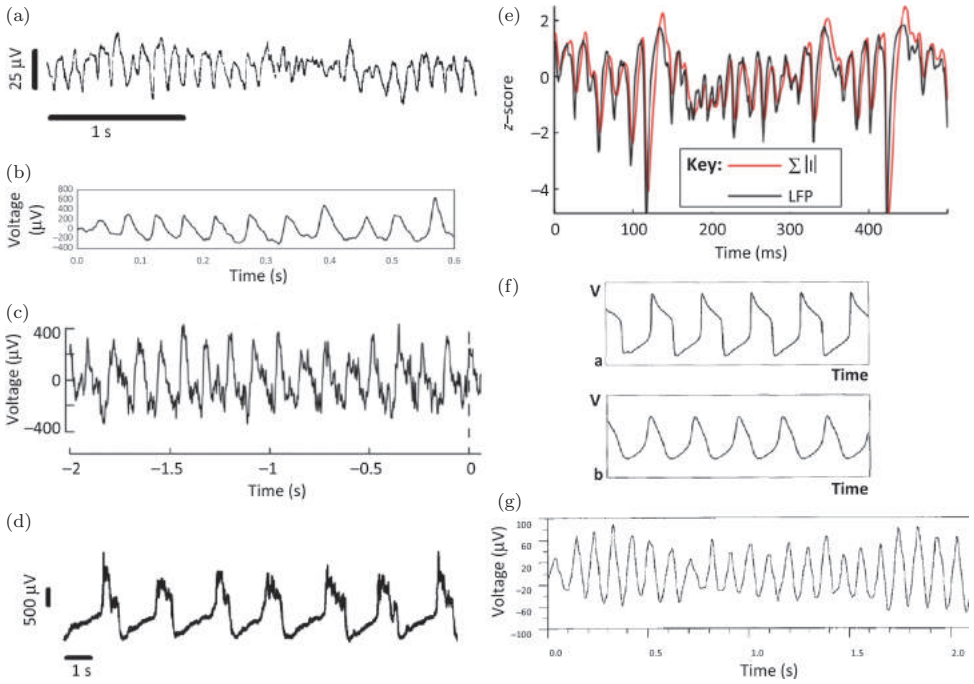

Figure 1.1. Non-sinusoidal oscillations recorded during various neurophysiological experiments: the mu rhythm (a), beta oscillations (b), theta oscillations (c), slow neocortex oscillations (d), gamma oscillations of pyramidal neurons (e), simulated oscillations in the Morris–Lecar model (f) and alpha oscillations in the rat gustatory cortex (g). Reproduced from Ref. [71] with permission. Copyright Cell Press 2017.

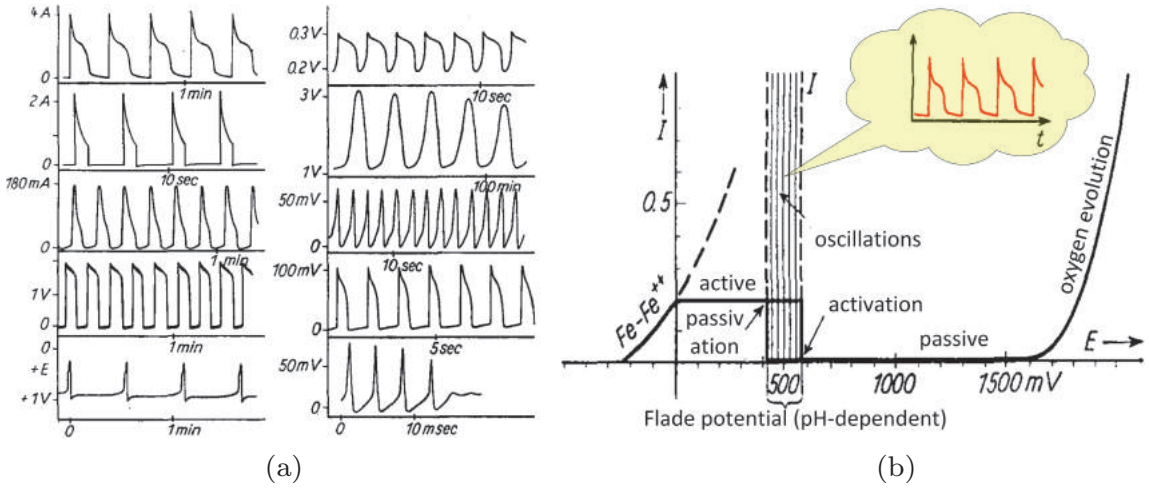

Figure 1.2. Electrochemical oscillations recorded in various corrosion experiments (a) and the oscillatory window determined for corrosion of iron in sulfuric acid solutions (b). Adapted from Ref. [72].

be found, then oscillations within the range of specific potential can occur (Figure 1.2(b)). It usually happens within the so-called Flade potential window, for example, a potential region on the boundary of passive and active zoned of metal surfaces exposed to electrolyte.[75]

As an example of anodic-based oscillator can serve the process of nickel dissolution during galvanostatic electropolishing in sulfuric acid or sodium sulfate in presence of chloride anions, as examined, respectively, by Doss and Deshmukh[76] as well as by Hoar and Mowad.[77]

The second group has observed periodically occurring dark brown layer on the surface of the electrode and proposed a mechanism based on two charge-transfer reactions following one another (1.4) and (1.5).

$$2\mathrm{Cl}^- \rightarrow \mathrm{Cl}_2 + e^- \tag{1.4}$$

$$\mathrm{Cl}_2 + \mathrm{Ni} \rightarrow \mathrm{Ni}^{2+} + 2\mathrm{Cl}^- \tag{1.5}$$

The first reaction was considered as slower and was depolarized by the second one. Furthermore, the oscillation has not been recorded until, at a certain value of current density, the concentration of chloride obtained adequate limit which promotes the anode dissolution (it can be called "the active state"). At some stage the transport of Cl^- slows down, which promotes the rise of electrode potential and

other reactions can take place (1.6)–(1.8).

$$SO_4^{2-} \rightarrow SO_4 + 2e^- \tag{1.6}$$

$$SO_4 + H_2O \rightarrow 2H^+ + SO_4^{2-} + O \tag{1.7}$$

$$Ni^{2+} \rightarrow Ni^{3+} + e^- \tag{1.8}$$

After immediate hydrolysis of Ni^{3+} ions the film of $Ni(OH)_3/NiOOH$ forms and blocks the surface of the electrode which in turn causes an increase of the cell potential. The last reaction (1.9) of this cycle occurs simultaneously and leads to the dissolution of blocking layer, the cell voltage decreases, surface becomes more porous and the whole process starts over.

$$Ni^{3+} + Cl^- \rightarrow Ni^{2+} + Cl \tag{1.9}$$

This type of oscillators is the most typical and often called "corrosion oscillator". Its mechanism is the best known and has a great potential for modeling. In the literature there are also systems based on anodic oxidation of non-metallic compounds such as formaldehyde[78] or hydrogen.[79] "Non-metallic anodic oscillators" more often consist of much more complex mechanisms with numerous intermediate radical products.

Cathodic processes are also known but they gather less attention because of the more complex nature/less visible effects. However some examples can easily be found in literature.[80] As an example the "In/SCN oscillator" can be shown, which was firstly described by De Levie,[81] but was successfully investigated by Koper and Sluyters[53,82] and others. Oscillations were observed during the thiocyanate-catalyzed reduction of indium ions on mercury electrode. This phenomena is based on two reactions, the first one (1.10) is slow due to diffusion of In^{3+} and the second faster (1.11) (responsible for negative resistance in the system) — increased desorption of thiocyanate anions and reduction of indium.

$$In^{3+} + 2SCN^- \rightarrow In\,(SCN)_2^+\,(ads) \tag{1.10}$$

$$In\,(SCN)_2^+\,(ads) + 3e^- \rightarrow In^o + 2SCN^- \tag{1.11}$$

The instabilities in the system are observed during slow potential scans. There is an interplay of potential-dependent thiocyanate absorption on mercury, diffusion of reagents and thiocyanate-catalyzed In^{3+} reduction at the mercury electrode. With decreasing negative polarization of the electrode after initial increase of current intensity, a decrease of the current is observed. Subsequently at more negative potentials the current starts to oscillate. It is associated with the electrostatic repulsion of free thiocyanate anions formed when surface indium thiocyanate complex is reduced (1.11). This results in apparent negative charge transfer resistance of the electrode. This in turn results in current oscillations, as the formal potential imposed on the working electrode is perturbed due to the influence of negative resistance on the potentiostat feedback loop.[83]

Looking at examples of the electrochemical oscillator, it is possible to create models with "active-passive" states based only on chemical reactions and their visible changes on the electrodes (thin film), however more accurate models should include diffusion and local concentrations of reagents, therefore more complex equivalent circuits for electrochemical impedance experiments are required.[84]

Regardless of whether the systems with anodic or cathodic type of oscillations will be considered, the similarity to biological systems, the possibility to model their behavior as well as the ability to time-space coupling, determine their potential as candidates for the development of such fields, which are discussed in this chapter. In the literature it has been reported by Okamoto *et al.* not only the analogy between oscillatory behavior of oxidation of formic acid and human nerve cell,[70] which share the characteristic features as a threshold, a refractory period and a stimulation-dependent response, but also Suzuki[85] proposed the mathematical model of single neuron which helped understand propagation of specific waveform and velocity in biological structures. But researchers are able go much further than simply mimicking the behavior of natural cells — Liao with co-workers[86] discovered material exhibiting a completely new feature, namely, electrochemical oscillations coupled with memory effects. This may lead to the conclusion that not only may the oscillations be the source of the neuromimetic effects, but also the reverse

causal relation should be considered. The newest approach to the application of electrochemical oscillators is based on exploration of the coupling phenomena. Coupling can be induced between two or more electrodes connected in series or arrays which was successfully described by Jia[87] and Zhai.[88] This kind of conjunction can emerge from different factors such as potential overlapping or mass transport — reagents can migrate from one point of the system to another and influence the behavior of the coupled sites.[89] Moreover, the coupling may have spatial[90] or spatio-temporal[91] character, which indicates that both static and dynamic patterns may result from coupled oscillatory processes. The occurrence of this phenomenon extends the possibility of using oscillators in chaotic,[92] synchronizing,[93] and decoding[57] systems as well as becoming great building blocks of artificial neural networks[94] and self-organizing matrices.[95] Maybe they are the future of cheap, biomimetic, and easily programmable *in materio* computers?[27]

1.3. Computation and Control in Dynamic Systems

1.3.1. *Computation in memristive devices and systems*

Recent findings in the field of computer science delivered stunning proof of capabilities of AI. However, the rapid development of AI is becoming more and more limited by the computational speed and power consumption of modern computers. As a result, training a large neural network can emit carbon dioxide in amounts 5 time larger than these emitted by a car during its lifetime.[96] These reasons lead to growth of interest in an alternative, unconventional computing concept, involving mimicking the learning processes in the human brain.

Despite operating with much slower frequencies than CPUs, our brains can process massive amounts of information in parallel fashion, requiring only a fraction of power consumed by computers performing similar tasks. It is estimated that performing complicated tasks, such as playing the game of Go, required the AlphaGo (equipped with 1202 CPUs and 176 GPUs) to consume even 50,000 times

more power than a human brain performing the same task.[97] The powerful processing abilities attracted attention to design devices and architectures that process information in a way inspired by neurons, but which could still be integrated with classical modern electronics. Nowadays, efforts to make machines compute in a more human manner have become a thoroughly investigated field of science, stretching from software implementations of neural networks and deep learning, through material design of neuromorphic devices to integration of physical artificial synapses on a chip.

The first ideas involving the concepts of *in materio computing* or *compute by physics* date back to the 1950s. The idea to utilize Kirchhoff's and Ohm's laws has been applied to solve partial differential equations, for image filtering, motion computing, and neural network algorithms.[98–101] Unfortunately, the performance of these systems was overshadowed by the rapid development of fast CMOS architectures and the *compute by physics* architectures lost their attractiveness.

Almost during the same time, the concept of *neuromorphic computing* was conceived. Although it dates back to the 1950s, the first practical applications employing neural networks appeared in the late 1980s only and originally involved mimicking the behavior of biological neural networks with analog electronics.[102] In recent years, this term has been stretched to many different implementations, including analog, digital, hardware, and software models of neural networks.

The development of novel non-volatile memories and memristive devices, however, brought growing interest in hardware neuromorphic circuits. The hardware realizations of neural networks with resistive switching devices, transistors, and memristors have proven to be promising alternatives to classical computing circuits, bringing together concepts of *in materio* and *neuromorphic* computing.

1.3.1.1. *Logic design with memristors/memristive devices*

One of the very first implementation of memristive devices for computing was their integration with the standard CMOS logic. Due to their variable (e.g., voltage- or charge-dependent) conductance,

memristors can act as controllable switches or latches that can be opened (high conductance state) or closed (low conductance state) with voltage of proper polarity.[103]

To be considered for logic design, simple circuits should be able to realize material implication (IMP or IMPLY) — a fundamental logic operation that together with FALSE (function that always yields 0 at the output) operation form a computationally complete logic basis for computing any Boolean function. Another great advantage of memristive devices in logic design is that they can both perform logic operations and store logical values as their conductances, making the logic stateful.

It has been showed that simple circuits consisting of resistors and two memristors can perform implication logic, while NAND operation requires three memristors.[103] A small number of memristors arranged in arrays have proven to be sufficient for effective computation of all Boolean functions.[104,105]

However, the limitation of IMPLY logic is that it requires additional circuit components like resistors and controllers, consumes a lot of power and demands high circuit complexity. Much simpler design can be obtained with memristor-only logic (Memristor-Aided LoGIC, MAGIC).[106] MAGIC takes the advantage of resistance switching process in memristors: depending on the direction of current flowing through the device, the conductance can be either increased or decreased. As a consequence, AND and OR gates can be easily implemented with two memristive devices and the final functionality depends on the orientation of memristors within the gate. NOT, NOR, and NAND gate can be built with three memristors, the last two of which are logically complete (the corresponding IMPLY logic gates require additional FALSE operation).[105,106] For practical implementations, it is crucial to decrease the memristive logic circuit footprint, for example, by stacking. Recent work show that design of 3D crossbar arrays is possible with logic primitives consisting of two antiparallel bipolar memristors. Furthermore, robustness of this design allows for implementation of any bipolar resistive switching device, paving the way for architectures with logic operations performed directly within the memory.[107]

1.3.1.2. *Matrix vector multiplication*

The need for manipulating massive data arrays is crucial for many applications, particularly linear transforms (discrete fourier transform, discrete cosine transform) and artificial neural networks (ANNs). However, due to the von Neumann bottleneck the computation and transfer costs are significant and limit the prospects of application of the ANN algorithms on a bigger scale. To train deep neural network (DNN), millions of synaptic weights need to be iteratively updated, demanding constant transfer of huge data structures between the CPU and RAM. This leads to high energy consumption of the order of kilowatts and days or even weeks of computational time. In the conventional von Neumann architecture, the computation of two numbers usually requires many multiply-accumulate (MAC) operations and constant data transfer between CPU and working memory. Despite the development of the hardware dedicated to accelerate these operations, such as tensor processing units, the manipulation of massive datasets is still considered a time- and energy-consuming computational step. In fact, the speed limitation of constant data moving and fetching is considered as one of the most important bottlenecks for the further development of AI.

The matrix vector multiplication (MVM) is a fundamental mathematical operation for many applications, for example, the training and inference of ANNs. In conventional computers, physical separation of processing unit and memory causes constant data shuttling, limiting the speed and causing significant energy consumption.

A potential solution to this problem is based on harvesting the inherent non-volatile memory of memristive devices connected together in a crossbar array. The design of such array involves many memristors placed at the intersections of perpendicular row and column electrodes. In such arrays, the computing and memory could be intertwined on a single chip with no need to move data between other components. More interestingly, arrays of memristive devices are capable of carrying out MVM in just a single step.[108]

The ability to compute MVM is a consequence of Ohm's law and Kirchhoff's law. The output current of any element in the matrix is

given by (1.12):

$$I = G \cdot U \tag{1.12}$$

where U is the applied voltage, I is the current read at the output of the device and G is the conductance of an element of the memristor array. As the voltage U_i is applied to the ith row, the resulting total current in the jth column (I_j) can be expressed as (1.13):

$$I_j = \sum_i G_{ij} U_i \tag{1.13}$$

where G_{ij} is the resistance of a memristive element located in ith row and jth column. To address a particular cell M_{ij} characterized with conductance G_{ij}, one simply needs to bias row i and column j with certain voltage. As a result, the measured output current $\mathbf{I} = (I_1, I_2, \ldots, I_n)$ is an analogue product of a conductance matrix $\mathbf{G}$ and an input voltage vector $\mathbf{U} = (U_1, U_2, \ldots, U_n)$, that is (1.14)

$$\mathbf{I} = \mathbf{G} \times \mathbf{U} \tag{1.14}$$

By incorporation of transimpedance amplifier into the circuit one can inverse the MVM operation (1.14) to obtain the division (1.15):[108]

$$\mathbf{U} = \mathbf{G}^{-1} \times \mathbf{I} \tag{1.15}$$

Recently, it has been shown that cross-point resistive memory arrays are capable of performing linear and logistic regression in just one step.[109] To find the vector minimizing the error in the regression analysis, one has to solve the Moore–Penrose inverse given by (1.16)

$$\mathbf{w} = \mathbf{X}^{+}\mathbf{y} = (\mathbf{X}^{\mathbf{T}}\mathbf{X})^{-1}\mathbf{X}^{\mathbf{T}}\mathbf{y}, \tag{1.16}$$

where $\mathbf{w}$ is the solution for $\mathbf{X}\mathbf{w} = \mathbf{y}$ equation. The equation can be solved by mapping matrix $\mathbf{X}$ on the array of conductances with vectors $\mathbf{w}$ and $\mathbf{y}$ corresponding to voltage and current, respectively. This system is capable of performing logistic regression as well, proving its usefulness in classification tasks.[109]

1.3.1.3. *Hardware artificial neural networks*

The last decade evidenced the power of AI with deep neural networks matching and even outperforming human capabilities in tasks previously regarded as extremely difficult for computers, such as speech, object, and face recognition.[110] However, the current DNNs demand for power will shortly become a bottleneck in the entire field of AI. To design an energy-efficient neuromorphic circuit crafted to deal with massive datasets and multiple MVM operations, it is necessary to mimic the processing of information by biological neural networks in a much more accurate way.[111]

The working principle of ANNs is loosely based on McCulloch–Pitt's mathematical model of neuron.[112] In classical feed-forward fully connected ANN, a neuron is considered as a node that receives, processes and transmits signals to other neurons. Each of the connections (analogy of biological synapses) is characterized with weight, indicating its strength. The neurons are grouped in layers, each connected with the neighboring ones. The learning process relies on adjustment of the connection strength between the neurons. Simple ANNs consists of only one layer between input and output layers, called hidden layers. Neural networks with more than one hidden layer are regarded as deep neural networks. The output signal of neuron is therefore a weighted sum of the outputs from preceding neurons (1.17):

$$y_j = \sum_i w_{ij} x_i, \tag{1.17}$$

where y is the output signal of the jth neuron that received input signal x_i from the ith neurons from the preceding layer, connected with the jth neuron by corresponding synaptic weights w_{ij}. Then, the output is processed through a nonlinear activation function, for example, tanh, sigmoid, or ReLU.[113] In the most frequently used supervised training algorithm — the backpropagation — the signal from the last layer (usually called the output layer) is compared with the correct values. The calculated error is then backpropagated to the first (input) layer of the network and the synaptic weights are

iteratively updated over many iterations (epochs) until the error is minimized. Finally, the prediction accuracy of the ANN is tested on new (test) dataset, serving as a benchmark.

Thanks to the presence of many neuromorphic effects the memristor-based artificial synapses are likely to play a crucial role in the design of neuromorphic circuits. The properties that distinguish memristive devices as building blocks for bio-plausible ANNs are the presence of more than two conductive states, low programming energy and ability to store the programmed conductance. Due to numerous effects responsible for conductance switching, many different devices are considered for implementation in neuromorphic hardware, namely, resistive switching random access memory (RRAM), the phase change memory (PCM), the ferroelectric and spin-transfer torque magnetic random access memories (FeRAM and STT-MRAM, respectively). RRAM and other resistive switching devices are able to store up to 6.5 bits of information and PCM devices even up to 8 bits.[114–116] The energy required to switch between distinct conductive states is as low as few femtojoules and nearly equals to this consumed by neurons and the data retention is estimated to in order of years for some state of the art devices.[113,117]

Arrays consisting of 32×32, 128×8, and 128×64 memristive one transistor–one resistor (1T1R) devices have proven to be effective in facial recognition, sparse encoding, and handwritten digit recognition.[101,118,119] The latter was able to achieve overall recognition accuracy of 89.9% on MNIST dataset, coming close to the software baseline. Convolutional neural networks (CNNs) deal with image recognition and object detection much better than classical ANNs and can be used to further improve the accuracy. Fully hardware implementation of memristive CNN consisting of eight 2048-cell memristive arrays arranged in five layers achieved 96.9% accuracy.[120]

Larger DNNs have been built with the use of PCM devices. Arrays consisting of 165,000 synapses achieved 82.2% on MNIST dataset and architecture with 1 million devices achieved 93.1% on CIFAR-10 dataset and 71.6% on ImageNet benchmark.[121,122] The accuracy is still lower than that achieved by software solutions, but

these results prove that hardware DNNs are capable of dealing with complex visual patterns.

The biggest promise of hardware neuromorphic circuits is to significantly decrease energy expenditure. Memristive cross-point arrays benefit from integrating computing unit and memory in one physical device, which significantly speeds up operations of the network. It is estimated that memristive neuromorphic architectures are able to operate at 115 TOPS W^{-1} (Tera Operations per Second per Watt) while performing MVM.[101] In comparison, digital CMOS-based technology doing the same task at lower accuracy is estimated to operate at 7 TOPS W^{-1} (see Ref. [119]). It is presumed that with proper architecture, energy consumption can even be 1000 times lower than that required by classical circuits.[118] However, the implementation of ANNs poses a significant challenge in the design of hardware neuromorphic circuits. In general, synaptic weight can have both positive and negative values, which require a modification to the simple crossbar architecture.[123] To obtain negative values, one has to calculate a relative synaptic weight as a difference between a pair of conductances (1.18)

$$w_{ij} = G_{ij} - G_{\text{ref}}, \tag{1.18}$$

where G_{ref} is some fixed, reference conductance.[124] However, this architecture is viable only for devices exhibiting bipolar switching behavior (i.e., when the conductance can be both increased and decreased). In case of unipolar switching devices, like PCM devices, in which conductance can be tuned only in one direction, the calculation of the synaptic weight requires second tunable conductance to yield both positive and negative values, that is (1.19)

$$w_{ij} = G_{ij}^{+} - G_{ij}^{-}. \tag{1.19}$$

Other significant issues posing learning ineffectiveness are device-to-device variations, nonlinearity of resistive switching and lack of symmetry of switching between high and low conductances, both leading to lower prediction accuracy.[125–127] It has been shown that even a few percent in linearity discrepancy between devices can lead

to decrease in the inference accuracy.[128] These issues can be overcome with feedback programming algorithms to introduce devices into the desired conductance state and selecting narrower conductance window.[101] Programming techniques that take into account the variability of the resistive switching among devices in the array to overcome have proven to effectively increase the inference accuracy as well.[125,129]

Spiking neural networks (SNNs) can emulate the behavior of biological neurons in a much more reliable way than classical ANNs. In the brain, both the time of neuron firing and its position in the network carries information.[130] The information is encoded with binary spikes and only specific spiking patterns induce neurons to emit the action potential. Thus, human brains are extremely efficient in processing complex, spatio-temporal data like speech and vision. Similar rate encoding approach is implemented in SNNs, where information is coded with the pulse width, frequency, and the relative time of its occurrence.[111]

CMOS-based SNNs neuromorphic technology circumventing von Neumann architecture limitations are already available, including SpiNNaker supercomputer, Intel Loihi, and IBM TrueNorth neuromorphic chips.[131–133] While being state of the art neuromorphic circuits, these solutions employ complex circuits of classical electronic elements to emulate synaptic behavior. Due to the innate presence of synaptic effects, memristive devices could significantly simplify the design of hardware SNNs. The presence of numerous neuromimetic effects including Hebbian learning rules, spike timing-dependent plasticity (STDP), spike rate-dependent plasticity, pulsed-pair facilitation, metaplasticity, associative, and non-associative learning allow direct and efficient implementing of spatio-temporal learning rules.[134–138]

Additionally, SNNs are able to carry out unsupervised training, where the network autonomously learns a pattern based on the data submitted to the input.[111,139] SNN consisting of only 16 synapses trained with unsupervised weights update via STDP showed the ability to learn static and track dynamic patterns.[140] It is noteworthy that in SNNs, only devices that receive a spike become active, while

the rest remain idle. This is a highly advantageous feature, as it will allow even further reduction of energy consumption.[141]

1.3.2. *Principles of control in dynamic systems — PID case*

The control theory deals with the analysis of various dynamic systems and methods of constructing controllers. The most common control systems are based on feedback loops, where the controlled signal is compared with the given reference signal, after which the differences between them (i.e., error) are used to calculate the corrective control action.[142–144] Currently one of the most widely used mechanisms of control is the proportional-integral-derivative (PID) controller.[142] The first theoretical work creating mathematical foundations and describing the operation of the PID controller appeared in 1922.[145] The purpose of Nicolas Minorsky's work was to determine the conditions of stability — in his work he used his sailing intuition, which was based on the fact that the helmsman controlled the ship not only based on the current error, but also took into account errors that occurred in the past and the current rate of change. His concepts were implemented on the battleship USS New Mexico to control angular velocity. The use of the "PI" controller (using only proportional and integral components) enabled the angular error to be reduced to $\pm 2^{\circ}$, while the addition of the "D" component helped reduce the error to $\pm 1/6^{\circ}$, which was much better than any helmsman could achieve.[146] Since then, the academic community has become deeply interested in the subject of PID controllers, as evidenced by international conferences and constantly developed models and emerging patents.[147–149]

The PID control device is based on continuous operation through the use of the feedback loop and appropriate corrective actions of its three calibrated components. The equation written in parallel form, specifying the output from the classic PID controller operating in a continuous manner is as follows (1.20):

$$u_{\mathrm{PID}}(t) = K_P e(t) + K_I \int_0^t e(t)\, dt + K_D \frac{de(t)}{dt}, \tag{1.20}$$

where u_{PID} is the output of the PID controller, K_P, K_I, and K_D denote coefficients of proportional, integer, and derivative gains, respectively, and $e(t)$ is the error. The standard form of representation of Equation (1.20) is often presented in the form (1.21):

$$u_{\mathrm{PID}}(t) = K_P\left(e(t) + \frac{1}{T_I}\int_0^t e(t)\,dt + T_D\frac{de(t)}{dt}\right), \tag{1.21}$$

where physical meaning of T_I and T_D are interpreted as time constants of integration or derivation processes. The block diagram of the PID controller is depicted in Figure 1.3. The principle of operation of the PID controller is as follows: The "P" component is responding to the error $e(t)$ with the proportional gain K_P. The use of a proportional component alone is not sufficient to achieve the desired system variable, due to the fact that when the error approaches zero, the correction applied also approaches zero. The integrating element attempts to counteract this by effectively accumulating the error result of the "P" component in order to increase the correction factor. However, instead of stopping the correction after reaching the goal, "I" attempts to reset the cumulative error to zero, which causes overshoot. The "D" component aims to minimize this overshoot by slowing down the correction factor applied as the desired system value is approached.

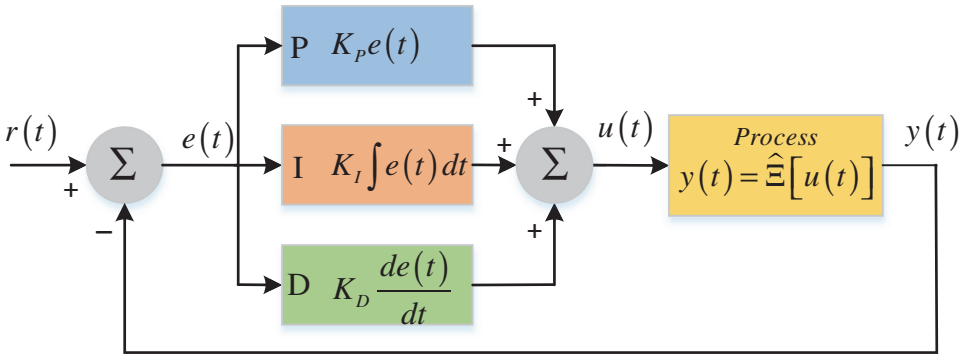

Figure 1.3. Schematic representation of PID controller. The symbols represent: $r(t)$ is desired process value, $e(t)$ is the error calculated from the difference of $r(t)$ and $y(t)$ — measured process value. Participation of P — proportional, I — integral, D — derivative components are summed and are applied to given process as $u(t)$ — control signal. The process itself transforms the control signal into a feedback $y(t)$. The $\hat{\Xi}$ operator can be regarded as a response function of the controlled process.

It is estimated that about 90% of industrial processes are controlled by PID systems.[150] They are used to regulate flow, temperature, pressure, humidity, level, velocity, or other parameters of industrial importance. The popularity of using this type of control is mainly due to its simplicity, applicability, and the intuitiveness of the impact of individual components on the system dynamics.[151] Many approaches towards tuning of PID controllers are used to obtain fast and acceptable performance of a given process, for example manual tuning, different heuristic methods, model based methods, or even auto-tuning provided by the supplier. Classic heuristic methods of tuning PID systems include methods by Cohen–Coon,[152] Ziegler–Nichols,[153] Tyreus–Luyben,[154] Åström–Hägglund[155] or Internal model control IMC-PID tuning rules by Rivera *et al.*[156]

When the dynamics of a given system is complex, nonlinear, nonstationary, difficult to accurately characterize or is subject to environmental uncertainty, there may be a need for more advanced control system. Intensive research is conducted on controllers using, for example, fractional calculus,[148,157] fuzzy logic,[149,158] artificial neural networks,[159,160] or using hybrid approaches.[161–163] In order to obtain a broader description of the methods of tuning PID control systems, the interested reader is referred to the topic reviews.[147,164–169]

More and more advanced methods of PID control are still being developed, aimed at better control over the time delay of the system response, avoiding overshoot or oscillations. At the same time, industry-related data present sobering results about operating PI and PID control systems. Industrial plant inspections show estimates that around 80% of used PID controllers are poorly tuned. It was found that 30% of PID controllers are in manual mode and that 25% of all installed PID controllers use the factory default settings, which means that they have not been tuned at all.[142,170,171] This does not change the fact that scientists are trying to develop and incorporate PID technology into larger control systems as well as develop related technologies that are based on similar concepts of feedback control which is the topic of the next section.

1.3.3. *Reservoir computing*

Just like in the case of the Internet, smartphones, 3D printing, e-cigarettes or electric cars to name a few, the development of artificial intelligence is becoming an integral part of human life. We use social media, online shopping, various video sharing platforms, communicators, etc. Each of these areas can be subjected to analysis and profiling to generate value through more personalized ads, news feeds, or videos which may be of interest to us.[172] This is intended to draw more human attention by suggesting personalized content — including aesthetic, intellectual, or political preferences. The collection and analysis of data translates into a real effect in the world in the form of monetary gains (e.g., AI supported product/stock market analysis[173,174]) or politics (the case of Cambridge Analytica affecting the presidential election in the USA[175]).

The analysis and processing of the data listed above (in addition to classical statistical methods) is carried out using concepts belonging to the field of machine learning (ML). One of ML's intensively developed branches are various ANNs.[176] In their functionality and/or structure they are modeled on the basis of the biological nervous systems. This is due to the brain's extremely optimal ability to recognize patterns and classify them as well as its ability to learn. For this reason, ANN are widely used for various tasks such as classification, prediction, generation, or filtering of the data. They turn out to be valuable tools if we are interested in modeling of various nonlinear processes treated as a "black box".

Generally, neural networks can be divided into two subclasses depending on the direction of the data flow — feedforward neural networks (FNNs) and recurrent neural networks (RNNs). Due to the characteristics of these networks, FNNs are more suitable for processing information that is *static* — that is, that are non-temporal dependent, whereas RNNs turn out to be more suitable for temporal data, where we are interested in modeling the *dynamics* of a given system.[177–179] Control systems are time-dependent entities, so in this chapter we will focus only on the description of new solutions from the RNN class. The flexibility and complexity of RNNs surpass the performance of classical PIDs, which are, by definition, limited

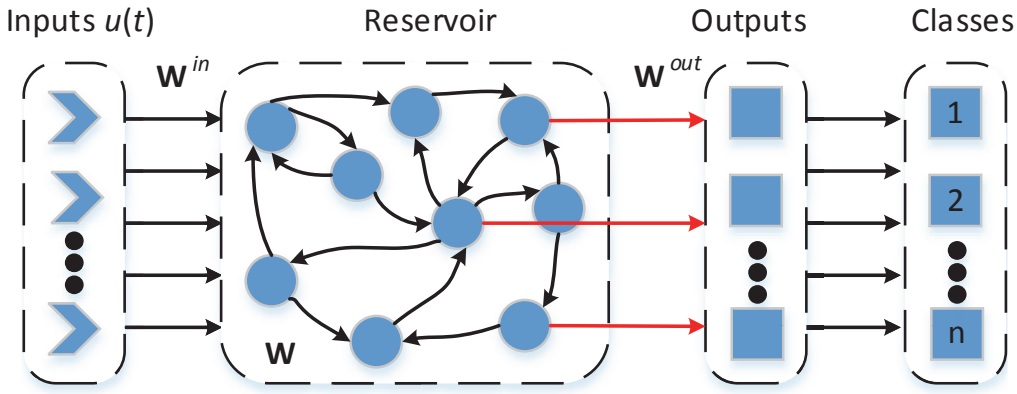

Figure 1.4. Schematic diagram of classical reservoir computing system. Connections between input layer and the reservoir layer, as well as the connections between hidden nodes in the reservoir are all fixed (black). The only trained connections can be found between the reservoir layer and the output layer (red). Output layer acts as a decoder of a particular reservoir parameters at a given time. Based on the obtained parameters, classification of input signals can be performed.

to a single feedback loop with no delay and a relatively simple nonlinear core.

One of the RNN approaches is particularly advantageous from the point of view of physical systems — reservoir computing (RC). In RC, a set of hidden neurons is called a "reservoir" intended for mapping input into higher dimensions through nonlinear transformations, so that it can be classified with linear transformations at the output layer (Figure 1.4). In the general case the response of a reservoir to the external input vector $\mathbf{u}$ can be described by a recursive equation (1.22)

$$\mathbf{x}(t) = \mathfrak{F}\left(\mathbf{W}\mathbf{x}(t-1), \mathbf{W}^{\text{in}}\mathbf{u}(t), \sum_{\delta=0}^{H} \mathbf{W}^{\text{fb}}\mathbf{y}(t-\delta)\right), \qquad (1.22)$$

where $\mathbf{x}(t)$ is the vector describing the internal state of the reservoir at discrete time t, $\mathbf{W}$ is the matrix of internal weights of reservoir, $\mathbf{W}^{\text{in}}$ is the matrix of input weights, $\mathbf{W}^{\text{fb}}$ is the matrix of feedback weights, y is the output signal used in feedback, H defines the depth of memory, and $\mathfrak{F}$ is the activation function of the reservoir. The state of the reservoir is a vector defined by the states of all of its

nodes, N (1.23)

$$\mathbf{x}(t) = (x_1(t), x_2(t), \ldots, x_N(t)), \quad N \in \mathbb{N}. \tag{1.23}$$

The readout layer may use only a subvector of the internal state of the reservoir, that is (1.24)

$$\mathbf{y}(t) = (x_1(t), x_2(t), \ldots, x_j(t)), \quad j \leq N. \tag{1.24}$$

No training is needed in the reservoir layer, which is a huge advantage in terms of speed of operation. The only training involves the readout later, which may be a simple linear transformation of the output vector (1.25):

$$\boldsymbol{\varphi}(t) = \mathbf{W}^{\text{out}}\psi(t), \tag{1.25}$$

and the delayed feedback in the more advanced cases (*vide infra).* It is especially important in the case of *in materio* implementations of reservoir computing, where no adjustments inside the physical reservoir can be done.[180,181] Because of this, the reservoir must be complex enough to perform nonlinear transformations suitable for data classification and modelling. Among all computational paradigms reservoir computing seems to be best suited for unconventional *in materio* implementations,[15] although selection of a proper physical platform is not a trivial task.[182,183]

The responses of the reservoir must possess properties of generalization and separability — similar inputs are mapped into similar states of the reservoir whereas differing inputs are mapped into its different states.[185] These features can be significantly improved by addition of additional trainable elements: a delayed feedback and a drive, as recently reported by Anathasiou and Konkoli (Figure 1.5).[184] Most importantly, the drive signal may influence the global dynamics of the reservoir in such a way that the reservoir can perform various computational tasks with the input data.

This approach enables decrease of reservoir complexity, allows at least partial control over internal reservoir dynamics and improves memory features, thus helping to beat the nonlinearity-memory trade-off. Other significant improvement of reservoir performance may be achieved by careful engineering of nodes — a combination of

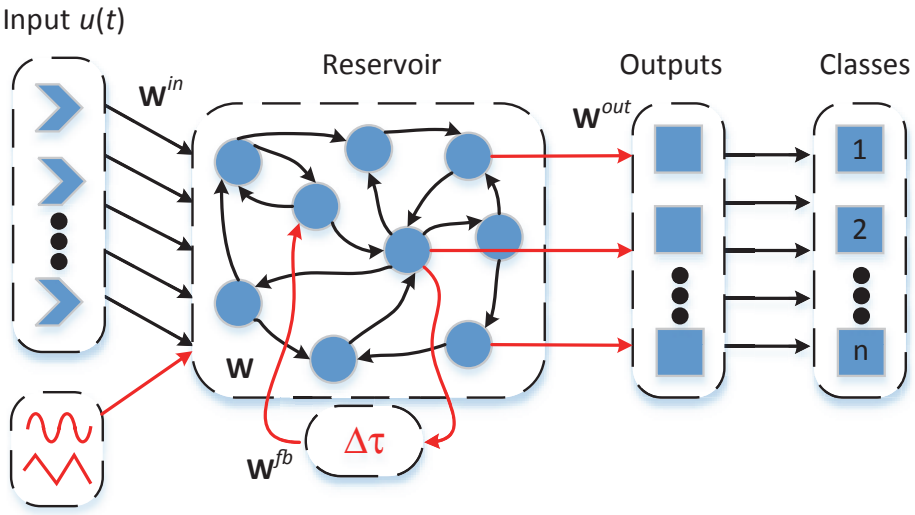

Figure 1.5. Schematic diagram of a modified reservoir computing systems. Additional feedback and the trainable drive library are marked in red. See Ref. [184] for details.

linear and nonlinear nodes helps to mitigate the memory-nonlinearity trade-off.[186] This approach, however is more suitable for software-based reservoirs, as in the case of *in materio* implementations it would require extensive control of materials at nanoscale. The interested reader is referred to broad literature for a formal description of its concepts.[27,184,187–194]

1.3.4. *Reservoir computing and control systems*

One can envision a full hardware integration of the controlled systems with the control system, where the processing of the multisensory data is carried out in an online manner. Such solutions are already available on the market (e.g., SPOT® from Boston Dynamics with +EDGE GPU), but they are not efficient compared to dedicated ML computing equipment[195] and are expensive. For this reason, research is being conducted on effective platforms that process information in a convenient way (e.g., memristor crossbars capable of matrix operations[101,196]) for ML applications.

Since RC is one of the efficient ML methods for processing nonlinear dynamic data, it seems natural to try to use this method for systems control applications. Relation of the RC with the control systems can be manifold. RC can be used in a similar way as

the PID control system (*vide infra*), or in parallel with the PID to enhance its operation, and can be trained on the basis of PID; in an inverse situation, system under control can be used as reservoir of states to perform computations. These approaches will be briefly illustrated with examples. It is worth mentioning that at first, presented applications for system control are based on a software implementation of RC, followed by some recent hardware RC implementations.

The relation between PIDs and RCs can be noticed at various levels. One of the widely used approaches to reservoir computing is the implementation of single node echo state machines.[197,198] They are based on a single nonlinear node placed in a feedback loop with appropriate delay and gain elements, which provide fading memory feature. The conceptual scheme of such a system is shown in Figure 1.6 and the block diagram of practical application in Figure 1.7. The input signal for such a system must be appropriately conditioned (e.g., divided into constant-time chunks, masked with appropriate masks, combined with proper drive signal, etc.)[199] and fed into the feedback loop at appropriate moments.

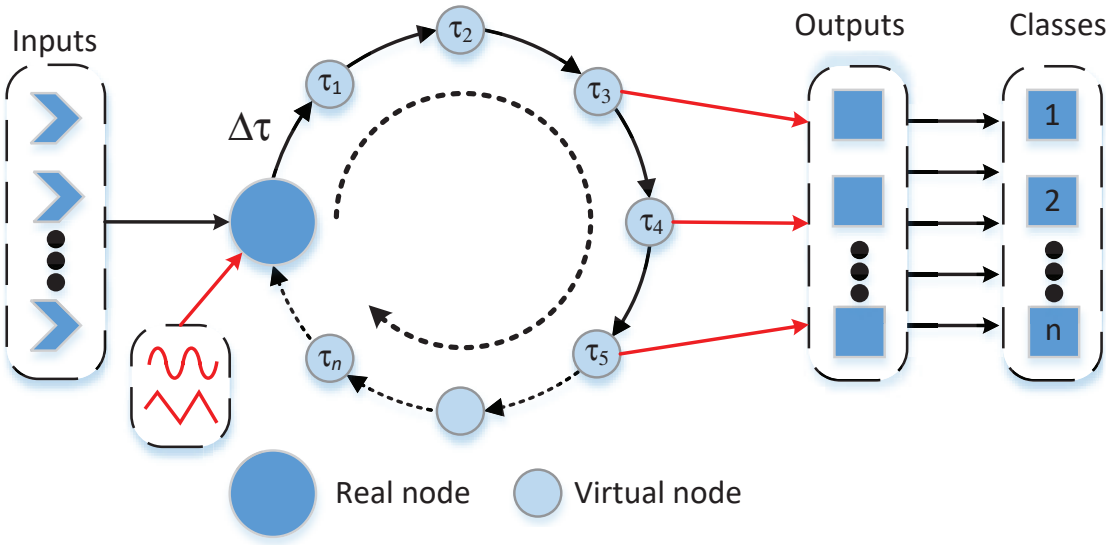

Figure 1.6. Single node implementation of a reservoir computing concept. The output layer follows the evolution of the input signal at various time instances. It is assumed that the node returns to its initial condition upon n steps, therefore single computational run lasts $(n+1)\cdot\Delta\tau$. Trained elements (drive and output layer weights) are marked in red.

In this approach signal chunks of the length not exceeding the given time interval of $\Delta\tau$ are fed into the feedback loop and the signal evolution is observed with the time spacing of $\Delta\tau$. In this way a series of virtual nodes presenting the input signal at different stages of evolution is obtained. The simplicity of this approach is a trade-off versus the performance. The number of virtual nodes and the length of the signal chunk determine the time-scale of the data processing, therefore this approach is mainly used in photonic systems,[200–207] however electronic implementations based on memristive elements are also known (Figure 1.7).[180, 208–210]

So far, hardware implementations of RC have been shown to act as efficient ANN *in materio* devices but without showing its possible application to control systems. Based on previous reports on RC software, it can be assumed that future research will include full hardware integration of the ANN control unit and the controlled system. RC's ability to work effectively in continuous online mode is a big advantage here. Some new RC hardware implementations are described below. Zhu *et al.*[211] presented hardware reservoir implemented on the single memristor operating in the feedback loop to capture and analyze neuronal spike trains in real time. The perovskite-based Ag/$CsPbI_3$/Ag memristor showed a good representation of the applied neural signal in its dynamics of operation, which was further enhanced by the feedback loop. In addition, low voltage (>100 mV) and low operating current (∼nA) made this

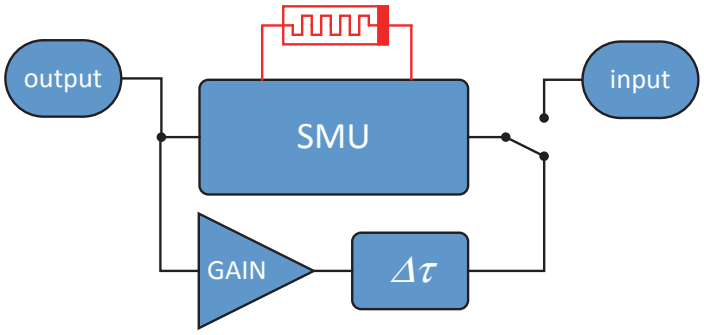

Figure 1.7. Block diagram of an experimental setup for memristor-based reservoir computer (a single node echo state machine). SMU stands for source-measure unit, GAIN for amplifier and the delay line is labelled $\Delta\tau$. Adapted from Ref. [28].

system suitable for working with a biological signal. Such a system could prove to be a good candidate for control systems due to its low power consumption and the possibility of continuous operation. In an attempt to reduce required information processing elements, Wlaźlak *et al.*[209] showed possibility to classify signals based on their amplitudes, without any necessity for readout neural network or any transformation whatsoever apart from simple threshold. The ITO/PbI_2/Ag memristive device operating in the feedback loop was used as the computational RC substrate. Furthermore, device exhibited spike-timing-dependent plasticity (STDP) and spike-rate-dependent plasticity (SRDP) Hebbian learning rules. Simplifying the required information processing while maintaining certain functionality may also be important from the point of view of control systems. In a different setup, Vandoorne *et al.* studied RC based on the photonic silicon chips. As this system did not show any nonlinear operation by itself, the desired nonlinearity was introduced at the readout layer. The great advantage of the system was its high speed of operation, enabling data processing at the level of 12.5 Gbit per second. More implementations can be found in recent review papers.[183,212]

In one study, Schwedersky *et al.*[213] explored performance of RC in comparison with PID system to control refrigerant compressor. Since this device shows areas of nonlinear operation, the RC-based control showed more than two times less relative error during operation when testing the experimental setup. Zhang *et al.*[214] showed comparison of RC with other classical ML techniques for a transmission faults monitoring of a 3D printer. In a situation where we have access to a small number of resources, a low-cost data acquisition and computation are crucial. In that scenario, RC presented outstanding performance in relation to other ML approaches. Wu *et al.*[215] studied joint system of RC and PID control of rehabilitation robotic arm showing better accuracy than simple PID controller. Sala *et al.*[216] showed that RC can be effectively trained on the basis of the PID responses and in effect was able to correct offsets of controlled robotic arm. Nakajima *et al.*[217] showed an interesting approach to employ

model of soft-robotic arm (inspired on the octopus tentacles) to use as a reservoir of states. Soft-robotics is characterized by the smooth movements observed in nature, which makes it be perceived as high-dimensional, elastic and nonlinear. The dynamics of a robot soft arm have been successfully used for approximation of three benchmark nonlinear dynamical systems. In the following work,[218] group presented hardware robotic arm used to perform computations. The interested reader will find more about soft robotics in the following subsections.

The single node echo state machine implementation of reservoir computer is structurally related to the PID controllers, which however do not have the explicitly defined delay line and their nonlinear response is strictly defined. The other difference related to the feedback loop — in the case of PIDs the delay/memory function can be embedded in the controlled element (e.g., in the form of its inertia). This analogy can be further explored for a very specific class of input data: signals satisfying the Dirichlet conditions for expansion of a function into a Fourier series. Such signals should be: (i) periodic functions absolutely integrable over its period, (ii) must be of bounded variation in any given bounded interval (i.e., it should have a finite number of local minima and maxima within a period) and (iii) must have a finite number of discontinuities in any bounded interval. All functions which obey the Dirichlet's criterion can be represented as Fourier series, for example, (1.26),

$$f(x) = A_0 + \sum_{n=1}^{N} A_n \sin(nx + \varphi_n). \tag{1.26}$$

Furthermore, operation of PID controller should be performed with integration time significantly shorter than the period of input oscillations. Thus, application of the two operators of PID to each of the Fourier components (it is possible due to the linearity of differential and integral operators) sin functions yields cosine functions (1.27) and (1.28):

$$\frac{d \sin x}{dx} = \cos x \tag{1.27}$$

and

$$\int \sin x dx = -\cos x. \tag{1.28}$$

Thus, the response function of PID for any Fourier component of the input signal will be given by (1.29)

$$f(x) = K_P \sin x + (K_D - K_I) \cos x \tag{1.29}$$

which simplifies to (1.30)

$$f(x) = \sqrt{K_P^2 + (K_D - K_I)^2} \sin(x + \phi) \tag{1.30}$$

with the phase shift equal to (1.31)

$$\phi = \begin{cases} \arctan \dfrac{K_D - K_I}{K_P}, & K_P \neq 0 \\ \operatorname{sgn}(K_D - K_I) \dfrac{\pi}{2}, & K_P = 0. \end{cases} \tag{1.31}$$

Thus, the nonlinear operator of PID can be represented by a fractional derivative[27,219–221] (following the sign convention used in memfractive devices[222]) of the order of (1.32)[223]:

$$\xi = -\frac{2\phi}{\pi} \tag{1.32}$$

which automatically leads to conclusion that the PID systems, when subjected to periodic signals satisfying the Dirichlet's conditions, have power-law memory features.[224,225] Thus, PID systems can be considered as simplified reservoirs with fading memory, provided that the process function $\widehat{\Xi}$ is: (i) a linear operator or (ii) a function, which satisfies the Dirichlet's conditions within the image of the input function $f(x)$. The detailed considerations on performance of such systems require spectral analysis of composite functions, discussed in detail by Bergner and Muraki.[226] Specific operating conditions (periodic input and a limited choice of process operators $\widehat{\Xi}$) are not usually met during operation of PID systems. However, this demonstrates close formal and functional relation between these

two systems, especially if $\widehat{\Xi}$ can induce additional phase shifts or represents a delay line. Detailed analysis of delayed PID systems was presented by Silva *et al.*[227] With appropriate properties of $\widehat{\Xi}$, PIDs can be applied to signal classification according to spectral features or signal filtration, which extracts desired signatures from complex input signals.

In summary, control systems can be implemented in a variety of ways, strictly depending on the dynamics of the system under consideration. Both classic control systems such as PID as well as more advanced ML-based systems open up many research paths aimed at increasing their accuracy and functionality compliance. It seems that the world is striving for more and more automation, using more and more advanced and sophisticated systems, which we have tried to briefly outline in this section in regard to PID and ML concepts.

1.4. Controllers Beyond PID: Fuzzy and Neuromorphic

1.4.1. *Fuzzy logic*

Human intelligence has the remarkable power of computing with both numbers and words. A good model of the human ability to make rational decisions by computing with words is fuzzy logic. Fuzzy logic has been defined as a rigorous logic of vague and approximate reasoning.[228] It is based on the theory of fuzzy sets proposed by the engineer Lotfi Zadeh.[229] A fuzzy set is different from a classical Boolean set because it breaks the law of Excluded Middle. An item may belong to a fuzzy set and its complement at the same time, with the same or different degrees of membership.

The degree of membership (μ) of an element to a fuzzy set can be any number included between 0 and 1. It derives that fuzzy logic is an infinite-valued logic. It is used to design controllers because it can describe any nonlinear cause and effect relationship. For this purpose, it is necessary to build a fuzzy logic system (FLS). The construction of any FLS requires three fundamental steps. First, the granulation of all the variables in fuzzy sets. The number, position, and shape

of the fuzzy sets are context-dependent. Second, the graduation of all the variables: each fuzzy set is labeled by a linguistic variable, often an adjective. Third, the relationships between input and output variables are described through syllogistic statements of the type "*If* ..., *Then* ...", which are named as fuzzy rules.

The "*If* ..." part is called the antecedent and involves the labels chosen for the input fuzzy sets. The "*Then* ..." part is called the consequent and involves the labels chosen for the output fuzzy sets. In the case of multiple input variables, these are connected through the AND, OR, NOT operators.[230] At the end of the three-steps procedure, an FLS is built; it is a predictive tool or a decision support system for the particular phenomenon it describes. The effectiveness of fuzzy logic in mimicking the human power of computing with words is due to the structural and functional analogies between any FLS and the human nervous system.[231] A significant challenge in the field of Chemical Artificial Intelligence is the design of strategies to process fuzzy logic by using molecules, macromolecules, and systems chemistry.[232]

1.4.2. *Processing fuzzy logic by using molecules*

The microscopic world is ruled by the laws of quantum mechanics that have some links with fuzzy logic.[233,234] The elementary unit of quantum information is the qubit. The qubit, $|\Psi\rangle$, is a quantum system that has two accessible states, labelled as $|0\rangle$ and $|1\rangle$, and it exists as a superposition of them (1.33)

$$|\Psi\rangle = a\,|0\rangle + b\,|1\rangle. \tag{1.33}$$

In Equation (1.33), a and b are complex numbers that satisfy the normalization condition $|a|^2+|b|^2 = 1$. Any logic operation on a qubit manipulates both states simultaneously. It determines an evolution of $|\Psi\rangle$ represented by the product of $|\Psi\rangle$ and an orthonormal operator $\widehat{\mathrm{O}}$. The new state $|\Psi'\rangle$ is given by (1.34)

$$\left|\Psi'\right\rangle = \widehat{\mathrm{O}}\,|\Psi\rangle. \tag{1.34}$$

The new state $|\Psi'\rangle$ still satisfies the normalization condition. In other words, (1.35):

$$\|\widehat{\mathrm{O}}|\Psi\rangle\| = \||\Psi\rangle\| = 1. \tag{1.35}$$

When a qubit undergoes any kind of measurement represented by a projector $\hat{p}$, the probability of an outcome is defined as (1.36)

$$\langle\Psi|\,\hat{p}\,|\Psi\rangle. \tag{1.36}$$

The projector (1.37)

$$\hat{p} = \sum_i |i\rangle\,\langle i| \tag{1.37}$$

is a linear operator defined over a set of orthonormal vectors $|i\rangle$. Multiplying a projector with a state vector $|\Psi\rangle$ means to project the vector onto the respective vector subspace. The probability value of Equation (1.36) equals the squared length of the state vector $|\Psi\rangle$ after its projection onto the subspace spanned by the vectors $|i\rangle$. Such value may be interpreted as the degree of membership of $|\Psi\rangle$ to the subspace spanned by $|i\rangle$.[234,235] The measurement determines the decoherence of the qubit.[137] The decoherence induces the collapse of any qubit in one of its two accessible states, either $|0\rangle$ or $|1\rangle$, with probabilities $|a|^2$ and $|b|^2$, respectively. The decoherence is also induced by deleterious interaction between the qubit and the surrounding environment, which is a heat reservoir. Whenever the decoherence is unavoidable, the single microscopic units can be used to process discrete logics, that is, binary or multi-valued crisp logics depending on the original number of qubits.[6,10]

The relation between quantum logic and fuzzy logic can be established also at topological level. It is possible to represent a real-valued qubit as a circle in two dimensional Hilbert space. It is homeomorphic with a unit square, which specifies two membership functions.[236] The intuitionistic analysis of fuzzy and quantum logic operators also points to striking similarities between fuzzy logic and quantum computing.[237] The intuitionistic argument should be, however, used consciously, as there are also marked formal and

practical differences between quantum and fuzzy logic. As pointed out by Lehrack *et al.*: "As main difference between fuzzy and quantum logic we identified the way how conditions are combined by conjunction and disjunction with respect to a given object: combination in quantum logic is performed *before* and in fuzzy logic *after* object evaluation takes place".[235]

Advanced microscopic techniques, reaching the atomic resolution, are required to carry out the computations with single molecules. Alternatively, large collections of molecules can be used to make computations. However, vast ensembles of molecules (if they are of the order of the Avogadro's number) are bulky materials. The inputs and outputs for making computations become macroscopic variables that can assume continuous values. When the function that relates input and output variables is steep, it is suitable to process discrete logic. On the other hand, when the function is smooth, it is suitable to implement an FLS.[238–241]

Every compound that exists as an ensemble of conformers works as a fuzzy set.[242] The types and the relative amounts of the different conformers depend on the physical and chemical contexts. Every compound is like a word of the natural language, the meaning of which is context-dependent. Conformational dynamics and heterogeneity enable context-specific functions to emerge in response to changing environmental conditions and allow the same compound to be used in multiple settings. The fuzziness of a macromolecule is usually more pronounced than that of a simpler molecule because it exists in a larger number of conformers. Among proteins, those that are completely or partially disordered are the fuzziest.[243] Their remarkable fuzziness makes them multifunctional and suitable to moonlight, that is, play distinct roles, depending on their context.[244]

When compounds that exist as a collection of conformers and that respond to the same type of either physical or chemical stimulus, are combined, they granulate the variable in a group of molecular fuzzy sets. They work in parallel and allow to discriminate different values of the same variable easily. This strategy is at the core of the sensory subsystems of the human nervous system.[231] Its imitation allows to develop artificial sensory systems that are

strongly sensitive. For instance, the imitation of the visual sensory system, by using a collection of adequately chosen direct thermally reversible photochromic compounds has allowed the implementation of artificial chemical systems that extend human vision from the visible to the UV. Such systems discriminate frequencies belonging to the UV-A, UV-B, and UV-C regions, respectively.[245,246]

Another attractive platform, in terms of both structural stability and flexibility of possible modifications (e.g., through intercalation of various small molecules), is provided by nucleic acids. These macromolecules provide a sufficient number of states to implement quasi-continuous variables, hence the definition of fuzzy sets, as well as the construction of a FLS, become relatively straightforward. These concepts were discussed by Deaton[247] and later by Zadegan,[248] who implemented functionalities of Boolean logic gates and designed an FLS based on the use of the Förster resonance energy transfer (FRET).

At the same time, simpler molecules may also be utilized for the realization of fuzzy logic operations owing to their electrochemical or photochemical properties. One of such compounds was presented by Karmakar[249] — the emission profiles of polypyridyl-imidazole based complex of ruthenium and their dependence on the presence of selected ions (Fe^{2+}, Zn^{2+}, F^{-}) were utilized in this instance.

1.4.3. *Implementation of fuzzy logic systems in solid-state devices*

Although the use of molecular systems in the context of fuzzy logic implementation opens a variety of paths towards future applications — especially in scenarios, where some degree of interaction with the environment is required — some major drawbacks are still present. This is mainly due to the necessity of working in solutions, which in turn hinders the concatenation of such devices, makes them incompatible with the conventional, silicon-based architectures and due to specific requirements concerning input/output operations, impede interfacing in general.

At the same time, a substantial amount of research effort is put into studies on the utilization of solid-state materials in the

construction of information processing devices realizing *in-materio computing* concept, based on multi-valued logic systems (including fuzzy logic).[5,194] These studies aim as well for the compatibility of new systems with classic electronics, which is achievable, since most of these devices utilize electrical signals as input and/or output. Moreover, this approach gives an opportunity to harness molecules, which may be used in a similar manner to the abovementioned (e.g., to facilitate interactions with the environment) or in order to modify the properties of a base material.

A good example of a solid-state element capable of realizing FLS functionalities is given in the work by Bhattacharjee[251] in which a tantalum oxide-based device, exhibiting some memristive properties is discussed, as a suitable platform for designing multi-valued logic gates. Another interesting approach was demonstrated by Xu and Yan, who realized sensing at the molecular level with the use of europium functionalized metal–organic frameworks, fluorescent response of which was used to define a so-called "Intelligent Molecular Searcher" utilizing some elements of the fuzzy logic formalism in order to detect changes in the concentration of selected ions.[252]

An interesting extension to the aforementioned devices may be realized with the use of light as one of the inputs. The authors of this chapter presented two hybrid materials, both composed of titanium dioxide modified with either anthraquinone (Figure 1.8)[250] or cyanocarbons,[5] as suitable platforms for the implementation of Fuzzy logic formalism. In these cases, we used the photocurrent generation patterns of the nanocomposites to assign fuzzy sets and define rule bases. Since the proposed devices may be controlled by both applied bias and the change of incident light wavelengths, it is possible to concatenate them with existing optoelectronic elements into more sophisticated networks capable of complex information processing tasks.

1.4.4. *Neuromorphic devices*

A closely related field, which also aims at mimicking some of the fundamental biological structures and processes, focuses on the

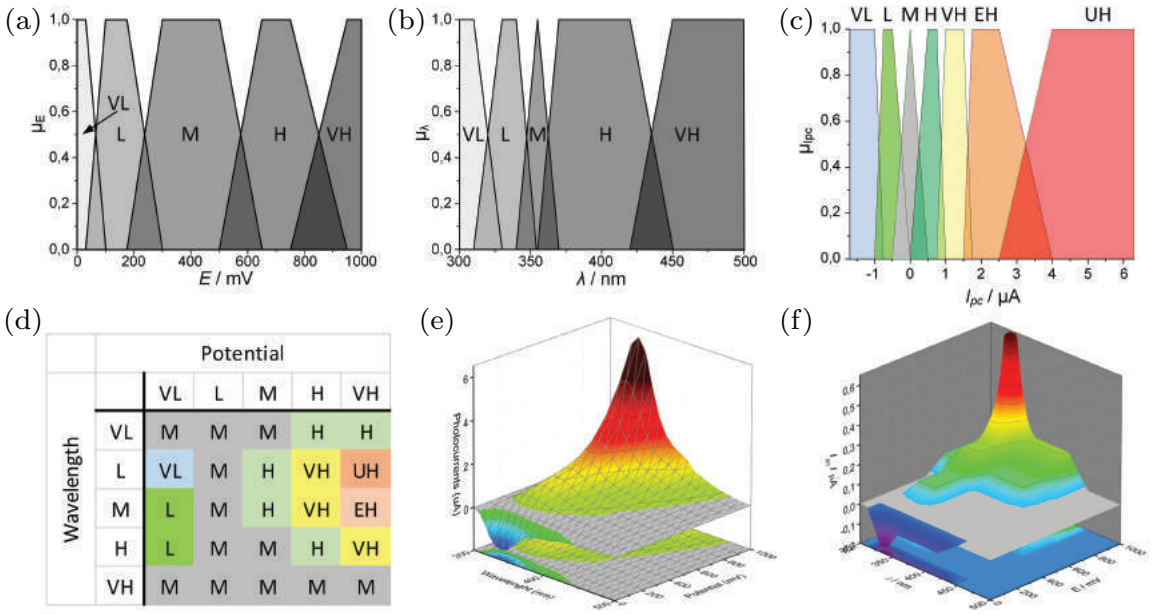

Figure 1.8. The process of fuzzification of input (a) and (b) and output (c) signals in the experiment involving titanium dioxide modified with anthraquinone is depicted. The rules base (d), the original photocurrent generation pattern (e) and the result of defuzzification is shown (f). Adapted from Ref. [250].

implementation of nervous system functionalities within software and hardware frameworks. Here, we discuss exclusively hardware realizations of the neuromorphic engineering concepts with a strong emphasis put on *in-materio* computing approach. This class of solutions gains substantial interest, as it opens ways for the utilization of unconventional information processing devices in scenarios — such as chemical sensing, multi-valued logic implementation, etc., — in which classic electronic elements are unsuitable. Moreover, the *in-materio* computing is more energy-efficient in some applications than the solutions based on CMOS architectures.[27,253–256]

The basic operation of neurons and synapses may be recreated within different systems capable of dynamical response to the external stimulus and evolution of its internal state in time. Selected concepts of neuromorphic engineering have already been realized within the *in-materio* computing framework with the use of both solution-based and solid-state systems. Ideally, these devices should be also easily concatenated into networks of higher complexity, allowing mimicking of neural networks with multiple nods, in order

to implement more sophisticated functionalities. In the former case (the use of molecules in solutions), this task seems to be difficult to achieve, hence this approach is rather underrepresented in the literature.

Nonetheless, one may find several realization of neuromimetic systems falling within this solution-based design — one of the commonly applied approaches assumes the use of chemical reactions, which exhibit a tendency to remain out of equilibrium.[232] A good platform meeting this requirement is provided by oscillating reactions, such as the Belousov–Zhabotinsky (BZ) reaction or the Briggs–Rauscher (BR) reaction, which may be used for recreation of spiking patterns observed in biological structures,[47,257] but also for such sophisticated tasks, as image and pattern recognition.[62]

An interesting variation of such systems is achieved, when luminescent or photochromic compounds are introduced to the system. Since BZ reaction is capable of modulating the optical input in the UV–vis region, these periodic changes will become a perturbation for other light-absorbing compounds, which will synchronize with BZ oscillations in one of two different ways: in-phase — if processes involving an additional agent are fast — or out-of-phase — in the case its response is slow.[50] This, in turn, allows realization of different dynamics characteristic for a variety of neural structures, including the functionality of so-called chaotic neurons — in this case the transport processes within solution play an important role[48,49,66,67] — the characteristics of which may be utilized in the cryptography or random number generation.

Finally, as mentioned before, the concatenation of individual cells is not an easy task, however some internal feedback loops exist within this class of systems, which open the way for the realization of simple neural networks. Changes in concentration and ratios between particular constituents of the system, as well as modifications various parameters describing both the device and optical input(s) enables implementation of different circuits — of both unidirectional and recurrent characters — and their dynamical reconfiguration.[50,68]

Despite the aforementioned possibilities of connecting solution-based systems into more complex architectures and their internal

capabilities to realize information processing in a manner similar to simple neural networks, there are some limitations to this approach. A more promising and versatile platform for the design of hardware neuromimetic systems is provided by solid-state elements. Here, three distinctive pathways may be defined: the first one assumes the use of classic, silicon-based electronics and existing, or slightly modified elements — this scenario, as discussed in the former sections of this chapter, is not always energy-efficient and lacks the flexibility (e.g., in terms of possible interactions with light or chemical entities)[195,258] — the second one, quite common nowadays, focuses on the use of memristors and memristive devices[194,259–261] and usually bases on the analysis of electrical inputs/outputs; this approach is discussed in the previous paragraphs — finally, the third one aims at the utilization of interactions of various materials (including nanocomposites) with small molecules, electrical stimuli and/or light, in an attempt to mimic the dynamics of individual neurons/synapses and complex neuronal structures.[262–265]

Here, we want to focus on the use of hybrid materials and their interactions with light — theses systems may offer response times close to the ones observed for the biological structures and can be fairly easily concatenated, as one of the inputs and an output of such a device are compatible (usually they are of electrical type). Moreover, the interplay between thermodynamic and kinetic aspects of charge carriers generation under irradiation in numerous nanocomposites provides the required level of complexity for the recreation of biological neurons and synapses dynamics (*vide infra*).[5] These features make light-sensitive hybrid materials a perfect platform for the realization of selected concepts falling within the neuromorphic engineering approach.

One of the good examples of neuromimetic devices exhibiting short-term memory effect is a binary hybrid composed of cadmium sulfide — which is responsible for the photocurrent generation — and multi-walled carbon nanotubes — which provide additional trapping states for electrons from the conduction band of CdS — sandwiched between two ITO@PET electrodes with an addition of ionic liquid.[266] Upon sample irradiation with a pulsed input the

device exhibits Hebbian-like plasticity.[267] Moreover, the profile of generated anodic photocurrent spikes can be controlled through even subtle changes in various experimental parameters (electrode potential, light wavelength, etc.) but also the time characteristics of the optical stimuli (e.g., the length of pulses, their number and interval between them).

It is noteworthy that, for a certain set of conditions it is possible to realize within the described system two fundamental modes of the synaptic response — potentiation (an increase in subsequent spikes intensity) and depression (a decrease in the subsequent output signals). This feature results directly from the electron trapping/detrapping (within MWCNTs) dynamics — the hypothesis proven based on the numerical calculations carried out for an appropriate equivalent circuit. Even more surprisingly, the application of mathematical formalism, used typically for the analysis of biological structures (defined within the SRDP and the STDP models) reveals that the characteristic time constants describing the device fit almost perfectly with the values observed for neural structures in living organisms.

Even more complex neuromimetic behavior may be implemented with the use of intrinsic charge carriers trapping/detrapping dynamics of nanocrystalline cadmium sulfide rich with additional electronic states present in the forbidden band. It was demonstrated that even a very rudiment photoelectrochemical device made of ITO@PET electrode covered with CdS in a simple three-electrode setup with the addition of an optical input is capable of sophisticated pattern recognition tasks realized typically by software Artificial Neural Networks — in this particular case the recognition of handwritten digits was carried out — with relatively high energy efficiency and satisfactory (taken into consideration the simplicity of the used system) separability.[268]

In this study, the non-trivial interplay between thermodynamics and kinetics of charge carriers generation and trapping events leads to a similar short-term memory effect as in the above-mentioned case, but here the train of light pulses is used as the stimuli encoding individual rows of pixels constituting a particular digit.

The dynamical response of the device, exhibiting an increasing intensity of subsequent photocurrent spikes generated within CdS (which results from various time constants characterizing processes involving two types of trapping states and the interfacial electron transfer), may be analyzed through the application of different threshold levels. Since encoded digits vary distinguishably in terms of pixels dispersion, the number of events, for which a specific threshold is exceeded fluctuates between the rows characteristically for each digit (Figure 1.9). When compared with a simple pixel counting method,

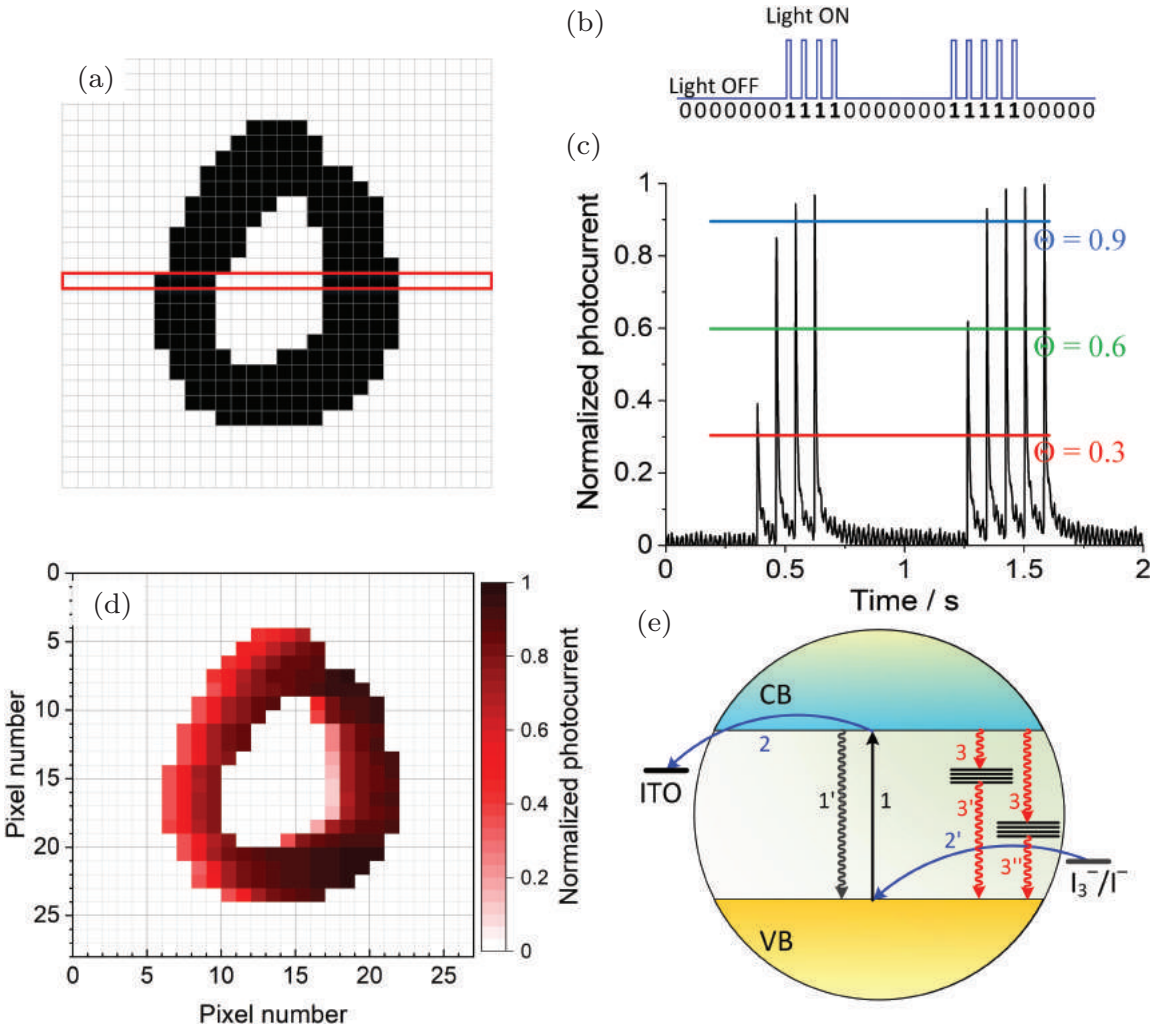

Figure 1.9. A handwritten character (a) encoded into a train of light pulses row by row (b). The resulting series of photocurrent spikes with three thresholds levels (c). The result of reconstruction (d). A simplified mechanism responsible for the short-term memory effect exhibited by nanocrystalline CdS (e). Adapted from Ref. [268].

one observes a significant increase in the recognition capability related to the use of proposed system.

1.5. Alternative Computing in Autonomous Robotics

The social request for the autonomous walking robot is growing. For example, in order to prevent secondary disasters during lifesaving, the autonomous robot is necessary to search and rescue in the harsh situations where humans cannot physically intervene.[269] Conventional autonomous walking robots had used the system modeling an assumed behavior pattern beforehand and choosing an action depending on the situation.[270] However, it is difficult to adapt to the unexpected situation because it is necessary for the conventional robot to assume enormous behavior patterns, and the action not modelled is impossible. Therefore, a new control system is necessary for choosing an appropriate action depending on the situation for the autonomous walking robot in order to walk in unknown environment.

Recently, natural computing inspired by physical systems in nature and biology[271] have attracted attention in computer hardware research field in terms of the efficient solution search for intractable problems. An interesting example is an amoeboid organism; it optimizes the body shape to maximize intake of the bait through trial and error.[272] Aono *et al.* developed amoeba-based solution search system, utilizing the search ability of the amoeboid organism and demonstrating the computing ability of the system by solving traveling salesman problem (TSP).[273]

In this section, we describe our amoeba-inspired autonomous walking robot that implements the amoeba-inspired electronic solution search system "electronic amoeba".[274] This robot successively searches for the appropriate footwork step by step to traverse uneven ground without any programming and pre-learning how to walk. Then we describe our approach to obtain environmental information and to take action utilizing physicality of the robot. Finally, we mention the amoeba-inspired autonomous control combined with reinforcement learning for achieving both adaptivity and efficient movement.

1.5.1. *Amoeba-based solution search system and electronic amoeba*

The electronic amoeba implemented for the autonomous robot control is inspired by the amoeba-based solution search system.[272] There are four essences of the amoeboid organism in terms of the searching: spreading pseudopods for maximizing intake of bait, avoiding harmful light, fluctuations in motion, and volume conservation. By utilizing these elements, the amoeboid organism achieves efficient solution search for the optimization problems. The electronic amoeba electronically implements the essence using an analog and/or digital electronic system.

Figure 1.10(a) shows a schematic illustration of the amoeba-based solution search system. The amoeboid organism placed on the

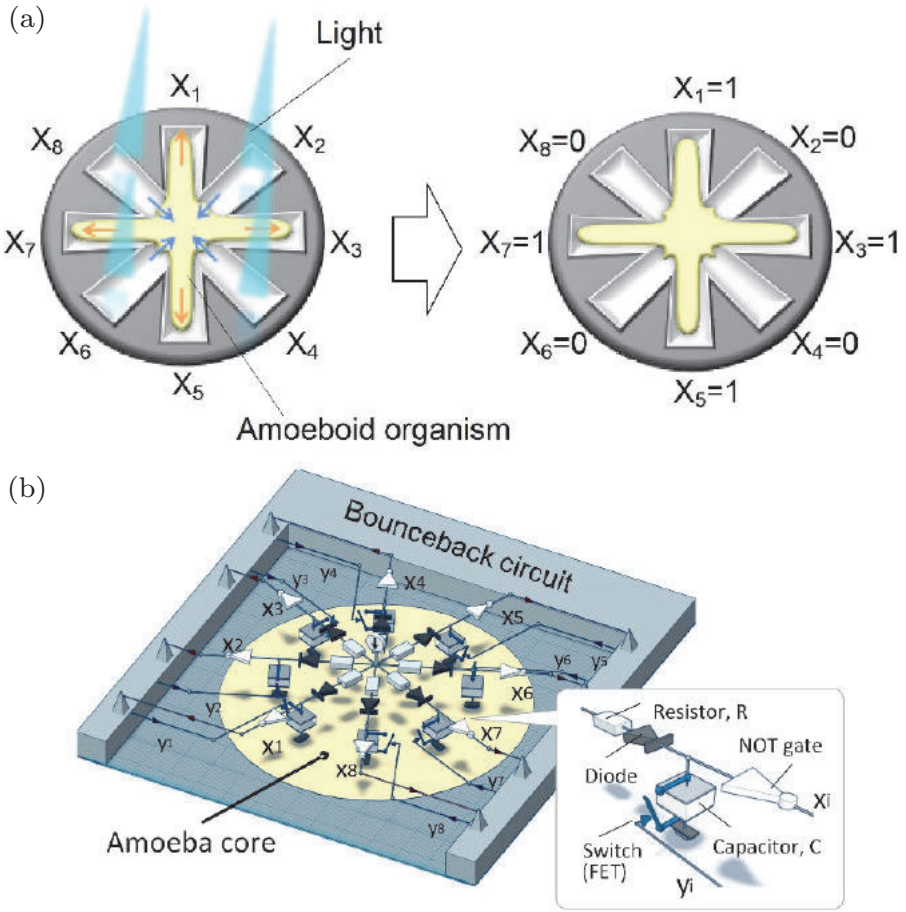

Figure 1.10. Schematic illustrations of (a) an amoeba-based solution search system for solving optimization problem and (b) an electronic amoeba mimicking the essential dynamics of the amoeboid organisms.

chip having grooves filled with agar spreads all pseudopods along the grooves to increase bait intake. When a groove lane is selectively irradiated by light, the amoeboid organism shrinks the pseudopod along the lane. The state variable X_i is assigned to ith groove; when the pseudopod extends to the groove i, $X_i = 1$, otherwise $X_i = 0$.

The amoeboid organism searches for the state that maximizes the bait intake by expanding and shrinking the pseudopods in the chip. To map the problem onto the system, we define a bounceback rule, which is a set of the light irradiation rules depending on the state variables. The bounceback rule is designed to prohibit the amoeboid organism from taking the state variables that violate the constraints of the problem. Deformation of the amoeboid organism and bounceback by the light irradiation are alternately proceeded. After that, the amoeboid organism becomes stable over time. The state variable at this time corresponds to the solution; there is no variable that violates the bounceback rule and the constraints are satisfied. The electronic amoeba (Figure 1.10(b)) follows the process of the amoeba-based system, however, it can proceed in the process much faster than the amoeba organism.

There are several options to map the bounceback rule for the electronic amoeba. A convenient way is to use a micro-controller having many I/O terminals. In many cases, the integrated development environment (IDE) is available and the rule can be directly written using Boolean operators implemented in the programming language. It is also easy to rewrite the instance. The state variable values of the amoeba core are sampled and they are processed in a digital manner. A disadvantage is that synchronous operation under clocking might cancel unique dynamics of the amoeba core working as an analog electronic circuit. Another option is full analog circuit implementation including the bounceback rule unit. Figure 1.11 shows a system with a crossbar implementing of the bouceback rule for maximum cut (Max-Cut) and TSP.[275] In these problems, an instance of the problem is represented by a weighted graph. The graph is physically implemented using a fully connected crossbar with resistors at appropriated cross points. The memristor crossbar

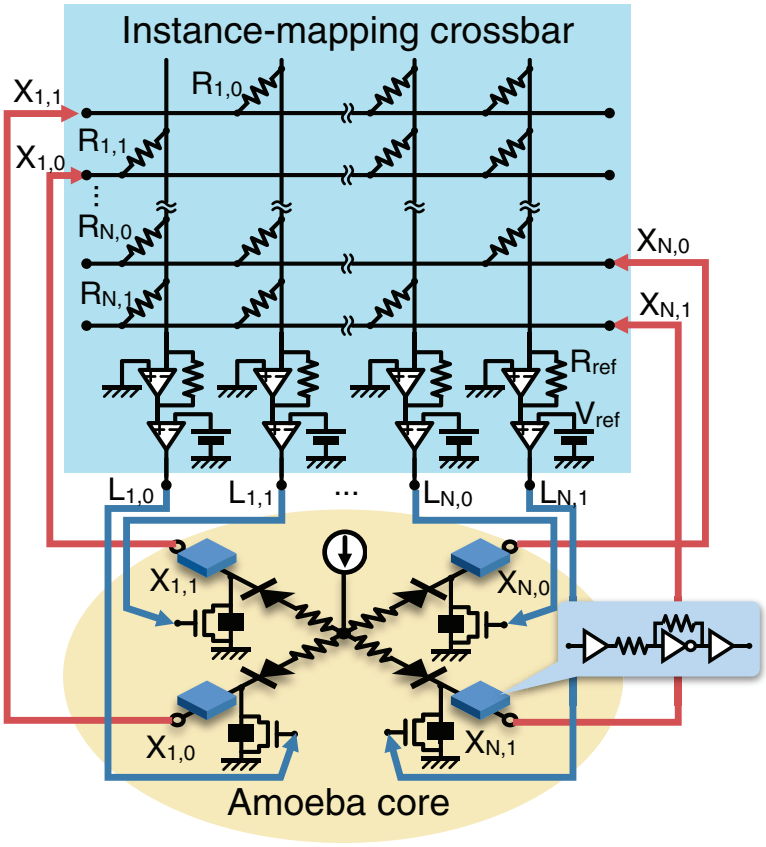

Figure 1.11. Electronic amoeba with a crossbar circuit for solving the Max-Cut and TSP problems.

is expected for reconfiguration of the graph, that is, rewrite the instance. Analog circuit operation of the whole system can fully utilize the dynamics of the electronic circuits, which should achieve efficient solution search with less power consumption.

1.5.2. *Amoeba-inspired autonomously walking robot*

The amoeba-inspired autonomous walking robot that we have developed consists of a commercially available four-legged robot and an electronic amoeba which is implemented in the microcomputer with amoeba-inspired solution search algorithm. Figure 1.12 shows the photograph of the robot. This robot has only a touch sensor on each toe and the sensor detects the ground contact of the leg. The electronic amoeba searches the leg bending motion as a variable

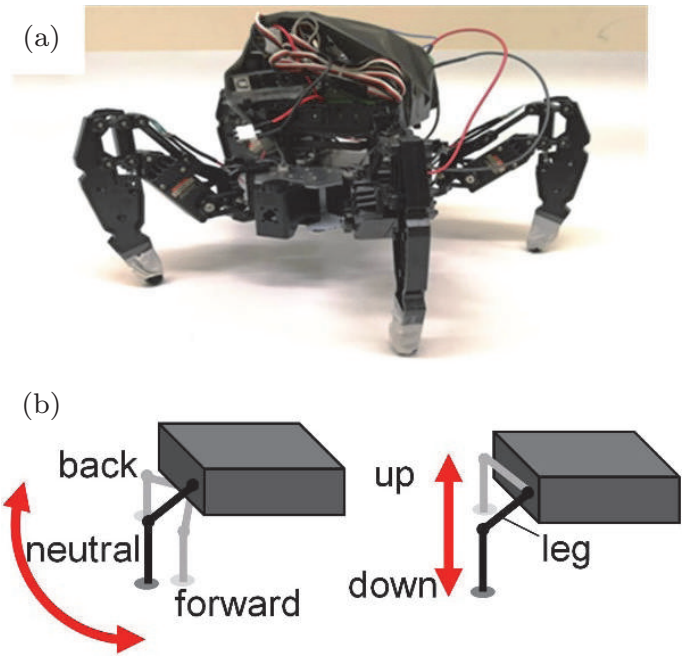

Figure 1.12. Amoeba-inspired autonomous walking robot: (a) photograph and (b) leg bending motions used in the robot walking.

of the optimization problem. There are six possible states for each leg and total 64 combinations are available as footwork for the robots. The electronic amoeba searches for the appropriate footwork at each walking step depending on the conditions of the ground and the robot.

To find optimal footwork for walking, it is necessary to formulate the constrain in terms of walking. We designed the bounceback rules so that the robot avoided the leg motions that led to falling or retreating based on information of the leg bending and the ground contact. We prepared 28 bounceback rules; for example, the rule prohibits an unstable posture that retracts two or more feet simultaneously. When the electronic amoeba finds a stable state that satisfies all rules, the robot stops walking. Therefore, to keep the robot walking, we added another mechanism to the algorithm that randomly canceled the bounceback with probability $\mathbf{W} = \{w_i\}, w_i \in [0, 1]$ at each step unless the robot fell or retreated. We selected eight rules as a subset $\boldsymbol{R}$ from the prepared 16 bounceback rules and ith rule, R_i, was weighted by w_i (Table 1.1).

Table 1.1. List of bounceback rules for autonomous waking.

1	When the robot starts, then reset all bounceback rules.
2	If Leg(i) in direction (j) is up at time (t), prohibit Leg(i) from down at the same time.
3	If Leg(i) in direction (j) is down at time (t), prohibit Leg(i) from up at the same time.
4	If number of legs with sensor on <2, then prohibit legs up.
5	If one of forelegs is twisted back, then prohibit another from moving back.
6	If one of hind legs is twisted forward, then prohibit another from moving forward.
7	If Leg(i) is twisted forward, prohibit leg in diagonal position from moving excepting forward.
8	If Leg(i) is twisted back, prohibit leg in diagonal position from moving excepting back.
9	If Sensor(i) is on, then prohibit Leg(i) from moving forward + down, and permit Leg(i) moving back + down, with a certain probability.
10	If Sensor(i) is off, then prohibit Leg(i) from moving back + up and permit Leg(i) moving forward + up, with a certain probability.
11	If Leg(i) is down and Sensor(i) is off, then permit Leg(i) moving laterally, with a certain probability.
12	If Leg(i) is up and Sensor(i) is off, then permit Leg(i) down and keeping lateral position, with a certain probability.
13	If Leg(i) is up and Sensor(i) is off, then permit Leg(i) down and laterally moving to another side, with a certain probability.
14	If Leg(i) is own and Sensor(i) is on, then permit Leg(i) up keeping lateral position, with a certain probability.
15	If Leg(i) is down and Sensor(i) is on, then permit Leg(i) up and laterally moving to another side, with a certain probability.
16	If Leg(i) is up and Sensor(i) is on, then permit Leg(i) down keeping lateral position, with a certain probability.

1.5.3. *Physicality for the identification of ground condition*

For smooth and efficient walking, information of the ground is important. Conventional robots use visual information to identify the ground condition. However, visual information processing has the drawback of large processing load. Therefore, we investigated a simple detection scheme of the ground condition focusing on physicality.

We implemented two walking modes in the robot, that is, the conventional footwork walking mode and the amoeba-inspired walking mode. In the conventional mode, the robot walked according to the programmed footwork routines. The robot could walk easily on the smooth ground in the conventional walking mode. On the other hand, the amoeba-inspired walking mode was necessary to walk on the rough ground. Thus, we investigated to use physicality to detect the ground condition in order to switch the walking modes depending on the condition. We used the body balance sensation and the tactile sensation to identify the ground condition without any visual information.

First, we explain how to use the balance sensation for identification. We attached an acceleration sensor to the head of the robot. From detailed observation of the walking robot, we found that the time series of the body tilt angle depended on the ground condition; the variation of the tilt angle was large when the robot walked on smooth ground; on the other hand, the variation was small when it walked on the rough.

Tactile sensation was used for identification of the ground condition as follows. We attached a pressure sensor to the toe of the robot. Looking into the correlation between the pressure of the feet and the ground condition, we found that the pressure on all feet were constant when the robot walked on smooth ground, whereas the pressures became unbalanced between the feet when it walked on rough ground.

Recently we experimentally demonstrated the feasibility of the above two physicality approaches in terms of detecting the ground condition in the vicinity of the robot, which will appear elsewhere. Our approach makes it possible to detect the environment condition with very low processing load.

1.5.4. *Integration of reinforcement learning for efficient walking*

An advantage of our amoeba-inspired walking robot is to have an ability to autonomously find out how to walk in unknown environment without any modification of the programming and learning.

On the other hand, an issue is to increase efficiency; it takes a long time to reach the destination, because the robot searches for the footwork at every step and the path of the robot is a quite meander; the robot does not learn how to walk. In this section, we investigate the way to implement learning capability into the amoeba-inspired walking robot.

The concept we consider to sophisticate the behavior of the robot is learning the weight **W** of the subset **R** of the bounceback rule, which has been introduced to avoid stopping the walking. We adopt the stochastic gradient ascent, which sequentially improves the selection probability of elemental motion. In our autonomous walking robot, the objective function is "walking forward without meandering". The robot learns w_i to maximize the objective function by means of the stochastic gradient ascent.

Figure 1.13 shows the concept of the reinforcement learning of the autonomous walking by integration of the footwork searching based

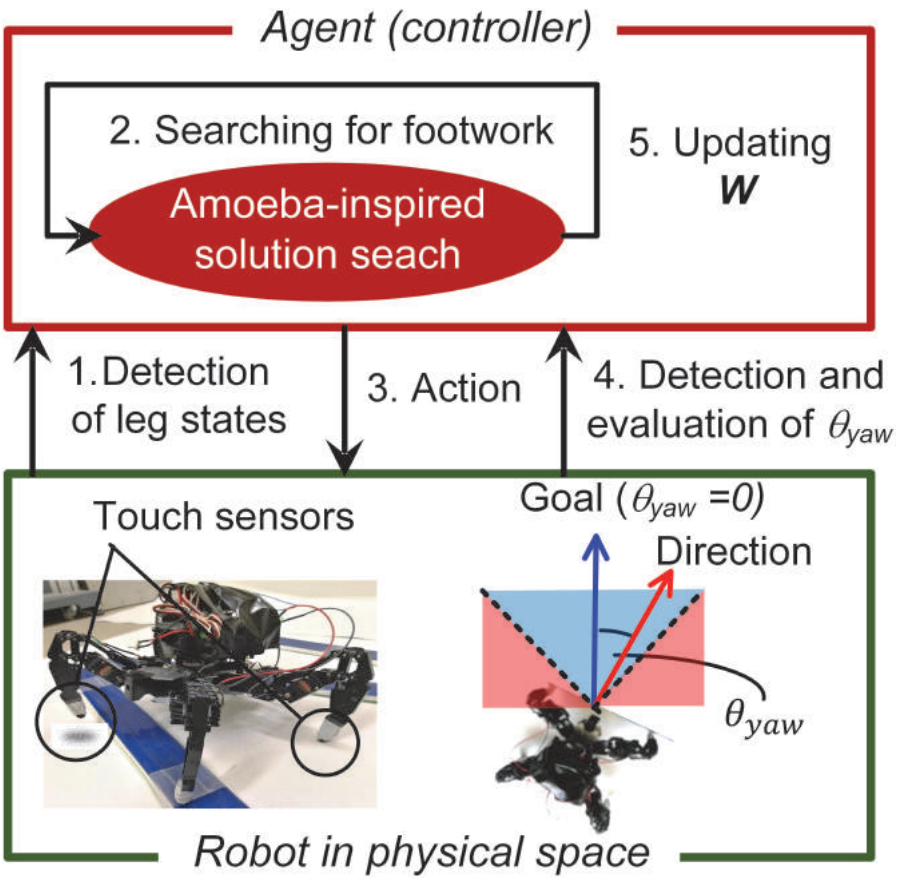

Figure 1.13. Amoeba-inspired autonomous walking control integrating reinforcement learning mechanism based on stochastic gradient ascent.

on the electronic amoeba and the learning based on the stochastic gradient ascent. Here, the process consists of a series of operations from 1 to 5 in Figure 1.13; detection of the lag states, searching for footwork under the bounceback rules, taking action according to the found footwork, evaluating the yaw and updating the weightings. In walking, the process is iterated. The footwork is decided based on the bounceback rule with **R** constraint. At this time, the yaw angle θ_{yaw} with respect to the destination of the robot is measured, and w_i is updated by the following Equation (1.38):

$$w_i\,(t+1) = \begin{cases} w_i\,(t) + a, & \text{if } |\theta_{\text{yaw}}| < \theta_{\text{th}} \\ w_i\,(t) - a, & \text{otherwise} \end{cases} \tag{1.38}$$

Here, θ_{th} is a threshold value for determining whether the robot meanders, and a is a correction value for $w_i(t)$ for R_i. If θ_{yaw} is smaller than θ_{th}, the robot is judged to increase the objective function and w_i is increased. Meanwhile, if θ_{yaw} is greater than θ_{th}, it is judged to meander and decrease the objective function, then w_i is reduced. When w_i is large, the robot frequently takes the footwork which is inhibited by R_i, because the probability of invoking the bounceback R_i is decreased. On the other hand, when w_i is small, it hardly takes the footwork. Thereby, the robot is expected to select appropriate footwork with higher probability for walking forward, avoiding fall and retreat movement, adapting the ground condition. This will enable the robot to carry out sophisticated walking without meandering. This autonomous robot control system is now under development.

The autonomous control system can be regarded as a reservoir computing circuit. The circuit operates in an oscillatory fashion, due to the feedback loops via the bounceback rules. The final state of each electronic pseudopod is thus a consequence of a random search algorithm implemented in a resistive-capacitive network. The fading memory feature is governed by the time constant of each pseudopod subcircuit. The present realization is an electronic hybrid reservoir with analog core and bounceback rules embedded in a digital circuit.[273] Furthermore, analogous circuit can be realized with charge controlled memristors, but this will require more complex

reset and signal conversion circuitry (a transistor and a NOT gate are sufficient for a capacitor-based circuit).

We have developed an autonomous walking robot based on the amoeba-inspired solution search for the optimization problem.[273] We successfully demonstrated the autonomous walking of the four-legged robot. We have also demonstrated that the robot had the ability to go over the obstacles without any information of the obstacles. We have investigated the identification of the ground condition using physicality without vision information. Furthermore, we proposed an approach to improve the walking efficiency by integrating reinforcement learning.

1.6. Alternative Computing and Soft Robotics

In many publications up to date, the term "soft robotics" is strictly connected to the mechanic aspects of robot movement. That is why this field of technology is usually full of terms "grippers" and "actuators",[276,277] although there are more and more trials for implementation of simple Boolean logic into non-rigid physical arrays.[278,279] Within the context presented here, we will focus rather on soft robotics as soft matter-based physical systems, capable of providing useful computations. These systems are necessary for the future design of independent processing units embedded in non-rigid entities. General strategy for that would be for the stimuli-responsive and switchable materials to be mixed into one entity, being able to adapt in various kind of situations. Soft machinery is currently very distant from the dystopian visions found in popular culture, yet possess some kind of independence, as the performed calculations are non-deterministic, based on the phenomena described in previous paragraphs.

The dominant developing idea throughout the literature for the controlling units for future robots is complete integration of the main processing unit, or units in cases of scattered logical units, with other robotic parts responsible for other functions — such as movement. Several examples of soft matter computer (SMC) were already proposed and presented.[280] This concept runs on three

computing principles: input encoding, physical mapping and output decoding. The system is based on a set of conductive fluid receptors (CFRs) — being similar to vascular system of living organisms. The same way as relay compounds (e.g., hormones) are released into the blood stream to spread information further, the stimuli are encoded spatially in the whole artificial soft body.

Mapping is performed as current measurement, done perpendicularly to the flow of fluids, making it possible to pass analog signal. Two types of immiscible fluids are introduced to such articular bloodstream — conductive and dielectric. Variations in time and intensity of current fluctuations make for information passing and signal amplification or filtration between set extreme values (e.g., $-2\,\mathrm{V}$ to $+2\,\mathrm{V}$). Digital computation is also possible — by joining several (at least two) conductive fluid receptors in parallel or in series. With two devices most of the Boolean logic gates (except for XOR) are possible to implement — depending on whether the receptors are connected by conducting fluid or not (Figure 1.14).

Three distinct applications in robot controllers were presented. The first one is a self-controlled softworm robot. Unfortunately, external peristaltic pump was used and should be circumvented for the next generation. Robot was capable of passing signal to actuators and CFRs through microchannel system — inducing movement, inching and wriggling — depending on the signal profile. No external control electronics was used only soft matter computer (Figure 1.15(a)). Non rigid logic gates were also implemented in soft gripper (Figure 1.15(b)). In this exemplary system, pressure on

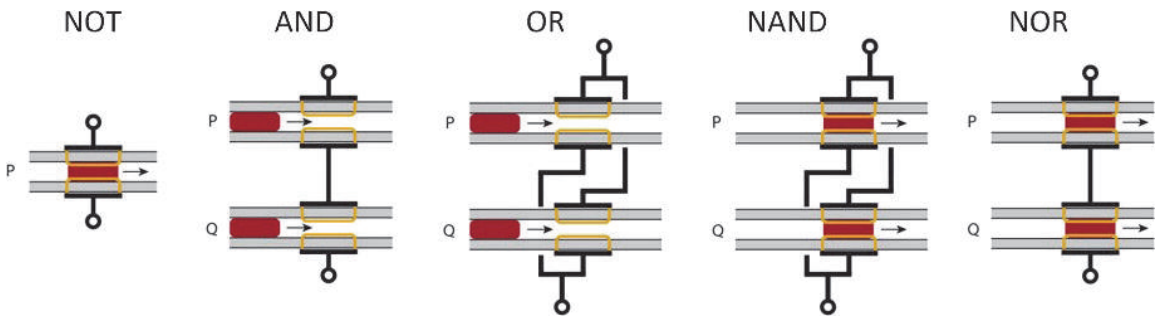

Figure 1.14. Simulation of logic gates by connecting two conductive fluid receptors (soft matter based) parallel. Colored section stands for conductive fluid volume. Adapted from Ref. [280]

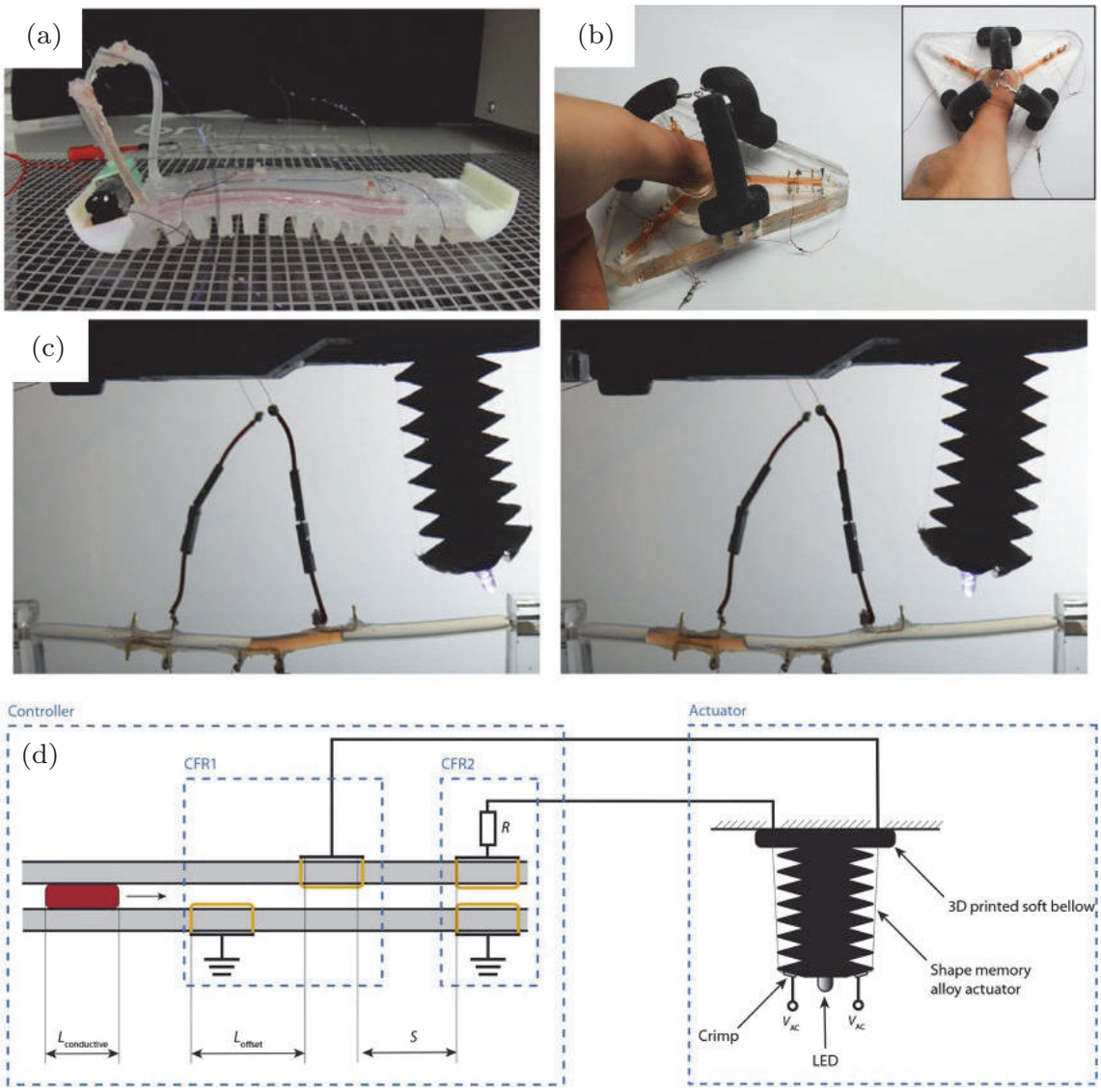

Figure 1.15. Demo devices built with non-rigid materials, controlled by soft matter computational systems: a softworm (a), a soft robotic gripper (b) and a two-degree of freedom bending actuator (c) with its blueprint (d). Adapted from Ref. [280].

the sensors controlled amount of released conductive fluid and the overall power of the grip. Authors suggest that this instance of soft matter computer can be used for delicate material handling, without use of commercial electronics controllers and sensor arrays, limiting number of building parts of the equipment.

In order to find ultimate solutions towards real-life applications, one should design flexible systems suitable for a variety of computational challenges. This should happen without tedious reconfiguration protocols and without requirement of external electronic devices

monitoring function of soft robot. That way soft robotic systems will be independent from the currently used silicon-based electronic microcontrollers. Development of said non-rigid systems will let us expand soft robotics field further, beyond just simple mimicking of biological movements — rather towards health and environmental monitoring, drug delivery, energy harvesting or pollution catalytic clean-up systems.

Scientists look not only into the animal world, but also facilitate robot design by mimicking plant body blueprints, such as machine-plant[281] or machine-fungus[282,283] interfaces. In such setup the latter act more as bio-sensors which are connected to external conventional electric signal measuring programmable devices. Plants used for the described purposes of computations/signal processing are: *Aloe vera* and *Echeveria suculentus* which were placed in Faraday cages. Devices which run on such setup can distinguish between environmental conditions. It is done by connecting sets of needle-type conductive electrodes to plants and probing them by pre-programmed set of electric pulses of several hundred Hz up to several kHz while introducing to external stimuli such as light or NaCl concentration. Electrical activity patterns are then distinguishably changed and allow for proper classification. Similar studies have been performed with *Pleurotus djamor*,[283] *Pleurotus ostreatus*[282] and *Physarum polycephalum*.[274,284]

These systems are yet very crude and additionally cannot be exactly classified as "soft" robots, even on the cellular level (cell walls) yet due to the semi-rigid character of specific computational parts are being described herein. They prove that hybrid approach is also a way of development for the whole soft robotics field. Plant computational systems will have a go in bio-sensing, pollution monitoring, agriculture certification. One can even think of such extraordinary applications as insect cooperation — such as when caterpillar-damaged plants tend to attract wasps for help.

The development of fully capable and independent robots with integrated processing units can be made in an evolutionary way. Several teams are trying to excel through next generations of soft

robots.[285,286] To achieve this task one must do several improvements simultaneously — provide better actuated and sensing solutions, signal amplification methods and protocols, computational schemes and patterns. And not forget to pack all of these functionalities into non-rigid, yet confined space.

In the end all parts of the mechanism can be encapsulated between lipid layer or liposomal membranes. Such encapsulation should firstly allow for conformational changes and locomotion as well as signal processing and computing. For these applications, neural network module processes the data collected by the sensors and makes decisions that are more than suitable. The coupling among the artificial neuron models can be not only optical[50] but also chemical and mechanical.[47,287–289] Motor proteins can act like actuators or motors. Energy for the system is supplied from chemical bond cleavage (e.g., from ATP molecules). That way amoeba or slime mold robots are being made. Next step of the hierarchical organization would be to gather, join and allow to interact/communicate molecular robots with each other. Similar to multi-cellular organisms and their existing complexity, each of the functional cell of soft robot should be compartmentalized into one main "body". For that purpose, methods of bio-printing mechanism need to be established, allowing in the future for facile construction of multi-cellular robots or hybrid robots with distinguishable functional organs. From the applications point of view each generation of such robots can help expand fields of both medical and pharmacological technologies — establishing novel drug delivery pathways or by advancing tissue engineering.

The futuristic vision of full integration of molecular scale soft robotics and *in materio* computing[285] is parallel to the visionary future of reservoir computing[182] — sensing, computing, and actuation is delegated to soft materials constituting at the same time the main body of the system. This crosses the boundary of artificial life,[290–292] where the boundaries between soft robotics and living structures as well as intelligence and AI become blurred.[4] This, however, at least presently, is a domain of science fiction.

1.7. Concluding Remarks

The nonlinear properties of physical materials, fractional character of numerous physical processes, and emergent properties of complex systems can be serendipitously harnessed for information processing purposes. Most of these systems cannot compete with contemporary silicon-based computers with von Neumann architecture, but it does not mean that the research on alternative computing paradigms utilizing unconventional materials (i.e., materials not explicitly meant for computation) is futile. It is a fascinating journey through unknown lands at the boundaries within various fields of science. This journey may bring breakthrough technologies for future information-based society and better healthcare. More importantly, it continuously pushes the limits of science in curiosity-driven research. What will this ultimately lead to? The best answer was given by K.K.V. Steincke: *It is difficult to make predictions, especially about the future.*[293]

Acknowledgments

Authors thank Professor Michał Zegrodnik for valuable discussions and Professor Kapela Pilaka for their support during preparation of the manuscript. The financial support from the Polish National Science Centre within the MAESTRO project (grant agreement No. UMO-2015/18/A/ST4/00058) is gratefully acknowledged. DP and PZ have been partly supported by the EU Project POWR.03.02.00-00-I004/16. SK and SO have been partly supported by JSPS KAKENHI, Grant Number JP16K14240, Japan. K.P. would like to thank the Foundation for Polish Science (FNP) for the financial support within START programme.

References

1. C. Truemann, Why data centres are the new frontier in the fight against climate change. (2019) https://www.computerworld.com/article/3431148/why-data-centres-are-the-new-frontier-in-the-fight-against-climate-change.html, accessed January 10th, 2020.
2. C. S. von Bartheld, J. Bahney, and S. Herculano-Houzel, The search for true numbers of neurons and glial cells in the human brain: A review of 150 years of cell counting. *J. Comp. Neurol.* **524**, 3865–3895 (2016).

3. S.-L. Ding, J. J. Royall, S. M. Sunkin, L. Ng, B. A. C. Facer, P. Lesnar, A. Guillozet-Bongaarts, B. McMurray, A. Szafer, T. A. Dolbeare, A. Stevens, L. Tirrell, T. Benner, S. Caldejon, R. A. Dalley, N. Dee, C. Lau, J. Nyhus, M. Reding, Z. L. Riley, D. Sandman, E. Shen, A. van der Kouwe, A. Varjabedian, M. Write, L. Zollei, C. Dang, J. A. Knowles, C. Koch, J. W. Phillips, N. Sestan, P. Wohnoutka, H. R. Zielke, J. G. Hohmann, A. R. Jones, A. Bernard, M. J. Hawrylycz, P. R. Hof, B. Fischl, and E. S. Lein, Comprehensive cellular-resolution atlas of the adult human brain. *J. Comp. Neurol.* **524**, 3127–3481 (2016).
4. G. R. Ivanitskii, The robot and the human. Where's their similarity limit? *Physics-Uspekhi* **61**, 871–895 (2018).
5. K. Pilarczyk, B. Daly, A. Podborska, P. Kwolek, V. A. D. Silverson, A. P. de Silva, and K. Szaciłowski, Coordination chemistry for information acquisition and processing. *Coord. Chem. Rev.* **325**, 135–160 (2016).
6. A. P. de Silva, *Molecular Logic-based Computation* (The Royal Society of Chemistry, Cambridge, 2012).
7. E. Katz, (ed.), *Biomolecular Information Processing* (Wiley-VCH, Weinheim, 2012).
8. E. Katz, (ed.), *Molecular and Supramolecular Information Processing* (Wiley-VCH, Weinheim, 2012).
9. K. Szaciłowski, *Infochemistry. Information Processing at the Nanoscale* (John Wiley & Sons, Chichester, 2012).
10. K. Szaciłowski, Digital information processing in molecular systems. *Chem. Rev.* **108**, 3481–3548 (2008).
11. M. Conrad, Molecular Computing. In M.C. Yovits (ed.), *Advances in Computers*, vol. 31, (Elsevier, 1990), pp. 235–324.
12. M. Conrad, R. R. Kampfner, K. G. Kirby, E. N. Rizki, G. Schleis, R. Smalz, and R. Trenary, Towards an artificial brain. *Biosystems* **23**, 175–218 (1989).
13. A. Adamatzky (ed.), *Advances in Unconventional Computing. Theory* (Springer International Publishing, 2017).
14. A. Adamatzky (ed.), *Advances in Unconventional Computing. Prototypes, Models and Algorithms* (Springer International Publishing, 2017).
15. S. Stepney, S. Rasmussen, and M. Amos, *Computational Matter* (Springer, Cham, 2018).
16. E. W. Plummer, R. Ismail, Matzdorf, A. V. Melechko, J. P. Pierce, and J. Zhang, Surfaces: A playground for physics with broken symmetry in reduced dimensionality. *Surf. Sci.* **500**, 1–27 (2002).
17. T. Calais and P. Valdivia y Alvarado, Advanced functional materials for soft robotics: Tuning physicochemical properties beyond rigidity control. *Multifunct. Mater.* **2**, 042001 (2019).
18. K. Nakajima, Muscular-Hydrostat Computers: Physical Reservoir Computing for Octopus-Inspired Soft Robots. In: S. Shigeno, Y. Murakami and T. Nomura (eds.), *Brain Evolution by Design: From Neural Origin to Cognitive Architecture* (Springer Japan, Tokyo, 2017), pp. 403–414.

19. K. Nakajima, H. Hauser, R. Kang, E. Guglielmino, D. G. Caldwell, and R. Pfeifer, Computing with a muscular-hydrostat system. In: *Proceedings of the 2013 IEEE International Conference on Robotics and Automation* (IEEE, Karlsruhe, 2013), pp. 1504–1511.
20. H.-L. Park, Y. Lee, N. Kim, D.-G. Seo, G.-T. Go, and T.-W. Lee, Flexible neuromorphic electronics for computing, soft robotics, and neuroprosthetics. *Adv. Mater.* **32**, 1903558 (2020).
21. Y. Lee and T.-W. Lee, Organic synapses for neuromorphic electronics: From brain-inspired computing to sensorimotor nervetronics. *Acc. Chem. Res.* **52**, 964–974 (2019).
22. G. Csaba and W. Porod, Coupled oscillators for computing: A review and perspective. *Appl. Phys. Rev.* **7**, 011302 (2020).
23. V. K. Vanag, "Cognitive" modes in small networks of almost identical chemical oscillators with pulsatile inhibitory coupling. *Chaos* **29**, 033106 (2019).
24. E. M. Izhikevich, *Dynamical Systems in Neuroscience* (MIT Press, Cambridge, 2007).
25. E. M. Izhikevich, Polychronization: Computation with spikes. *Neural Comput.* **18**, 245–282 (2006).
26. E. M. Izhikevich, Hybrid spiking models. *Phil. Trans. Royal Soc. A* **368**, 5061–5070 (2010).
27. E. Wlaźlak, D. Przyczyna, R. Gutierrez, G. Cuniberti, and K. Szaciłowski, Towards synthetic neural networks: Can artificial electrochemical neurons be coupled with artificial memristive synapses? *Jpn. J. Appl. Phys.* **59**, SI0801 (2020).
28. D. Przyczyna, P. Zawal, T. Mazur, M. Strzelecki, P. L. Gentili, and K. Szaciłowski, In-materio neuromimetic devices: Dynamics, information processing and pattern recognition. *Jpn. J. Appl. Phys.* **59**, 050504 (2020).
29. F. Rahma and S. Muneam, *Memristive Electronic Circuits. Dynamics, Synchronization and Applications* (Springer, Cham, 2019).
30. N. Kasabov, *Time-Space, Spiking Neural Networks and Brain-Inpired Artificial Intelligence* (Springer-verlag GmbH, Berlin, 2019).
31. L. F. Seoane, Evolutionary aspects of reservoir computing. *Phil. Trans. B* **374**, 20180377 (2019).
32. J. D. Hart, L. Larger, T. E. Murphy, and R. Roy, Delayed dynamical systems: Networks, chimeras abd reservoir computing. *Phil Trans. A* **377**, 20180123 (2019).
33. B. Kia, J. F. Lindner, and W. L. Ditto, Nonlinear dynamics as an engine of computation. *Philos. Trans. Roy. Soc. A: Math., Phys. Eng. Sci.* **375**, 20160222 (2017).
34. Monty Python, The spanish Inquisition. *Monty Python's Flying Curcus*, Series 2, Episode 2 (1970).
35. A. Otto, W. Just, and G. Radons, Nonlinear dynamics of delay systems: An overview. *Philos. Trans. Roy. Soc. A: Math. Phys. Eng. Sci.* **377**, 20180389 (2019).

36. D. Buonomano, *Your Brain Is a Time Machine: The Neuroscience and Physics of Time* (W. W. Norton & Company, New York, 2017).
37. M. I. Rabinovich, P. Verona, A. I. Selverston, and H. D. I. Abarbanel, Dynamical principles in neuroscience. *Rev. Mod. Phys.* **78**, 1213–1265 (2006).
38. P. L. Gentili, *Untangling Complex Systems. A Grand Challenge for Science* (CRC Press, Boca Raton, 2018).
39. D. Verstraeten, J. Dambre, X. Dutoit, and B. Schrauwen, Memory versus non-linearity in reservoirs. In: *The 2010 International Joint Conference on Neural Networks (IJCNN)* (2010), pp. 1–8.
40. H. Wang and X. Yan, Reservoir computing with sensitivity analysis input scaling regulation and redundant unit pruning for modeling fed-batch bioprocesses. *Ind. Eng. Chem. Res.* **53**, 6789–6797 (2014).
41. J. Dambre, D. Verstraeten, B. Schrauwen, and S. Massar, Information processing capacity of dynamical systems. *Sci. Rep.* **2**, 514 (2012).
42. J. T. Lizier, JIDT: An information-theoretic toolkit for studying the dynamics of complex systems. *Front. Robot. AI* **1**, 11 (2014).
43. S. Marzen and J. P. Crutchfield, Information anatomy of stochastic equlibria. *Entropy* **16**, 4713–4748 (2014).
44. R. D. Beer and P. L. Williams, Information processing and dynamics in minimally cognitive agents. *Cogn. Sci.* **39**, 1–38 (2015).
45. P. Barančok and I. Farkaš, Memory capacity of input-driven echo state networks at the edge of chaos. In: S. Wermter, C. Weber, W. Duch, T. Honkela, P. Koprinkova-Hristova, S. Magg, G. Palm, and A. E. P. Villa (eds.), *Artificial Neural Networks and Machine Learning — ICANN 2014* (Springer International Publishing, Cham, 2014), pp. 41–48.
46. P. L. Gentili, V. Horvath, V. K. Vanag, and I. R. Epstein, Belousov-Zhabotinsky "chemical neuron" as a binary and fuzzy logic processor. *Int. J. Uncov. Comput.* **8**, 177–192 (2012).
47. V. Horvath, P. L. Gentili, V. K. Vanag, and I. R. Epstein, Pulse-coupled chemical oscillators with time delay. *Angew. Chem. Int. Ed.* **51**, 6878–6881 (2012).
48. P. L. Gentili, M. Dolnik, and I. R. Epstein, "Photochemical oscillator": Colored hydrodynamic oscillations and waves in a photochromic system. *J. Phys. Chem. C* **118**, 598–608 (2014).
49. P. L. Gentili, M. S. Giubila, R. Germani, and B. M. Heron, Photochromic and luminescent compounds as artificial neuron models. *Dyes Pigments* **156**, 149–159 (2018).
50. P. L. Gentili, M. S. Giubila, R. Germani, A. Romani, A. Nicoziani, A. Spalletti, and B. M. Heron, Optical communication among oscillatory reactions and photo-excitable systems: UV and visible radiation can synchronize artificial neuron models. *Angew. Chem. Int. Ed.* **56**, 7535–7540 (2017).

51. H. Möllencamp, B. Flintjer, and W. Jansen, 200 Jahre "Pulsierendes Quecksilberherz" Zur Geschichte und Theorie eines faszinierenden elektrochemischen Versuchs. *CHEMKON* **1**, 117–125 (1994).
52. F. F. Runge, Merkwürdiges Verhalten des Quecksilbers in Berührung mit Salpetersäure und Eisen. *Ann. Phys.* **91**, 95–98 (1829).
53. M. T. M. Koper and J. H. Sluyters, Electrochemical oscillators: An experimental study of the indium/thiocyanate oscillator. *J. Electr. Chem. Interf. Electrochem.* **303**, 65–72 (1991).
54. O. Lev, A. Wolffberg, M. Sheintuch, and L. M. Pismen, Bifurcations to periodic and chaotic motions in anodic nickel dissolution. *Chem. Eng. Sci.* **43**, 1339–1353 (1988).
55. M. Orlik, *Self-Organization in Electrochemical Systems I. General Principles of Self-Organization. Temporal Instabilities* (Springer-Verlag, Heilderberg, 2012).
56. M. Orlik, *Self-Organization in Electrochemical Systems II. Spatiotemporal Patterns and Control of Chaos* (Springer-Verlag, Heilderberg, 2012).
57. Y. Jia and I. Z. Kiss, Decoding network structure in on-chip integrated flow cells with synchronization of electrochemical oscillators. *Sci. Rep.* **7**, 46027 (2017).
58. M. Wickramasinghe and I. Z. Kiss, Synchronization of electrochemical oscillators with differential coupling. *Phys. Rev. E* **88**, 062911 (2013).
59. J. Liu, L. Sheng, and Z. Z. He, *Liquid Metal Soft Machines* (Springer Nature, Singapore, 2019).
60. A. Adamatzky, A. Chiolerio, and K. Szaciłowski, Liquid metal droplet solves maze. *Soft Matter* **16**, 1455–1462 (2020).
61. M.-A. Tsompanas, C. Fullarton, and A. Adamatzky, Belousov-Zhabotinsky liquid marbles in robot control. *Sensors Actuators B: Chem.* **295**, 194–203 (2019).
62. P. L. Gentili and J.-C. Micheau, Light and chemical oscillations: Review and perspectives. *J. Photochem. Photobiol. C* **43**, 100321 (2020).
63. A. Adamatzky, M.-A. Tsompanas, T. C. Draper, C. Fullarton, and R. Mayne, Liquid marble photosensor. *ChemPhysChem* **21**, 90–98 (2020).
64. M. Iranifam, M. A. Segundo, J. L. M. Santos, J. L. F. C. Lima and M. H. Sorouraddin, Oscillating chemiluminescence systems: State of the art. *Luminescence* **25**, 409–418 (2010).
65. P. L. Gentili, M. S. Giubila, and B. M. Heron, Processing binary and fuzzy logic by chaotic time series generated by a hydrodynamic photochemical oscillator. *ChemPhysChem* **18**, 1831–1841 (2017).
66. P. L. Gentili, H. Gotoda, M. Dolnik, and I. R. Epstein, Analysis and prediction of aperiodic hydrodynamic oscillatory time series by feed-forward neural networks, fuzzy logic, and a local nonlinear predictor. *Chaos* **25**, 013104 (2015).
67. K. Hayashi, H. Gotoda, and P. L. Gentili, Probing and exploiting the chaotic dynamics of a hydrodynamic photochemical oscillator to implement all the basic binary logic functions. *Chaos* **26**, 053102 (2016).

68. B. Bartolomei, B. M. Heron, and P. L. Gentili, A contribution to neuromorphic engineering: Neuromodulation implemented through photochromic compounds maintained out of equilibrium by UV–visible radiation. *Rendiconti Lincei. Sci. Fis. Natur.* **31**, 39–52 (2020).
69. M. G. T. Fechner, Zur Elektrochemie. Über die Umkehrung der Polarität in der einfachen Kette. *Schweiggers J. Chem. Phys.* **53**, 129 (1828).
70. H. Okamoto, N. Tanaka, and M. Naito, Analogy between the stimulus-response characteristics of neuronal and electrochemical cells. *Chem. Phys. Lett.* **237**, 432–436 (1995).
71. S. R. Cole and B. Voytek, Brain oscillations and the importance of waveform shape. *Trends Cogn. Sci.* **21**, 137–149 (2017).
72. U. F. Franck and R. Fitzhugh, Periodische Elektrodenprozesse und ihre Beschreibung durch ein mathematisches modell. *Z. Elektrochem., Ber. Bunsenges. Phys. Chem.* **65**, 156–168 (1961).
73. H. Degn, Theory of electrochemical oscillations. *Trans. Faraday Soc.* **64**, 1348–1358 (1968).
74. J. L. Hudson and T. T. Tsotsis, Electrochemical reaction dynamics: A review. *Chem. Eng. Sci.* **49**, 1493–1572 (1994).
75. H. H. Uhlig and P. F. King, The flade potential of iron passivated by various inorganic corrosion inhibitors. *J. Electrochem. Soc.* **106**, 1 (1959).
76. K. S. G. Doss and D. Deshmukh, Electrochemical potential oscillations: The nickel-sulphuric acid system. *J. Electroanal. Chem. Interf. Electrochem.* **70**, 141–156 (1976).
77. T. P. Hoar and J. A. S. Mowat, Mechanism of electropolishing. *Nature* **165**, 64–65 (1950).
78. Y. E. Seidel, Z. Jusys, R. W. Lindström, M. Stenfeldt, B. Kasemo, and K. Krischer, Oscillatory behaviour in galvanostatic formaldehyde oxidation on nanostructured pt/glassy carbon model electrodes. *ChemPhysChem* **11**, 1405–1415 (2010).
79. T. Yamazaki and T. Kodera, Potential oscillation during anodic oxidation of hydrogen at a platinum electrode — I. experimental. *Electrochim. Acta* **34**, 969–975 (1989).
80. J. Wojtowicz, Oscillatory behavior in electrochemical systems. In J. O. Bockris and y. B. E. Conwa (eds.), *Modern Aspects of Electrochemistry* (Springer, Boston, 1972).
81. R. De Levie, On the electrocemical oscillator. *J. Electroanal. Chem. Interf. Electrochem.* **25**, 257–273 (1970).
82. M. T. M. Koper and J. H. Sluyters, Electrochemical oscillators: Their description through a mathematical model. *J. Electroanal. Chem. Interf. Electrochem.* **303**, 73–94 (1991).
83. M. Rudolph, M. Hromadova, and R. de Levie, Demystifying an electrochemical oscillator. *J. Phys. Chem. A* **102**, 4405–4410 (1998).
84. R. A. Spangler and F. M. Snell, Transfer function analysis of chemical kinetic systems. *J. Theor. Biol.* **16**, 366–380 (1967).
85. R. Suzuki, Electrochemical neuron model. *Adv. Biophys.* 115–156 (1976).

86. L. Zhang, Y. Qu, J. Huang, X. Feng, D. Li, and Y. Chen, Memory-effect-induced electrochemical oscillation of an Al-doped Li4Ti5O12 composite in Li-ion batteries. *Chem. Commun.* **55**, 1279–1282 (2019).
87. Y. Jia and I. Z. Kiss, Spontaneously synchronized electrochemical micro-oscillators with nickel electrodissolution. *J. Phys. Chem. C* **116**, 19290–19299 (2012).
88. S. Zhan, J. F. Miller, and A. M. Tyrrell, An evolutionary system using development and artificial genetic regulatory networks for electronic circuit design. *Biosystems* **98**, 176–192 (2009).
89. M. Rivera, G. Martínez Mekler, and P. Parmananda, Synchronization phenomena for a pair of locally coupled chaotic electrochemical oscillators: A survey. *Chaos* **16**, 037105 (2006).
90. N. Mazouz, K. Krischer, G. Flätgen, and G. Ertl, Synchronization and pattern formation in electrochemical oscillators: Model calculations. *J. Phys. Chem. B* **101**, 2403–2410 (1997).
91. A. Karantonis, M. Pagitsas, Y. Miyakita, and S. Nakabayashi, Manipulation of spatio-temporal patterns in networks of relaxation electrochemical oscillators. *Electrochim. Acta* **50**, 5056–5064 (2005).
92. I. Z. Kiss, V. Gáspár, and J. L. Hudson, Experiments on synchronization and control of chaos on coupled electrochemical oscillators. *J. Phys. Chem. B* **104**, 7554–7560 (2000).
93. Y. Liu, M. Sebek, F. Mori, and I. Z. Kiss, Synchronization of three electrochemical oscillators: From local to global coupling. *Chaos* **28**, 045104 (2018).
94. T. Chouzouris, I. Omelchenko, A. Zakharova, J. Hlinka, P. Jiruska, and E. Schöll, Chimera states in brain networks: Empirical neural vs. modular fractal connectivity. *Chaos* **28**, 045112 (2018).
95. K. Fukami, S. Nakanishi, H. Yamasaki, T. Tada, K. Sonoda, N. Kamikawa, N. Tsuji, H. Sakaguchi, and Y. Nakato, General mechanism for the synchronization of electrochemical oscillations and self-organized dendrite electrodeposition of metals with ordered 2D and 3D microstructures. *J. Phys. Chem. C* **111**, 1150–1160 (2007).
96. E. Strubell, A. Ganesh, and A. McCallum, Energy and policy considerations for deep learning in NLP (2019). arXiv, 1906.02243.
97. D. Silver, A. Huang, C. J. Maddison, A. Guez, L. Sifre, G. van den Driessche, J. Schrittwieser, I. Antonoglou, V. Panneershelvam, M. Lanctot, S. Dieleman, D. Grewe, J. Nham, N. Kalchbrenner, I. Sutskever, T. Lillicrap, M. Leach, K. Kavukcuoglu, T. Graepel, and D. Hassabis, Mastering the game of Go with deep neural networks and tree search. *Nature* **529**, 484–489 (2016).
98. G. Liebmann, Solution of partial differential equations with a resistance network analogue. *Br. J. Appl. Phys.* **1**, 92–103 (1950).
99. H. Kobayashi, J. L. White, and A. A. Abidi, An active resistor network for Gaussian filtering of images. *IEEE J. Solid-State Circ.* **26**, 738–748 (1991).

100. J. Hutchinson, C. Koch, J. Luo, and C. Mead, Computing motion using analog and binary resistive networks. *Computer* **21**, 52–63 (1988).
101. M. Hu, C. E. Graves, C. Li, Y. Li, N. Ge, E. Montgomery, N. Davila, H. Jiang, R. S. Williams, and J. J. Yang, Memristor-based analog computation and neural network classification with a dot product engine. *Adv. Mater.* **30**, 1705914 (2018).
102. J. J. Hopfield, Artificial neural networks. *IEEE Circ. Devi.* **4**, 3–10 (1988).
103. J. Borghetti, G. S. Snider, P. J. Kuekes, J. J. Yang, D. R. Stewart, and R. S. Williams, 'Memristive' switches enable 'stateful' logic operations via material implication. *Nature* **464**, 873–876 (2010).
104. E. Lehtonen and M. Laiho, Stateful implication logic with memristors. In *2009 IEEE/ACM International Symposium on Nanoscale Architectures* (2009), pp. 33–36.
105. S. Kvatinsky, G. Satat, N. Wald, E. G. Friedman, A. Kolodny, and U. C. Weiser, Memristor-based material implication (IMPLY) logic: Design principles and methodologies. *IEEE Trans. VLSI Syst.* **22**, 2054–2066 (2014).
106. S. Kvatinsky, D. Belousov, S. Liman, G. Satat, N. Wald, E. G. Friedman, A. Kolodny, and U. C. Weiser, MAGIC — Memristor-aided logic. *IEEE Trans. Circ. Syst. II: Express Briefs* **61**, 895–899 (2014).
107. N. Xu, T. G. Park, H. J. Kim, X. Shao, K. J. Yoon, T. H. Park, L. Fang, K. M. Kim, and C. S. Hwang, A stateful logic family based on a new logic primitive circuit composed of two antiparallel bipolar memristors. *Adv. Intellig. Syst.* **2**, 1900082 (2020).
108. Z. Sun, G. Pedretti, E. Ambrosi, A. Bricalli, W. Wang, and D. Ielmini, Solving matrix equations in one step with cross-point resistive arrays. *Proc. Nat. Acad. Sci.* **116**, 4123 (2019).
109. Z. Sun, G. Pedretti, A. Bricalli, and D. Ielmini, One-step regression and classification with cross-point resistive memory arrays. *Sci. Adv.* **6**, eaay2378 (2020).
110. Y. Taigman, M. Yang, M. Ranzato, and L. Wolf, DeepFace: Closing the gap to human-level performance in face verification. In *2014 IEEE Conference on Computer Vision and Pattern Recognition* (2014), pp. 1701–1708.
111. D. Ielmini and S. Ambrogio, 16 — Neuromorphic computing with resistive switching memory devices. In B. Magyari-Köpe and Y. Nishi (eds.), *Advances in Non-Volatile Memory and Storage Technology (Second Edition)* (Woodhead Publishing, 2019), pp. 603–631.
112. W. S. McCulloch and W. Pitts, A logical calculus of the ideas immanent in nervous activity. *Bull. Math. Biophys.* **5**, 115–133 (1943).
113. Q. Xia and J. J. Yang, Memristive crossbar arrays for brain-inspired computing. *Nat. Mater.* **18**, 309–323 (2019).
114. S. Stathopoulos, A. Khiat, M. Trapatseli, S. Cortese, A. Serb, I. Valov, and T. Prodromakis, Multibit memory operation of metal-oxide bi-layer memristors. *Sci. Rep.* **7**, 17532 (2017).

115. W. Banerjee and H. Hwang, Quantized conduction device with 6-bit storage based on electrically controllable break junctions. *Adv. Electron. Mater.* **5**, 1900744 (2019).
116. Q. Cao, W. Lü, X. R. Wang, X. Guan, L. Wang, S. Yan, T. Wu, and X. Wang, Nonvolatile multistates memories for high-density data storage. *ACS Appl. Mater. Interfaces* **12**, 42449–42471 (2020).
117. H. Zhao, Z. Dong, H. Tian, D. DiMarzi, M.-G. Han, L. Zhang, X. Yan, F. Liu, L. Shen, S.-J. Han, S. Cronin, W. Wu, J. Tice, J. Guo, and H. Wang, Atomically thin femtojoule memristive device. *Adv. Mater.* **29**, 1703232 (2017).
118. P. Yao, H. Wu, B. Gao, S. B. Eryilmaz, X. Huang, W. Zhang, Q. Zhang, N. Deng, L. Shi, H. S. P. Wong, and H. Qian, Face classification using electronic synapses. *Nat. Commun.* **8**, 15199 (2017).
119. P. M. Sheridan, F. Cai, C. Du, W. Ma, Z. Zhang, and W. D. Lu, Sparse coding with memristor networks. *Nat. Nanotech.* **12**, 784–789 (2017).
120. P. Yao, H. Wu, B. Gao, J. Tang, Q. Zhang, W. Zhang, J. J. Yang, and H. Qian, Fully hardware-implemented memristor convolutional neural network. *Nature* **577**, 641–646 (2020).
121. G. W. Burr, R. M. Shelby, S. Sidler, C. d. Nolfo, J. Jang, I. Boybat, R. S. Shenoy, P. Narayanan, K. Virwani, E. U. Giacometti, B. N. Kurdi, and H. Hwang, Experimental demonstration and tolerancing of a large-scale neural network (165 000 synapses) using phase-change memory as the synaptic weight element. *IEEE Trans. Electr. Dev.* **62**, 3498–3507 (2015).
122. V. Joshi, M. Le Gallo, S. Haefeli, I. Boybat, S. R. Nandakumar, C. Piveteau, M. Dazzi, B. Rajendran, A. Sebastian, and E. Eleftheriou, Accurate deep neural network inference using computational phase-change memory. *Nat. Commun.* **11**, 2473 (2020).
123. N. K. Upadhyay, H. Jiang, Z. Wang, S. Asapu, Q. Xia, and J. Joshua Yang, Emerging memory devices for neuromorphic computing. *Adv. Mater. Technol.* **4**, 1800589 (2019).
124. J. Jang, S. Park, G. W. Burr, H. Hwang, and Y. Jeong, Optimization of conductance change in Pr1–xCaxMnO3-based synaptic devices for neuromorphic systems. *IEEE Elect. Dev. Lett.* **36**, 457–459 (2015).
125. D. Joksas, P. Freitas, Z. Chai, W. H. Ng, M. Buckwell, C. Li, W. D. Zhang, Q. Xia, A. J. Kenyon, and A. Mehonic, Committee machines — a universal method to deal with non-idealities in memristor-based neural networks. *Nat. Commun.* **11**, 4273 (2020).
126. A. Chen and M. Lin, Variability of resistive switching memories and its impact on crossbar array performance. In *2011 International Reliability Physics Symposium*, (2011), pp. MY.7.1–MY.7.4.
127. H. Tsai, S. Ambrogio, P. Narayanan, R. M. Shelby, and G. W. Burr, Recent progress in analog memory-based accelerators for deep learning. *J. Phys. D: Appl. Phys.* **51**, 283001 (2018).

128. T. Gokmen and Y. Vlasov, Acceleration of deep neural network training with resistive cross-point devices: Design considerations. *Front. Neurosci.* **10**, 333 (2016).
129. M. Hu, J. P. Strachan, L. Zhiyong, R. Stanley, and Williams, Dot-product engine as computing memory to accelerate machine learning algorithms. In *2016 17th International Symposium on Quality Electronic Design (ISQED)*, (2016), pp. 374–379.
130. T. Deneux, A. Kempf, A. Daret, E. Ponsot, and B. Bathellier, Temporal asymmetries in auditory coding and perception reflect multi-layered nonlinearities. *Nat. Commun.* **7**, 12682 (2016).
131. S. B. Furber, F. Galluppi, S. Temple, and L. A. Plana, The SpiNNaker project. *Proc. IEEE* **102**, 652–665 (2014).
132. P. A. Merolla, J. V. Arthur, R. Alvarez-Icaza, A. S. Cassidy, J. Sawada, F. Akopyan, B. L. Jackson, N. Imam, C. Guo, Y. Nakamura, B. Brezzo, I. Vo, S. K. Esser, R. Appuswamy, B. Taba, A. Amir, M. D. Flickner, W. P. Risk, R. Manohar, and D. S. Modha, A million spiking-neuron integrated circuit with a scalable communication network and interface. *Science* **345**, 668 (2014).
133. M. Davies, Putting the learning, in machine learning processors: An introduction to the Loihi neuromorphic research chip. *Zenodo* (2018), doi:10.5281/zenodo.1313406.
134. Z. Xiao and J. Huang, Energy-efficient hybrid perovskite memristors and synaptic devices. *Adv. Electron. Mater.* **2**, 1600100 (2016).
135. T. Mazur, P. Zawal, and K. Szaciłowski, Synaptic plasticity, metaplasticity and memory effects in hybrid organic–inorganic bismuth-based materials. *Nanoscale* **11**, 1080–1090 (2019).
136. M. Ziegler, R. Soni, T. Patelczyk, M. Ignatov, T. Bartsch, P. Meuffels, and H. Kohlstedt, An electronic version of Pavlov's dog. *Adv. Func. Mater.* **22**, 2744–2749 (2012).
137. X. Yang, Y. Fang, Z. Yu, Z. Wang, T. Zhang, M. Yin, M. Lin, Y. Yang, Y. Cai, and R. Huang, Nonassociative learning implementation by a single memristor-based multi-terminal synaptic device. *Nanoscale* **8**, 18897–18904 (2016).
138. W. Wang, G. Pedretti, V. Milo, R. Carboni, A. Calderoni, N. Ramaswamy, A. S. Spinelli, and D. Ielmini, Learning of spatiotemporal patterns in a spiking neural network with resistive switching synapses. *Sci. Adv.* **4**, eaat4752 (2018).
139. Z. Wang, S. Joshi, S. Savel'ev, W. Song, R. Midya, Y. Li, M. Rao, P. Yan, S. Asapu, Y. Zhuo, H. Jiang, P. Lin, C. Li, J. H. Yoon, N. K. Upadhyay, J. Zhang, M. Hu, J. P. Strachan, M. Barnell, Q. Wu, H. Wu, R. S. Williams, Q. Xia, and J. J. Yang, Fully memristive neural networks for pattern classification with unsupervised learning. *Nat. Electron.* **1**, 137–145 (2018).
140. G. Pedretti, V. Milo, S. Ambrogio, R. Carboni, S. Bianchi, A. Calderoni, N. Ramaswamy, A. S. Spinelli, and D. Ielmini, Memristive neural network for on-line learning and tracking with brain-inspired spike timing dependent plasticity. *Sci. Rep.* **7**, 5288 (2017).

141. I. Chakraborty, A. Jaiswal, A. K. Saha, S. K. Gupta, and K. Roy, Pathways to efficient neuromorphic computing with non-volatile memory technologies. *Appl. Phys. Rev.* **7**, 021308 (2020).
142. R. Vilanova and A. Visioli, *PID Control in the Third Millennium* (Springer 2012).
143. J. C. Doyle, B. A. Francis, and A. R. Tannenbaum, *Feedback Control Theory* (Courier Corporation, 2013).
144. T. Glad and L. Ljung, *Control Theory* (CRC press, 2018).
145. N. Minorsky, Directional stability of automatically steered bodies. *J. Am. Soc. Naval Eng.* **34**, 280–309 (1922).
146. S. Bennett, *A History of Control Engineering, 1930–1955* (IET, 1993).
147. K. H. Ang, G. Chong, and Y. Li, PID control system analysis, design, and techology. *IEEE Trans. Control Syst. Technol.* **13**, 559–576 (2005).
148. P. Shah and S. Agashe, Review of fractional PID controller. *Mechatronics* **38**, 29–41 (2016).
149. V. Kumar, B. Nakra, and A. Mittal, A review on classical and fuzzy PID controllers. *Int. J. Intell. Control Syst.* **16**, 170–181 (2011).
150. W. S. Levine, *The Control Handbook (three volume set)* (CRC press, 2018).
151. L. Wang, T. Barnes, and W. R. Cluett, New frequency-domain design method for PID controllers. *IEE Proc. Control Theor. Appl.* **142**, 265–271 (1995).
152. G. Cohen, Theoretical consideration of retarded control. *Trans. Am. Soc. Mech. Eng.* **75**, 827–834 (1953).
153. J. G. Ziegler and N. B. Nichols, Optimum settings for automatic controllers. *Trans. Am. Soc. Mech. Eng.* **64**, (1942).
154. B. D. Tyreus and W. L. Luyben, Tuning PI controllers for integrator/dead time processes. *Ind. Eng. Chem. Res.* **31**, 2625–2628 (1992).
155. K. J. Åström and T. Hägglund, Automatic tuning of simple regulators with specifications on phase and amplitude margins. *Automatica* **20**, 645–651 (1984).
156. D. E. Rivera, M. Morari, and S. Skogestad, Internal model control: PID controller design. *Ind. Eng. Chem. Proc. Des. Devel.* **25**, 252–265 (1986).
157. B. M. Vinagre, C. A. Monje, A. J. Calderón, and J. I. Suárez, Fractional PID controllers for industry application. A brief introduction. *J. Vibrat. Control* **13**, 1419–1429 (2007).
158. H. Baogang and Y. Hao, Review of fuzzy PID control techniques and some important issues. *Acta Autom. Sin.* **27**, 567–584 (2001).
159. H. Shu and Y. Pi, PID neural networks for time-delay systems. *Comput. Chem. Eng.* **24**, 859–862 (2000).
160. J. Kang, W. Meng, A. Abraham, and H. Liu, An adaptive PID neural network for complex nonlinear system control. *Neurocomputing* **135**, 79–85 (2014).
161. L. Liu, F. Pan, and D. Xue, Variable-order fuzzy fractional PID controller. *ISA Trans.* **55**, 227–233 (2015).

162. S. Das, I. Pan, S. Das, and A. Gupta, A novel fractional order fuzzy PID controller and its optimal time domain tuning based on integral performance indices. *Eng. App. Art. Intellig.* **25**, 430–442 (2012).
163. I. Pan and S. Das, Fractional order fuzzy control of hybrid power system with renewable generation using chaotic PSO. *ISA Trans.* **62**, 19–29 (2016).
164. H. O. Bansal, R. Sharma, and P. Shreeraman, PID controller tuning techniques: A review. *J. Control Eng. Technol.* **2**, 168–176 (2012).
165. D. E. Seborg, A perspective on advanced strategies for process control (revisited). In *Advances in Control* (Springer, 1999), pp. 103–134.
166. B. W. Bequette, Nonlinear control of chemical processes: A review. *Ind. Eng. Chem. Res.* **30**, 1391–1413 (1991).
167. P. de Moura Oliveira, Modern heuristics review for PID control optimization: A teaching experiment. In *2005 International Conference on Control and Automation*, vol. 2, (IEEE, 2005), pp. 828–833.
168. G. Stephanopoulos and C. Han, Intelligent systems in process engineering: A review. *Comput. Chem. Eng.* **20**, 743–791 (1996).
169. K. J. Åström and T. Hägglund, The future of PID control. *Contr. Eng. Prac.* **9**, 1163–1175 (2001).
170. S. Yamamoto and I. Hashimoto, Present status and future needs: The view form Japanese industry. In Y. Arkun and W. H. Ray (eds.), *Proceedings of the 4th International Conference on Chemical Process Control* (CACHE, Austin, 1991).
171. D. B. Ender, Process control performance: Not as good as you think. *Control Eng.* **40**, 180–190 (1993).
172. R. Zafarani, M. A. Abbasi, and H. Liu, *Social Media Mining: An Introduction* (Cambridge University Press, 2014).
173. T. K. Lee, J. H. Cho, D. S. Kwon, and S. Y. Sohn, Global stock market investment strategies based on financial network indicators using machine learning techniques. *Exp. Syst. Appl.* **117**, 228–242 (2019).
174. M. Tkáč and R. Verner, Artificial neural networks in business: Two decades of research. *App. Soft Comput.* **38**, 788–804 (2016).
175. R. Rathi, Effect of Cambridge Analytica's Facebook ads on the 2016 US Presidential Election. (2019). https://towardsdatascience.com/effect-of-cambridge-analyticas-facebook-ads-on-the-2016-us-presidential-election-dacb5462155d, accessed 02.09.2020, 2020.
176. I. N. Da Silva, D. H. Spatti, R. A. Flauzino, L. H. B. Liboni, and S. F. dos Reis Alves, Artificial neural network architectures and training processes. In *Artificial Neural Networks* (Springer, 2017), pp. 21–28.
177. Y.-M. Chiang, L.-C. Chang, and F.-J. Chang, Comparison of static-feedforward and dynamic-feedback neural networks for rainfall–runoff modeling. *J. Hydrol.* **290**, 297–311 (2004).
178. P. Wallisch, M. E. Lusignan, M. D. Benayoun, T. I. Baker, A. S. Dickey, and N. G. Hatsopoulos, *MATLAB for Neuroscientists: An Introduction to Scientific Computing in MATLAB* (Academic Press, 2014).

179. S. Moshiri, N. E. Cameron, and D. Scuse, Static, dynamic, and hybrid neural networks in forecasting inflation. *Computat. Econom.* **14**, 219–235 (1999).
180. C. Du, F. Cai, M. A. Zidan, W. Ma, S. H. Lee, and W. D. Lu, Reservoir computing using dynamic memristors for temporal information processing. *Nat. Commun.* **8**, 1–10 (2017).
181. J. Moon, W. Ma, J. H. Shin, F. Cai, C. Du, S. H. Lee, and W. D. Lu, Temporal data classification and forecasting using a memristor-based reservoir computing system. *Nat. Electron.* **2**, 480–487 (2019).
182. K. Nakajima, Physical reservoir computing — an introductory perspective. *Jpn. J. Appl. Phys.* **59**, 060501 (2020).
183. G. Tanaka, T. Yamane, J. B. Héroux, R. Nakane, N. Kanazawa, S. Takeda, H. Numata, D. Nakano, and A. Hirose, Recent advances in physical reservoir computing: A review. *Neural Networks* **115**, 100–123 (2019).
184. V. Athanasiou and Z. Konkoli, On improving the computing capacity of dynamical systems. *Sci. Rep.* **10**, 9191 (2020).
185. V. Athanasiou and Z. Konkoli, On mathematics of universal computation with generic dynamical systems. In A. Adamatzky, S. G. Akl and G. C. Sirakoulis (eds.), *From Parallel to Emergent Computing* (CRC Press, London, 2019).
186. M. Inubushi and K. Yoshimura, Reservoir computing beyond memory-nonlinearity trade-off. *Sci. Rep.* **7**, 10199 (2017).
187. B. Schrauwen, D. Verstraeten, and J. Van Campenhout, An overview of reservoir computing: Theory, applications and implementations. In *Proceedings of the 15th European Symposium on Artificial Neural Networks*, (2007), pp. 471–482.
188. Y. Paquot, F. Duport, A. Smerieri, J. Dambre, B. Schrauwen, M. Haelterman, and S. Massar, Optoelectronic reservoir computing. *Sci. Rep.* **2**, 287 (2012).
189. M. Lukoševičius and H. Jaeger, Reservoir computing approaches to recurrent neural network training. *Comput. Sci. Rev.* **3**, 127–149 (2009).
190. H. Jaeger, The "echo state" approach to analysing and training recurrent neural networks-with an erratum note. German National Research Center for Information Technology GMD Technical Report, 148, (2001).
191. W. Maass, T. Natschläger, and H. Markram, Real-time computing without stable states: A new framework for neural computation based on perturbations. *Neural Comput.* **14**, 2531–2560 (2002).
192. Z. Konkoli, On developing theory of reservoir computing for sensing applications: The state weaving environment echo tracker (SWEET) algorithm. *Int. J. Parallel Emergent Distrib. Syst.* **33**, 121–143 (2018).
193. M. Dale, J. F. Miller, and S. Stepney, Reservoir computing as a model for in-materio computing. In *Advances in Unconventional Computing* (Springer, 2017), pp. 533–571.
194. K. Pilarczyk, E. Wlaźlak, D. Przyczyna, A. Blachecki, A. Podborska, V. Anathasiou, Z. Konkoli, and K. Szaciłowski, Molecules, semiconductors,

light and information: Towards future sensing and computing paradigms. *Coord. Chem. Rev.* **365**, 23–40 (2018).
195. F. Akopyan, J. Sawada, A. Cassidy, R. Alvarez-Icaza, J. Arthur, P. Merolla, N. Imam, Y. Nakamura, P. Datta, and G.-J. Nam, Truenorth: Design and tool flow of a 65 mw 1 million neuron programmable neurosynaptic chip. *IEEE Trans. Comp.-Aided Des. Integr. Circ. Syst.* **34**, 1537–1557 (2015).
196. F. Cai, J. M. Correll, S. H. Lee, Y. Lim, V. Bothra, Z. Zhang, M. P. Flynn, and W. D. Lu, A fully integrated reprogrammable memristor–CMOS system for efficient multiply–accumulate operations. *Nat. Electron.* **2**, 290–299 (2019).
197. A. Röhm and K. Lüdge, Multiplexed networks: Reservoir computing with virtual and real nodes. *J. Phys. Commun.* **2**, 085007 (2018).
198. G. Dion, S. Mejaouri, and J. Sylvestre, Reservoir computing with a single delay-coupled non-linear mechanical oscillator. *J. Appl. Phys.* **124**, 152132 (2018).
199. L. Appeltant, G. Van der Sande, J. Danckaert, and I. Fischer, Constructing optimized binary masks for reservoir computing with delay systems. *Sci. Rep.* **4**, 3629 (2014).
200. C. Ríos, N. Youngblood, Z. Cheng, M. Le Gallo, W. H. P. Pernice, C. D. Wright, A. Sebastian, and H. Bhaskaran, In-memory computing on a photonic platform. *Sci. Adv.* **5**, eaau5759 (2019).
201. D. Brunner, B. Penkovsky, B. A. Marquez, M. Jacquot, I. Fischer, and L. Larger, Tutorial: Photonic neural networks in delay systems. *J. Appl. Phys.* **124**, 152004 (2018).
202. G. Van der Sande, D. Brunner, and M. C. Soriano, Advances in photonic reservoir computing. *Nanophotonics* **6**, 561–576 (2017).
203. L. Larger, A. Baylón-Fuentes, R. Martinenghi, V. S. Udaltsov, Y. K. Chembo, and M. Jacquot, High-speed photonic reservoir computing using a time-delay-based architecture: Million words per second classification. *Phys. Rev. X* **7**, 011015 (2017).
204. P. Antonik, M. Hermans, M. Haelterman, and S. Massar, Photonic reservoir computer with output feedback for chaotic time series prediction. In *IEEE International Joint Conference on Neural Networks 2017* (IEEE, 2017), pp. 2407–2413.
205. P. Antonik, M. Haelterman, and S. Massar, Online training for high-performance analogue readout layers in photonic reservoir computers. *Cognit. Comput.* **9**, 297–306 (2017).
206. F. Duport, A. Smerieri, A. Akrout, M. Haeterman, and S. Massar, Fully analogue photonic reservoir computer. *Sci. Rep.* **6**, 22381 (2016).
207. S. Guy Van der, B. Daniel, and C. S. Miguel, Advances in photonic reservoir computing. *Nanophotonics* **6**, 561–576 (2017).
208. E. Wlaźlak, P. Zawal, and K. Szaciłowski, Neuromorphic applications of a multivalued [SnI4 {(C6H5) 2SO}2] memristor incorporated in the echo state machine. *ACS Appl. Electron. Mater.* **2**, 329–338 (2020).

209. E. Wlaźlak, M. Marzec, P. Zawal, and K. Szaciłowski, Memristor in a reservoir system — experimental evidence for high-level computing and neuromorphic behavior of PbI2. *ACS Appl. Mater. Interfaces*, **11**, 17009–17018 (2019).
210. D. Przyczyna, S. Pecqueur, D. Vuillaume, and K. Szaciłowski, Reservoir computing for sensing — an experimental approach. *Int. J. Unconv. Comput.* **14**, 267–284 (2019).
211. X. Zhu, Q. Wang, and W. D. Lu, Memristor networks for real-time neural activity analysis. *Nat. Commun.* **11**, 1–9 (2020).
212. A. Kurenkov, S. Fukami, and H. Ohno, Neuromorphic computing with antiferromagnetic spintronics. *J. Appl. Phys.* **128**, 010902 (2020).
213. B. B. Schwedersky, R. C. C. Flesch, H. A. S. Dangui, and L. A. Iervolino, Practical nonlinear model predictive control using an echo state network model. In *2018 International Joint Conference on Neural Networks (IJCNN)* (IEEE, 2018), pp. 1–8.
214. S. Zhang, K. He, D. Cabrera, C. Li, Y. Bai, and J. Long, Transmission condition monitoring of 3d printers based on the echo state network. *Appl. Sci.* **9**, 3058 (2019).
215. J. Wu, J. Huang, Y. Wang, and K. Xing, RLS-ESN based PID control for rehabilitation robotic arms driven by PM-TS actuators. In *Proceedings of the 2010 International Conference on Modelling, Identification and Control* (IEEE, 2010), pp. 511–516.
216. D. A. Sala, V. J. Brusamarello, R. de Azambuja, and A. Cangelosi, Positioning control on a collaborative robot by sensor fusion with liquid state machines. In *2017 IEEE International Instrumentation and Measurement Technology Conference (I2MTC)* (IEEE, 2017), pp. 1–6.
217. K. Nakajima, H. Hauser, R. Kang, E. Guglielmino, D. G. Caldwell, and R. Pfeifer, A soft body as a reservoir: Case studies in a dynamic model of octopus-inspired soft robotic arm. *Front. Comput. Neurosci.* **7**, 91 (2013).
218. K. Nakajima, H. Hauser, T. Li, and R. Pfeifer, Information processing via physical soft body. *Sci. Rep.* **5**, 10487 (2015).
219. B. J. West, *Fractional Calculus View of Complexity: Tomorrow's Science* (CRC Press, Boca Raton, 2015).
220. M. D. Ortigueira and J. A. Tereiro Machado, What is a fractional derivative? *J. Comput. Phys.* **293**, 4–13 (2015).
221. R. Herrmann, *Fractional Calculus: An Introduction for Physicists* (World Scientific Publishing Company, Singapore, 2014).
222. M.-S. Abdelouahab, R. Lozi, and L. Chua, Memfractance: A mathematical paradigm for circuit elements with memory. *Int. J. Bifurc. Chaos* **24**, 1430023 (2014).
223. R. Garrappa, E. Kaslik, and M. Popolizio, Evaluation of fractional integrals and derivatives of elementary functions: Overview and tutorial. *Mathematics* **7**, 407 (2019).
224. S. Westerlund, Dead matter has memory! *Phys. Scr.* **43**, 174–179 (1991).

225. M. Edelman, Universality in systems with power-law memory and fractional dynamics. In M. Edelman, E. E. N. Macau and M. A. F. Sanjuan (eds.), *Chaotic, Fractional, and Complex Dynamics: New Insights and Perspectives* (Springer International Publishing, Cham, 2018), pp. 147–171.
226. S. Bergner, T. Moller, D. Weiskopf, and D. J. Muraki, A spectral analysis of function composition and its implications for sampling in direct volume visualization. *IEEE Trans. Vis. Comput. Graph.* **12**, 1353–1360 (2006).
227. G. J. Silva, A. Datta, and S. R. Bhattacharyya, *PID Controllers for Time-Delay Systems* (Birkhäuser, Boston, 2005).
228. L. A. Zadeh, Toward human level machine intelligence — is it achievable? the need for a paradigm shift. *IEEE Comput. Intell. Mag.* **3**, 11–22 (2008).
229. L. A. Zadeh, Fuzzy sets. *Inform. Control* **8**, 338–353 (1965).
230. J. M. Mendel, Fuzzy logic systems for engineering: A tutorial. *Proc. IEEE* **83**, 345–377 (1995).
231. P. L. Gentili, The human sensory system as a collection of specialized fuzzyfiers: A conceptual framework to inspire new artificial intelligent systems computing with words. *Int. J. Intell. Fuzzy Syst.* **27**, 2137–2151 (2014).
232. P. L. Gentili, Small steps towards the development of chemical artificial intelligent systems. *RSC Adv.* **3**, 25523–25549 (2013).
233. P. L. Gentili, The fuzziness of the molecular world and its perspectives. *Molecules* **23**, 2074 (2018).
234. J. Pykacz, Fuzzy quantum logic I. *Int. J. Theor. Phys.* **32**, 1691–1708 (1993).
235. I. Schmitt, A. Nürnberger, and S. Lehrack, On the relation between fuzzy and quantum logic. In R. Seising (ed.), *Views on Fuzzy Sets and Systems from Different Perspectives: Philosophy and Logic, Criticisms and Applications* (Springer Berlin Heidelberg, Berlin, Heidelberg, 2009), pp. 417–438.
236. M. S. Hannachi, Y. Hatakeyama, and K. Hirota, Emulating qubits with fuzzy logic. *J. Adv. Comput. Intell. Intelligent Inf.* **11**, 242–249 (2007).
237. R. Reiser, A. Lemke, A. Avila, J. Vieira, M. Pilla, and A. Du Bois, Interpretations on quantum fuzzy computing: Intuitionistic fuzzy operations × quantum operators. *Electr. Notes Theoret. Comput. Sci.* **324**, 135–150 (2016).
238. P. L. Gentili, Molecular processors: From qubits to fuzzy logic. *ChemPhysChem* **12**, 739–745 (2011).
239. P. L. Gentili, The fundamental fuzzy logic operators and some complex-oolean logic circuits implemented by the chomogenism of a spirooxazine. *Phys. Chem. Chem. Phys* **13**, 20335–20344 (2011).
240. P. L. Gentili, Boolean and fuzzy logic gates based on the interaction of flindersine with bovine serum albumin and tryptophan. *J. Phys. Chem. A* **112**, 11992–11997 (2008).
241. P. L. Gentili, Boolean and fuzzy logic implemented at the molecular level. *Chem. Phys.* **336**, 64–73 (2007).

242. P. L. Gentili, The fuzziness of a chromogenic spiroxazine. *Dyes Pigments* **110**, 235–248 (2014).
243. M. Fuxreiter, Towards a stochastic paradigm: From fuzzy ensembles to cellular functions. *Molecules* **23**, 3008 (2018).
244. C. J. Jeffery, An introduction to protein moonlighting. *Biochem. Soc. Trans.* **42**, 1679–1683 (2014).
245. P. L. Gentili, A. L. Rightler, B. M. Heron, and C. D. Gabbutt, Discriminating between the UV-A, UV-B and UV-C regions by novel biologically inspired photochromic fuzzy logic (BIPFUL) systems: A detailed comparative study. *Dyes Pigments* **135**, 169–176 (2016).
246. P. L. Gentili, A. L. Rightler, B. M. Heron, and C. D. Gabbutt, Extending human perception of electromagnetic radiation to the UV region through biologically inspired photochromic fuzzy logic (BIPFUL) systems. *Chem. Commun.* **52**, 1474–1477 (2016).
247. R. Deaton and M. Garzon, Fuzzy logic with biomolecules. *Soft Comput.* **5**, 2–9 (2001).
248. R. M. Zadegan, M. D. E. Jepsen, L. L. Hildebrandt, V. Birkedal, and J. Kjems, Construction of a fuzzy and boolean logic gates based on DNA. *Small* **11**, 1811–1817 (2015).
249. S. Karmakar, M. Nandi, S. Mukherjee, and S. Baitalik, Polypyridylimidazole based smart Ru(II) complex mimicking advanced Boolean and Fuzzy logic functions. *Inorg. Chim. Acta* **454**, 76–88 (2017).
250. A. Blachecki, J. Mech-Piskorz, M. Gajewska, K. Mech, K. Pilarczyk, and K. Szaciłowski, Organotitania-based nanostructures as a suitable platform for the implementation of binary, ternary, and fuzzy logic systems. *ChemPhysChem* **18**, 1798–1810 (2017).
251. D. Bhattacharjee, W. Kim, A. Chattopadhyay, R. Waser, and V. Rana, Multi-valued and fuzzy logic realization using TaOx memristive devices. *Sci. Rep.* **8**, 8 (2018).
252. X.-Y. Xu and B. Yan, Intelligent molecular searcher from logic computing network based on Eu(III) functionalized UMOFs for environmental monitoring. *Adv. Funct. Mater.* **27**, 1700247-n/a (2017).
253. W. Liu, Z. Wang, X. Liu, N. Zeng, Y. Liu, and F. E. Alsaadi, A survey of deep neural network architectures and their applications. *Neurocomputing* **234**, 11–26 (2017).
254. R. A. Nawrocki, R. M. Voyles, and S. E. Shaheen, A mini review of neuromorphic architectures and implementations. *IEEE Trans. Electron Dev.* **63**, 3819–3829 (2016).
255. C. Horsman, S. Stepney, R. C. Wagner, and V. Kendon, When does a physical system compute? *Proc. Royal. Soc. A* **470**, 20140182 (2014).
256. S. Stepney, The neglected pillar of material computation. *Physica D* **237**, 1157–1164 (2008).
257. V. Horvath, D. J. Kutner, J. T. Chavis Iii, and I. R. Epstein, Pulse-coupled BZ oscillators with unequal coupling strengths. *Phys. Chem. Chem. Phys.* **17**, 4664–4676 (2015).

258. K. M. Hynna and K. Boahen, Thermodynamically equivalent silicon models of voltage-dependent ion channels. *Neural Comput.* **19**, 327–350 (2007).
259. V. Erokhin, T. Berzina, A. Smerieri, P. Camorani, S. Erokhina, and M. P. Fontana, Bio-inspired adaptive networks based on organic memristors. *Nano Commun. Networks* **1**, 108–117 (2010).
260. V. Erokhin, T. Berzina, P. Camorani, A. Smerieri, D. Vavoulis, J. Feng, and M. P. Fontana, Material memristive device circuits with synaptic plasticity: Learning and memory. *BioNanoSci.* **1**, 24–30 (2011).
261. T. Berzina, A. Smerieri, M. Barnabó, A. Pucci, G. Ruggieri, V. Erokhin, and M. P. Fontana, Optimization of an organic memristor as an adaptive memory element. *J. Appl. Phys.* **105**, 124515 (2009).
262. K. Kim, C.-L. Chen, Q. Truong, A. M. Shen, and Y. Chen, A Carbon nanotube synapse with dynamic logic and learning. *Adv. Mater.* **25**, 1693–1698 (2013).
263. O. Bichler, W. Zhao, F. Alibart, S. Pleutin, D. Vuillaume, and C. Gamrat, Functional model of a nanoparticle organic memory transistor for use as a spiking synapse. *IEEE Trans. Electron Dev.* **57**, 3115–3122 (2010).
264. V. Erokhin, T. Berzina, P. Camorani, and M. P. Fontana, Non-equlibrium electrical behaviour of polymeric electrochemical junctions. *J. Phys. Condens. Matter* **19**, 205111 (2007).
265. T. Ohno, T. Hasegawa, T. Tsuruoka, K. Terabe, J. K. Gimzewski, and M. Aono, Short-term plasticity and long-term potentiation mimicked in single inorganic synapses. *Nat. Mater.* **10**, 591–595 (2010).
266. K. Pilarczyk, A. Podborska, M. Lis, M. Kawa, D. Migdał, and K. Szaciłowski, Synaptic behavior in an optoelectronic device based on semiconductor-nanotube hybrid. *Adv. Electr. Mater.* 1500471 (2016).
267. W. Gerstner and W. M. Kistler, Mathematical formulations of Hebbian learning. *Biol. Cybern.* **87**, 404–415 (2002).
268. D. Przyczyna, M. Lis, K. Pilarczyk, and K. Szaciłowski, Hardware realization of the pattern recognition with an artificial neuromorphic device exhibiting a short-term memory. *Molecules* **24**, 2738 (2019).
269. H.-W. Park, P. M. Wensing, and S. Kim, Online planning for autonomous running jumps over obstacles in high-speed quadrupeds. In L. E. Kavraki, D. Hsu and J. Buchli (eds.), *Robotics: Science and Systems* (Sapienza University of Rome, Rome, 2015).
270. M. Raibert, K. Blankespoor, G. Nelson, and R. Playter, BigDog, the rough-terrain quadruped robot. *IFAC Proceedings Volumes*, **41**, 10822–10825 (2008).
271. G. Rozenberg, T. Bäck, and J. N. Kok, *Handbook of Natural Computing* (Springer-Verlag, Berlin, 2012).
272. T. Nakagaki, H. Yamada, and Á. Tóth, Maze-solving by an amoeboid organism. *Nature* **407**, 470–470 (2000).
273. K. Saito, N. Suefuji, and S. Kasai, Amoeba-inpired electronic solution-searching system and its application to finding walking maneuver of a multi-legged robot. In *Proceedings of the 48th International Symposium on Multiple-Valued Logic*, (2019), pp. 127–131.

274. M. Aono, M. Hara, and K. Aihara, Amoeba-based neurocomputing with chaotic dynamic. *Commun ACM* **50**, 69–72 (2007).
275. K. Saito, S. Kasai, and M. Aono, Evaluation of solution search performance of amoeba-inspired electronic computing system for solving maximum cut problem. In T. Kousaka and H. Aomori (eds.), *Proceedings of 2020 International Symposium on Nonlinear Theory and Its Applications* (2020).
276. R. V. Martinez, A. C. Glavan, C. Keplinger, A. I. Oyetibo, and G. M. Whitesides, Soft actuators and robots that are resistant to mechanical damage. *Adv. Func. Mater.* **24**, 3003–3010 (2014).
277. B. Mosadegh, P. Polygerinos, C. Keplinger, S. Wennstedt, R. F. Shepherd, U. Gupta, J. Shim, K. Bertoldi, C. J. Walsh, and G. M. Whitesides, Pneumatic networks for soft robotics that actuate rapidly. *Adv. Func. Mater.* **24**, 2163–2170 (2014).
278. M. Wehner, R. L. Truby, D. J. Fitzgerald, B. Mosadegh, G. M. Whitesides, J. A. Lewis, and R. J. Wood, An integrated design and fabrication strategy for entirely soft, autonomous robots. *Nature* **536**, 451–455 (2016).
279. M. P. Nemitz, C. K. Abrahamsson, L. Wille, A. A. Stokes, D. J. Preston, and G. M. Whitesides, Soft non-volatile memory for non-electronic information storage in soft robots. In R. Kramer-Bottiglio and M. Tolley (eds.), *Proceedings of the 3rd IEEE International Conference on Soft Robotics*, vol. 2, (IEEE, New Haven CT, 2020), pp. 89–94.
280. M. Garrad, G. Soter, A. T. Conn, H. Hauser, and J. Rossiter, A soft matter computer for soft robots. *Sci. Rob.* **4**, eaaw6060 (2019).
281. S. Nichele, S. Risi, G. Tufte, and L. Beloff, Towards a plant bio-machine. In *Proceesings of the IEEE Symposium Series on Computational Intelligence* (IEEE Comput. Intelligence Society, Honolulu, 2017).
282. A. Adamatzky, Towards fungal computer. *Interface Focus* **8**, 20180029 (2018).
283. A. Adamatzky, On spiking behaviour of oyster fungi Pleurotus djamor. *Sci. Rep.* **8**, 7873 (2018).
284. A. Adamatzky (ed.), *Advances in Physarum Machines. Sensing and Computing with Slime Mold* (Springer International Publishing, Switzerland, 2016).
285. M. Hagiya, A. Konagaya, S. Kobayashi, H. Saito, and S. Murata, Molecular robots with sensors and intelligence. *Acc. Chem. Res.* **47**, 1681–1690 (2014).
286. H. Hess and J. L. Ross, Non-equilibrium assembly of microtubules: From molecules to autonomous chemical robots. *Chem. Soc. Rev.* **46**, 5570–5587 (2017).
287. P. R. Buskohl, R. C. Kramb, and R. A. Vaia, Synchronicity in composite hydrogels: Belousov–Zhabotinsky (BZ) active nodes in gelatin. *J. Phys. Chem. B* **119**, 3595–3602 (2015).
288. A. F. Taylor, M. R. Tinsley, and K. Showalter, Insights into collective cell behaviour from populations of coupled chemical oscillators. *Phys. Chem. Chem. Phys.* **17**, 20047–20055 (2015).

289. M. Toiya, V. K. Vanag, and I. R. Epstein, Diffusively coupled chemical oscillators in a microfluidic assembly. *Angew. Chem. Int. Ed.* **47**, 7753–7755 (2008).
290. W. Aguilar, G. Santamaría-Bonfil, T. Froese, and C. Gershenson, The past, present, and future of artificial life. *Front. Robot. AI* **1** (2014).
291. R. Belk, M. Humayun, and A. Gopaldas, Artificial life. *J. Macromarket.* **40**, 221–236 (2020).
292. M. M. Hanczyc, J. M. Parrilla, A. Nicholson, K. Yanev, and K. Stoy, Creating and maintaining chemical artificial life by robotic symbiosis. *Artif. Life* **21**, 47–54 (2014).
293. K. K. V. Steincke, Og saa til Slut et Par parlamentariske Sprogblomster. In K. K. V. Steincke (ed.) *Farvel Og Tak: Minder Og Meninger* (Forlaget Fremad, Copenhagen, 1948).

Nanoscale

PAPER

View Article Online
View Journal | View Issue

Check for updates

Cite this: *Nanoscale*, 2019, **11**, 1080

Synaptic plasticity, metaplasticity and memory effects in hybrid organic–inorganic bismuth-based materials†

Tomasz Mazur, *‡[a] Piotr Zawal *‡[a,b] and Konrad Szaciłowski *[a]

Received 21st November 2018,
Accepted 7th December 2018

DOI: 10.1039/c8nr09413f

rsc.li/nanoscale

Since the discovery of memristors, their application in computing systems utilizing multivalued logic and a neuromimetic approach is of great interest. A thin film device made of methylammonium bismuth iodide exhibits a wide variety of neuromorphic effects simultaneously, and is thus able to mimic synaptic behaviour and learning phenomena. Standard learning protocols, such as spike-timing dependent plasticity and spike-rate dependent plasticity might be further modulated *via* metaplasticity in order to amplify or alter changes in the synaptic weight. Moreover, transfer of information from short-term to long-term memory is observed. These effects show that the diversity of functions of memristive devices can be strongly affected by the pre-treatment of the sample. Modulation of the resistive switching amplitude is of great importance for the application of memristive elements in computational applications, as additional substates might be utilized in multi-valued logic systems and metaplasticity and memory consolidation will contribute to the development of more efficient bioinspired computational schemes.

Introduction

Modern age computers are getting more computing power each year, roughly following Moore's law – doubling performance every 2 years. Predictions estimate that due to simple physical limitations it will not be possible to follow such a rapid development. In fact, the fastest growth so far has already happened.[1] Even in the case of some miraculous achievement, today's chip architecture will still be not sufficient for more complex and non-linear tasks. This phenomenon is known as the von Neumann bottleneck[2] and cannot be circumvented in any different way other than moving towards neural-like electronics based on the non-von Neumann computer architecture. Another type of limitation of the computational problem is known as Amdahl's law,[3] which states that every parallel computation speedup is limited and thus requires a change in solution paradigms to achieve higher computing performance.

Each of the presented class of problems can currently be successfully addressed by switching the design of electronic circuits to memristor based ones.[4] This is achievable as these basic passive electronic elements[5] combine both computing and storage (memory) functions. The term *memristor* describes a specific class of resistive devices, the state (conductance) of which is dependent on the history of the device. To memristors' fingerprints one can include a pinched *I–V* hysteresis loop, which either changes its shape or entirely disappears with a high scanning frequency, and passive, non-volatile memory.[6–8] Since their discovery they have attracted great attention due to a variety of possible applications in wide-ranging areas: as passive memory devices, elements in many-valued and fuzzy logic and neuromorphic computing. One of the very first application examples were memristors based on TiO_2[9] and other oxide semiconductors.[10] To this day, the memristive effect has been observed in a variety of different materials, such as oxides,[11–13] lead halide hybrid perovskites,[14–16] sulphides,[17] polymers,[18,19] and organic molecules.[20] These devices, however, do not offer immediate progress in computational power due to connectivity problems: the extraordinary complexity of the human brain cannot be easily achieved.[21] This problem can be addressed by novel memristive devices of more complex functionality, *e.g.* by multi-terminal memtransistors.[22] Another approach is closer to the principle of *in-materio* computation,[23] in which specific physical properties of the material are explored to boost the computational power of devices.

[a]*Academic Centre for Materials and Nanotechnology AGH University of Science and Technology al. A. Mickiewicza 30, 30-059 Kraków, Poland.*
E-mail: tmazur@agh.edu.pl, zawal@agh.edu.pl, szacilow@agh.edu.pl
[b]*Faculty of Physics and Applied Computer Science AGH University of Science and Technology al. A. Mickiewicza 30, 30-059 Kraków, Poland*
†Electronic supplementary information (ESI) available. See DOI: 10.1039/c8nr09413f
‡These authors contributed equally to this work.

Perovskites and their analogues are a particularly interesting group of materials as the future of solar electronics and replacement of silicon – mostly in photovoltaic applications.[24,25] A promising alternative to perovskites are methylammonium bismuth iodides[26,27] – despite their low efficiency as solar cells, compared to organic–inorganic lead perovskites, they have superior stability in humid atmosphere[28] and are reported to be less toxic and to have a lesser environmental impact.[29] In addition, a recently published article presents the memristive properties of methylammonium bismuth iodide in the context of high-speed multilevel data storage.[30] All of the above were the reasons for our group to investigate the neural-like behaviour of these materials, as the future prominent candidate for next-age computing.

Although the exact resistive switching mechanism in hybrid organic–inorganic bismuth materials has not been thoroughly studied yet, several plausible mechanisms presumed to be responsible for the memristive effect have been proposed for lead halide perovskites.[31] Many different types of defects might affect resistive switching properties, to which one can include ion migration under the gradient of external potential,[14] especially electromigration of MA^+ cations,[32] creation of a Schottky barrier at the perovskite/metal interface,[14] population and depopulation of electronic trap sites,[30] and drift and redistribution of $V_I^{\bullet}/V_I^{\times}$ iodine vacancies.[33] The resistive switching can be further modulated by redox reactions at electrochemically active electrodes,[34] the film thickness[35] and illumination.[33–35] The latter effect is particularly interesting due to the entirely new field of study resulting from the intersection of optoelectronics and memristor technology.[36]

One of the most intriguing properties of memristors is the ability to emulate the behaviour of biological synapses.[37] In the nervous system learning is governed by the synaptic plasticity, *i.e.* the ability of neurons to either amplify or attenuate the strength of synaptic connections, thus modifying their synaptic weight to store and process information.[38] An incoming action potential from the presynaptic neuron induces the release of neurotransmitter molecules which then diffuse through the synaptic cleft and depolarize the membrane of the postsynaptic neuron (Fig. 1a). This process causes the generation of the excitatory postsynaptic potential or current (EPSP and EPSC, respectively) and affects the synaptic weight. In analogy to biological neurons, when under an appropriate electrical stimulus, the conductivity of the memristive layer changes, which corresponds to changes in the synaptic weight of the biological system.

In neural networks the weight of the synaptic connection can be adjusted *via* learning protocols, such as spike-timing dependent plasticity (STDP) and spike-rate dependent plasticity (SRDP), the former representing the famous Hebbian learning rule, postulating that "*who fire together, wire together*".[39] For a long-lasting increase in synaptic efficacy a long-term potentiation (LTP) term has been coined. The converse of LTP is long-term depression (LTD), resulting in lowering of the synaptic weight.[40] These two mechanisms are responsible for retaining new information in neurons and are

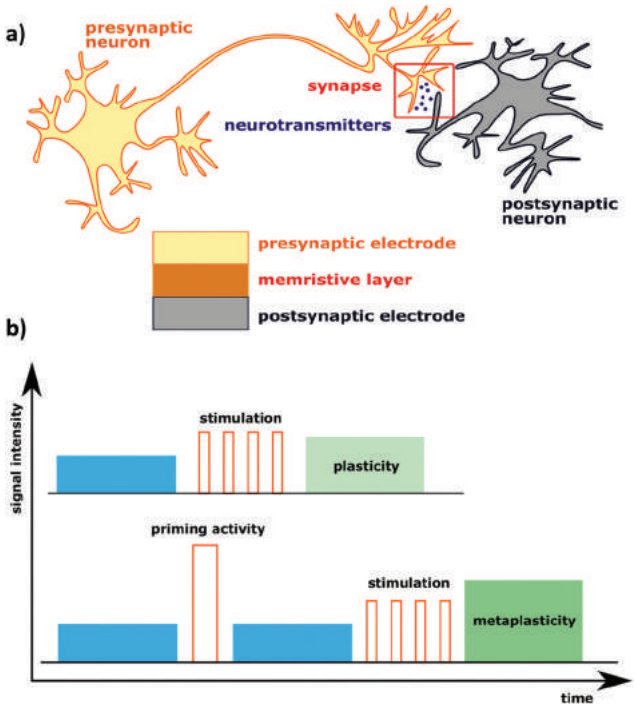

Fig. 1 Conceptual representation of biological neurons connected by a synapse (a) and corresponding schematic of the memristive device with a memristive layer acting as a synapse and pre- and postsynaptic electrodes as appropriate neurons. Representation of the metaplasticity (b). The priming activity causes no immediate changes in the plasticity, but enables further modulation of the synaptic weight ("the plasticity of the plasticity").

presumed to play a significant role in learning processes in the brain. However, simultaneous to LTP and LTD, a different kind of regulating process occurs.

Metaplasticity, *i.e.* "*the plasticity of plasticity*", is a phenomenon observed when LTP/LTD exhibition in neurons is altered due to some other neuronal activity (Fig. 1b). From a biological point of view, the metaplasticity is responsible for maintaining synaptic plasticity within a dynamic range.[41] Such an effect has already been reported in the literature for WO_3[42] and HfO_2 based memristors,[43–45,50] MoS_2 thin layers[46] and monolayer memtransistors.[22] Here we show for the first time that by employing a specific primary electric impulse one is able to modulate synaptic plasticity[47] in non-oxide artificial memristive devices.

To the authors' best knowledge, this is the first time that a device exhibiting both learning protocols (STDP and SRDP) modulated by metaplasticity is presented. The usual way of testing neural learning strategies is to look for materials suitable for example for STDP only[48,49] or STDP with SRDP only.[52] By metaplastic modulation of these learning protocols, additional sub-states can be created between the two extreme high and low conductive states of the memristor, creating a new branch for future research towards neuromorphic computing and application of the memristors in analogue electronics.

Results and discussion

Morphology of the samples

Methylammonium tetraiodobismuthate (MABiI) layers were prepared by the one-step spin-coating technique by varying the ratio between methylammonium iodide and bismuth iodide (see the Materials and methods section and Table S1†). The structure of thin layer devices was examined with scanning electron microscopy (SEM). The cross-sectional SEM image of the MABiI thin film is presented in Fig. 2a. The FTO (bottom layer) thickness was found to be ~30 nm, PEDOT : PSS (middle layer) was ~15 nm and the thickness of the MABiI thin film (top layer) was ~375 nm. Modifications of the MAI : BiI_3 ratio did not cause significant macroscopic changes in sample morphologies, yet the colour changed from bright orange-red (3 : 1, excess of MAI) to dark brown (1 : 3, excess of BiI_3), as depicted in Fig. 2b.

Thin film XRD measurement results

Each peak of the experimental diffractograms presented in Fig. 3 has been attributed to the previously reported $(CH_3NH_3)_3(Bi_2I_9)$ phase.[29,30,51,52] It is worth mentioning that there had been some inconsistencies in the literature regarding the MABiI space group.[53] Here, peaks are attributed assuming the $P6_3/mmc$ space group.[29,53] Interestingly, in the sample with an excess of BiI_3 (1 : 3 ratio) the peaks attributed to planes (100), (102), (103) and (006) disappear. Moreover, the diffraction peak attributed to the (101) plane is slightly shifted (14.8°) in comparison with the same peak in other samples (14.6°). Furthermore, the relative intensity of this peak is also much higher than those in other studied cases. In general, the ratio of (202) : (101) peak intensities increases with increasing MAI : BiI_3 ratio, indicating structural changes in the crystal structure.

UV-Vis spectra

The UV-Vis spectra of each solution (for the same BiI_3 concentrations) are presented in Fig. 4a (precursor solution spectra have been provided in Fig. S1†). It can be seen that the band at *ca.* 450 nm, which can be attributed to tetraiodobismuthate, $[BiI_4]^-$, or its higher homologues, $[BiI_4]_n^{n-}$, is present only at

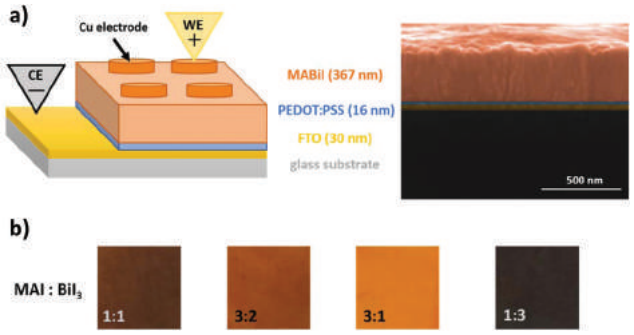

Fig. 2 Experimental setup and the MABiI device. Schematic structure of the experimental device with several metal electrodes pressed to the material layer alongside (right side of the picture) with the cross-sectional SEM image of the MABiI memristive device. Three visible layers are, from bottom to top, FTO, PEDOT : PSS and MABiI (a). Photos of the as-prepared thin films on the FTO + PEDOT : PSS substrates (b). Samples differ by the MAI : BiI_3 ratio used for starting solution preparation.

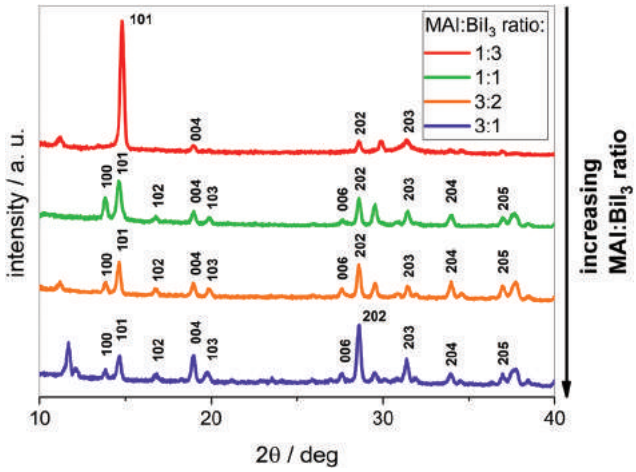

Fig. 3 Thin film XRD patterns of MABiI materials synthesized from solutions with various substrate ratios.

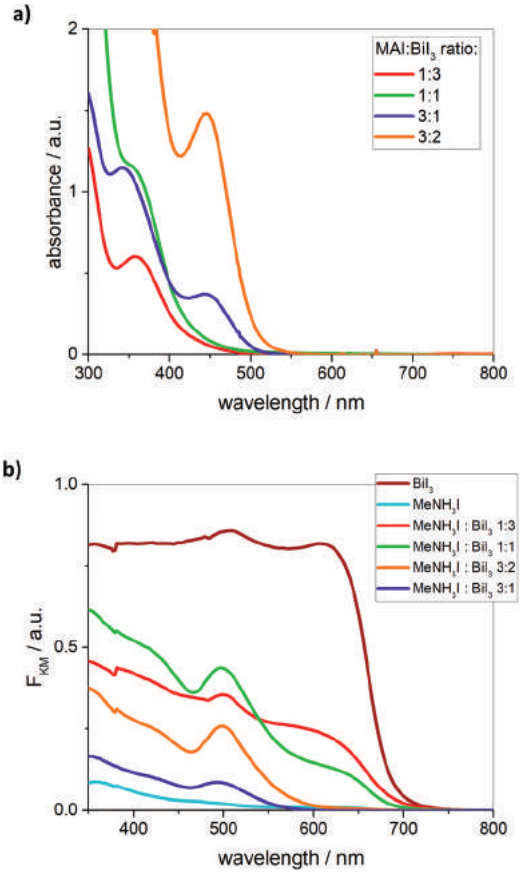

Fig. 4 UV-Vis spectra of the precursor solutions in DMF for each MAI : BiI_3 ratio. Note the emerging peak at 449 nm with increasing concentration of the substrates, corresponding to $[BiI_4]^-$ ions (a). Absorption spectra of MABiI thin films crystallized from different starting solutions (b).

sufficiently high iodide concentrations.[54] Upon evaporation of these solutions, films of various absorptivities are formed (Fig. 4b). In the case of an excess of iodide films with the clearly visible band at *ca.* 500 nm are formed, which correspond to structures with the tetraiodobismuthate unit.[55,56] At lower iodide concentrations an additional absorption with features characteristic of BiI_3 (absorption onset at *ca.* 700 nm) becomes dominant. These observations indicate that the solid phase may be significantly defective and rich in various polymeric forms of tetraiodobismuthate.[57]

I–V curves and electrochemical characterization

The memristive characteristics of the devices were initially evaluated using cyclic voltammetry within the ±3 V potential range. Recorded voltamperograms show characteristic hysteresis loops (Fig. 5a), independently on thin film stoichiometry. This clearly indicates the memristive character of the studied devices, as the pinched hysteresis loop is a fundamental fingerprint of a memristor.[6,58] Relative differences between high (HRS) and low resistive states (LRS) were higher upon negative working electrode polarizations. Differences in the current values are due to two factors – the first one is the number of mobile charge carriers, which in turn depends on the sample constitution. The second one is the electrode surface effectively in contact with the perovskite surface. The non-stoichiometric samples acted better as memristors, with more distinguishable "ON" and "OFF" states. The stoichiometric material shows only a weak memristive character (measured as the ON/OFF current ratio), whereas nonstoichiometric ones show very significant resistive switching. Asymmetry of the *I–V* characteristics must be noted. Current intensities at positive bias voltage are significantly higher than those recorded at negative bias voltage. This indicates the partially rectifying character of the MABiI/copper junction, presumably due to the formation of a Schottky junction at the interface. This effect depends on the stoichiometry of the film and is negligible for a stoichiometric 3 : 2 MAI : BiI_3 ratio. In this case a junction of an almost ohmic character is observed, whereas any deviation from this composition results in a significantly rectifying junction. Therefore the crucial role of various lattice and interfacial defects for both rectification and memristive behaviour may be postulated. This observation supports the hypothesis that a part of the memristive behaviour of MABiI is a consequence of charge carrier migration – either methylammonium ions or iodide vacancies/anions.[32,33] This cannot be the dominant effect though, as for a series of scanning speeds (from 10 mV s^{-1} up to 20 V s^{-1}) the hysteresis loop diminishes only to some extent (see Fig. 5b).

The other origin of the memristive behaviour of studied junctions may be metal-induced gap states (MIGS). They are formed at the metal–semiconductor interface due to the wave function of the metal tailing into the band gap of the semiconductor. Depending on the charge neutrality level MIGS can exhibit both donor- and acceptor-like properties.[59–61] Polycrystallinity of the copper electrodes and their tendency to oxidize at the surface may further contribute to the formation of trap states at the interface. These states, in turn, may modulate the height of the Schottky barrier thus constituting the observed memristive effect. This mechanism also delivers an

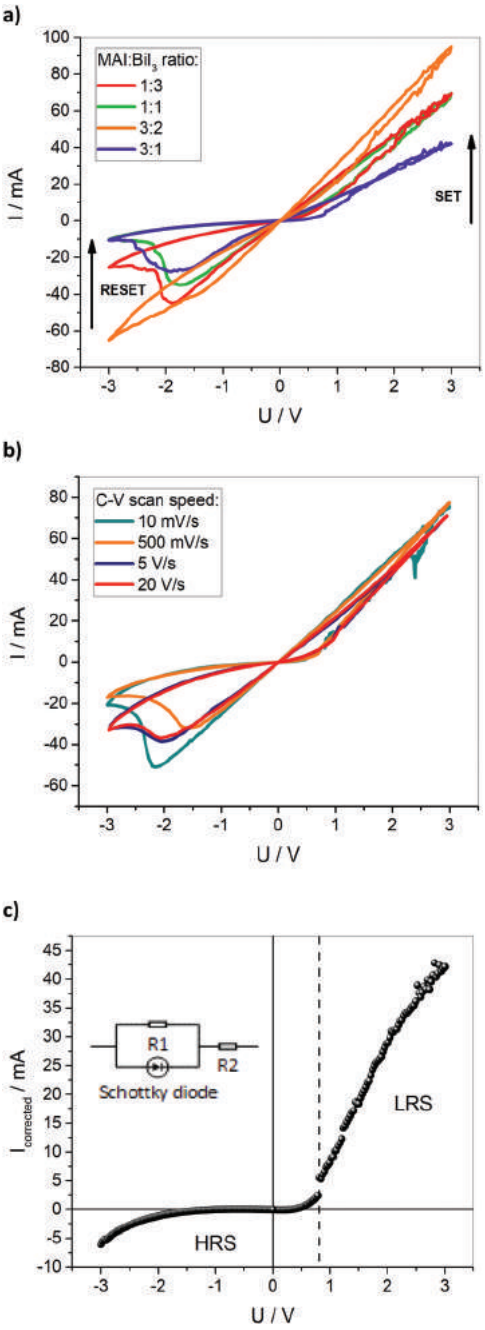

Fig. 5 Current–voltage characteristics with a distinct hysteresis loop. For thin films prepared from solutions with different MAI : BiI_3 ratios the smallest resistive switching was observed for the 3 : 2 stoichiometric sample. Scanning speed was kept constant at 500 mV s^{-1} (a). Measured *I–V* curve for the MAI : BiI_3 3 : 1 ratio sample with varying scanning frequency from 10 mV s^{-1} to 20 V s^{-1} (b). The diode-like part of the current–voltage measurement of the MABiI 3 : 1 sample after subtraction of the ohmic component calculated assuming the equivalent circuit presented in the inset (c). At 0.8 V (denoted with the dashed line) a change from Schottky-type to ohmic-type junction occurs, resulting in a switch from LRS to HRS.

explanation for the asymmetry of the hysteresis loop. In the region of negative bias, the acceptor electron states are being gradually occupied, resulting in an increase of the Schottky barrier and transition from LRS to HRS. The existence of a Schottky-type interface causes a diode-like characteristic of the HRS state, whereas LRS corresponds to a typical Ohmic conduction type (Fig. 5c). We have further investigated the Schottky diode-like behaviour employing the thermionic emission theory to extract the barrier height from the *I–V* characteristics. Assuming the equivalent circuit presented in the inset of Fig. 5c and using the Richardson equation we have calculated the Schottky barrier height to be 0.55 eV (see the ESI, section 3, Fig. S2–S5†).

Switching effect stability

It has been previously shown that the stability of the state is dependent on the switching voltage.[62] In order to investigate the stability of switching effects, the MABiI 3 : 1 sample was tested accordingly. Firstly, the sample was switched to a state of choice – either HRS or LRS with negative or positive voltage bias respectively. The initial state of the memristor was probed for 10 s with −0.5 V readout voltage (black-coloured data points in Fig. 6). The memristor state was then subsequently switched to the desired state with 2 s voltage of the given amplitude in the range from −3 V to +3 V. The state-reading procedure was applied again after 10 s (red in Fig. 6) and 30 min (blue in Fig. 6). For the tested sample, the switching effect is very stable for the HRS to LRS transition, *i.e.* when a positive bias voltage exceeding +1.5 V was used, whereas some short-term instabilities can be observed for the HRS to LRS transition if the bias voltages were below +1.5 V. In consequence, the output current is dependent on the applied writing voltage. The least degradation of HRS and the most stable read current were observed after writing with +3 V. When the memristor is biased with +1 V, which is close to the switching voltage, the measurement shows fast relaxation to the initial HRS state. However, high positive voltages advance the degradation of MABiI. For this reason, in the STDP tests we have chosen +1.5 V as the switching voltage from HRS to LRS. In order to ascertain full RESET, from LRS to HRS the switching was done with −3 V. The decrease in output current, meaning switching even more to HRS, for positive voltage bias is related to the readout method done at −0.5 V. Upon first voltage bias layer(s) of different materials constituting the experimental device act as capacitor(s) – additional negative voltage (necessary for readout) charges the capacitor up, decreasing the current allowed to flow. This effect is also present for positive voltage bias, yet in such cases, the relaxation to HRS is the most dominant factor there. This effect indicated the significant contribution of the surface states at the interface (*e.g.* MIGS) to the resistive switching process. When a low switching voltage is applied (up to 1.5 V) only shallow trap states are involved. They have a relatively short lifetime due to the possibility of thermal depopulation and therefore memory retention time is short and they (at least partially) return to a high resistive state. An appropriately high switching potential (over 2 V) populates deep traps as well. Due to the high energy barrier, they cannot be thermally depopulated and the state retention time is much longer.

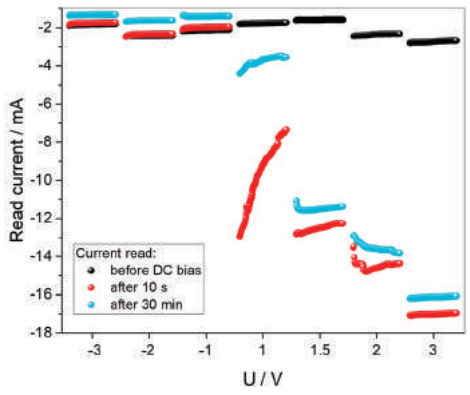

Fig. 6 Dependence of the memristor state stability on the SET voltage. Black lines indicate the initial state of a device measured at −0.5 V for 10 s. After switching the MABiI memristor to LRS (with positive voltage) or HRS (negative voltage), the reading current was measured with −0.5 V as indicated by the red lines. Finally, after 30 minutes, the device state was read again for 10 s (blue lines).

Simple neuromorphic functions – learning and forgetting

Controlled and lasting resistance switching can be used for multilevel resistive state programming by the application of several consequent pulses of chosen polarity. Here, the sample was subjected to a train of 15 poling spikes with an amplitude of ±1.2 V and a duration of 5 ms. After each spike, the state of the device was read with ±0.5 V pulses. A lower reading voltage was chosen in order to avoid perturbation of the memristor state. The results of the described procedure are presented in Fig. 7a–c. The learning process was observed for all studied samples, but the strongest effects were seen for the MABiI 3 : 1 sample (*cf.* Fig. 8c and d). Therefore, this material has been chosen for further studies.

The current increases upon stimulation with the train of positive pulses, which is a result of gradual switching of the device into the LRS state. This process is associated with learning phenomenon and has been already described in the literature.[14,63] On the other hand, decreasing conductance is observed upon negative voltage pulses – the device is thus forgetting the provided information. Such enhancement and decrease in passed electric signal strength is easily parallelized into weight changes in the synaptic connection between two neurons and can be used for building artificial neural networks from memristive devices.[64,65] To investigate learning and forgetting time constants, an exponential function of the form (1) was fitted to the current values obtained from ±0.5 V reading pulses:

$$I = I_0 + A \cdot \exp(-(t - t_0)/\tau), \quad (1)$$

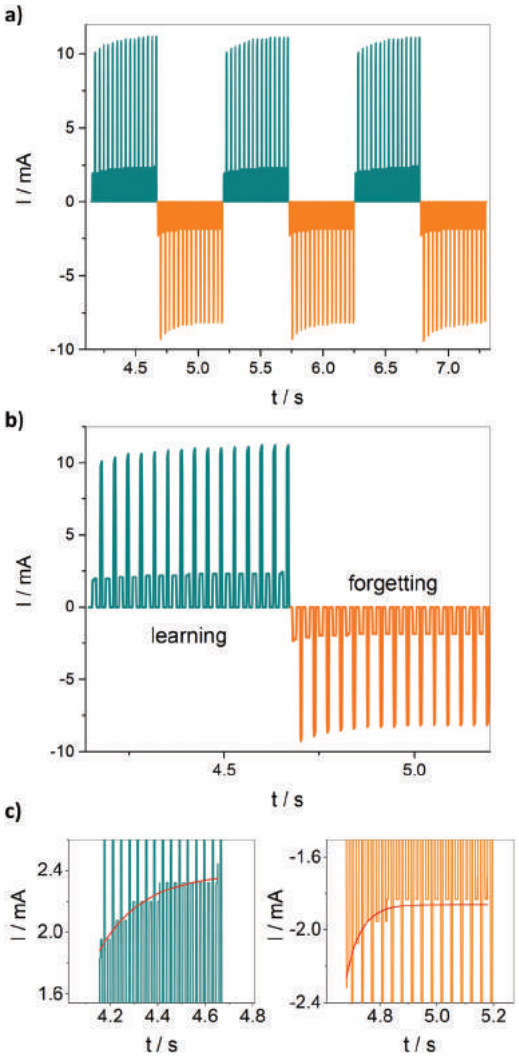

Fig. 7 Learning and forgetting effect in the MABiI 3 : 1 sample. Visible increase in the current value upon poling with +1.2 V spikes and current decrease while poling with −1.2 V spikes are analogous with learning and forgetting processes in neurons. Between poling spikes there are ±0.5 V pulses used for reading without perturbing the memristor state (a). Enlarged single cycle of learning and forgetting with distinct poling and reading spikes (b). In subplots (c) we present a fitted single-exponent function (eqn (1)) to both sample learning and forgetting regimes.

where I_0 is a parameter used to add or subtract the current offset, t_0 is a fixed parameter corresponding to the position of the first spike and τ is the learning/forgetting time constant. Determined time constants τ were estimated to be 186 ± 6 ms (R^2 = 0.92) for learning and 52 ± 4 ms (R^2 = 0.82) for forgetting (full fitting results have been provided in the ESI, Fig. S6†). This means that the forgetting process, which is attributed to switching the device from the LRS to HRS state and resulting in current decrease, occurs much faster than the opposite learning process. In analogy to neural behaviour, the investigated system tends to forget information significantly faster than is able to learn a new one. On the other hand, if one considers memristors as a memory device, erasing the information would occur much faster than writing the new one into a memristor. This observation can be explained when the asymmetry of the Schottky junction is considered. The charge transfer is easier in the forward voltage scan direction than in the reverse direction. As the memristive state is dependent on the charge (by the Chua's definition of the memristor) and the electron flow is faster in the forward polarization of the Schottky junction, the switching from LRS to HRS occurs significantly faster.

Metaplastic modulation of spike timing-dependent plasticity (STDP)

All of the aforementioned characteristics of bismuth-based materials can be incorporated to achieve the most popular learning technique designed for neural networks, either for biological or artificial, which is STDP. The procedure allows both strengthening and weakening of synaptic connections, yet contrary to the spike-rate-dependent plasticity process (see the next section), two-electrode stimulation (presynaptic and postsynaptic) is necessary. Depending on the test spike characteristic, various synaptic weight *vs.* time functions can be achieved.[14,66] In the presented experiments, spikes typical for the antisymmetric Hebbian learning rule were used (see Fig. S7† for experimental voltage patterns).

Before incorporating STDP learning methods for different material types, optimal pre-treatment bias voltage values were established. This was done for the sample with an MAI : BiI_3 ratio of 3 : 1 and the purpose of the pretreatment procedure was to switch the sample state either way (to HRS or LRS) in a repeatable manner. Usually devices are set or reset by means of simple voltage scans – same as for the *I*–*V* experiments. The results of STDP after this pre-treatment are presented in Fig. 8a, both for depression and potentiation. The outcome of the STDP experiment, the synaptic weight change Δw, is defined as:

$$\Delta w = ((I_{\text{after}} - I_{\text{before}})/I_{\text{before}}) \cdot 100\% \quad (2)$$

where I_{before} is the current measured at −0.5 V before applying the voltage stimulation procedure and I_{after} is the current measured at −0.5 V after the stimulation. The maximum signal potentiation is set to be above 500%. However, this outcome can be either enhanced or decreased by switching the pre-treatment procedure to DC bias for a short period of time – 2 s in our case. As can be established from the results shown in Fig. 8b, the bias voltage before the potentiation STDP sequence (*i.e.* $\Delta t > 0$) should be −3 V. When −2 V and −1 V biases were applied, the synaptic weight changes were significantly smaller. In the case of depression ($\Delta t < 0$), optimal results are achieved while using +1.5 V bias voltage – below that threshold synaptic weight changes are almost stochastic (see Fig. S8 in the ESI†). This shows that the synaptic plasticity might be efficiently modulated by DC pre-treatment of a suitable amplitude. With STDP measurement parameters established, MABiI materials with varying MAI : BiI_3 ratios were investigated. The decrease of the synaptic weight in the

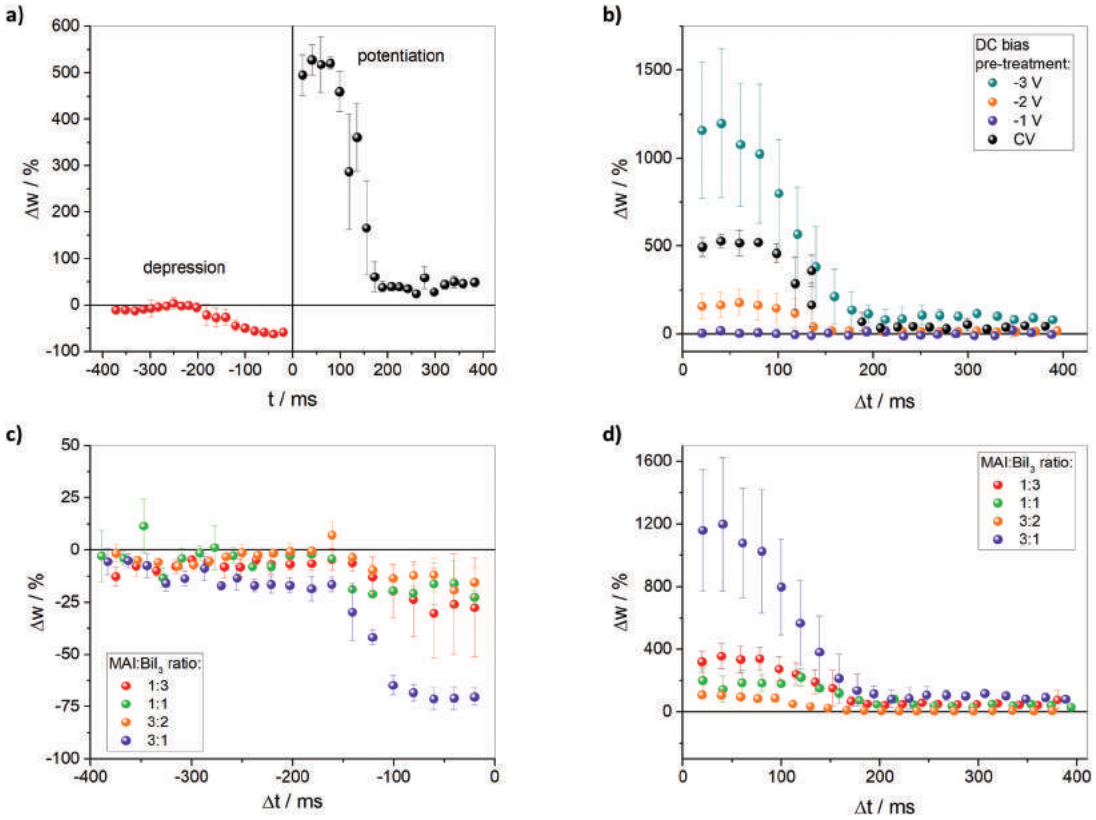

Fig. 8 Standard STDP learning protocol and metaplastic modulation of STDP. Full STDP with *I*–*V* scans between the consecutive poling spikes for the MABiI 3 : 1 sample (a). Potentiation regime of the STDP measurement (b). The changed parameter is DC bias voltage applied before each measurement. The comparison of Δw for samples pre-treated with DC bias and *I*–*V* scans reveals that the type and amplitude of the priming activity can effectively modulate the potentiation. The measurement was conducted on the MABiI 3 : 1 sample. Depression (c) and potentiation (d) regimes of STDP for samples with various MAI : BiI_3 ratios. Experimental parameters were DC bias equal to −3 V for potentiation and +1.5 V for depression regimes. In each case, the STDP voltage pattern consists of poling spikes of ±1.6 V.

depression regime does not exceed 75% for all of the samples, with a sample of the MAI : BiI_3 3 : 1 ratio possessing the highest susceptibility to change in the synaptic weight in the LTD regime (see Fig. 8c). The differences in results are much more dynamic in the case of the potentiation mode (Fig. 8d) – the most significant synaptic weight change is measured at 1198% relative increase, however, at the expense of precision – standard deviation was equal to 424%. In the case of the stoichiometric sample (MAI : BiI_3 ratio 3 : 2) the highest potentiation effect for optimal Δt did not exceed 150%, indicating that introducing additional defects resulting from the non-stoichiometric MABiI composition can significantly influence the outcome of neuromorphic measurements.

Metaplastic modulation of spike rate-dependent plasticity (SRDP)

Synapse potentiation might be also achieved by increasing the frequency between poling spikes, emulating spike rate-dependent plasticity, sometimes in the literature denoted also as rate-driven plasticity.[67,68] In SRDP the synaptic weight depends solely on the time interval Δt between consecutive pre-synaptic spikes of the same polarity and increases with the rate of the spikes. In this section we present the results for the MABiI sample with an MAI : BiI_3 1 : 3 ratio.

The voltage pattern utilized in SRDP and an exemplary current response measurement is presented in Fig. 9. When the time interval Δt between poling spikes is sufficiently long, no potentiation occurs as the system relaxes back to its original state before the next spike arrives (Fig. 9a). However, when the frequency is increased, one can observe a modification of the state of the device, which can be attributed to memory effects (Fig. 9b and c). Under poling with the set of spikes, an increase in current is observed and is identified as the short-term plasticity (STP) effect.[63] Immediately after the train one can observe a gradual decrease in the reading current, which is attributed to the relaxation process of memory. However, when a certain threshold level is reached while poling, the transition from short-term plasticity to long-term plasticity (LTP) occurs.[18,69] Here, when the plateau is reached (Fig. 9c), the readout current is at a higher level than it was before the poling spike train. As the time regime is significantly different from the relaxation rate, this means that the state of the device is maintained due to the LTP effect and satisfies the demand of memristor's non-volatile memory.

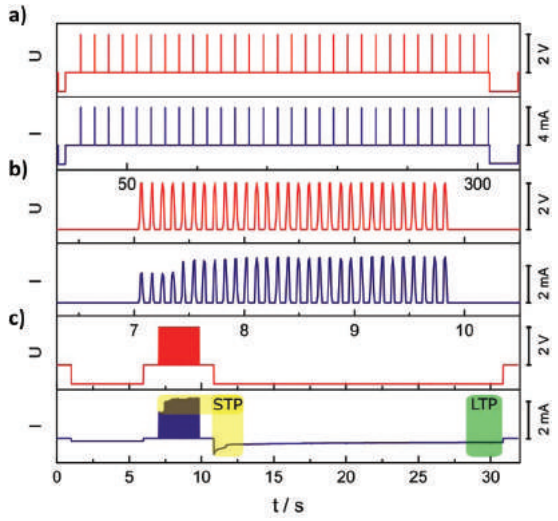

Fig. 9 Memory consolidation after the SRDP measurement. Exemplary voltage pattern (red lines) and the corresponding current response (blue line) in SRDP measurements. In part (a) with time interval Δt = 10 s no potentiation occurs, as the system relaxes between consecutive spikes (top). Potentiation revealed by an increase in current intensity as the interval decreases to Δt = 70 ms (middle). Full SRDP experiment pattern including the dynamic changes immediately after the poling procedure is completed, which implies the consolidation process of STP to LTP (bottom). The measurement was conducted on the MABiI 3 : 1 sample.

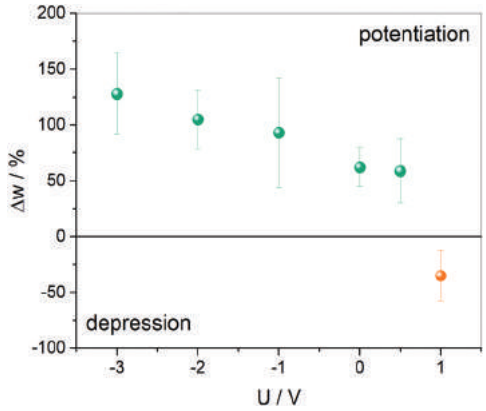

Fig. 10 Metaplasticity in the SRDP measurement induced *via* the DC bias pre-treatment. Before SRDP measurement with a fixed time interval Δt = 30 ms, the MABiI sample 3 : 1 was treated with a DC bias of the given amplitude. When the bias was in range of −3 V to +0.5 V, a potentiation is observed. However, when the initial bias was +1 V, the synaptic weight decreased, resulting in depression.

This behaviour strongly resembles memory consolidation in the human brain.[70] In physiological systems in order for information to be retained in the memory, a time-dependent stabilization process is necessary. Whereas in the brain synthesis of new proteins and RNA in the hippocampus is required for the consolidation, in the case of the investigated materials this is supposedly caused by filling of deep, thermally stable electron traps. It can be parallelized into a situation when learning something new, part of the information is forgotten (STP regime), although another part is consolidated (LTP regime). Such an effect was not present in STDP measurements – the memristor was rather transferred directly into the LTP regime (see Fig. S9†).

In order to investigate how the DC pretreatment affects plasticity in the SRDP experiment, before each measurement the MABiI 3 : 1 sample was poled for 2 s with different voltages (Fig. 10). Next, a single SRDP sequence consisting of 30 poling spikes of 1.2 V voltage was applied. The duration of a single poling spike was t = 25 ms and the time interval between spikes was set to Δt = 30 ms. The current was read with −0.5 V before and 21 s after the poling spike train. As in the previous STDP experiment, the highest LTP occurs when the sample is pre-treated with −3 V. Interestingly, when the pre-treatment voltage was +1 V (which is a voltage below the threshold switching value from HRS to LRS) the state of the device was transferred to the LTD regime. This proves that the pre-treatment of the sample might strongly affect or even alter the SRDP output.

For each of the four investigated samples we have performed the SRDP measurement with varying time intervals Δt between poling spikes. Each sample was pretreated with −3 V for 2 s prior to the measurement. The synaptic weight change Δw was calculated as previously and plotted against the time interval between poling spikes (Fig. S10 and S11†). For all measured samples the LTP increases as Δt approaches 0; however, the magnitude of changes is different for different samples. The smallest relative differences are observed for the 3 : 2 ratio and the biggest one for 3 : 1, following a similar trend as in STDP measurements – the MABiI 3 : 1 sample also showed high potentiation even at large Δt values (Fig. S11†). However, the data for non-stoichiometric samples cannot be interpreted considering single-exponential functions. A careful analysis indicated a more complex character of SRDP responses in non-stoichiometric samples (see section 8 in the ESI†). The existence of two types of electron traps with distinct dynamics (trapping time) might be responsible for the memory consolidation process as well.

Conclusions

With neuromorphic computing overcoming silicon electronics limitations, such as Moore's law and von Neumann's bottleneck, seems to be achievable. For now, memristors are a good candidate for non-linear computing elements due to the ability to store multilevel information as a passive electrical element. Here we present a reliable and air-stable[30] candidate for future memristive network devices – based on non-stoichiometric methylammonium iodobismuthate thin layers, which can be easily and inexpensively prepared *via* a simple spin-coating technique and, depending on the pretreatment potential, can mimic various neural features: STDP, SRDP, metaplasticity and memory consolidation.

Our results show that the memristive properties of MABiI are a consequence of several cooperative effects. The most dominant are charge carrier dynamics and electron trap mechanisms. The proposed putative memristance mechanism entails further research though – mostly spectroscopic investigations towards unravelling the true electronic structure with the inclusion of all inter- and intra-layer interactions.

Memristive materials based on BiI_3 and MAI have the potential to become universal cells in artificial neural networks mostly due to their ability to change the synaptic weight (*i.e.* learn) *via* many strategies, including SRDP and STDP, which can be further modulated by metaplasticity. The metaplasticity can be exceptionally beneficial for neuromorphic computing since it allows the increase of synaptic weight changes in both SRDP and STDP and thus the creation of many additional, separate memristive states, which can be easily utilized in many-value logic. Moreover, the light-modulated energy of iodine vacancies being able to affect the memristive effect makes them potential promising candidates for a new field of research in neuromorphic optoelectronics.

Materials and methods

Bismuth methylammonium iodobismuthate (MABiI) layers were prepared by a one-step spin coating method. Methylammonium iodide (MAI) was mixed with bismuth iodide (BiI_3) and dissolved in *N*,*N*-dimethylformamide (DMF) in the following molar ratios of MAI : BiI_3: 1 : 3, 1 : 1, 3 : 2, and 3 : 1. Prior to spin coating, inks were sonicated in 70 °C for 20 minutes and then filtered through a PTFE 0.45 μm syringe filter. The initial masses and concentrations for each ratio are presented in the ESI, section 1.† The FTO/glass substrate was cleaned sequentially (20 minutes of sonication in 50 °C) with deionized water with a small amount of 2% Hellmanex, deionized water and isopropanol and dried in air. Next, 50 μl of PEDOT : PSS solution in water (Sigma Aldrich) was spin coated on the cleaned FTO at 2000 RPM for 30 s. The layer was next dried on a hotplate at 100 °C for 20 minutes under an ambient atmosphere. The ink $MABiI_3$ layer was spin-coated at 2000 RPM for 30 s and dried on a hotplate at 100 °C for 20 minutes.

All the samples were measured in a device of our design in order to assure the highest possible measurement reproducibility. Briefly, the sample is put in a holder and a plastic cylinder with incorporated metal rods acting as working electrodes is pressed against the sample surface with a fixed force, thus creating electrical contact on the MABI/metal interface. In our experiments 99.99% pure Cu metal rods (Sigma Aldrich) with a diameter of 2 mm were used, which let us estimate the surface contact area to be 3.14 mm^2. Prior to each measurement, the electrode surface was polished with abrasive paper (4000 grade) to a mirror-like surface. However, as the contact is purely mechanical and might depend both on the metal rod texture and the sample surface roughness, the effective contact surface might vary a little from sample to sample.

The measurements were conducted under an ambient atmosphere. Current–voltage characteristic (*I*–*V*) and spike-timing-dependent plasticity (STDP) experiments were performed on a Keithley 4200 SCS system with two SMUs connected respectively to a FTO and Cu electrode (see Fig. 2a for the experimental setup). For the *I*–*V* measurements, the applied DC voltage sweep direction was 0 V → 3 V → 0 V → −3 V → 0 V at 500 mV s^{-1}. In each technique, readout pulses were set up at −0.5 V.

In the STDP measurements the voltage pulse sequence was as follows: first, the memristor state was read three times with −0.5 V. Then symmetric bipolar sawtooth pulses of ±1.6 V were applied on the pre- and postsynaptic electrode with a fixed time interval. Then, the state was read again with three −0.5 V pulses (for schematics of the utilized voltage pattern please see the ESI, section 5†). After the measurement the memristive device was reset to the initial state with either *I*–*V* scan or DC voltage bias (as indicated in the text). To induce long-term potentiation, the time interval between the two poling pulses was gradually decreased.

Spike-rate-dependent plasticity (SRDP) and memristor's state retention measurements were performed on a Metrohm Autolab PGSTAT302N system with a two-electrode setup. The working electrode (WE) was connected to Cu electrodes, while the counter electrode (CE) and reference electrode (RE) were short-circuited and connected directly to the FTO layer. Before conducting the actual experiments, samples were conditioned with multiple *I*–*V* scans (typically about 30) at 500 mV s^{-1}. Voltage and current sequences are presented in the ESI, section 5.†

An X-ray diffractometer (XRD, RINT 2100, Rigaku) with Co Kα1 radiation (λ = 1.78892 Å) was used to record the X-ray diffraction diagram at 10° to 100° at a scanning step of 0.01° s^{-1}. The presented results were recalculated for Cu Kα1 (λ = 1.54056 Å) to compare diffractograms with the literature data.

Conflicts of interest

There are no conflicts to declare.

Acknowledgements

The authors thank Dr Mateusz Marzec for UPS measurements, Dr Katarzyna Berent for the SEM image and Ewelina Wlaźlak for her help with calculations of the Schottky barrier height. Special thanks are addressed to Prof. Piotr Bała and Prof. Kapela Pilaka for a fruitful discussion and support during the preparation of the manuscript.

The authors acknowledge the support of Higher National Science Centre (Poland) within the MAESTRO project (grant agreement No. UMO-2015/18/A/ST4/00058) and Polish Ministry of Science and Higher Education.

Notes and references

1 M. Hilbert and P. López, *Science*, 2011, **332**, 60–65.
2 J. Backus, *Commun. ACM*, 1978, **21**, 613–641.
3 D. P. Rodgers, *ACM SIGARCH Comput. Archit. News*, 1985, **13**, 225–231.
4 M. A. Zidan, J. Paul Strachan, W. D. Lu, J. P. Strachan and W. D. Lu, *Nat. Electron.*, 2018, **1**, 22–29.
5 L. O. Chua, *IEEE Trans. Circuit Theory*, 1971, **18**, 507–519.
6 L. Chua, *Semicond. Sci. Technolgy*, 2014, **29**, 104001.
7 T. Prodromakis, C. Toumazou and L. Chua, *Nat. Mater.*, 2012, **11**, 478–481.
8 P. Maier, F. Hartmann, M. Emmerling, C. Schneider, M. Kamp, S. Höfling and L. Worschech, *Phys. Rev. Appl.*, 2016, **5**, 1–9.
9 D. B. Strukov, G. S. Snider, D. R. Stewart and R. S. Williams, *Nature*, 2008, **453**, 80–83.
10 R. S. Williams, J. Yang and D. Stewart, *US* 8450711B2, 2009.
11 D. B. Strukov, G. S. Snider, D. R. Stewart and R. S. Williams, *Nature*, 2008, **453**, 80–83.
12 A. Bera, H. Peng, J. Lourembam, Y. Shen, X. W. Sun and T. Wu, *Adv. Funct. Mater.*, 2013, **23**, 4977–4984.
13 N. M. Samardžić, B. Bajac, J. Bajić, E. Đurđić, B. Miljević, V. V. Srdić and G. M. Stojanović, *Microelectron. Eng.*, 2018, **187–188**, 139–143.
14 Z. Xiao and J. Huang, *Adv. Electron. Mater.*, 2016, **2**, 1600100.
15 H. S. Kim and N. G. Park, *J. Phys. Chem. Lett.*, 2014, **5**, 2927–2934.
16 G. Lin, Y. Lin, R. Cui, H. Huang, X. X. X. Guo, C. Li, J. Dong, X. X. X. Guo and B. Sun, *J. Mater. Chem. C*, 2015, **3**, 10793–10798.
17 W. Wang, G. N. Panin, X. Fu, L. Zhang, P. Ilanchezhiyan, V. O. Pelenovich, D. Fu and T. W. Kang, *Sci. Rep.*, 2016, **6**, 33107.
18 Y. Chen, G. Liu, C. Wang, W. Zhang, R.-W. Li and L. Wang, *Mater. Horiz.*, 2014, **1**, 489.
19 D. A. A. Lapkin, A. V. V. Emelyanov, V. A. A. Demin, T. S. S. Berzina and V. V. V. Erokhin, *Microelectron. Eng.*, 2018, **185–186**, 43–47.
20 Y. Van De Burgt, E. Lubberman, E. J. Fuller, S. T. Keene, G. C. Faria, S. Agarwal, M. J. Marinella, A. Alec Talin and A. Salleo, *Nat. Mater.*, 2017, **16**, 414–418.
21 D. Li and X. Liang, *Nature*, 2018, **554**, 472–473.
22 V. K. Sangwan, H. S. Lee, H. Bergeron, I. Balla, M. E. Beck, K. S. Chen and M. C. Hersam, *Nature*, 2018, **554**, 500–504.
23 J. F. Miller, S. L. Harding and G. Tufte, *Evol. Intell.*, 2014, **7**, 49–67.
24 N. J. Jeon, J. H. Noh, W. S. Yang, Y. C. Kim, S. Ryu, J. Seo and S. Il Seok, *Nature*, 2015, **517**, 476–480.
25 H.-L. L. Hsu, C.-P. P. Chen, J.-Y. Y. Chang, Y.-Y. Y. Yu and Y.-K. K. Shen, *Nanoscale*, 2014, **6**, 10281–10288.
26 C. Lan, J. Luo, S. Zhao, C. Zhang, W. Liu, S. Hayase and T. Ma, *J. Alloys Compd.*, 2017, **701**, 834–840.
27 B. Hwang and J.-S. S. Lee, *Sci. Rep.*, 2017, **7**, 673.
28 B. W. Park, B. Philippe, X. Zhang, H. Rensmo, G. Boschloo and E. M. J. Johansson, *Adv. Mater.*, 2015, **27**, 6806–6813.
29 M. Lyu, J. H. Yun, M. Cai, Y. Jiao, P. V. Bernhardt, M. Zhang, Q. Wang, A. Du, H. Wang, G. Liu and L. Wang, *Nano Res.*, 2016, **9**, 692–702.
30 B. Hwang and J. S. Lee, *Nanoscale*, 2018, **10**, 8578–8584.
31 J. M. Frost and A. Walsh, *Acc. Chem. Res.*, 2016, **49**, 528–535.
32 Y. Yuan, J. Chae, Y. Shao, Q. Wang, Z. Xiao, A. Centrone and J. Huang, *Adv. Energy Mater.*, 2015, **5**, 1–7.
33 X. Zhu and W. D. Lu, *ACS Nano*, 2018, **12**, 1242–1249.
34 X. Zhu, J. Lee and W. D. Lu, *Adv. Mater.*, 2017, **29**, 1–8.
35 Y. Sun, M. Tai, C. Song, Z. Wang, J. Yin, F. Li, H. Wu, F. Zeng, H. Lin and F. Pan, *J. Phys. Chem. C*, 2018, **122**, 6431–6436.
36 A. H. Jaafar, R. J. Gray, E. Verrelli, M. O'Neill, S. M. Kelly and N. T. Kemp, *Nanoscale*, 2017, **9**, 17091–17098.
37 B. Linares-Barranco and T. Serrano-Gotarredona, *Nat. Preced.*, 2009, 2–5.
38 S. Kim, C. Du, P. Sheridan, W. Ma, S. Choi and W. D. Lu, *Nano Lett.*, 2015, **15**, 2203–2211.
39 D. O. Hebb, *The organization of behavior: A neurophysiological approach*, Wiley and Sons, New York, 1949.
40 W. C. Abraham, *Nat. Rev. Neurosci.*, 2008, **9**, 387–399.
41 X. Zhu, C. Du, Y. Jeong and W. D. Lu, *Nanoscale*, 2017, **9**, 45–51.
42 Z. H. Tan, R. Yang, K. Terabe, X. B. Yin, X. D. Zhang and X. Guo, *Adv. Mater.*, 2016, **28**, 377–384.
43 J. Yin, F. Zeng, Q. Wan, F. Li, Y. Sun, Y. Hu, J. Liu, G. Li and F. Pan, *Adv. Funct. Mater.*, 2018, **28**(19), 1706927.
44 Q. Wu, H. Wang, Q. Luo, W. Banerjee, J. Cao, X. Zhang, F. Wu, Q. Liu, L. Li and M. Liu, *Nanoscale*, 2018, **10**, 5875–5881.
45 H. Tan, G. Liu, H. Yang, X. Yi, L. Pan, J. Shang, S. Long, M. Liu, Y. Wu and R.-W. Li, *ACS Nano*, 2017, **11**(11), 11298–11305.
46 R. A. John, F. Liu, N. A. Chien, M. R. Kulkarni, C. Zhu, Q. Fu, A. Basu, Z. Liu and N. Mathews, *Adv. Mater.*, 2018, **30**(25), 1800220.
47 W. C. Abraham and M. F. Bear, *Trends Neurosci.*, 1996, **19**, 126–130.
48 S. H. Jo, T. Chang, I. Ebong, B. B. Bhadviya, P. Mazumder and W. Lu, *Nano Lett.*, 2010, **10**, 1297–1301.
49 J. X. Shen, D. S. Shang, Y. S. Chai, S. G. Wang, B. G. Shen and Y. Sun, *Adv. Mater.*, 2018, **30**, 1706717.
50 X. Yang, Y. Fang, Z. Yu, Z. Wang, T. Zhang, M. Yin, M. Lin, Y. Yang, Y. Cai and R. Huang, *Nanoscale*, 2016, **8**, 18897–18904.
51 R. L. Z. Hoye, R. E. Brandt, A. Osherov, V. Stevanovic, S. D. Stranks, M. W. B. Wilson, H. Kim, A. J. Akey, J. D. Perkins, R. C. Kurchin, J. R. Poindexter, E. N. Wang, M. G. Bawendi, V. Bulovic and T. Buonassisi, *Chem. – Eur. J.*, 2016, **22**, 2605–2610.
52 H. Wang, J. Tian, K. Jiang, Y. Zhang, H. Fan, J. Huang, L. Yang, B. Guan and Y. Song, *RSC Adv.*, 2017, **7**, 43826–43830.

53 K. Eckhardt, V. Bon, J. Getzschmann, J. Grothe, F. M. Wisser and S. Kaskel, *Chem. Commun.*, 2016, **52**, 3058–3060.
54 O. Horváth and I. Mikó, *Spectra, equilibrium and photoredox chemistry of iodobismuthate (III) complexes in acetonitrile*, Elsevier, 2000, vol. 304.
55 H. A. Evans, J. G. Labram, S. R. Smock, G. Wu, M. L. Chabinyc, R. Seshadri and F. Wudl, *Inorg. Chem.*, 2017, **56**, 395–401.
56 J. Haruyama, K. Sodeyama, L. Han and Y. Tateyama, *Acc. Chem. Res.*, 2016, **49**, 554–561.
57 L. M. Wu, X. T. Wu and L. Chen, *Coord. Chem. Rev.*, 2009, **253**, 2787–2804.
58 L. Chua, V. Sbitnev and H. Kim, *Int. J. Bifurcation Chaos*, 2012, **22**, 1230011.
59 W. Mönch, *J. Vac. Sci. Technol., B: Microelectron. Nanometer Struct. – Process., Meas., Phenom.*, 1999, **17**, 1867.
60 T. Nishimura, K. Kita and A. Toriumi, *Appl. Phys. Lett.*, 2007, **91**, 23702.
61 H. Vázquez, W. Gao, F. Flores and A. Kahn, *Phys. Rev. B: Condens. Matter Mater. Phys.*, 2005, **71**, 041306.
62 N. Du, M. Kiani, C. G. Mayr, T. You, D. Bürger, I. Skorupa, O. G. Schmidt and H. Schmidt, *Front. Neurosci.*, 2015, **9**, 1–10.
63 K. Pilarczyk, A. Podborska, M. Lis, M. Kawa, D. Migdal and K. Szaciłowski, *Adv. Electron. Mater.*, 2016, **2**, 1500471.
64 Y. Park and J. S. Lee, *ACS Nano*, 2017, **11**, 8962–8969.
65 A. Thomas, *J. Phys. D: Appl. Phys.*, 2013, **46**, 093001.
66 C. Zamarreño-Ramos, L. A. Camuñas-Mesa, J. A. Perez-Carrasco, T. Masquelier, T. Serrano-Gotarredona and B. Linares-Barranco, *Front. Neurosci.*, 2011, **5**, 1–22.
67 C. Du, W. Ma, T. Chang, P. Sheridan and W. D. Lu, *Adv. Funct. Mater.*, 2015, **25**, 4290–4299.
68 S. Li, F. Zeng, C. Chen, H. Liu, G. Tang, S. Gao, C. Song, Y. Lin, F. Pan and D. Guo, *J. Mater. Chem. C*, 2013, **1**, 5292–5298.
69 C. Mayr, S. Sheik, C. Bartolozzi and E. Chicca, *Synaptic Plasticity for Neuromorphic Systems*, Frontiers Media SA, 2016.
70 J. L. McGaugh, *Science*, 2000, **287**, 248–251.

RSC Nanoscale

ARTICLE

Synaptic plasticity, metaplasticity and memory effects in hybrid organic-inorganic bismuth-based materials

Tomasz Mazur, [†a]* Piotr Zawal[†b]* and Konrad Szaciłowski [a]

Supporting Information

1. Preparation of bismuth perovskite starting solutions

Weighted amounts of methylammonium iodide (M_{MAI} = 159 g/mol) were mixed with bismuth iodide (M_{BiI3} = 590 g/mol) and dissolved in 0.5 mL of N,N-dimethylformamide (DMF) with following molar ratios:

Table S1 Substrates used in MABiI thin films preparation.

MAI:BiI_3 ratio	mass of MAI	mass of BiI_3
1:3	26.5 mg	295.0 mg
1:1	79.5 mg	295.0 mg
3:2	59.6 mg	147.5 mg
3:1	159.0 mg	196.7 mg

2. UV-Vis spectra of pure precursors solutions in DMF

UV-Vis spectrum (325 nm – 800 nm) of pure MAI in DMF is characterized by one absorption maximum at 366 nm (MAI) and BiI_3 in DMF has a maximum at 435 nm, originating from $[BiI_4]^-$ complexes.

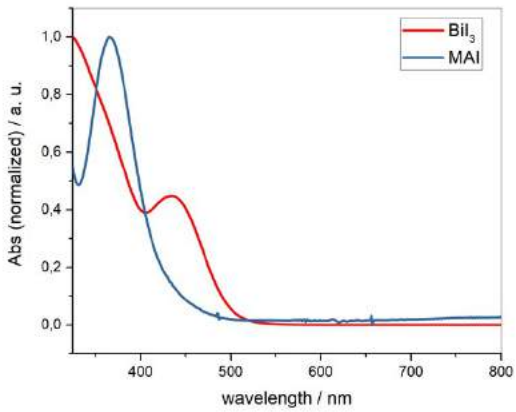

Figure S1 UV-Vis spectrum of pure precursors - methylammonium iodide (MAI) and bismuth triodide BiI_3 - dissolved in DMF.

3. Calculation of Schottky barrier height

To study the character of the interface we have employed the thermionic emission theory to extract the information from the I-V measurement curve. The Schottky character of the MABiI3/Cu junction is clearly visible while scanning from 0 V to 0.8 V. The reverse saturation current and the ideality factor can be calculated from the equation defining Schottky diode current for forward bias voltages:

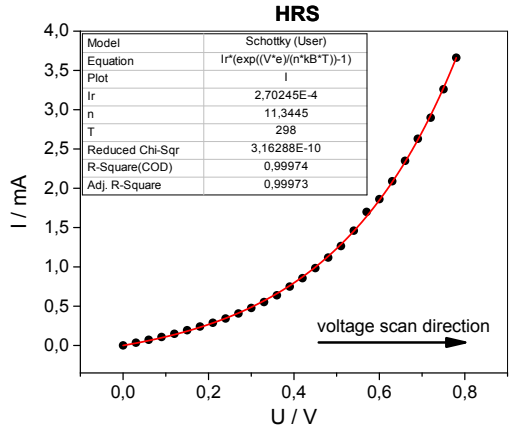

$$I_s = I_r\left(\exp\left(\frac{ev}{k_B T}\right) - 1\right) \quad (1)$$

Figure S2 Schottky diode-like I-V characteristics during forward voltage scan direction.

The fitting results are presented in Figure S2. The calculated saturation current is I_r = 0.27 mA and the ideality parameter is 11.35, indicating strong deviance from the ideal current values. This might originate from the fact, that investigated device is not just a pure diode, but rather can be described as a circuit. The character of the junction changes from Schottky-like to Ohmic when the memristor is in LRS (Figure S3).

One can exclude the filament formation, as the switching is not abrupt but rather changes gradually, which might result from changes in junction properties. Moreover, the prepared devices did not need any electroforming procedure in order to exhibit memristive behaviour, which is often necessary for memristors with filament resistive switching mechanism.[1] As mentioned before, the current flowing through the junction at the MABiI/Cu interface is not ideal (as indicated by the n parameter). To further investigate this behaviour we have focused only on one part of the loop, strongly resembling the Schottky diode characteristic (consisting of 0 V → +3 V and -3 V → 0 V parts of the I-V curve). Since the current

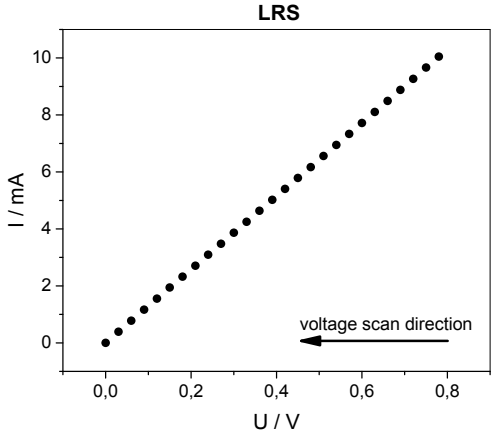

Figure S3 Ohmic I-V characteristic during the reverse voltage scan direction.

response differs from this for the ideal diode and the Ohmic component is present, we suggest that the junction acts not as a single diode, but rather a circuit as shown on the diagram in Figure S4:

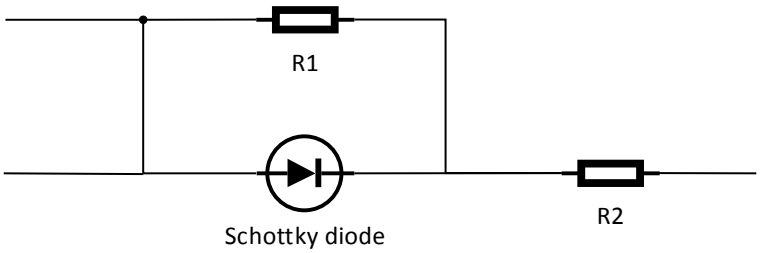

Figure S4 Equivalent circuit consisting of parallel connected Schottky diode and resistor R1 with additional resistor R2 in series. The former was used to take into the consideration the higher resistance of HRS.

When the diode is polarized with a forward bias, the total circuit resistance is approximately equal to R2. Under reverse bias polarization, the sum of two resistors determines the circuit resistance, which accounts for the transition to HRS. In order to calculate the resistance, the linear function has been fitted to both regions of the data (Figure S5).

In the HRS the function has been fitted only to the linear current response. The calculated resistances from slopes of fitted functions are: *R2* = 49.90 Ω (LRS part) and *R1+R2* = 689.66 Ω (HRS part), meaning *R1* = 639.76 Ω. To calculate the reverse saturation current, we have eliminated the Ohmic component by subtracting the theoretical current flowing through *R2* from the measured current values. As the *R2* resistance is present only in HRS, the correction was made only for voltages below the switching voltage, i.e. 0.8 V (as indicated in Figure S5 by the vertical line):

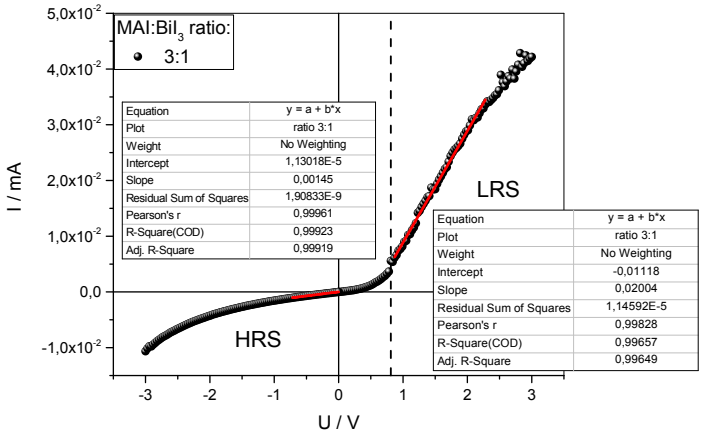

Figure S5 The fitting data of linear functions used to estimate resistance of R1 and R2. The functions were fitted to linear current response in both HRS and LRS to determine R1+R2 and R2, respectively.

These calculations led us to estimate the reverse saturation current of the diode to J_0 = 4.87×10-2 mA (calculated as the average current for voltages in the linear range from -1 V to 0 V). After these calculations, the Schottky barrier height can be calculated from the Richardson equation:

$$J_0 = A^* \cdot T^2 \exp\left(\frac{q_e \varphi_B}{kT}\right) \quad (2)$$

where J_0 is the reverse saturation current, T is temperature, q_e is the elementary charge, φ_B is Schottky barrier height, k is the Boltzmann constant and A^* is the effective Richardson constant defined as follows: $A^* = 4\pi q_e m_e^* k^2 h^{-3}$, where m_e^* is the electron effective mass and h is the Planck constant. In $MA_3Bi_2I_9$ the effective mass $m_e^*_{A\text{-}H}$ was calculated to be 0.54[2] and the temperature at which the measurements were conducted was 23 °C. Thus, the calculated Schottky barrier height on the MABI/Cu junction is φ_B = 0.55 eV. We have additionaly investigated the Schottky barrier with Ultraviolet Photoelectron Spectroscopy (UPS). The measured barrier height was 0.5 V on MABiI/Cu interface, whereas at MABiI/PEDOT:PSS interface the height was 0 V, indicating Ohmic type of this junction.

4. Simple neuromorphic functions – learning and forgetting (fitting data)

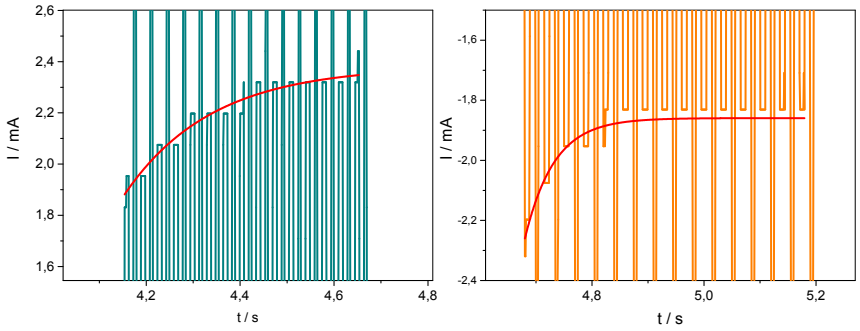

Model	ExpDecay1
Equation	y = y0 + A1*exp(-(x-x0)/t1)
Plot	current
y0	0,00238 ± 0
x0	4,14025 ± 0
A1	-5,3841E-4 ± 1,1468E-5
t1	0,1857 ± 0,00588
Reduced Chi-Sqr	1,58938E-9
R-Square(COD)	0,92366
Adj. R-Square	0,92311

Model	ExpDecay1
Equation	y = y0 + A1*exp(-(x-x0)/t1)
Plot	current
y0	-0,00186 ± 0
x0	4,67898 ± 0
A1	-4,11021E-4 ± 1,92253E-5
t1	0,05212 ± 0,00416
Reduced Chi-Sqr	2,51065E-9
R-Square(COD)	0,81905
Adj. R-Square	0,81782

Figure S6 Fitting data of exponential function fitted to learning (right panel) and forgetting (left panel).

5. Electric impulses sequences

Here, in we present voltage sequences for most crucial experiments in current publication. Voltage levels have been established empirically, based on preliminary tests for each type of sample (Figure S7a, b, c).

a. **Voltage sequence for I-V hysteresis -** before main neuromorphic measurements for each sample, each sample was tested with I-V scans – several, typically 20 voltage scans, within -3.5 V to 3.5 V range, with moderate scan speed – 200 mV/s.

b. **Sequence for STDP measurements -** typically, each sample was measured 3 times for each Δt value.

c. **Sequence for SRDP measurements**

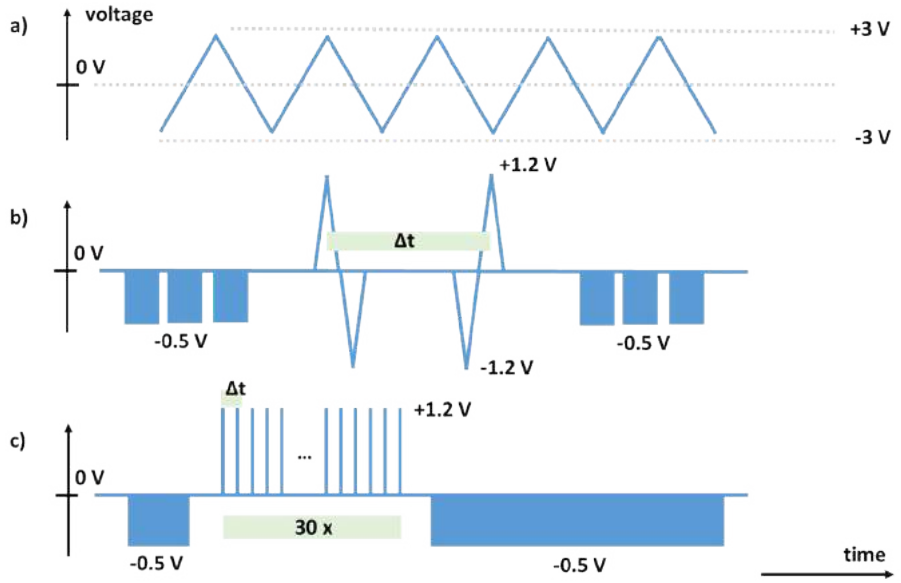

Figure S7 Voltage sequences used in I-V hysteresis curve experiment (a), STDP experiments – in case of $\Delta t < 0$, the two spikes exchange places (b), SRDP experiments (c).

6. STDP – DC bias results for negative Δt (LTD regime)

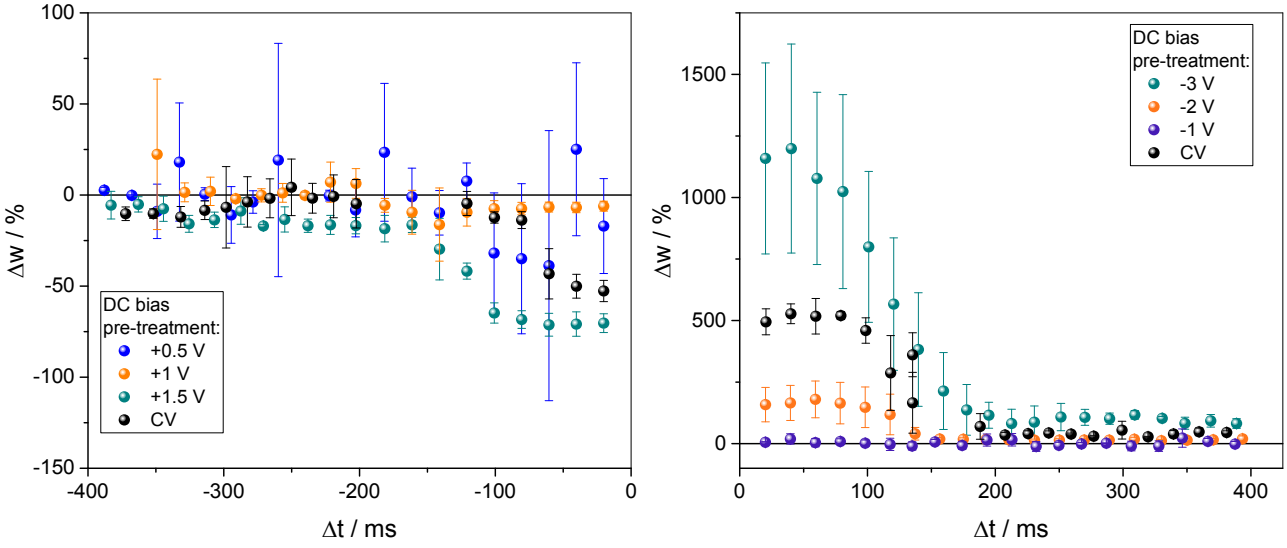

Figure S8 STDP curve comparison between conventional experiments (CV scan performed before the poling spikes sequence) and experiments with the priming activity (DC bias pre-treatment before the sequence). The figure shows results of two plasticity regimes – left part is for depression regime (LTD) and the right part is for potentiation regime (LTP).

7. STDP – non-volatile learning

In Figure S9 we present the direct transition into LTP regime after the STDP measurement.

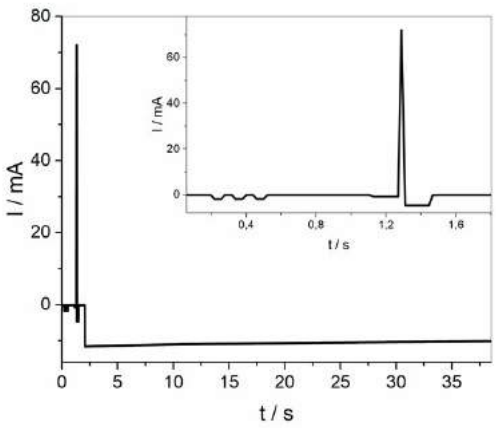

Figure S9 STDP measured as current response for 36 s after applying pair of spikes with Δt = 20 ms. No significant change in current suggests that observed effect belongs to LTP regime. Before poling the sample current was read three times at -0.5 V (depicted in inset).

8. SRDP measured for materials made with different MAI:BiI_3 ratio.

The SRDP of the two least defected samples, i.e. MABiI 1:1 and 3:2, can be described with single exponential function. The long time constant τ_l (the constant is called "long" for the sake of the further discussion) for MABiI 3:2 is 560±397 ms and 533±210 ms for MABiI 1:1. However this fit is not ideal due to significant scatter of the data points, the tendency is quite explicit. In the range of the estimated uncertainty both time constants can be considered as equal (Figure S10).

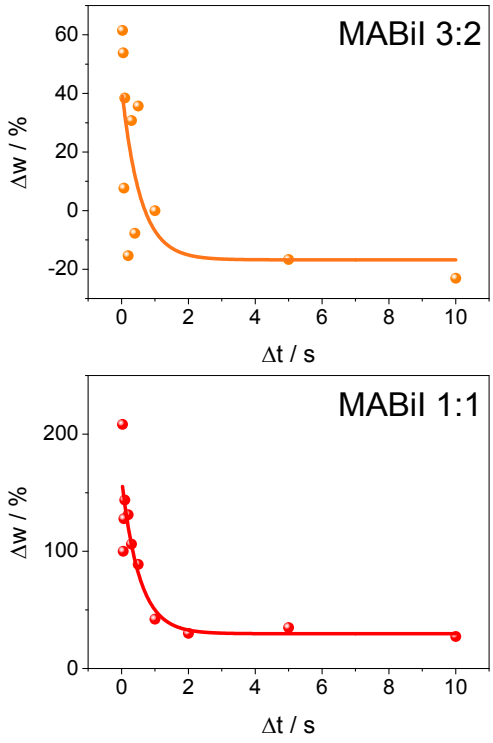

Model	ExpDecay1
Equation	y = y0 + A1*exp(-(x-x0)
Plot	3:2
y0	-16.79082 ± 0
x0	-0.10459 ± 0
A1	71.09364 ± 25.10971
t1	0.55986 ± 0.39763
Reduced Chi-Sq	513.07134
R-Square(COD)	0.49101
Adj. R-Square	0.43446

Model	ExpDecay1
Equation	y = y0 + A1*exp(-(x-x0)
Plot	1:1
y0	29.70713 ± 0
x0	-0.0737 ± 0
A1	152.63723 ± 25.91378
t1	0.53264 ± 0.2096
Reduced Chi-Sq	666.46867
R-Square(COD)	0.81827
Adj. R-Square	0.79808

Figure S10 Single-exponent functions fitted to MABil 1:1 and 3:2 samples in SRDP measurement.

However, this simple exponential function doesn't describe well the data collected for MABil 1:3 and 3:1. The closer look at the data collected for this samples reveals that the data can be better described with a more sophisticated equation consisting of the following form:

$$I = \begin{cases} I_0 + A_d + A_g\left(e^{-\frac{t_c}{\tau_s}} - e^{-\frac{t}{\tau_l}}\right) & t < t_c \\ I_0 + A_d e^{-(t-t_c)/\tau_l} & t > t_c \end{cases} \quad (3)$$

where y_o is the reading current offset, A_d and A_g are amplitudes for growth and decay region of the function, t_c is the time interval value with the highest current amplitude, τ_s and τ_l are the short and long time constants, respectively.

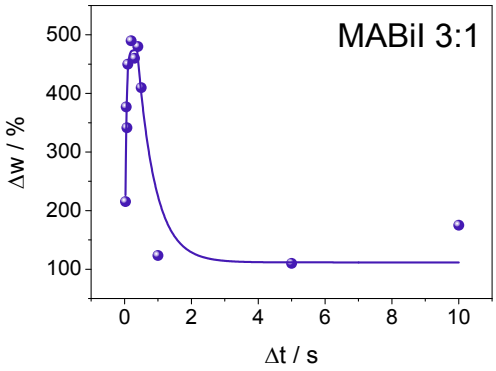

Model	ExpGrowDec
Equation	y = x<xc ? y0+Ad+Ag*(exp(-xc/tg)-exp(-x/tg)) : y0+Ad*exp(-(x-xc)/td);
Plot	3:1
y0	111.67264 ± 44.81469
xc	0.37992 ± 0.11006
Ag	566.49488 ± 356.91897
tg	0.03619 ± 0.02439
Ad	362.25289 ± 64.00157
td	0.53264 ± 0.30254
Reduced Chi-Sqr	4021.37584
R-Square(COD)	0.90705
Adj. R-Square	0.81411

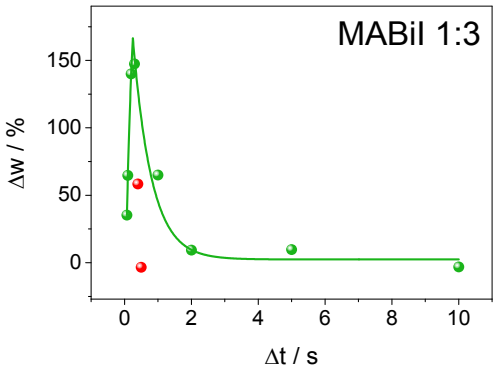

Model	ExpGrowDec
Equation	y = x<xc ? y0+Ad+Ag*(exp(-xc/tg)-exp(-x/tg)) : y0+Ad*exp(-(x-xc)/td);
Plot	1:3
y0	2.40152 ± 0
xc	0.24871 ± 0.0506
Ag	333.4306 ± 435.86766
tg	0.23727 ± 0.69672
Ad	164.21751 ± 16.73121
td	0.55986 ± 0.12884
Reduced Chi-Sqr	164.58121
R-Square(COD)	0.97921
Adj. R-Square	0.95149

Figure S11 Two-exponential function fitting for MABiI 3:1 and 1:3 samples in SRDP measurement. The points marked in red were excluded from the fitting procedure and *y_0 parameter (y-axis offset) was fixed in the fit for MABiI 1:3*.

This suggests that for more defected samples another process with different time constant occurs with a significantly shorter time constant. The estimated constants are τ_l = 533±303 ms and τ_s = 36±24 ms for MABiI 3:1 and τ_l = 560±129 ms and τ_s = 237±697 ms for MABiI 1:3. However the fits are far from being perfect and should be treated rather as qualitative than a quantitative experiment, the presence of the short time constant is obvious in the mentioned samples. To improve the output of the measurement, we suggest that sputtered electrodes and current compliance should be introduced to reduce the data points scatter.

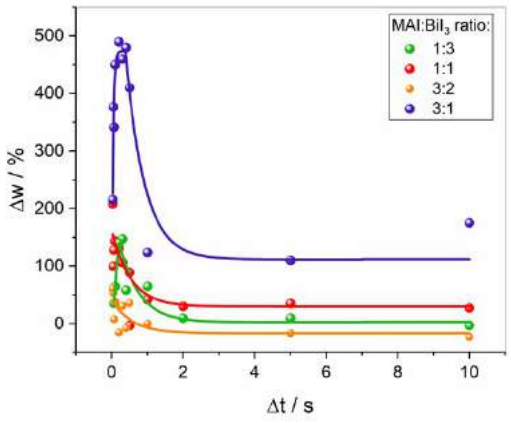

Figure S12 Collective graph of SRDP measurement output for different MAI:BiI_3 with fitted functions.

The presence of two significantly different time constants indicated the possibility of material evolution, i.e. relaxation processes that change the occupancy of the trap states and hence the conductivity and synaptic weights. The presence of two types of electron traps with different dynamics (trapping time) might also be significant in memory consolidation process. Once again, we conclude that more defected materials presented higher and more stable synaptic weight changes, proving indirectly the significant role of lattice defects in the charge trapping processes and hence the observed memristive effects. It does not exclude, however the role of ion migration, as it has already been postulated for stoichiometric samples of MABiI.

Bibliography:

1 M. Hansen, M. Ziegler, L. Kolberg, R. Soni, S. Dirkmann, T. Mussenbrock and H. Kohlstedt, *Sci. Rep.*, 2015, **5**, 13753.

2 M. Pazoki, M. B. Johansson, H. Zhu, P. Broqvist, T. Edvinsson, G. Boschloo and E. M. J. Johansson, *J. Phys. Chem. C*, 2016, **120**, 29039–29046.

Journal of Materials Chemistry C

ROYAL SOCIETY OF CHEMISTRY

PAPER

View Article Online
View Journal

Cite this: DOI: 10.1039/d0tc00679c

Bismuth triiodide complexes: structure, spectroscopy, electronic properties, and memristive properties†

Ewelina Wlaźlak, *[a] Justyna Kalinowska-Tłuścik, [b] Dawid Przyczyna,[ac] Piotr Zawal [ac] and Konrad Szaciłowski *[a]

Received 10th February 2020,
Accepted 28th March 2020

DOI: 10.1039/d0tc00679c

rsc.li/materials-c

A new class of semiconducting materials has been prepared based on bismuth(III) iodide in reaction with ternary amine *N*-oxides, sulfoxides, and phosphinoxides. Depending on the nature of the ligand, various structures originating from fragments of the BiI_3 lattice are formed. The band structure of these materials, optical spectroscopy, and work function measurements indicate the importance of metal–ligand and intraligand interactions in the electronic properties of these complexes. These materials are usually p-type semiconductors, but bidentate benzo(*c*)cinnoline-*N*,*N*′-dioxide results in an n-type semiconducting complex. They can be used for fabrication of MIM (metal–insulator–metal) type devices, which show interesting memristive properties, including modulation of the memristive properties simply due to the change of the type of metallic contact. The operation of the presented devices is based solely on the interface effects and the modulation of the Schottky barrier height. The change of only one of the two electrodes leads to a change from the clockwise to the anticlockwise direction of propagation of the hysteresis loop as well as from the Hebbian to the anti-Hebbian learning mode.

Introduction

Bismuth(III) halide systems form a variety of molecular and ionic structures in which mono- and polynuclear structures can be found.[1–9] Bismuth(III) halide organic–inorganic hybrid semiconductors attract increasing attention due to their application as absorbers in photovoltaic cells. One of the reasons behind the intensive studies on $(CH_3NH_3)_3Bi_2I_9$ and related structures is the much lower toxicity of bismuth in comparison to lead, present in the most efficient perovskite solar cells (*e.g.*, $CH_3NH_3PbI_3$).[10–13] In general, bismuth(III) halides have several interesting optical properties, like photoluminescence,[14,15] thermo- and photochromism,[16,17] and other favorable features like solubility in organic solvents and air stability.[18]

Besides the undeniable contribution to the field of photovoltaics, both lead- and bismuth iodide compounds marked their presence in modern electronics, especially in neuromorphic and memory applications.[19–23] The hysteresis loop observed in the current–voltage characteristics of those materials is often called a fingerprint of the memristor.[24] A memristor is the fourth fundamental passive electrical circuit element postulated by Leon Chua as early as 1971.[25] For a long time, it was considered only as a scientific curiosity, but in 2008, for the first time, a physical device was linked to the theoretical construct called the ''memristor,'' as postulated by Leon Chua. R. S. Williams and coworkers at HP Labs presented a MIM (metal–insulator–metal) device based on a thin layer of TiO_2 sandwiched between Pt contacts.[26] It is important to mention that devices with this feature were reported much earlier.[27,28] There are various potential applications of those devices: memory, logic synthesis, cryptography, analog computing, and neuromorphic applications.[29–35]

Neuromorphic applications of memristors are possible for many reasons. First, memristors have two or more (resistive) states. Second, the switching between the states is time-dependent. Finally, memristors have non-volatile memory and (voltage) thresholds that enable the change of the state of the device.[36] In memristive devices different plasticity types

[a] AGH University of Science and Technology, Academic Centre for Materials and Nanotechnology, al. A. Mickiewicza 30, 30-059 Kraków, Poland. E-mail: ewlazlak@agh.edu.pl, szacilow@agh.edu.pl
[b] Faculty of Chemistry, Jagiellonian University, ul. Gronostajowa 2, 30-060 Kraków, Poland
[c] Faculty of Physics and Applied Computer Science, AGH University of Science and Technology, al. A. Mickiewicza 30, 30-059 Kraków, Poland

† Electronic supplementary information (ESI) available: Crystal/experimental data and structure refinement results; packing in crystals of the complexes and the most important intermolecular interactions; Tauc plots and the band gaps of the studied compounds; current–voltage characteristics of all compounds in Au and Cu variants; the persistence test of the FTO/$[BiI_3\{(C_6H_5)_2SO\}_{1.5}]_4$/Au device. CCDC 1941005–1941008. For ESI and crystallographic data in CIF or other electronic format see DOI: 10.1039/d0tc00679c

and learning rules were observed: spike-timing dependent plasticity (STDP), spike-rate dependent plasticity (SRDP), long-term potentiation (LTP) and depression (LTD), habituation and metaplasticity.[21,37–42] Among them, STDP seems to be the most common indicator of synapse-like behavior.[43,44] The memristive properties displayed by various solid-state devices can be a consequence of several physical and chemical processes, including the formation of conductive filaments,[45–47] the migration of ions and/or dopants,[48] or the modulation of the Schottky barrier height.[49–53]

Taking into account the successes of ionic bismuth-halide perovskite-like compounds, we turned our attention to molecular organic complexes of BiI_3. Complexes with bulky organic ligands usually are less prone to hydrolysis but large ligands like triphelylphosine oxide or tribenzylamine and triphenylarsine oxide do not promote stacking interactions in the crystal structure.[54,55] It can result in very low conductivity of the new material. Therefore, besides two complexes with large organic ligands, we synthesized two compounds with organic ligands more prone to develop stacking interactions.

Here we present a group of new bismuth(III) iodide hybrid organic–inorganic complexes with bulky organic ligands. The ligand-dependent disruption of the initial layered structure of BiI_3 has consequences in the optical and electrical properties of the compounds. Different numbers of atoms coordinated in the first sphere of the Bi atom, as well as various metal–ligand electronic interactions, result in different conductivity types observed *via* SPV measurements. Moreover, a memristive device can be prepared when thin layers of the presented complexes are placed between two electrodes, and the conductivity type is a crucial factor governing the shape of the hysteresis loop. Those devices offer an uncommon mechanism of memristive switching – trap state modulation of the Schottky barrier height.[21] What is presented here for the first time is the change of current propagation in the pinched hysteresis loop from clockwise to anticlockwise when only one metal electrode was changed (Au to Cu). The effect is caused by the change in surface charging upon the formation of a metal/semiconductor junction. The direct consequence is the change from Hebbian to anti-Hebbian learning observed during STDP measurements obtained for the device based on the same compound, but in contact with two different metals – an effect that has never been described before. A hardware neural network based on the $[BiI_3\{(C_6H_5)_3PO\}_2]_2$ or $[BiI_3\{(C_6H_5)_2SO\}_{1.5}]_4$ complexes would have a unique property. A chip design to take advantage of this unusual Hebbian to anti-Hebbian learning rule change could allow one to apply a particular training method: the Remote Supervised Method (ReSuMe).[56]

Results and discussion

Crystal structure description

Bismuth iodide reacts in refluxing methanol with various *O*-donor ligands: ternary amine *N*-oxides, sulfoxides, and phosphinoxides. The resulting compounds are stable crystalline, orange and red-colored solids, soluble in organic solvents and insoluble in water. In contact with water, they undergo slow hydrolysis but are stable under ambient conditions for at least one year without any signs of hydrolysis or decomposition. The coordination of the bismuth ion is octahedral (Fig. 1a–c) in all but one crystal structure. The mentioned exception is observed for $[BiI_3(C_{12}H_8N_2O_2)]$, in the case of which, due to the chelating character of the organic moiety, seven atoms are in the first coordination sphere of the central ion (Fig. 1d). In the architecture of $[BiI_3\{(C_6H_5)_3PO\}_2]_2$ (described previously[57]) and $[BiI_3\{(C_6H_5)_2SO\}_{1.5}]_4$ crystals, isolated coordination motifs can be distinguished. For the first-mentioned crystal structure, centrosymmetric dimers are observed, formed by two bismuth

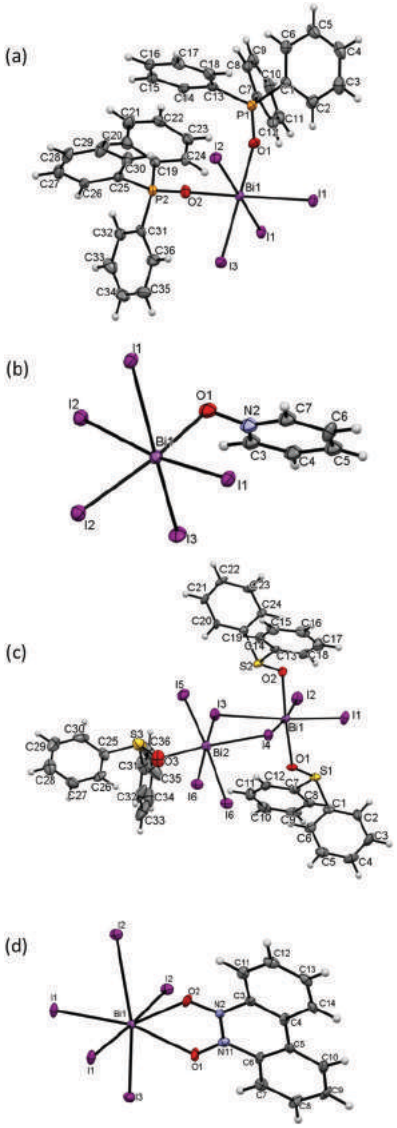

Fig. 1 Molecular geometry observed in the crystal structures of $[BiI_3\{(C_6H_5)_3PO\}_2]_2$ (a), $[BiI_3(C_5H_5NO)]_n$ (b), $[BiI_3\{(C_6H_5)_2SO\}_{1.5}]_4$ (c) and $[BiI_3(C_{12}H_8N_2O_2)]_n$ (d), showing the atom labeling scheme. Here, asymmetric units are shown, completed by the symmetry equivalent atoms to present the bismuth coordination sphere. Displacement ellipsoids of non-hydrogen atoms are drawn at the 50% probability level. H atoms are presented as small spheres with an arbitrary radius.

cations bridged by two iodide ions. In the case of $[BiI_3\{(C_6H_5)_2SO\}_{1.5}]_4$, the motif is more complicated due to two non-equivalent bismuth coordination schemes. In the Bi1 coordination sphere, there are 4 iodide anions in the equatorial position of the distorted octahedron with 2 oxygen atoms occupying axial positions, while B2 is surrounded by 5 iodides and only one oxygen atom. Thus, the isolated motif consists of four bismuth cations, bridged by iodide ions, forming three 4-member rings fused at the bismuth position. The angle between the mean planes defined for these rings is 81.90(1)°. Additionally, the motifs are linked by centrosymmetric I1···I1 interactions (distance 3.75(1) Å), forming waving chains propagating parallel to the [001] direction. In contrast to the abovementioned structures, the coordination spheres of bismuth in $[BiI_3(C_5H_5NO)]_n$ and $[BiI_3(C_{12}H_8N_2O_2)]_n$ form only chain motifs, propagating parallel to the [100] axis along the crystal. The angles between the mean planes defined for similarly linked 4-member rings are 88.51(1) and 80.36(1)° for $[BiI_3(C_5H_5NO)]_n$ and $[BiI_3(C_{12}H_8N_2O_2)]_n$, respectively. In the octahedral coordination of the central ion, the Bi–O distances vary between 2.31(1) and 2.47(1) Å. In $[BiI_3(C_{12}H_8N_2O_2)]_n$ the chelating character of the organic ligand results in longer Bi–O distances, being 2.54(1) Å and 2.88(1) Å for O1 and O2, respectively. The Bi–I distances differ, depending on the bridging or free character of the considered anion. Ions which act as the bridging agents are distanced from bismuth more (in the range 2.89(1)–3.23(1) Å; mean value 3.19(1) Å) than the free iodide ligands, for which the distance varies in a smaller range of 2.86(1)–2.95(1) Å.

The main interactions in the presented structures are related to the coordination of Bi. Additional forces stabilizing the crystals are C–H···I contacts (H···I distance approx. 3.2 Å), which are observed in structures $[BiI_3\{(C_6H_5)_3PO\}_2]_2$, $[BiI_3(C_5H_5NO)]_n$, and $[BiI_3(C_{12}H_8N_2O_2)]_n$. In the case of $[BiI_3\{(C_6H_5)_2SO\}_{1.5}]_4$, such an interaction is not observed due to the abovementioned I···I chaining contacts.

Interactions that may be responsible for the electronic properties of the described materials are based on short contacts between aromatic moieties. Only in $[BiI_3(C_{12}H_8N_2O_2)]$ crystals are the classical π···π interactions observed (distance between the closest atoms 3.4 Å), formed by well-overlapping aromatic systems of two molecules related *via* the center of symmetry. This dimer is arranged in a parallel fashion with respect to the aromatic ring of the translated molecule. However, in the last-mentioned contact, the edges of the aromatic rings slightly overlap (shortest distances 3.40 Å and 3.45 Å for C9···C13 and C10···C14, respectively). Contacts between aromatic rings are also observed in the $[BiI_3\{(C_6H_5)_2SO\}_{1.5}]_4$ crystal. The shortest distances and the level of overlap do not imply the π···π interaction directly. However, the aromatic rings C1–C6 and C25–C30 are relatively close (approx. 3.6 Å) and surrounded by sequential C19–C24 rings arranged parallel to the aromatic moieties mentioned earlier. Interesting contacts between pyridine *N*-oxide rings are observed in the crystal structure of $[BiI_3(C_5H_5NO)]_n$. In this case, centrosymmetric dimers are formed with O1···C3 interactions (distance 3.19(1) Å), followed by small edge overlapping of the parallel ring of the translated dimer (the shortest C···C distance 3.65(1) Å). Only in the crystal structure of $[BiI_3\{(C_6H_5)_3PO\}_2]_2$ were the π···π interactions/contacts not observed. There are several stabilizing C–H···π interactions instead, which were also observed in the $[BiI_3\{(C_6H_5)_2SO\}_{1.5}]_4$ structure. The packing projections, as well as the interaction/contact motifs between aromatic moieties, are shown in the ESI† file (Fig. S1–S7).

UV-vis absorption spectra

The absorption spectra (and zoom at the absorption band edges) of the studied complexes and BiI_3 are presented in Fig. 2. Bismuth(III) iodide has a broad absorption spectrum with the absorption onset at *ca.* 750 nm. In the case of each complex, the absorption band edge shifts towards shorter wavelengths, which is tightly associated with the disruption of the strongly bonded BiI_3 layers. The coordination of bulky triphenylphosphine oxide ligands in $[BiI_3\{(C_6H_5)_3PO\}_2]_2$ results in the presence of the dimer of BiI_4L_2 octahedra in the structure. Among the four complexes, it is the strongest disruption of the 2D structure of BiI_3. Furthermore, this is the complex with the smallest number of iodine atoms around the Bi atom; therefore, the blue shift (up to 550 nm) of the absorption onset is the most distinct. Intermediate positions of optical absorption onsets are observed for $[BiI_3\{(C_6H_5)_2SO\}_{1.5}]_4$, $[BiI_3(C_{12}H_8N_2O_2)]_n$ and $[BiI_3(C_5H_5NO)]_n$, in which chain-like 1D structures are formed by coordinated

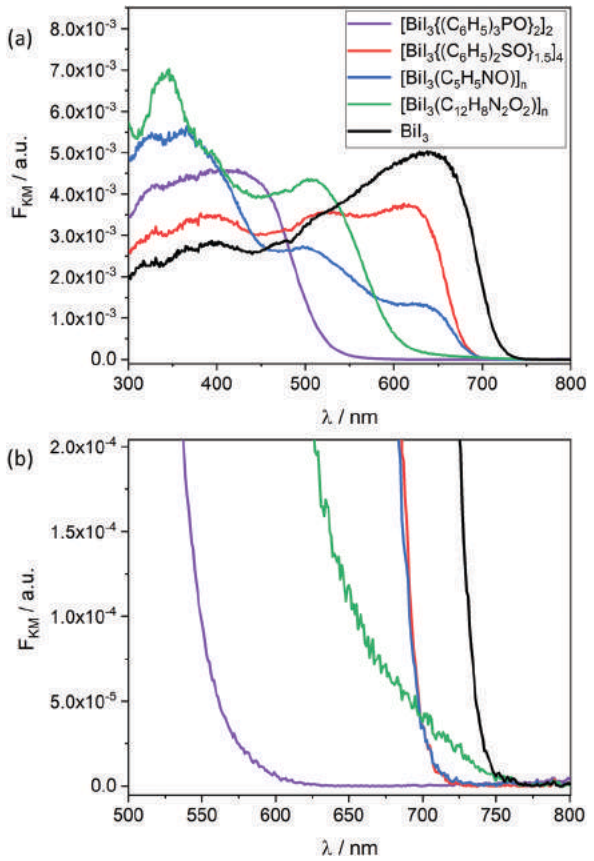

Fig. 2 Solid-state electronic spectra of the four studied complexes and BiI_3 (a) and magnification of the absorption edges of those compounds (b).

bismuth(III) atoms. The spectrum of the $[BiI_3(C_{12}H_8N_2O_2)]_n$ complex significantly differs from the others presented in Fig. 2. It has a strong absorption band with a maximum of 520 nm but also small absorption bands in the range 650–750 nm (Fig. 2b). This band is related to the stacking of benzo(*c*)cinnoline conjugated rings – in the rest of the compounds, the bismuth(III) iodide chains are the only long-range arrangements present in the structure.

Diffuse reflectance spectroscopy and Tauc plots were used to determine the optical band gap of the studied compounds. By plotting $(F_{KM}*h\nu)^n$ *vs.* $h\nu$ one can estimate the optical energy gap value of indirect (n = 1/2) or direct (n = 2) transitions. For organic compounds in which there is a lack of strong intermolecular interactions, the n factor is usually equal to unity.[58] The studied BiI_3 sample has an indirect optical band gap of 1.68 eV (Fig. S8, see the ESI†), which is consistent with the literature value of 1.67 eV for a single crystal.[59] The nature of the optical transition in the four complexes is not so obvious. Therefore the three most common possibilities of the n factor in a Tauc plot were explored (Fig. S9–S11, see the ESI†).

Due to the lack of any strong intermolecular interactions in the crystal structure of $[BiI_3\{(C_6H_5)_3PO\}_2]_2$, n = 1 seems to be the most reasonable choice, which leads to a value of 2.37 eV. For complexes $[BiI_3\{(C_6H_5)_2SO\}_{1.5}]_4$, $[BiI_3(C_{12}H_8N_2O_2)]_n$ and $[BiI_3(C_5H_5NO)]_n$, one can take into consideration the types of band gaps obtained with DFT calculations. Assuming that $[BiI_3\{(C_6H_5)_2SO\}_{1.5}]_4$ has a direct bandgap, the value would be 1.86 eV, while $[BiI_3(C_{12}H_8N_2O_2)]_n$ and $[BiI_3(C_5H_5NO)]_n$ have indirect band gaps of values 1.56 eV and 1.75 eV respectively. The values of experimentally obtained band gaps and their theoretical predictions are summarized in Table S2 in the ESI.†

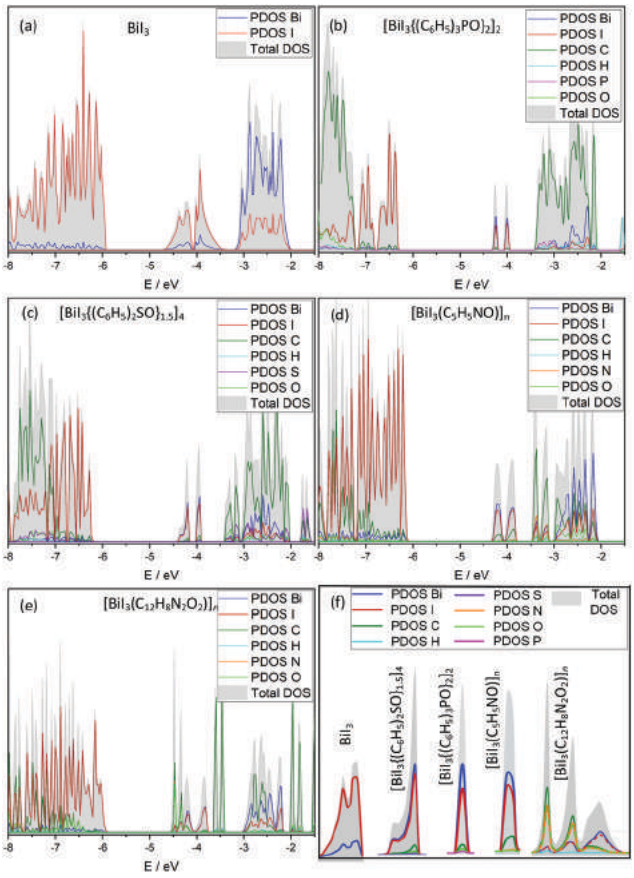

Fig. 3 Density of state distributions of BiI_3 (a), $[BiI_3\{(C_6H_5)_3PO\}_2]_2$ (b), $[BiI_3\{(C_6H_5)_2SO\}_{1.5}]_4$ (c), $[BiI_3(C_5H_5NO)]_n$ (d) and $[BiI_3(C_{12}H_8N_2O_2)]_n$ (e). The magnified conduction bands of the studied compounds (f).

The density of states (DOS)

The DOS distributions of the four studied complexes and BiI_3 are presented in Fig. 3. The main similarity between BiI_3 and the studied complexes is the dominance of iodine atom orbitals in the composition of the valence band of all five compounds, as can be observed in the partial DOS distributions. The width of the valence band is the smallest in the case of the $[BiI_3\{(C_6H_5)_3PO\}_2]_2$ complex, which is consistent with the most drastic disruption of the 2D structure of BiI_6 octahedra. The decreased width observed in the case of the other complexes can also be attributed to the partial disruption of the polymeric structure of bismuth iodide. This process is associated with a gradual change in the composition of the conduction band in the series BiI_3, $[BiI_3\{(C_6H_5)_3PO\}_2]_2$, $[BiI_3\{(C_6H_5)_2SO\}_{1.5}]_4$, $[BiI_3(C_5H_5NO)]_n$ and $[BiI_3(C_{12}H_8N_2O_2)]_n$.

The conduction band of bismuth iodide (at least its low energy fragment) is composed mainly of iodine orbitals with only a small contribution of bismuth orbitals (which are also present in the valence band). Such a situation indicates a significant covalent character of the bismuth–iodine bond. The three complexes with monodentate ligands present an increased contribution of bismuth orbitals in the lower part of the conduction band and also a significantly growing contribution of electronic orbitals belonging to organic ligands. This contribution is quite small in the case of $[BiI_3\{(C_6H_5)_3PO\}_2]_2$ and $[BiI_3\{(C_6H_5)_2SO\}_{1.5}]_4$, which correlates with the lack of any strong interactions in the crystal structure that involve the aromatic rings of the ligands. This contribution is slightly increased in the case of the $[BiI_3(C_5H_5NO)]_n$ complex and originates from the short distance interaction between pyridine *N*-oxide ligands in two adjacent polymeric chains (*cf.* Fig. 1b). The bidentate complex $[BiI_3(C_{12}H_8N_2O_2)]_n$ presents an entirely different composition of the conduction band. In this case, the dominating contribution of orbitals from organic ligands is justified by strong intermolecular interactions of extended aromatic moieties in neighboring chains within the $[BiI_3(C_{12}H_8N_2O_2)]_n$ crystal lattice.

Surface photovoltage (SPV) measurements

SPV spectra are useful for determining the nature of majority charge carriers in semiconducting materials. This method is based on the change of the surface and near-surface potential distribution under illumination. Under illumination, the minority charge carriers travel to the surface, which results in the flattening of the band bending. The bands bend upwards in the n-type semiconductor (due to the formation of a near-surface depletion layer) and downwards in the p-type semiconductor (due to the presence of the accumulation layer). In general:

$$e\Delta CPD = -e\Delta SPV$$

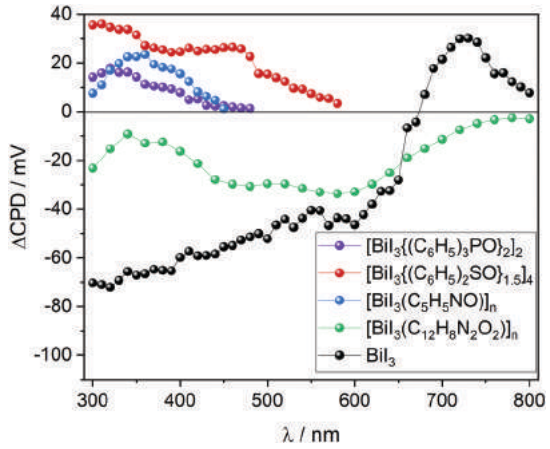

Fig. 4 Differential surface photovoltage spectra of BiI_3 and its complexes.

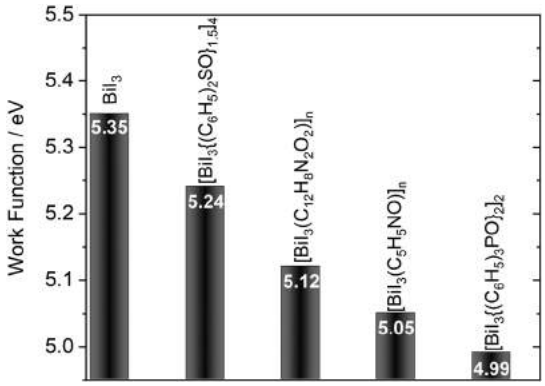

Fig. 5 Work function values of BiI_3 and BiI_3 complexes measured in ambient conditions.

where e is the electric charge, SPV is the surface photovoltage, and ΔCPD is the contact potential difference.[60] The studied bismuth complexes might be p-type or n-type semiconductors if the crystal structure would allow an excess of intercalated iodine atoms or the presence of iodine vacancies, respectively. Fig. 4 presents the SPV spectra of BiI_3 and the studied complexes. Bismuth triiodide is an n-type semiconductor due to the tendency to lose iodine, so ΔCPD is negative in most of its absorption range.[61,62] The positive ΔCPD below 650 nm is related to additional surface states induced most probably by the OH groups present at the surface. The $[BiI_3(C_{12}H_8N_2O_2)]_n$ complex also exhibits the tendency to lose some of the iodine atoms. In this complex, a chelating ligand enforces a coordination number of seven, which is higher than usually found in bismuth complexes. We speculate that this kind of coordination geometry might have a tendency to lose one iodine atom to form a more relaxed octahedral coordination site. Complexes $[BiI_3\{(C_6H_5)_3PO\}]_2$, $[BiI_3\{(C_6H_5)_2SO\}_{1.5}]_4$ and $[BiI_3(C_5H_5NO)]_n$ have typical octahedral coordination geometry around the Bi atom, and their p-type conductivity might be associated with iodine intercalation.

Work function measurements

The reduction of the work function values after coordination of electron-donating ligands to BiI_3 is presented in Fig. 5. The work function values of all five compounds are in the 5.35–4.99 eV range. The literature work function value of polycrystalline Au and Cu surfaces under a vacuum is 5.2 and 4.6 eV, respectively.[63] The work function of the metal surface is extremely sensitive to the conditions in which the metal is measured (vacuum or ambient, humidity level, presence of absorbable gases) as well as the surface type (crystallographic orientation) and its roughness.[64–70] The decreasing values of the work function reflect the increasing electron donor properties of the applied ligands.

The largest change is observed in the case of triphenylphosphine oxide, which is a ligand that induces a significant decrease of the Racah B parameter, *i.e.*, the formation of a coordination bond between a metal ion and a ligand results in electron cloud expansion and reduction of electron–electron repulsion. This effect is usually attributed to the partial covalent metal–ligand bond character.[71] While on the basis of sole work function measurements the nephelauxetic effects cannot be unambiguously elucidated, the partial density of state distributions corroborate this analysis – a significant increase of the contribution of ligand orbitals to the valence and conduction band indicates covalent character of the metal–ligand interaction, which is associated with an increase in electron density at metal centers and, consequently, a decreased work function.

Current–voltage (I–V) characteristics

The conductivity type verified with SPV measurements is crucial in the construction of Schottky junction-based devices,[72,73] including memristors – a two-terminal component whose resistance depends on the current that is passed through the device.[25,74,75] Usually, there are two distinct states of the device: high and low resistive states (labeled HRS and LRS, respectively), but multistate memristive devices are also known.[76] Memristive devices usually consist of two metallic contacts and layers of a compound (a metal oxide, chalcogenide, metal iodide perovskite, polymer, or another medium in which ions can travel). Depending on the compound and electrode material, different mechanisms are responsible for the performance of the memristive device and the shape of its fingerprint: the pinched hysteresis loop always crossing the origin of the voltage–current plane when driven by any periodic input (voltage or current) with zero DC component.[24,75] In most cases, memristors (or more generally memristive elements) consist of a layer of active material sandwiched between two identical contacts. However, in order to observe the role of interfacial processes, an asymmetrical arrangement with one metallic and one indium-tin oxide-based contact has been used. Moreover, the metallic contact has been neither sputtered nor evaporated in order to leave the surface of the semiconductor layer undisturbed. On the contrary, the semiconductor layer has been spin-coated on FTO glass, and the metallic contact has been tightly pressed (with controlled force) against the thin layer. The same setup was found to be very successful in recent studies on other lead- and bismuth-based semiconductors.[21,77] Typical hysteresis curves are observed in all studied cases.

Moreover, devices based on n-type materials exhibit rectifying character of the junction, however with a low on/off current ratio. Thus, the device can be approximated with a Schottky diode and a low resistance resistor (or memristor) in parallel, as discussed previously.[21,77]

The presented devices are analog memristive devices based on BiI_3 or $[BiI_3L]$ complexes, a metal electrode (Au or Cu), and an FTO second electrode.[30] The performance of these devices relies on the surface interaction between the metal and semiconductor surfaces. A Schottky barrier forms at the metal/semiconductor interface and the height of this barrier depends on the charge collected at the interface. This resultant charge has three main components:

(i) Surface states resulting solely from the character of the semiconductor, *i.e.*, n-type (p-type) semiconductors, tend to cumulate negative (positive) charge on the surface and have upward (downward) band bending. It is a result of the presence of surface states that originate from crystal imperfections, surface adsorbates, dangling bonds, and electron delocalization at the interface.

(ii) Metal induced gap states (MIGS) arising from abrupt termination of metal and semiconductor lattices (which renders some of the forbidden states allowed), followed by electron flow between the metal and semiconductor in order to equilibrate the Fermi levels of both materials. The sign of the cumulated charge of MIGS depends on the work function of the metal ϕ_M and semiconductor ϕ_S. Electron density can shift toward the semiconductor if $\phi_M < \phi_S$, which results in downward band bending and positive interface charge. By analogy, when $\phi_M > \phi_S$ the bands bend upwards due to negative interface charge. Most likely MIGS add a small positive charge to the surface because the work functions of the five compounds are quite high (5.35–4.99 eV) in relation to the literature value of ϕ_{Cu} and ϕ_{Au}, especially due to the tendency of the metal to reduce its work function in the presence of humidity or surface roughness – which is the case of the presented metal electrodes (see the Methods section).

Finally, (iii) states that are a result of the formation of chemical bonds between the metal and the semiconductor also lead to a charge carrier shift at the interface. As a result, the copper/complex interfaces gain additional negative charge due to the formation of I–Cu bonds.

It is extremely difficult to measure the individual contributions of the three components, but the overall outcome is easy to assess by measurement of the *I–V* characteristics. In the case of a negatively charged interface, a neutral or negative bias (*i.e.*, the junction polarized in the reverse direction, Fig. 6a) results in charge accumulation in traps, which increases the height of the Schottky barrier, resulting in a high resistivity state. When a forward (positive) bias is applied, the traps are gradually emptied, which at some point leads to abrupt shrinkage of the barrier and switching to the low resistivity state (Fig. 6b). If the surface state has a donor-like character, and the surface is charged positively (Fig. 6c), then the application of a positive bias increases the barrier height and leads to a more positive surface charge (Fig. 6d).

Moreover, the memory effect can be only observed if the rate of the depopulation of the trap states is higher than the reverse

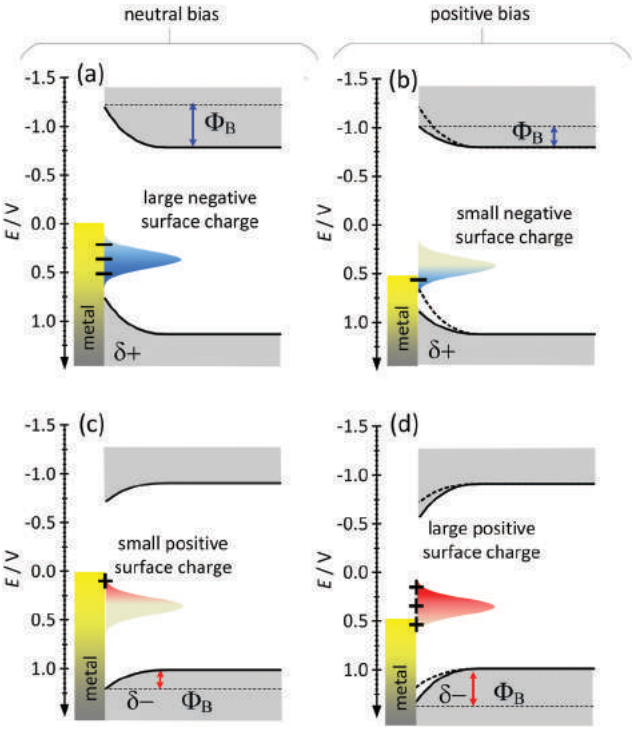

Fig. 6 The diagrams present: negative interface charge upon neutral (a) or positive (b) bias; and positive interface charge upon neutral (c) or positive (d) bias applied to the metal electrode.

process (in other words, the activation energy for discharging the trap states is lower than the activation energy of charge trapping at reverse bias), therefore along with weak rectification a pinched hysteresis loop is observed. As already reported, such processes can be a source of memristive behavior in organic[78] and coordination compounds,[21,79] and inorganic[80–82] materials.

Fig. 7 presents the current–voltage characteristics of $[BiI_3(C_{12}H_8N_2O_2)]_n$ and $[BiI_3\{(C_6H_5)_2SO\}_{1.5}]_4$ (for *I–V* characteristics of all five studied compounds see Fig. S13 in the ESI†). The blue curve represents *I–V* of the device that is negatively charged at the interface (Fig. 7a, c and d), while the red represents a positive interface charge (Fig. 7b).

Irrespective of the sign of the charge accumulated at the interface, all devices exhibit bipolar switching. The insets present the most likely contributions of the three components.

Fig. 7a and c present devices with the Au metal electrode. With the lack of interfacial chemical bonding (iii) at the metal/semiconductor interface, the dominant factor in the overall interface charge is the presence of the surface states that originate from the semiconductor itself (i), *i.e.*, negative charge for n-type $[BiI_3(C_{12}H_8N_2O_2)]_n$ and positive charge for p-type $[BiI_3\{(C_6H_5)_2SO\}_{1.5}]_4$.

When the second electrode is made of a metal with a more reactive metal electrode (*i.e.*, Cu, Fig. 7b and d), the situation is different. The results clearly show that all examined devices in contact with copper have a negative interface charge and the same direction of changes in the current–voltage characteristics (Fig. S13, ESI†). The fact that the p-type semiconductor in the

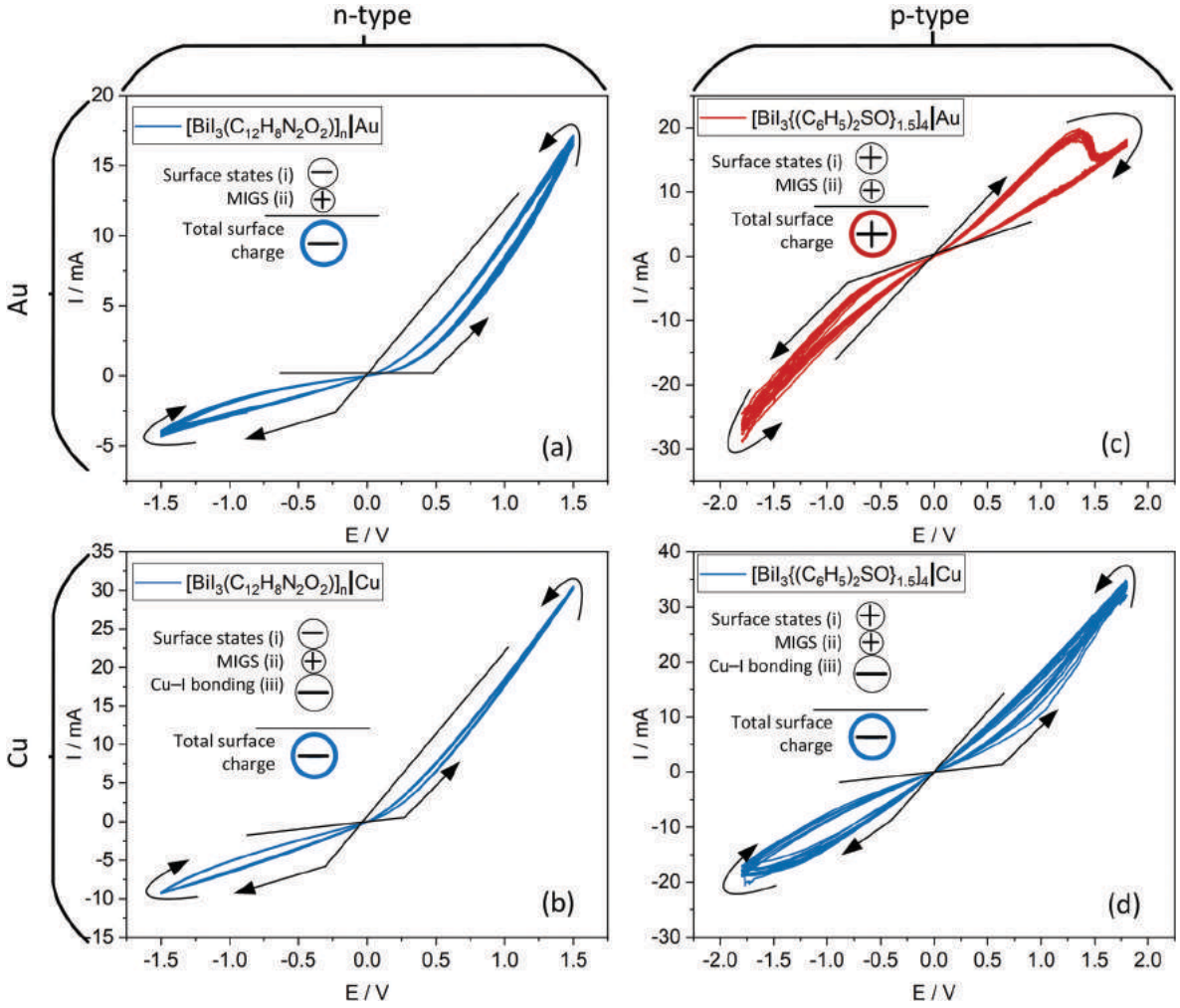

Fig. 7 Current–voltage characteristics of $[BiI_3(C_{12}H_8N_2O_2)]_n$ memristors measured with Au (a) and Cu (b) as the second electrode and $[BiI_3\{(C_6H_5)_2SO\}_{1.5}]_4$ memristors measured with Au (c) and Cu (d) as the second electrode. Ten scans with a 100 mV s^{-1} rate.

presence of positively charged MIGS (ii) and positively charged surface states (i) is charged negatively at the interface with a metal of small ϕ means that a surface reaction took place, and copper atoms attracted iodide anions closer to the surface forming negative charge (iii). It is a dominant factor that contributes to the interface charge of the $[BiI_3L]$/Cu junction. Therefore, by the change of only the metal electrode from Au to Cu, the direction of the hysteresis loop propagation changes from clockwise into anticlockwise.

The weak interaction between the metal electrode and the semiconductor layer allows observation of these subtle effects. Sputtered or evaporated electrodes provide much stronger interaction between the metal and semiconductor and are usually involved in the formation of conductive filaments within the active layer. These effects dominate the more subtle charge trapping processes involving MIGS and other interfacial states. In the case of filament formation, the metal-dependent switching characteristics (Fig. 7c and d) could not be observed. Filamentary processes involving different metals should only affect the ON/OFF ratio and the rate of switching, but not the symmetry of the hysteresis loop. The mechanical contacts presented here offer an additional possibility of subtle control of Schottky barrier properties with the interface devoid of any defects which can be formed under harsh sputtering conditions. The devices presented here can be regarded as analog memristive devices – their ON/OFF ratio is low, but they show significantly nonlinear characteristics. Therefore, while not very useful for memory application, they should demonstrate their utility in neuromorphic and signal processing devices, as postulated by Chen *et al.*[30] Other materials with similar electrical properties were successfully applied in reservoir computing systems.[77,79]

Chronoamperometric measurements

The analysis of the current–voltage characteristics presented in Fig. 7 and Fig. S13 (ESI†) allows determining the potential windows in which the state of the devices can be read. In the case of the memristor based on the $[BiI_3\{(C_6H_5)_2SO\}_{1.5}]_4$/Au interface, the state of the device should be read in the −0.5 to 1 V range. Fig. 9 presents two series of chronoamperometric

measurements in which the switching behavior of the memristor was tested. In both series, the set impulses (which induce the change from the HRS to the LRS) have an amplitude of −2.5 V and a duration of 0.25 s, and the reset impulses (which induce the change from the LRS to the HRS) have an amplitude of 2.5 V and duration of 0.5 s. The series have different read potentials: Fig. 8a–c present the data in which the state of the memristor was checked at 0.3 V, while Fig. 8d–f show the data acquired with a read potential of −0.3 V. In each series the state of the device was changed from the HRS to the LRS and from the LRS to the HRS about 1000 times to test the endurance of the device. In both series, the points representing the HRS have the lower interquartile range (IQR). In general, the points acquired with a read potential of −0.3 V are more dispersed and seem to drift slightly towards smaller currents, but the HR states are still well separated from the LR states. The LRS/HRS ratios are 1.28 and 1.17 for measurements performed with 0.3 V and −0.3 V, respectively. These values are rather modest, especially when compared with sulphide or oxide-based memristors, which the switching mechanism is usually based on the formation of conductive filaments;[83] however, the devices presented in this work were not optimized for the best performance or On/Off ratio but rather to get reliable qualitative results. Among devices based on metal-halide organic perovskites higher ratios (∼10) have been observed, even in memristors with an interface-type resistive switching mechanism.[48,84] Interestingly, in the devices built with organic metal-halide perovskites various types of the resistive switching source were proved. The reported memristors differ in the compound layer type and thickness, type of metal contact, surface area, and thin-film preparation methods, and as a result both filamentary and interfacial mechanisms were observed.[23] The memristive devices presented in this work do not show any typical indicators of filament formation and seem to be governed by the modulation of the Schottky barrier hight. This type of switching in general ensures better cycle-to-cycle uniformity (see Fig. 7) than that based on creation and rupture of CFs. This results in small current variance within each resistance state and allows one to easily distinguish the HRS and LRS, even with the measured HRS/LRS ratios. The persistence of the states was also tested. Both the HRS and LRS last for at least 1 h when the read potential (0.3 or −0.3 V) is applied. The stability measurements are presented in Fig. S14 (see the ESI†). The collected data highlight the durability and versatility of the $[BiI_3\{(C_6H_5)_2SO\}_{1.5}]_4$/Au memristor. The possibility to operate the memristor in both positive and negative read potential ranges might be significant when a crossbar architecture is applied or during integration with other elements.

Synaptic-like behavior

Due to the ability to mimic some of the functions of biological neurons, memristors are often investigated in terms of artificial synapses. The communication between neurons relies on the modulation of the conductance of the synapse – the connection between two neural cells. The phenomenon of adjustment of the strength of this connection is called synaptic plasticity and is considered to be responsible for learning and memory processes in the brain.

Spike-timing dependent plasticity is a form of Hebbian learning in which the change and direction of the synaptic weight are dependent both on the order and temporal interval

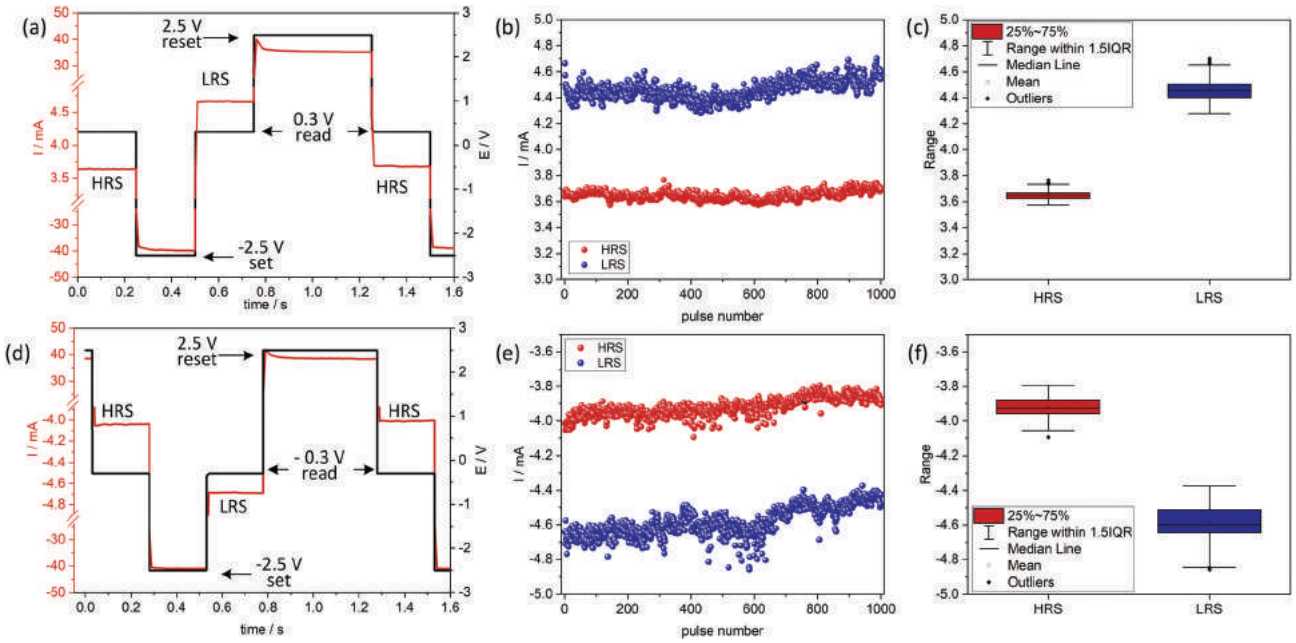

Fig. 8 Chronoamperometric measurements performed on the $[BiI_3\{(C_6H_5)_2SO\}_{1.5}]_4$/Au device. Voltage pattern (black line) used to test the switching behavior of the memristor and the corresponding current response (red line) (read potential of 0.3 V (a), read potential of −0.3 V (d)), endurance test of the resistive switching (1000 cycles) (read potential of 0.3 V (b), read potential of −0.3 V (e)), and boxplots depicting the stability of the resistive switching (read potential of 0.3 V (c), read potential of −0.3 V (f)).

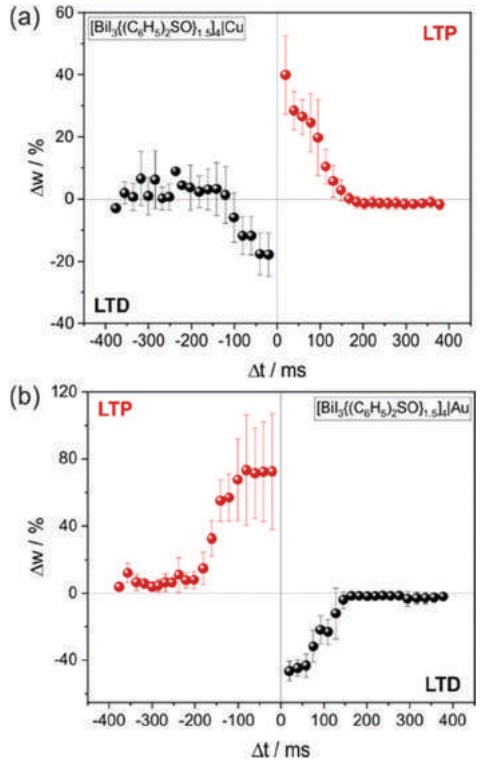

Fig. 9 STDP of $[BiI_3\{(C_6H_5)_2SO\}_{1.5}]_4$. Hebbian learning rule obtained with the Cu electrode (a). Anti-Hebbian learning rule obtained with the Au electrode (b).

between the pre- and the postsynaptic spike.[85] According to the canonical asymmetric Hebbian learning rule, as the time interval between pre-synaptic and post-synaptic decreases, the synapse exhibits long-term potentiation (LTP). Inversely, when the post-synaptic spike precedes the pre-synaptic one, the conductance of the synaptic connection decreases, resulting in long-term depression (LTD).[86] The magnitude of the resulting synaptic weight changes is governed by the time intervals between the pre- and post-synaptic spikes. This learning rule is frequently summarized as "neurons that fire together, wire together," which, on the other hand, cannot be understood literally.[87] In memristors, the synaptic plasticity is realized through gradual resistive switching between the HRS and LRS as a response to trains of pulses with variable time intervals.[88,89]

The STDP with Hebbian learning is presented in Fig. 9a for $[BiI_3\{(C_6H_5)_2SO\}_{1.5}]_4$ with the Cu electrode. The pre-synaptic spike preceding the post-synaptic spike ($\Delta t > 0$) leads to LTP, whereas when the post-synaptic spike arrives before the pre-synaptic spike ($\Delta t < 0$) LTD is observed. Interestingly, with the same voltage pattern applied to $[BiI_3\{(C_6H_5)_2SO\}_{1.5}]_4$ with the Au electrode, we have obtained anti-Hebbian learning with roughly the same temporal windows for LTP and LTD (Fig. 9b). This effect coincides with the reversal of the pinched hysteresis loop on the change of the metallic contact from Cu to Au. The STDP in memristive materials depends on many parameters, such as the amplitude, shape,[20,90] number, and frequency of spikes[89] and pre-treatment of the sample.[21] In the case of the presented materials, the inversion of the STDP symmetry is induced by the same mechanisms that govern the changes in the *I–V* loop direction. Therefore, in addition to the already known mechanisms, modulation of synaptic plasticity can be achieved by changing the electrode material as well (Fig. S15 and S16, ESI†). Therefore, the presented system shows unprecedented flexibility, leading to a variation of the hysteresis loop shape as well as of the learning scheme (Hebbian *vs.* anti-Hebbian) within the same material. This learning rule variability can be utilized in the remote supervised method (ReSuMe) and implemented on a memristor array for supervised learning application in Spiking Neural Networks (SNNs).[91] ReSuMe relies on balancing two opposite (Hebbian and anit-Hebbian) learning rules between remote "teacher" and "student" neurons and the resulting synaptic efficacy is dependent on the correlation of their activities. This method has already proven to be a highly successful supervised SNN algorithm, as the memristor array-based SNNs trained with this method have achieved ~96% accuracy in handwritten digit recognition, approaching the limit of human capabilities.[56]

Conclusions

New bismuth complexes with bulky organic ligands show pronounced semiconducting properties. The band structure of these materials, along with optical spectroscopy and work function measurements, indicated the importance of metal–ligand and intraligand interactions in the electronic properties of bulk materials. They have relatively low bandgap energies ranging from 1.6 to 2.4 eV and electrical conductivity high enough to sustain an electric current in the milliampere range. Thin layer devices with metallic (Cu and Au) and FTO contacts show analog memristive switching. The dependence of the switching characteristics on the nature of the metal contact and conductivity type allows elucidation of the switching mechanism as modulation of Schottky barrier parameters associated with trapping of electrons at the interface states. These phenomena can be observed in the case of unperturbed interfaces, therefore sputtering or evaporation of metallic contacts is avoided. Mechanical pressing seems a less viable methodology, but in this way one can avoid partial decomposition of soft materials.

The differences in the electronic and crystal structures in the series of complexes led to different semiconducting properties (*e.g.*, n and p-type conductivity). As a result, different interface charging and different types of *I–V* hysteresis patterns are observed. What is interesting is that both clockwise and anti-clockwise *I–V* curves can be observed in devices based on the same compound, but in contact with different metals. The opposing behavior of the complex/Au and complex/Cu junctions may be a result of the higher reactivity of copper, which leads to the formation of Cu···I bonds at the metal/complex interface.

The different *I–V* characteristics result in Hebbian and anti-Hebbian learning rules obtained for the same compound in contact with two different metals – such an effect has never been described before. This dualistic behavior should

be observed in devices based on other representatives of the metal halide family if other processes like conductive filament formation or ionic movement will not interfere.

The interfacial phenomena reported here open a pathway towards the design of information processing devices based on interfacial processes and charge trapping dynamics. Elucidation of the mechanistic details governing the nonlinearity of the electrical characteristics and memristive switching allows the design of devices with desired characteristics. While the technology of fabrication is not matured, further exploration of memristive materials susceptible to interfacial control of resistivity may contribute to new electronic devices with prospective applications in *in-materio* computing.

Experimental section

Caution! These syntheses are potentially hazardous due to the toxic, irritating, and lachrymatory properties of iodine. Appropriate means of personal protection should be applied. All waste should be properly disposed of due to high toxicity toward aquatic organisms.

Material synthesis

Benzo(*c*)cinnoline *N*,*N*′-dioxide synthesis was performed according to ref. 92 Commercially available BiI_3, triphenylphosphine oxide, diphenyl sulphoxide, pyridine *N*-oxide (Sigma Aldrich), methanol, toluene, and acetonitrile (Avantor) were used without prior purification. The methanol used during the syntheses has up to 0.01% of water.

$[BiI_3\{(C_6H_5)_3PO\}_2]_2$. Triphenylphosphine oxide (2.2 mmol) was dissolved in 15 ml of methanol and added dropwise to bismuth triiodide (1 mmol) dissolved in methanol (100 ml) under reflux. The solution was filtered and condensed to about 1/3 of the volume. Light orange, cubic crystals precipitated from the solution (yield 45%). Elemental analysis: C, 38.14%, H, 2.53%.

$[BiI_3\{(C_6H_5)_2SO\}_{1.5}]_4$. Diphenyl sulphoxide (3 mmol) was dissolved in 15 ml of methanol and added dropwise to bismuth triiodide (1 mmol) dissolved in methanol (100 ml) under reflux. The solution was filtered and condensed to about 1/3 of the volume. The crystals precipitated from the solution were fine and orange (yield 25%). Elemental analysis: C, 25.08%; H, 1.71%, S, 5.50%.

$[BiI_3(C_5H_5NO)]_n$. Pyridine *N*-oxide (2.2 mmol) was dissolved in 15 ml of methanol and added dropwise to bismuth triiodide (1 mmol) dissolved in methanol (100 ml) under reflux. An orange, fine solid precipitated immediately. The product was recrystallized from a mixture of toluene and acetonitrile (10 : 1 v/v) (yield 52%). Elemental analysis: C, 10.55%, H, 0.93%, N, 2.27%.

$[BiI_3(C_{12}H_8N_2O_2)]_n$. Benzo(*c*)cinnoline *N*,*N*-dioxide (1.05 mmol) was dissolved in 15 ml of methanol and added dropwise to bismuth triiodide (1 mmol) dissolved in methanol (100 ml) under reflux. The solution was filtered and methanol was evaporated. A dark red solid was recrystallized from toluene: methanol mixture (3 : 1 v/v). The final product has a form of red-orange crystals (yield 25%). Elemental analysis: C, 18.48%, H, 1.05%, N: 3.54%.

Crystal structure determination

X-ray diffraction data for single crystals of the presented compounds were collected at 130(2) K, using a SuperNova (Rigaku – Oxford Diffraction) four circle diffractometer with a mirror monochromator and a microfocus MoKα radiation source (λ = 0.71073 Å). The obtained data sets were processed with CrysAlisPro.[93] The phase problem was solved with SIR2004[94] or SUPERFLIP[95] software. The parameters of the obtained models were refined by full-matrix least-squares on F^2 using SHELXL-2014/6.[96] All non-hydrogen atoms were refined anisotropically. Hydrogen atoms were positioned at the idealized geometry and refined using the riding model with the isotropic displacement parameter $U_{iso}[H] = 1.2U_{eq}[C]$. Crystal/experimental data and structure refinement results are shown in Table S1 in the ESI.† Calculations were performed using the WinGX integrated system (ver. 2014.1).[97] Figures were prepared with Mercury 4.0.[98]

Crystallographic data have been deposited with the Cambridge Crystallographic Data Centre as supplementary publication no.: CCDC 1941007 $[BiI_3\{(C_6H_5)_3PO\}_2]_2$, 1941005 $[BiI_3C_5H_5NO]_n$, 1941008 $[BiI_3\{(C_6H_5)_2SO\}_{1.5}]_4$ and 1941006 $[BiI_3(C_{12}H_8N_2O_2)]_n$.†

UV-vis spectroscopy

Diffuse reflectance spectra were recorded on a Lambda 750 (PerkinElmer, USA) spectrophotometer in a spectrally pure $BaSO_4$ matrix. The same material was used as a reference sample.

Computational details

All calculations were performed using density functional theory with the generalized gradient approximation (GGA) of the Perdew–Burke–Ernzerhof (PBE) exchange–correlation functional and dispersion correction proposed by Grimme,[99] with Becke and Johnson damping (PBE-D3(BJ)) and scalar relativistic corrections within the Zero Order Regular Approximation (ZORA)[100] implemented in the BAND2018 SCM package.[101–104] Basis functions of valence triple zeta quality with two polarization functions (TZ2P) were adopted with a medium frozen core. The geometry optimization of the atomic positions was carried out with fixed experimental lattice parameters. The *k*-point mesh over the first Brillouin zone was sampled according to the Wiesenekker–Baerends scheme.[105]

Kelvin probe measurements

Surface photovoltage (SPV) measurements were performed using a Kelvin probe-based surface photovoltage spectrometer (Instytut Fotonowy, Poland, and Besocke Delta Phi, Germany) equipped with a 150 W xenon arc lamp and a monochromator. The measured compounds were deposited on the ITO surface by the drop-casting method. The work function measurements were performed under ambient conditions.

Device fabrication and electrical measurements

The compounds were dissolved in dimethylformamide (except $[BiI_3\{(C_6H_5)_3PO\}_2]_2$, which was dissolved in methanol) and spin-coated on the surface of an FTO/glass substrate. A solid polished (with an aqueous suspension of Al_2O_3) piece of gold or copper metal was pressed against the BiI_3 or $[BiI_3L_n]$ complex layer. The electrical measurements were conducted in a two-electrode setup with working and counter electrodes connected to the metal and FTO electrodes, respectively. Current–voltage characteristics and chronoamperometric measurements were recorded on a Biologic SP-150 potentiostat. Devices were prepared and measured under an ambient atmosphere at room temperature. STDP was measured with a Keithley 4200-SCS in a two-electrode setup with the following voltage pattern: firstly, the resistive state of the device was read with −0.5 V pulses. In order to induce LTP (LTD), a pair of temporally correlated +/− 1.6 V symmetric sawtooth spikes was applied firstly to the top (bottom) electrode and to the bottom (top) electrode. The state of the device was subsequently read with −0.5 V voltage pulses (for the full voltage pattern see the Supporting Information SXX). The time interval between the poling spikes was measured from peak to peak and changed from 400 ms to 20 ms.

Conflicts of interest

There are no conflicts to declare.

Acknowledgements

The authors acknowledge the support of the National Science Centre (Poland) within the MAESTRO (grant agreement No. UMO-2015/18/A/ST4/00058) and PRELUDIUM (grant agreement No. UMO-2015/19/N/ST5/00533) projects. The crystal structure determination was carried out with the equipment purchased thanks to the financial support of the European Regional Development Fund in the framework of the Polish Innovation Economy Operational Program (contract no. POIG.02.01.00-12-023/08). DP and PZ have been partly supported by the EU Project POWR.03.02.00-00-I004/16. This research was supported in part by PL-Grid Infrastructure (grant id: iodide2)

References

1 A. N. Usoltsev, S. A. Adonin, P. A. Abramov, I. V. Korolkov, I. V. Yushina, O. V. Antonova, M. N. Sokolov and V. P. Fedin, *Inorg. Chim. Acta*, 2017, **462**, 323–328.
2 M. A. Tershansy, A. M. Goforth, M. D. Smith and H.-C. zur Loye, *J. Chem. Crystallogr.*, 2008, **38**, 453–459.
3 A. J. Dennington and M. T. Weller, *Dalton Trans.*, 2018, **47**, 3469–3484.
4 V. V. Sharutin, I. V. Yegorova, N. N. Klepikov, E. A. Boyarkina and O. K. Sharutina, *Russ. J. Inorg. Chem.*, 2009, **54**, 52–68.
5 A. W. Kelly, A. M. Wheaton, A. D. Nicholas, H. H. Patterson and R. D. Pike, *J. Inorg. Organomet. Polym.*, 2018, **28**, 528–534.
6 S. A. Adonin, M. N. Sokolov and V. P. Fedin, *Coord. Chem. Rev.*, 2016, **312**, 1–21.
7 L.-M. Wu, X.-T. Wu and L. Chen, *Coord. Chem. Rev.*, 2009, **253**, 2787–2804.
8 G. A. Fisher and N. C. Norman, in *Adv. Inorg. Chem.*, ed. A. G. Sykes, Academic Press, 1994, vol. 41, pp. 233–271.
9 W. Travis, C. E. Knapp, C. N. Savory, A. M. Ganose, P. Kafourou, X. Song, Z. Sharif, J. K. Cockcroft, D. O. Scanlon, H. Bronstein and R. G. Palgrave, *Inorg. Chem.*, 2016, **55**, 3393–3400.
10 S. M. Jain, T. Edvinsson and J. R. Durrant, *Chem. Commun.*, 2019, **2**, 91.
11 S. M. Jain, D. Phuyal, M. L. Davies, M. Li, B. Philippe, C. De Castro, Z. Qiu, J. Kim, T. Watson, W. C. Tsoi, O. Karis, H. Rensmo, G. Boschloo, T. Edvinsson and J. R. Durrant, *Nano Energy*, 2018, **49**, 614–624.
12 M. Kong, H. Hu, L. Wan, M. Chen, Y. Gan, J. Wang, F. Chen, B. Dong, D. Eder and S. Wang, *RSC Adv.*, 2017, **7**, 35549–35557.
13 M. A. Green, A. Ho-Baillie and H. J. Snaith, *Nat. Photonics*, 2014, **8**, 506.
14 M. Leng, Z. Chen, Y. Yang, Z. Li, K. Zeng, K. Li, G. Niu, Y. He, Q. Zhou and J. Tang, *Angew. Chem., Int. Ed.*, 2016, **55**, 15012–15016.
15 O. Toma, N. Mercier and C. Botta, *Eur. J. Inorg. Chem.*, 2013, 1113–1117.
16 G. Xu, G.-C. Guo, M.-S. Wang, Z.-J. Zhang, W.-T. Chen and J.-S. Huang, *Angew. Chem., Int. Ed.*, 2007, **46**, 3249–3251.
17 A. M. Goforth, M. A. Tershansy, M. D. Smith, L. Peterson, J. G. Kelley, W. J. I. DeBenedetti and H.-C. zur Loye, *J. Am. Chem. Soc.*, 2011, **133**, 603–612.
18 R. L. Z. Hoye, R. E. Brandt, A. Osherov, V. Stevanović, S. D. Stranks, M. W. B. Wilson, H. Kim, A. J. Akey, J. D. Perkins, R. C. Kurchin, J. R. Poindexter, E. N. Wang, M. G. Bawendi, V. Bulović and T. Buonassisi, *Chem. – Eur. J.*, 2016, **22**, 2605–2610.
19 B. Hwang and J.-S. Lee, *Nanoscale*, 2018, **10**, 8578–8584.
20 K. Yan, M. Peng, X. Yu, X. Cai, S. Chen, H. Hu, B. Chen, X. Gao, B. Dong and D. Zou, *J. Mater. Chem. C*, 2016, **4**, 1375–1381.
21 T. Mazur, P. Zawal and K. Szaciłowski, *Nanoscale*, 2019, **11**, 1080–1090.
22 Y. Hu, S. Zhang, X. Miao, L. Su, F. Bai, T. Qiu, J. Liu and G. Yuan, *Adv. Mater. Interfaces*, 2017, **4**, 1700131.
23 X. Zhao, H. Xu, Z. Wang, Y. Lin and Y. Liu, *InfoMat*, 2019, **1**, 183–210.
24 S. P. Adhikari, M. P. Sah, H. Kim and L. O. Chua, *IEEE Trans. Circuits Syst.*, 2013, **60**, 3008–3021.
25 L. O. Chua, *IEEE Trans. Circuit Theory*, 1971, **CT-18**, 507–519.
26 D. B. Strukov, G. S. Snider, D. R. Stewart and R. S. Williams, *Nature*, 2008, **453**, 80–83.
27 J.-M. Ginoux and B. Rosetto, in *Chaos, CNN, Memristors and Beyond*, ed. A. Adamatzky and G. Chen, World Scientific, 2012, p. 564, , DOI: 10.1142/8590.
28 T. Prodromakis, in *Chaos, CNN, Memristors and Beyond*, ed. A. Adamatzky and G. Chen, World Scientific, 2012, p. 564, DOI: 10.1142/8590.

29 H. Li, B. Liu, X. Liu, M. Mao, Y. Chen, Q. Wu and Q. Qiu, *IEEE Int. Symp. Circ. Syst. (ISCAS)*, 2015, 17–20, DOI: 10.1109/ISCAS.2015.7168559.
30 Y. Chen, G. Liu, C. Wang, W. Zhang, R.-W. Li and L. Wang, *Mater. Horiz.*, 2014, **1**, 489–506.
31 G. Liu, C. Wang, W. Zhang, L. Pan, C. Zhang, X. Yang, F. Fan, Y. Chen and R.-W. Li, *Adv. Electron. Mater.*, 2016, **2**, 1500298.
32 K.-H. Kim, S. Gaba, D. Wheeler, J. M. Cruz-Albrecht, T. Hussain, N. Srinivasa and W. Lu, *Nano Lett.*, 2012, **12**, 389–395.
33 Y. Gao, D. C. Ranasinghe, S. F. Al-Sarawi, O. Kavehei and D. Abbott, *Sci. Rep.*, 2015, **5**, 12785.
34 R. Zhang, H. Jiang, Z. R. Wang, P. Lin, Y. Zhuo, D. Holcomb, D. H. Zhang, J. J. Yang and Q. Xia, *Nanoscale*, 2018, **10**, 2721–2726.
35 I. Vourkas and G. C. Sirakoulis, *IEEE Circ. Syst. Mag.*, 2016, **16**, 15–30.
36 G. Ding, Y. Wang, G. Zhang, K. Zhou, K. Zeng, Z. Li, Y. Zhou, C. Zhang, X. Chen and S.-T. Han, *Adv. Funct. Mater.*, 2019, **29**, 1806637.
37 T. Shi, J.-F. Wu, Y. Liu, R. Yang and X. Guo, *Adv. Electron. Mater.*, 2017, 1700046.
38 Ella M. Gale, *Faraday Discuss.*, 2019, **213**, 521–551.
39 B.-Y. Kim, H.-G. Hwang, J.-U. Woo, W.-H. Lee, T.-H. Lee, C.-Y. Kang and S. Nahm, *NPG Asia Mater.*, 2017, **9**, e381.
40 T.-H. Lee, H.-G. Hwang, J.-U. Woo, D.-H. Kim, T.-W. Kim and S. Nahm, *ACS Appl. Mater. Interfaces*, 2018, **10**, 25673–25682.
41 B. Liu, Z. Liu, I.-S. Chiu, M. Di, Y. Wu, J.-C. Wang, T.-H. Hou and C.-S. Lai, *ACS Appl. Mater. Interfaces*, 2018, **10**, 20237–20243.
42 Q. Wu, H. Wang, Q. Luo, W. Banerjee, J. Cao, X. Zhang, F. Wu, Q. Liu, L. Li and M. Liu, *Nanoscale*, 2018, **10**, 5875–5881.
43 T. Serrano-Gotarredona, T. Masquelier, T. Prodromakis, G. Indiveri and B. Linares-Barranco, *Front. Neurosci.*, 2013, **7**, 2.
44 K. E. Nikiruy, A. V. Emelyanov, V. A. Demin, A. V. Sitnikov, A. A. Minnekhanov, V. V. Rylkov, P. K. Kashkarov and M. V. Kovalchuk, *AIP Adv.*, 2019, **9**, 065116.
45 A. Younis, D. Chu and S. Li, *Sci. Rep.*, 2015, **5**, 13599.
46 Y. Yang, P. Gao, S. Gaba, T. Chang, X. Pan and W. Lu, *Nat. Commun.*, 2012, **3**, 732.
47 Y. Yang and W. Lu, *Nanoscale*, 2013, **5**, 10076–10092.
48 B. Hwang and J.-S. Lee, *Sci. Rep.*, 2017, **7**, 673.
49 A. Sawa, *Mater. Today*, 2008, **11**, 28–36.
50 C. Baeumer, C. Schmitz, A. Marchewka, D. N. Mueller, R. Valenta, J. Hackl, N. Raab, S. P. Rogers, M. I. Khan, S. Nemsak, M. Shim, S. Menzel, C. M. Schneider, R. Waser and R. Dittmann, *Nat. Commun.*, 2016, **7**, 12398.
51 Y. Tian, L. Jiang, X. Zhang, G. Zhang and Q. Zhu, *AIP Adv.*, 2018, **8**, 035105.
52 M. Hansen, M. Ziegler, L. Kolberg, R. Soni, S. Dirkmann, T. Mussenbrock and H. Kohlstedt, *Sci. Rep.*, 2015, **5**, 13753.
53 H. Ma, W. Wang, H. Xu, Z. Wang, Y. Tao, P. Chen, W. Liu, X. Zhang, J. Ma and Y. Liu, *ACS Appl. Mater. Interfaces*, 2018, **10**, 21755–21763.
54 E. Wlaźlak, J. Kalinowska-Tłuścik, W. Nitek, S. Klejna, K. Mech, W. Macyk and K. Szaciłowski, *ChemElectroChem*, 2018, **5**, 3486–3497.
55 E. Wlaźlak, W. Macyk, W. Nitek and K. Szaciłowski, *Inorg. Chem.*, 2016, **55**, 5935–5945.
56 C. Chang, P. Chen, B. Hudec, P. Liu and T. Hou, *IEEE Int. Electron Devices Meet.*, 2018, 15.15.11–15.15.14.
57 F. Lazarini and S. Milićev, *Acta Crystallogr., Sect. B: Struct. Crystallogr. Cryst. Chem.*, 1976, **32**, 2873–2875.
58 J. Singh and K. Shimakawa, *Advances in amorphous semiconductors*, Taylor & Francis, London, 2003.
59 N. J. Podraza, W. Qiu, B. B. Hinojosa, H. Xu, M. A. Motyka, S. R. Phillpot, J. E. Baciak, S. Trolier-McKinstry and J. C. Nino, *J. Appl. Phys.*, 2013, **114**, 033110.
60 L. Kronik and Y. Shapira, *Surf. Sci. Rep.*, 1999, **37**, 1–206.
61 A. Kulkarni, T. Singh, A. Jena, P. Pinpithak, M. Ikegami and T. Miyasaka, *ACS Appl. Mater. Interfaces*, 2018, **10**, 9547–9554.
62 H. Han, M. Hong, S. S. Gokhale, S. B. Sinnott, K. Jordan, J. E. Baciak and J. C. Nino, *J. Phys. Chem. C*, 2014, **118**, 3244–3250.
63 N. D. Lang and W. Kohn, *Phys. Rev. B: Solid State*, 1971, **3**, 1215–1223.
64 F. Musumeci and G. H. Pollack, *Chem. Phys. Lett.*, 2012, **536**, 65–67.
65 Y. Wan, Y. Li, Q. Wang, K. Zhang and Y. Wu, *Int. J. Electrochem. Sci.*, 2012, **7**, 5204–5216.
66 M. Xue, H. Wu, J. Ou, F. Wang, X. Li, W. Li and Z. Jiang, *J. Appl. Phys.*, 2012, **111**, 123714.
67 E. E. Huber Jr and C. T. Kirk Jr, *Surf. Sci.*, 1966, **5**, 447–465.
68 D. Yamashita and A. Ishizaki, *Appl. Surf. Sci.*, 2016, **363**, 240–244.
69 C. Hückstädt, S. Schmidt, S. Hüfner, F. Forster, F. Reinert and M. Springborg, *Phys. Rev. B: Condens. Matter Mater. Phys.*, 2006, **73**, 075409.
70 J. M. Heras and L. Viscido, *Appl. Surf. Sci.*, 1980, **4**, 238–241.
71 P. L. Giggin, in *Comprehensive Coordination Chemistry*, ed. G. F. Wilkinson, Pergamon Press, Oxford, 1987.
72 R. T. Tung, *Mater. Sci. Eng.*, 2001, **R35**, 1–138.
73 R. T. Tung, *Appl. Phys. Rev.*, 2014, **1**, 011304.
74 L. Chua, in *Memristors and Memristive Systems*, ed. R. Tetzlaff, Springer, New York, NY, 2014, pp. 17–90, DOI: 10.1007/978-1-4614-9068-5_2.
75 L. Chua, *Radioengineering*, 2015, **24**, 319–368.
76 K. Lu, Y. Li, W. F. He, J. Chen, Y. X. Zhou, N. Duan, M. M. Jin, W. Gu, K. H. Xue, H. J. Sun and X. S. Miao, *Appl. Phys. A: Mater. Sci. Process.*, 2018, **124**, 438.
77 E. Wlaźlak, M. Marzec, P. Zawal and K. Szaciłowski, *ACS Appl. Mater. Interfaces*, 2019, **11**, 17009–17018.
78 S. Majumdar, H. Tan, Q. H. Qin and S. van Dijken, *Adv. Electron. Mater.*, 2019, **5**, 1800795.
79 E. Wlaźlak, P. Zawal and K. Szaciłowski, *ACS Appl. Electron. Mater.*, 2020, **2**, 329–338.
80 A. Odagawa, H. Sato, I. H. Inoue, H. Atoh, M. Kawasaki and Y. Tokura, *Phys. Rev. B: Condens. Matter Mater. Phys.*, 2004, **70**, 224403.

81 A. Sawa, T. Fujii, M. Kawasaki and Y. Tokura, *Appl. Phys. Lett.*, 2004, **85**, 4073–4075.
82 D. S. Shang, Q. Wang, L. D. Chen, R. Dong, X. M. Li and W. Q. Zhang, *Phys. Rev. B: Condens. Matter Mater. Phys.*, 2006, **73**, 245427.
83 B. Mohammad, M. A. Jaoude, V. Kumar, D. M. A. Homouz, H. Abu Nahla, M. Al-Qutayri and N. Christoforou, *Nanotechnol. Rev.*, 2016, **5**, 311–329.
84 E. J. Yoo, M. Lyu, J.-H. Yun, C. J. Kang, Y. J. Choi and L. Wang, *Adv. Mater.*, 2015, **27**, 6170–6175.
85 D. O. Hebb, *The organization of behavior; a neuropsychological theory*, Wiley, Oxford, England, 1949.
86 Daniel E. Feldman, *Neuron*, 2012, **75**, 556–571.
87 S. Lowel and W. Singer, *Science*, 1992, **255**, 209.
88 Z. Xiao and J. Huang, *Adv. Electron. Mater.*, 2016, **2**, 1600100.
89 W. He, K. Huang, N. Ning, K. Ramanathan, G. Li, Y. Jiang, J. Sze, L. Shi, R. Zhao and J. Pei, *Sci. Rep.*, 2014, **4**, 4755.
90 S. Saïghi, C. G. Mayr, T. Serrano-Gotarredona, H. Schmidt, G. Lecerf, J. Tomas, J. Grollier, S. Boyn, A. F. Vincent, D. Querlioz, S. La Barbera, F. Alibart, D. Vuillaume, O. Bichler, C. Gamrat and B. Linares-Barranco, *Front. Neurosci.*, 2015, **9**, 51.
91 F. Ponulak and A. Kasiński, *Neural Comput.*, 2010, **22**, 467–510.
92 K. Ohe, S. Uemura, N. Sugita, H. Masuda and T. Taga, *J. Org. Chem.*, 1989, **54**, 4169–4174.
93 H.-A. Chen and C.-W. Pao, *ACS Omega*, 2019, **4**, 10950–10959.
94 M. C. Burla, R. Caliandro, M. Camalli, B. Carrozzini, G. L. Cascarano, L. De Caro, C. Giacovazzo, G. Polidori and R. Spagna, *J. Appl. Crystallogr.*, 2005, **38**, 381–388.
95 L. Palatinus and G. Chapuis, *J. Appl. Crystallogr.*, 2007, **40**, 786–790.
96 G. Sheldrick, *Acta Crystallogr., Sect. A: Found. Crystallogr.*, 2008, **64**, 112–122.
97 L. Farrugia, *J. Appl. Crystallogr.*, 1999, **32**, 837–838.
98 C. F. Macrae, P. R. Edgington, P. McCabe, E. Pidcock, G. P. Shields, R. Taylor, M. Towler and J. van de Streek, *J. Appl. Crystallogr.*, 2006, **39**, 453–457.
99 S. Grimme, *J. Comput. Chem.*, 2006, **27**, 1787–1799.
100 P. H. T. Philipsen, E. van Lenthe, J. G. Snijders and E. J. Baerends, *Phys. Rev. B: Condens. Matter Mater. Phys.*, 1997, **56**, 13556–13562.
101 J. del Valle, J. Ramirez, M. Rozenberg and I. Schuller, *J. Appl. Phys.*, 2018, **124**, 211101.
102 G. te Velde and E. J. Baerends, *Phys. Rev. B: Condens. Matter Mater. Phys.*, 1991, **44**, 7888–7903.
103 M. Franchini, P. H. T. Philipsen and L. Visscher, *J. Comput. Chem.*, 2013, **34**, 1819–1827.
104 M. Franchini, P. H. T. Philipsen, E. van Lenthe and L. Visscher, *J. Chem. Theory Comput.*, 2014, **10**, 1994–2004.
105 G. Wiesenekker and E. J. Baerends, *J. Phys.: Condens. Matter*, 1991, **3**, 6721–6742.

Electronic Supplementary Material (ESI) for Journal of Materials Chemistry C.

Bismuth Triiodide Complexes: Structure, Spectroscopy, Electronic Properties, and Memristive Properties

Ewelina Wlaźlak,*[a] Justyna Kalinowska-Tłuścik,[b] Dawid Przyczyna,[ac] Piotr Zawal,[ac] and Konrad Szaciłowski*[a]

[a]AGH University of Science and Technology, Academic Centre for Materials and Nanotechnology, al. A. Mickiewicza 30, 30-059 Kraków, Poland.

[b]Faculty of Chemistry, Jagiellonian University, ul. Gronostajowa 2, 30-060 Kraków, Poland.

[c]Faculty of Physics and Applied Computer Science AGH University of Science and Technology al. A. Mickiewicza 30, 30-059 Kraków, Poland.

*corresponding authors

Content

Crystallographic details

Table S1. Crystal/experimental data and structure refinement results

Empirical moiety formula	$[BiI_3\{(C_6H_5)_3PO\}_2]$	$[BiI_3(C_5H_5NO)]$	$[BiI_3\{(C_6H_5)_2SO\}_{1.5}]_2$	$[BiI_3(C_{12}H_8N_2O_2)]$
Formula weight [g/mol]	1146.22	684.78	1786.14	801.88
Crystal system	Monoclinic	Triclinic	Triclinic	Triclinic
Space group	$P2_1/c$	$P\bar{1}$	$P\bar{1}$	$P\bar{1}$
Unite cell dimensions	a = 12.7693(3) Å b = 11.7066(1) Å c = 30.5274(7) Å a= 90.0° b= 127.090(3)° g= 90.0°	a = 7.6306(7) Å b = 8.6042 (9)Å c = 9.2988(9) Å a= 80.893(8)° b= 86.043(8)° g= 80.695(8)°	a = 11.2571(4)Å b = 13.8388(5)Å c = 16.8099(7)Å a= 82.885(3)° b= 77.008(3)° g= 67.450(4)°	a = 7.6873(3)Å b = 9.9765(4)Å c = 11.2378(4)Å a= 104.186(4)° b= 93.222(3)° g= 99.194(4)°
Volume [$Å^3$]	3640.17(17)	594.30(10)	2354.54(17)	820.73(6)
Z	4	2	2	2
D_{calc} [Mg/m^3]	2.091	3.827	2.519	3.245
μ [mm^{-1}]	7.506	22.582	11.561	16.385
F(000)	2136	584	1604	704
Crystal size [mm^3]	0.3 x 0.2 x 0.2	0.2 x 0.1 x 0.1	0.1 x 0.08 x 0.08	0.1 x 0.1 x 0.1
Θ range	3.05° to 28.57°	3.04° to 28.45°	2.98° to 28.57°	3.13° to 28.65°
Index ranges	-15 ≤ h ≤ 17, -15 ≤ k ≤ 14, -40 ≤ l ≤ 39	-7 ≤ h ≤ 10, -10 ≤ k ≤ 11, -12 ≤ l ≤ 12	-14 ≤ h ≤ 15, -18 ≤ k ≤ 17, -22 ≤ l ≤ 21	-10 ≤ h ≤ 9, -12 ≤ k ≤ 13, -15 ≤ l ≤ 14
Refl. collected	48661	4361	32076	10984
Independent reflections	8712 [R(int) = 0.1173]	2659 [R(int) = 0.0721]	10795 [R(int) = 0.0713]	3820 [R(int) = 0.0501]
Completeness [%] to Θ = 25.24°	99.8	99.8	99.8	99.9
Absorption correction	Analytical *)	Analytical	Analytical	Multi-scan
Tmin. and Tmax.	0. 073 and 0.295	0.178 and 0.644	0.384 and 0.605	0.859 and 1.000
Data/ restraints/parameters	8712 / 0 / 397	2659 / 0 / 70	10795 / 0 / 433	3820 / 0 / 181
GooF on F2	1.048	1.089	1.035	1.019
Final R indices [I>2sigma(I)]	R1= 0.0464, wR2= 0.1015	R1= 0.0629, wR2= 0.1157	R1= 0.0464, wR2= 0.0598	R1= 0.0268, wR2= 0.0493
R indices (all data)	R1= 0.0544, wR2= 0.1099	R1= 0.0969, wR2= 0.1417	R1= 0.0903, wR2= 0.0738	R1= 0.0333, wR2= 0.0520
$\Delta\rho_{max}$, $\Delta\rho_{min}$ [$e \cdot Å^{-3}$]	3.20 and -2.57	3.56 and -3.77	2.54 and -1.36	0.99 and -1.61

*) CrysAlisPro 1.171.40.14e (Rigaku Oxford Diffraction, 2018); Analytical numeric absorption correction using a multifaceted crystal model based on expressions derived by R.C. Clark & J.S. (Clark, R. C. & Reid, J. S. (1995). Acta Cryst. A51, 887-897)

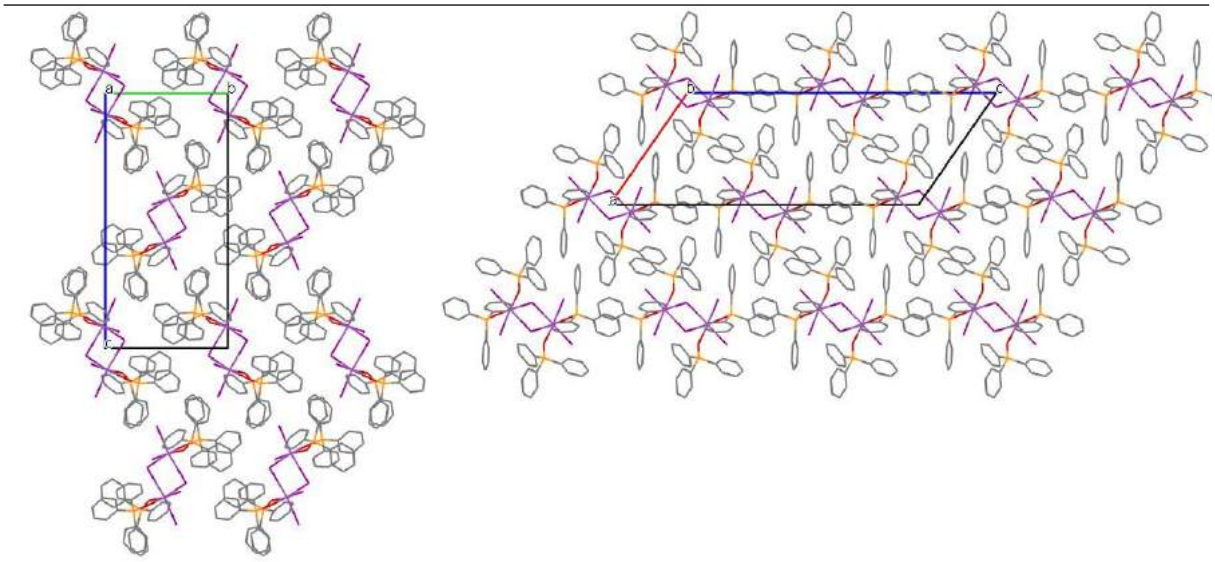

View along [100] View along [010]

Figure S1. Packing in the crystal of [BiI3{(C6H5)3PO}2]2 showing isolated centrosymmetric dimers. Hydrogen atoms were omitted for figure clarity.

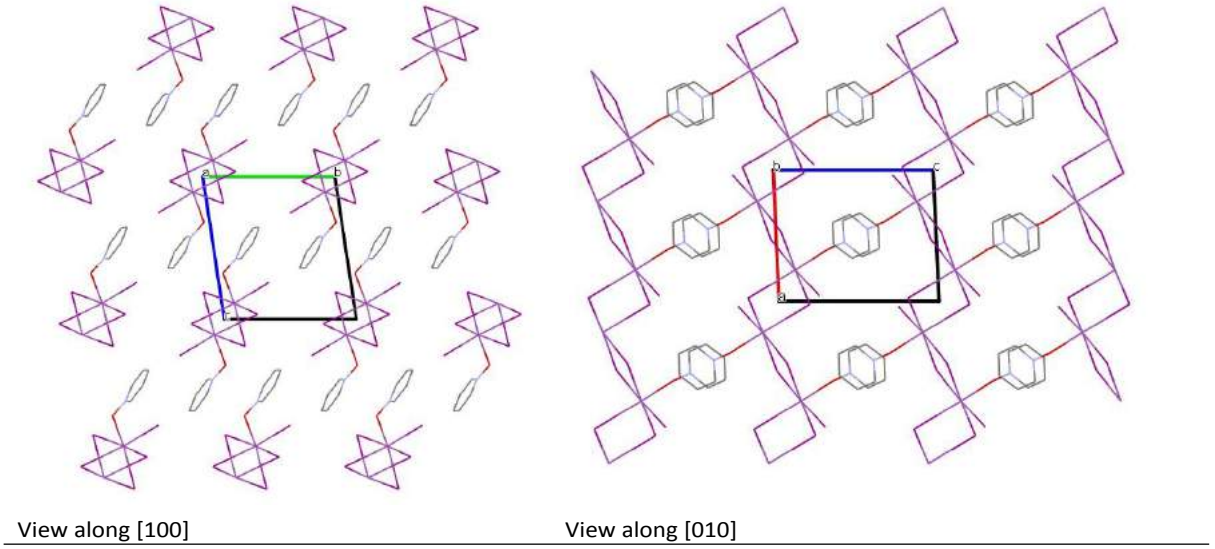

View along [100] View along [010]

Figure S2. Packing in the crystal of $[BiI_3(C_5H_5NO)]_n$ showing bismuth-iodide chains propagating parallel to [100] axis. Hydrogen atoms were omitted for figure clarity.

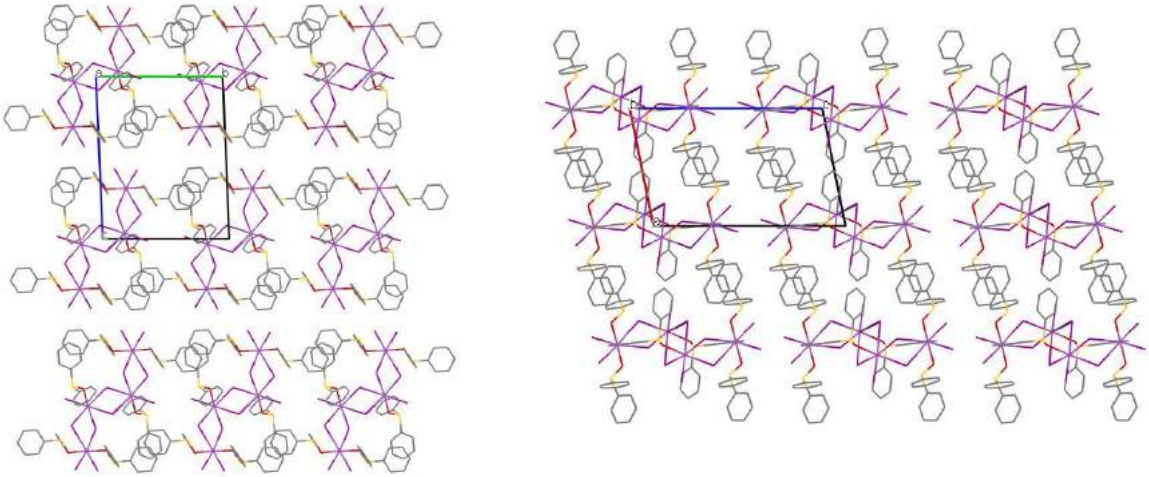

View along [100] View along [010]

Figure S3. Packing in the crystal of $[BiI_3\{(C_6H_5)_2SO\}_{1.5}]_4$ showing the isolated motives formed by 4 bismuth ions, bridged by iodide. Hydrogen atoms were omitted for figure clarity.

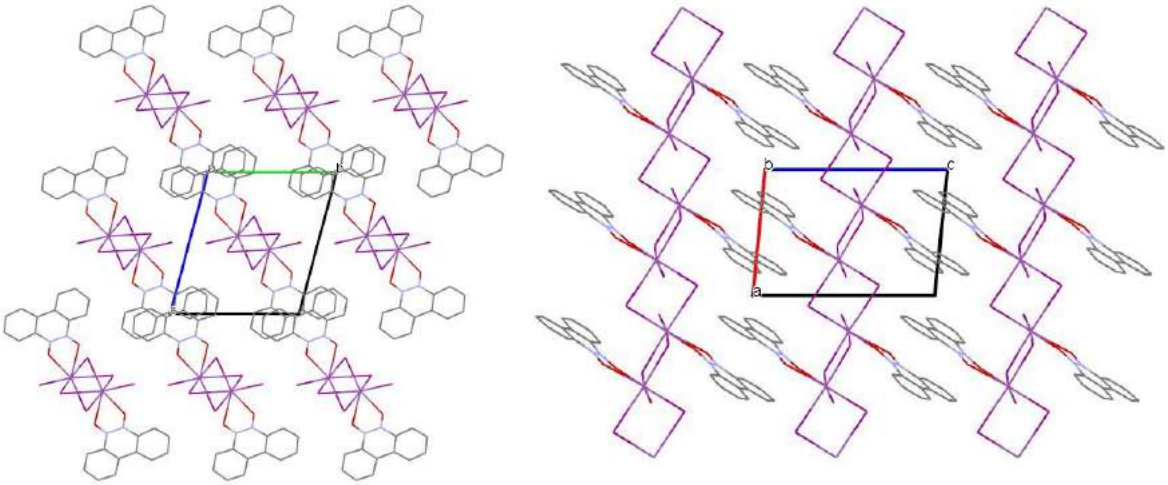

View along [100] View along [010]

Figure S4. Packing in the crystal of $[BiI_3(C_{12}H_8N_2O_2)]_n$ showing bismuth-iodide chains propagating parallel to [100] axis. Hydrogen atoms were omitted for figure clarity.

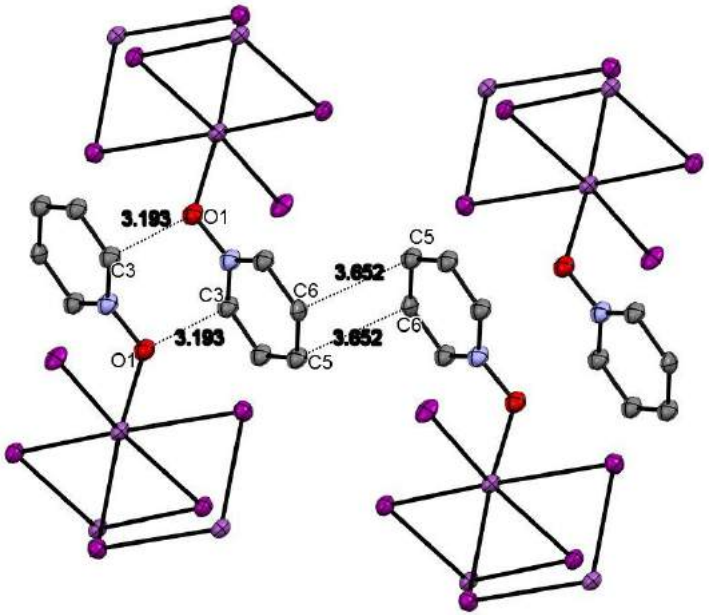

Figure S5. C...O short contacts between aromatic moieties in the crystal of $[BiI_3(C_5H_5NO)]_n$. Hydrogen atoms were omitted for figure clarity.

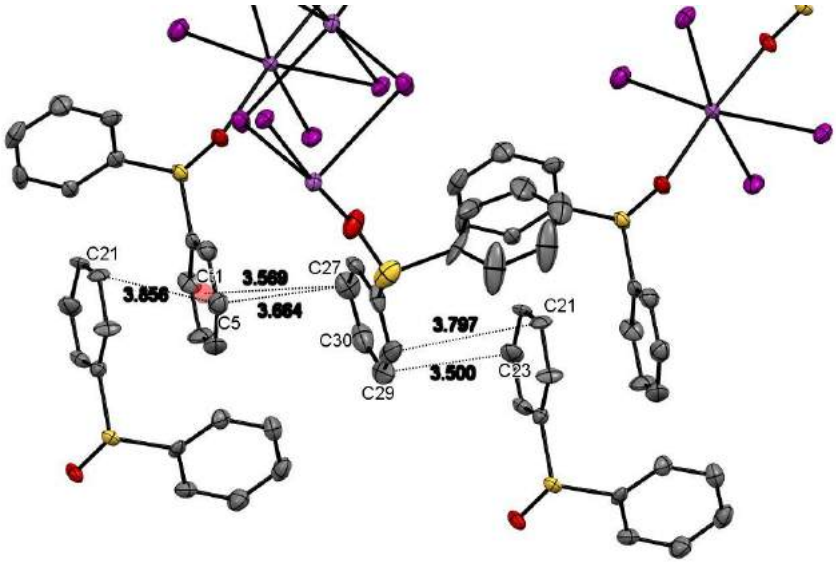

Figure S6. Short contacts between aromatic moieties (ring C1-C6, with shown Ct1 centre of gravity) in the crystal of $[BiI_3\{(C_6H_5)_2SO\}_{1.5}]_4$. Hydrogen atoms were omitted for figure clarity.

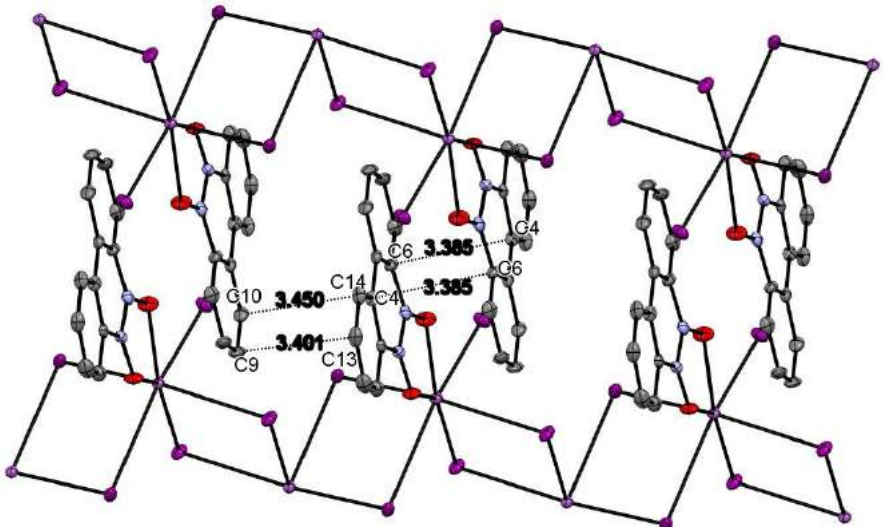

Figure S7. Short contacts and π...π interactions between aromatic moieties in the crystal of $[BiI_3(C_{12}H_8N_2O_2)]_n$. Hydrogen atoms were omitted for figure clarity.

Tauc plots and band gaps

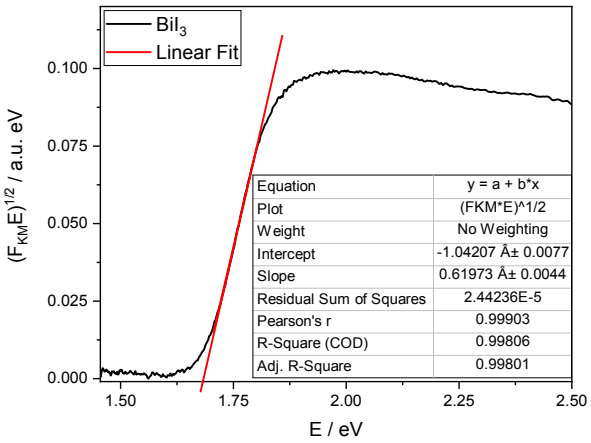

Figure S8. Tauc plots for BiI_3.

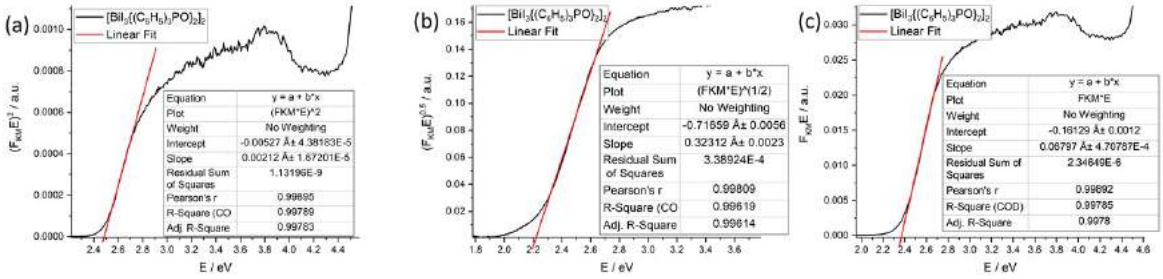

Figure S9. Tauc plots for $[BiI_3\{(C_6H_5)_3PO\}_2]_2$.

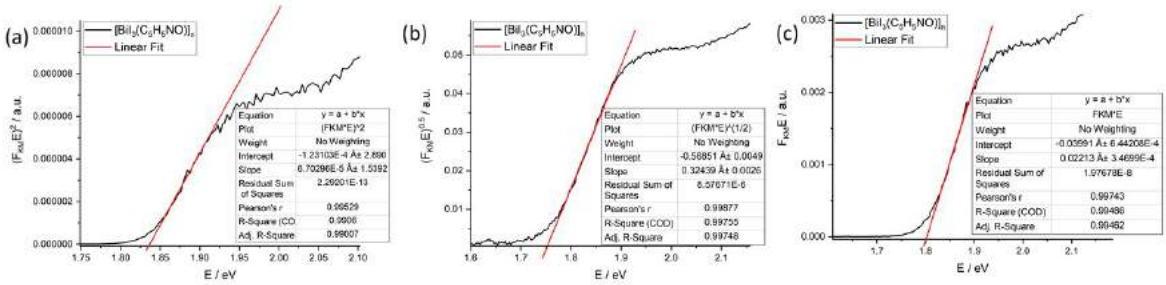

Figure S10. Tauc plots for $[BiI_3(C_5H_5NO)]_n$.

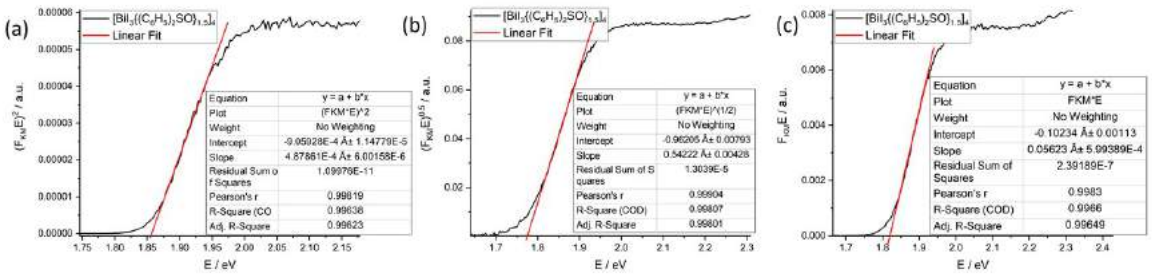

Figure S11. Tauc plots for $[BiI_3\{(C_6H_5)_2SO\}_{1.5}]$.

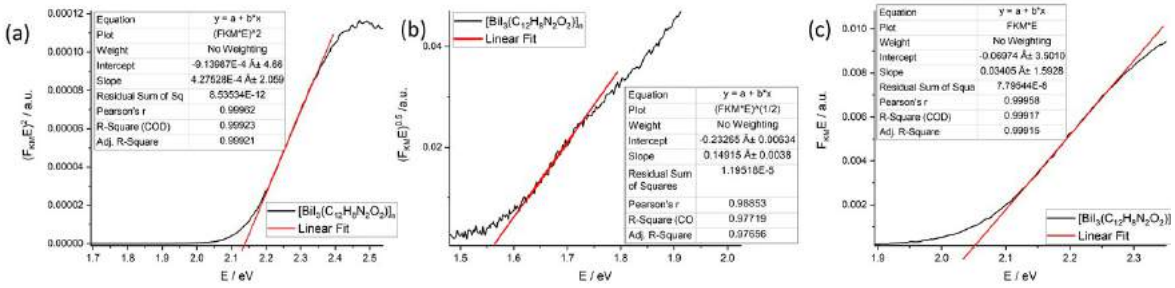

Figure S12. Tauc plots for $[BiI_3(C_{12}H_8N_2O_2)]_n$.

Table S2. Experimental and theoretical band gaps of studied compounds.

Compound	Experimental band gap / eV			Theoretical band gap / eV
	Direct	Indirect	Undefined	
BiI_3	–	**1.68**	–	indirect 1.18
$[BiI_3\{(C_6H_5)_3PO\}_2]_2$	2.49	2.22	**2.37**	Indirect 2.12
$[BiI_3\{(C_6H_5)_2SO\}_{1.5}]_4$	**1.86**	1.77	1.82	direct 1.87
$[BiI_3C_5H_5NO]_n$	1.84	**1.75**	1.8	indirect 1.81
$[BiI_3(C_{12}H_8N_2O_2)]_n$	2.13	**1.56**	2.05	indirect 1.33

Current-voltage characteristics

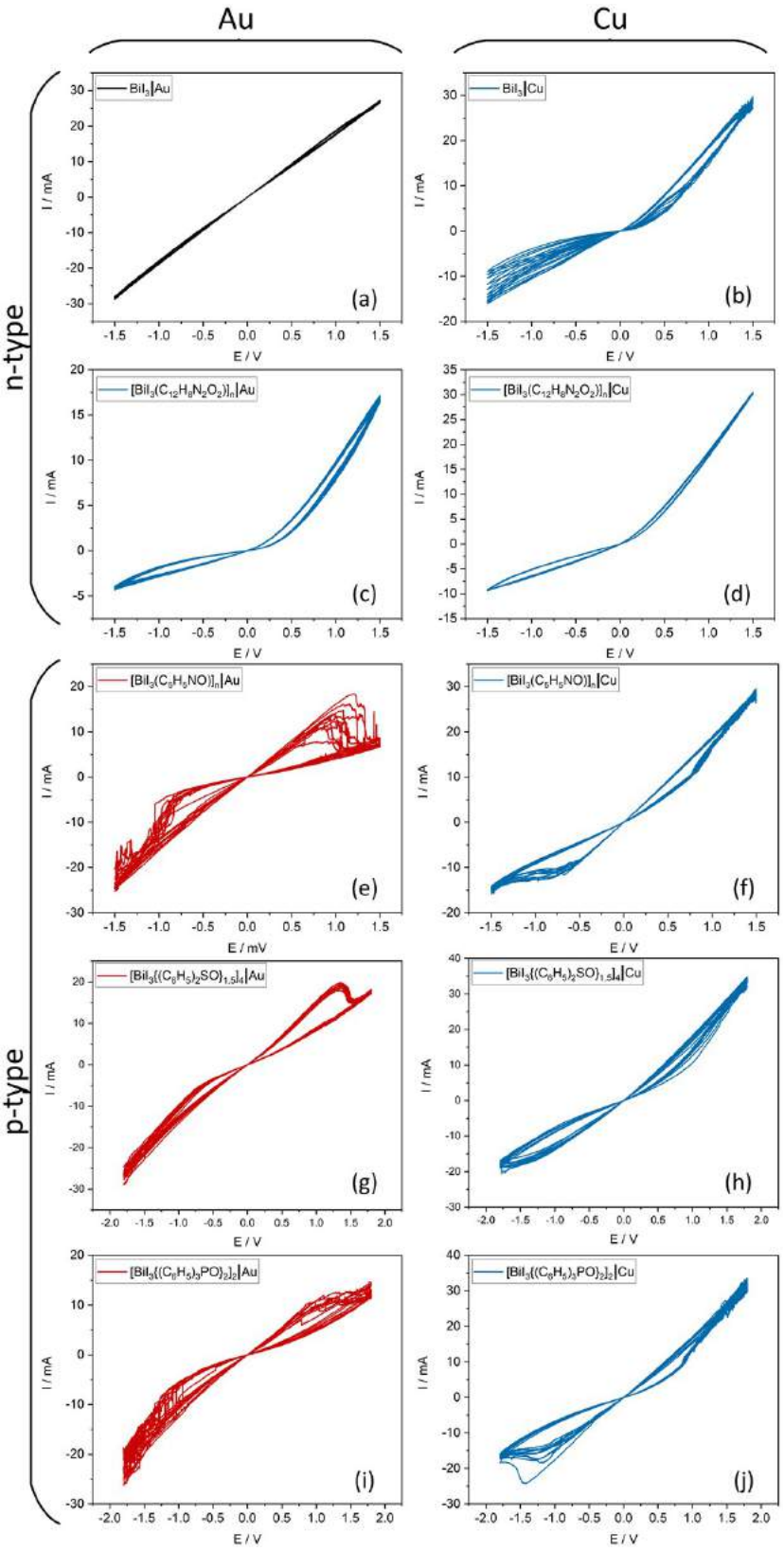

Figure S13. Current-voltage characteristics of BiI_3 memristors measured with Au (a) and Cu (b) as second electrode, $[BiI_3(C_{12}H_8N_2O_2)]_n$ memristors measured with Au (c) and Cu (d) as second electrode $[BiI_3(C_5H_5NO)]_n$ memristors measured with Au (e) and Cu (f) as second electrode, $[BiI_3\{(C_6H_5)_2SO\}_{1.5}]_4$ memristors measured with Au (g) and Cu (h) as second electrode, $[BiI_3\{(C_6H_5)_3PO\}]_2$ memristors measured with Au (i) and Cu (j) as second electrode. Ten scans with 100 S13

The stability of the states

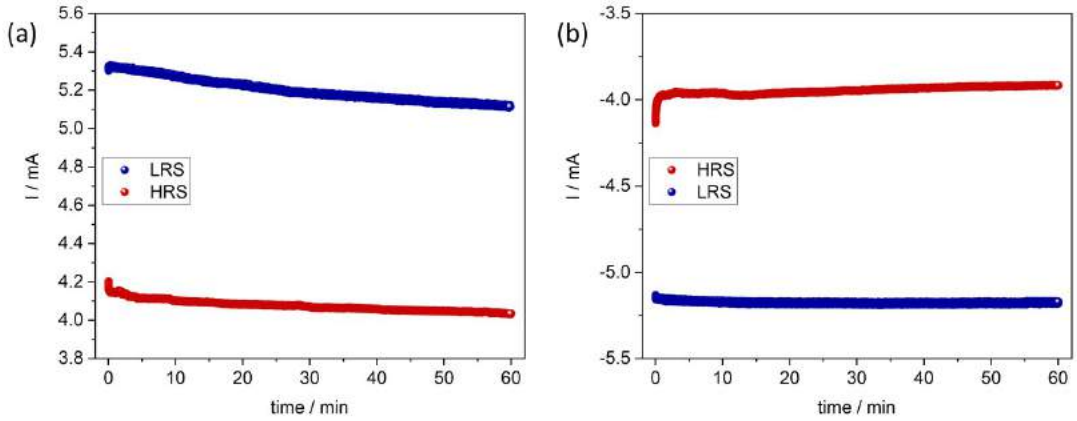

Figure S14. The persistence of the states measured at 0.3 V (a) and –0.3 V (b). The device (FTO/[BiI3{(C6H5)2SO}1.5]4/Au) was set to HRS with the 2.5 V (30 s) impulse and LRS with the –2.5 V (30 s) impulse.

Spike-timing dependent plasticity

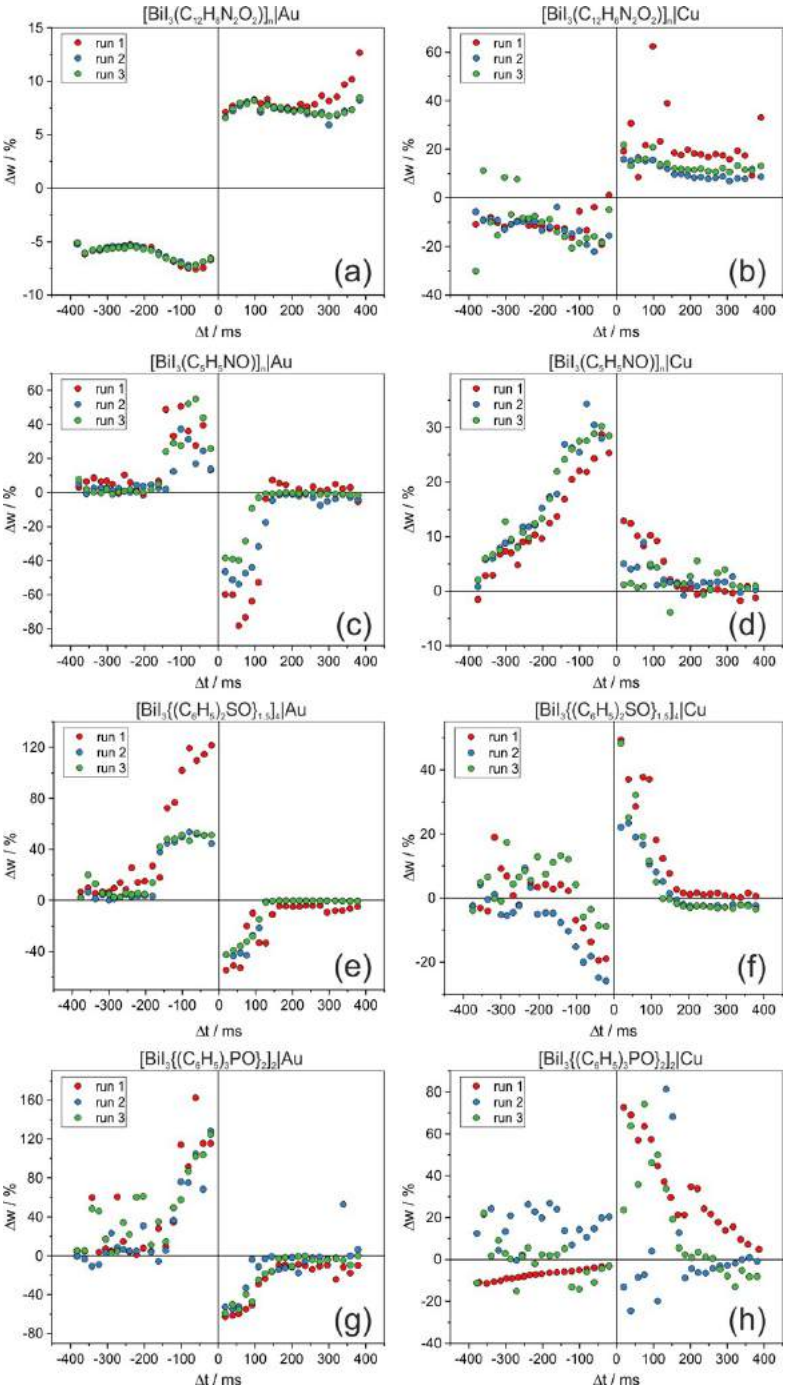

Figure S15. Spike-timing dependent plasticity (STDP) of the memristive materials measured of BiI_3 memristors measured with Au (left column) and Cu (right column) as second electrode, $[BiI_3(C_{12}H_8N_2O_2)]_n$ memristors measured with Au (a) and Cu (b) as second electrode $[BiI_3(C_5H_5NO)]_n$ memristors measured with Au (c) and Cu (d) as second electrode, $[BiI_3\{(C_6H_5)_2SO\}_{1.5}]_4$ memristors measured with Au (e) and Cu (f) as second electrode, $[BiI_3\{(C_6H_5)_3PO\}]_2$ memristors measured with Au (g) and Cu (h) as second electrode.

$[BiI_3(C_{12}H_8N_2O_2)]_n$

Due to narrow hysteresis loop in the I-V scan and rectifying character of the junction, $[BiI_3(C_{12}H_8N_2O_2)]_n$ shows no synaptic plasticity. Synaptic weight changes that can be seen both in Figure S14(a) and (b) are almost of constant value. This suggests that the applied voltage pattern caused only slight resistive switching, independent on the temporal interval between the spikes.

$[BiI_3(C_5H_5NO)]_n$

While $[BiI_3(C_5H_5NO)]_n|Au$ shows the expected antisymmetric anti-Hebbian behaviour, we have observed unipolar Hebbian learning rule with the Cu electrode. This phenomenon occurred due to instability of the current response to the applied voltage pattern or DC bias during the STDP measurement. The instability was monitored with I-V scans performed during the STDP measurements. The direction of resistive switching changes throughout the measurement.

$[BiI_3\{(C_6H_5)_2SO\}_{1.5}]_4$

This material was presented and described in the main text of the article (with the averaged Δw and error bars calculated as standard deviation). Here, we present the data collected during the 3 runs of the measurement.

$[BiI_3\{(C_6H_5)_3PO\}]_2$

Similarly to other materials measured with the Au electrode, $[BiI_3\{(C_6H_5)_3PO\}]_2$ also exhibits anti-Hebbian learning rule. However, data collected during the measurement with the Cu electrode is considerably scattered and differs among the measurement series. This material show instability in the I-V scans during the STDP measurement as well.

RESEARCH ARTICLE

ADVANCED ELECTRONIC MATERIALS
www.advelectronicmat.de

Light-Induced Synaptic Effects Controlled by Incorporation of Charge-Trapping Layer into Hybrid Perovskite Memristor

Piotr Zawal, Tomasz Mazur,* Maria Lis, Alessandro Chiolerio, and Konrad Szaciłowski*

Organic-inorganic perovskites despite being known for their extraordinary performance in solar cell research areas are also a workhorse in the field of unconventional information processing. Here, a neuromimetic behaviour is presented in a perovskite device with the potential to act as an artificial synapse. In addition, perovskite layer is combined with one of the non-stoichiometric polymeric forms of carbon nitride (C_3N_4). Such a device can operate not only according to the principles of non-von Neumann architecture but also utilizes two different stimuli as information carriers—electric current and/or light. This in turn can lead towards the development of next-generation information processing/storage units.

1. Introduction

Organic-inorganic perovskites possess a unique set of optoelectronic properties.[1] The high absorption coefficient, defect tolerance, and low exciton dissociation energy make them suitable for solar cell applications. So far, perovskites achieved efficiencies comparable with traditional silicon solar cells. On the other hand, the low activation energy of defect migration and memristive properties make perovskite materials intensively investigated for neuromorphic applications.[2] Many learning rules and synaptic effects can be induced by applying a proper set of voltage spikes to the memristive device. It was found, however, that even non-volatile memristive devices have limited information retention time. Each readout operation induces subtle changes in their electronic structure and therefore the number of readout cycles is limited.[3] Despite the fact that volatility of the memristor is undesirable in memory application,[4] it is an advantageous feature for the application in Spiking Neural Networks and reservoir computing[5] and for mimicking neuromorphic effects such as synaptic plasticity. Moreover, despite numerous studies, the relation between memristive and photoelectric phenomena is still not fully recognized, though it could lead to the development of novel devices, such as mem-sensors[6] and extend the applicability and functionality of synaptic devices to optoelectronic and photonic systems.[7] Particularly, the interplay between memristive properties and light-induced synaptic plasticity still remains to be thoroughly investigated due to its remarkable potential in the field of neuromorphic computing. Lead iodide perovskites or, more generally hybrid organic-inorganic perovskites (HOIPs) seem to be materials of choice for these applications: they show very well-characterized memristive properties[2d,8] and their leading position in solar energy conversion is unquestioned.[9] The exploration of HOIPs in photomemristive devices requires appropriate interface engineering in order to activate processes which are detrimental for solar cells, but highly desired for memristive devices (e.g., extended hysteresis, charge trapping, charge carrier recombination). On the basis of our former reports[10] charge trapping at the chosen interface seems to be here the most desired feature of a photomemristive device. Therefore, carbon nitride, especially in the form of nanoparticles, has been considered as a charge trapping material for a new generation of memristive devices: its well-known electron acceptor character[11] combined with relatively high band gap energy[12] suits very well the desired performance of the device.

Here we present novel memristive photoactive devices based on a thin lead iodide perovskite ($CH_3NH_3PbI_3$) layer sandwiched between conductive pads. We have additionally incorporated carbon nitride nanoparticles (CN-NPs) exhibiting charge-trapping properties into the perovskite-based memristive device. We found that the addition of this layer provides new neuromimetic features to the studied devices: a tenfold increase in Hebbian learning efficiency, a decrease in response time by two orders of magnitude as well as long-term depression/fading memory features. The latter may be very important for nonstandard computational applications, e.g. in reservoir computing.[13]

By illuminating the perovskite device with short light pulses (200 ms, 465 nm), we have observed an increase in the photocurrent with consecutive pulses. However, the device with additional charge-trapping layers exhibits an altered mode of

P. Zawal, T. Mazur, M. Lis, K. Szaciłowski
Academic Centre for Materials and Nanotechnology
AGH University of Science and Technology
al. Mickiewicza 30, Krakow, Poland
E-mail: zawal@agh.edu.pl; tmazur@agh.edu.pl
P. Zawal
Faculty of Physics and Applied Computer Science
AGH University of Science and Technology
al. Mickiewicza 30, Krakow, Poland
M. Lis
Faculty of Materials Science and Ceramics
AGH University of Science and Technology
al. Mickiewicza 30, Krakow, Poland
A. Chiolerio
Center for Sustainable Future Technologies
Istituto Italiano di Tecnologia
Via Livorno 60, Torino 10144, Italy

The ORCID identification number(s) for the author(s) of this article can be found under https://doi.org/10.1002/aelm.202100838.

DOI: 10.1002/aelm.202100838

learning. After initial fast photocurrent growth, a slow decrease, presenting dynamic features and a time scale of long term plasticity, is observed. Here, we present a fabrication and properties of synaptic devices which operate either stimulated by optical or electrical signals. We report that incorporation of a thin layer of C_3N_4 nanoparticles into the HOIP memristive device significantly changes its performance regarding optical stimulation (SRDP mode), whereas the response to electrical stimulation (STDP mode) is not affected by this modification. Our results show that light-induced synaptic effects can be qualitatively altered by the incorporation of a charge-trapping layer into a perovskite-based memristor, whereas the dark characteristics is only slightly modified. The understanding of the mechanisms that govern the observed effects would be an important step towards the design of light-sensitive artificial synapses.

2. Results and Discussion

2.1. Spectroscopic Characterization of Components and Devices

The C_3N_4 nanoparticles have been prepared by the hydrothermal decomposition of thiourea according to a previously reported protocol.[14] The identity of the polyheptazine modifier was confirmed by FTIR and UV–Vis spectroscopies (SI Sections 4, 5 and 6) alongside with TEM imaging in Section 2. Both spectra are almost identical to those previously reported.[15] FTIR spectrum suggests the presence of cyano groups (ν_{CN} = 2090 cm^{-1}) bonded with the carbon framework. The strong shift of this oscillation with respect to potassium melonate (tris(cyanamidoheptazinate), ν_{CN} = 2166 cm^{-1})[16] suggests either partial carbodiimide (C =N =C) character of nitrogen centres, or their interaction with electron acceptor moieties (e.g., polyheptazine–like structures). Considering further observations (vide infra), the latter option seems more justified.

UV–Vis absorption spectrum of nanoparticles suspension shows a broad shoulder within 300–450 nm range as shown in **Figure 1**c. The profile of the spectrum is almost identical to previous reports, moreover, it closely resembles a blue-shifted spectrum of a polyheptazine sample.[17] The low energy tail shows a series of low intensity narrow peaks within 315–370 nm, which may be associated with weak electronic transitions involving a group of various trap states of slightly different energies. The photoluminescence spectrum (Figure 1d) exhibits one strong and broad emission centred at 450 nm (with excitation at 370 nm), which gradually shifts towards lower energies with decreasing excitation energy. Two energy regions with linear non-unity slope of the Stokes shift (inset in Figure 1d) are separated by a narrow (≈0.3 eV) region of a constant Stokes shift, which may be interpreted in terms of the so-called red edge effect,[18] which is a consequence of the heterogeneity of the luminescent species and their environment[19] and is frequently observed in nanoparticles suspensions.[20] In the

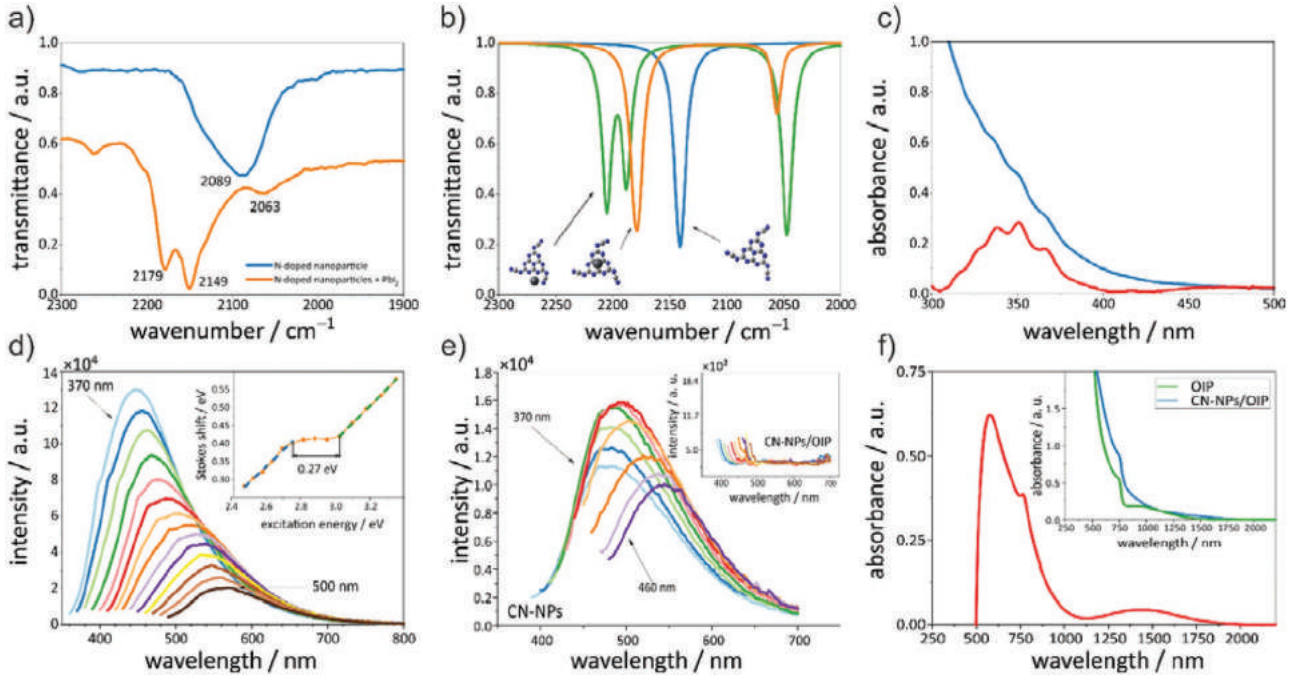

Figure 1. a) FT-IR spectra (normalized transmittance) of CN-NPs purified by Soxhlet extraction and purified CN-NPs mixed with crystalline PbI_2. b) The theoretical IR spectrum of the pure CN-NP model–tris(cyanamidoheptazinate) and its two lead(II) complexes, serving as perovskite- CN-NPs models. A significant splitting and red shift is a fingerprint of this interaction. c) UV–Vis absorption spectrum of a colloidal solution of CN-NPs in toluene. Red line represents a magnified section of the isolated spectral component related to the trap states manifold. d) Fluorescence spectra of purified CN-NPs in toluene. Excitation wavelengths range from 370 to 500 nm. Inset shows Stokes shifts versus the excitation energy. e) Fluorescence spectra of purified CN-NPs on a glass substrate. Excitation wavelengths range from 370 to 460 nm. Inset shows the same sample after deposing of OIP layer on top of the CN-NPs. f) Differential UV-Vis spectrum showing absorption attributed to the charge trapping process together with absorption spectra of OIP and CN-NPs/OIP thin layer devices.

studied case the observed red edge effect implies the presence of two intraband gap states, the shallow non-emissive state and a deeper, emissive one, at least 0.3 eV below the shallow trap state. Interestingly, these spectral features are observed also in thin (≈50 nm) films of polyheptazine nanoparticles (Figure 1e). This explanation is corroborated by the weak trap-related peaks in the absorption spectrum spanning the range of ≈0.5 eV (cf. Figure 1c). These luminescent transitions are completely quenched when a thin layer (≈340 nm) of lead iodide perovskite is deposited on top of this layer (inset in Figure 1e), which may indicate an efficient photoinduced electron transfer involving perovskite as an electron donor and polyheptazine nanoparticles as an electron acceptor. Such a hypothesis is fully justified in the light of the well-known electron acceptor character of g-C_3N_4 and other polyheptazine (nano)materials[17,21] and is consistent with previous reports of similar systems.[22]

The interaction between the C_3N_4 nanoparticles and HOIP has been investigated by the means of FTIR spectroscopy. Experimental results have been supplemented with the DFT modelling. It can be assumed that among all components of HOIP only lead ions can be engaged in interactions with CN-NPs, especially those with cyanamido terminations: lone electron pairs on these ligands can interact with empty 6p orbitals of Pb^{2+}. Indeed, the FTIR spectra of CN-NPs impregnated with PbI_2 solution show a significant rearrangement of the vibrational spectrum in the ν_{CN} region: the single band is the ν_{CN} band is split into three bands, two of which are bathochromically shifted (red shifted) with respect to the ν_{CN} vibration in nanoparticles as depicted in Figure 1a.

The same effect was observed in the case of a theoretical model system, in which the lead ion was complexed with tris(cyanamidoheptazinate) anion. Interestingly, the splitting and shifts were observed irrespectively of the binding mode (side-on versus face-on, cf. Figure 1b), however only side-on interaction results in the pattern observed in the experiment.

UV–Vis transmission spectra of these films of perovskite layers are consistent with a direct bandgap semiconductor character of methylammonium iodoplumbate of $E_g = 1.5$ eV.[23] The absorption spectra of layered structures are, however, significantly different. Whereas the band gap of the perovskite material seems to be unaffected, new transitions at ≈565 and 1403 nm appear (Figure 1f). These new transitions may be attributed to the absorption spectra of anionic forms of polyheptazine nanoparticles, i.e., electron-trapped forms. Electron trapping in polyheptazine materials is usually accompanied by a broad absorption spanning across the visible range[21] or significant spectral changes at 530 and 1300 nm,[24] however the contribution of metal-to-ligand charge transfer processes in heptazine-lead(II) assemblies cannot be excluded.

Finally, the acceptor character of polyheptazine nanoparticles can be deduced from work function measurements (Supporting Information, SI, Section 7). The work function of freshly prepared perovskite layers of ITO was estimated to be 4.60 ± 0.01 eV in ambient air. Upon deposition of nanoparticles the work function of the surface increased by ≈0.51 eV yielding the final value of 5.11 ± 0.01 eV under identical experimental conditions. This behavior is fully consistent with the presence of an electron acceptor at the semiconductor's surface resulting in a dipole moment perpendicular to the surface.[25]

All these observations constitute solid evidence not only for strong electronic interactions between perovskite layers and polyheptazine nanoparticles, but more importantly, they indicate a significant electron transfer process which results in electron trapping at nanoparticles. This in turn should have a profound influence on resistive switching and the dynamics of resistive devices based on these materials.

2.2. Memristive Properties and Synaptic Plasticity

The memristive properties of the device are indicated by a pinched hysteresis loop in current-voltage measurements (**Figure 2**a,b). The device is gradually switched from a high resistance state (HRS) into a low resistance state (LRS) with increasing positive polarization–for the configuration where the metal electrode acts as a working electrode. The reset process occurs during the negative scan, setting the device back into HRS. This indicates that the device is the n-type semiconductor Schottky-junction type memristor.[10b,26] Interestingly, the resistive switching performance of the Au/HOIP/ITO and Au/HOIP/CN-NPs/ITO observed under potentiodynamic conditions are the same and do not depend on illumination (Figure 2c). This indicates, that the resistive switching (observed here as an I/V hysteresis loop) does not engage the HOIP/ITO interface but should be attributed to the switching via modulation of the Schottly barrier at the Au/HOIP interface. This conclusion is fully consistent with our previous observations in related systems.[10a,26] The device structures are presented in Figure 2d. Figure 2e,f contain spike-timing dependent plasticity (STDP) represented with an antisymmetric Hebbian learning rule. STDP relies on adjusting the synaptic weights Δw according to the order and temporal correlation of pre- and post-synaptic spikes. When the presynaptic spike precedes the postsynaptic one, the Δw is positive and the synaptic connection is strengthened (potentiated). Conversely, when the postsynaptic spike arrives before the presynaptic one, the Δw is negative and the synaptic connection is weakened (depressed). In the Hebbian learning, as the time interval Δt decreases, the magnitude of Δw increases for the potentiation and decreases for the depression. The type of learning curve obtained in STDP experiments is strongly correlated with the shape of the pre- and post-spike voltage scheme.[27] For Hebbian learning we chose bipolar switching pulses.

We measured the current upon the application of a symmetric bipolar voltage pattern to the top Au (presynaptic) and bottom ITO (postsynaptic) electrode and calculated the Δw according to the formula: $\Delta w = \frac{i_{post} - i_{pre}}{i_{pre}}$, where i_{pre} and i_{post} are the currents measured before and after the sequence of the voltage pulses (see Section 8.2 in SI).

Despite that the character of the Hebbian learning is the same among the devices, the observed Δw changes are approximately an order of magnitude higher in CN-NPs/OIP/Au device. On the other hand, the Δw values became more scattered but the antisymmetric character of the Hebbian learning curve is more pronounced in the CN-NPs/OIP/Au device. We emphasize that the crucial feature here is the presence of antisymmetric Hebbian rules in both of the devices. Along

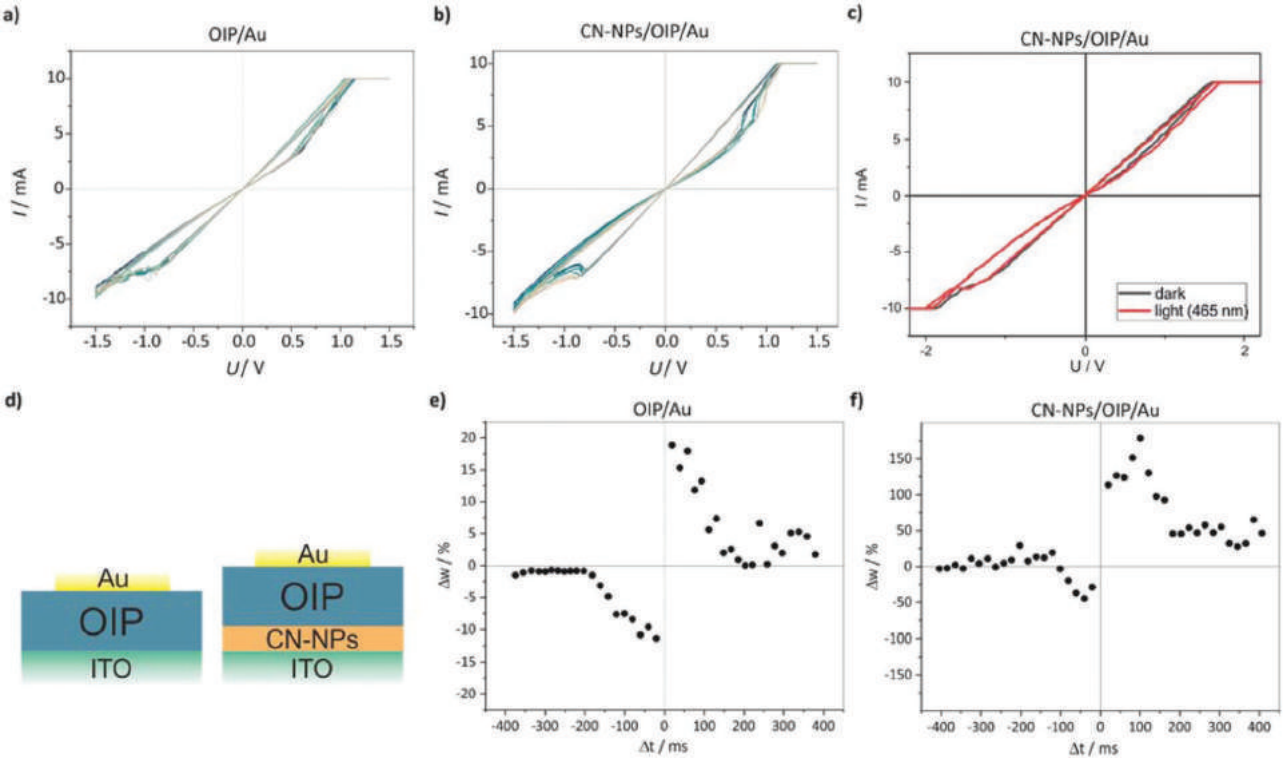

Figure 2. a) *I–V* scans of OIP/Au and b) CN-NPs/OIP/Au. Pinched hysteresis loops indicate memristive character of both types of the devices. c) Comparison of *I–V* scans of CN-NPs/OIP/Au device, performed in dark and with 465 nm light. No significant changes in the hysteresis loops were observed. Current compliance was set to 10 mA. d) Schematic representation of the layered devices. Hebbian learning rule represented by spike-timing dependent plasticity (STDP). e,f) The character of Hebbian learning of the memristive device remained the same after incorporation of CN-NPs layer, yet the Δw increased ten-fold.

with improved Hebbian learning features, the interaction with light has been significantly altered by the incorporation of the charge-trapping material. Owing to their high absorption coefficient, defect tolerance, long charge carrier lifetimes and low exciton binding energies, perovskites can efficiently generate charge carriers upon illumination. The influence of light on memristive properties involves modulation of the Schottky barrier height.[28] Illuminating perovskite memristive devices increases the energy barrier for migration of iodine vacancies in the electric field gradient, which in turn allows tuning synaptic functions with light.[29] However, the field of light-sensitive artificial synapses still remains largely uninvestigated.

I–V scans were performed in the voltage range of ±1.5 V and with current compliance (CC) set to 10 mA to prevent electrical breakdown of the devices. The potential was applied to the top Au electrode with the bottom ITO electrode grounded.

In order to compare the conducting mechanisms between the OIP/Au and CN-NPs/OIP/Au, we fitted the *I–V* curves according to different conducting mechanisms. In both devices, the LRS is dominated by ohmic conduction. The high symmetry of *I–V* curves in positive and negative regimes suggests that no Schottky barrier (or very low barrier) is present at the Au/OIP interfaces. This is a consequence of the similar work functions of OIP and Au (**Figure 3**).

However, the HRS contains more complex conduction mechanisms. Both devices exhibit large ohmic components with the addition of space-charge limited current (SCLC). However, the slope of the line fitted in the non-Ohmic conduction mechanism regime shows an increase from 1.12 to 1.33, which is not present in OIP/Au device. Moreover, in the CN-NPs/OIP/Au device, switching occurs at 0.87 V, which is a higher potential value than in OIP/Au device (0.62 V). The observed current amplitude changes were higher in CN-NPs/OIP/Au device. All these observations suggest a different kind of charge traps and a higher charge trap concentration in the CN-NPs/OIP/Au device.

To investigate the possibility of inducing synaptic effects with light, we have applied trains of light pulses (t = 200 ms, Δt = 200 ms, λ = 465 nm, I = 60 mW cm^{-2}) to devices switched to HRS with different voltages. Devices at LRS generated photocurrent orders of magnitude lower, which is again consistent with the Schottky junction memristor properties (see SI, Figure S8). The putative mechanism of this behavior is described in the subsequent section. The OIP/Au devices generate photocurrent, the amplitude of which gradually increases with time and finally reaches a plateau. The facilitation is produced by a train of 5 Hz light pulses and closely resembles the short-term facilitation (STF), which is a form of short-term synaptic plasticity (**Figure 4**a).[30] Interestingly, we have observed that incorporation of a charge-trapping layer altered the photocurrent generation dynamics, resulting in different types of synaptic learning. In the CN-NPs/OIP/Au device, after a short increase of photocurrent amplitude, we have observed a gradual decrease of photocurrent amplitude with

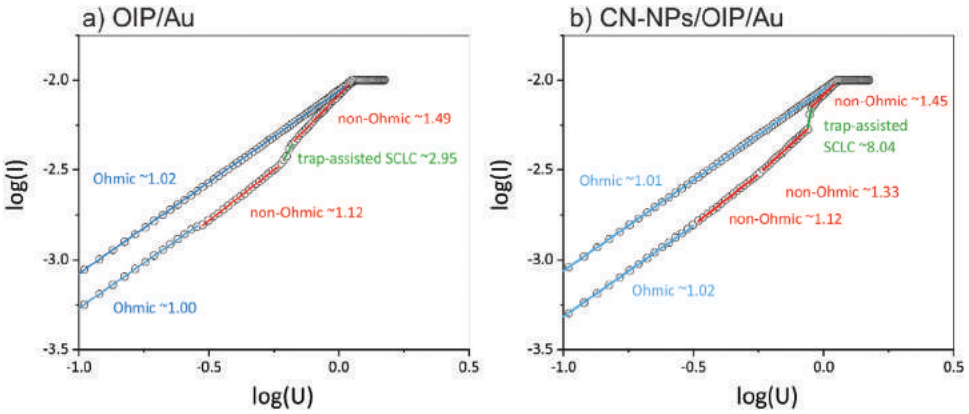

Figure 3. Current-voltage characteristics of a) OIP/Au and b) CN-NPs/OIP/Au devices in a double logarithmic plot, positive bias. The different conduction mechanisms and corresponding slopes are listed in the plots.

each consecutive spike (Figure 4b). This behaviour is analogous to long-term depression (LTD), a phenomenon occurring in synapses experiencing depletion of neurotransmitters (vide infra, cf. Equation 1). Here, the long term is associated with timescales of particular effect which are several orders of magnitude larger than the initial excitation phenomena. STF and LTD both play an important role in adjusting the sensitivity of sensory networks to correctly process sensory signals.[31] It is noteworthy, that the initial growth in the photocurrent amplitude is observed regardless of the switching voltage pulse length and waiting period after switching (see SI, Section 9.1). Moreover, the photocurrent amplitude depends on the conductivity of the device and can be used for optical reading of the resistive states (see SI, Section 9.2).

There are some reports on light-controlled memristive devices,[6a] which in principle belong to three classes: transistor-like structures, where light excitation changes the conductivity of the channel,[32] systems in which excitation increases the conductivity due to the efficient removal of oxygen vacancies,[33] and devices in which light disrupts conductive filaments,[29] no light-induced plastic behavior in a memristive system have been reported so far, however some recent contributions indicate the importance of such features for the development of self-powered neuromorphic computing systems.[7] We have presented a short comparison of the available systems in **Table 1**. A term solaristor has been conned for light-sensitive hybrid devices, combining features of phototransistor with that of a ferroelectric memory cell.[34] The current study shows a new implementation of this idea: a light-sensitive memristor, with two different plasticities: voltage-driven and light-driven, which operates with various inputs and at different time scales. This device also offers a possibility for facile realization of light-induced neuromorphic functions in a simple two-terminal device based on common materials.

2.3. Photomemristive Switching Mechanism

OIP and related materials usually form Schottky junctions with metal electrodes, whereas junctions with ITO are close to Ohmic ones.[10b,26] The electronic structure of the Au/OIP/ITO cell is shown in **Figure 5**a,b.

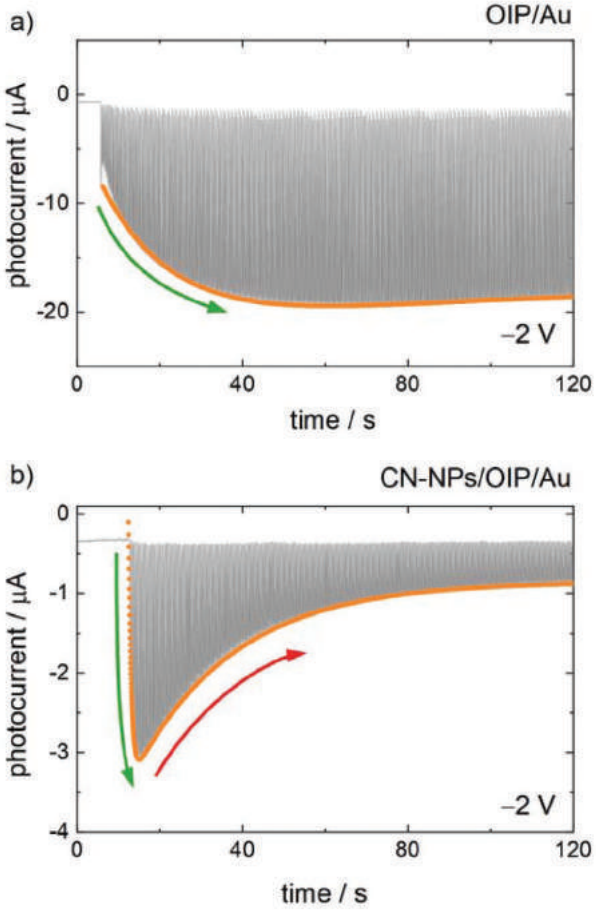

Figure 4. a) The distinct dynamics of photocurrent generation measured in perovskite device (OIP/Au) and perovskite memristive device with incorporated charge trapping layer of carbon nitride nanoparticles (CN-NPs /OIP/Au). The devices were irradiated from the side of the ITO electrode with short (200 ms) 465 nm light pulses with frequency of 5 Hz and the photocurrent was measured at the Au electrode. Without the charge-trapping layer, the photocurrent amplitude and generation dynamics are independent on switching voltage. The gradual growth of photocurrent can be attributed to learning (green arrow). b) When the charge-trapping layer was incorporated, after the initial growth (short-term facilitation, green arrow), we observed a gradual decrease of photocurrent amplitude (long-term depression, red arrow).

Table 1. Memristive Devices Systems with both Light and Electric-Driven Functionalities.

Device structure	Device unique features	ELECTRIC signal characteristics (working voltage ranges)	PHOTONIC signal characteristics	Neuromorphic functionalities	Ref.
Au/Pentacene/Al_2O_3/**$CsPbBr_3$**/SiO2	Due to asymmetric structure, it is possible to reversibly accumulate charge in the semiconductors junction.	SET: +40 V; RESET: −60V; electric impulses of 35 V/0.5 s	light pulses of 365 nm	electric: hysteresis (non-linear behavior), PPF, STDP, Potentiation/depression light response: PPF	[35]
Au/Pentacene/ PMMA/ **2D imine polymer** (2DP)/SiO_2	Very low operating voltage and ultralow energy consumption of ~0.29 pJ per synaptic event. Electron trapping in 2D polymer layer.	the devices exhibit obvious synaptic responses under a voltage of −0.1 V	light pulses of 400 nm and 450 nm	electric: hysteresis, electric excitatory postsynaptic current (EPSC) light response: EPSC, PPF, STM to LTM transition, and dynamic filtering	[36]
Au/**$MAI_xFAI_{1-x}PbI_3$**/ITO	MA halide-doped perovskite artificial synapse can be tuned by light irradiation and electric stimulus simultaneously.	electric impulses: (−1 V, 0.21 s up to −5 V)	white light pulses	electric STP, LTP, potentiation and depression have been achieved light response: changes in plasticity (metaplasticity)	[37]
Au–**MoS_2 nanospheres**–Au (planar design)	One of the first multiresistive photoswitchable devices. Under irradiation ON/OFF resistance ratio increases.	CV scans from 0 V to 8 V, electric pulses of +8 V	light pulses from the ranges of MoS_2 bandgap (1.5–1.9 eV)	boolean logic gates–TRUE, AND; "fuzzy logic"–IF; sample application for photo image acquisition and compression hysteresis curve and HRS/ multiple LRS switching	[38]
Au/PMMA/**(CdSe/ZnS QDs)/ $CsPbBr_3$ QDs**/ITO	Photonic plasticity is attributed to charge trapping/de-trapping processes in CdSe/ZnS nanoparticles.	CV scans from 0 to −3 V and from 0 to +3 V, separately	light pulses of 405 nm, from 0.06 mW cm^{-2} to 168 Mw cm^{-2})	electric response: potentiation, depression, EPSC, STP, LTP light induced-learning/forgetting, STM to LTM transition; In addition: devices stay fully operable under bending tests	[39]
Au/**$MAPbI_3$/CN-NPs**/ITO	Exhibits plasticity effect upon stimulation with light; different plasticity type then for the device without charge-trapping layer.	CV sans form −2 V to +2 V; STDP with pulses of +/−1.6 V	light pulses of 465 nm	electric response: hysteresis, STDP light response: SRDP, STF behavior	this work

In the low resistive state the metal-induced gap states (MIGS) as well as other intragap states, are empty and therefore the Schottky barrier at the metal/semiconductor interface is low. At the bias voltage close to zero it results in a high hole injection barrier, the situation close to the flatband state of the semiconductor favors exciton annihilation or efficient recombination of electrons and holes. This situation should lead to low photocurrent intensity (Figure 5a and SI Figure S8). This is actually being observed in the case of LRS devices. Switching to HRS requires high negative polarization of the metal electrode. It results in the filling of intra-gap states, resulting in an increased Schottky barrier and consequently efficient photocurrent generation due to intrinsic electric field gradient (Figure 5b). Incorporation of carbon nitride nanoparticles introduces another family of intra-gap states (located near the ITO electrode), which are strongly coupled to the lead centres within the perovskite layer (cf. Figure 1). These states, which originally are only partially filled induce the formation of a second Schottky-like barrier at the OIP/ITO interface (Figure 5c). This barrier, however, should be very low due to the passivation of perovskite surface states by interaction with terminal cyano groups (cf. Figure 1).[22b] During illumination some photogenerated electrons are trapped at CN-NPs (as heptazine derivatives are very efficient electron traps),[40] which in turn results in an increase of Schottky barrier height. In consequence, photocurrent intensity is decreased due to possible charge carrier recombination and disfavored electron transfer to the ITO substrate (Figure 5d). The interplay between two charge trapping processes (at MIGS of the Au/OIP junction and CN-NPs ones) results in complex photocurrent profiles, which, by analogy to biological systems,[41] can be approximated with the exponential growth/decay function (Equation 1):

$$I_{\text{photocurr}}(t) = A_f e^{-t/\tau_1} - A_d e^{-t/\tau_2} \quad (1)$$

where A_f is the facilitation coefficient and A_d is the depression coefficient, whereas τ_1 and τ_2 are time constants for facilitation and depression processes, respectively. Based on fitted function the time constants were 12.3 s and 207.0 s for the facilitation and depression of the OIP/Au device, respectively, with the depression coefficient being negligibly small. Thus almost only potentiation signal is registered for undoped samples. For the carbon nitride enriched sample much faster photocurrent dynamics is present. The two exponential function indicate a dynamic

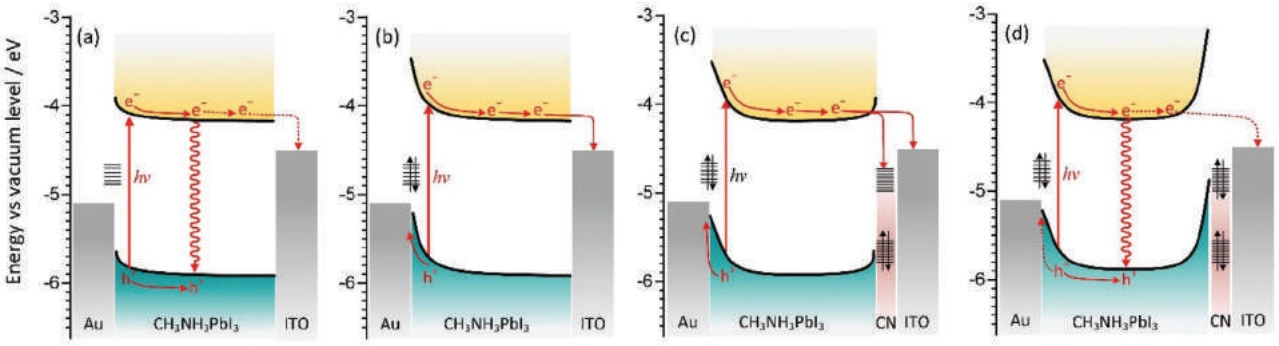

Figure 5. A tentative mechanism of resistive switching and photocurrent generation in a,b) Au/OIP/ITO and c,d) Au/OIP/CN-NPs/ITO devices: charge carrier recombination in the LRS state (a) and efficient photocurrent generation in the HRS state (b); photocurrent generation and charge trapping at CN-NPs in the HRS state (c) results in a built-up of a second barrier, which effectively prevents photocurrent generation (d). Band edge potentials of OIP are taken from Ref. [42] the position of trap stated of carbon nitride nanoparticles is estimated according to Ref. [43] CN stands for carbon nitride nanoparticles.

change for both growth/decay–time constants were 0.640 s and 24.1 s for facilitation and depression, respectively. Difference between constants of two orders of magnitude alongside with comparison: time constant–pulse length indicates long-term character of described depression effects.

Incorporation of charge trapping particles at one of the interfaces enables electrical and optical control of two energy barriers at both sides of the device, which translates into improved Hebbian learning (but with slightly distorted symmetry, in which facilitation is more pronounced than depression in the case of reversed order of pre- and post-synaptic pulses, which is observed in the case of resistive switching involving ferroelectric materials[44]), much faster responsivity (facilitation time constant increases by two orders of magnitude, and the depression one by one order of magnitude) and a complex resistive switching. The lack of symmetry of learning curves is a consequence of different time scales for facilitation and depression processes,[45] i.e. different rate constants of charge trapping near the Au and ITO terminals.

In spite of previous reports (vide supra), mutual charge trapping at two interfaces with different yields results in a unique plastic behavior, combining short time facilitation and short time depression within a single structure. This unprecedented behavior may be useful for advanced information processing approaches which utilize dynamic memory and a continuum of resistive states, e.g. reservoir computers and liquid state machines.[46]

3. Conclusions

In the present study, we have demonstrated that incorporation of a charge-trapping layer to the HOIP-based memristor does not induce its electrical plasticity in a qualitative way, but deeply modifies a parallel, light-induced plasticity. The two parallel plasticity regimes are a result of charge trapping phenomena at the device's interfaces: they are separated in space due to the device's architecture and in time due to the different time scale of voltage- and light-induced phenomena. The possibility of independent modification of one plasticity regime created a possibility of the construction of novel optoelectronic synaptic devices with complexity much higher than the devices reported so far. We have shown that both Au/HOIP/ITO and Au/HOIP/CN-NPS/ITO devices exhibit a very similar form of spike-timing dependent plasticity, however, two distinct types of plasticity effects (short-term facilitation and long-term depression) were observed in these devices upon stimulation with light. We have attributed the different characters of light-induced synaptic-like effects to the trapping properties of the CN-NPs layer. We have also demonstrated that light-induced processes may be used for optical reading of the resistive state of perovskite memristive devices.

4. Experimental Section

Synthesis of carbon nitride nanoparticles was conducted with a modified method described elsewhere.[14] Thiourea (0.46 g) and citric acid (0.42 g) were dissolved in 10 ml of water, colorless solution was placed in an ERTEC microwave reactor where hydrothermal synthesis was carried out at 200 °C for 2 h at a working pressure between 14–16 atm. The black solution was obtained and then water was evaporated on a rotary evaporator to give a dark green product insoluble in toluene. The purification of the synthesis from the organic contamination consisted of the extraction in toluene using the Soxhlet apparatus for 4 h following the literature.[47] As a result of this process, a greenish-yellow toluene solution was received and subjected to further spectroscopic examination. To synthesize comparative carbon QDs, the same synthesis with glucose (0.54 g) instead of thiourea was performed. The purification process was the same as for CN-NPs.

Methylammonium lead iodide (OIP) was synthesized with the conventional two-step method. All the steps were conducted in the ambient atmosphere. PbI2 (Sigma Aldrich) solution was prepared by dissolving 461 mg of PbI2 in DMF and stirred at 70 °C for several hours. Immediately before spin coating, the solution was filtered with a 200 µm PTFE filter. 0.3 M methylammonium iodide (MAI, Ossila) solution was prepared by dissolving 53 mg of MAI in 1 ml of isopropyl alcohol. ITO substrates were sonicated for 5 min in a 1% solution of Hellmanex in hot water, followed by the same protocol executed in hot water and in isopropanol. The last cleaning stage consisted of exposing ITO to oxygen plasma for 10 min.

The CN-NPs layer was deposited at 3000 rpm and placed on the hotplate at 70 °C for 10 min. The heated substrate was subsequently coated with a PbI2 layer (4000 rpm, 45 s) and dried for 10 min at 70 °C on a hotplate. Next, 100 µl of MAI solution was spin coated (3000 rpm, 60 s) on the hot substrate and within 6–8 s later 200 µl of ethyl acetate was dripped on the spinning surface. The substrate was subsequently placed on a hotplate for 10 min at 100 °C to crystallize. Finally, 70 nm thick Au electrodes were sputtered on top through a shadow mask. The active area of the device was 2.25 mm^2. To measure the thicknesses

of the OIP and CN-NPs layers, the layers on silicon substrates were deposited according to the above protocol. The thickness was measured with the Bruker Dimension ICON XR AFM. The OIP and CN-NPs layers were determined to be 300 nm and 33 nm thick, respectively. (Figure S2 in the Supporting Information).

UV-Vis spectra of the as-prepared $CH_3NH_3PbI_3$ were measured on Bruker Lambda 750 spectrophotometer in transmission mode. The absorbance spectrum is shown in Figure S3, Supporting Information.

FT-IR spectra were measured on a Bruker Tensor II FTIR spectrophotometer. The NEC QDs sample was dried by evaporation of toluene and the dry product was transferred on ATR crystal. To prepare the CN-NPs/PbI2 sample, the toluene was evaporated from the CN-NPs sample, added dry CN-NPs to PbI_2 dissolved in DMF, sonicated for 20 min and dried on the microscope substrate. The dry powder was scraped, transferred onto ATR crystal (Ge) and measured in the ATR mode.

Fluorescence measurements were conducted using an Edinburgh Instruments Spectrofluorometer FS5 in standard 1 cm quartz cells (solutions) or in the Front Face sample holder (solid samples).

Work functions of samples have been measured using the KP020 ambient Kelvin probe system (KP Technologies, UK) with 1 mm and 5 mm sensor electrodes. 1000 measurements have been collected for gold reference and studied samples in the dark. The OIP sample was prepared according to the previously described protocol. For the measurement, CN-NPs were spincoated (3000 rpm) on top of the OIP layer.

The *I–V* scans and spike-timing dependent plasticity (STDP) measurements were performed on Keithley 4200-SCS in a two-electrode setup with Au as the active electrode and the bottom ITO electrode grounded. The electrical connections to ITO and Au electrodes were established by pressing a tungsten probing tip (Everbeing Int'l Corp.) installed in micropositioners to the corresponding electrodes. *I–V* scans were performed within the ±1.5 V voltage range with current compliance (CC) set to 10 mA to prevent electrical breakdown of the sample. The potential was applied to the top Au electrode with the bottom ITO electrode grounded.

DFT modelling has been performed using the Gaussian 09 Rev. E.01 software package at the B3LYP/SDD level of theory. This choice is motivated by simplification of computational approach: the SDD basis set comprises the D95 basis set[48] for lighter elements and a Stuttgart/Dresden Effective Core Potential[49] for heavier ones, therefore can be used for the whole system containing both light and heavy elements, and yield results of satisfactory quality.

Supporting Information

Supporting Information is available from the Wiley Online Library or from the author.

Acknowledgements

The authors thank Prof. Grzegorz Hess (Faculty of Biology, Jagiellonian University) for consultations regarding the interpretation of synaptic-like effects. The authors thank Dr. Marta Gajewska (Academic Centre for Materials and Nanotechnology, AGH University of Science and Technology) for TEM imaging of the samples. The authors acknowledge the financial support from the Polish National Science Center within the MAESTRO (grant agreement No. UMO-2015/18/A/ST4/00058) and PRELUDIUM (grant agreement No. UMO-2018/31/N/ST5/03215) projects. PZ has been partly supported by the EU Project POWR.03.02.00-00-I004/16. DFT calculations were performed at the Academic Computer Centre CYFRONET AGH within computational grant PLGSURFACE2. This research was partly supported by program "Excellence initiative–research university" for the AGH University of Science and Technology.

Conflict of Interest

The authors declare no conflict of interest.

Author Contributions

Conceptualization, P. Z., T. M., K. S.; Methodology P. Z., T. M., A.C., K. S.; Investigation, P. Z., T. M., M. L., K. S; Writing – Original Draft, P. Z., T. M., M. L., A.C., K. S.; Preparation, P. Z., T. M., M. L., K. S.; Visualization, P. Z., T. M., M. L., A.C., K. S.; Funding Acquisition, K. S., P. Z. All authors have given approval to the final version of the manuscript. P.Z. and T.M. contributed equally to this work. The authors declare no conflicts of interest. Data Availability Statement.

Data Availability Statement

The data that support the findings of this study are available from the corresponding author upon reasonable request.

Keywords

carbon nitride (C_3N_4), neuromimetic behavior, organic-inorganic perovskites, unconventional information processing

Received: August 10, 2021
Revised: November 2, 2021
Published online:

[1] a) J. Shamsi, A. S. Urban, M. Imran, L. De Trizio, L. Manna, *Chem. Rev.* **2019**, *119*, 3296; (b) L. N. Quan, B. P. Rand, R. H. Friend, S. G. Mhaisalkar, T. W. Lee, E. H. Sargent, *Chem. Rev.* **2019**, *119*, 7444; (c) A. K. Jena, A. Kulkarni, T. Miyasaka, *Chem. Rev.* **2019**, *119*, 3036; (d) S. Klejna, T. Mazur, E. Wlaźlak, P. Zawal, H. S. Soo, K. Szaciłowski, *Coord. Chem. Rev.* **2020**, *415*, 213316.

[2] a) Y. Sun, M. Tai, C. Song, Z. Wang, J. Yin, F. Li, H. Wu, F. Zeng, H. Lin, F. Pan, *J. Phys. Chem. C* **2018**, *122*, 6431; b) Z. Xiao, J. Huang, *Adv. Electron. Mater.* **2016**, *2*, 1600100; c) G. Cao, C. Cheng, H. Zhang, H. Zhang, R. Chen, B. Huang, X. Yan, W. Pei, H. Chen, *J. Semicond.* **2020**, *41*, 051205; d) X. Xiao, J. Hu, S. Tang, K. Yan, B. Gao, H. Chen, D. Zou, *Adv. Mater. Technol.* **2020**, *5*, 1900914.

[3] Y. V. Pershin, M. Di Ventra, *Adv. Phys.* **2011**, *60*, 145.

[4] R. Wang, J.-Q. Yang, J.-Y. Mao, Z.-P. Wang, S. Wu, M. Zhou, T. Chen, Y. Zhou, S.-T. Han, *Adv. Intell. Syst.* **2020**, *2*, 2000055.

[5] a) R. Midya, Z. Wang, S. Asapu, S. Joshi, Y. Li, Y. Zhuo, W. Song, H. Jiang, N. Upadhay, M. Rao, P. Lin, C. Li, Q. Xia, J. J. Yang, *Adv. Electron. Mater.* **2019**, *5*, 1900060; b) E. Wlaźlak, D. Przyczyna, R. Gutierrez, G. Cuniberti, K. Szaciłowski, *Jpn. J. Appl. Phys.* **2020**, *59*, SI0801.

[6] a) K. Pilarczyk, E. Wlaźlak, D. Przyczyna, A. Blachecki, A. Podborska, V. Anathasiou, Z. Konkoli, K. Szaciłowski, *Coord. Chem . Rev.* **2018**, *365*, 23; b) A. Chiolerio, I. Roppolo, V. Cauda, M. Crepaldi, S. Bocchini, K. Bejtka, A. Verna, C. F. Pirri, *Nano Res.* **2015**, *8*, 1956.

[7] A. Pérez-Tomás, *Adv. Mater. Interfaces* **2019**, *6*, 1900471.

[8] Y. Fang, S. Zhai, L. Chu, J. Zhong, *ACS Appl. Mater. Interfaces* **2021**, *13*, 17141.

[9] J. Y. Kim, J.-W. Lee, H. S. Jung, H. Shin, N.-G. Park, *Chem. Rev.* **2020**, *120*, 7867.

[10] a) T. Mazur, P. Zawal, K. Szaciłowski, *Nanoscale* **2019**, *11*, 1080; b) E. Wlaźlak, P. Zawal, K. Szaciłowski, *ACS Appl. Electron. Mater.* **2020**, *2*, 329.

[11] a) G. Seo, Y. Saito, M. Nakamichi, K. Nakano, K. Tajima, K. Kanai, *Sci. Rep.* **2021**, *11*, 17833; b) R. Godin, Y. Wang, M. A. Zwijnenburg, J. Tang, J. R. Durrant, *J. Am. Chem. Soc.* **2017**, *139*, 5216.

[12] N. Liu, T. Li, Z. Zhao, J. Liu, X. Luo, X. Yuan, K. Luo, J. He, D. Yu, Y. Zhao, *ACS Omega* **2020**, *5*, 12557.

[13] L. F. Seoane, *Phil. Trans. B* **2019**, *374*, 20180377.
[14] A.-J. Wang, H. Li, H. Huang, Z.-S. Qian, J.-J. Feng, *J. Mater. Chem. C* **2016**, *4*, 8146.
[15] H. Li, F.-Q. Shao, H. Huang, J.-J. Feng, A.-J. Wang, *Sens. Actuators, B* **2016**, *226*, 506.
[16] A. Sattler, W. Schnick, *Eur. J. Inorg. Chem.* **2009**, *2009*, 4972.
[17] H. Schlomberg, J. Kröger, G. Savasci, M. W. Terban, S. Bette, I. Moudrakovski, V. Duppel, F. Podjaski, R. Siegel, J. Senker, R. E. Dinnebier, C. Ochsenfeld, B. V. Lotsch, *Chem. Mater.* **2019**, *31*, 7478.
[18] a) A. P. Demchenko, in *Perspectives on Fluorescence: A Tribute to Gregorio Weber*, (Ed.: D. M. Jameson), Springer International Publishing, Cham **2016**, pp. 95–141; b) A. P. Demchenko, *Luminescence* **2002**, *17*, 19.
[19] K. A. Al-Hassan, T. Azumi, *Chem. Phys. Lett.* **1988**, *150*, 344.
[20] T. A. Dolenko, S. A. Burikov, A. M. Vervald, A. A. Khomich, O. S. Kudryavtsev, O. A. Shenderova, I. I. Vlasov, *J. Appl. Spectrosc.* **2016**, *83*, 294.
[21] Y. Markushyna, P. Lamagni, C. Teutloff, J. Catalano, N. Lock, G. Zhang, M. Antonietti, A. Savateev, *J. Mater. Chem. A* **2019**, *7*, 24771.
[22] a) M. Ou, W. Tu, S. Yin, W. Xing, S. Wu, H. Wang, S. Wan, Q. Zhong, R. Xu, *Angew. Chem., Int. Ed.* **2018**, *57*, 13570; b) L.-L. Jiang, Z.-K. Wang, M. Li, C.-C. Zhang, Q.-Q. Ye, K.-H. Hu, D.-Z. Lu, P.-F. Fang, L.-S. Liao, *Adv. Funct. Mater.* **2018**, *28*, 1705875; c) Q. Wang, S. Yu, W. Qin, X. Wu, *Nanoscale Adv.* **2020**, *2*, 274.
[23] E. M. Hutter, M. C. Gélvez-Rueda, A. Osherov, V. Bulović, F. C. Grozema, S. D. Stranks, T. J. Savenije, *Nat. Mater.* **2017**, *16*, 115.
[24] A. Savateev, N. V. Tarakina, V. Strauss, T. Hussain, K. ten Brummelhuis, J. M. Sánchez Vadillo, Y. Markushyna, S. Mazzanti, A. P. Tyutyunnik, R. Walczak, M. Oschatz, D. M. Guldi, A. Karton, M. Antonietti, *Angew. Chem., Int. Ed.* **2020**, *59*, 15061.
[25] a) G. Heimel, L. Romener, E. Zojer, J.-L. Bredas, *Acc. Chem. Res.* **2008**, *41*, 721; b) E. Zojer, T. C. Taucher, O. T. Hofmann, *Adv. Mater. Interfaces* **2019**, *6*, 1900581; c) M. V. Lebedev, P. A. Dementev, T. V. Lvova, V. L. Berkovits, *J. Mater. Chem. C* **2019**, *7*, 7327; d) W. E. Ford, D. Gao, N. Knorr, R. Wirtz, F. Scholz, Z. Karipidou, K. Ogasawara, S. Rosselli, V. Rodin, G. Nelles, F. von Wrochem, *ACS Nano* **2014**, *8*, 9173; e) J. Duch, P. Kubisiak, K. H. Adolfsson, M. Hakkarainen, M. Golda-Cepa, A. Kotarba, *Appl. Surf. Sci.* **2017**, *419*, 439.
[26] E. Wlaźlak, M. Marzec, P. Zawal, K. Szaciłowski, *ACS Appl. Mater. Interfaces* **2019**, *11*, 17009.
[27] a) T. Serrano-Gotarredona, T. Masquelier, T. Prodromakis, G. Indiveri, B. Linares-Barranco, *Front. Neurosci.* **2013**, *7*, 00002; b) D. E. Feldman, *Neuron* **2012**, *75*, 556.
[28] F. Zhou, Y. Liu, X. Shen, M. Wang, F. Yuan, Y. Chai, *Adv. Funct. Mater.* **2018**, *28*, 1800080.
[29] X. Zhu, W. D. Lu, *ACS Nano* **2018**, *12*, 1242.
[30] S. L. Jackman, W. G. Regehr, *Neuron* **2017**, *94*, 447.
[31] H. Anwar, X. Li, D. Bucher, F. Nadim, *Curr. Opin. Neurobiol.* **2017**, *43*, 71.
[32] a) W. Wang, G. N. Panin, X. Fu, L. Zhang, P. Ilanchezhiyan, V. O. Pelenovich, D. Fu, T. W. Kang, *Sci. Rep.* **2016**, *6*, 31224; b) P. Maier, F. Hartmann, M. Emmerling, C. Schneider, M. Kamp, S. Höfling, L. Worschech, *Phys. Rev. Appl.* **2016**, *5*, 054011; c) P. Maier, F. Hartmann, M. R. S. Dias, M. Emmerling, C. Schneider, L. K. Castelano, M. Kamp, G. E. Marques, V. Lopez-Richard, L. Worschech, S. Höfling, *Appl. Phys. Lett.* **2016**, *109*, 023501; d) Z.-D. Luo, X. Xia, M.-M. Yang, N. R. Wilson, A. Gruverman, M. Alexe, *ACS Nano* **2020**, *14*, 746; e) Y. Sun, L. Qian, D. Xie, Y. Lin, M. Sun, W. Li, L. Ding, T. Ren, T. Palacios, *Adv. Funct. Mater.* **2019**, *29*, 1902538.
[33] a) D. Berco, D. S. Ang, H. Z. Zhang, *Adv. Intell. Syst.* **2020**, *2*, 1900115; b) J.-Y. Mao, L. Zhou, X. Zhu, Y. Zhou, S.-T. Han, *Adv. Opt. Mater.* **2019**, *7*, 1900766.
[34] A. Pérez-Tomás, A. Lima, Q. Billon, I. Shirley, G. Catalan, M. Lira-Cantú, *Adv. Funct. Mater.* **2018**, *28*, 1707099.
[35] Y. Gong, Y. Wang, R. Li, J.-Q. Yang, Z. Lv, X. Xing, Q. Liao, J. Wang, J. Chen, Y. Zhou, S.-T. Han, *J. Mater. Chem. C* **2020**, *8*, 2985.
[36] J. Zhang, Q. Shi, R. Wang, X. Zhang, L. Li, J. Zhang, L. Tian, L. Xiong, J. Huang, *InfoMat* **2021**, *3*, 904.
[37] J. Gong, H. Wei, Y. Ni, S. Zhang, Y. Du, W. Xu, *Mater. Today Phys.* **2021**, *21*, 100540.
[38] W. Wang, G. N. Panin, X. Fu, L. Zhang, P. Ilanchezhiyan, V. O. Pelenovich, D. Fu, T. W. Kang, *Sci. Rep.* **2016**, *6*, 31224.
[39] Z. Chen, Y. Yu, L. Jin, Y. Li, Q. Li, T. Li, Y. Zhang, H. Dai, J. Yao, *Mater. Des.* **2020**, *188*, 108415.
[40] a) V. W.-h. Lau, V. W.-z. Yu, F. Ehrat, T. Botari, I. Moudrakovski, T. Simon, V. Duppel, E. Medina, J. K. Stolarczyk, J. Feldmann, V. Blum, B. V. Lotsch, *Adv. Enegry Mater.* **2017**, *7*, 1602251; b) X. Wang, K. Maeda, A. Thomas, K. Takanabe, G. Xin, J. M. Carlsson, K. Domen, M. Antonietti, *Nat. Mater.* **2009**, *8*, 76.
[41] a) G. Q. Bi, M. M. Poo, *J. Neurosci.* **1998**, *18*, 10464; b) R. Legenstein, D. Pecevski, W. Maass, *PLoS Comput. Biol.* **2008**, *4*, e1000180.
[42] J.-M. Yang, Y. Luo, Q. Bao, Y.-Q. Li, J.-X. Tang, *Adv. Mater. Interfaces* **2019**, *6*, 1801351.
[43] H. Z. Wu, L. M. Liu, S. J. Zhao, *Phys. Chem. Chem. Phys.* **2014**, *16*, 3299.
[44] S. Majumdar, H. Tan, Q. H. Qin, S. van Dijken, *Adv. Electron. Mater.* **2019**, *5*, 1800795.
[45] S. Zappacosta, F. Mannella, M. Mirolli, G. Baldassarre, *P. L.oS. Comp. Biol* **2018**, *14*, e1006227.
[46] a) S. B. Cooper, A. Sorbi, *Computability in Context: Computation and Logic in the Real World*, Imperial College Press, London, **2011**, p. 420; b) G. Tanaka, T. Yamane, J. B. Héroux, R. Nakane, N. Kanazawa, S. Takeda, H. Numata, D. Nakano, A. Hirose, *Neural Networks* **2019**, *115*, 100; c) D. Przyczyna, P. Zawal, T. Mazur, M. Strzelecki, P. L. Gentili, K. Szaciłowski, *Jpn. J. Appl. Phys.* **2020**, *59*, 050504; d) A. Chiolerio, *Adv. Intell. Syst.* **2020**, *2*, 2000120.
[47] J. R. Holst, E. G. Gillan, *J. Am. Chem. Soc.* **2008**, *130*, 7373.
[48] T. H. Dunning, P. J. Hay, in *Methods of Electronic Structure Theory*, (Ed.: H. F. Schaefer), Springer US, Boston, MA **1977**, pp. 1–27.
[49] U. Wedig, M. Dolg, H. Stoll, H. Preuss, in *Quantum Chemistry: The Challenge of Transition Metals and Coordination Chemistry*, (Ed.: A. Veillard), Springer Netherlands, Dordrecht **1986**, pp. 79–89.

ADVANCED ELECTRONIC MATERIALS

Supporting Information

for *Adv. Electron. Mater.,* DOI: 10.1002/aelm.202100838

Light-Induced Synaptic Effects Controlled by Incorporation of Charge-Trapping Layer into Hybrid Perovskite Memristor

Piotr Zawal, Tomasz Mazur,* Maria Lis, Alessandro Chiolerio, and Konrad Szaciłowski*

Supporting Information (SI) for:

Light-induced synaptic effects controlled by incorporation of charge-trapping layer into hybrid perovskite memristor

Piotr Zawal[*,a,b], *Tomasz Mazur*[*,‡,b], *Maria Lis*[b,c], *Alessandro Chiolerio*[d] *and Konrad Szaciłowski*[b]

Piotr Zawal, Tomasz Mazur, Maria Lis, Konrad Szaciłowski
Academic Centre for Materials and Nanotechnology, AGH University of Science and Technology, al. Mickiewicza 30, Krakow, Poland
E-mail: zawal@agh.edu.pl; tmazur@agh.edu.pl

Piotr Zawal
Faculty of Physics and Applied Computer Science, AGH University of Science and Technology, al. Mickiewicza 30, Krakow, Poland

Maria Lis
Faculty of Materials Science and Ceramics, AGH University of Science and Technology, al. Mickiewicza 30, Krakow, Poland

Alessandro Chiolerio
Center for Sustainable Future Technologies, Istituto Italiano di Tecnologia, Via Livorno 60, 10144 Torino, Italy

1. Synthesis of carbon nitride nanoparticles (CN-NPs)

Synthesis of carbon nitride nanoparticles was conducted with modified method described elsewhere.[1]> Thiourea (0.46 g) and citric acid (0.42 g) were dissolved in 10 ml water, colorless solution was placed in ERTEC microwave reactor where hydrothermal synthesis was carried out at 200°C for 2 h at working pressure between 14-16 atm. The black solution was obtained and then water was evaporated on a rotary evaporator to give a dark green product insoluble in toluene. The purification of the synthesis from the organic contamination consisted of the extraction in toluene using the Soxhlet apparatus for 4 h following the literature.[2] As a result of this process greenish-yellow toluene solution was received and subjected to further spectroscopic examination.

To synthesize comparative carbon QDs, we have performed the same synthesis with glucose (0.54 g) instead of thiourea. The purification process was the same as for CN-NPs.

2. TEM measurements

Transmission electron microscopy (TEM) images were obtained by Tecnai TF 20 X-TWIN (FEI) operated at accelerating voltage of 200 keV to confirm the presence of nanoparticles and estimate their size.

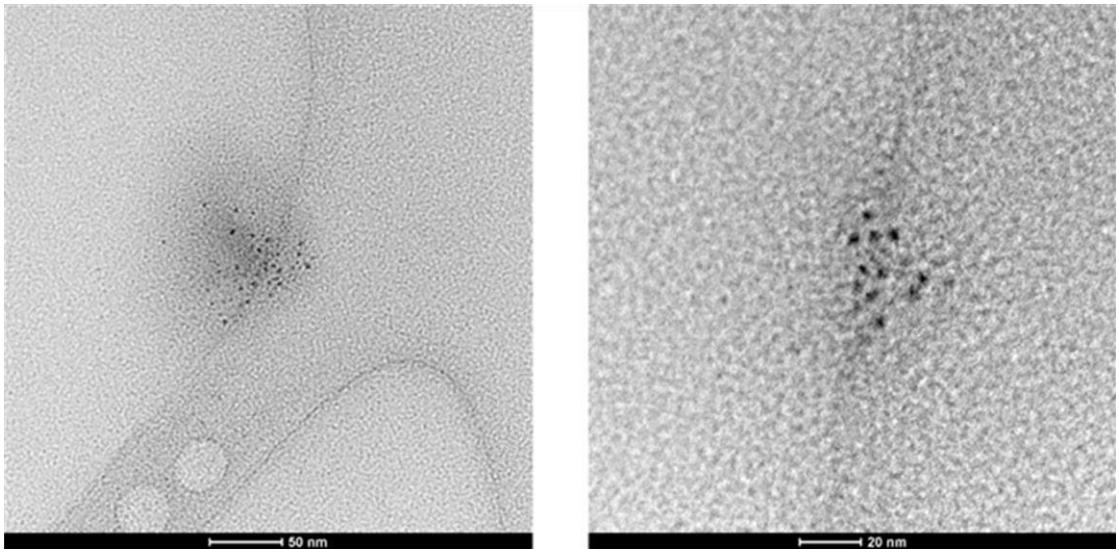

Figure S1. *TEM image of purified CN-NPs samples.*

3. Device preparation

Methylammonium lead iodide (OIP) was synthesized with the conventional two-step method. All the steps were conducted in the ambient atmosphere. PbI_2 (Sigma Aldrich) solution was prepared by dissolving 461 mg of PbI_2 in DMF and stirred at 70°C for several hours. Immediately before spin coating, the solution was filtered with 200 µm PTFE filter. 0.3 M methylammonium iodide (MAI, Ossila) solution was prepared by dissolving 53 mg of MAI in 1 ml of isopropyl alcohol. ITO substrates were sonicated for 5 minutes in 1% solution of Hellmanex in hot water, followed by the same protocol executed in hot water and in isopropanol. Last cleaning stage consisted of exposing ITO to oxygen plasma for 10 minutes.

The CN-NPs layer was deposited at 3000 rpm and placed on the hotplate at 70°C for 10 minutes. The heated substrate was subsequently coated with a PbI_2 layer (4000 rpm, 45 s) and dried for 10 minutes at 70°C on a hotplate. Next, 100 µl of MAI solution was spincoated (3000 rpm, 60 s) on the hot substrate and within 6-8 s later 200 µl of ethyl acetate was dripped on the spinning surface. The substrate was subsequently placed on a hotplate for 10 min at 100°C to crystallize. Finally, 70 nm

thick Au electrodes were sputtered on top through shadow mask. The active area of the device was 2.25 mm^2. To measure the thicknesses of OIP and CN-NPs layer we have deposited the layers on silicon substrates according to the above protocol. The surface was scratched and thickness was measured with Bruker Dimension ICON XR AFM. The OIP and CN-NPs layers were 300 nm and 33 nm thick.

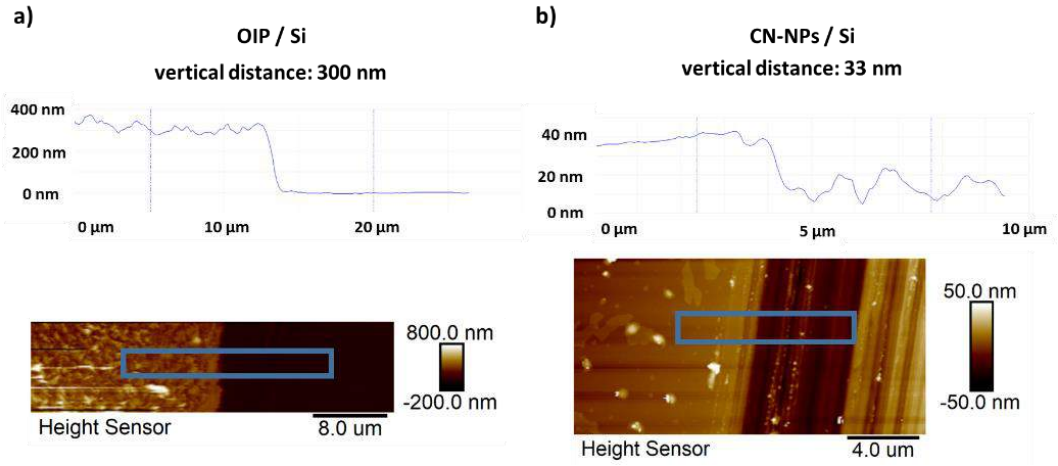

Figure S2. *AFM images of Surface height profiles of a) OIP on Si substrate layer and b) CN-NPs on Si substrate layer*

4. UV-Vis spectroscopy

UV-Vis spectra of the as-prepared $CH_3NH_3PbI_3$ were measured on Bruker Lambda 750 spectrophotometer in transmission mode. The absorbance spectrum is shown in **Error! Reference source not found.**. The measured spectrum exhibits steep onset at ~788 nm and rising absorption for lower wavelengths – the typical features of lead iodide perovskite.[3]> We have chosen the wavelength of 465 nm for the photosynaptic experiments to fall within the absorption spectrum of the perovskite layer and out of absorption spectrum of CN-NPs (see Figure 1c in the main text) in order to assure the generation of charge carriers in the perovskite layer only.

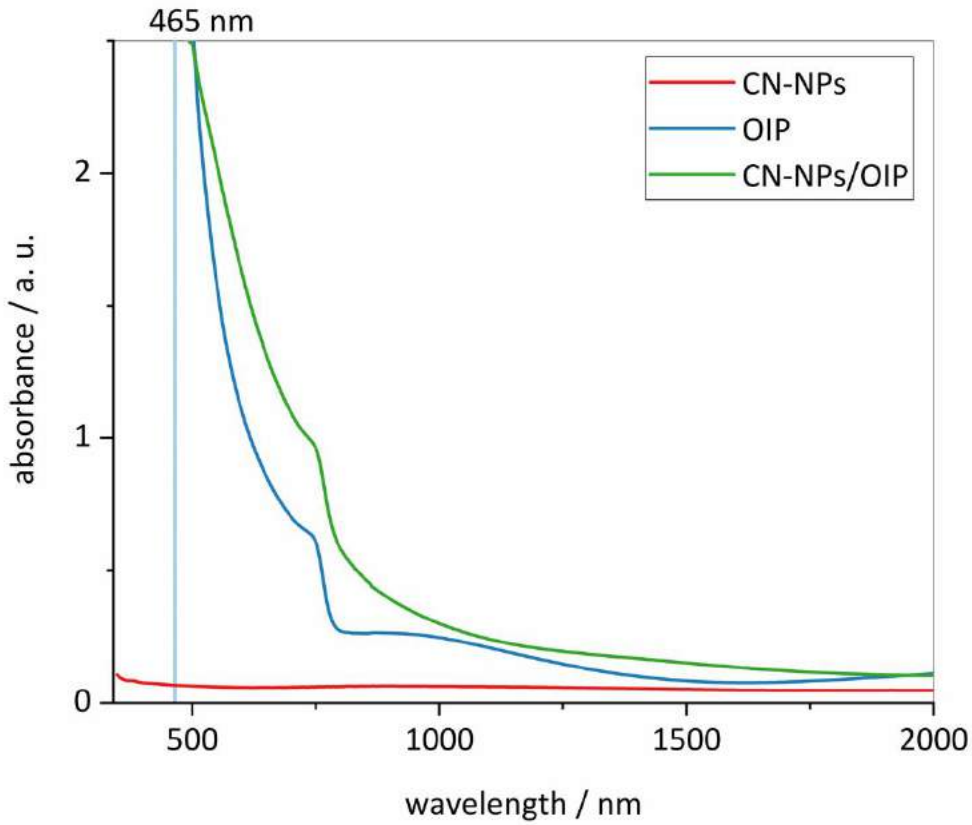

Figure S3. *UV-Vis spectra of CN-NPs, OIP and CN-NPs/OIP layers deposited on glass. The 465 nm wavelength (marked with vertical line) chosen for irradiation falls within the absorption band of OIP layer*

5. FTIR spectra

FTIR measurement was performed to identify characteristic vibrations of bonds in QDs and to examine interactions with the lead(II) iodide using spectrophotometer FTIR Tensor II (Bruker). The NEC QDs sample was dried by evaporation of toluene and dry product was transferred on ATR crystal. To prepare the CN-NPs/PbI_2 sample, we have evaporated the toluene from CN-NPs sample, added dry CN-NPs to PbI_2 dissolved in DMF, sonicated for 20 min and dried on microscope substrate. The dry powder was scraped, transferred onto ATR crystal (Ge) and measured in ATR mode.

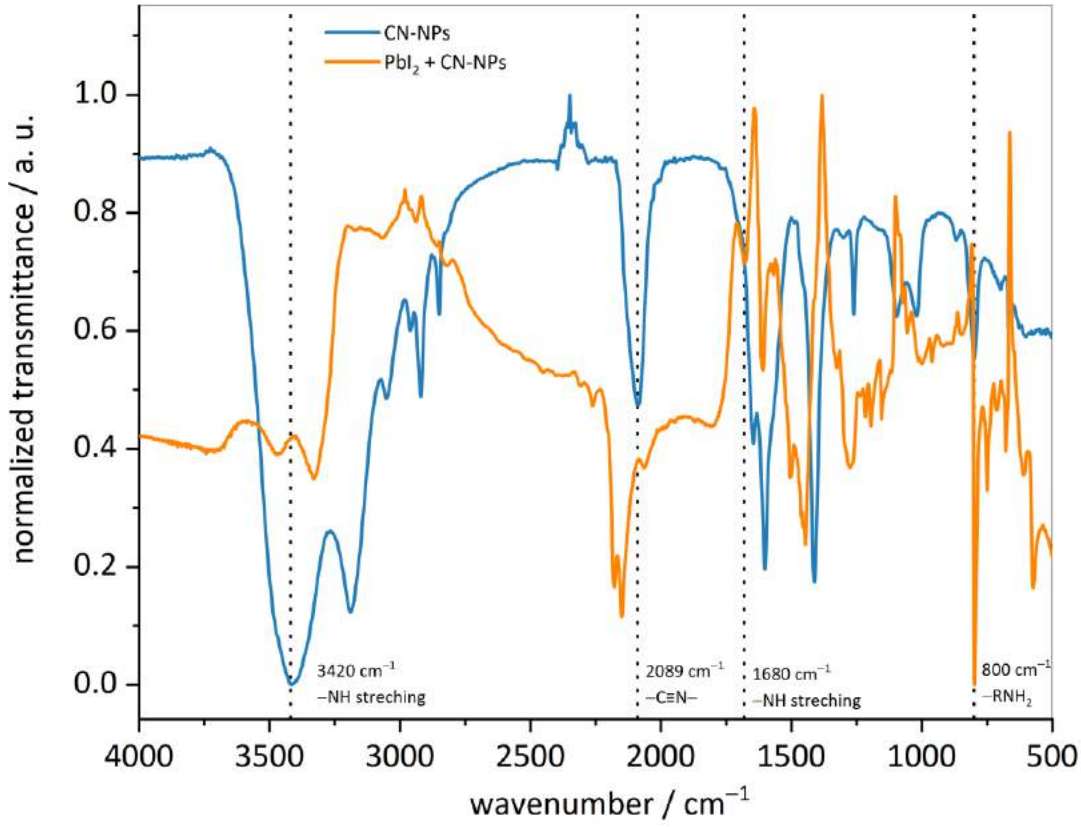

Figure S4. *FT-IR spectra of CN-NPs species (blue) alongside with PbI_2 + CN-NPs mix (orange). In both cases peaks arising from –N-H interactions are present.*

6. Fluorescence measurements

To confirm the fluorescent properties and of nitrogen-enriched carbon quantum dots in comparison to carbon quantum dots, the fluorescence maps were obtained using Edinburgh Instruments Spectrofluorometer FS5. 100 µl of basic solutions of CN NPs and carbon QDs were dissolved in the 2.5ml of toluene, exact concentrations of initial solutions are impossible to designate. The intensity of fluorescence of carbon QDs is significantly lower than CN-NPs, despite using more excitation energy (broader slit). No evidence of Stokes shift in regard of excitation energy is present, what implies only the nitrogen doped QDs own trapping states in structure.

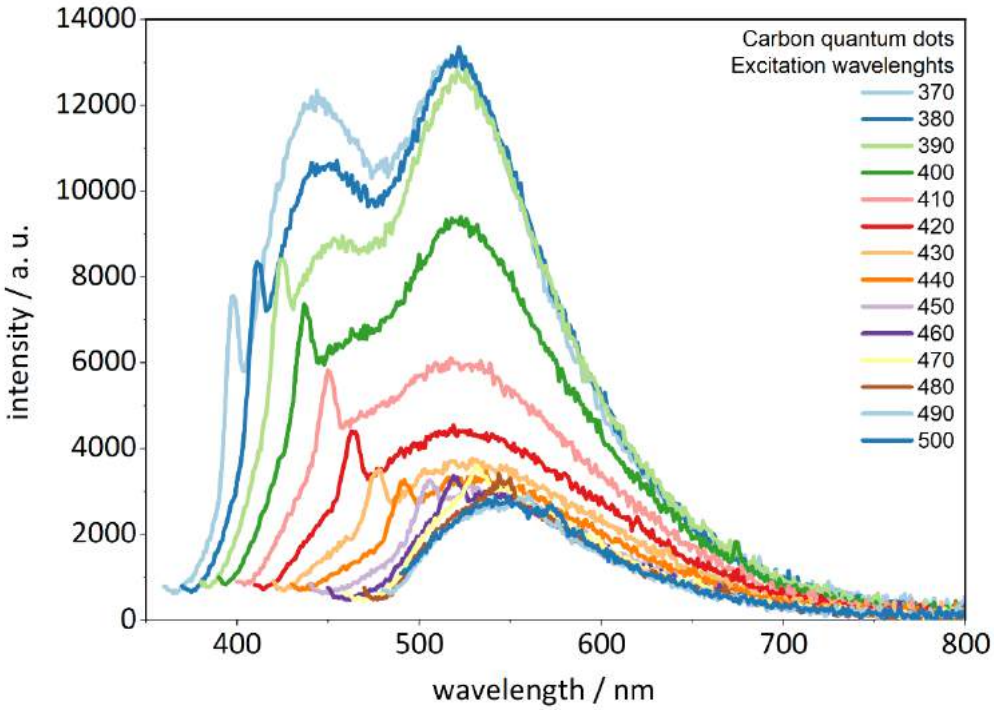

Figure S5. *Fluorescence spectra of carbon QDs measured at excitation wavelength increasing from 370 nm to 500 nm.*

7. Work function measurements

Work functions of samples have been measured using KP020 ambient Kelvin probe system (KP Technologies, UK) with 1 mm and 5 mm sensor electrodes. 1000 measurements have been collected for gold reference and studied samples in the dark. The OIP sample was prepared according to previously described protocol. For the measurement, CN-NPs were spincoated (3000 rpm) on top of OIP layer .

8. Electrical measurements

The I-V scans and spike-timing dependent plasticity (STDP) measurements were performed on Keithley 4200-SCS in two electrode setup with Au as the active electrode and the bottom ITO electrode grounded. The electrical connections to ITO and Au electrode were established by pressing tungsten probing tip (Everbeing Int'l Corp.) installed in micropositioners to the corresponding electrodes.

8.1. Spike-timing dependent plasticity (STDP)

To measure STDP – a form of Hebbian learning – we have used symmetric sawtooth pulses of ±1.6 V lasting 300 ms which were applied to the top and bottom electrode with varying time interval (**Figure S6**). To induce potentiation, the voltage was firstly applied to the top Au electrode acting as a presynaptic neuron. After given time, the same voltage pattern was applied to the bottom ITO electrode (postsynaptic neuron). To induce the depression we have changed the temporal order of the voltage pattern, applying first pulse to the bottom (presynaptic) electrode and the second to the top (postsynaptic) one. To calculate the synaptic weight Δw, the state of the device was read three times at −0.5 V for 60 ms before and after applying the voltage spike pair. The time interval between pulses varied between 20 ms and 400 ms to induce changes in the magnitude of Δw.

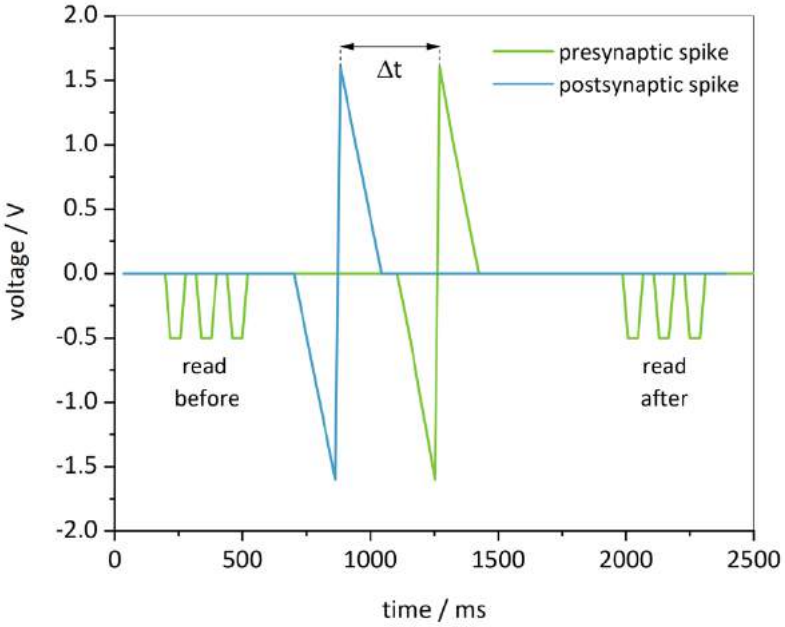

Figure S6.*Voltage pattern used for STDP measurements. The presynaptic spike occurs before the postsynaptic spike, inducing potentiation. To induce depression, the spike order was altered so that postsynaptic spike was applied before presynaptic one.*

9. Photocurrent generation

9.1. Photocurrent transient – influence of switching voltage time stamp

In order to investigate the switching mechanism, we have measured the photocurrent after switching with −2 V DC voltage (to high resistivity state, HRS) for 10 s (as compared to standard 60 s). The amplitude of the photocurrent, observed after longer voltage bias (60 s) was higher, yet there were no significant changes in the characteristic of further photocurrent evolution (exponential decay). To assert that response to light pulses does not originate from some kind of intrinsic electrical or thermal relaxation of the device, we have switched the sample into HRS state and left for 3 minutes in the dark. After this time, we started measuring photocurrents. We found that the photocurrent amplitude was lower as compared to when the device was irradiated immediately after switching. The photocurrent decreased with time, reaching the same plateau as in the alternate experiments. During the measurement, the , the long-term photocurrent amplitude was approximately the same height – cf. results after 100 s.

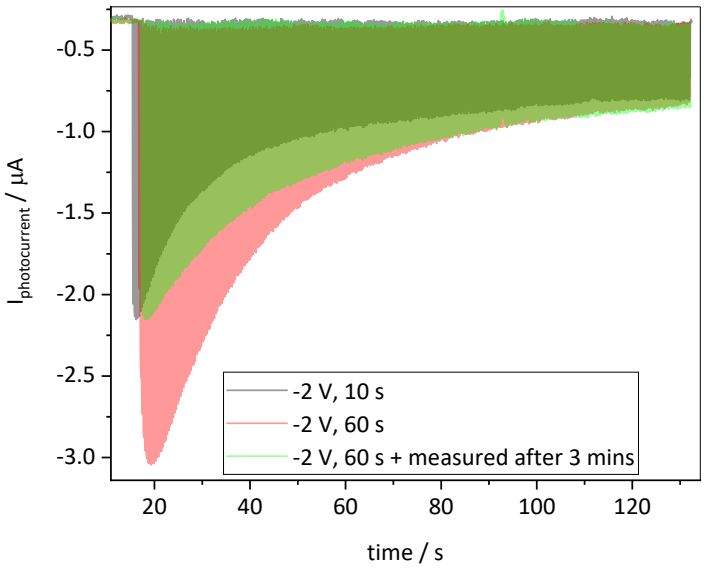

Figure S7. *Relaxation processes of the CN NPs/OIP/Au devices, probed with varying switching parameters: DC bias −2 V for 10 s (grey), DC bias −2 V for 60 s (red) and DC bias −2 V for 60 s and 3 min delay after photoirradiation (green).*

9.2. Photocurrents - switching voltage dependency (dependence on resistive state)

To assess the possibility of reading the resistive state of the CN-NPs/OIP/Au, we have measured the photocurrents in the device switched to HRS with −2 V and to LRS (+2 V). Despite that photocurrent generation dynamics remained unchanged, the amplitude in LRS was significantly lower than in HRS. Therefore, the state of the device can be inferred from photocurrent value. It is noteworthy, that optical reading is generally considered as having lower impact on the resistive state, as it has been shown that numerous voltage read cycles in non-volatile memristors can affect the conductance.[4]

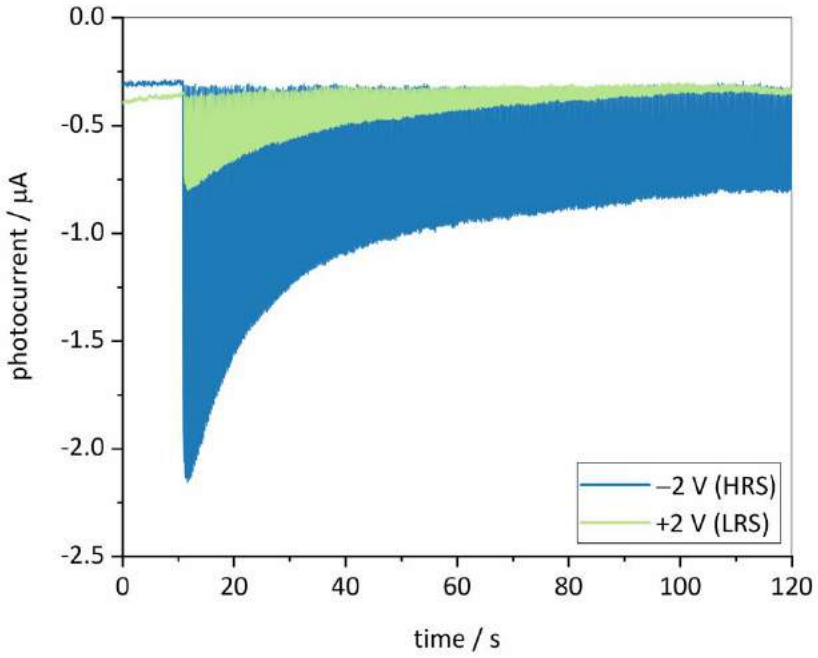

Figure S8. *Photocurrents measured in the CN-NPs/OIP/Au device switched to high resistive state (HRS) with −2V and to low resistive state (LRS) with +2 V. The distinguishable photocurrent amplitude in two different states can be used to read the resistive state of memristive device by measuring photocurrent.*

9.3. Photocurrents – pulse frequency dependency

Device photoresponses were also tested with varying pulse frequency. In each case before photocurrent generation, sample was switched to HRS (−2 V DC voltage for 30 s). The length of 465 nm light pulses was 200 ms. Variations of the time between pulses (*dt)* are different for the OIP/Au and CN NPs/OIP/Au devices. First separation time is of the order of pulse length, second one is 2-3 times longer, third one falls within the 7-15 times longer regime.

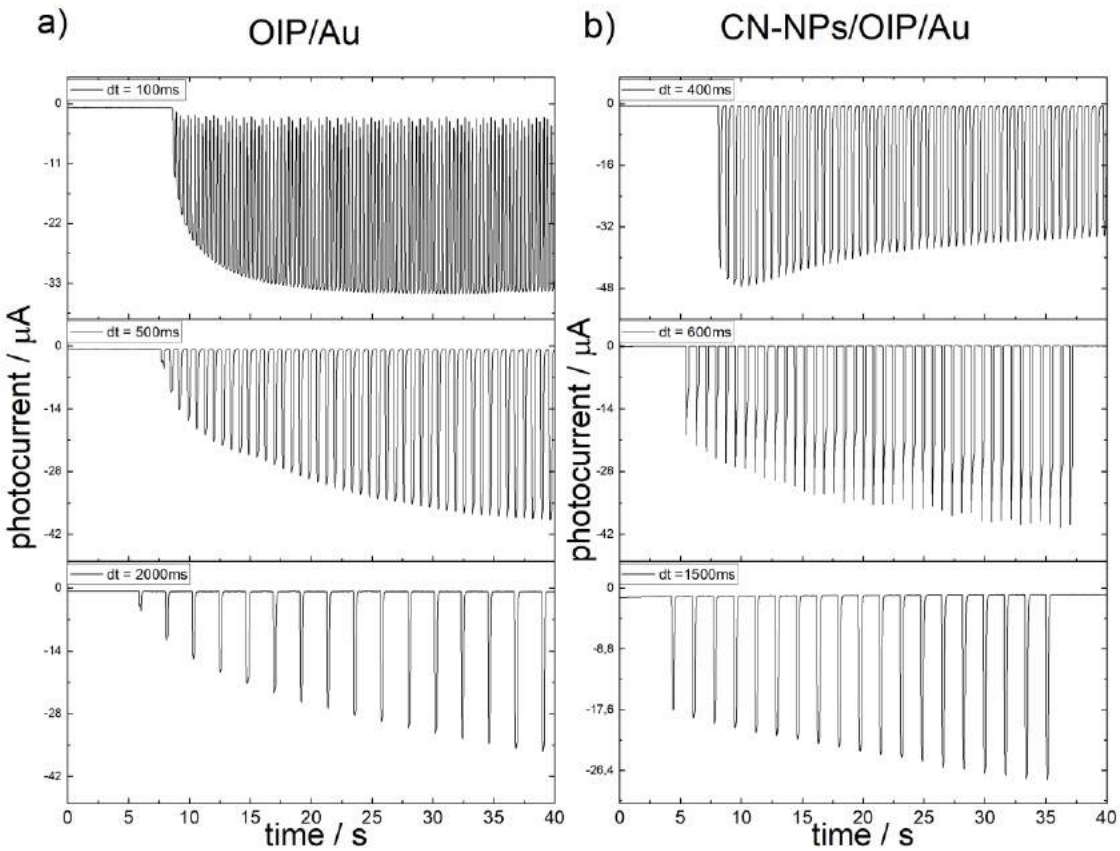

Figure S9. *Photocurrent transients during first 40 s of measurements, with varied time between pulses, dt, for OIP/Au device (a) and CN-NPs/OIP/Au device (b).*

Bibliography

[1] A.-J. Wang, H. Li, H. Huang, Z.-S. Qian, J.-J. Feng, *J. Mater. Chem. C* **2016**, *4*, 8146.

[2] J. R. Holst, Synthesis of Inorganic Heptazine-Based Materials, University of Iowa, **2009**.

[3] S. De Wolf, J. Holovsky, S. J. Moon, P. Löper, B. Niesen, M. Ledinsky, F. J. Haug, J. H. Yum, C. Ballif, *J. Phys. Chem. Lett.* **2014**, *5*, 1035.

[4] Y. V Pershin, M. Di Ventra, *Adv. Phys.* **2011**, *60*, 145.

Leaky integrate-and-fire model and short-term synaptic plasticity emulated in a novel bismuth-based diffusive memristor

P. Zawal,[a,b] D. Das,[c] M. Gryl,[d] A. Sławek,[a] G. Abdi,[a] E. Gerouville,[e] M. Marciszko-Wiąckowska,[a] M. Marzec,[a] G. Hess,[f] D. G. Georgiadou,[e] K. Szaciłowski[a]

a – Academic Centre for Materials and Nanotechnology, AGH University of Science and Technology, al. Mickiewicza 30, Krakow, Poland

b – Faculty of Physics and Applied Computer Science, AGH University of Science and Technology, al. Mickiewicza 30, Krakow, Poland

c – Department of Physics, School of Natural Sciences, Shiv Nadar University, Delhi-NCR, NH-91, Dadri, Gautam Buddha Nagar, Uttar Pradesh 201314, India

d – Crystal Engineering and Structural Analysis Group, Department of Crystal Chemistry and Crystal Physics, Faculty of Chemistry, Jagiellonian University in Kraków, ul. Gronostajowa 2, 30-387 Kraków, Poland

e – Electronics and Computer Science, University of Southampton, Southampton SO17 1BJ, UK

f – Department of Neurophysiology and Chronobiology, Institute of Zoology and Biomedical Research, Jagiellonian University, 30-387 Krakow, Poland

ABSTRACT

Among many artificial neural network architectures, spiking neural networks are the ones capable of processing information in a biologically faithful manner. For their development, the search for devices that could efficiently implement the spiking signal system of the brain is a crucial task. Among the potential candidates, volatile memories exhibit properties that are advantageous for temporal data processing with short-term synaptic plasticity. Here, we introduce a diffusive memristor based on a novel compound – butylammonium bismuth iodide (BABI) – and evaluate its memristive and neuromorphic properties. In contrast to non-volatile memristors, the BABI memristors exhibit diffusive dynamics which enable them to store the information only for show periods of time. We utilized this property to mimic the short-term synaptic plasticity described by the leaky integrate-and-fire model of a biological neuron. Combined with high switching uniformity and self-rectifying memory, these devices showed high classification accuracy in artificial neural networks simulations, paving the way for their application in neuromorphic computing systems.

KEYWORDS

diffusive memristor, neuromorphic computing, synaptic plasticity, resistive switching

INTRODUCTION

Information processing is a highly demanding process. High-performance supercomputers, as well as large data centers, consume huge amounts of energy, comparable to the energy demands of cities and countries[1]. Neuromorphic computing, performing the same tasks, holds promise to consume much smaller amounts of energy due to (i) different physical background

of computation and (ii) different systems architecture, free from von Neumann bottleneck and other limitations of current CMOS technologies[2]. One of the devices that are considered the workhorse of unconventional and, more specifically, neuromorphic computing are memristors and related elements. Since the introduction of the memristor as the fourth – next to the resistor, conductor and capacitor – passive electronic element[3] and its first physical implementation[4], high effort is paid to the development of new memristive devices, their characterization, and application in different types of unconventional computing systems.

Memristors are two-terminal electronic devices with the ability to store information as their physical property – conductance – which can be further modulated either by voltage or current to alter the information stored in them. Their low energy consumption[5], multibit memory[6,7], exceptional ON/OFF ratio[8], potential for downscaling[8,9] and integration in 3D with CMOS compatibility[10,11] contributed to their widespread application in neuromorphic implementations, such as hardware neural networks and data storage[12].

With regard to the ability to retain the resistive state, memristors can be categorized into non-volatile and volatile devices. While the former can retain the low resistance state (LRS) for a long time ranging from minutes to months[13,14], the volatile (diffusive) memristors spontaneously return to the high resistance state (HRS) after the removal of the external voltage bias within nanoseconds to seconds[15]. Non-volatile devices have already shown to be suitable for a variety of applications, stretching from memory storage, implementation of physically unclonable functions[16], matrix multiplication[17,18] and optoelectronics[19] to non-conventional computing[20]. In particular, the ability of memristors to mimic synaptic plasticity makes them potential candidates for future systems for neuromorphic computing. On the other hand, although the diffusive memristors can't be utilized for information storage, the volatility of the resistive state allows mimicking the synaptic plasticity in a more biomimetic way by encoding the temporal information with sparse and asynchronous binary spikes, thus paving the way for

their application in spiking neural networks (SNNs)[21]. Benefitting from the time domain encoding, low energy consumption, and spatiotemporal learning, SNNs are more accurate emulations of the way in which human brain processes information. Furthermore, the simple two-terminal device architecture of the memristor provides a unique opportunity for high-density neuromorphic computing in a crossbar array (CBA). However, rapid usage of CBA is hindered by the well-known sneak path current-related issue, which limits the read-out efficiency. The use of a selector element accompanying the memory cell is proposed as a viable approach to overcome such a sneak path issue. For example, Sasago *et al*.[22] utilized poly-Si diodes and Zhang *et al.*[23] used epitaxial Si-diode selectors. However, the complex fabrication method and high production costs introduce challenges for using such selector elements. Therefore, the development of a self-rectifying memory cell using a simple and low-cost fabrication method is crucial.

Here, we show hybrid bismuth-based memristive devices fabricated with low-cost chemical methods that exhibit polarity-dependent hysteretic behavior and self-rectifying characteristics. Such a simple fabrication method not only eases the production cost but also enables multifunctional device features. The devices show filamentary resistive switching and exhibit volatile memory, the retention time of which can be tuned with voltage. The same devices are also capable of mimicking neuron-like behaviors with distinct characteristics depending on the frequency of the stimulus. At low frequency, the device generates random spikes with firing probability dependent on the voltage of the stimulus, whereas synaptic facilitation rules in the high-frequency regime.

For the production of the devices, a new type of hybrid organic-inorganic bismuth-based material was used: butylammonium bismuth iodide (BABI) for which we determined its structural, optoelectronic and memristive properties. With a simple spin coating method, we fabricated memristors with diffusive resistive switching characteristics that consist of BABI as

the active layer, which was sandwiched between two conductive electrodes, yielding a two-terminal device. We showed that the resistive switching in BABI memristors is volatile in nature and that the LRS can be retained only for a short time ranging from milliseconds to seconds with the relaxation time constant being modulated by the input voltage amplitude and duration. Using these properties, we showed that the device can efficiently mimic the behavior of biological neurons, in particular, the functions described by the leaky integrate-and-fire neuron model.

The I-V measurements showed that the switching occurs only in the negative branch of the scan, indicating the inability to retain the LRS. The activation energy estimated from the Arrhenius plots suggests that the resistive switching originates from the movement of iodine vacancies within the BABI structure. Therefore, we propose the transfer to LRS originating from the creation of conductive filaments that are formed by iodine vacancies migrating in the gradient of the external electric field as the physical mechanism responsible for resistive switching. Because of the innate instability of the filament, after spontaneous rupture or dissolution, the device rapidly returns to the original HRS, resulting in volatile memory and self-rectifying properties of the device.

Despite the fact that long retention times are generally desirable for memory applications, we show that this type of volatile memory can be effectively utilized to emulate the behaviour of a leaky integrate-and-fire neuron. For low frequency (2 Hz) pulses of varying amplitude, we have shown that the device generates current spikes randomly with spiking probability rising with the voltage amplitude. By moving into a high-frequency regime (0.2, 0.5, 1 and 2 kHz), the train of short voltage pulses causes an increase in the magnitude of currents, therefore mimicking the frequency facilitation of the neurons. The memristive characteristics of the device indicate that it can be incorporated into artificial neural networks performing classification tasks. The simulation showed that even simple BABI-based network is capable

of recognizing handwritten digits with high accuracy, reaching nearly 95% just within 50 training epochs.

In this study, we report the first diffusive memristor based on a bismuth compound (BABI) with the resistive switching mechanism governed by the movement of iodine vacancies. Using the volatility of the device's resistive states of the device, we showed that it is possible to emulate the functions of the biological leaky integrate-and-fire neuron model. The presented results indicate that BABI can be a potential candidate for building blocks of spiking neural networks.

RESULTS AND DISCUSSION

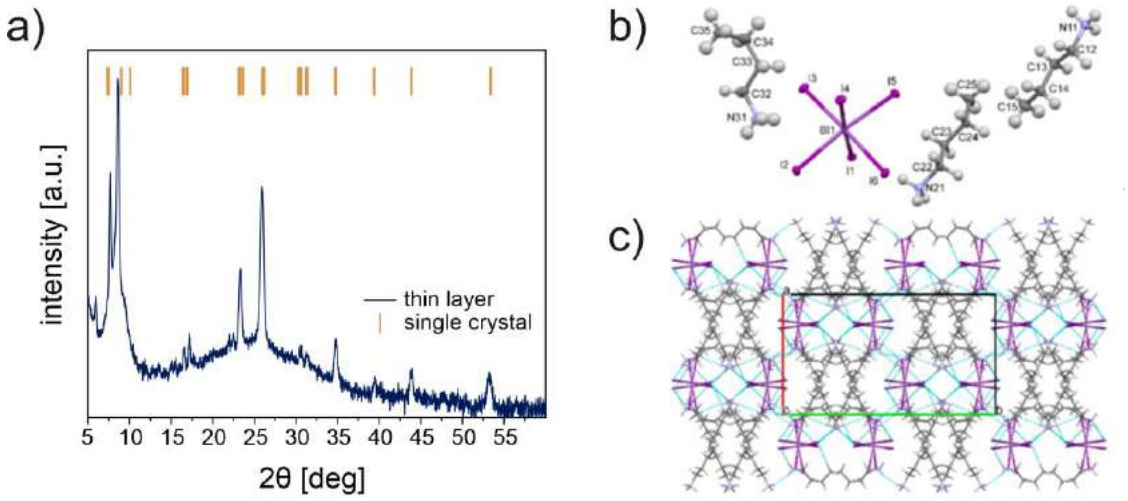

Figure 1. a) Diffractogram of n-BABI thin layer together with the theoretical peak positions calculated from the resolved crystal structure. b) Asymmetric unit of the BABI structure with the non-hydrogen atom numbering scheme. c) Packing of the structural components as seen along the [001] direction with marked hydrogen bonds.

To determine the crystal structure of BABI, the compound was studied using XRD methods both in the single-crystalline form and as a thin layer with the results shown in **Fig. 1a.** The diffractogram presents the diffraction pattern of the BABI thin layer crystallized from 0.5 M solution containing 3:2 BAI:BiI_3 ratio while the vertical lines indicate the position of the peaks in the BABI single crystal. The diffractogram of the BABI thin layer reveals the presence of sharp and well-defined diffraction peaks, therefore indicating a high degree of crystallinity. The calculated lattice parameters were found to be a = 13.5986(1) A˚, b = 24.1005(2) A˚ and c = 17.5189(2) A˚ with the unit cell volume of 5741.53 $Å^3$. The average grain size calculated using the Sherrer equation was estimated as 46(1) nm.

Single-crystal XRD measurements at low temperature (T = 120 K) showed that the structure of BABI is orthorhombic and centrosymmetric (*P*ccn space group). **Table S1** contains crystal data and details of the refinement procedure. The asymmetric unit comprises three *n*-

butylammonium cations and one BiI_6 anion as shown in **Fig. 1b**. The three cations differ in conformation (**Fig. S1**, **Table S2**) and intermolecular interactions. The BiI_6 anion has a slightly distorted octahedral geometry, with the I-Bi-I angles ranging from 86.47° to 94.36°. Structural components are connected via hydrogen bonds of N-H···I and C-H···I type (**Fig. 1c**). The N-H···I interactions in this structure are an example of charge-assisted hydrogen bonds, where both the donor and the acceptor are charged species. The N-H···I^- interactions are quite rare and can be found in ca. 0.08 % of CSD database entries (CSD 5.42). Some of the N-H···I^- interactions (**Table S3**) can be considered relatively strong, based on the H···I distance (below 2.8 Å) and DHA angles (above 170°) analysis[24,25]. Fingerprint plots for the three butylammonium cations are visible in **Fig. S2**. From the percentage of interactions, it is clear that the cations are involved in only two different types of interactions, H···I and H···H, with a different contribution to the fingerprint for each of the cations.

Interestingly, analysis of single-crystal diffraction data recorded at room temperature reveals only the presence of the inorganic part, whereas the organic sub-lattice seems to be totally disordered and thus invisible in XRD measurements. This observation suggests the possibility of rotational movements of *n*-butylammonium chains within voids in the lattice. This, in turn, significantly influences the temperature impact on the conductivity in BABI-based thin layer devices (*vide infra*).

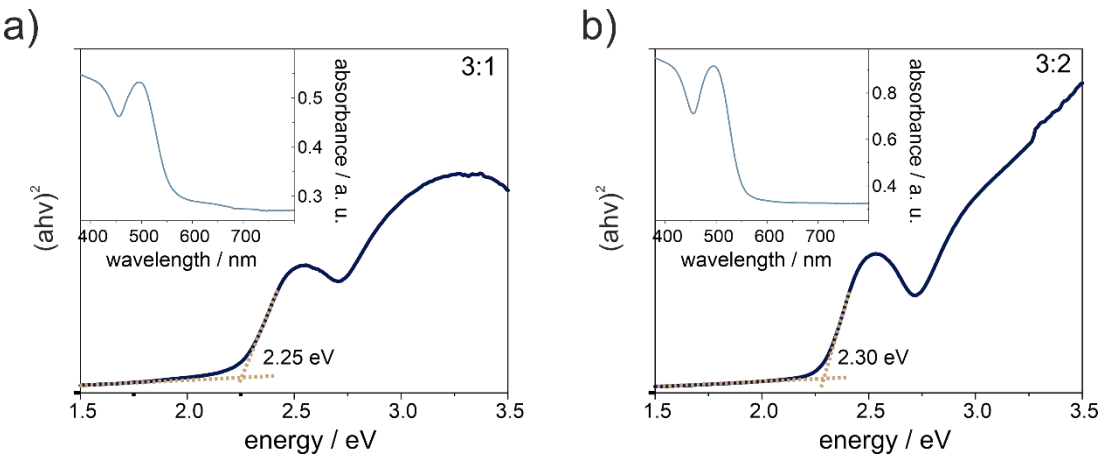

Figure 2. Tauc plots of BABI thin layers synthesized from the 3:1 (a) and 3:2 (b) BAI:BiI_3 ratio with their corresponding absorption spectra in the insets. The change in the precursor ratio from 3:1 to 3:2 increases the optical band gap from 2.25 eV to 2.30 eV. It is noteworthy that the absorption of the 3:1 sample is nearly twice lower than that synthesized from 3:2 solution (cf. the insets).

XRD experiments revealed that the BABI stoichiometry is 3:1 which differed from our initial assumption that BABI will crystallize in a 3:2 cation to anion ratio. The assumption was based on the stoichiometry of methylammonium bismuth iodide, which is a compound analogous to BABI but containing methylammonium cation instead of the *n*-butylammonium one[26]. Therefore, the BABI crystallized from the solution containing the non-stoichiometric BAI to BiI_3 ratio of 3:2 is expected to have more structural defects due to the excess amounts of BiI_3 which in turn affect the optoelectronic properties of the material.

Diffuse reflectance spectroscopy (DRS) was applied to estimate the optical band gap of synthesized materials. The Tauc plots shown in **Fig. 2** were prepared to determine the optical gap. The coefficient *r* in $(\alpha h\nu)^{1/r}$ formula fixed at ½ turned out to be the most suitable for the investigated samples, suggesting that direct transitions occur regardless of the preparation ratio. The optical gap of pristine BiI_3 was estimated to be 1.67 eV[27], whereas the BABI samples exhibited significantly higher band gap values: 2.25 eV for stoichiometric samples (3:1) and 2.30 eV for nonstoichiometric (3:2) ones. As expected, increasing the ratio of *n*-butylammonium iodide to BiI_3 leads to a noticeable widening of the optical gap. This observation can be explained by the Burstein-Moss effect[28]. Any deviation from stoichiometry results in lattice defects, which naturally increase the doping state. Increased charge concentration, in turn, results in an apparent increase in the band gap value, due to partial filling of the low-lying conduction band states. This makes the energies of the lowest allowed transitions slightly higher[29–31].

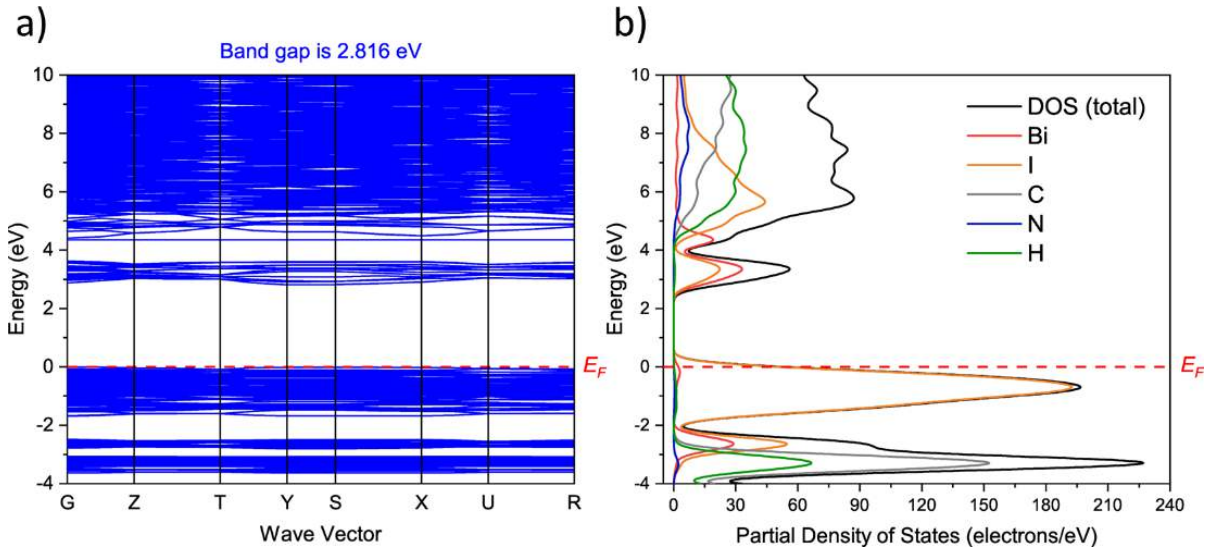

Figure 3. Band structure (a) and total and partial density of states of BABI material (b) as calculated using DTF approach.

The determination of the semiconductor's band structure is crucial for its potential application in optoelectronic devices. We optimized the geometry of the BABI structure and calculated electronic spectroscopy using the density functional theory (DFT) method. The calculated band structure is shown in **Fig. 3a**, where the Fermi level is marked with a red dotted line. BABI is a *p*-type semiconductor and it can be seen that the studied material has a direct band gap because both the valence band maximum (VBM) and the conduction band minimum (CBM) are located at the same symmetry points within the Brillouin zone. In fact, the positions of the bands do not significantly depend on the wave vector. This indicates that the studied structure, being an ionic crystal, should have heavy electrons and holes (high effective mass), which result in low conductivity. The calculated band gap value is 2.816 eV, which is slightly overestimated in relation to the experimental value of 2.25-2.3 eV (**Fig. 2**).

To fully understand the band structure of BABI, we calculated the density of states (DOS) and the partial density of states (PDOS). The DOS presented in **Fig. 3b** shows broad maxima between −2 and 0 eV indicating that these filled valence bands are quite close to each other. On

the other hand, one may observe much fewer unfilled conduction bands between 2.8 and 3.6 eV, resulting in lower density of states. In-depth analysis of PDOS for individual atoms (**Fig. S3a–S3f**) reveal that the most prominent HOMO–LUMO electronic transitions are from p-type iodide orbitals to p-type iodide and p-type bismuth orbitals, while the remaining atoms do not contribute to DOS near the bad bap region.

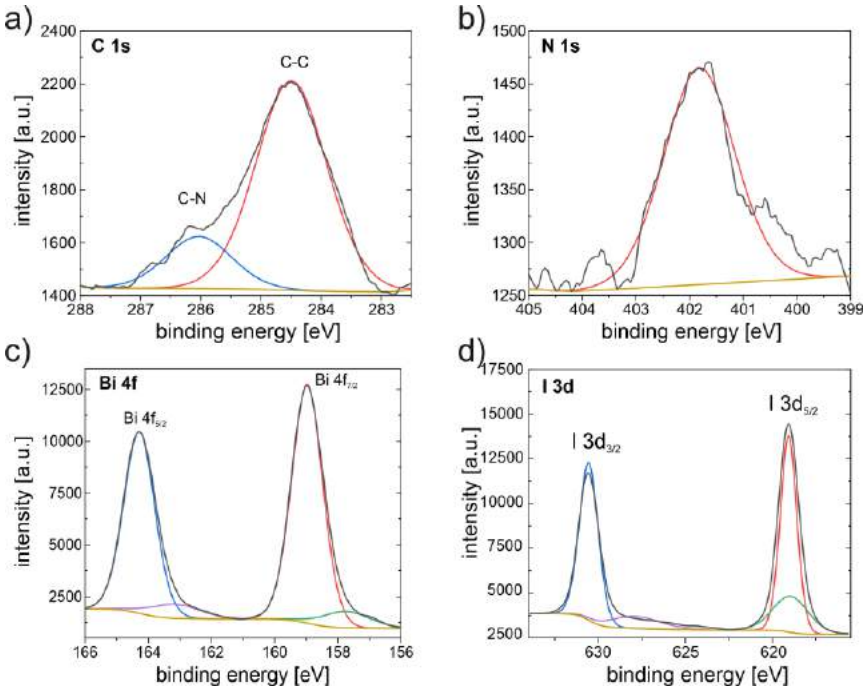

Figure 4. XPS spectra of a) C 1s, b) N 1s, c) Bi 4f, and d) I 3d of the BA*B*I film prepared from the 3:*2* precursor ratio.

X-ray photoelectron spectroscopy (XPS) was also performed on the BABI films to probe the elemental composition at the surface of the film. The obtained XPS spectra are presented in **Fig. 4** and show the characteristic peaks for bismuth, iodine, nitrogen, and carbon. More specifically, the C 1s spectrum (**Fig. 4a**) shows both the C-C and C-N bonds, as expected due to the butyl ammonium cation, and their calculated ratio is reasonable with slightly higher content of adventitious carbon (23.18% C-C *vs* 4.97% C-N). The N 1s signal, due to the butylammonium cation, is found at around 402 eV (**Fig. 4b**), as expected. The Bi 4f spectrum (**Fig. 4c**) shows that Bi is predominantly in the +3 oxidation state with a spin-orbit splitting of

around 5.3 eV, while a small amount of metallic (undercoordinated) Bi also exists on the surface. However, the Bi $4f_{7/2}$ appears at 159.48 eV, close to what is expected for the BiI_3 compound[32]. The shoulders on both the $4f_{7/2}$ and $4f_{5/2}$ peaks are due to a difference in neighbors: the main peaks are due to Bi connected to iodine, while the shoulders are due to Bi connected to iodine vacancies. Finally, in the I 3d spectrum (**Fig. 4d)**, the peaks at 631.1 and 619.6 eV correspond to I $3d_{3/2}$ and I $3d_{5/2}$ of I^- ions. These results indicate the presence of iodine vacancies which have been already reported to be responsible for the resistive switching phenomena in the related types of materials[33,34].

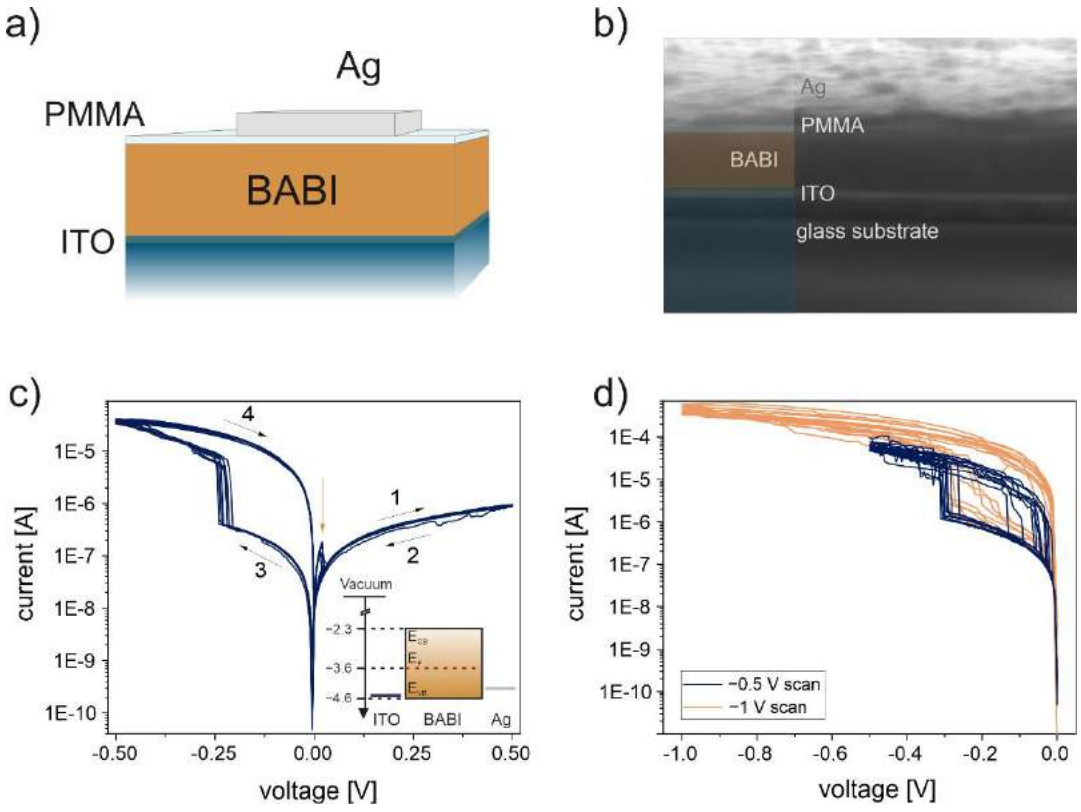

Figure 5. a) Schematic illustration of a single BABI memristor's cross-section with the active layer sandwiched between ITO and Ag as bottom and top electrodes, respectively, and PMMA interlayer. b) SEM cross-section photo of BABI memristor. c) 10 consecutive I-V scans with

arrows depicting the resistive switching direction. d) Negative-only I-V scans showed that the low resistive state is not retained from scan to scan.

The memristive devices were prepared by spin-coating the *n*-butylammonium bismuth iodide solution in DMF on ITO substrate followed by annealing at high temperature and subsequent spin coating of the PMMA interlayer and magnetron sputtering of the Ag electrode. The schematic drawing of the device is shown in **Fig. 5a** while **Fig. 5b** presents the SEM picture of the cross-section of BABI memristor. The BABI and PMMA layers showed high uniformity with their respective thicknesses of ~300 nm and ~20 nm as determined by stylus profilometry. A PMMA interlayer was used to prevent the reaction of Ag with BABI, which led to rapid degradation of the device just within a couple of hours when Ag was deposited directly on BABI and resulted in an overall high scan-to-scan variability (**Fig. S4**). With PMMA, the lifetime of the devices was significantly increased and the devices exhibited stable resistive switching for more than a week of measurements conducted in the ambient air, although it should be noted that the devices were stored under an argon atmosphere overnights.

One of the fingerprints of the memristors resulting from their nonlinear dynamics is the pinched hysteresis loop when the device is subjected to bipolar voltage sweeps. I-V scans of the BABI memristive device are shown in **Fig. 5c.** During the initial voltage scan, 0 V → 0.5 V → 0 V (arrow no. 1 in the graph), almost no resistance switching is observed. When submitted to the voltage sweep with the opposite polarity (arrows 2-3), the device that initially was in the high resistance state (HRS) switched abruptly to the low resistance state (LRS) at a low threshold voltage of ~0.23 V, which is only twice the threshold voltage of the atomic-scale state of the art synapses based on 2D MoS_2[35]. Moreover, the process of resistive switching falls within a narrow range, indicating a high cycle-to-cycle uniformity of the BABI device. Switching to LRS resulted in a current increase from 3.1×10^{-7} A to 1.6×10^{-5} A (measured at −200 mV) which is 50 times higher than the initial current. However, we also obtained devices

in which the resistive switching window was as high as 10^4, indicating that the investigated devices can be further optimized to maximize the HRS/LRS ratio (**Fig. S5**). During the final −0.5 V -> 0 V part of the sweep (arrow 4), the device spontaneously returns to its initial HRS, characterized by low current amplitudes during the next I-V scan. Whereas the rapid return to HRS holds for most of the measurements, several scans show that LRS is being retained in the low-voltage range during the positive scan from 0 to 0.5 V with the abrupt conductance drop at around 25 mV as indicated by the vertical arrow (cf. **Fig. S5)**. More precisely, during the positive scan (denoted with arrow 4), initially the devices were in LRS and then made a transition from LRS to the HRS at a notably low voltage ~0.025 V (formally called the reset process). Finally, above 0.025 V, the hysteresis contracted rapidly and the devices exhibited mostly self-rectifying behavior until 0.5 V. These results indicate that BABl is a potential multifunctional device that organizes self-rectifying memory behavior without using any additional selector element, and therefore it could very attractive for its implementation in large-scale CBA.

The spontaneous return to the low conductivity was further confirmed by performing negative-only scans in the −0.5 V range (**Fig. 5d**). Resistive switching was present during each scan, showing that the LRS is not retained and the decay to LRS occurred even when the voltage scan range was extended to −1 V. Interestingly, the currents in LRS were higher than compared to −0.5 V range, indicating that the device can exhibit states of different conductivity, although none of these states is retained from scan to scan. Such abrupt transition to LRS with a relatively high LRS/HRS currents ratio is characteristic for the creation of the conductive filament whereas the relaxation to HRS occurs probably due to its spontaneous rupture of dissolution.

The electronic structure of BABI was further investigated with UPS measurements which revealed that BABI crystallized from the 3:2 ratio is a p-type semiconductor with an optical band gap of 2.3 eV and the valence band located 1.0 eV below the Fermi level. The structure is

presented in the inset of **Fig. 5c** where the ITO and Ag work functions of −4.6 eV and −4.26 eV, respectively, were taken[36,37]. It is noteworthy that conducting the UPS measurements on a 3:1 sample was impossible due to the excess charging of the sample indicating the insulating character of the material crystallized from the stoichiometric ratio of substrates. Meanwhile, the non-stoichiometric material did not charge which additionally signalled the role of the structural defects in the BABI conduction mechanism. To support this hypothesis, we analyzed the logarithmic form of the I-V scans from which the physical mechanism that governs the resistive switching phenomena can be deduced. **Fig. 6a** shows the log-log plot of the negative branch of the I-V scan with slopes obtained by fitting the linear functions to the I-V scan data. The small gray points were excluded from the fits. The fitting values around 1 suggest that the majority of the conduction mechanism is governed by Ohmic conduction. Increasing the negative bias lead to an increase from almost purely Ohmic (slope 1.12) to non-Ohmic (1.35) conduction followed by an abrupt increase in conductance. Subsequently, decreasing the bias resulted in an increase from 1.18 to 1.59 followed by 0.98 and 0.91 regions, which showed that – except for one region – LRS is also dominated by Ohmic conduction. This mechanism is primarily observed in memristors with resistive switching based on the formation of conductive filaments.

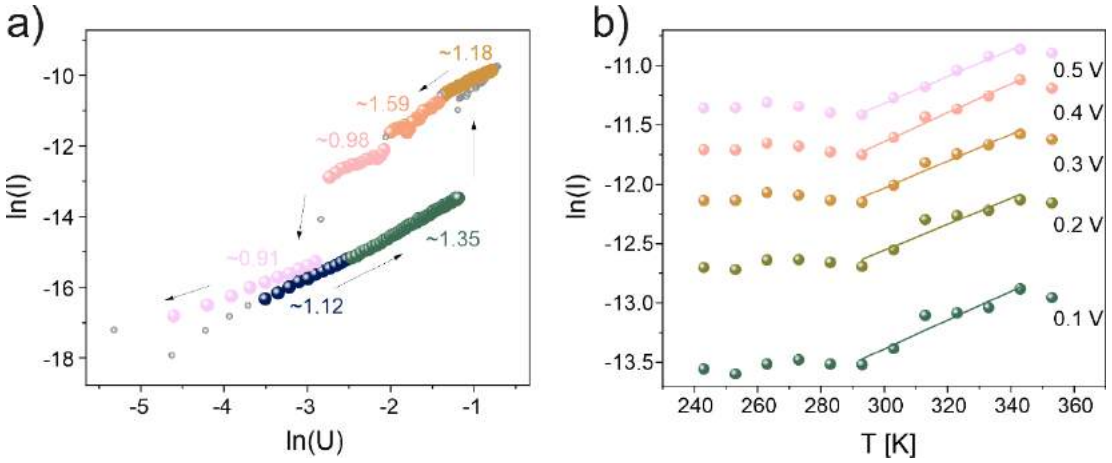

Figure 6. a) log-log plot of the negative part of the I-V scan. The linear dependence between the current logarithms and the voltage with slope ~1 indicates that conduction has Ohmic character in both in HRS and LRS. b) Arrhenius plot showing the temperature dependence of

the currents in the positive branch of I-V collected at different voltages in the non-switching branch.

To extract more information on the transport properties, we recorded the I-V scans at temperatures from 373 K to 243 K every 10 degrees (**Fig. S6**) from which the current values at varying temperatures were extracted to form an Arrhenius plot shown in **Fig. 6b**. We observed a rapid degradation of the device above 373 K; therefore, 373 K was the highest operational temperature. To ensure the device is in the non-switching voltage regime, the data points were extracted from the positive branch of the I-V scans[38]. It can be noticed that the conductivity of the devices is almost constant (within experimental error) in the range 243-293 K; however, at higher voltages, a small decrease of conductivity with increasing temperature can be observed. As it was indicated by the XRD measurements, at room temperature cations were strongly disordered, yielding a flexible structure that may affect the electronic transport within the material. Therefore, the observed lowering of conductivity is presumably due to the rotational movements of *n*-butylammonium cations in the BABI lattice which result in an increased electron scattering. At higher temperatures (293-373 K), a significant increase in current amplitudes was observed which was linearly correlated with the temperature. This behavior suggests a complex electrical transport phenomenon and not just a simple conductivity mechanism. Since BABI is a *p*-type semiconductor, the low-temperature energy regions may be attributed to electron conductivity in a heavily doped semiconductor, whereas the high-temperature region to a thermally-activated ionic transport. The value of activation energy was extracted from the linear fit (1):

$$\ln(I) \sim -\frac{1}{T}\frac{E_a}{k_B} + \ln(A) \quad (1)$$

where E_a is the activation energy, T is the temperature, k_B is Boltzmann constant, and A is a constant. The calculated value of E_a was ∼0.1 eV, corresponding to the reported energy barrier for iodine vacancies migrating in the external electric field in perovskites which was calculated

to be in the range of 0.1-0.6 eV[33,39]. For BiI_3, the energies of activation of iodine vacancies were calculated to be 0.73 eV but only 0.16 eV for the material with a deviation from stoichiometry, meaning that the defects in bismuth iodide form much easier compared to its lead counterpart[40]. Migration of iodine vacancies and the formation of iodine vacancies-rich regions which subsequently build conductive paths throughout the material is considered the major factor behind the resistive switching in iodide materials[33,34,41]. Both results in **Fig. 6a** and **6b**, supported by the conclusions from the spectroscopic measurements, indicate that the formation and spontaneous dissolution of the conductive filaments made of iodine vacancies is the most plausible mechanism of resistive switching in the case of BABI. When sufficiently high voltage is applied (i.e. above 0.25 V as seen in the I-Vs) the iodide vacancies form a conductive path moving the memristor into LRS. Upon removal of the voltage, the filament can be maintained only for a short period of time. When it spontaneously dissolves in the structure, the device returns to HRS. The decay of the resistive state is a significant distinction from the nonvolatile memristors, in which usually voltage of opposite polarity is required to reset the device[42].

Artificial memristor-based synapses have already been shown to be capable of efficiently emulating synaptic plasticity and other various neuromorphic effects[43–47]. Communication between biological neurons relies on sending and receiving short pulses of electrical activity. When one neuron releases neurotransmitter molecules into the synaptic cleft, they diffuse towards the membrane of the other cell. As soon as they reach the second neuron, they trigger a set of reactions that lead to a diffusion of Na^+ ions from the extracellular fluid into the neuron's body. The flux of ions depolarizes the membrane and, when a certain threshold is reached, the neuron produces an action potential – a short electrical pulse acting as a basic unit of the neural signal transmission. Among several mathematical models describing the neuronal dynamics, the leaky integrate-and-fire (LIF) model seizes the temporal dynamics of the membrane potential which is prone to spontaneous decay regardless of whether the action potential was

generated or not. In the latter case, the more frequently the neuron receives a stimulus, the more likely it is to fire a spike (integration). On the contrary, if stimulation occurs at intervals longer than the relaxation time constant, spiking is much less likely[48].

Owing to the diffusive dynamics, i.e. the spontaneous return to HRS, BABI memristor can emulate the leaky function of the LIF model. **Fig. 7a** shows the current relaxation dynamics after applying a short pulse with an amplitude ranging from −0.5 V to −5 V. For low voltages the current decayed at much higher rates than for the high ones. However, regardless of the amplitude, the system relaxed to the original HRS in just several seconds. Similar relaxation behaviour was measured when the voltage had fixed amplitude of −3 V but the pulse duration was decreased from 100 ms to 20 ms as shown in **Fig. 7b**. For a 100 ms pulse, the device required around 10 seconds to return to HRS, whereas for 20 ms the relaxation was almost instantaneous. **Fig. 7c** shows the dependence of the relaxation time constant t_0 as a function of the switching pulse voltage that was extracted from the data presented in **Fig. 7a** by modeling the relaxation dynamics with an exponential function:

$$I(t) = I_0 + Aexp\left(\frac{-t}{t_0}\right) \quad (2)$$

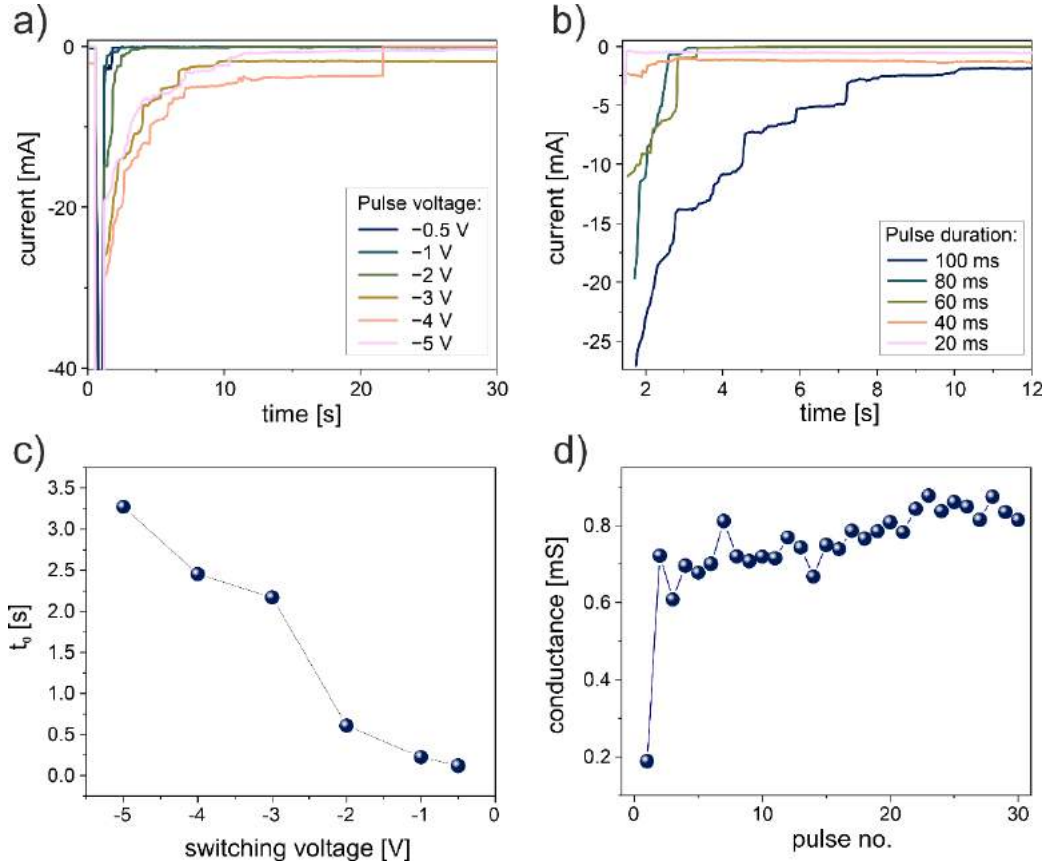

Figure 7. a) Relaxation dynamics of the BABI device after applying 100 ms single voltage pulse of different amplitudes and b) single voltage pulse with fixed −3 V amplitude and different duration. The relaxation time increases with both the amplitude and the duration. c) The relaxation time constant as a function of the pulse voltage shows that as the voltage becomes more negative, the device takes longer to return to HRS from LRS. d) Conductance adjustment with 30 voltage pulses (–2 V, 100 ms) read at –50 mV that show a rapid increase in conductance followed by steady growth.

The relaxation constant increases almost linearly with the voltage amplitude and increases almost 30x from 0.12 s for –0.5 V to 3.27 s for –5 V. This effect can be attributed to the movement of iodine vacancies – under external bias the vacancies are being displaced from their equilibrium positions and the higher the bias amplitude, the more iodine species moves and/or further they are displaced, which results in a longer relaxation time. Unfortunately, due to abrupt current drops, a similar analysis could not be fitted reliably to the data in **Fig. 7b**.

Although the BABI memristor can retain information only for short time, this feature can be used to temporarily tune the conductance of the memristive device. **Fig. 7d** shows the evolution of the conductance with 30 consecutive voltage pulses with –2 V amplitude and 100 ms duration separated by 100 ms interval. Immediately after each pulse, the resistive state was measured with –50 mV for 100 ms, showing that the conductance of the device can be adjusted with the number of pulses.

The communication between neurons is based on the exchange of short voltage spikes known as action potentials. We investigated the behaviour of BABI under pulse mode operation by applying a voltage pattern consisting of short 100 ms pulses separated by 50 ms intervals. After each measurement, the voltage was increased, resulting in the device randomly firing current spikes as shown in **Fig. 8a**. When the voltage amplitude of the stimulus was −300 mV, the device did not produce any output spikes. Increasing the voltage to −500 mV, −800 mV and −1000 mV caused the device to fire more frequently and −1500 mV voltage induced the current spikes almost with every pulse. This behavior closely mimics the integrating function of the LIF neuron, where the local graded potential (LGP) resulting from spatial and temporal summation of synaptic inputs to the neuron has to exceed a certain threshold value above which the neuron generates an action potential in an all-or-none fashion. It is noteworthy that upon integration of a certain set of input voltage pulses and firing high-amplitude current spikes, the device returns to its resting state with lower currents (**Fig. S7**) which complies with the leaky function of the LIF model[49,50]. This model may be thus interpreted as consisting of a part performing the synaptic signal integration function that is implemented by the memristor and a part performing the action potential firing function that has to be implemented by an additional external circuit[51]. As seen in the graphs, higher voltage pulse amplitudes result in an increased probability of firing a current spike. To represent this behavior quantitatively, we calculated the probability of spiking as a function of the voltage (**Fig. 8b**). Due to the large variance in the

current amplitudes, the threshold above which the output signals were considered a spike was arbitrarily chosen as 30% of the highest current in the given set and was indicated with dashed horizontal lines in **Fig. 8a**. Therefore, every current spike exceeding this threshold value was considered as a suprathreshold event representing the LGP that can trigger an all-or-none action potential in the LIF neuron[51]. The calculated probability of spike generation rose slowly to 5% for voltages from –300 mV to –1000 mV but jumped to 30% when the voltage was set to –1500 mV. This abrupt change is presumably related to the narrow voltage window within which the conductive filament is formed. The high amplitude pulses are more likely to induce filament formation, which transfers the device to LRS and results in high current spikes. Upon dissolution of the filament, the device switches back to HRS exhibiting low-amplitude currents.

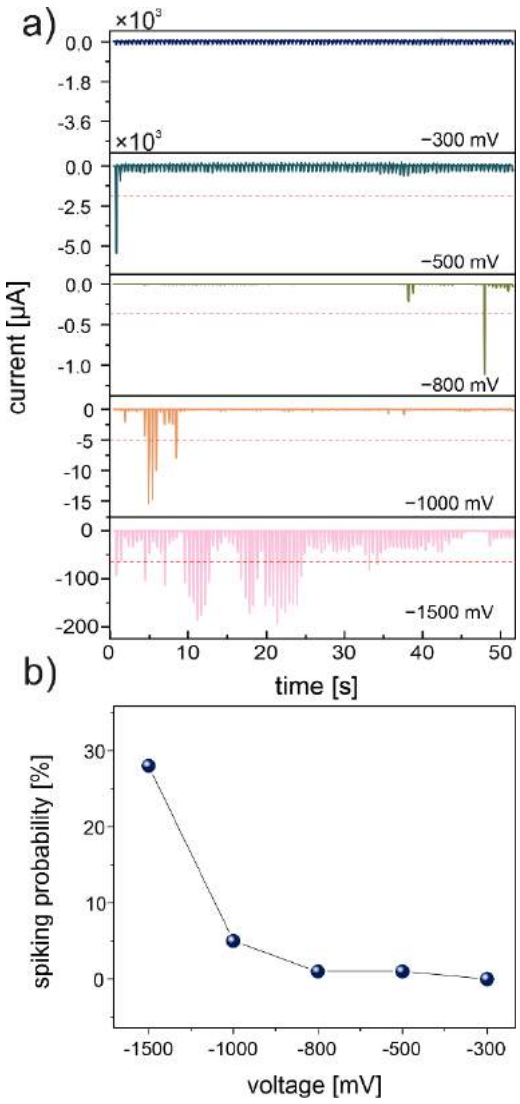

Figure 8. a) Current spikes randomly generated by applying 100 voltage pulses. The number of spikes exceeding the threshold in each set increases with the voltage of the stimulus. The red dashed lines indicate the threshold amplitude above which the current spike was classified as "neuron firing". b) Spiking probability as a function of voltage calculated as the percentage of current spikes exceeding the threshold (red dashed lines in plot a).

The volatile character of memory can be utilized to emulate another short-term synaptic plasticity effect: synaptic facilitation. The efficacy of some biological synapses can be temporarily increased by a train of unipolar, closely spaced pulses in a process termed synaptic facilitation. Facilitation of excitatory postsynaptic potentials during bursts of activity of presynaptic neurons allows synapses to influence postsynaptic cells stronger[52]. When

presynaptic trains consist of only two pulses, paired-pulse facilitation (PPF) occurs. As the time interval separating these two stimuli becomes shorter, the magnitude of enhancement increases. Thus, pulses that are distant from each other in terms of time will cause a lower enhancement than pulses applied with high frequency. Despite the fact that PPF involves only two pulses, it can be extended to include numerous pulses, which is known as frequency facilitation. In memristors, the synaptic enhancement will manifest itself as a gradual increase in the currents with the magnitude of this enhancement dependent on the frequency of the applied bias. The enhancement of the current with frequency can be explained by the volatility of the BABI memristor. When the system relaxes after being stimulated with a voltage pulse and the second pulse arrives before it fully returns to the HRS, the current induced by the second voltage pulse will have a higher amplitude. **Fig. 9** shows the current induced by a train of short 100 μs pulses at different frequencies. Here, shorter pulses were used to stretch the current enhancement over time, since longer pulses caused abrupt facilitation followed by a plateau, as shown in **Fig. 7d**. For 200 Hz behaviour similar to random spiking was observed, suggesting that the same effect can be obtained with shorter pulses at higher frequencies. Increasing the frequency to 500 Hz leads to the generation of a block of spikes in the latter part of the train with higher amplitude than those observed for 200 Hz. Increasing the frequency further leads to even higher currents. For 1000 Hz after rapid increase within several first pulses, steady growth of amplitude was maintained over the pulses train. Similar behavior was observed for 2000 Hz; however, in this case, the growth that occurred during the measurement was the most significant along with the highest amplitudes. These results show that the current facilitation is dependent on the frequency of the voltage train, mimicking the behavior of frequency facilitation in biological synapses in the brain.

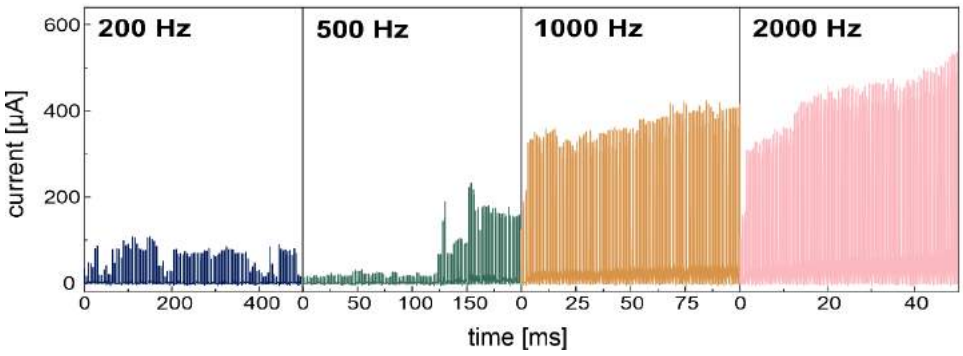

Figure 9. Frequency facilitation is represented as an increase in the current growth dynamics with frequency. Short voltage pulses (−3 V, 100 μs) of high frequency induced overall higher currents with noticeably faster growth dynamics.

The fabricated BABI memristive devices were investigated for synaptic potentiation and depression characteristics similar to those of biological synapses. To achieve such features, the devices first exposed 158 pulses of −2 V amplitude and duration of 25 ms followed by 159 pulses with an amplitude of +2 V were exposed on the devices, facilitating a gradual change in post-synaptic conductivity (**Fig. S8**). This alteration of synaptic conductivity is presented on a double normalized scale (**Fig. 10a**) and was fitted with the following equations to extract the non-linear weight parameter γ for LTP (γ = 4.5) and LTD (γ = 0.01).

$$G_{LTP} = G_{min} + G_0 \left(1 - \exp\left(\frac{P}{\gamma}\right)\right) \quad (3)$$

$$G_{LTD} = G_{max} - G_0 \left(1 - exp\left(-\frac{P - P_{max}}{\gamma}\right)\right) \quad (4)$$

$$G_0 = \frac{G_{max} - G_{min}}{1 - exp\left(\frac{-P_{max}}{\gamma}\right)} \quad (5)$$

In the above equations, G_{max} and G_{min} represent the maximum and minimum conductance values obtained at the LTP and LTD, respectively, and P denotes the number of pulses used in the experiment.

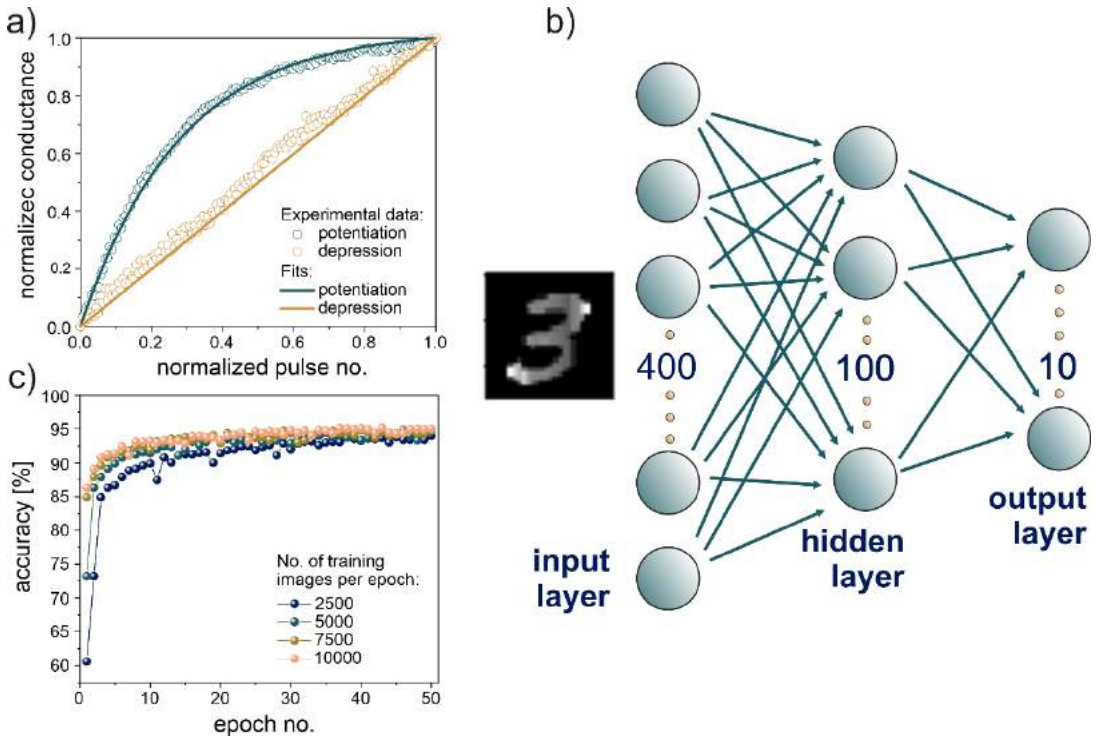

Figure 10. a) Variation of normalized conductance with normalized pulse no. b) Schematic representation of ANN with fully connected layers. c) Classification accuracy (~95%) of MNIST handwritten digits using the BABI memristor device parameters for the different numbers of training images used per epoch.

Next, artificial neural network (ANN) simulations were run based on the experimentally extracted parameters of BABI memristors to find the classification accuracy of the modified National Institute of Standards and Technology (MNIST) database of handwritten digits, which includes 10000 images in the training set and 60000 in the testing set. The ANN used for simulation (**Fig. 10b**) consisted of three layers that were connected with the standard feedforward algorithm. The input layer, the hidden layer, and an output layer are composed of 400, 100, and 10 neurons, respectively. To minimize recognition inaccuracy, the stochastic gradient descent optimizer was used. A systematic improvement in the classification accuracy was achieved (**Fig. 10c**) by varying the number of train images per epoch from 2500 to 10000. In general, the proposed model achieved an excellent classification accuracy of ~95% within

just 50 epochs, highlighting the potential of current research for the hardware accelerator of neural network hardware accelerator[53,54].

CONCLUSION

We exploited volatile memristor based on a novel butylammonium bismuth iodide active layer to mimic short-term dynamics. Despite the close compositional similarity with methylammonium bismuth iodide that crystallizes in a perovskite-like structure, this novel type of hybrid material was determined to be an ionic crystal. With simple and low-cost chemical methods, memristive devices with diffusive resistive switching dynamics were prepared and investigated for their application in neuromorphic information processing. The resistive switching in BABI is presumably due to the migration of iodine vacancies in the external electric fields, which form a conductive filament, transferring the device from HRS to LRS. However, the high-conductance state is not retained and the device returns to its HRS, which can be attributed to the instability of the filament. Using this phenomenon, we achieved firing response behaviors corresponding to the leaky function of the LIF neuron model, namely relaxation rate dependence on both voltage and duration of the switching pulse. Upon low-frequency input, the BABI memristor generated current spikes randomly, but the probability of firing depended on the voltage of the voltage pulses, mimicking the integrating capabilities of neurons described by the LIF model. In the high-frequency regime, the BABI mimics the frequency facilitation by exhibiting both an increase in amplitude with the frequency and facilitation with the number of pulses. Finally, we showed the possibility of utilizing BABI diffusive memristors in artificial neural networks by conducting simulations with the resistive switching dynamics extracted from the pulse experiments. By using the MNIST handwritten digits dataset, the simulated ANN achieved nearly 95% recognition accuracy within only 50 epochs.

In summary, this work shows an application of a novel type of hybrid bismuth-based material in a volatile memristor capable of mimicking the short-term behaviors of biological neurons. With their diffusive dynamics, high resistive switching window, low production costs and long stability in the ambient atmosphere compared to the hybrid perovskite-based artificial synapses, BABI memristors could potentially serve as a building block of neural networks for the next generation of brain-inspired computing platforms.

METHODS

Synthesis of n-butylammonium bismuth iodide (BABI). Complexes of n-butylammonium bismuth iodide were synthesized using an antisolvent precipitation process as a promising technique to prepare ultrafine crystals. The n-butylammonium iodide (3 mmol; 0.60315 g) and bismuth iodide (2 mmol; 1.18 g) were dissolved in methanol and exposed to dichloromethane as an antisolvent (in which they are insoluble) in a large jar; gradually the evaporation of solvents results in pure crystalline materials.

Device fabrication. Devices used in this work consisted of BABI as the active material, with ITO and Ag serving as the bottom and top electrodes, respectively. Before device preparation, ITO substrates (Ossilla Ltd.) were cleaned in an ultrasonic bath with water with detergent (Hellmanex), DI water, acetone and isopropyl alcohol and subsequently dried with N_2. Immediately before spin coating, ITO substrates were cleaned with O_2 plasma for 10 min.

To form the BABI solution, bismuth(III) iodide (BiI_3) (Sigma Aldrich) and butylammonium bismuth iodide (BAI) (Ossilla Ltd.) were dissolved in N,N-dimethylformamide (DMF) to obtain a concentration of 32% by weight and stirred for 30 min. To deposit the PMMA buffer layer, a solution of 5 mg ml^{-1} PMMA (120,000 MW, Sigma Aldrich) was prepared by dissolving the polymer in toluene and stirring for 12 h.

The BABI layer was formed by spin coating the solution on the ITO substrates at 2000 rpm for 60 s, after which the substrate was immediately transferred to a hotplate and annealed at 100 °C for 30 mins. Then the PMMA solution was spin-coated on top of the substrate at the same speed and annealed on the hotplate at 100 °C for 10 mins. All of the preparation steps, including the preparation of the solutions, were conducted under an inert atmosphere. The fabrication of the device was completed by sputtering 70 nm of Ag with a shadow mask, producing metal-semiconductor-metal structures with an electrode area of 2.25 mm^2.

UV-vis spectroscopy. BABI thin layers for spectroscopic measurements were prepared in the same way as the memristive devices, excluding the sputtering of the top electrode. UV-vis spectra were collected with a PerkinElmer Lambda750 spectrophotometer in transmission mode.

Electrical measurements. Electrical measurements were conducted with Keithley 4200-SCS using Everbeing manual probe station equipped with micropositioners to connect to the electrodes. During the measurements, the Ag electrode was the working electrode whereas the ITO electrode was grounded. All electrical measurements were conducted in ambient air.

X-ray diffraction. SCXRD measurements were conducted on an XtaLAB Synergy-S X-ray diffractometer using MoKα radiation at 130 K. The CrysalisPro 1.171.41.122a (Rigaku OD, 2021) software was used for data collection and reduction. The structure was solved using direct methods (SHELXT) and refined using the least squares procedure (SHELXL incorporated into a WinGX package)[55–57]. Thin layer XRD measurements were performed at room temperature on the Empyrean diffractometer (PANalytical) with Cu Kα radiation in the reflection mode. The data were collected during a continuous scan performed applying parallel beam geometry (Göbel mirror in the incident beam optics and parallel plate collimator in the diffracted beam optics).

Computational methods. The electron band structure was determined by Density Functional Theory (DFT)[58–60] calculations using the CASTEP software[61,62]. To describe the non-local exchange correlation energy we used the generalized gradient approximation (GGA) with the Perdew-Burker-Ernzerhof (PBE) functional. CASTEP-specific On-the-Fly Generated Ultrasoft (OFTG Ultrasoft) pseudopotentials were adopted with a plane-wave kinetic energy cutoff of 517 eV (fine quality) for further accuracy. To include wan der Waals interactions in the system, a semi-empirical dispersion correction was applied with the Tkatchenko-Scheffler (TS) scheme. The studied material was considered not magnetic, therefore the spin polarization effects were omitted. Before we performed the band structure calculations, we conducted the geometry optimization. The BABI structure is characterized by a relatively large unit cell (approximately 5742 $Å^3$), so the Γ-point sampling of the irreducible part of the first Brillouin zone turned out to be sufficient. The calculations for geometry optimization and electron spectroscopy were considered convergent when the energy change per atom was less than 10^{-5} and 10^{-6} eV, respectively. Gaussian-like Fermi smearing was used. The distance cut-off point for bond populations was set to 3.0 Å.

AUTHOR INFORMATION

Corresponding Author

Piotr Zawal

Email: zawal@agh.edu.pl

Notes

The authors declare no competing financial interest.

ACKNOWLEDGEMENTS

Authors acknowledge the financial support of the Polish National Science Center within the ETIUDA (grant agreement No. UMO-2020/36/T/ST5/00421) and PRELUDIUM (grant agreement No. UMO-2018/31/N/ST5/03215) projects. PZ has been partly supported by the EU project POWR.03.02.00- 00-I004/16. This research was partly supported by the program "Excellence initiative–research university" for the AGH University of Science and Technology. The authors thank Dr. Katarzyna Berent for performing SEM measurements of the thin layers. DFT calculations were performed at Academic Computer Centre Cyfronet AGH within computational grant PLGSURFACE3.

In this study, the Scientific colour map batlow (https://doi.org/10.5281/zenodo.5501399) is used to prevent visual distortion of the data and exclusion of readers with colour vision deficiencies (https://doi.org/10.5281/zenodo.1243862).

SUPPORTING INFORMATION

XRD structure refinement details, torsion angles, geometry of hydrogen bonds and weak interactions, fingerprint plots, Partial Density of States calculations results, I-V curves without buffer layer, I-V curves with high resistive switching window, temperature dependence of I-V curves, stochastic current generation, current facilitation and depression (PDF).

REFERENCES

(1) Klejna, S.; Mazur, T.; Wlaźlak, E.; Zawal, P.; Soo, H. Sen; Szaciłowski, K. Halogen-Containing Semiconductors: From Artificial Photosynthesis to Unconventional Computing. *Coord. Chem. Rev.* **2020**, *415*, 213316. https://doi.org/10.1016/j.ccr.2020.213316.

(2) Athanasiou, V.; Konkoli, Z. Computing with Modest Resources: How to Have Your Cake and Eat It Too. In *Handbook of Unconventional Computing*; 2021; pp 341–361. https://doi.org/10.1142/9789811235726_0009.

(3) Chua, L. Memristor - The Missing Circuit Element. *IEEE Trans. Circuit Theory* **1971**, *C*.

(4) Strukov, D. B.; Snider, G. S.; Stewart, D. R.; Williams, R. S. The Missing Memristor Found. *Nature* **2008**, *453* (7191), 80–83. https://doi.org/10.1038/nature06932.

(5) Liu, B.; Liu, Z.; Chiu, I.-S.; Di, M.; Wu, Y.; Wang, J.-C.; Hou, T.-H.; Lai, C.-S. Programmable Synaptic Metaplasticity and below Femtojoule Spiking Energy Realized in Graphene-Based Neuromorphic Memristor. *ACS Appl. Mater. Interfaces* **2018**, *10* (24), 20237–20243. https://doi.org/10.1021/acsami.8b04685.

(6) Balatti, S.; Larentis, S.; Gilmer, D. C.; Ielmini, D. Multiple Memory States in Resistive Switching Devices Through Controlled Size and Orientation of the Conductive Filament. *Adv. Mater.* **2013**, *25* (10), 1474–1478. https://doi.org/10.1002/adma.201204097.

(7) Stathopoulos, S.; Khiat, A.; Trapatseli, M.; Cortese, S.; Serb, A.; Valov, I.; Prodromakis, T. Multibit Memory Operation of Metal-Oxide Bi-Layer Memristors. *Sci. Rep.* **2017**, *7* (1), 17532. https://doi.org/10.1038/s41598-017-17785-1.

(8) So-Yeon Kim; June-Mo Yang; Sun-Ho Lee; Nam-Gyu Park. A Layered (n -C 4 H 9 NH 3) 2 CsAgBiBr 7 Perovskite for Bipolar Resistive Switching Memory with a High ON/OFF Ratio. *Nanoscale* **2021**, *13* (29), 12475–12483. https://doi.org/10.1039/D1NR03245C.

(9) Milano, G.; Luebben, M.; Ma, Z.; Dunin-Borkowski, R.; Boarino, L.; Pirri, C. F.; Waser, R.; Ricciardi, C.; Valov, I. Self-Limited Single Nanowire Systems Combining All-in-One

Memristive and Neuromorphic Functionalities. *Nat. Commun. 2018 91* **2018**, *9* (1), 1–10. https://doi.org/10.1038/s41467-018-07330-7.

(10) Yu, M.; Cai, Y.; Wang, Z.; Fang, Y.; Liu, Y.; Yu, Z.; Pan, Y.; Zhang, Z.; Tan, J.; Yang, X.; Li, M.; Huang, R. Novel Vertical 3D Structure of TaOx-Based RRAM with Self-Localized Switching Region by Sidewall Electrode Oxidation. *Sci. Reports 2016 61* **2016**, *6* (1), 1–10. https://doi.org/10.1038/srep21020.

(11) Banerjee, W.; Zhang, X.; Luo, Q.; Lv, H.; Liu, Q.; Long, S.; Liu, M. Design of CMOS Compatible, High-Speed, Highly-Stable Complementary Switching with Multilevel Operation in 3D Vertically Stacked Novel HfO2/Al2O3/TiOx (HAT) RRAM. *Adv. Electron. Mater.* **2018**, *4* (2), 1700561. https://doi.org/10.1002/aelm.201700561.

(12) Xiao, T. P.; Bennett, C.; Feinberg, B.; Agarwal, S.; Marinella, M. Analog Architectures for Neural Network Acceleration Based on Non-Volatile Memory. *Appl. Phys. Rev.* **2020**, *7* (3), 031301. https://doi.org/10.1063/1.5143815.

(13) Luo, Z.-D.; Yang, M.-M.; Alexe, M. Dissolvable Memristors for Physically Transient Neuromorphic Computing Applications. **2019**. https://doi.org/10.1021/acsaelm.9b00670.

(14) Jiang, H.; Han, L.; Lin, P.; Wang, Z.; Jang, M. H.; Wu, Q.; Barnell, M.; Yang, J. J.; Xin, H. L.; Xia, Q. Sub-10 Nm Ta Channel Responsible for Superior Performance of a HfO 2 Memristor OPEN. *Nat. Publ. Gr.* **2016**. https://doi.org/10.1038/srep28525.

(15) Wang, R.; Yang, J.; Mao, J.; Wang, Z.; Wu, S.; Zhou, M.; Chen, T.; Zhou, Y.; Han, S. Recent Advances of Volatile Memristors: Devices, Mechanisms, and Applications. *Adv. Intell. Syst.* **2020**, *2* (9), 2000055. https://doi.org/10.1002/aisy.202000055.

(16) Carboni, R.; Ielmini, D. Applications of Resistive Switching Memory as Hardware Security Primitive. *Springer Ser. Adv. Microelectron.* **2020**, *63*, 93–131. https://doi.org/10.1007/978-981-13-8379-3_4.

(17) Sun, Z.; Pedretti, G.; Ambrosi, E.; Bricalli, A.; Wang, W.; Ielmini, D. Solving Matrix Equations in One Step with Cross-Point Resistive Arrays. *Proc. Natl. Acad. Sci. U. S. A.* **2019**, *116* (10), 4123–4128. https://doi.org/10.1073/pnas.1815682116.

(18) Sun, Z.; Pedretti, G.; Bricalli, A.; Ielmini, D. One-Step Regression and Classification with Cross-Point Resistive Memory Arrays. *Sci. Adv.* **2020**, *6* (5), eaay2378. https://doi.org/10.1126/sciadv.aay2378.

(19) Song, S.; Kim, J.; Kwon, S. M.; Jo, J.-W.; Park, S. K.; Kim, Y.-H. Recent Progress of Optoelectronic and All-Optical Neuromorphic Devices: A Comprehensive Review of Device Structures, Materials, and Applications. *Adv. Intell. Syst.* **2021**, *3* (4), 2000119. https://doi.org/10.1002/aisy.202000119.

(20) Ielmini, D.; Wang, Z.; Liu, Y. Brain-Inspired Computing via Memory Device Physics. *APL Mater.* **2021**, *9* (5). https://doi.org/10.1063/5.0047641.

(21) Stoliar, P.; Tranchant, J.; Corraze, B.; Janod, E.; Besland, M. P.; Tesler, F.; Rozenberg, M.; Cario, L. A Leaky-Integrate-and-Fire Neuron Analog Realized with a Mott Insulator. *Adv. Funct. Mater.* **2017**, *27* (11). https://doi.org/10.1002/adfm.201604740.

(22) Sasago, Y.; Kinoshita, M.; Morikawa, T.; Kurotsuchi, K.; Hanzawa, S.; Mine, T.; Shima, A.; Fujisaki, Y.; Kume, H.; Moriya, H.; Takaura, N.; Torii, K. Cross-Point Phase Change Memory with 4F2 Cell Size Driven by Low-Contact-Resistivity Poly-Si Diode. *Dig. Tech. Pap. - Symp. VLSI Technol.* **2009**, *772* (2006), 24–25.

(23) Zhang, C.; Song, Z. T.; Wu, G. P.; Liu, B.; Wan, X. D.; Wang, L.; Wang, L. H.; Yang, Z. Y.; Chen, B.; Feng, S. L. Design and Fabrication of Dual-Trench Epitaxial Diode Array for High-Density Phase-Change Memory. *IEEE Electron Device Lett.* **2011**, *32* (8), 1014–1016. https://doi.org/10.1109/LED.2011.2155028.

(24) Gilli, G.; Gilli, P. Towards an Unified Hydrogen-Bond Theory. *J. Mol. Struct.* **2000**, *552* (1–3), 1–15. https://doi.org/10.1016/S0022-2860(00)00454-3.

(25) Palusiak, M.; Janowska, I.; Zakrzewski, J.; Grabowski, S. J. Charge-Assisted N—H...I and C—H...I Hydrogen Bonding in (1 R ,2 S)-1-(Ferrocenylmethyl)-2-(Methoxymethyl)Pyrrolidinium Iodide. *Acta Crystallogr. Sect. C Cryst. Struct. Commun.* **2005**, *61* (1), m55–m57. https://doi.org/10.1107/S0108270104027581.

(26) Hwang, B.; Lee, J.-S. Lead-Free, Air-Stable Hybrid Organic–Inorganic Perovskite Resistive Switching Memory with Ultrafast Switching and Multilevel Data Storage. *Nanoscale* **2018**, *10* (18), 8578–8584. https://doi.org/10.1039/C8NR00863A.

(27) Podraza, N. J.; Qiu, W.; Hinojosa, B. B.; Motyka, M. A.; Phillpot, S. R.; Baciak, J. E.; Trolier-McKinstry, S.; Nino, J. C. Band Gap and Structure of Single Crystal BiI3 : Resolving Discrepancies in Literature. *J. Appl. Phys.* **2013**, *114* (3), 033110. https://doi.org/10.1063/1.4813486.

(28) Moss, T. S. The Interpretation of the Properties of Indium Antimonide. *Proc. Phys. Soc. Sect. B* **1954**, *67* (10), 775–782. https://doi.org/10.1088/0370-1301/67/10/306.

(29) Pankove, J. I.; Kiewit, D. A. *Optical Processes in Semiconductors*; Courier Corporation, 1972; Vol. 119. https://doi.org/10.1149/1.2404256.

(30) Savill, K. J.; Ulatowski, A. M.; Herz, L. M. Optoelectronic Properties of Tin-Lead Halide Perovskites. *ACS Energy Lett.* **2021**, *6* (7), 2413–2426. https://doi.org/10.1021/acsenergylett.1c00776.

(31) Zarhri, Z.; Cano, A. D.; Oubram, O.; Ziat, Y.; Bassam, A. Optical Measurements and Burstein Moss Effect in Optical Properties of Nb-Doped BaSnO3 Perovskite. *Micro and Nanostructures* **2022**, 207223. https://doi.org/10.1016/j.micrna.2022.207223.

(32) National Institute of Standards and Technology. NIST X-ray Photoelectron Spectroscopy Database https://srdata.nist.gov/xps/XPSDetailPage.aspx?AllDataNo=31255. https://doi.org/10.18434/T4T88K.

(33) Zhu, X.; Lu, W. D. Optogenetics-Inspired Tunable Synaptic Functions in Memristors. *ACS Nano* **2018**, *12* (2), 1242–1249. https://doi.org/10.1021/acsnano.7b07317.

(34) Sun, Y.; Tai, M.; Song, C.; Wang, Z.; Yin, J.; Li, F.; Wu, H.; Zeng, F.; Lin, H.; Pan, F.; Sun, Y.; Tai, M.; Yin, J.; Li, F.; Wu, H.; Zeng, F.; Lin, H.; Pan, F.; Song, C.; Wang, Z.; Yin, J.; Li, F.; Wu, H.; Zeng, F.; Lin, H.; Pan, F. Competition between Metallic and Vacancy Defect Conductive Filaments in a CH3NH3PbI3-Based Memory Device. *J. Phys. Chem. C* **2018**, *122* (11), 6431–6436. https://doi.org/10.1021/acs.jpcc.7b12817.

(35) Xu, R.; Jang, H.; Lee, M.-H.; Amanov, D.; Cho, Y.; Kim, H.; Park, S.; Shin, H.-J.; Ham, D. Vertical MoS 2 Double-Layer Memristor with Electrochemical Metallization as an Atomic-Scale Synapse with Switching Thresholds Approaching 100 MV. **2019**, *28*, 54. https://doi.org/10.1021/acs.nanolett.8b05140.

(36) Dweydari, A. W.; Mee, C. H. B. Work Function Measurements on (100) and (110) Surfaces of Silver. *Phys. Status Solidi* **1975**, *27* (1), 223–230. https://doi.org/10.1002/pssa.2210270126.

(37) Zawal, P.; Mazur, T.; Lis, M.; Chiolerio, A.; Szaciłowski, K. Light-Induced Synaptic Effects Controlled by Incorporation of Charge-Trapping Layer into Hybrid Perovskite Memristor. *Adv. Electron. Mater.* **2021**, 2100838. https://doi.org/10.1002/aelm.202100838.

(38) Michalas, L.; Stathopoulos, S.; Khiat, A.; Prodromakis, T. An Electrical Characterisation Methodology for Identifying the Switching Mechanism in TiO2 Memristive Stacks. *Sci. Rep.* **2019**, *9* (1), 1–8. https://doi.org/10.1038/s41598-019-44607-3.

(39) Azpiroz, J. M.; Mosconi, E.; Bisquert, J.; De Angelis, F. Defect Migration in Methylammonium Lead Iodide and Its Role in Perovskite Solar Cell Operation. *Energy Environ. Sci.* **2015**, *8* (7), 2118–2127. https://doi.org/10.1039/c5ee01265a.

(40) Dmitriyev, Y. N.; Bennett, P. R.; Cirignano, L. J.; Klugerman, M. B.; Shah, K. S. Bismuth Iodide Crystals as a Detector Material: Some Optical and Electrical Properties. *Hard X-Ray, Gamma-Ray, Neutron Detect. Phys.* **1999**, *3768* (July), 521. https://doi.org/10.1117/12.366625.

(41) Zhu, X.; Lee, J.; Lu, W. D. Iodine Vacancy Redistribution in Organic–Inorganic Halide Perovskite Films and Resistive Switching Effects. *Adv. Mater.* **2017**, *29* (29), 1–8. https://doi.org/10.1002/adma.201700527.

(42) Lv, F.; Gao, C.; Zhou, H.-A.; Zhang, P.; Mi, K.; Liu, X. Nonvolatile Bipolar Resistive Switching Behavior in the Perovskite-like ($CH_3NH_3)_2FeCl_4$. *ACS Appl. Mater. Interfaces* **2016**, acsami.6b04464. https://doi.org/10.1021/acsami.6b04464.

(43) Xiao, Z.; Huang, J. Energy-Efficient Hybrid Perovskite Memristors and Synaptic Devices. *Adv. Electron. Mater.* **2016**, *2* (7), 1600100. https://doi.org/10.1002/aelm.201600100.

(44) Mazur, T.; Zawal, P.; Szaciłowski, K. Synaptic Plasticity, Metaplasticity and Memory Effects in Hybrid Organic-Inorganic Bismuth-Based Materials. *Nanoscale* **2019**, *11* (3), 1080–1090. https://doi.org/10.1039/c8nr09413f.

(45) Chang, C.-C. C.; Chen, P.-C. C.; Hudec, B.; Liu, P.-T. T.; Hou, T.-H. H. Interchangeable Hebbian and Anti-Hebbian STDP Applied to Supervised Learning in Spiking Neural Network; pp 15.5.1-15.5.4. https://doi.org/10.1109/IEDM.2018.8614648.

(46) Milo, V.; Malavena, G.; Compagnoni, C. M.; Ielmini, D. Memristive and CMOS Devices for Neuromorphic Computing. *Materials (Basel).* **2020**, *13* (1), 166. https://doi.org/10.3390/ma13010166.

(47) Upadhyay, N. K.; Jiang, H.; Wang, Z.; Asapu, S.; Xia, Q.; Joshua Yang, J. Emerging Memory Devices for Neuromorphic Computing. *Adv. Mater. Technol.* **2019**, *4* (4), 1–13. https://doi.org/10.1002/admt.201800589.

(48) Gerstner, W.; Kistler, W. M.; Naud, R.; Paninski, L. *Neuronal Dynamics: From Single Neurons to Networks and Models of Cognition*; 2014. https://doi.org/10.1017/CBO9781107447615.

(49) Huang, H. M.; Yang, R.; Tan, Z. H.; He, H. K.; Zhou, W.; Xiong, J.; Guo, X. Quasi-Hodgkin–Huxley Neurons with Leaky Integrate-and-Fire Functions Physically Realized with Memristive Devices. *Adv. Mater.* **2019**, *31* (3), 1–8. https://doi.org/10.1002/adma.201803849.

(50) Hao, S.; Ji, X.; Zhong, S.; Pang, K. Y.; Lim, K. G.; Chong, T. C.; Zhao, R. A Monolayer Leaky Integrate-and-Fire Neuron for 2D Memristive Neuromorphic Networks. *Adv. Electron. Mater.* **2020**, *6* (4), 1–8. https://doi.org/10.1002/aelm.201901335.

(51) Yang, J.-Q.; Wang, R.; Wang, Z.-P.; Ma, Q.-Y.; Mao, J.-Y.; Ren, Y.; Yang, X.; Zhou, Y.; Han, S.-T. Leaky Integrate-and-Fire Neurons Based on Perovskite Memristor for Spiking

Neural Networks. *Nano Energy* **2020**, *74*, 104828. https://doi.org/10.1016/j.nanoen.2020.104828.

(52) Jackman, S. L.; Regehr, W. G. The Mechanisms and Functions of Synaptic Facilitation. *Neuron* **2017**, *94* (3), 447–464. https://doi.org/10.1016/j.neuron.2017.02.047.

(53) Zeng, F.; Guo, Y.; Hu, W.; Tan, Y.; Zhang, X.; Feng, J.; Tang, X. Opportunity of the Lead-Free All-Inorganic Cs3Cu2I5 Perovskite Film for Memristor and Neuromorphic Computing Applications. *ACS Appl. Mater. Interfaces* **2020**, *12* (20), 23094–23101. https://doi.org/10.1021/acsami.0c03106.

(54) Hu, M.; Graves, C. E.; Li, C.; Li, Y.; Ge, N.; Montgomery, E.; Davila, N.; Jiang, H.; Williams, R. S.; Yang, J. J.; Xia, Q.; Strachan, J. P. Memristor-Based Analog Computation and Neural Network Classification with a Dot Product Engine. *Adv. Mater.* **2018**, *30* (9), 1705914. https://doi.org/10.1002/adma.201705914.

(55) Sheldrick, G. M. SHELXT – Integrated Space-Group and Crystal-Structure Determination. *Acta Crystallogr. Sect. A Found. Adv.* **2015**, *71* (1), 3–8. https://doi.org/10.1107/S2053273314026370.

(56) Sheldrick, G. M. Crystal Structure Refinement with SHELXL. *Acta Crystallogr. Sect. C Struct. Chem.* **2015**, *71* (1), 3–8. https://doi.org/10.1107/S2053229614024218.

(57) Farrugia, L. J. WinGX and ORTEP for Windows : An Update. *J. Appl. Crystallogr.* **2012**, *45* (4), 849–854. https://doi.org/10.1107/S0021889812029111.

(58) Hohenberg, P.; Kohn, W. Inhomogeneous Electron Gas. *Phys. Rev.* **1964**, *136* (3B), B864–B871. https://doi.org/10.1103/PhysRev.136.B864.

(59) Kohn, W.; Sham, L. J. Self-Consistent Equations Including Exchange and Correlation Effects. *Phys. Rev.* **1965**, *140* (4A), A1133–A1138. https://doi.org/10.1103/PhysRev.140.A1133.

(60) Francis, G. P.; Payne, M. C. Finite Basis Set Corrections to Total Energy Pseudopotential Calculations. *J. Phys. Condens. Matter* **1990**, *2* (19), 4395–4404. https://doi.org/10.1088/0953-8984/2/19/007.

(61) Clark, S. J.; Segall, M. D.; Pickard, C. J.; Hasnip, P. J.; Probert, M. I. J.; Refson, K.; Payne, M. C. First Principles Methods Using CASTEP. *Zeitschrift für Krist. - Cryst. Mater.* **2005**, *220* (5–6), 567–570. https://doi.org/10.1524/zkri.220.5.567.65075.

(62) Segall, M. D.; Lindan, P. J. D.; Probert, M. J.; Pickard, C. J.; Hasnip, P. J.; Clark, S. J.; Payne, M. C. First-Principles Simulation: Ideas, Illustrations and the CASTEP Code. *J. Phys. Condens. Matter* **2002**, *14* (11), 2717–2744. https://doi.org/10.1088/0953-8984/14/11/301.

Supporting Information

Leaky integrate-and-fire model and short-term synaptic plasticity emulated in a novel bismuth-based diffusive memristor

P. Zawal,[a,b] D. Das,[c] M. Gryl,[d] A. Sławek,[a] G. Abdi,[a] E. Gerouville,[e] M. Marciszko-Wiąckowska,[a] M. Marzec,[a] G. Hess,[f] D. G. Georgiadou,[e] K. Szaciłowski[a]

a – Academic Centre for Materials and Nanotechnology, AGH University of Science and Technology, al. Mickiewicza 30, Krakow, Poland

b – Faculty of Physics and Applied Computer Science, AGH University of Science and Technology, al. Mickiewicza 30, Krakow, Poland

c – Department of Physics, School of Natural Sciences, Shiv Nadar University, Delhi-NCR, NH-91, Dadri, Gautam Buddha Nagar, Uttar Pradesh 201314, India

d – Crystal Engineering and Structural Analysis Group, Department of Crystal Chemistry and Crystal Physics, Faculty of Chemistry, Jagiellonian University in Kraków, ul. Gronostajowa 2, 30-387 Kraków, Poland

e – Electronics and Computer Science, University of Southampton, Southampton SO17 1BJ, UK

f – Department of Neurophysiology and Chronobiology, Institute of Zoology and Biomedical Research, Jagiellonian University, 30-387 Krakow, Poland

Table S1. Crystal data, measurement conditions and structure refinement details.

Chemical formula	$C_{12}H_{36}B_iI_6N_3$
M_r	1192.82
Crystal system, space group	orthorhombic, *P*ccn
Lattice parameters (Å)	a = 13.5986(1)
	b = 24.1005(2)
	c = 17.5189(2)
T (K)	130(1)
V (Å^3)	5741.52(9)
Z	8
D_x(g/cm^3)	2.760
Radiation type	MoKα
μ (mm^{-1})	12.596
Theta range	2.540 to 33.596°
Diffractometer	Rigaku, XtaLAB Synergy S
Absorption correction	multi-scan
Crystal size (mm)	0.120 x 0.120 x 0.030
Reflections collected	63360
Independent reflections	9897 [R(int) = 0.0356]
Tmin/Tmax	1.000 and 0.336
Data / restraints / parameters	9897 / 9 / 229
Goodness-of-fit	1.023
Final R indices [I>2sigma(I)]	R_1 = 0.0257, wR_2 = 0.0456
$\Delta\rho_{min}/\Delta\rho_{max}$ (e/Å^3)	1.631 and -1.364

Table S2. Selected torsion angles observed in the studied crystal structure (°).

atoms	Torsion angles
C(14)-C(13)-C(12)-N(11)	179.7(3)
N(31)-C(32)-C(33)-C(34)	-177.1(3)
N(21)-C(22)-C(23)-C(24)	-179.0(3)
C(12)-C(13)-C(14)-C(15)	-176.2(3)
C(22)-C(23)-C(24)-C(25)	-176.0(3)
C(32)-C(33)-C(34)-C(35)	73.0(5)

Table S3. Experimental geometry of hydrogen bonds and weak interactions (Å,°).

D-H···A	d(D-H)	d(H···A)	d(D···A)	<(DHA)
N(11)-H(11A)...I(5)$^{\#1}$	0.91(1)	2.88(3)	3.641(3)	142(3)
N(11)-H(11A)...I(4)$^{\#2}$	0.91(1)	3.02(3)	3.641(3)	127(3)
N(11)-H(11B)...I(6)$^{\#2}$	0.91(1)	2.92(1)	3.825(3)	170(3)
N(11)-H(11C)...I(3)$^{\#3}$	0.91(1)	2.86(2)	3.692(3)	153(3)
N(21)-H(21A)...I(1)$^{\#4}$	0.91(1)	3.14(4)	3.618(3)	115(3)
N(21)-H(21A)...I(2)$^{\#4}$	0.91(1)	2.85(2)	3.611(3)	142(3)
N(21)-H(21C)...I(1)	0.91(1)	2.68(1)	3.590(3)	174(3)
N(21)-H(21B)...I(6)$^{\#4}$	0.90(1)	2.77(2)	3.637(3)	160(3)
N(31)-H(31A)...I(3)$^{\#5}$	0.91(1)	3.04(2)	3.821(4)	145(3)
N(31)-H(31B)...I(5)$^{\#6}$	0.91(1)	2.84(2)	3.682(3)	155(4)
N(31)-H(31C)...I(2)	0.91(1)	2.94(4)	3.595(3)	130(4)
C(32)-H(32A)...I(1)$^{\#5}$	0.99	3.32	4.156(4)	143.3
C(32)-H(32A)...I(6)$^{\#6}$	0.99	3.27	4.019(4)	133.6
C(32)-H(32B)...I(2)$^{\#5}$	0.99	3.17	4.078(3)	153.7

C(22)-H(22B)...I(6)	0.99	3.31	4.050(4)	132.9
C(12)-H(12A)...I(1)$^{\#3}$	0.99	3.26	3.931(4)	126.3

Symmetry transformations used to generate equivalent atoms:

#1 x-1/2,-y+1,-z+1/2; #2 x-1,y,z; #3 -x+1/2,y,z-1/2; #4 -x+3/2,-y+1/2,z; #5 -x+2,-y+1,-z+1; #6 x+1/2,-y+1,-z+1/2

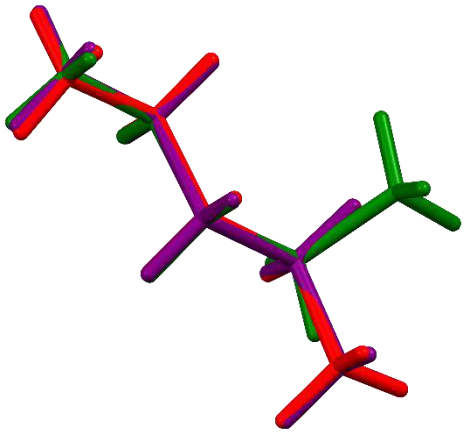

Figure S1. Three butylammonium cations: A: marked in red (atoms as viewed from the top: N11, C12, C13, C14, C15), B- marked in violet (atoms N21, C22, C23, C24, C25) and C- marked in green (atoms N31, C31, C32, C33, C34, C35).

The conformation of cations A and B (marked in red and violet in **Fig. S1**, respectively) is almost identical, whereas the C- cation (drawn in green) has a different carbon chain torsion angle (73.13° in C, −175.85° in A and −176.16° in B).

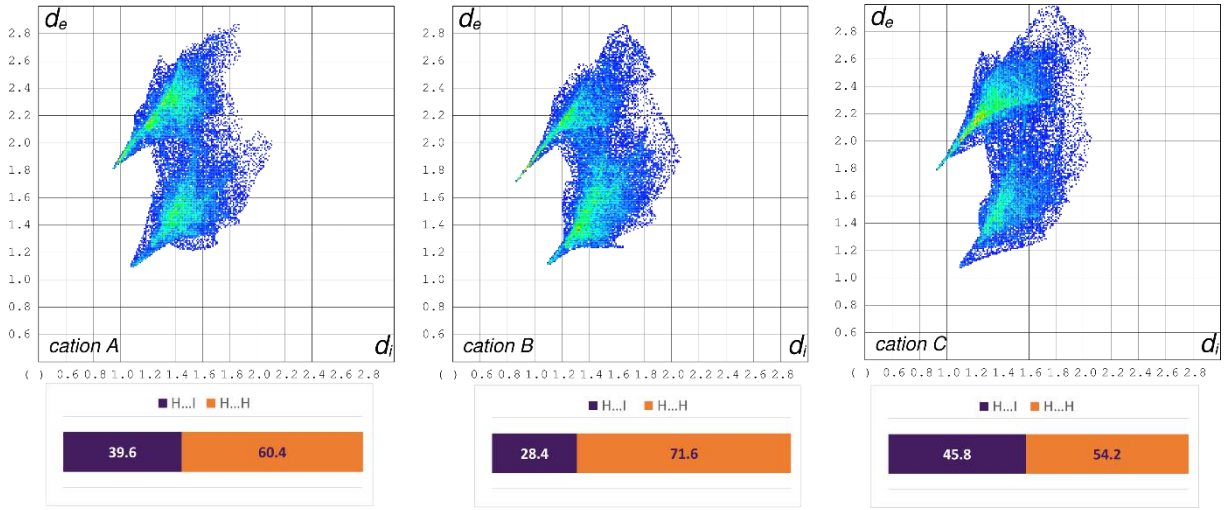

Figure S2. Fingerprint plots for the three butylammonium cations.

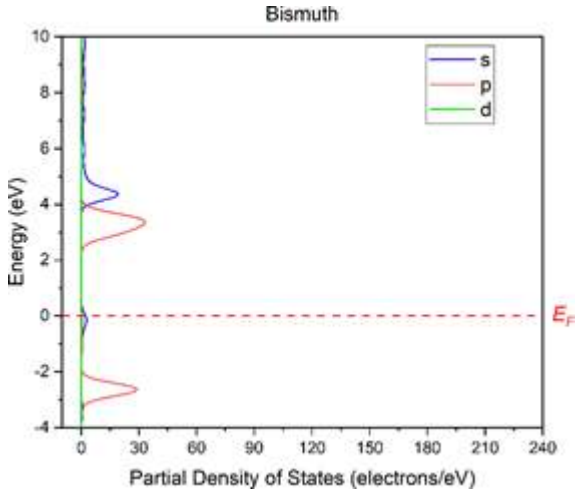

Figure S3a. PDOS for bismuth atoms in the BABI structure, the division into orbitals is shown.

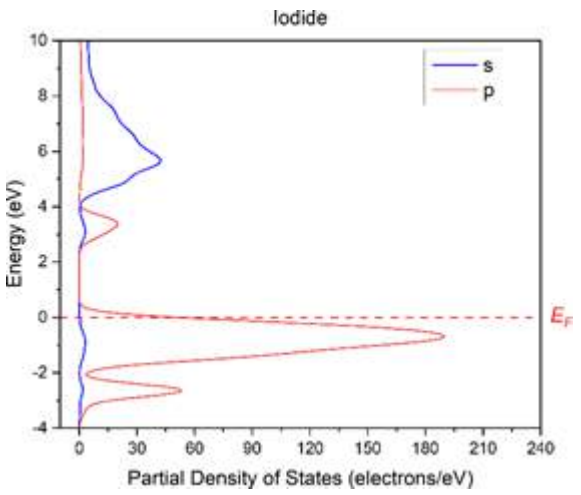

Figure S3b. PDOS for iodide atoms in the BABI structure, the division into orbitals is shown.

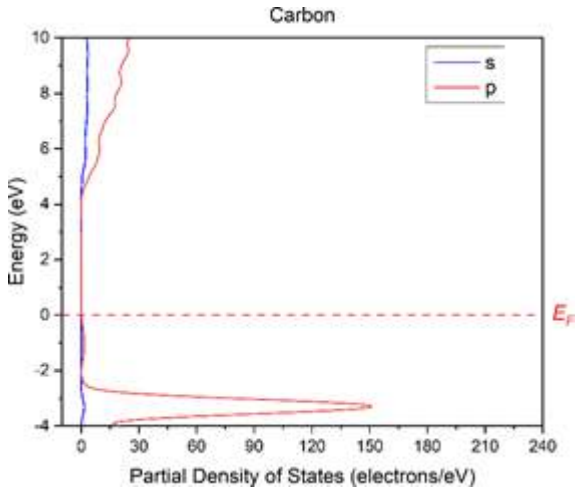

Figure S3c. PDOS for carbon atoms in the BABI structure, the division into orbitals is shown.

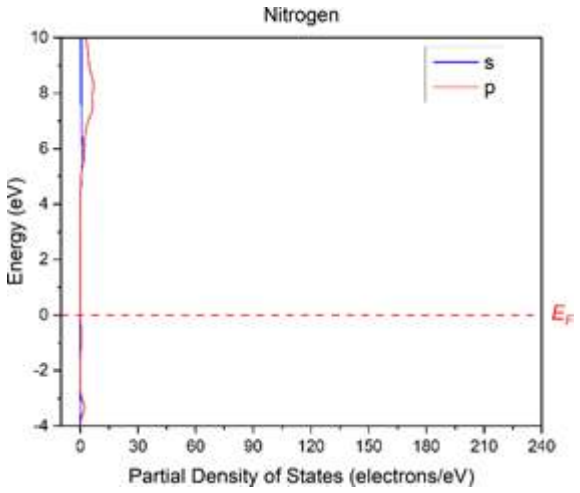

Figure S3d. PDOS for nitrogen atoms in the BABI structure, the division into orbitals is shown.

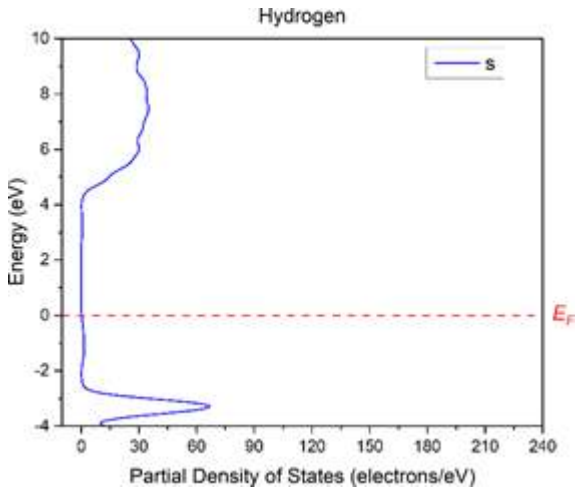

Figure S3e. PDOS for hydrogen atoms in the BABI structure, the division into orbitals is shown.

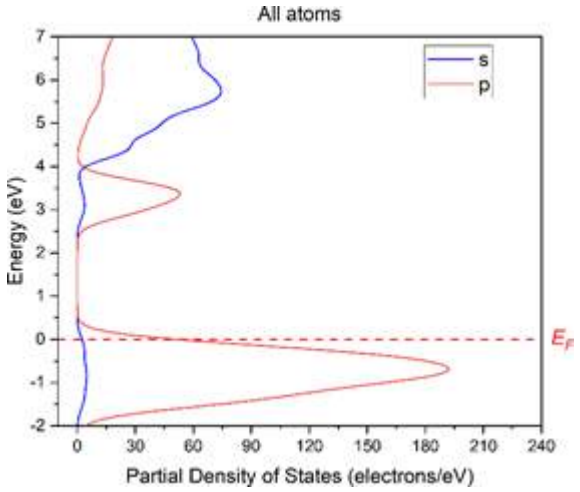

Figure S3f. PDOS for all atoms in the BABI structure, the division into orbitals is shown.

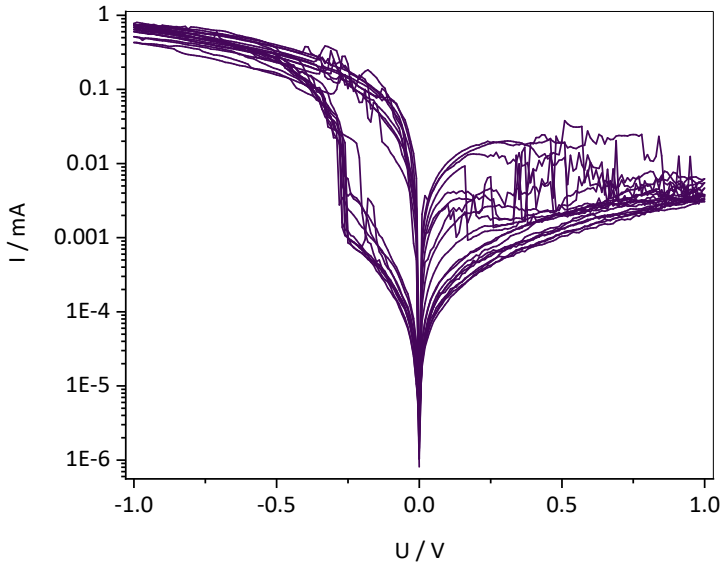

Figure S4. I-V scans of BABI/Ag memristor without PMMA buffer layer.

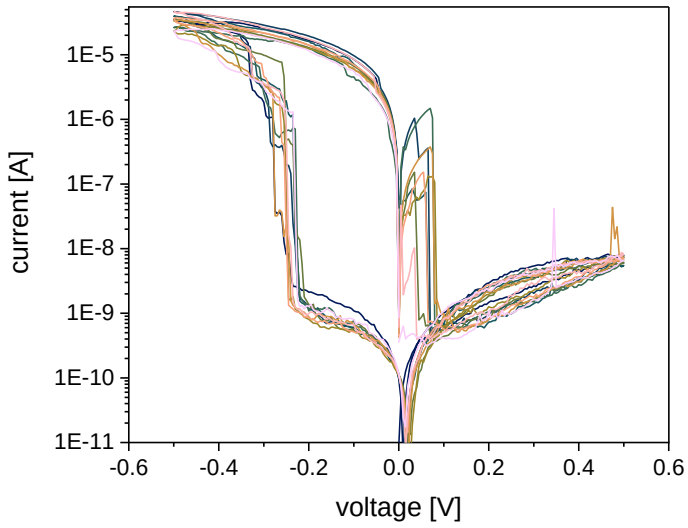

Figure S5. I-V scans of a device exhibiting large HRS/LRS ratio.

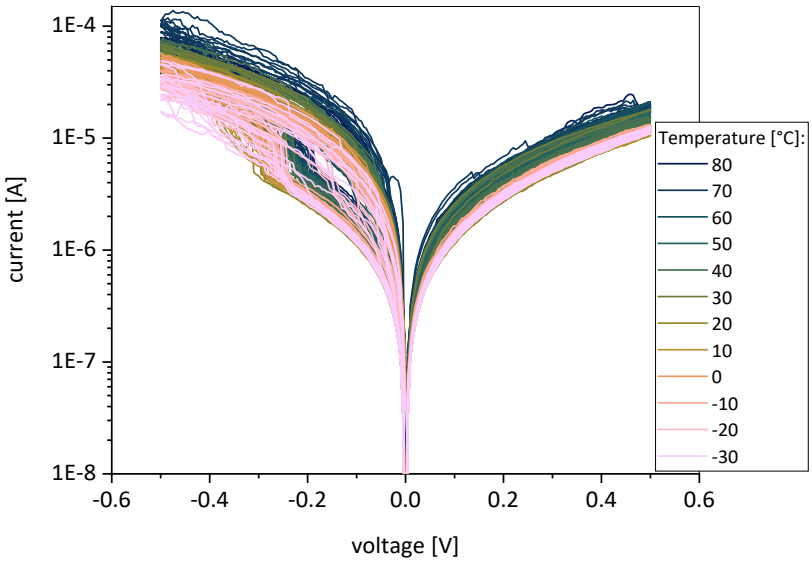

Figure S6. I-V scans at different temperatures. The data for Arrhenius plot was extracted from the positive branch of the scan to assure the device is in the non-switching regime.

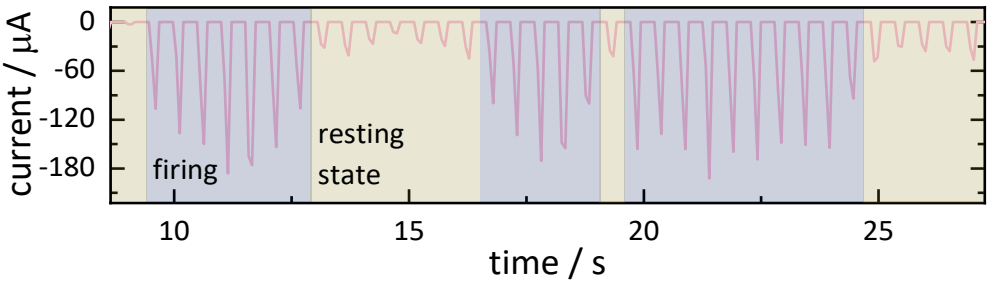

Figure S7. After firing several high-current pulses the device spontaneously returns to its resting state with low current spikes.

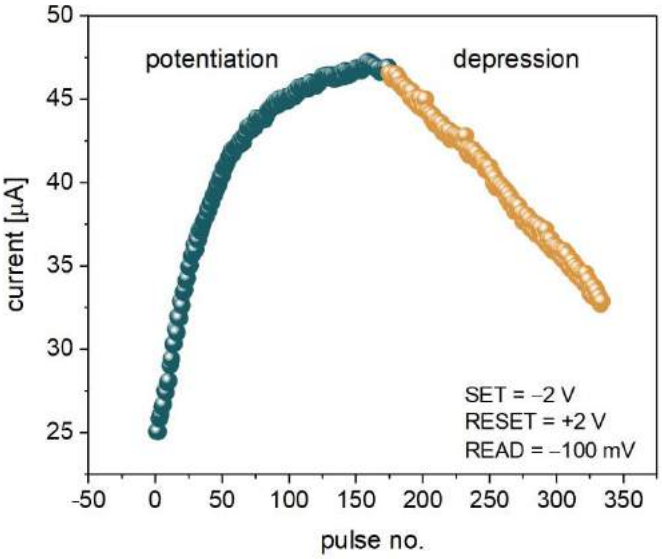

Figure S8. Synaptic potentiation and depression represented as current increase and decrease upon applying sets of negative and positive voltage pulses. The current values were read after each SET or RESET pulse at −100 mV.

4.2. Oświadczenia współautorów

AKADEMIA GÓRNICZO–HUTNICZA
IM. STANISŁAWA STASZICA W KRAKOWIE
Akademickie Centrum Materiałów i Nanotechnologii
Prof. dr hab. Konrad Szaciłowski

Kraków 30.06.2022

Oświadczenie o udziale w publikacjach mgr Piotra Zawala

Ja, niżej podpisany Konrad Szaciłowski oświadczam, że mój udział w wymienionych poniżej publikacjach mgr. Piotra Zawala polegał na:

1. Klejna, S., Mazur, T., Wlaźlak, E., Zawal, P., Soo, H. S., Szaciłowski, K. Halogen-containing semiconductors: From artificial photosynthesis to unconventional computing, Coordination Chemistry Reviews, 2020, 415, 213316:

napisaniu dwóch pierwszych rozdziałów publikacji oraz korekcie scaleniu wszystkich pozostałych fragmentów;

2. Lis, M., Onuma, S., Przyczyna, D., Zawal, P., Mazur, T., Pilarczyk, K., Gentili, P. L., Kasai, S., Szaciłowski, K. From Oscillatory Reactions to Robotics: A Serendipitous Journey Through Chemistry, Physics and Computation, Handbook of Unconventional Computing, 2021, 1-79:

napisaniu fragmentów dotyczących analizy energetycznej przetwarzania informacji, fragment analizy porównawczej PID/rezerwuar oraz ontegracji tekstu całego rozdziału;

3. Przyczyna, D., Zawal, P., Mazur, T., Strzelecki, M., Gentili, P. L., Szaciłowski, K. In-materio neuromimetic devices: dynamics, information processing and pattern recognition, Japanese Journal of Applied Physics, 2020, 59 (5), 050504:

napisaniu fragment poświęconego synapsom fotoelektrochemicznym, prztwarzaniu sygnałów akustycznych oraz kryptografii, a także końcowej redakcji tekstu;

4. Mazur, T.∗, Zawal, P.∗, Szaciłowski, K. Synaptic plasticity, metaplasticity and memory effects in hybrid organic-inorganic bismuth-based materials, Nanoscale, 2019, 11 (3), 1080-109:

analizie danych spektroskopowych oraz nadzorze nad przebiegiem pomiarów elektrycznych, koordynowaniu badań, oraz końcowej korekcie manuskryptu;

5. Wlaźlak, E., Kalinowska-Tłuścik, J., Przyczyna, D., Zawal, P., Szaciłowski, K. Bismuth triiodide complexes: Structure, spectroscopy, electronic properties, and memristive properties, Journal of Materials Chemistry C, 2020, 8 (18), 6136-6148:

analizie danych spektroksopowych i interpretacji zmian pracy wyjścia próbek,

6. Zawal, P.∗, Mazur, T.∗, Lis, M., Chiolerio, A., Szaciłowski, K. Light-Induced Synaptic Effects Controlled by Incorporation of Charge-Trapping Layer into Hybrid Perovskite Memristor, Advanced Electronic Materials, 2022, 8 (4), 2100838:

opracowaniu modeli teoretycznych, planowaniu i częściowej realizacji pomiarów spektroskopowych oraz wykonaniu pomiarów pracy wyjścia materiałów a także pomocy w określeniu mechanizmu generowania fotoprądu;

7. Zawal, P., Das, D., Gryl, M., Sławek, A., Abdi, G., Gerouville, E., Marciszko-Wiąckowska, M., Marzec, M., Hess, G., Georgiadou, D., Szaciłowski, K. Leaky integrate-and-fire model and short-term synaptic plasticity emulated in a novel bismuth-based diffusive memristor, Advanced Electronic Materials (w recenzji):

projektowaniu pomiarów temperaturowych oraz pomocy w interpretacji wyników.

Kraków, 19.09.2022

Oświadczam, że mój wkład w powstanie artykułu:

Klejna, S., Mazur, T., Wlaźlak, E., Zawal, P., Soo, H. S., Szaciłowski, K. Halogen-containing semiconductors: From artificial photosynthesis to unconventional computing, Coordination Chemistry Reviews, 2020, 415, 213316.

polegał na:

- badaniach literaturowych
- opisie mechanizmów procesów fotokatalitycznych dla układów z Bi oraz Pb
- napisaniu fragmentu tekstu oraz poprawie całości tekstu

Tomasz Mazur

Kraków, 19.09.2022

Oświadczam, że mój wkład w powstanie artykułu:

Lis, M., Onuma, S., Przyczyna, D., Zawal, P., Mazur, T., Pilarczyk, K., Gentili,P. L., Kasai, S., Szaciłowski, K. From Oscillatory Reactions to Robotics: A Serendipitous Journey Through Chemistry, Physics and Computation, Handbook of Unconventional Computing, 2021, 1-79.

polegał na:

- badaniach literaturowych
- opisie badań nad robotami z materiałów elestycznych
- opisie badań nad niekonwencjonalnymi metodami obliczeniowymi
- napisaniu i poprawie manuskryptu

Tomasz Mazur

Kraków, 19.09.2022

Oświadczam, że mój wkład w powstanie artykułu:

Przyczyna, D., Zawal, P., Mazur, T., Strzelecki, M., Gentili, P. L., Szaciłowski,K. In-materio neuromimetic devices: dynamics, information processing and patternrecognition, Japanese Journal of Applied Physics, 2020, 59 (5), 050504.

polegał na:

- badaniach literaturowych
- opisie badań nad klasyfikacją i transformacją sygnałów
- napisaniu i poprawie manuskryptu

Tomasz Mazur

Kraków, 19.09.2022

Oświadczam, że mój wkład w powstanie artykułu:

Mazur, T.*, Zawal, P.*, Szaciłowski, K. Synaptic plasticity, metaplasticity and me-mory effects in hybrid organic-inorganic bismuth-based materials, Nanoscale, 2019,11 (3), 1080-1090.

polegał na:

- opracowaniu metodologii eksperymentalnej;
- wykonaniu badań spektroskopowych, elektrochemicznych i neuromorficznych;
- analizie i interpretacji wyników;
- napisaniu i poprawie manuskryptu;

Tomasz Mazur

Kraków, 19.09.2022

Oświadczam, że mój wkład w powstanie artykułu:

Zawal, P.*, Mazur, T.*, Lis, M., Chiolerio, A., Szaciłowski, K. Light-Induced Sy-naptic Effects Controlled by Incorporation of Charge-Trapping Layer into HybridPerovskite Memristor, Advanced Electronic Materials, 2022, 8 (4), 2100838.

polegał na:

- opracowaniu metodologii eksperymentalnej;
- wykonaniu badań spektroskopowych, elektrochemicznych i neuromorficznych;
- analizie i interpretacji wyników;
- napisaniu i poprawie manuskryptu;

Tomasz Mazur

Dr Ewelina Wlaźlak,
University of California, Santa Barbara
Department of Electrical and Computer Engineering
Harold Frank Hall
wlazlak@ucsb.edu

Oświadczam, że mój wkład w powstanie artykułu:

Klejna, S., Mazur, T., Wlaźlak, E., Zawal, P., Soo, H. S., Szaciłowski, K. Halogen-containing semiconductors: From artificial photosynthesis to unconventional computing, Coordination Chemistry Reviews, 2020, 415, 213316.

polegał na:
- zestawieniu i interpretacji wyników dotyczących memrystywnych właściwości wybranych jodków metali w rozdziale 7,
- wraz z innymi autorami brałam również udział w redakcji całości artykułu.

Oświadczam, że mój wkład w powstanie artykułu:

Wlaźlak, E., Kalinowska-Tłuścik, J., Przyczyna, D., Zawal, P., Szaciłowski, K. Bismuth triiodide complexes: Structure, spectroscopy, electronic properties, and memristive properties, Journal of Materials Chemistry C, 2020, 8 (18), 6136-6148.

polegał na:

- syntezie badanych związków, analizie oddziaływań w otrzymanych strukturach
- rejestracji i analizie widm UV-Vis
- pomiarze prac wyjścia badanych związków z wykorzystaniem Sondy Kelvina
- analizie i interpretacji wyników uzyskanych z pozostałych pomiarów (wraz ze współautorami)
- wykonaniu części pomiarów elektrycznych, w szczególności chronoamperometrycznych
- napisaniu większości manuskryptu.

Ewelina Wlaźlak

Kraków, 26.09.2022

Oświadczam, że mój wkład w powstanie artykułu:

Klejna, S., Mazur, T., Wlaźlak, E., Zawal, P., Soo, H. S., Szaciłowski, K. Halogen-containing semiconductors: From artificial photosynthesis to unconventional computing, Coordination Chemistry Reviews, 2020, 415, 213316.

wynosił 16.66 % i polegał na:

- badaniach literaturowych
- opisie struktury krystalicznej i elektronowej perowskitów
- napisaniu fragmentu tekstu oraz poprawie całości tekstu

Sylwia Klejna

Sylwia Klejna

AKADEMIA
GÓRNICZO–HUTNICZA
IM. STANISŁAWA
STASZICA W KRAKOWIE
Akademickie Centrum Materiałów i Nanotechnol

Prof. dr hab. Konrad Szaciłowski

Kraków 16.10.2022

Oświadczenie o udziale w publikacjach mgr Piotra Zawala

Z uwagi na brak możliwości kontaktu z współautorką wymienionych poniżej prac, ja, niżej podpisany Konrad Szaciłowski oświadczam, że:

1. W publikacji "From Oscillatory Reactions to Robotics: A Serendipitous Journey Through Chemistry, Physics and Computation", *Handbook of Unconventional Computing*, **2021**, 1-79 (autorzy Lis, M., Onuma, S., Przyczyna, D., Zawal, P., Mazur, T., Pilarczyk, K., Gentili, P. L., Kasai, S., Szaciłowski, K.) udział Marii Lis polegał na napisaniu fragmentu poświęconego elektrochemicznym reakcjom oscylacyjnym (podrozdział 1.2.2, strony 8-14).

2. W publikacji „Light-Induced Synaptic Effects Controlled by Incorporation of Charge-Trapping Layer into Hybrid Perovskite Memristor", *Advanced Electronic Materials*, **2022**, 8 (4), 2100838 (autorzy Zawal, P., Mazur, T., Lis, M., Chiolerio, A., Szaciłowski, K.) rola Marii Lis polegała na udziale w syntezie nanocząstek azotku węgla, wykonaniu części pomiarów fotoluminescencji oraz pomiarów techniką FTIR wraz z analizą i wizualizacją wyników tych pomiarów oraz przygotowaniu fragmentu teksu publikacji opisującego te wyniki.

October 14, 2022

Re: Author Contribution Statement

This letter is to confirm that in the book chapter entitled "From Oscillatory Reactions to Robotics: A Serendipitous Journey Through Chemistry, Physics and Computation" by Lis, M., Onuma, S., Przyczyna, D., Zawal, P., Mazur, T., Pilarczyk, K., Gentili, P. L., Kasai, S., Szaciłowski, K. in Handbook of Unconventional Computing, 2021, pp.1-79, I have contributed concept design, manuscript writing, proof read, and commented on the final version of the article.

Your sincerely,

Seiya Kasai

Seiya Kasai, Dr.
Professor
Research Center for Integrated Quantum Electronics and
Graduate School of Information Science & Technology
Hokkaido University

4 October 2022

Re: Author Contribution Statement

This letter is to confirm that in the book chapter entitled "From Oscillatory Reactions to Robotics: A Serendipitous Journey Through Chemistry, Physics and Computation" by Lis, M., Onuma, S., Przyczyna, D., Zawal, P., Mazur, T., Pilarczyk, K., Gentili, P. L., Kasai, S., Szaciłowski, K. in Handbook of Unconventional Computing, 2021, pp.1-79, I have contributed robot system design, manuscript writing, proof read, and commented on the final version of the article.

Your sincerely,

Shu Onuma

Shu Onuma
Research Center for Integrated Quantum Electronics and
Graduate School of Information Science & Technology
Hokkaido University
(Current Affiliation Nikon Corporation)

Akademia Górniczo–Hutnicza
im. Stanisława Staszica w Krakowie
Akademickie Centrum Materiałów i Nanotechnologii

Mgr inż Dawid Przyczna

Kraków 19.09.2022

Oświadczenie o udziale w publikacji mgr Piotra Zawala

Ja, niżej podpisany Dawid Przyczyna oświadczam, że mój udział w wymienionych poniżej publikacjach mgr. Piotra Zawala polegał na:

- Przyczyna, D., Zawal, P., Mazur, T., Strzelecki, M., Gentili, P. L., Szaciłowski, K. In-materio neuromimetic devices: dynamics, information processing and pattern recognition, Japanese Journal of Applied Physics, 2020, 59 (5), 050504.

przeglądzie literaturowym oraz opisie generacji wyższych harmonicznych oraz liczb losowych w urządzeniach memrystywnych.

- Lis, M., Onuma, S., Przyczyna, D., Zawal, P., Mazur, T., Pilarczyk, K., Gentili, P. L., Kasai, S., Szaciłowski, K. From Oscillatory Reactions to Robotics: A Se- rendipitous Journey Through Chemistry, Physics and Computation, Handbook of Unconventional Computing, 2021, 1-79

przeglądzie literaturowym i opisie regulatorów PID oraz tematyki obliczania rezerwuarowego

- Wlaźlak, E., Kalinowska-Tłuścik, J., Przyczyna, D., Zawal, P., Szaciłowski, K. Bi- smuth triiodide complexes: Structure, spectroscopy, electronic properties, and mem- ristive properties, Journal of Materials Chemistry C, 2020, 8 (18), 6136-6148.

wykonaniu pomiarów absorpcji UV-Vis, fotonapięcia powierzchniowego, pracy wyjścia oraz cyklicznej woltamperometrii badanych próbek

Dawid Przyczyna

.....

Podpis

Akademia Górniczo–Hutnicza
Akademickie Centrum Materiałów i Nanotechnologii
al. A. Mickiewicza 30, 30–059 Kraków
tel. +48 12 617 5283
e–mail: szacilow@agh.edu.pl

AKADEMIA GÓRNICZO-HUTNICZA
IM. STANISŁAWA STASZICA W KRAKOWIE

Wydział Fizyki i Informatyki Stosowanej
dr inż. Kacper Pilarczyk

Leuven, 20.09.2022

OŚWIADCZENIE WSPÓŁAUTORA

Jako współautor wymienionej poniżej publikacji:

Maria Lis, Shu Onuma, Dawid Przyczyna, Piotr Zawal, Tomasz Mazur, **Kacper Pilarczyk**, Pier Luigi Gentili, Seiya Kasai, Konrad Szaciłowski
From Oscillatory Reactions to Robotics: A Serendipitous Journey Through Chemistry, Physics and Computation
In Handbook of Unconventional Computing, Volume 2: Implementations (ed. Andrew Adamatzky), 2021, World Scientific Publishing

oświadczam, iż byłem odpowiedzialny za powstanie rozdziału 1.4. (Controllers Beyond PID: Fuzzy and Neuromorphic) - w szczególności podrozdziałów 1.4.3. oraz 1.4.4. – oraz za redakcję innych, pomniejszych fragmentów pracy.

dr inż. Kacper Pilarczyk

al. A. Mickiewicza 30, 30-059 Kraków
Wydział Fizyki i Informatyki Stosowanej
ul. Reymonta 19, budynek D-10
e-mail: kpilarcz@agh.edu.pl

A.D. 1308
unipg
UNIVERSITÀ DEGLI STUDI
DI PERUGIA

Prof. Pier Luigi Gentili
Chemistry, Biology, and Biotechnology Department
UNIVERSITÀ DEGLI STUDI DI PERUGIA
Via Elce di Sotto, 8 - 06123 PERUGIA
Tel. 075/5855573
E-mail: pierluigi.gentili@unipg.it
Website: http://www.dcbb.unipg.it/pierluigi
Twitter: @Pier_Complexity

Perugia, the 10th of October 2022

Author contribution statements

In the review paper "Przyczyna, D., Zawal, P., Mazur, T., Strzelecki, M., Gentili, P. L., Szaciłowski, K. "In-materio neuromimetic devices: dynamics, information processing and pattern recognition." Japanese Journal of Applied Physics, 2020, 59 (5), 050504" Piotr Zawal wrote section 6.2 on the physical unclonable functions built with memristors.

In the book's chapter "Lis, M., Onuma, S., Przyczyna, D., Zawal, P., Mazur, T., Pilarczyk, K., Gentili, P. L., Kasai, S., Szaciłowski, K. "From Oscillatory Reactions to Robotics: A Serendipitous Journey Through Chemistry, Physics and Computation." Handbook of Unconventional Computing, 2021, 1-79" Piotr Zawal wrote section 1.3.1 on the implementation of memristors in hardware for computing.

Best Regards.

Prof. Pier Luigi Gentili

Marcin Strzelecki

marcin.strzelecki@amuz.krakow.pl

Kraków, 1 października 2022 r.

Oświadczam, że mój wkład w powstanie publikacji:

Przyczyna, D., Zawal, P., Mazur, T., Strzelecki, M., Gentili, P. L., Szaciłowski, K. *In-materio neuromimetic devices: dynamics, information processing and pattern recognition*, Japanese Journal of Applied Physics, 2020, 59 (5), 050504.

polegał na:

opracowaniu części dotyczącej problemów muzycznych, w szczególności definicji interwałów muzycznych, z rozróżnieniem na dysonanse i konsonanse, a także problemów wyższego poziomu, jak skale muzyczne, tonalność i harmonia.

NANYANG TECHNOLOGICAL UNIVERSITY SINGAPORE

Reg. No. 200604393R

3 October 2022

Piotr Zawal
Academic Center for Materials and Nanotechnology
Faculty of Physics and Applied Computer Science,
AGH University of Science and Technology
al. Mickiewicza 30,
30-059 Kraków
Poland

Dear Piotr Zawal,

Re: Author Contributions for Halogen-Containing Semiconductors: From Artificial Photosynthesis to Unconventional Computing

I am writing this letter to confirm that I wrote Section 6: Artificial photosynthesis in perovskite systems in the following publication:

Sylwia Klejna, Tomasz Mazur, Ewelina Wlaźlak, Piotr Zawal, Han Sen Soo, Konrad Szaciłowski, Halogen Containing Semiconductors: From Artificial Photosynthesis to Unconventional Computing, *Coordination Chemistry Reviews*, **2020**, *415*, 213316.

In addition, I helped to edit and proofread the entire paper.

Yours sincerely,

Han Sen **Soo**
Associate Professor
hansen@ntu.edu.sg
+65 65923182
School of Chemistry, Chemical Engineering and Biotechnology
Nanyang Technological University, Singapore
CCEB-05-03
21 Nanyang Link
Singapore 637371
Singapore

dr hab. Justyna Kalinowska-Tłuścik
Zespół Biokrystalografii
Zakład Krystalochemii i Krystalofizyki
Wydział Chemii UJ
Gronostajowa 2, 30-387 Kraków

Kraków, 01.10.2022

Oświadczenie współautora

Oświadczam, że mój wkład w powstanie publikacji:

Bismuth triiodide complexes: structure,spectroscopy, electronic properties, and memristive properties

E. Wlaźlak, J. Kalinowska-Tłuścik, D. Przyczyna, P. Zawal, K. Szaciłowski;

Journal of Materials Chemistry C, 2020, Vol. 8 (18), 6136 - 6148
DOI: 10.1039/d0tc00679c

polegał na wykonaniu pomiarów dyfrakcji promieniowania rentgenowskiego dla czterech monokryształów związków kompleksowych bizmutu, opracowaniu uzyskanych wyników oraz przygotowaniu fragmentów publikacji związanych z opisem struktury krystalicznej badanych związków.

Justyna Kalinowska-Tłuścik

ISTITUTO ITALIANO
DI TECNOLOGIA

Torino, 4th October 2022

Subject: Author contribution statement

This letter is to confirm that in the research paper "Light-Induced Synaptic Effects Controlled by Incorporation of Charge-Trapping Layer into Hybrid Perovskite Memristor", by Piotr Zawal, Tomasz Mazur, Maria Lis, Alessandro Chiolerio, Konrad Szaciłowski, I have contributed to the resistive switching mechanism discussion and proof reading and commented the final version of the paper.

Yours faithfully,

Alessandro Chiolerio

Alessandro Chiolerio

Prof. Alessandro Chiolerio, PhD, MsC, Eng.

Fondazione Istituto Italiano di Tecnologia
Bioinspired Soft Robotics
Via Morego 30, 16165 Genova (GE), Italia

dr hab. Marlena Gryl
Zespół Inżynierii Krystalicznej i Analizy Strukturalnej
Zakład Krystalochemii i Krystalofizyki
Wydział Chemii Uniwersytetu Jagiellońskiego
ul. Gronostajowa 2, 30-387 Kraków

UNIWERSYTET JAGIELLOŃSKI W KRAKOWIE

Wydział Chemii

OŚWIADCZENIE

Oświadczam, że mój wkład w powstanie manuskryptu publikacji:

Zawal, P., Das, D., Gryl, M., Sławek, A., Abdi, G., Gerouville, E., Marciszko-Wiąckowska, M., Marzec, M., Hess, G., Georgiadou, D., Szaciłowski, K.
Leaky integrate-and-fire model and short-term synaptic plasticity emulated in a novel bismuth-based diffusive memristor

polegał na:

- wykonaniu pomiarów dyfrakcyjnych dla monokryształów tytułowego związku oraz na rozwiązaniu i udokładnieniu modelu struktury krystalicznej
- analizie i interpretacji wyników badań strukturalnych
- obliczeniu powierzchni Hirshfelda oraz map fingerprint

/Marlena Gryl/

Kraków dnia 2022-10-04

ul. Gronostajowa 2
30-387 Kraków
tel. +48 12 686 26 00
fax +48 12 686 27 50
sekretar@chemia.uj.edu.pl
www.chemia.uj.edu.pl

Electronics and Computer Science

UNIVERSITY OF Southampton

Dr Dimitra G. Georgiadou
Associate Professor
UKRI Future Leaders Fellow
Flexible and Organic Nanoelectronics

Electronics and Computer Science
University of Southampton
Highfield Campus, University Road, Building 59 (Zepler)
Southampton SO17 1BJ, United Kingdom

E-mail: D.Georgiadou@soton.ac.uk
Webpage: https://www.ecs.soton.ac.uk/people/dg1v19

19 September 2022

Re: Author Contribution Statement

This letter is to confirm that in the research paper "Leaky integrate-and-fire model and short-term synaptic plasticity emulated in a novel bismuth-based diffusive memristor" by Zawal, P., Das, D., Gryl, M., Sławek, A., Abdi, G., Gerouville, E., Marciszko-Wiąckowska, M., Marzec, M., Hess, G., Georgiadou, D., Szaciłowski, K., I have contributed in the XPS discussion and proof read and commented on the final version of the article.

Yours faithfully,

Dr Dimitra Georgiadou

University of Southampton 19/09/2022

Author Contribution Statement

In the paper: *Leaky integrate-and-fire model and short-term synaptic plasticity emulated in a novel bismuth-based diffusive memristor*, under review in ACS Applied Materials & Interfaces, 2022, I have written the paragraph that discussed the XPS measurement and the XPS data treatment.

Oświadczenie współautora

Ja, Andrzej Sławek, oświadczam, że moim wkładem w pracę:

I. Zawal, P., Das, D., Gryl, M., Sławek, A., Abdi, G., Gerouville, E., Marciszko-Wiąckowska, M., Marzec, M., Hess, M., Georgiadoum, G., Szaciłowski, K. "Leaky integrate-and-fire model and short-term synaptic plasticity emulated in a novel bismuth-based diffusive memristor ", (praca wysłana do recenzji)

Było przeprowadzenie modelowania molekularnego z wykorzystaniem teorii funkcjonału gęstości (DFT), opracowanie oraz analiza wyników obliczeń oraz pomoc w przygotowaniu manuskryptu w części dotyczącej modelowania DFT.

Andrzej Sławek

Co-Author Statement

I, Gisya Abdi, hereby declare that my contribution to publication:

I. Zawal, P., Das, D., Gryl, M., Sławek, **A., Abdi**, G., Gerouville, E., Marciszko-Wiąckowska, M., Marzec, M., Hess, G., Georgiadou, D., Szaciłowski, K. "Leaky integrate-and-fire model and short-term synaptic plasticity emulated in a novel bismuth-based diffusive memristor"

Was Synthesis of single crystal of butylammonium bismuth iodide (BABI) and performing Diffuse Reflectance Spectroscopy (DRS) of thin layers on ITO glasses for studying optical band gaps of the synthesized materials.

19/09/2022

Dr. Dip Das
Email: dd209@snu.edu.in
Shiv Nadar University, India.

Author contribution statement

I am glad to contribute to the research titled “Leaky integrate-and-fire model and short-term synaptic plasticity emulated in a novel bismuth-based diffusive memristor” by Zawal et al. Here, I performed the simulations for checking the learning accuracy of the MNIST handwritten data sets based on the experimentally observed BABI memristive device parameters. Besides, I analyzed a portion of experimental results and wrote a couple of lines in the introduction and the results sections that justify the self-rectifying behavior of the BABI memristor.

Thanking you!

Date: 20/09/2022

Best wishes,

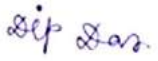

OŚWIADCZENIE

Deklaruje się, że każdy z Autorów przeczytał finalną wersję manuskryptu a wkład merytoryczny poszczególnych Autorów w powstanie artykułu:

Zawal, P., Das, D., Gryl, M., Sławek, A., Abdi, G., Gerouville, E., Marciszko-Wiąckowska, M., Marzec, M., Hess, G., Georgiadou, D., Szaciłowski, K. „Leaky integrate-and-fire model and short-term synaptic plasticity emulated in a novel bismuth-based diffusive memristor"

jest następujący:

Marianna Marciszko-Wiąckowska

- przeprowadzenie pomiarów XRD,
- analizie i dyskusji wyników eksperymentalnych,
- korekta gotowego manuskryptu.

20.09.2022, Marianna Marciszko-Wiąckowska

data, podpis

Kraków, 10 października 2022 r.

Dr inż. Mateusz Marzec
Akademia Górniczo-Hutnicza
im. St. Staszica w Krakowie
Akademickie Centrum
Materiałów i Nanotechnologii

OŚWIADCZENIE

Oświadczam, że mój wkład w powstanie publikacji:

Zawal, P., Das, D., Gryl, M., Sławek, A., Abdi, G., Gerouville, E., Marciszko-Wiąckowska, M., Marzec, M., Hess, G., Georgiadou, D., Szaciłowski, K.

Leaky integrate-and-fire model and short-term synaptic plasticity emulated in a novel bismuth-based diffusive memristor

polegał na:

- wykonaniu badań metodą spektroskopii fotoelektronów w zakresie nadfioletu

- analizie i interpretacji wyników

Prof. dr hab. Grzegorz Hess

Zakład Neurofizjologii I Chronobiologii
Instytut Zoologii i Badań Biomedycznych Uniwersytetu Jagiellońskiego
ul. Gronostajowa 9
30-387 Kraków

Kraków, 12.10.2022 r.

Oświadczenie o udziale w publikacji

Oświadczam, że mój udział w publikacji:

Zawal, P., Das, D., Gryl, M., Sławek, A., Abdi, G., Gerouville, E., Marciszko-Wiąckowska, M., Marzec, M., Hess, G., Georgiadou, D., Szaciłowski, K. Leaky integrate-and-fire model and short-term synaptic plasticity emulated in a novel bismuth-based diffusive memristor

- polegał na interpretacji części uzyskanych wyników w kontekście plastyczności synaptycznej, napisaniu fragmentu dyskusji oraz redakcji manuskryptu.